NATIONAL TECHNICAL UNIVERSITY OF ATHENS
SCHOOL OF MECHANICAL ENGINEERING
SECTION OF FLUIDS
LABORATORY OF AERODYNAMICS

Development of Computational Methods for the Aeroelastic Analysis of Rotors using Grid Based and/or Particle Techniques. Application to Wind Turbine and Helicopter Rotors.

A Thesis submitted for the degree of Doctor of Philosophy

PH.D. THESIS

of

NIKOLAOS SPYROPOULOS

Athens, September 2023

NATIONAL TECHNICAL UNIVERSITY OF ATHENS

SCHOOL OF MECHANICAL ENGINEERING

SECTION OF FLUIDS

Development of Computational Methods for the Aeroelastic Analysis of Rotors using Grid Based and/or Particle Techniques. Application to Wind Turbine and Helicopter Rotors.

A Thesis submitted for the degree of Doctor of Philosophy

PH.D. THESIS

of

NIKOLAOS SPYROPOULOS

Supervisor: Vasilis A. Riziotis

Associate Professor, NTUA, School of Mechanical Engineering

Approved by the examination committee on 14th September 2023.

Giovanni Bernandini   Associate Professor, Roma Tre, Department of Civil, Computer Science and Aeronautical Technologies Engineering

Massimo Gennaretti   Professor, Roma Tre, Department of Civil, Computer Science and Aeronautical Technologies Engineering

Manolis Angelou   Assistant Professor, NTUA, School of Naval Architecture and Marine Engineering

George Papadakis   Assistant Professor, NTUA, School of Naval Architecture and Marine Engineering

Kyriakos C. Giannakoglou*   Professor, NTUA, School of Mechanical Engineering

Spyros G. Voutsinas*   Professor, NTUA, School of Mechanical Engineering

Vasilis A. Riziotis*   Associate Professor, NTUA, School of Mechanical Engineering

*Member of the advisory committee

Athens, September 2023

NATIONAL TECHNICAL UNIVERSITY OF ATHENS

SCHOOL OF MECHANICAL ENGINEERING

SECTION OF FLUIDS

DISCLAIMER ON ACADEMIC ETHICS AND INTELLECTUAL PROPERTY RIGHTS

Being fully aware of the implications of copyright laws, I expressly state that this Ph.D.
thesis, as well as the electronic files and source codes developed or modified in the course
of this thesis, are solely the product of my personal work and do not infringe any rights of
intellectual property, personality and personal data of third parties, do not contain work
/ contributions of third parties for which the permission of the authors / beneficiaries is
required and are not a product of partial or complete plagiarism, while the sources used
are limited to the bibliographic references only and meet the rules of scientific citing. The
points where I have used ideas, text, files and / or sources of other authors are clearly
mentioned in the text with the appropriate citation and the relevant complete reference
is included in the bibliographic references section. I fully, individually and personally
undertake all legal and administrative consequences that may arise in the event that it is
proven, in the course of time, that this thesis or part of it does not belong to me because
it is a product of plagiarism.

(Signature)

. . . .
Nikolaos Spyropoulos

14th September 2023

Acknowledgements

I would like to take the opportunity to thank those who supported me in completing this thesis; professionally, personally or both.

Words cannot express my gratitude to my supervisor, Associate Professor Vasilis Riziotis. He has has been standing firm behind me throughout this demanding work, generously providing me with knowledge and guidance, but also respecting my personal nature and way of thinking. I feel blessed to have met him and hope we can continue to collaborate in the future.

I would like to extend my sincere thanks to the rest of the Advisory Committee members; Professor Spyros Voutsinas and Professor Kyriakos Giannakoglou. Professor Spyros Voutsinas has always been available to discuss and share his profound knowledge. Professor Kyriakos Giannakoglou was an exceptional teacher during my under–graduate studies and provided me with valuable comments and suggestions, that helped me shape the final form of this thesis.

I am also grateful to the rest of the members of the Examination Committee for closely following my work throughout this period and making constructive comments. More specifically, I am extremely grateful to Assistant Professor George Papadakis, for dedicating so much of his personal time to assist me in my research. He essentially functioned as the 4th member of my Advisory Committee.

Special thanks to Dr. John Prospathopoulos and Dr. Petros Chasapogiannis who generously provided knowledge and expertise and have been valuable collaborators through these years.

I would also like to thank the Greek Research & Technology Network (GRNET) in the National HPC facility ARIS for supporting my research by granting computational time under projects "ELASTODYN" with ID $pr010013\_thin$, "HELIHOP" with IDs $pr012024\_thin$ and $pr012024\_fat$ and "WINDHOP" with ID $pr013022\_thin$. Moreover, I would like to acknowledge "BETA_CAE Systems S.A." for allowing me to use the ANSA CAE pre-processor to generate the computational grids needed for this study.

Furthermore, I would like to express how lucky I feel to have met and collaborated with numerous exceptional scientists in the Laboratory of Aerodynamics; Dr. Dimitris Manolas, Dr. Konstantinos Diakakis, Dr. Theologos Andronikos, Giannis Serafeim, Dimitris Ntouras and Dimitris Vlastos. Appart from excellent colleagues, I am fortunate enough to now call them friends. I would also like to thank Christos Bakirtzoglou, Dimitra Anevlavi and Iro Malefaki for being great neighbours at work. I am also grateful to have my friends and classmates, Katerina Smyrli and Konstantinos Anagnostopoulos, by my side throughout these years.

Of course, I could not have undertaken this journey without the love and support of my family; my mother Margarita, my father Andreas, my brother Dimitris and my second mother Maria.

Lastly, I would be remiss in not mentioning my partner Anastasia, for supporting me and putting up with me all those years. She has been an inseparable part of my life and my identity! I would also like to thank my dogs; Ramon, Melanie, Roxy, Bruno and Dorian for all the entertainment and emotional support and I would like to apologise to them for my absence during the past months.

Athens, September 2023

Nikolaos Spyropoulos

Κι αν είσαι στο σκαλί το πρώτο, πρέπει
νά'σαι υπερήφανος κ' ευτυχισμένος.
Εδώ που έφθασες, λίγο δεν είναι·
τόσο που έκαμες, μεγάλη δόξα.

Κ.Π. Καβάφης, «Το Πρώτο Σκαλί»

Abstract

In this thesis, a high fidelity aeroelastic analysis solver for rotor configurations has been developed. This newly formed computational tool is capable of analyzing complex flow phenomena over a wide part of the sub–sonic region and under the same computational framework. The structural dynamics problem is solved by GAST, an in–house elasto–dynamic analysis module, the development of which started in previous theses [1, 2] and continued in the present. In previous versions of GAST, a Wind Turbine (WT) configuration was approximated as an assembly of linear full stiffness matrix Timoshenko beams [3] discretized through a $1D$ Finite Element Method (FEM) approach and being sequentially connected in the context of a generic multi–body dynamics representation, not restrained to sequential configurations. During the present thesis, the kinematic and dynamic analysis part was reformed to follow a multi–body dynamics methodology. As a result, GAST may now be used for the structural dynamics analysis of any arbitrary configuration of multiple load paths and connections between slender components (beams). The aerodynamic analysis is based on MaPFlow and HoPFlow [4]. MaPFlow is an in–house conventional Eulerian CFD solver which solves the compressible unsteady Reynolds averaged Navier–Stokes equations under a cell–centered finite volume discretization. Flows in the incompressible region are simulated using Low Mach Preconditioning [5]. HoPFlow is a hybrid Eulerian–Lagrangian compressible CFD solver that combines the standard Eulerian CFD formulation implemented in MaPFlow close to the solid boundaries, with a Lagrangian CFD approach for the rest of the computational space, through a domain decomposition approach. The Fluid Structure Interaction (FSI) framework is formed through a proper communication protocol that has been developed in the present work and connects the individual structural and aerodynamic modules under a strong coupling approach.

To have the option of an holistic and cost–effective design tool, especially for WTs, and for rotor applications in general, the Actuator Line (AL) methodology has been implemented in MaPFlow. In the AL approach, the blades of a rotor are simulated as a set of control points along their axes; they are allowed to move freely inside the computational grid and their aerodynamic loads are applied to the flow–field as source terms on the computational cells they slice during their rotation. In this way, multi–body and aeroelastic simulations are facilitated, while computational cost is restrained. AL has been widely used in studying the generation and convection of WT rotor wakes [6, 7], due to the detailed description of the flow–field that the CFD framework offers. However, in this study, it is found capable of predicting also the loads of both WT and helicopter rotor blades in accuracy and under moderate computational requirements. Moreover,

to reproduce the true (atmospheric) conditions in which a WT operates, the method of Generation Zone (GZ) has been implemented in MaPFlow and is used for the first time in order to impose pre–defined turbulent fields (produced with Mann's model [8]) onto an averaged flow–field within a CFD context. It is found that GZ is able to create turbulent fields that are closer to the turbulent field produced by the Mann's model, compared to conventional methodologies found in literature.

The validation of this new high accuracy, but cost–effective aeroelastic module (coupled GAST–AL module) consists of:

i) aeroelastic simulations of the DTU 10MW Reference Wind Turbine (DTU 10MW RWT) [9] under constant wind and atmospheric (turbulent) conditions;

ii) aeroelastic simulations of the Main Rotor (MR) of the model BO105 helicopter used in the HeliNoVi experimental campaign [10], under low, medium and high flight speed in forward flight conditions.

AL results are compared against Blade Element Momentum Theory (BEMT) and Lifting Line (LL) models results in the case of the WT, whereas LL and measured data are considered in the helicopter cases. AL results show significant differences compared to BEMT predictions that get more intense as the flow conditions get more complex. However, excellent agreement between AL and LL is observed in all the examined cases, due to the detailed representation of the flow–field by the CFD and the Free Vortex Wake frameworks respectively. Hence, AL proves to be as reliable as LL in terms of loads and deflections predictions. The main advantage of the AL method, is that the effect of the rotor and ground on the local turbulent inflow can be accounted for in detail within the CFD context, under moderate computational requirements.

Simulations of both WT and helicopter rotors, considering the actual geometry of the rotor blades, are performed using the coupled GAST–HoPFlow aeroelastic solver. The simulated cases concern:

i) aerodynamic analysis of the model WT rotor used in the New MEXICO experimental campaign [11, 12] for an axial flow case at 14.7 m/s;

ii) aeroelastic analysis of the MR of the model BO105 helicopter used in the HARTII experimental campaign [13] for the Base–Line descent case at 33 m/s flight speed.

The accuracy and the features of this newly formed, high fidelity aeroelastic solver are assessed in complex local flow conditions and over a wide part of the sub–sonic region. In the root region of a WT rotor, characterized by lower Mach values, detached flow conditions occur. On the other, weak shock waves appear near the blades tip of the helicopter rotor, where higher Mach values are encountered. Results are compared against experimental measurements and predictions produced by other CFD based aeroelastic codes. In both cases, the aerodynamic loads of the blades are predicted in great accuracy (comparable to that of standard CFD solvers). The resulting structural loads and the corresponding deflections are estimated fairly well. The same remark is made for the flow–field developed in the region close to the rotors. The above remarks confirm that the coupling method

between the Eulerian and the Lagrangian sub–domains that determines the boundary conditions for the confined Eulerian grid is adequate and consistent. The same conclusion is drawn for the coupling between the structural module and the aerodynamic solver.

Keywords

FSI, multi–body dynamics, CFD, hybrid CFD solvers, actuator line, atmospheric conditions, wind turbine rotor, DTU 10MW RWT, New MEXICO, helicopter rotor, HeliNoVi, HARTII

Table of Contents

List of Abbreviations

FSI Fluid Structure Interaction

FEM Finite Element Method

ROM Reduced Order Models

CFD Computational Fluid Dynamics

FDM Finite Differences Method

FVM Finite Volume Method

DGM Discontinuous Galerkin Method

BDF Backwards Difference Formulae

GCL Geometric Conservation Law

RBF Radial Basis Functions

FFT Fast Fourier Transform

RANS Reynolds Averaged Navier Stokes

URANS Unsteady Reynolds Averaged Navier Stokes

DNS Direct Numerical Simulation

LES Large Eddy Simulation

DES Detached Eddy Simulation

DDES Delayed Detached Eddy Simulation

SGS Sub-Grid Scale

IBM Immersed Boundary Method

BEMT Blade Element Momentum Theory

LL Lifting Line

BEM Boundary Element Methods

FVW Free Vortex Wake

AD Actuator Disk

AL Actuator Line

GZ Generation Zone

TI Turbulence Intensity

ABL Atmospheric Boundary Layer

SPH Smooth Particle Hydrodynamics

VPM Vortex Particles Methods

PM Particle Mesh

RHS Right Hand Side

WT Wind Turbine

DTU 10MW RWT DTU 10MW Reference Wind Turbine

1P once per rotor revolution (preferred in **wind turbines** terminology)

3P three times per rotor revolution (preferred in **wind turbines** terminology)

5P five times per rotor revolution (preferred in **wind turbines** terminology)

RFC Rain-Flow Counting

DEL Damage Equivalent Loads

MR Main Rotor

BVI Blade Vortex Interaction

1/rev once per rotor revolution (preferred in **helicopters** terminology)

2/rev twice per rotor revolution (preferred in **helicopters** terminology)

3/rev three times per rotor revolution (preferred in **helicopters** terminology)

4/rev four times per rotor revolution (preferred in **helicopters** terminology)

HeliNoVi Helicopter Noise and Vibration

HARTII second higher Harmonic control and Aeroacoustic Rotor Test

HHC Higher Harmonic Control

ERF European Rotorcraft Forum

SPR Stero Pattern Recognition

PIV Particle Image Velocimetry

DNW German-Dutch wind tunnel

ECD Eurocopter Deutschland GmbH

DLR German Aerospace Center

ONERA French Aerospace Lab

NLR Netherlands Aerospace Center

AFDD U.S. Army Aero-Flight Dynamics Directorate

NL NASA Langley

NTUA National Technical University of Athens

Chapter 1

Introduction

In this introductory chapter, the context of the present thesis is defined. First, the technological framework of wind turbines and helicopters is examined and the relevance of aeroelasticity with these technological fields is highlighted. The goal of the thesis for developing a high fidelity aeroelastic analysis tool is then justified. In support to that, an overview of the current state of the art in structural dynamics and aerodynamics analysis tools is given. An outline of the contributions of the present work, alongside with a summary of the examined test cases and the foremost remarks are then briefly presented. Finally, the structure of the following chapters of the thesis is explained.

1.1 Aeroelasticity and technology

Wind Turbines (WTs) and helicopters are substantial paradigms of human technology in which atmospheric air flow through a rotor is leveraged for producing useful work. Wind exploitation for electric power generation has been long time feasible thanks to WTs. In helicopter technology, rapid development is noted again nowadays to support not only transport, but also numerous commercial uses including fire fighting, agricultural crop spraying, medical evacuation, etc. and in this way upgrade the quantity and quality of the provided services to the society. Technological improvement is desirable in both fields, so that performance is enhanced alongside with cost reduction. To that end, research is today directed towards the development of high fidelity computational tools, capable of concurrently addressing all the underlying processes that take place when the airflow passes through the rotors. The goal is to use them in order to identify and better understand the significance of the various and different physical phenomena taking place during the operation of both WTs and helicopters. By supplementing the procedure of design with high fidelity numerical tools, performance and safety may be improved.

In the effort to reduce wind energy cost, wind energy sector is directed towards increasing the size and flexibility of modern WT rotors. To that end, rotor blades are becoming larger and more slender, undergoing large deflections which increases the complexity of both the structural model and the flow–field formed in their wake and thus makes difficult the aeroelastic analysis of the full configuration. For their part, helicopter rotors and their drive train systems are characterized as fundamentally aeroelastic systems of high complexity and non–linear responses. It therefore follows that, in order for highly

flexible and complex constructions to be efficiently developed, design procedure needs to be equipped with accurate numerical tools applying elaborated and physically motivated models, able to account in detail for aeroelastic phenomena which play a decisive role in determining the dynamic behaviour and loads of rotating blades. This calls for sophisticated computational models both for the elasto–dynamic and the aerodynamic analysis of the blades, which combined comprise the fields of aeroelasticity.

1.2 Scope of the thesis

The aim of the present work is the development and validation of a general application and high fidelity computational tool for the aeroelastic analysis of rotors. This newly developed tool is tested on aerodynamic and aeroelastic simulations of both WT and helicopter rotors, and its accuracy is evaluated by comparing the produced results against experimental data and predictions by other computational tools of similar accuracy. Moreover, it is compared against already validated in–house computational tools that use lower fidelity aerodynamic models such as Blade Element Momentum Theory (BEMT) and Lifting Line (LL), which are considered as state of the art in WT and helicopter design respectively. In this case, simple flow cases are examined first, where the less sophisticated models are considered to be reliable and then more complex flow cases are addressed, so that the advantages of the new high fidelity model may be assessed.

For the newly developed tool to be general enough and perform analyses of high accuracy, kinematics and dynamics are based on a multi–body dynamics framework, whereas the aerodynamic analysis is performed through Computational Fluid Dynamics (CFD) techniques. In order to enable easy interchange between different individual models of varying cost and accuracy, the two systems, the elasto–dynamic and the aerodynamic one, are solved separately and get coupled through a proper aeroelastic interface framework that has been developed during the present thesis.

The elasto–dynamic analysis tool can simulate any structure with long and slender components, that can be legitimately modelled as beams interconnected by joints acted upon by forces and restricted by constraints. Rigid body and elastic motion due to structural flexibility are concurrently accounted for within the multi–body dynamics framework, alongside the non–linear inertial and structural effects and geometric couplings imposed by large deflections of highly flexible components. These highly flexible components are approximated as assemblies of Timoshenko beams discretized through Finite Element Method (FEM). In this way, the non–linear geometric phenomena are accurately resolved in the structural analysis.

General application and high accuracy in terms of aerodynamics is accomplished by employing CFD techniques. In this way, load–driving conditions related to compressibility and viscous effects (e.g. shock waves, stall–induced effects) are properly accounted for and complex flow phenomena may be resolved with great accuracy. In order to investigate the interaction between the rotating blades and stationary bodies (e.g. ground, WT tower or helicopter fuselage), an Actuator Line (AL) approach may be employed within a standard Eulerian CFD framework, that does not resolve the actual geometry of the rotor blades,

rather than models them as a set of control points forming lines along their axes. These lines, are allowed to move and deform freely within the computational grid and communicate with the flow through body–forces. In this way, aeroelastic analysis is facilitated and computational cost is restrained. However, in cases where flow phenomena related to the exact geometry of the simulated body (e.g. shock waves, flow separation) are to be investigated, the actual geometry of the rotor blades is resolved and multi–body configurations (interaction between arbitrarily moving bodies) are realized through a hybrid CFD code that employs a domain decomposition approach, like overset methodologies do, in order to combine an Eulerian approach close to solid–wall boundaries with a Lagrangian one for the rest of the domain.

The two systems are solved separately but get tightly coupled through a Fluid Structure Interaction (FSI) protocol that carries out the required information communication between the two distinct systems. Intercommunication is performed multiple times within every time–step of a time–marching procedure until both systems converge, so that the full aero–mechanic system is analyzed in accuracy. The aero–elastic coupling framework developed is capable of dealing only with beam structured configurations.

1.3 Literature survey

The aeroelastic analysis of a complete WT or helicopter configuration consists of various fields of analysis that alternatively could be studied separately, such us aerodynamics, structural and dynamic analysis and control. However, in order to accurately approach the complex subject of aeroelasticity in such advanced technological applications, those distinct fields need to be concurrently analyzed, so that interaction is properly taken into account. In order to facilitate the present survey, the available modelling options for the individual fields of structural dynamics (elasto–dynamic analysis) and aerodynamics are considered first, based on the accuracy of the produced results and their computational requirements.

1.3.1 Structural dynamics models

The discretisation of a WT or helicopter structure may be theoretically performed through 3D FEM, which however are rejected due to prohibitive computational requirements. In practice, structural discretization is based on either quasi–3D shell elements or beam modelling (1D FEM) of the various components of the structure which are then connected under a multi–body formulation.

Beam models are usually preferred over 3D FEM mainly due to the fact that the slender components of WT and helicopter configurations (e.g. rotor blades) may be very well approximated as beams. Full 3D FEM structural modelling could be applied to certain areas such as the WT hub and the nacelle, where beam theory fails to provide design information. It needs to be stressed, however, that beam models rely on prior cross–sectional analysis in order to obtain the cross-sectional properties of the blades (e.g. cross–sectional stiffness and mass per unit length) at various span–wise stations. Furthermore, with the ever increasing use of composite materials in WT and helicopter blades manufacturing,

transverse shear deformation, cross–sectional warping, and elastic coupling caused by material anisotropy are becoming significant in elastic analyses. Composite blades can be discretised using $3D$ composite shell elements, which are capable of describing composite layer characteristics throughout the shell thickness and predict such $3D$ phenomena in accuracy. Even so, instead of a $3D$ FEM analysis, the most computationally effective approach to modelling this complex beam problem is to split the basic $3D$, geometrically non–linear elasticity problem into two separate problems: i) a geometrically nonlinear $1D$ problem of a beam in the span–wise direction, where cross–sections are assumed to be rigid [14] and ii) a $2D$ linear elastic problem at the various span–wise stations, from which the cross–sectional warping is determined [15, 16, 17]. Such approaches have been followed in [18, 19].

Another essential motivation for applying beam modelling instead of $3D$ FEM is the fact that beam models are very well validated against analytic solutions and have proven to provide predictions of sufficient accuracy even for large deformation problems. On the other hand, $3D$ FEM based structural analysis may be coupled with CFD aerodynamic models in order to form a full $3D$ FSI analysis framework [20]. However, computational cost of such approaches is usually prohibitive, unless coarse discretization of doubtful accuracy is employed. The excessively lower computational requirements of beam models compared to higher fidelity options has led to structural modelling of WT and helicopters being almost exclusively based on beam theory [21, 22, 23]. Consequently, the vast majority of computational resources may be utilized in the aerodynamic analysis.

A number of different beam model based approaches of varying fidelity for the structural analysis of a WT or helicopter configuration may be adopted. One is a modal approach, where the description of the various bodies deflections can be made as a linear combination of some physical realistic modes; typically the lowest eigen–modes [24, 25, 26]. Modal approaches are usually referred to as Reduced Order Models (ROM) to substantially reduce computational cost in view of a long list of simulations during design. When higher fidelity approaches of more degrees of freedom are to be adopted $1D$ FEM discretization of beam models is followed. Early developments were based on simple linear beam models, such as the Euler–Bernoulli [27] or the Timoshenko [28] beam models, enhanced with certain important non linear contributions such as rotational stiffening effect. Both the Euler–Bernoulli and Timoshenko beam models contain the assumption of small deflections. However, as the configurations increase in size, rotors become larger and the rotor blades get highly slender and undergo large deflections. As a result, non–linear beam models are required in order to accurately predict the geometric non–linearities brought about by large deflections. With respect to accounting for non–linear structural phenomena there are two options;

- higher order beam models, such as the 2nd order Euler–Bernoulli model presented in [29] that was based on the earlier developments of Hodges and Dowell [30] and geometrically exact models developed by Simo and Reissner [31], Hodges [32, 33] or more recent works such as the one of Meier [34, 35] that are based on the Kirchhoff–Love beam models and usually adopt an intrinsic formulation of beam

theory (instead of expressing variations in terms of displacements and rotations they use linear and angular velocities)

- multi–body formulations [36, 37, 38] where a slender body undergoing large deflections is considered as an assembly of linear beams, each having its own co–ordinate system with respect to which deflections and rotations are assumed small. In this case, large deflections and rotations are gradually built by imposing to each beam local co–ordinate system, the deflections and rotations of the preceding ones as large rigid–body motions. The connection between consecutive beams is accomplished by satisfying proper kinematic and dynamic conditions at the connection points (joints) [39]. In an alternative approach, the components of a configuration may be divided into a number of interconnected rigid elements, supplemented with concentrated springs at the connection points in order to account for the flexibility of the component.

1.3.2 Aerodynamic models

There are multiple options of varying fidelity for performing aerodynamic analysis of rotating blades; compute their aerodynamic forces and assess the disturbances they bring about on the flow–field. The different options may be classified based on their computational cost and the accuracy of the results they produce. Simplified engineering tools, such as BEMT [40] based models or linearised dynamic wake models [41], are very fast and reliable in simple flow cases. For this reason, they are widely employed in design and analysis tools. A more elaborate option is LL panel codes employing Free Vortex Wake (FVW) modelling [42]. The latter can handle complex aerodynamic phenomena (yaw misalignment, high shear of the Atmospheric Boundary Layer (ABL)) with greater accuracy [43]. However, they are essentially inviscid and incompressible, which means that load driving conditions related to compressible and viscous effects (such as shock waves or stall induced effects), can only be considered through engineering correction models. On the other end, the highest fidelity option is fully resolved, grid–based CFD solvers that solve the Navier-Stokes equations on grids composed of millions cells [44]. Despite being computationally expensive, they have the ability to take into account compressibility and viscous effects of the flow or unsteady and 3D phenomena related to the geometry of the blades. Viscous effects are important when studying the rotor wake interaction with the boundary layer developed on surrounding bodies, such as the WT tower or the ground [45].

The various modelling options may be classified as well into grid–based (Eulerian) or grid–free (Lagrangian) ones according to the formulation in which the flow equations are expressed. In Eulerian formulations the computational space is discretised in grid cells and the flow–field evolution is described by recording the values of the flow quantities on the grid nodes. In Lagrangian (material) formulations the flow properties are carried by numerical particles which act as flow markers and the flow–field description is accomplished by following the properties of the particles along their trajectories.

Simplified aerodynamic models

The most widely known and used simplified aerodynamic models are based on BEMT combined with engineering correction models in order to account for dynamic inflow conditions [46]. In such methodologies the rotor is modelled as a disk and gets discretized in annular elements (rings). The lateral boundaries of these elements are assumed to consist of streamlines, which means that no flow across the elements is permitted. This hypothesis dictates a strong 2D character of the method. The equations for momentum and angular momentum conservation (1D momentum theory) are solved on the plane of each annular element, whereas the dynamic closure of the equations is accomplished with the use of the blade element approach. Consequently, the computation of the aerodynamic loads of the rings depends on tabulated airfoil data (2D polars) of the airfoil section that characterizes the ring.. The aerodynamic loading of each ring is considered to be constant across its surface, corresponding to a rotor with an infinite number of blades. In order to correct the latter assumption a tip loss correction model was introduced by Prandtl [47]. BEMT models have proven to be quite accurate in predicting the steady state rotor loads. Combined with engineering correction models they are also able to take into account, in a simplified approach, unsteady phenomena such as the dynamic response of a quasi–steady wake [48, 49, 46] or the asymmetric distribution of the induced velocities over the rotor disk due to wake skewness [48, 49, 46]. Moreover, unsteady and highly viscous phenomena related to the geometry of the blades, such us flow separation, may be accounted for by using Dynamic Stall models [50, 51, 52]. Their validity in simple flow cases under low computational requirements is the main asset of simplified BEMT based models, rendering them suitable for rotor design and performance analysis, where large series of simulations need to be performed. For this reason, they are regarded as state of the art in WT design.

As a higher fidelity approach in complex flow cases (e.g. yaw misalignment cases), more sophisticated dynamic wake models are usually combined with the blade element approach in order to describe the flow–field close to the rotor plane (near wake region) in greater accuracy. In this way, the unsteady response of a dynamic wake and its varying induction on the rotor plane are properly taken in to account. Such are the linear theory for describing the dynamic wake response developed by Pitt and Peters [53] or the near wake models for the trailing vorticity [54]. In practice, the latter depend on a LL modelling of the rotor blades, where only a part of the wake structure (e.g. quarter revolution) is described as circular vortex paths originating from the rotor blades.

Grid–free (Lagrangian) methodologies

A much more elaborate option would be to represent the flow–field in Lagrangian (material) form. In such formulations, the flow is approximated by a set of numerical particles that cover the entire computational space and act as flow markers, approximating the flow–field at discrete positions. The flow–field evolution is described by following the trajectories of the numerical particles while recording the values of the flow quantities they are assigned with. In that sense, particle methods are grid–free, self–adaptive and

(in theory) have zero numerical diffusion. Furthermore, no truncation of the computational domain is needed and the true velocity conditions are satisfied at infinity [55]. On the other hand, the treatment of wall boundary conditions constitutes a major challenge, involving costly convolution operations and large number of particles [56, 57]. Another drawback is the fact that computational cost rises proportionally to N^2 (N is the number of particles), unless special techniques such as Particle Mesh (PM) [58, 59, 60] or multi–pole expansions [61, 62, 63] are adopted. Furthermore, the ability of particles to move freely within the computational domain may lead to excessive clustering or spreading which in turn may bring about loss of accuracy and/or numerical instabilities. To prevent this, re–meshing, which is a typical procedure in particle methods that redistributes the particles regularly in space, may be employed. In this way, full coverage of the computational domain is recovered and regular distribution of the numerical particles is ensured.

According to the flow quantities that the particles carry, the Lagrangian formulations may be distinguished in Smooth Particle Hydrodynamics (SPH) [64, 65, 66] methods or Vortex Particles Methods (VPM) [55, 67, 68]. In the former ones momentum and energy are used as the primary flow variables of the particles, whereas dilatation, vorticity and pressure are preferred in the latter. Due to their robustness in pressure variations, VPM are quite popular in external aerodynamics applications. They are usually combined with Boundary Element Methods (BEM) [42] and have been widely used for capturing the 3D wake behind rotating bodies like WTs rotors [43], Helicopter rotors [69], but also Airplanes [70]. Their popularity is mainly attributed to the use of non–diffusive properties (primarily vorticity) that makes them befitting for wake modelling, especially in cases where the interaction between lifting bodies and free wake structures, known as Blade Vortex Interaction (BVI) [71], is to be studied.

There are various blades modelling options to be combined with a Lagrangian flow–field representation approach. The simplest one would be the LL method of Prandtl [72, 73], where a blade can be modelled as a single or an assembly of vortex filaments with constant circulation along its quarter–chord ($c/4$) line. In the context of BEM, the blade geometry can be represented as a set of boundary elements (panels) attached to the actual blade surface (thick representation of a lifting body) or its camber surface (thin representation of a lifting body as a Lifting Surface). In the Lifting Surface methodology [74] the blades are modelled as a surface distribution of dipoles along its camber surface, whereas in the thick body approach the actual blade geometry can be represented as a distribution of potential value ϕ under a *direct* [75] or a distribution of sources and dipoles under an *indirect* [76] formulation. Alternatively, the Lagrangian flow–field representation may be combined with a CFD modelling of the aerodynamic bodies in order to take into account the viscous and compressibility phenomena related to the body geometry in maximum accuracy. Such approaches are known as hybrid CFD methodologies.

Grid–based (Eulerian) methodologies

Eulerian CFD is the most popular simulation method in aerodynamics, due to the high accuracy it provides in describing the flow–field close to a body. This stems from the

fact that the Navier–Stokes equations are solved. Hence, the evolution of the flow both in space and time is described in detail. Complex flow patterns may be accurately analyzed, whereas compressible and viscous phenomena are properly accounted for when the flow interacts with the simulated bodies. Moreover, the accurate treatment of wall boundaries (no–penetration and no–slip conditions may be exactly satisfied) leads to a good estimation of the development of the boundary layer of a body. Therefore, aerodynamic phenomena that are strongly related to the geometry of the body (e.g. shock waves, flow separation) may be consistently predicted.

Computational space is discretized in "stationary" grid nodes through which the fluid moves and on whom the flow properties are recorded. The discrete flow equations can be formulated based on a variety of approaches, namely the Finite Differences Method (FDM) [77], the Finite Volume Method (FVM) [78], the Discontinuous Galerkin Method (DGM) [79] or the Spectral Method [80].

Turbulence may be accounted for through multiple approaches of varying fidelity and computational cost. In Reynolds Averaged Navier Stokes (RANS) [81], the spectrum of turbulent fluctuations is averaged in frequency. By applying this kind of averaging to the flow equations, the so–called Reynolds stress terms appear in the momentum and energy equations leading to a closure problem. There are several closures ranging from simple algebraic up to multi–equation differential models. To the other end, in Direct Numerical Simulation (DNS) [82] turbulence modelling is not needed and turbulent fluctuations are resolved, provided that sufficient grid and time resolution are employed. Large Eddy Simulation (LES) [83] stands in between. Instead of averaging over the frequency range, space filtering is carried out that distinguishes large scales which are resolved from the smaller ones, which are modelled through a sub–grid scale model. The grid requirements in DNS are very demanding while in LES more manageable sizes are needed. Still, in High Reynolds flows the grid requirements are very high and hence hybrid RANS/LES models have been developed [84].

The outer boundaries of the computational domain are typically located far away from the simulated bodies, so that the corresponding boundary conditions may approximate those of the undisturbed flow at infinity. A typical distance of the outer boundaries in the case of flow around an airfoil is 50 to 100 chords length. This distance can be shortened without loss of accuracy only if special techniques are followed, such as vortex correction [85]. Still, truncation of the computational domain at a finite distance is a numerical approximation that leads to errors perceived by the flow as reflections of acoustic waves. This is considered as significant drawback in external aerodynamics applications. Damping of such high frequency waves is typically accomplished through special techniques, such as the multigrid method [86] or a conventional gradual grid coarsening towards the outer boundaries, which however increases numerical diffusion and adds errors as well. Local grid refinement seems like an obvious remedy, but it comes with a substantial increase in computational cost. Moreover, the consideration of the interaction between independently moving and deflecting bodies is usually implemented through the application of special methodologies like Immersed Boundary Methods (IBMs) [87], Sliding grids [88], Overset grids [89] or Deforming grids [90]. Each method raises different issues, such

as temporal discontinuity of regional cells, loss of conservativeness or deterioration of grid quality and penalizes computational cost. In certain cases, this problem may be overcome using Actuator methods [91, 92], in which bodies are simulated as a set of control points that may move freely within the computational space, while their forces are simulated as source terms in the momentum and energy equations. Nevertheless, when Actuator methods are employed, the accuracy of the produced flow–field close to the bodies gets lower, while flow phenomena that are strongly related to the geometry of the body (e.g. shock wave, flow separation) cannot be analyzed.

Lagrangian vs Eulerian methodologies

To sum up, Lagrangian methodologies are more effective in the off–body region, due to the lower numerical diffusion of the Lagrangian formulation of the flow equations and the fact that they satisfy the true far–field boundary conditions. On the other hand, Eulerian methodologies are very effective in the region close to the solid–wall boundaries due to the fact that wall boundary conditions are accurately satisfied. Hence, high fidelity computation of the near–body flow–field is possible with proper grid resolution. It is therefore reasonable to combine the two methodologies in order to enhance accuracy and reduce computational cost.

Hybrid (Lagrangian–Eulerian) methodologies

Lagrangian and Eulerian methodologies may be combined in a hybrid formulation by following a domain decomposition approach. The sub–domains may either overlap or not. Strong viscous–inviscid interaction models [93, 29] and RANS-Vortex coupled ones [94, 95] are examples of completely overlapping hybrid methodologies that combine an inviscid Lagrangian formulation for the entire flow with a viscous layer close to the solid boundaries and define coupling conditions for pressure and velocity on the outer boundary of the viscous layer. Coupling in this case is approximate, not only because the two formulations are not equivalent, but also because the sub–domains overlap. Exact coupling consists of imposing continuity to all flow quantities which in principle refers to non–overlapping sub–domains. In this case, the coupling conditions take the form of integral equations (also known as Neumann to Dirichlet map) defined on the boundary interface [96, 97]. While in $2D$ problems the extra cost is manageable, the penalty in $3D$ can be substantial. For this reason, certain hybrid methods have at least some degree of overlapping, in the form of a buffer area, [98], while others directly approximate the coupling conditions. In [99, 100] compressible RANS solvers were coupled with viscous vortex methods implementing non–overlapping decomposition. Vortex particles are defined outside the Eulerian domain based on the flux of vorticity across the interface while the computation of the velocity on the interface includes the vorticity within the Eulerian domain. Finally, in [101] a compressible particles formulation has been combined with an Euler code.

1.4   Outline of the thesis

The main objective of this thesis is the development of a high fidelity aeroelastic analysis tool that can be applied on all type of rotor based configurations (e.g. vertical and horizontal wind turbines, helicopters, propeller driven air–crafts, etc.) and model very complex load–path configurations on both open–loop and closed–loop topologies. The different modules (elasto–dynamic analysis and CFD based aerodynamic codes) of this new tool have been developed at the National Technical University of Athens in previous Ph.D. theses as stand–alone tools. In this work, however, the elasto–dynamic module has significantly been modified in order to enlarge its scope, whereas additional modelling options have been added to the standard CFD code in order to allow its use as a high fidelity but affordable computational tool for a few WT design cases defined in the IEC standard [102] (computational cost may be overwhelming for a full list of simulations). Moreover, these improved individual modules have now been coupled under an FSI framework into a general application and high fidelity aeroelastic analysis tool.

1.4.1   General application GAST

The elasto–dynamic analysis module of this newly developed tool is a new version of GAST [1] and hGAST [2]. The structural analysis of the various components of a configuration is based on a Timoshenko beam modelling discretized in space by combining the method of virtual work with the FEM approach. This part of the analysis has been inherited by the previous versions of GAST. However, the kinematic and dynamic analyses followed in order to connect the different components into a full operational configuration exceeds the previous ad–hoc approaches that mainly focused on wind turbines. This is accomplished by employing a multi–body dynamics methodology that connects the different arbitrarily moving beams through joints and dynamic constraints that are realized by satisfying non–linear connection equations [36]. As a result, the new GAST is now capable of simulating any arbitrary configuration that may be validly modelled as an assembly of beams. On its previous versions, GAST has been coupled with RAFT [103], a simplified low fidelity BEMT based aerodynamic model, and GenUVP [42], a more sophisticated medium fidelity model employing panel formulations within a FVW context. Nevertheless, in order to be able to analyze in detail the aerodynamic behaviour of not only thin (lifting), but also bluff bodies, and in order to be able to account for aerodynamic phenomena driven by compressibility and viscous effects, this new elasto–dynamic tool is herein coupled with CFD based aerodynamic models. The CFD codes used for the aerodynamic analysis are MaPFlow and HoPFlow [4].

1.4.2   MaPFlow–AL modelled rotor blades

MaPFlow solves the compressible Unsteady Reynolds Averaged Navier Stokes (URANS) equations under a cell–centered finite volume spatial discretization scheme and can handle both structured and unstructured grids. Low Mach Preconditioning is applied on the equations solved when the local Mach number gets close zero, which is typical for

WT applications. 2nd order schemes are used for space and time integration. In order to facilitate multi–body configurations, where independently moving bodies interact with each other (e.g. blades–ground or blades–tower interaction), and in the same time restrain computational cost (e.g. when multiple WTs are to be simulated in a wind farm set–up) the AL technique [92] for modelling rotor blades has been implemented in MaPFlow during this thesis. The new coupled GAST–AL model is tested on aeroelastic simulations of both WT and helicopter rotors. Its accuracy is evaluated by comparing the produced results against experimental measurements and predictions by already validated in–house computational tools that use lower fidelity aerodynamic models based on BEMT and LL theories, which are considered as state of the art in WT and helicopter design respectively.

Smooth free–stream flow cases

In the WT cases, axial and yaw misalignment flows are tested at various wind speeds and comparison is made among the AL module, the standard BEMT model and the LL approach. At simple axial cases, good agreement is achieved between all three models in terms of loads and deflections prediction. Deviations occur between BEMT and the other two models at yawed free–stream flow conditions. These differences become more pronounced as the yaw angle increases. However, excellent agreement is observed between AL and LL at all the examined cases. For the helicopter simulations, AL predictions are validated against LL simulation results and wind tunnel measurements of the HeliNoVi experiment [10]. In general, predictions are close to the experimental measurements and, when differences occur, the two models results seem to agree very well with each other.

Turbulent flow cases

In order to simulate the operation of a WT in true atmospheric conditions, the model of Mann [104, 105, 8] has been used in order to create a synthetic $3D$ turbulent field and a new technique for imposing the produced turbulent field into a CFD context has been developed and implemented in MaPFlow. This new technique is based on the Generation Zone (GZ) concept presented in [106] and is able to create a spectrum which is less diffused compared to the one produced by the conventional methodology of the Actuator Disk (AD) [107] and hence closer to the initial one produced by the model of Mann. The new coupled GAST–AL model, alongside with the new internal module of MaPFlow to generate turbulent wind fields within a CFD context is tested on aeroelastic simulations of an isolated WT rotor at an axial and yaw misalignment flow case. A full WT configuration (rotor, shaft and tower) operating inside the ABL under turbulent free-stream flow is also examined. The produced results are compared against the ones obtained by the standard BEMT model. As in the smooth free–stream flow cases, good agreement is achieved between BEMT and AL predictions at the simple axial flow case, whereas differences show up at the more complex flow cases. At all the examined cases it is shown that the main advantage of AL over BEMT is the consideration of the mutual interaction of the rotor and the surrounding bodies (ground) with the ambient turbulence and the nearby inflow, thanks to the CFD representation of the flow–field.

1.4.3 HoPFlow–fully resolved rotor blades

There are cases in which the actual blade geometry (or the geometry of any other body) needs to be simulated, no matter the increased computational cost. This is inevitable when flow phenomena that are directly related to the body geometry (e.g. development of boundary layer) are to be investigated. In these cases, HoPFlow is used as the aerodynamic module of the new aeroelastic code. HoPFlow is a hybrid CFD code that employs a domain decomposition approach, like overset methodologies do, in order to combine an Eulerian approach (the one followed in MaPFlow) close to solid–wall boundaries with a Lagrangian one for the rest of the domain. In the Lagrangian sub–domain, flow–field is represented by following the evolution of a number of particles along their trajectories. In the Lagrangian approach implemented in HoPFlow, numerical particles are assigned with mass, dilatation, vorticity, pressure and volume. The velocity field is computed using the Helmholtz's decomposition theorem in conjunction with the PM technique in order to solve the resulting Poisson equations for the scalar potential ϕ and the vector potential $\vec{\psi}$. The domain decomposition employed in HoPFlow is suitable for multi–body and aeroelastic configurations within a CFD context, without minimizing the accuracy of the produced near–body flow–field that the AL methodology brings about. HoPFlow is tested on an aerodynamic simulation of a WT model rotor used in the New MEXICO experimental campaign [11] and the coupled GAST–HoPFlow aeroelastic tool is tested on an aeroelastic simulation of a helicopter model rotor used in the HARTII experiment [13]. In both cases the rotor blades are fully resolved. The accuracy of the produced results is evaluated by comparing them against experimental measurements and predictions by other computational tools of similar accuracy (coupling between beam structural models and CFD based aerodynamic analyses) developed by other institutions and research centers.

Aerodynamic analysis case

In the case of the aerodynamic analysis of the WT model rotor it is shown that the accuracy of the boundary layer solution (near–body flow–field) of the hybrid solver is comparable with that produced by a standard Eulerian CFD code. This confirms that the coupling method that determines the boundary conditions for the confined Eulerian grid is adequate and consistent. It is also shown that the reduced numerical diffusion of the Lagrangian formulation followed in the off–body region leads to better preservation of far–wake structures and, thus, to a more accurate estimation of the wake deficit compared to its Eulerian counterpart MaPFlow.

Aeroelastic analysis case

In the case of the aeroelastic analysis of the helicopter model rotor the procedure followed to couple GAST with HoPFlow is validated as well. It is shown that the aerodynamic and structural loads, the corresponding deflections and the produced nearby flow–field predicted by this new high fidelity aeroelastic solver is in good agreement with the experimentally measured data and comparable to the predictions by other high fidelity aeroelastic tools.

Regarding the validation cases examined in the present study, emphasis has been given to WT and helicopter configurations. However, the capabilities of this newly created aeroelastic tool exceed those cases and it may as well be used on drones, aircraft and marine propellers, including their drive–train systems, cluster of photovoltaic panels and any other structure that consist of long and slender components and may be legitimately modelled as assemblies of beams that interact with fluid flows.

1.5   Structure of the thesis

In Chapter 2, the theoretical base of the individual modules of this new aero–elastic tool is presented. It includes the multi–body dynamics and the modelling of the structural dynamics through beam theory, the aerodynamic analysis following Eulerian and hybrid CFD approaches and the aeroelastic coupling procedure followed in all the different aerodynamic modelling options.

In Chapter 3, the capabilities of the new GAST–AL aeroelastic model are validated for the analysis of both WT and helicopter rotors operating under different constant wind speeds and flight speeds respectively. The produced results are compared against experimental measurements and computational predictions when BEMT and LL models are used instead of AL, which are considered as state of the art in WT and helicopter rotors design respectively. Furthermore, in the same chapter, the aeroelastic analysis of a WT under turbulent free–stream flows is performed. AL results are now compared against the results obtained by the standard BEMT model. The goal is to assess the benefit from incorporating CFD in WT analysis.

In Chapter 4 the accuracy of the new GAST–HoPFlow aeroelastic model is tested on an aerodynamic simulation of a WT model rotor and an aeroelastic simulation of a helicopter model rotor. The produced results are compared against experimentally measured data and predictions by other computational tools of similar accuracy developed by other institutions and research centers.

In Chapter 5, the thesis is concluded by summarizing the work and highlighting the most significant findings made in the previous chapters. Finally, a few interesting topics for future research using this new high fidelity aeroelastic tool are indicated.

Chapter **2**

Methodology

The aim of this chapter is to provide the theoretical background and the equations of the simulation codes used in the present research along with some numerical implementation details of the models. Firstly, the structural dynamics theoretical background followed in beam–structured configurations and implemented in GAST is detailed. The different CFD based aerodynamic options of varying fidelity that have been employed in the study are then analyzed in some detail. Both the standard Eulerian approach followed in MaPFlow and the hybrid Eulerian–Lagrangian approach implemented in HoPFlow are presented. Finally, the procedure followed to accomplish the interaction and communication between two separate solvers, the structural dynamics one with any of the various aerodynamic modules, is presented. The herein presented coupling interface focuses essentially in beam–structured configurations.

2.1   Multi–body dynamics of beam–structured configurations

The structural and dynamic response of a configuration is accounted for using GAST [1, 29, 37, 38]. GAST is a servo–aero–elasto–dynamic solver based on a multi–body approach, in which all the structure components are considered as flexible generalized Timoshenko beams, structurally modelled by full stiffness matrix [3] and solved based on a $1D$ F.E.M. approximation. In this way a full structure configuration may be modelled, in which all flexible components (e.g. rotor blades, shaft and tower constitute a WT configuration) are included. Rigid body and elastic motion due to structural flexibility are concurrently accounted for within the multibody dynamics framework, alongside with the non–linear inertial and structural effects and the geometric couplings imposed by large deflections of highly flexible components (e.g. rotor blades). The flexible components (bodies) are approximated as an assembly of linear Timoshenko beam elements (hereafter called sub–bodies). The assembly of all the separate components into the full system is carried out by imposing appropriate non–linear kinematic and dynamic constraint equations at their connection points. In this way, non–linear effects due to high deflections are accounted for using linear beam theory at the sub–body level, but considering non–linear effects at the connection of different sub–bodies [38]. Following this approach, multiple load path joints can be easily introduced. In brief, the multi–body approach employed in this work demands that in case of multiple connected sub–bodies one of the connected compo-

nents specifies the position (displacements) and orientation (rotations), while all others contribute their reaction loads (see Figure 2.1).
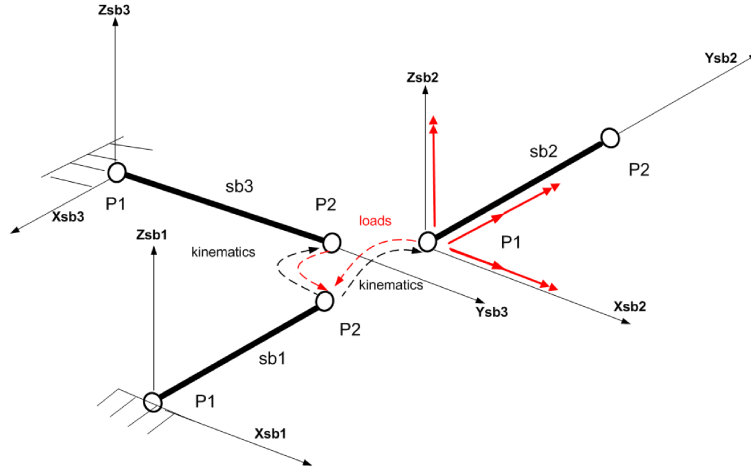
Figure 2.1. *Connection conditions. Example between 3 interconnected sub-bodies. A single point (P2 of sb1) provides the kinematics, while all the others (P1 of sb2 and P2 of sb3) contribute their reaction loads.*

2.1.1 Multi–body kinematics

A local coordinate system $[O(x, y, z)]$ (see Figure 2.1) is attached to one end of the sub–body which is considered as the start point ($P1$), with respect to which linear elastic displacements are defined. The y axis of the local system is chosen to coincide with the beam (sub–body) elastic axis. The local frame of the sub–body is subjected to (a) rigid body and (b) elastic motions. Rigid body motions are divided into two kinds. There are rigid body motions that bodies undergo by themselves and motions induced by other bodies that are connected to them.

Let $\mathbf{q}^k = \left[\mathbf{q}_t^k, \mathbf{q}_r^k\right]^T$ denote the set of (rigid body) translations $\left(\mathbf{q}_t^k\right)$ and rotations $\left(\mathbf{q}_r^k\right)$ that define the origin and orientation of the local system of the kth body in its initial undeformed state. Both $\mathbf{q}_t^k$ and $\mathbf{q}_r^k$ may be time varying. The $\mathbf{q}^k$ vector contains i) all time invariant translations and rotations that define local the co–ordinate system of the beam with respect to the inertial frame, ii) time variant self sub–body motions (e.g pitching motion of the blade), iii) global rigid body kinematic degrees of freedom (dofs) undergone by a collection of bodies including the kth body (eg. rotor rotational speed, floater motion). The latter are either prescribed (constant rotational speed) or determined through the solution of a dynamic equation (floater motion).

$\mathbf{q}_0^k = \left[\mathbf{q}_{0t}^k, \mathbf{q}_{0r}^k\right]^T$ is a 6-component vector including 3 translations $\left(\mathbf{q}_{0t}^k\right)$ and 3 rotations $\left(\mathbf{q}_{0r}^k\right)$ denoting motions induced by other bodies, in particular the elasto–dynamic motions induced by other bodies that are connected to the kth body (e.q. tower deflections as shown in Figure 2.2). $\mathbf{q}_0^k$ values are determined by satisfying proper non–linear connection equations. Hence $\mathbf{q}_0^k$ is responsible for moving the kth body, so that is stays connected to its preceding bodies (e.g. shaft shown in Figure 2.2). In that sense, it can be said that the elastic deflections of the other bodies that are connected to the kth body (e.q. tower

and shaft deflections shown in Figure 2.2) are summed up to $\mathbf{q}_0^k$ as rigid body motion.

It is noted that with regard to rigid body motion dofs, there is not always clear distinction between $\mathbf{q}$ and $\mathbf{q}_0$. Some dofs may belong to either of the two sets. For example rotor blades rotation could be included in the $\mathbf{q}$ vector of the shaft and through that they can be communicated to the $\mathbf{q}_0$ vector of all the blades connected to the shaft (directly or indirectly). But also, rotor azimuthal rotation can be considered (as a global rotation dof) in the $\mathbf{q}$ vector of all rotating components.

Rigid translations (denoted by sub-script "t") will displace the body as a whole to positions denoted by $\mathbf{R}_p^k$ and $\mathbf{R}_0^k$ respectively for the two types of motions, while rigid rotations (denoted by sub-script "r") lead to rotation matrices $\mathbf{T}_p^k$ and $\mathbf{T}_0^k$. Based on the above, the (global) position vector $\mathbf{r}_G^k$, the velocity $\dot{\mathbf{r}}_G^k$ and the acceleration $\ddot{\mathbf{r}}_G^k$ of an arbitrary point P of the deflected k^{th} body with respect to the global (inertial) frame $[O_G\,(x_G, y_G, z_G)]$ (see Figure 2.3) are expressed as follows:

$$
\begin{aligned}
\mathbf{r}_G^k &= \mathbf{R}_p^k\!\left(\mathbf{q}^k, t\right) + \mathbf{T}_p^k\!\left(\mathbf{q}_r^k, t\right)\!\left(\mathbf{R}_0^k\!\left(\mathbf{q}_0^k, t\right) + \mathbf{T}_0^k\!\left(\mathbf{q}_{0r}^k, t\right)\!\left(\mathbf{r}_L^k + \mathbf{S}\mathbf{u}^k\left(t\right)\right)\right) \Rightarrow \\
\mathbf{r}_G^k &= \underbrace{\left(\mathbf{R}_p^k\!\left(\mathbf{q}^k, t\right) + \mathbf{T}_p^k\!\left(\mathbf{q}_r^k, t\right)\mathbf{R}_0^k\!\left(\mathbf{q}_0^k, t\right)\right)}_{\mathbf{R}^k} + \underbrace{\mathbf{T}_p^k\!\left(\mathbf{q}_r^k, t\right)\mathbf{T}_0^k\!\left(\mathbf{q}_{0r}^k, t\right)}_{\mathbf{T}^k}\!\left(\mathbf{r}_L^k + \mathbf{S}\mathbf{u}^k\left(t\right)\right) \Rightarrow \\
\mathbf{r}_G^k &= \mathbf{R}^k + \mathbf{T}^k\left(\mathbf{r}_L^k + \mathbf{S}\mathbf{u}^k\left(t\right)\right) \\
\dot{\mathbf{r}}_G^k &= \dot{\mathbf{R}}^k + \dot{\mathbf{T}}^k\left(\mathbf{r}_L^k + \mathbf{S}\mathbf{u}^k\left(t\right)\right) + \mathbf{T}^k\left(\mathbf{S}\dot{\mathbf{u}}^k\left(t\right)\right) \\
\ddot{\mathbf{r}}_G^k &= \ddot{\mathbf{R}}^k + \ddot{\mathbf{T}}^k\left(\mathbf{r}_L^k + \mathbf{S}\mathbf{u}^k\left(t\right)\right) + 2\dot{\mathbf{T}}^k\left(\mathbf{S}\dot{\mathbf{u}}^k\left(t\right)\right) + \mathbf{T}^k\left(\mathbf{S}\ddot{\mathbf{u}}^k\left(t\right)\right)
\end{aligned}
\tag{2.1}
$$

where $\mathbf{R}_p^k$ and $\mathbf{T}_p^k$ are the translation vector and rotation matrix that express the rigid body motion up to the 1st node of the sub–body, whereas $\mathbf{R}_0^k$ and $\mathbf{T}_0^k$ are the translation vector and rotation matrix of the 1st node of the sub–body that are defined by the elasto–dynamic motion induced by other bodies that are connected to the sub-body. $\mathbf{r}_L^k = \left(x_L^k, y_L^k, z_L^k\right)^T$ is the local position vector of P in the initial undeformed state, $\mathbf{u}^k = \left(u^k, v^k, w^k, \theta_x^k, \theta_y^k, \theta_z^k\right)^T$ is the vector of the local elastic deflections (displacements and rotations), $\dot{\mathbf{u}}^k = \left(\dot{u}^k, \dot{v}^k, \dot{w}^k, \dot{\theta}_x^k, \dot{\theta}_y^k, \dot{\theta}_z^k\right)^T$ and $\ddot{\mathbf{u}}^k = \left(\ddot{u}^k, \ddot{v}^k, \ddot{w}^k, \ddot{\theta}_x^k, \ddot{\theta}_y^k, \ddot{\theta}_z^k\right)^T$ are the corresponding velocities and accelerations (all defined in the local coordinate system of the body). Matrix $\mathbf{S}$ is given by:

$$
\mathbf{S} = \begin{bmatrix} 1 & 0 & 0 & 0 & z_L^k & 0 \\ 0 & 1 & 0 & -z_L^k & 0 & x_L^k \\ 0 & 0 & 1 & 0 & -x_L^k & 0 \end{bmatrix}
\tag{2.2}
$$

where the right 3×3 part of $\mathbf{S}$ takes into account the extra displacements of a point that is offset with respect to the elastic axis, due to the elastic rotation of the axis.

It is noted that $\mathbf{T}_p^k$ and $\mathbf{T}_0^k$ are all expressed as a sequence of successive elementary rotations about a single axis:

$$
\mathbf{T} = \mathbf{T}_1\left(q_r^1\right)\mathbf{T}_2\left(q_r^2\right)\cdots\mathbf{T}_{m-1}\left(q_r^{m-1}\right)\mathbf{T}_m\left(q_r^m\right)
$$

whereas, $\mathbf{R}_p^k$ and $\mathbf{R}_0^k$ are expressed as a sum of elementary rotations (around one axis) multiplied with an elementary translation:

$$\mathbf{R} = \mathbf{R}_1\left(q_t^1\right) + \mathbf{T}_1\left(q_r^1\right)\left(\mathbf{R}_2\left(q_t^2\right) + \mathbf{T}_2\left(q_r^2\right)\cdots\mathbf{R}_{m-1}\left(q_t^{m-1}\right) + \mathbf{T}_{m-1}\left(q_r^{m-1}\right)\mathbf{R}_m\left(q_t^m\right)\right)$$

where $m = 6$ for $\mathbf{R}_0^k$ and $\mathbf{T}_0^k$.

In equation (2.1) $\mathbf{R}^k$ and $\mathbf{T}^k$ are the translation vector and rotation matrix following the connection of the 1st node of the kth sub–body with another sub–body.
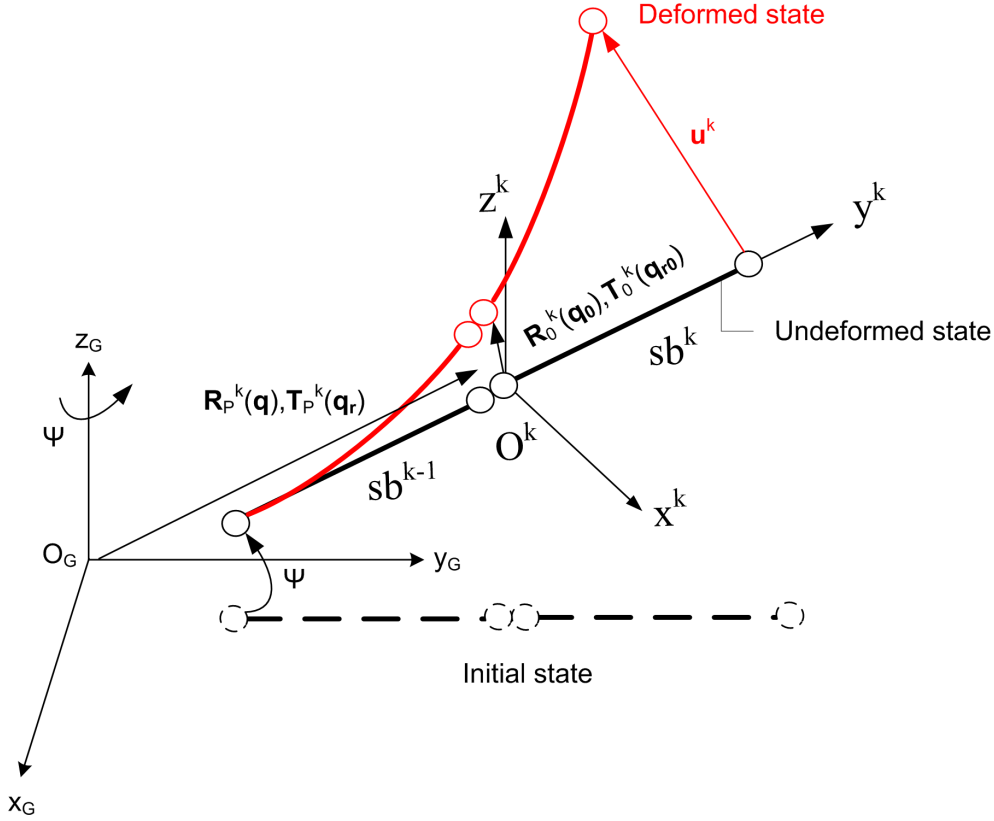
Figure 2.2. *Realization of a rotating blade consisting of 2 sub-bodies. Initial undeformed state depicted in black dashed line, current undeformed state (after azimuthal rotation) depicted in black continuous line and deformed state (after azimuthal rotation and elastic deflections) depicted in red continuous line. Distinction between $\mathbf{q}$ and $\mathbf{q}_0$ vectors. $\mathbf{q}$ expresses the rigid body motion of a body (azimuthal rotation), while $\mathbf{q}_0$ is defined by the elasto-dynamic motion induced by other bodies that are connected to this body. Hence, in this simple example, the position vectors and rotation matrices of sub-bodies $k-1$ and k are defined as:*

$$\mathbf{T}^{k-1} = \mathbf{R}_3\left(\Psi\right), \qquad \mathbf{R}^{k-1} = \mathbf{T}^{k-1}\begin{pmatrix} 0 \\ R_{hub} \\ 0 \end{pmatrix}, \qquad \mathbf{T}_P^k = \mathbf{T}_{k-1}, \qquad \mathbf{R}_P^k = \mathbf{R}_{k-1} + \mathbf{T}_{k-1}\begin{pmatrix} 0 \\ L^{k-1} \\ 0 \end{pmatrix},$$

$$\mathbf{T}_0^k = \begin{bmatrix} 0 & -\theta_z & \theta_y \\ \theta_z & 0 & -\theta_x \\ -\theta_y & \theta_x & 0 \end{bmatrix}^{k-1} (P2), \mathbf{R}_0^k = \begin{pmatrix} u \\ v \\ w \end{pmatrix}^{k-1} (P2), \mathbf{T}^k = \mathbf{T}_P^k\mathbf{T}_0^k = \mathbf{T}^{k-1}\begin{bmatrix} 0 & -\theta_z & \theta_y \\ \theta_z & 0 & -\theta_x \\ -\theta_y & \theta_x & 0 \end{bmatrix}^{k-1} (P2),$$

$$\mathbf{R}^k = \mathbf{R}_P^k + \mathbf{T}_P^k\mathbf{R}_0^k = \mathbf{R}^{k-1} + \mathbf{T}^{k-1}\left[\begin{pmatrix} 0 \\ L^{k-1} \\ 0 \end{pmatrix} + \begin{pmatrix} u \\ v \\ w \end{pmatrix}^{k-1} (P2)\right].$$
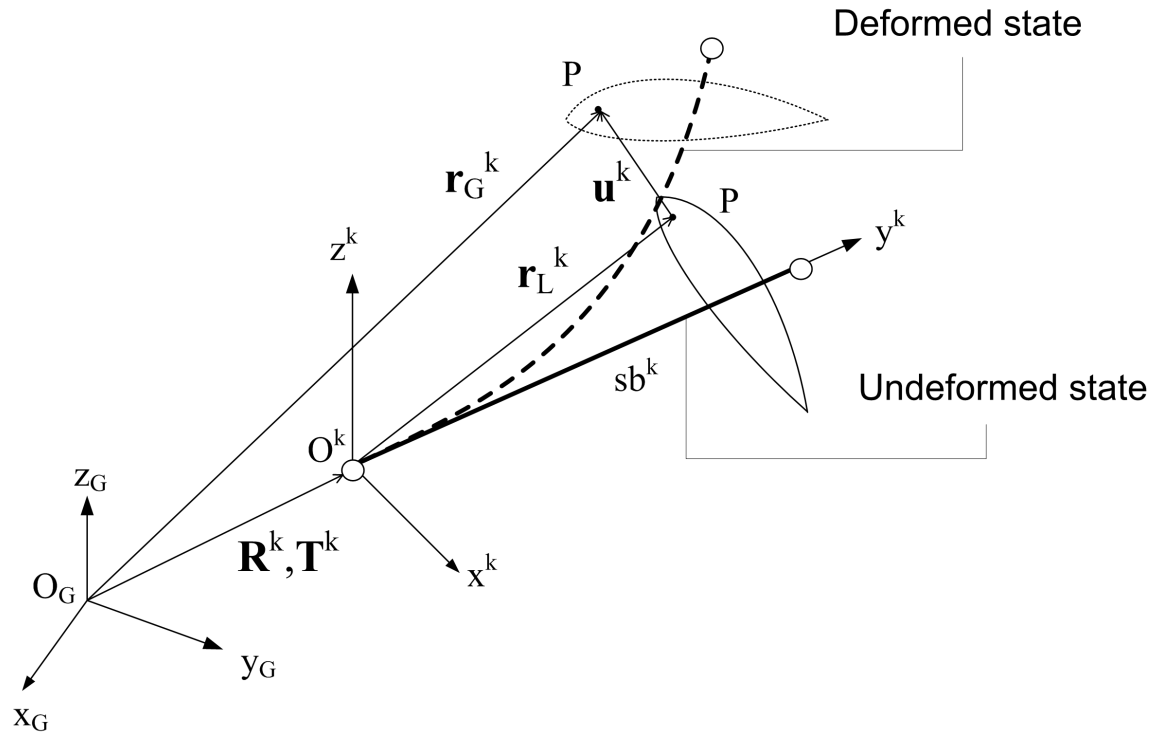
Figure 2.3. *The kinematics of an arbitrary point P can be defined through the multi–body dynamics equations (2.1), based on the initial local coordinates and elastic deflections with respect to the body it belongs to, the position vector and the rotation matrix of the body.*

It is important that the above multi–body formulation is here extended to the body level. Highly flexible bodies, such as the blades, are divided into a number of interconnected sub–bodies, each considered as a single or as an assembly of linear beam finite elements. Large deflections and rotations gradually build up and non–linear dynamics are introduced by imposing the deflections and rotations of preceding sub–bodies as rigid body motions to each sub–body. Dynamic coupling of the sub–bodies is introduced by communicating the reaction loads (3 forces and 3 moments) at the first node of every sub–body to the free node of the previous sub–body as external loading. Illustration of the extension of the multi–body framework on the level of a body is illustrated in Figure 2.4. Moreover, Figure 2.5 shows how a body (local co–ordinate system $[O_B(x_B, y_B, z_B)]$) can be discretized into a number of interconnected sub–bodies (local co–ordinate system $[O(x, y, z)]$) and every sub–body into a sequence of linear Timoshenko beam elements.
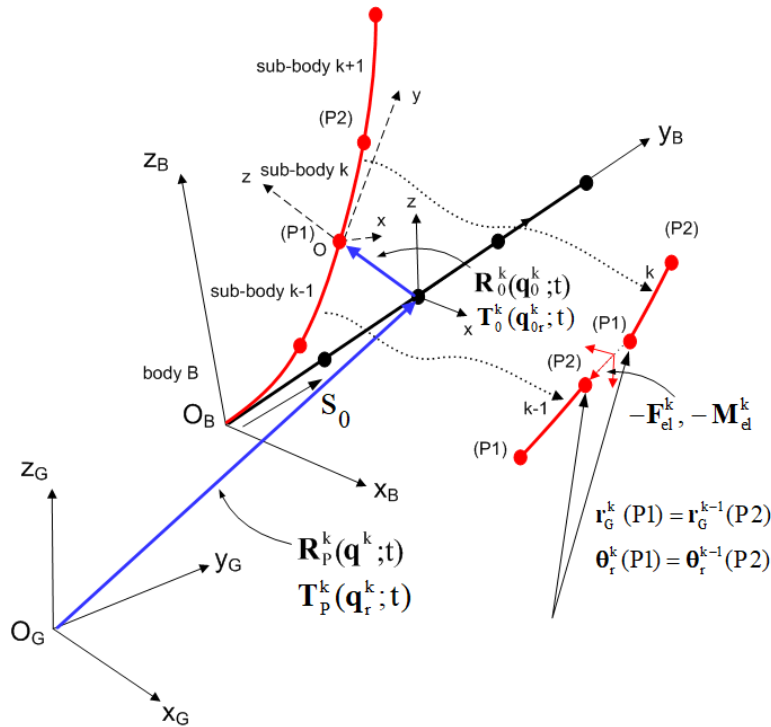
Figure 2.4. *Application of multi-body dynamics for modelling of non-linear bodies as a sequence of linear inter-connected beams. Non-linear effects are included at the connection points.*
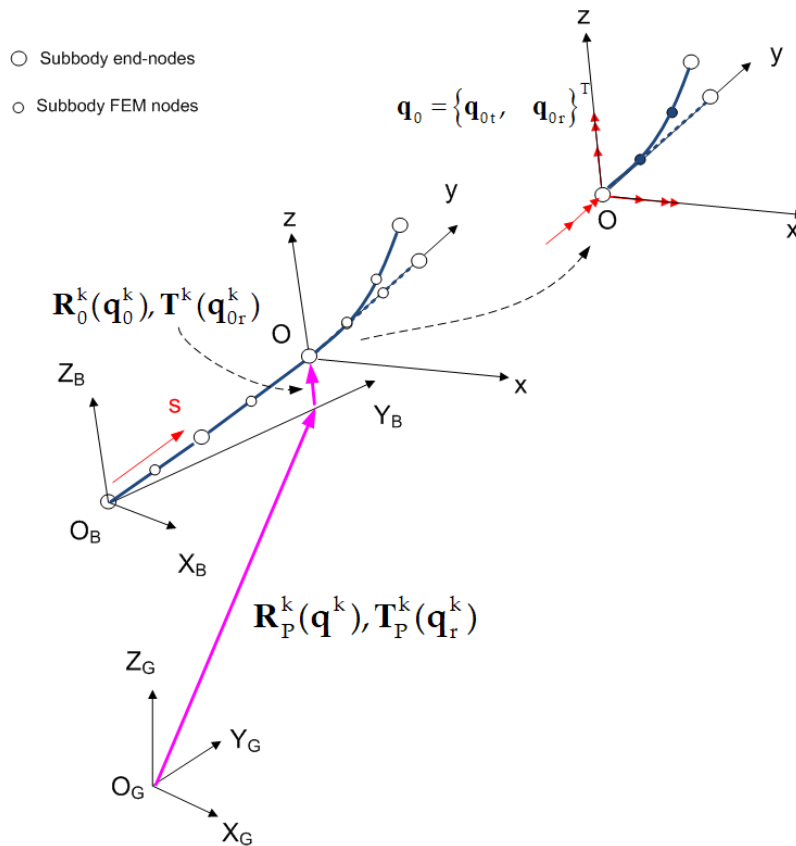
Figure 2.5. *Discretization of a non-linear body. Bodies are divided into a sequence of inter-connected sub-bodies, which in turn are discretized into a number of linear Timoshenko finite elements.*

2.1.2   Timoshenko beam model
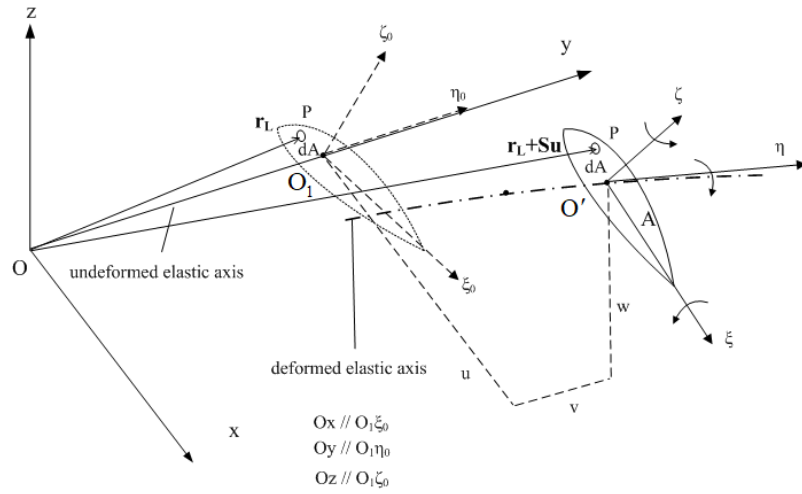
Figure 2.6. *Definition of the beam local coordinate system and local deflections.*

2.1.2.1   Equations of structural equilibrium

Linear Timoshenko beam modelling is applied in order to account for the local deflections vector $\mathbf{u}^k$ of a flexible body. The body fitted coordinate system $[O'\,(\xi, \eta, \zeta)]$ shown in Figure 2.6 is the cross section local system. Around the axes of this system, local bending and torsion rotation take place. The set of dynamic equilibrium equations (3 forces and 3 moments equations) of the kth body takes the form:

$$\int_A \rho \mathbf{S}^T \mathbf{T}^{k^T} \ddot{\mathbf{r}}_G^k \, dA = \begin{bmatrix} F_x' \\ F_y' \\ F_z' \\ M_x' + F_z - F_y w' \\ M_y' \\ M_x' - F_x + F_y u' \end{bmatrix}^k + \left\{ \begin{array}{c} \textit{external loads including} \\ \textit{reaction loads communicated} \\ \textit{by connected bodies} \end{array} \right\} \qquad (2.3)$$

where $()' = \frac{\partial}{\partial y}$ denotes derivative with respect to the beam–wise local y direction. The terms $F_y w'$ and $F_y u'$ in the moment x and z equations are the only non–linear terms retained in this analysis. This is because they are expected to contribute significantly, especially in the case of rotating beams in which axial force increases due to the centrifugal effect. The two terms give rise to virtual stiffening of the beam proportionally to the square of the rotational speed. It is noted that equilibrium equations (2.3) are written with respect to the local co–ordinate system of the sub–body.

The acceleration of an arbitrary point P with respect to the local co–ordinate system of the body it belongs to is written as:

$$\mathbf{T}^{k^T} \ddot{\mathbf{r}}_G^k = \underbrace{\mathbf{T}^{k^T} \ddot{\mathbf{R}}^k}_{\text{acceleration of origin}} + \underbrace{\mathbf{T}^{k^T} \ddot{\mathbf{T}}^k \left(\mathbf{r}_L^k + \mathbf{S}\mathbf{u}^k(t) \right)}_{\text{Centrifugal}} + \underbrace{2\mathbf{T}^{k^T} \dot{\mathbf{T}}^k \left(\mathbf{S}\dot{\mathbf{u}}^k(t) \right)}_{\text{Coriolis}} + \underbrace{\left(\mathbf{S}\ddot{\mathbf{u}}^k(t) \right)}_{\text{local acceleration}} \qquad (2.4)$$

As indicated under every term of equation (2.4), in addition to local acceleration due to local deflection of the sub–body, the acceleration of the origin of the local sub–body co–ordinate system and the centrifugal and Coriolis terms due to the rotation of the local sub-body co–ordinate system are taken into account in the analysis. It is noted that the first, second and third term of equation (2.4) depend linearly on $\mathbf{q}^k = \left[\mathbf{q}_t^k, \mathbf{q}_r^k\right]^T$ and $\mathbf{q}_0^k = \left[\mathbf{q}_{0t}^k, \mathbf{q}_{0r}^k\right]^T$.

The constitutive relation between the generalized structural loads over a cross section of a beam and the strains-curvatures is given by:

$$\mathbf{F}^k = \mathbf{K}^k \epsilon^k \Rightarrow$$

$$
\underbrace{\begin{bmatrix} F_x \\ F_y \\ F_z \\ M_x \\ M_y \\ M_x \end{bmatrix}^k}_{\mathbf{F}^k}
=
\underbrace{\begin{bmatrix} K_{xx}^A & K_{xy}^A & K_{xz}^A & K_{xx}^B & K_{xy}^B & K_{xz}^B \\ & K_{yy}^A & K_{yz}^A & K_{yx}^B & K_{yy}^B & K_{yz}^B \\ & & K_{zz}^A & K_{zx}^B & K_{zy}^B & K_{zz}^B \\ & sym. & & K_{xx}^C & K_{xy}^C & K_{xz}^C \\ & & & & K_{yy}^C & K_{yz}^C \\ & & & & & K_{zz}^C \end{bmatrix}^k}_{\mathbf{K}^k}
\underbrace{\begin{bmatrix} u' + \theta_z \\ v' \\ w' - \theta_x \\ \theta_x' \\ \theta_y' \\ \theta_z' \end{bmatrix}^k}_{\epsilon^k}
\Rightarrow
$$

$$
\underbrace{\begin{bmatrix} F_x \\ F_y \\ F_z \\ M_x \\ M_y \\ M_x \end{bmatrix}^k}
=
\underbrace{\begin{bmatrix} K_{xx}^A & K_{xy}^A & K_{xz}^A & K_{xx}^B & K_{xy}^B & K_{xz}^B \\ & K_{yy}^A & K_{yz}^A & K_{yx}^B & K_{yy}^B & K_{yz}^B \\ & & K_{zz}^A & K_{zx}^B & K_{zy}^B & K_{zz}^B \\ & sym. & & K_{xx}^C & K_{xy}^C & K_{xz}^C \\ & & & & K_{yy}^C & K_{yz}^C \\ & & & & & K_{zz}^C \end{bmatrix}^k}_{\mathbf{K}_1^k = \mathbf{K}^k}
\underbrace{\begin{bmatrix} u' \\ v' \\ w' \\ \theta_x' \\ \theta_y' \\ \theta_z' \end{bmatrix}^k}_{\mathbf{u'}^k}
+
\underbrace{\begin{bmatrix} 0 & 0 & 0 & -K_{xz}^A & 0 & K_{xx}^A \\ 0 & 0 & 0 & -K_{yz}^A & 0 & K_{xy}^A \\ 0 & 0 & 0 & -K_{zz}^A & 0 & K_{xz}^A \\ 0 & 0 & 0 & -K_{zx}^B & 0 & K_{xx}^B \\ 0 & 0 & 0 & -K_{yz}^B & 0 & K_{xy}^B \\ 0 & 0 & 0 & -K_{xz}^B & 0 & K_{xz}^B \end{bmatrix}^k}_{\mathbf{K}_2^k}
\underbrace{\begin{bmatrix} u \\ v \\ w \\ \theta_x \\ \theta_y \\ \theta_z \end{bmatrix}^k}_{\mathbf{u}^k}
\Rightarrow
$$

$$\mathbf{F}^k = \mathbf{K}_1^k \mathbf{u'}^k + \mathbf{K}_2^k \mathbf{u}^k \tag{2.5}$$

$\mathbf{K}^k$ is the sectional Timoshenko full stiffness matrix.

With respect to a standard Timoshenko beam approach the elements K_{xx}^A and K_{zz}^A signify transverse shear rigidity, K_{yy}^A axial stiffness, K_{xx}^C and K_{zz}^C flexural stiffness in flap–wise and edge–wise directions respectively and K_{yy}^C torsional stiffness. The off–diagonal elements K_{xy}^C and K_{yz}^C signify bend–twist coupling.

By substituting equation (2.5) into equation (2.3) the dynamic equations are expressed with respect to the local deflections dofs in the form:

$$\int_A \rho \mathbf{S}^T \mathbf{T}^{k^T} \ddot{\mathbf{r}}_G^k dA = \left(\mathbf{K}_1^k \mathbf{u'}^k\right)' + \left(\mathbf{K}_2^k \mathbf{u}^k\right)' + \left(\mathbf{K}_3^k \mathbf{u'}^k\right) + \left(\mathbf{K}_4^k \mathbf{u}^k\right) + external\ loads \tag{2.6}$$

where,

$$\mathbf{K}_3^k = \begin{bmatrix} 0 & 0 & 0 & 0 & 0 & 0 \\ 0 & 0 & 0 & 0 & 0 & 0 \\ 0 & 0 & 0 & 0 & 0 & 0 \\ K_{xz}^A & K_{yz}^A & K_{zz}^A - F_y & K_{zx}^B & K_{zy}^B & K_{zz}^B \\ 0 & 0 & 0 & 0 & 0 & 0 \\ -K_{xx}^A + F_y & -K_{xy}^A & -K_{xz}^A & -K_{xx}^B & -K_{xy}^B & -K_{xz}^B \end{bmatrix}^k$$

$$\mathbf{K}_4^k = \begin{bmatrix} 0 & 0 & 0 & 0 & 0 & 0 \\ 0 & 0 & 0 & 0 & 0 & 0 \\ 0 & 0 & 0 & 0 & 0 & 0 \\ 0 & 0 & 0 & -K_{zz}^A & 0 & K_{xz}^A \\ 0 & 0 & 0 & 0 & 0 & 0 \\ 0 & 0 & 0 & K_{xz}^A & 0 & -K_{xx}^A \end{bmatrix}^k$$

For uniform/isotropic material beams, matrices $\mathbf{K}_1^k$, $\mathbf{K}_2^k$, $\mathbf{K}_3^k$, $\mathbf{K}_4^k$ take the form:

$$\mathbf{K}_1^k = \begin{bmatrix} G_x A & 0 & 0 & 0 & G_x Ax & 0 \\ 0 & EA & 0 & -EAx & 0 & EAz \\ 0 & 0 & G_z A & 0 & -G_z Az & 0 \\ 0 & -EAx & 0 & EIxx & 0 & -EIxz \\ G_x Ax & 0 & -G_z Az & 0 & GIt & 0 \\ 0 & EAz & 0 & -EIxz & 0 & EIzz \end{bmatrix}^k \tag{2.7}$$

$$\mathbf{K}_2^k = \begin{bmatrix} 0 & 0 & 0 & 0 & 0 & G_x A \\ 0 & 0 & 0 & 0 & 0 & 0 \\ 0 & 0 & 0 & -G_z A & 0 & 0 \\ 0 & 0 & 0 & 0 & 0 & 0 \\ 0 & 0 & 0 & G_z Az & 0 & G_x Ax \\ 0 & 0 & 0 & 0 & 0 & 0 \end{bmatrix}^k \tag{2.8}$$

$$\mathbf{K}_3^k = \begin{bmatrix} 0 & 0 & 0 & 0 & 0 & 0 \\ 0 & 0 & 0 & 0 & 0 & 0 \\ 0 & 0 & 0 & 0 & 0 & 0 \\ 0 & 0 & G_z A - F_y & 0 & -G_z Az & 0 \\ 0 & 0 & 0 & 0 & 0 & 0 \\ -G_x A + F_y & 0 & 0 & 0 & -G_x Ax & 0 \end{bmatrix}^k \tag{2.9}$$

$$\mathbf{K}_4^k = \begin{bmatrix} 0 & 0 & 0 & 0 & 0 & 0 \\ 0 & 0 & 0 & 0 & 0 & 0 \\ 0 & 0 & 0 & 0 & 0 & 0 \\ 0 & 0 & 0 & -G_z A & 0 & 0 \\ 0 & 0 & 0 & 0 & 0 & 0 \\ 0 & 0 & 0 & 0 & 0 & -G_x A \end{bmatrix}^k \tag{2.10}$$

where

$$EIxx = \int_A Ez^2 \, dA, \quad EIzz = \int_A Ex^2 \, dA, \quad EIxz = \int_A Exz \, dA$$

$$EA = \int_A E \, dA, \quad EAx = \int_A Ez \, dA, \quad EAz = \int_A Ex \, dA$$

$$G_x A = \kappa_x \int_A G \, dA, \quad G_z A = \kappa_z \int_A G \, dA$$

$$G_x Ax = \kappa_x \int_A Gz \, dA, \quad G_z Az = \kappa_z \int_A Gx \, dA, \quad GIt = \int_A \left(\kappa_x Gz^2 + \kappa_z Gx^2 \right) dA$$

κ_x and κ_z are the shear correction factors that depend on the direction of the cross–section. In *GIt* calculation warping is neglected.

2.1.2.2 FEM approximation of the beam dynamic equations

By applying the principle of virtual work, equation (2.6) takes its weak form:

$$\int_L \delta \mathbf{u}^{kT} \left[\int_A \rho \mathbf{S}^T \mathbf{T}^{kT} \ddot{\mathbf{r}}_G^k \, dA \right] dy = \int_L \delta \mathbf{u}^{kT} \left(\mathbf{K}_1^k \mathbf{u}'^k \right)' dy + \int_L \delta \mathbf{u}^{kT} \left(\mathbf{K}_2^k \mathbf{u}^k \right)' dy$$

$$+ \int_L \delta \mathbf{u}^{kT} \left(\mathbf{K}_3^k \mathbf{u}'^k \right) dy + \int_L \delta \mathbf{u}^{kT} \left(\mathbf{K}_4^k \mathbf{u}^k \right) dy$$

$$+ \ work \ of \ external \ loads \Rightarrow$$

$$\int_L \delta \mathbf{u}^{kT} \left[\int_A \rho \mathbf{S}^T \mathbf{T}^{kT} \ddot{\mathbf{r}}_G^k \, dA \right] dy = \underbrace{\left[\delta \mathbf{u}^{kT} \left(\mathbf{K}_1^k \mathbf{u}'^k \right) \right]_0^L + \left[\delta \mathbf{u}^{kT} \left(\mathbf{K}_2^k \mathbf{u}^k \right) \right]_0^L}_{\text{boundary terms}}$$

$$- \int_L \delta \mathbf{u}'^{kT} \left(\mathbf{K}_1^k \mathbf{u}'^k \right) dy - \int_L \delta \mathbf{u}'^{kT} \left(\mathbf{K}_2^k \mathbf{u}^k \right) dy$$

$$+ \int_L \delta \mathbf{u}^{kT} \left(\mathbf{K}_3^k \mathbf{u}'^k \right) dy + \int_L \delta \mathbf{u}^{kT} \left(\mathbf{K}_4^k \mathbf{u}^k \right) dy$$

$$+ \ work \ of \ external \ loads \Rightarrow$$

$$\int_L \delta \mathbf{u}^{kT} \left[\int_A \rho \mathbf{S}^T \mathbf{T}^{kT} \ddot{\mathbf{r}}_G^k \, dA \right] dy = - \int_L \delta \mathbf{u}'^{kT} \left(\mathbf{K}_1^k \mathbf{u}'^k \right) dy - \int_L \delta \mathbf{u}'^{kT} \left(\mathbf{K}_2^k \mathbf{u}^k \right) dy$$

$$+ \int_L \delta \mathbf{u}^{kT} \left(\mathbf{K}_3^k \mathbf{u}'^k \right) dy + \int_L \delta \mathbf{u}^{kT} \left(\mathbf{K}_4^k \mathbf{u}^k \right) dy \qquad (2.11)$$

$$+ \ work \ of \ external \ loads + boundary \ terms$$

The boundary terms represent the virtual work done by the reacting forces and moments at the support points (edges) of the beam. If a kinematic condition is specified there, then the virtual term vanishes ($\delta \mathbf{u}^{kT} = 0$), because there is no admissible displacement. On the contrary, if a dynamic condition is specified (communication of force/moment from a connected body) then the work done by the reaction load is added (as indicated in equation (2.11) through the boundary terms).

The local deflections along every element (of length L_e) of the beam are approximated through discrete dofs $\hat{\mathbf{u}}$ at the nodes of the finite element:

$$\mathbf{u}(y, t) = \mathbf{N}(y) \, \hat{\mathbf{u}}(t) \qquad (2.12)$$

where $\mathbf{N}$ is the shape function matrix of the element. 1st order shape functions are used for tension and torsion, and modified C^1 Hermitian functions for the two bending displacements [108] that prevent shear locking effect [109] (by satisfying static equilibrium compatibility relations for a Timoshenko beam with uniform properties).

In equation (2.12),

$$\hat{\mathbf{u}}\left(t\right) = \left(u^1, v^1, w^1, \theta_x^1, \theta_y^1, \theta_z^1, u^2, v^2, w^2, \theta_x^2, \theta_y^2, \theta_z^2\right)^T$$

where ^{1} and ^{2} indicate the first and the second node of the element respectively and

$$\mathbf{N}\left(y\right) = \begin{bmatrix} N_{1u}^1 & 0 & 0 & 0 & 0 & N_{2u}^1 & N_{1u}^2 & 0 & 0 & 0 & 0 & N_{2u}^2 \\ 0 & N_v^1 & 0 & 0 & 0 & 0 & 0 & N_v^2 & 0 & 0 & 0 & 0 \\ 0 & 0 & N_{1w}^1 & N_{2w}^1 & 0 & 0 & 0 & 0 & N_{1w}^2 & N_{2w}^2 & 0 & 0 \\ 0 & 0 & N_{1\theta_x}^1 & N_{2\theta_x}^1 & 0 & 0 & 0 & 0 & N_{1\theta_x}^2 & N_{2\theta_x}^2 & 0 & 0 \\ 0 & 0 & 0 & 0 & N_{\theta_y}^1 & 0 & 0 & 0 & 0 & 0 & N_{\theta_y}^2 & 0 \\ N_{1\theta_z}^1 & 0 & 0 & 0 & 0 & N_{2\theta_z}^1 & N_{1\theta_z}^2 & 0 & 0 & 0 & 0 & N_{2\theta_z}^2 \end{bmatrix}$$

$$N_v^1(\xi) = N_{\theta_y}^1(\xi) = 1 - \xi$$

$$N_v^2(\xi) = N_{\theta_y}^2(\xi) = \xi$$

$$N_{1u,w}^1(\xi) = 1 - \xi\Phi_{x,z1} - 3\xi^2\Phi_{x,z2} + 2\xi^3\Phi_{x,z2}$$

$$N_{1u,w}^2(\xi) = 1 - N_{1u,w}^1(\xi)$$

$$N_{2u,w}^1(\xi) = \left(-\xi + 0.5\xi\Phi_{x,z1} + 0.5\xi^2\Phi_{x,z1} + 2\xi^2\Phi_{x,z2} - \xi^3\Phi_{x,z2}\right)L_e$$

$$N_{2u,w}^2(\xi) = \left(0.5\xi\Phi_{x,z1} - 0.5\xi^2\Phi_{x,z1} + \xi^2\Phi_{x,z2} - \xi^3\Phi_{x,z2}\right)L_e$$

$$N_{1\theta_z,\theta_x}^1(\xi) = 6\xi(1 - \xi)\Phi_{x,z1}/L_e$$

$$N_{1\theta_z,\theta_x}^2(\xi) = -N_{1\theta_z,\theta_x}^1(\xi)$$

$$N_{2\theta_z,\theta_x}^1(\xi) = 1 - \xi\Phi_{x,z1} + \xi(-4 + 3\xi)\Phi_{x,z1}$$

$$N_{2\theta_z,\theta_x}^2(\xi) = -\xi\Phi_{x,z1} + \xi(-2 + 3\xi)\Phi_{x,z1}$$

where v and θ_y indicate tension and torsion respectively, u and w indicate bending displacements in x and z axes respectively, and θ_z and θ_x are the corresponding bending angles. $\xi = y/L_e \; \epsilon \; [0,1]$ and

$$\Phi_{x,z1} = \frac{\phi_{x,z}}{1 + \phi_{x,z}}, \quad \Phi_{x,z2} = \frac{1}{1 + \phi_{x,z}}, \quad \phi_{x,z} = \frac{12\overline{EIzz,xx}}{\overline{G_{x,z}A}L_e^2}$$

where $\overline{EIzz,xx}$, $\overline{G_{x,z}A}$ are the average bending stiffness and shear rigidity over the element in x or z directions.

2.1.2.3 Linearization of the beam dynamic equations

Non–linear equations (2.11) are linearized and written in perturbed (Δ) form with respect to a reference (steady state, periodic state or intermediate solution) denoted by the superscript 0. It is thereby assumed that:

$$\mathbf{q}^k = \mathbf{q}^{k^0} + \Delta\mathbf{q}^k, \ \dot{\mathbf{q}}^k = \dot{\mathbf{q}}^{k^0} + \Delta\dot{\mathbf{q}}^k, \ \ddot{\mathbf{q}}^k = \ddot{\mathbf{q}}^{k^0} + \Delta\ddot{\mathbf{q}}^k$$

$$\mathbf{u}^k = \mathbf{u}^{k^0} + \Delta\mathbf{u}^k, \ \dot{\mathbf{u}}^k = \dot{\mathbf{u}}^{k^0} + \Delta\dot{\mathbf{u}}^k, \ \ddot{\mathbf{u}}^k = \ddot{\mathbf{u}}^{k^0} + \Delta\ddot{\mathbf{u}}^k$$

By keeping the 1st order terms in equations (2.4), the following approximations are introduced:

$$\mathbf{T}^{k^T}\ddot{\mathbf{R}}^k = \left(\mathbf{T}^{k^T}\ddot{\mathbf{R}}^k\right)^0 + \partial_{\mathbf{q}}\left(\mathbf{T}^{k^T}\ddot{\mathbf{R}}^k\right)^0\Delta\mathbf{q}^k + \partial_{\dot{\mathbf{q}}}\left(\mathbf{T}^{k^T}\ddot{\mathbf{R}}^k\right)^0\Delta\dot{\mathbf{q}}^k + \partial_{\ddot{\mathbf{q}}}\left(\mathbf{T}^{k^T}\ddot{\mathbf{R}}^k\right)^0\Delta\ddot{\mathbf{q}}^k$$

$$\mathbf{T}^{k^T}\dot{\mathbf{T}}^k = \left(\mathbf{T}^{k^T}\dot{\mathbf{T}}^k\right)^0 + \partial_{\mathbf{q}}\left(\mathbf{T}^{k^T}\dot{\mathbf{T}}^k\right)^0\Delta\mathbf{q}^k + \partial_{\dot{\mathbf{q}}}\left(\mathbf{T}^{k^T}\dot{\mathbf{T}}^k\right)^0\Delta\dot{\mathbf{q}}^k \qquad (2.13)$$

$$\mathbf{T}^{k^T}\ddot{\mathbf{T}}^k = \left(\mathbf{T}^{k^T}\ddot{\mathbf{T}}^k\right)^0 + \partial_{\mathbf{q}}\left(\mathbf{T}^{k^T}\ddot{\mathbf{T}}^k\right)^0\Delta\mathbf{q}^k + \partial_{\dot{\mathbf{q}}}\left(\mathbf{T}^{k^T}\ddot{\mathbf{T}}^k\right)^0\Delta\dot{\mathbf{q}}^k + \partial_{\ddot{\mathbf{q}}}\left(\mathbf{T}^{k^T}\ddot{\mathbf{T}}^k\right)^0\Delta\ddot{\mathbf{q}}^k$$

where $\partial_{\mathbf{q}}$, $\partial_{\dot{\mathbf{q}}}$ and $\partial_{\ddot{\mathbf{q}}}$ are the derivatives with respect to the kinematic degrees of freedom $\mathbf{q}$, $\dot{\mathbf{q}}$ and $\ddot{\mathbf{q}}$ respectively.

By combining equations (2.11), (2.12) and (2.13) and by eliminating the virtual displacements $\delta\hat{\mathbf{u}}^T$, the linearized dynamic equations of a finite element can be written in the following matrix form:

$$\mathbf{M}_e^a\Delta\ddot{\mathbf{u}} + \mathbf{C}_e^a\Delta\dot{\mathbf{u}} + \mathbf{K}_e^a\Delta\mathbf{u} + \mathbf{M}_e^q\Delta\ddot{\mathbf{q}} + \mathbf{C}_e^q\Delta\dot{\mathbf{q}} + \mathbf{K}_e^q\Delta\mathbf{q} = \mathbf{Q}_e \qquad (2.14)$$

where the local linearized mass, damping and stiffness matrices of every FEM element along the beam are expressed as follows:

$$\mathbf{M}_e^a = \int_{L_e}\left(\mathbf{N}^T\left(\int_A \rho\mathbf{S}^T\mathbf{S}dA\right)\mathbf{N}\right)dy$$

$$\mathbf{C}_e^a = \int_{L_e}\left(\mathbf{N}^T\left(\int_A \rho\mathbf{S}^T 2\left(\mathbf{T}^{k^T}\dot{\mathbf{T}}^k\right)^0\mathbf{S}dA\right)\mathbf{N}\right)dy$$

$$\mathbf{K}_e^a = \int_{L_e}\left(\mathbf{N}^T\left(\int_A \rho\mathbf{S}^T\left(\mathbf{T}^{k^T}\ddot{\mathbf{T}}^k\right)^0\mathbf{S}dA\right)\mathbf{N}\right)dy$$

$$+ \int_{L_e}\left(\mathbf{N}'^T\mathbf{K}_1\mathbf{N}'\right)dy + \int_{L_e}\left(\mathbf{N}'^T\mathbf{K}_2\mathbf{N}\right)dy - \int_{L_e}\left(\mathbf{N}^T\mathbf{K}_3\mathbf{N}'\right)dy - \int_{L_e}\left(\mathbf{N}^T\mathbf{K}_4\mathbf{N}\right)dy$$

$$\mathbf{M}_e^q = \int_{L_e}\left(\int_A \rho\mathbf{N}^T\mathbf{S}^T\partial_{\ddot{\mathbf{q}}}\left(\mathbf{T}^{k^T}\ddot{\mathbf{R}}^k\right)^0 dA\right)dy + \int_{L_e}\left(\int_A \rho\mathbf{N}^T\mathbf{S}^T\partial_{\ddot{\mathbf{q}}}\left(\mathbf{T}^{k^T}\ddot{\mathbf{T}}^k\right)^0\left(\mathbf{r}_L^k + \mathbf{S}\mathbf{u}^{k^0}\right)dA\right)dy$$

$$\mathbf{C}_e^q = \int_{L_e}\left(\int_A \rho\mathbf{N}^T\mathbf{S}^T\partial_{\dot{\mathbf{q}}}\left(\mathbf{T}^{k^T}\ddot{\mathbf{R}}^k\right)^0 dA\right)dy + \int_{L_e}\left(\int_A \rho\mathbf{N}^T\mathbf{S}^T\partial_{\dot{\mathbf{q}}}\left(\mathbf{T}^{k^T}\ddot{\mathbf{T}}^k\right)^0\left(\mathbf{r}_L^k + \mathbf{S}\mathbf{u}^{k^0}\right)dA\right)dy$$

$$+ \int_{L_e}\left(\int_A \rho\mathbf{N}^T\mathbf{S}^T 2\partial_{\dot{\mathbf{q}}}\left(\mathbf{T}^{k^T}\dot{\mathbf{T}}^k\right)^0\left(\mathbf{S}\dot{\mathbf{u}}^{k^0}\right)dA\right)dy$$

$$\mathbf{K}_e^q = \int_{L_e} \left(\int_A \rho \mathbf{N}^T \mathbf{S}^T \partial_\mathbf{q} \left(\mathbf{T}^{k\,T} \ddot{\mathbf{R}}^k \right)^0 dA \right) dy + \int_{L_e} \left(\int_A \rho \mathbf{N}^T \mathbf{S}^T \partial_\mathbf{q} \left(\mathbf{T}^{k\,T} \ddot{\mathbf{T}}^k \right)^0 \left(\mathbf{r}_L^k + \mathbf{S}\mathbf{u}^{k0} \right) dA \right) dy$$

$$+ \int_{L_e} \left(\int_A \rho \mathbf{N}^T \mathbf{S}^T 2\partial_\mathbf{q} \left(\mathbf{T}^{k\,T} \dot{\mathbf{T}}^k \right)^0 \left(\mathbf{S}\dot{\mathbf{u}}^{k0} \right) dA \right) dy - \int_{L_e} \left(\mathbf{N}^T \partial_\mathbf{q} \left(\mathbf{T}^{k\,T} \right)^0 \mathbf{F}_{ext} \right) dy$$

$$\mathbf{Q}_e = + \int_{L_e} \left(\mathbf{N}^T \left(\mathbf{T}^{k\,T} \right)^0 \mathbf{F}_{ext} \right) dy$$

$$- \int_{L_e} \left(\int_A \rho \mathbf{N}^T \mathbf{S}^T \left(\mathbf{T}^{k\,T} \ddot{\mathbf{R}}^k \right)^0 dA \right) dy - \int_{L_e} \left(\int_A \rho \mathbf{N}^T \mathbf{S}^T \left(\mathbf{T}^{k\,T} \ddot{\mathbf{T}}^k \right)^0 \left(\mathbf{r}_L^k + \mathbf{S}\mathbf{u}^{k0} \right) dA \right) dy$$

$$- \int_{L_e} \left(\int_A \rho \mathbf{N}^T \mathbf{S}^T 2 \left(\mathbf{T}^{k\,T} \dot{\mathbf{T}}^k \right)^0 \left(\mathbf{S}\dot{\mathbf{u}}^{k0} \right) dA \right) dy - \int_{L_e} \left(\int_A \rho \mathbf{N}^T \mathbf{S}^T \left(\mathbf{S}\ddot{\mathbf{u}}^{k0} \right) dA \right) dy$$

$$- \int_{L_e} \left(\mathbf{N}'^T \mathbf{K}_1 \mathbf{N}' \mathbf{u}^{k0} \right) dy - \int_{L_e} \left(\mathbf{N}'^T \mathbf{K}_2 \mathbf{N} \mathbf{u}^{k0} \right) dy + \int_{L_e} \left(\mathbf{N}^T \mathbf{K}_3 \mathbf{N}' \mathbf{u}^{k0} \right) dy + \int_{L_e} \left(\mathbf{N}^T \mathbf{K}_4 \mathbf{N} \mathbf{u}^{k0} \right) dy$$

where $\mathbf{F}_{ext}$ are the external loads of the finite element, which are dependent on the reference state $\mathbf{q}^{k0}$ and $\mathbf{u}^{k0}$.

By directly assembling the local matrices over the successive finite elements of a beam, the dynamic system of a single beam takes the form of Figure 2.7. This procedure is valid, because the beams are assumed to be rectilinear and thus they have the same orientation with their finite elements. Otherwise, the local matrices of a finite element e should be pre–multiplied by $\mathbf{T}^{k\,T}\mathbf{T}^e$ and post–multiplied by $\mathbf{T}^{e\,T}\mathbf{T}^k$ in order to be expressed into the local co–ordinate system of the beam that the element belongs to, where $\mathbf{T}^e$ denotes the rotation matrix of the finite element e and $\mathbf{T}^k$ the rotation matrix of its beam k. It is also noted that the boundary terms between adjacent elements (representing internal reaction loads) will counteract each other. So, the only boundary terms that remain are those of the first and the last node of the beam. When the end of the beam is a free–end (e.g. blade tip) reactions will be equal to zero since free–ends are load free. At the first node, deflections are usually constrained (Dirichlet condition is applied) and, therefore, boundary terms also vanish. In cases that the beam is connected to some other body, reaction loads from the adjacent body should be communicated. Such boundary reaction loads are equivalent to external loading terms and are included to the external loading terms that depend on the dofs of this other sub–body. They also contribute in $\mathbf{M}$, $\mathbf{C}$ and $\mathbf{K}$ matrices, as is shown in the following section.

The global $\mathbf{M}$, $\mathbf{C}$, $\mathbf{K}$ and $\mathbf{Q}$ matrices of the complete dynamic system consisting of an assembly of sub–bodies (which are not yet connected to each other – see next section for the definition of constraint equations), takes the form of Figure 2.8. It is noted that when assembling the matrices of the full dynamic system, $\mathbf{q}_0^k$ dofs of every sub–body are grouped together with its local deflection dofs $\mathbf{u}^k$ while the global $\mathbf{q}^k$ dofs are placed at the bottom of the vector of the unknowns. Separate equations must be defined for every time dependent $\mathbf{q}^k$ dof. In the example of the Figure 2.8 two non–connected sub–bodies are considered.
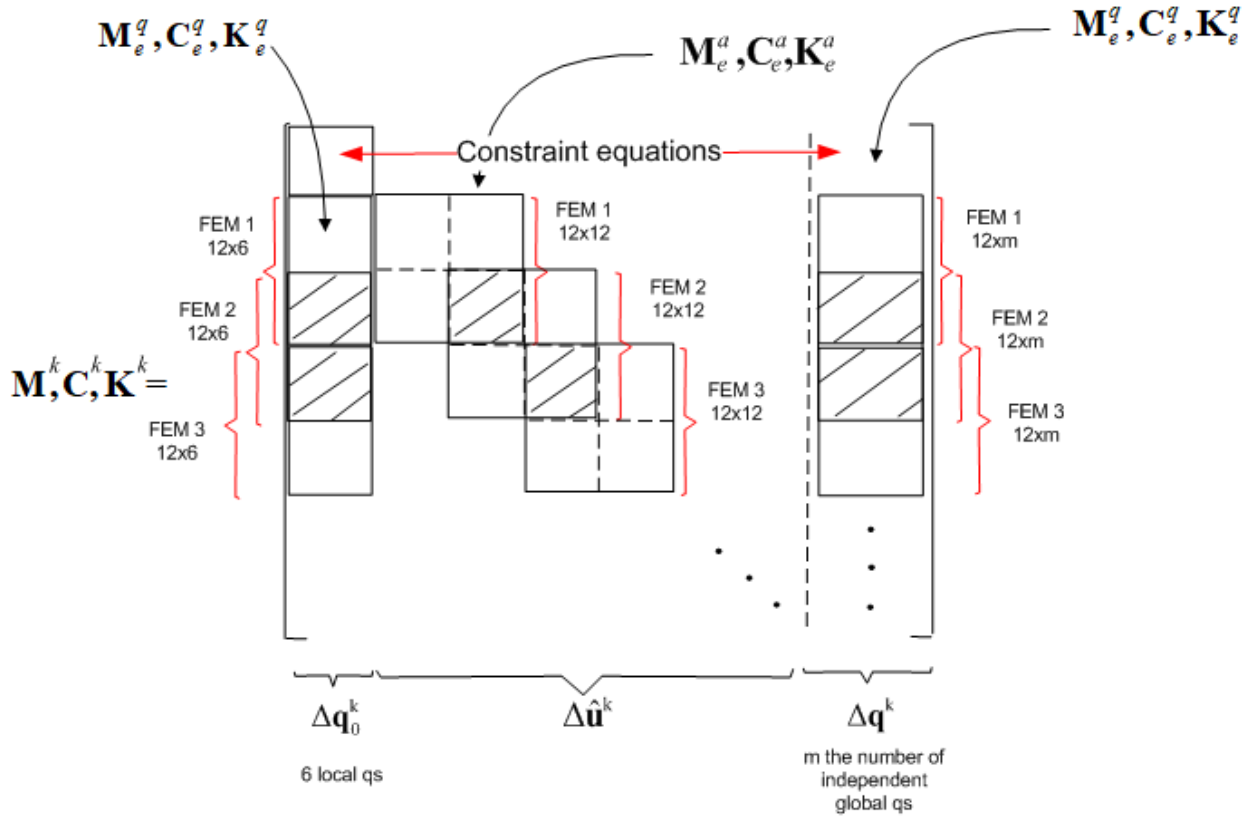
Figure 2.7. *System form for a single beam. By assuming the beam to be rectilinear, its matrices are created by directly assembling the local matrices of its successive finite elements.*
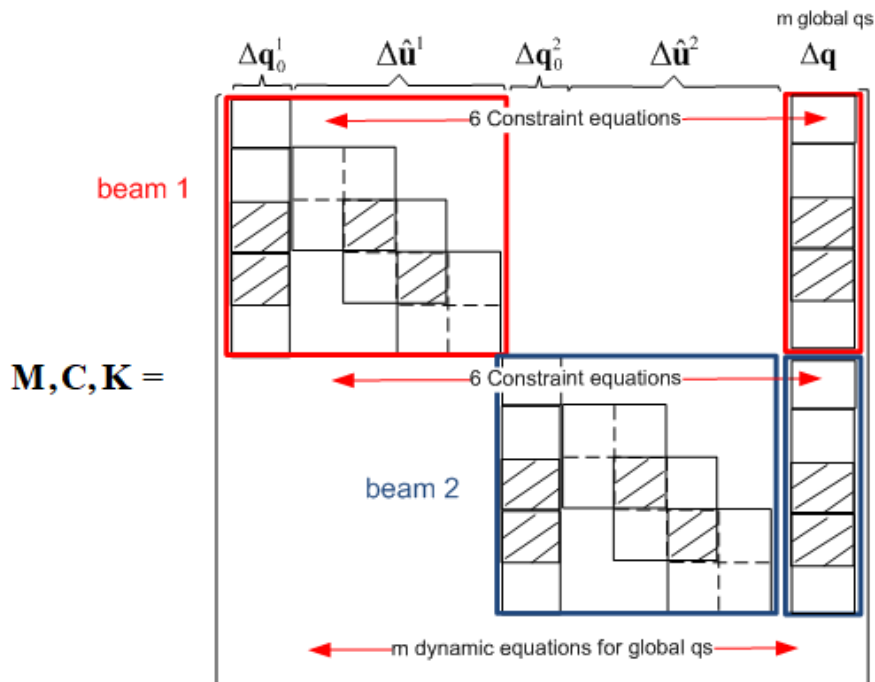
Figure 2.8. *System form for two non-connected beams.* $\mathbf{q}_0^k$ *dofs of every beam are grouped together with its local deflection dofs* $\mathbf{u}^k$*, while the global* $\mathbf{q}^k$ *dofs are placed at the bottom of the vector of the unknowns.*

2.1.3 Multi–body constraint equations

The closure of equation (2.11) is accomplished by defining the work of the external loads (this is carried out through the coupling of the structural dynamics solver with an aerodynamic one) and the boundary terms $\left[\delta\mathbf{u}^{kT}\left(\mathbf{K}_1^k\mathbf{u}'^k + \mathbf{K}_2^k\mathbf{u}^k\right)\right]_0^L$ at the root ($y = 0$) and the tip ($y = L$) of every sub–body. Boundary conditions can be divided into two categories; kinematic and dynamic conditions. Kinematic conditions are usually expressed in Dirichlet form. In that case, there is no admissible displacement for this FEM node $\left(\delta\mathbf{u}^{kT} = 0\right)$, equation (2.11) degenerates into a trivial one $\mathbf{0} = \mathbf{0}$ and cannot be used in order to define the respective dofs. Instead, the position (displacement and/or rotation) of the node is specified through an appropriate compatibility equation, resulting in a Dirichlet condition for the corresponding dofs. Dynamic conditions are considered as external loads that need to be applied at either ends of the beam in order to maintain equilibrium. In most cases, the position of the root of the beam is constrained through a kinematic condition, whereas the loads at the tip are set to a specific value that may be either the sum of the reaction loads contributed by the connected beams, or zero if the tip is a free–end. This is usually true for single load–path structures (e.g. consecutive sub–bodies forming a non–linear blade), however it may not be the case in multiple load–path configurations.

2.1.3.1 Kinematic boundary conditions

For the simulation of a **stiff connection** between two beams r and m (see Figure 2.9), 3 translation and 3 rotation non–linear constraint equations are defined:

$$\mathbf{r}_G^m\,(P1 \text{ or } P2) - \mathbf{r}_G^r\,(P1 \text{ or } P2) - \mathbf{d}_0^{r,m} = \mathbf{0}$$
$$\boldsymbol{\theta}^{r,m} - \boldsymbol{\theta}_0^{r,m} = \mathbf{0} \tag{2.15}$$

where $\mathbf{d}_0^{r,m}$, $\boldsymbol{\theta}_0^{r,m}$ is a vector, column matrix containing the relative distance, angle between the the local coordinate systems that are attached to the connected nodes (P1 or P2 of sub–body r and P1 or P2 of sub–body m). In the simple case of a straight beam consisting of two sub–bodies, $\mathbf{d}_0^{r,m}$ and $\boldsymbol{\theta}_0^{r,m}$ are set to zero.

The position of the connected nodes expressed in the global co–ordinate system (see Figure 2.9a) are given by:

$$\mathbf{r}_G^r = \mathbf{R}^r + \mathbf{T}^r\left[\mathbf{r}_L^r + \begin{pmatrix} u \\ v \\ w \end{pmatrix}^r\right]$$

$$\mathbf{r}_G^m = \mathbf{R}^m + \mathbf{T}^m\left[\mathbf{r}_L^m + \begin{pmatrix} u \\ v \\ w \end{pmatrix}^m\right] \tag{2.16}$$

$$\mathbf{d}_0^{r,m} = \mathbf{T}^r\left[\mathbf{d}_0^r + \begin{pmatrix} \theta_x \\ \theta_y \\ \theta_z \end{pmatrix}^r \times \mathbf{d}_0^r\right]$$

The term $\mathbf{Su}(t)$ of equation (2.1) results in $\begin{pmatrix} u \\ v \\ w \end{pmatrix}$, as the sub–bodies are assumed to be rectilinear and therefore $x_L = z_L = 0$ in equation (2.2) for all the nodes of a sub–body. The term $\begin{pmatrix} \theta_x \\ \theta_y \\ \theta_z \end{pmatrix}^r \times \mathbf{d}_0^r$ is added in $\mathbf{d}_0^{r,m}$ computation in order to ensure that the extra displacement due to the angular deformation of the connected node of sub–body r, will be taken into account when an initial offset $\mathbf{d}_0^r$ (computed in the initial undeformed state and expressed in the local co–ordinate system of sub–body r) is present.

The relative angles $\boldsymbol{\theta}^{r,m}$ with respect to the 3 local axes of sub–body r are given by [36]:

$$\cos \theta_i^{r,m} \left(\mathbf{e}_j^m \cdot \mathbf{e}_k^r \right) - \sin \theta_i^{r,m} \left(\mathbf{e}_k^m \cdot \mathbf{e}_k^r \right) = 0 \tag{2.17}$$

$$\begin{aligned} \cos \theta_i^{r,m} &= \left(\mathbf{e}_k^m \cdot \mathbf{e}_k^r \right) \\ \sin \theta_i^{r,m} &= \left(\mathbf{e}_j^m \cdot \mathbf{e}_k^r \right) \end{aligned} \tag{2.18}$$

where $\mathbf{e}_{i,j,k}^r$ and $\mathbf{e}_{i,j,k}^m$ are the two unit vector bases defining the local orientation of the connected nodes of the sub–bodies r and m respectively (see Figure 2.9b). So $\theta_i^{r,m}$ is the relative rotation about axis $\mathbf{e}_i^r$ of the local basis attached to the node of sub–body m with respect to the local basis attached to the node of sub–body r. No Einstein convention is used in equations (2.17) and (2.18) and thus repeated indices do not imply summation. It is noted that vectors $\mathbf{e}_{i,j,k}$ are formed by the columns of the rotation matrix $\mathbf{T}^n$ of the node, which is equal to the rotation matrix $\mathbf{T}$ of the sub–body it belongs to when referring to P1 or with $\mathbf{T}\mathbf{T}_L$ where

$$\mathbf{T}_L = \begin{bmatrix} 1 & -\theta_z(P2) & \theta_y(P2) \\ \theta_z(P2) & 1 & -\theta_x(P2) \\ -\theta_y(P2) & \theta_x(P2) & 1 \end{bmatrix}$$

when referring to P2. In the definition of $\mathbf{T}_L$ it is implied that local deflection angles at end node P2 are small. This is consistent with the linear Timoshenko beam theory applied to sub–bodies.

The angular constraint equations of (2.15) are valid only in cases where the relative rotations vanish in the reference configuration (initial undeformed state) [39]. In cases where the beams to be connected do not initially share the same orientation between their connection points, one or more angles $\theta_i^{r,m}$ are not properly defined. As a result, the corresponding constraint equations are not linearly independent from the rest. To overcome this problem, the local basis vectors of sub–body m are rotated by $\mathbf{T}^{mr}$. $\mathbf{T}^{mr}$ is a time invariant matrix that describes the rotation from the local co–ordinate system of sub–body m to the local co–ordinate system of sub–body r as defined in the initial undeformed state $\left(\mathbf{T}^{mr} = \mathbf{T}^{mT}(\mathbf{q}_0^m = \mathbf{0}, t = 0)\mathbf{T}^r(\mathbf{q}_0^r = \mathbf{0}, t = 0) \right)$. Consequently, the connection angles may be perceived as the difference in the relative rotation from the initial relative angles $\boldsymbol{\theta}_r^{r,m} = \boldsymbol{\theta}^{r,m} - \boldsymbol{\theta}_0^{r,m}$. For a stiff connection between two beams $\boldsymbol{\theta}_r^{r,m} = \mathbf{0}$ and as a result of

equation (2.17), the angular constraint equations defined in this way may be simplified in:

$$\theta_{ri}^{r,m} = 0 \Rightarrow \mathbf{e}_j^m \cdot \mathbf{e}_k^r = 0$$

where

$$\begin{bmatrix} \mathbf{e}_1^{r\,T} & \mathbf{e}_2^{r\,T} & \mathbf{e}_3^{r\,T} \end{bmatrix} = \begin{cases} \mathbf{T}^r, & \text{when referring to } P1 \\ \mathbf{T}^r \mathbf{T}_L^r, & \text{when referring to } P2 \end{cases}$$

$$\begin{bmatrix} \mathbf{e}_1^{mT} & \mathbf{e}_2^{mT} & \mathbf{e}_3^{mT} \end{bmatrix} = \begin{cases} \mathbf{T}^m \mathbf{T}^{mr}, & \text{when referring to } P1 \\ \mathbf{T}^m \mathbf{T}_L^m \mathbf{T}^{mr}, & \text{when referring to } P2 \end{cases}$$

Relative rotations and therefore constraint equations can be also applied with respect to a predefined arbitrary system as shown in Figure 2.9b, which is typically referred to as the *local co-ordinate system of the joint*. The rotation matrix of the joint $\mathbf{T}^j = \begin{bmatrix} \mathbf{e}_1^{j\,T} & \mathbf{e}_2^{j\,T} & \mathbf{e}_3^{j\,T} \end{bmatrix}$ may easily be defined as a time invariant rotation $\mathbf{T}^{rj}$ with respect to the local co–ordinate system of sub–body r: $\mathbf{T}^j = \mathbf{T}^r \mathbf{T}^{rj}$. Consequently the vectors $\mathbf{e}_i$ are formed by the columns of the rotation matrices $\mathbf{T}^n \mathbf{T}^{rj}$ of the nodes to be connected.

To sum up, the constraint equations for a stiff connection between two beams r and m expressed in the local co–ordinate system of the joint are defined as:

$$\mathbf{T}^{jT} \left[\mathbf{r}_G^m (P1 \text{ or } P2) - \mathbf{r}_G^r (P1 \text{ or } P2) - \mathbf{d}_0^{r,m} \right] = \mathbf{0}$$
$$\theta_{ri}^{r,m} = 0 \Rightarrow \mathbf{e}_j^m \cdot \mathbf{e}_k^r = 0$$

(2.19)

where

$$\mathbf{d}_0^{r,m} = \mathbf{T}^r \left[\mathbf{d}_0^r + \begin{pmatrix} \theta_x \\ \theta_y \\ \theta_z \end{pmatrix}^r \times \mathbf{d}_0^r \right]$$

$$\begin{bmatrix} \mathbf{e}_1^{r\,T} & \mathbf{e}_2^{r\,T} & \mathbf{e}_3^{r\,T} \end{bmatrix} = \begin{cases} \mathbf{T}^r \mathbf{T}^{rj}, & \text{when referring to } P1 \\ \mathbf{T}^r \mathbf{T}_L^r \mathbf{T}^{rj}, & \text{when referring to } P2 \end{cases}$$

$$\begin{bmatrix} \mathbf{e}_1^{mT} & \mathbf{e}_2^{mT} & \mathbf{e}_3^{mT} \end{bmatrix} = \begin{cases} \mathbf{T}^m \mathbf{T}^{mr} \mathbf{T}^{rj}, & \text{when referring to } P1 \\ \mathbf{T}^m \mathbf{T}_L^m \mathbf{T}^{mr} \mathbf{T}^{rj}, & \text{when referring to } P2 \end{cases}$$

(2.20)

$$\mathbf{T}_L = \begin{bmatrix} 1 & -\theta_z(P2) & \theta_y(P2) \\ \theta_z(P2) & 1 & -\theta_x(P2) \\ -\theta_y(P2) & \theta_x(P2) & 1 \end{bmatrix}$$

$$\mathbf{T}^{mr} = \mathbf{T}^{mT}(\mathbf{q}_0^m = \mathbf{0}, t = 0) \mathbf{T}^r(\mathbf{q}_0^r = \mathbf{0}, t = 0)$$

$$\mathbf{T}^{rj} = \mathbf{T}^{rT}(\mathbf{q}_0^r = \mathbf{0}, t = 0) \mathbf{T}^j(\mathbf{q}_0^r = \mathbf{0}, t = 0)$$
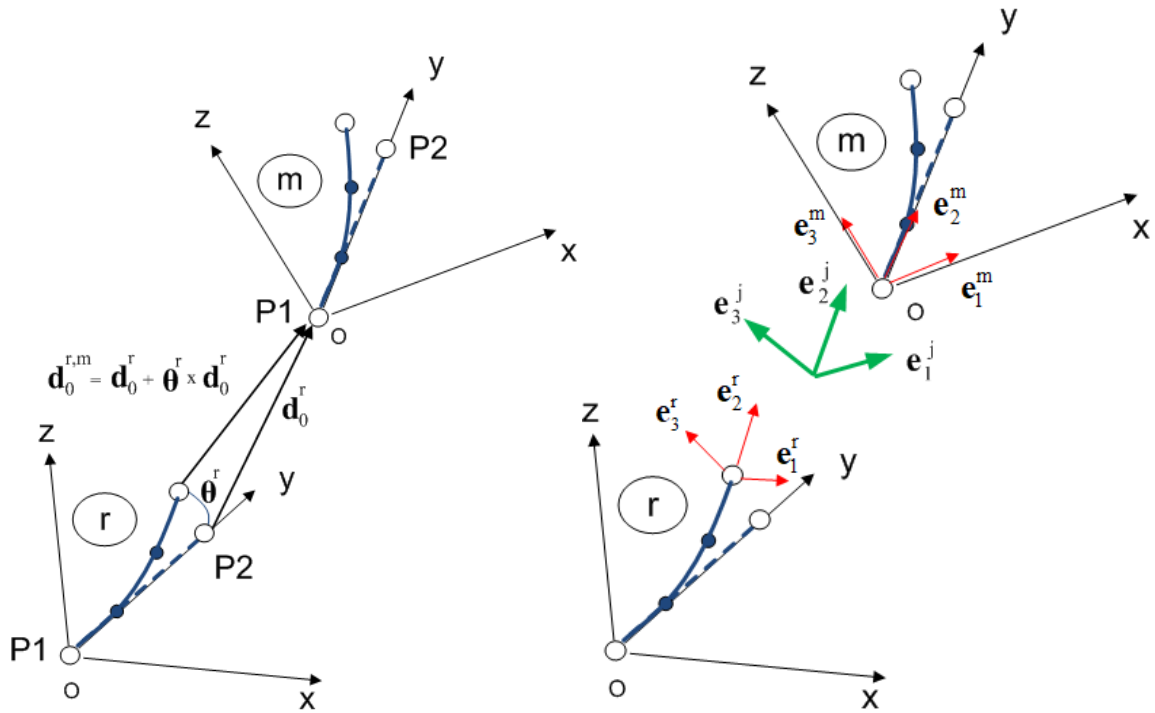
(a) *Definition of relative distance between two connected sub–bodies r and m. The relative distance needs to be retained in stiff connections.*

(b) *Definition of unit bases $\mathbf{e}_i^r$ and $\mathbf{e}_i^m$ of two connected sub–bodies r and m. The unit base $\mathbf{e}_i^j$ defines the local co–ordinate system of the joint, with respect to which the angular constraint equations are applied.*

Figure 2.9. *Basic definitions concerning the linear (a) and angular (b) constraint equations applied at the end nodes of two connected beams r and m.*

2.1.3.2 Dynamic boundary conditions

In a stiff connection, one sub–body defines the kinematics (in the example sub–body *r*) and the others provide **reaction loads** (see Figure 2.1). These reactions loads (3 forces and 3 moments) are applied as external point forces/moments to the node which defines the kinematics. The reaction loads $\mathbf{Q}^R = \left(\mathbf{F}^R, \mathbf{M}^R\right)^T$, where $\mathbf{F}^R = \left(F_x^R, F_y^R, F_z^R\right)^T$ and $\mathbf{M}^R = \left(M_x^R, M_y^R, M_z^R\right)^T$, at a connection point are obtained as the reaction loads of a FEM node 1 or 2 (1 indicating the start and 2 the end node of the finite element) and can be expressed as linear functions of the local deflection dofs $\hat{\mathbf{u}}$ of the element and the global and local $\mathbf{q}$ and $\mathbf{q}_0$ dofs respectively of the sub–body that the element belongs to. Consequently, based on equation (2.14), the reaction loads at the edges of a finite element can be computed as:

$$\begin{bmatrix} \mathbf{Q}^R(1) \\ \mathbf{Q}^R(2) \end{bmatrix} = \mathbf{M}_e^a \Delta \ddot{\mathbf{u}} + \mathbf{C}_e^a \Delta \dot{\mathbf{u}} + \mathbf{K}_e^a \Delta \mathbf{u} + \mathbf{M}_e^q \Delta \ddot{\mathbf{q}} + \mathbf{C}_e^q \Delta \dot{\mathbf{q}} + \mathbf{K}_e^q \Delta \mathbf{q} - \mathbf{Q}_e \qquad (2.21)$$

The first six rows $\mathbf{Q}^R(1)^T$ are the reaction loads (forces and moments) at the 1st node of the element, while the last six $\mathbf{Q}^R(2)^T$ are the reaction loads at the 2nd node. The reaction loads at the edges of the element represent the boundary terms that are eliminated when the element is connected to an adjacent one, or when the displacement of the node is

specified through a Dirichlet kinematic condition. Otherwise, if the loading is specified, then the reaction loads must equal this given value. It needs to be stressed that the loads $\mathbf{Q}^R$ are computed with respect to the local co–ordinate system of the sub–body that the element belongs to. So, in order to be transferred to another sub–body, they have to be rotated to its local co–ordinate system:

$$\mathbf{Q}^R(2)^r = -\mathbf{T}^{rT}\mathbf{T}^m\mathbf{Q}^R(1)^m \tag{2.22}$$

Based on the above, the global matrices $\mathbf{M}, \mathbf{C}, \mathbf{K}, \mathbf{Q}$ of Figure 2.8, take the form of Figure 2.10 for a stiff connection between two sub–bodies.
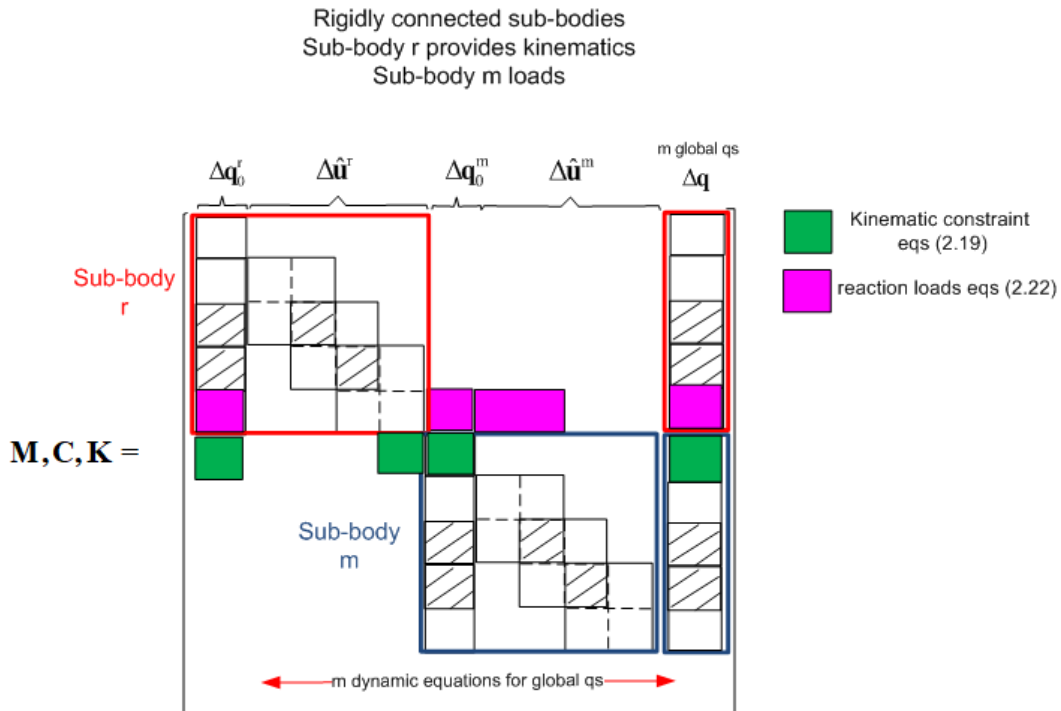
Figure 2.10. *System form for a stiff connection between sub–bodies r and m. Sub–body r defines the kinematics and sub–body m provides reaction loads.*

For the simulation of a **free or elastic connection** between two sub–bodies r and m (as shown in Figure 2.11), the position of the node that receives kinematics is defined by solving the dynamic conditions of a soft joint (linear/angular spring and/or damper):

$$\begin{aligned}
\mathbf{F}^R_{x,y,z} &= \mathbf{k}^t_{x,y,z}\left[\mathbf{T}^{jT}\left(\mathbf{r}^m_G - \mathbf{r}^r_G - \mathbf{d}^{r,m}_0\right)\right] + \mathbf{c}^t_{x,y,z}\left[\mathbf{T}^{jT}\left(\dot{\mathbf{r}}^m_G - \dot{\mathbf{r}}^r_G\right)\right] \\
\mathbf{M}^R_{x,y,z} &= \mathbf{k}^r_{x,y,z}\left[\boldsymbol{\theta}^{r,m}_r\right] + \mathbf{c}^r_{x,y,z}\left[\dot{\boldsymbol{\theta}}^{r,m}_r\right]
\end{aligned} \tag{2.23}$$

where $\mathbf{F}^R_{x,y,z}$, $\mathbf{M}^R_{x,y,z}$ are the reaction loads at the edges of the joint, $\mathbf{k}^t_{x,y,z}$, $\mathbf{c}^t_{x,y,z}$ are the linear and $\mathbf{k}^r_{x,y,z}$, $\mathbf{c}^r_{x,y,z}$ are the angular stiffness and damping properties of the joint, defined in its local co–ordinate system.

$\dot{\mathbf{r}}_G$ is given by equation (2.1), whereas the relative angular velocities $\dot{\boldsymbol{\theta}}^{r,m}_r$ expressed with respect the local co–ordinate system of the joint can be computed by differentiating

equation (2.17) in time and by exploiting equation (2.18):

$$\cos\theta_{ri}^{r,m}\left(\mathbf{e}_j^m\cdot\mathbf{e}_k^r\right)-\sin\theta_{ri}^{r,m}\left(\mathbf{e}_k^m\cdot\mathbf{e}_k^r\right)=0\Rightarrow$$

$$-\dot\theta_{ri}^{r,m}\sin\theta_{ri}^{r,m}\left(\mathbf{e}_j^m\cdot\mathbf{e}_k^r\right)+\cos\theta_{ri}^{r,m}\overline{\left(\mathbf{e}_j^m\cdot\mathbf{e}_k^r\right)}-\dot\theta_{ri}^{r,m}\cos\theta_{ri}^{r,m}\left(\mathbf{e}_k^m\cdot\mathbf{e}_k^r\right)-\sin\theta_{ri}^{r,m}\overline{\left(\mathbf{e}_k^m\cdot\mathbf{e}_k^r\right)}=0\Rightarrow$$

$$\dot\theta_{ri}^{r,m}\left[\sin\theta_{ri}^{r,m}\left(\mathbf{e}_j^m\cdot\mathbf{e}_k^r\right)+\cos\theta_{ri}^{r,m}\left(\mathbf{e}_k^m\cdot\mathbf{e}_k^r\right)\right]=\cos\theta_{ri}^{r,m}\overline{\left(\mathbf{e}_j^m\cdot\mathbf{e}_k^r\right)}-\sin\theta_{ri}^{r,m}\overline{\left(\mathbf{e}_k^m\cdot\mathbf{e}_k^r\right)}\Rightarrow$$

$$\dot\theta_{ri}^{r,m}\left[(\sin\theta_{ri}^{r,m})^2+(\cos\theta_{ri}^{r,m})^2\right]=\left(\mathbf{e}_k^m\cdot\mathbf{e}_k^r\right)\overline{\left(\mathbf{e}_j^m\cdot\mathbf{e}_k^r\right)}-\left(\mathbf{e}_j^m\cdot\mathbf{e}_k^r\right)\overline{\left(\mathbf{e}_k^m\cdot\mathbf{e}_k^r\right)}\Rightarrow$$

$$\dot\theta_{ri}^{r,m}=\left(\mathbf{e}_k^m\cdot\mathbf{e}_k^r\right)\overline{\left(\mathbf{e}_j^m\cdot\mathbf{e}_k^r\right)}-\left(\mathbf{e}_j^m\cdot\mathbf{e}_k^r\right)\overline{\left(\mathbf{e}_k^m\cdot\mathbf{e}_k^r\right)} \tag{2.24}$$

where

$$\begin{bmatrix}\dot{\mathbf{e}}_1^{r^T} & \dot{\mathbf{e}}_2^{r^T} & \dot{\mathbf{e}}_3^{r^T}\end{bmatrix}=\begin{cases}\dot{\mathbf{T}}^r\mathbf{T}^{rj}, & \text{when referring to } P1\\ \dot{\mathbf{T}}^r\mathbf{T}_L^r\mathbf{T}^{rj}+\mathbf{T}^r\dot{\mathbf{T}}_L^r\mathbf{T}^{rj}, & \text{when referring to } P2\end{cases}$$

$$\begin{bmatrix}\dot{\mathbf{e}}_1^{m^T} & \dot{\mathbf{e}}_2^{m^T} & \dot{\mathbf{e}}_3^{m^T}\end{bmatrix}=\begin{cases}\dot{\mathbf{T}}^m\mathbf{T}^{mr}\mathbf{T}^{rj}, & \text{when referring to } P1\\ \dot{\mathbf{T}}^m\mathbf{T}_L^m\mathbf{T}^{mr}\mathbf{T}^{rj}+\mathbf{T}^m\dot{\mathbf{T}}_L^m\mathbf{T}^{mr}\mathbf{T}^{rj}, & \text{when referring to } P2\end{cases} \tag{2.25}$$

$$\dot{\mathbf{T}}_L=\begin{bmatrix}0 & -\dot\theta_z(P2) & \dot\theta_y(P2)\\ \dot\theta_z(P2) & 0 & -\dot\theta_x(P2)\\ -\dot\theta_y(P2) & \dot\theta_x(P2) & 0\end{bmatrix}$$

As in the case of a stiff connection between two sub–bodies, the node that receives kinematics transfers its reaction loads to the node that provides kinematics according to equation (2.22).
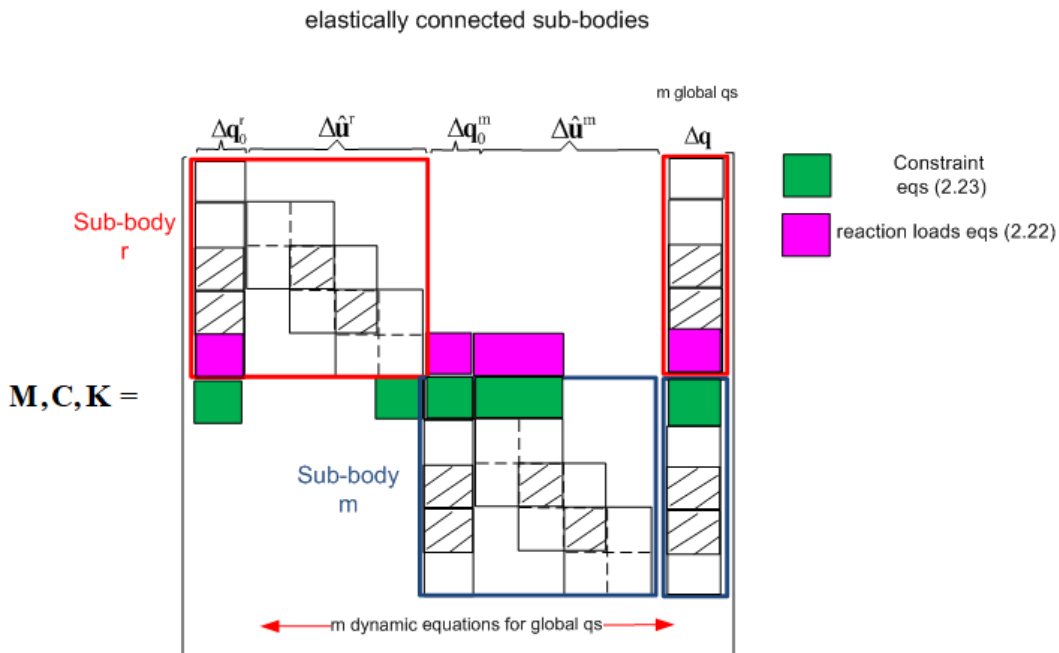
Figure 2.11. *System form for a free/elastic connection between sub-bodies r and m. Sub-body r defines the kinematics through dynamic conditions and sub-body m provides reaction loads.*

By choosing arbitrarily large values for $\mathbf{k}^t_{x,y,z}$ and $\mathbf{k}^r_{x,y,z}$ in equation (2.23), rigid connections between sub–bodies may be realized in a dynamic approach. In this way, a node receives kinematics without zeroing out its admissible displacement $\left(\delta\mathbf{u}^{k^T} \neq \mathbf{0}\right)$. Consequently, this node is also allowed to receive reaction loads. When equations (2.15) and (2.23) are satisfied on the same co–ordinate system, they can efficiently be combined, covering all possible assemblies of connected sub–bodies and realizing multiple load–path configurations.

Finally, it needs to be stressed that an important advantage of the herein presented multi–body approach compared to other similar implementations is that the dynamic equations, including those of constraints, are linearized allowing thus to perform eigenvalue stability analyses. The system of dynamic equations is provided in a linearized state space form.

2.2 Aerodynamic modelling

In the present section, the theoretical part of the various CFD based aerodynamic models that have been used in this study is presented. Details for the medium–fidelity Lifting Line (LL) model can be found in [110], and for the low–fidelity Blade Element Momentum Theory (BEMT) based aerodynamic model in [1, 2]. Both are used as an extra reference, additional to experimental data, in order to validate the higher–fidelity CFD models, as they are considered as state of the art in helicopter and Wind Turbine (WT) rotors design respectively.

2.2.1 The Eulerian CFD solver MaPFlow

The most accurate way to simulate flows in the presence of solid bodies, is to solve the Eulerian expression of the Navier–Stokes equations. This ensures that the boundary conditions on solid–wall boundaries are accurately satisfied. The main advantage of employing CFD in rotor analyses is related to its capability to account in maximum detail for viscous and compressible effects (flow separation, formation of boundary layers, shock waves). These are dominant in wind farm simulations, where rotor wake evolution has an impact on the performance of downwind turbines. Furthermore, viscous effects are important when studying the rotor wake interaction with the boundary layer developed on surrounding bodies, such as the WT tower or even the ground. Such interactions affect the rotor performance and the loading of the blades.

In this section, the basic concept and add–ons of MaPFlow, an in–house Eulerian CFD solver developed in [4], are described. MaPFlow solves the compressible Unsteady Reynolds Averaged Navier Stokes (URANS) equations under a cell-centered finite volume spatial discretization scheme. MaPFlow can handle both structured and unstructured grids; it is parallelized under the MPI protocol, and the grid partitioning is performed using the METIS library [111]. The convective fluxes are evaluated by solving the preconditioned local Riemann problem between the neighboring cells of each face, using the Roe's approximate Riemann solver [112] with the Venkatakrishnan limiter [113]. The viscous fluxes are discretized using a central 2nd order scheme. For the reconstruction of variables at the interface, a piecewise linear interpolation scheme is used. The evaluation of the spatial gradients of the primitive variables is done using the Green–Gauss formula, with a centered scheme approximation. Multiple options are available for turbulence modelling, such as the one-equation model of Spalart–Allmaras [114] or the two-equation model $k - \omega\ SST$ of Menter [115]. Regarding laminar to turbulent flow transition modelling, the $\gamma - Re_\theta$ model of Menter [116] is used. A Delayed Detached Eddy Simulation (DDES) approach is also implemented in MaPFlow, following the suggestions of [117]. Unsteady simulations are performed through an implicit 2nd order backwards difference scheme [118], along with a dual time-stepping technique [119] in order to facilitate convergence. Flows in the incompressible region are simulated using Low Mach Preconditioning [5]. Finally, the implicit operator inversion is accomplished with the use of the Gauss–Seidel iterative method alongside the reverse Cuthill–Mckee

reordering scheme [120].

2.2.1.1 Governing Equations and Implementation

Let D denote a volume of fluid and ∂D its boundary. By integrating the governing equations over D, the following integral form is obtained:

$$\frac{\partial}{\partial t} \int_D \mathbf{U} dD + \oint_{\partial D} (\mathbf{F_c} - \mathbf{F_v}) \, dS = \int_D \mathbf{Q} dD \tag{2.26}$$

In equation (2.26), $\vec{U}$ is the vector of the Conservative Flow Variables:

$$\mathbf{U} = \begin{pmatrix} \rho \\ \rho u \\ \rho v \\ \rho w \\ \rho E \end{pmatrix} \tag{2.27}$$

where ρ denotes density, (u, v, w) the three components of the velocity field and E the total energy, while $\mathbf{F_c}$ and $\mathbf{F_v}$ denote the Convective and Viscous Fluxes respectively:

$$\mathbf{F_c} = \begin{pmatrix} \rho V \\ \rho u V + n_x p \\ \rho v V + n_y p \\ \rho w V + n_z p \\ \rho(E + \frac{p}{\rho})V \end{pmatrix} \tag{2.28}$$

$$\mathbf{F_v} = \begin{pmatrix} 0 \\ n_x \tau_{xx} + n_y \tau_{xy} + n_z \tau_{xz} \\ n_x \tau_{yx} + n_y \tau_{yy} + n_z \tau_{yz} \\ n_x \tau_{zx} + n_y \tau_{zy} + n_z \tau_{zz} \\ n_x \Theta_x + n_y \Theta_y + n_z \partial_z \end{pmatrix} \tag{2.29}$$

In equations (2.28) and (2.29) $V = \mathbf{u} \cdot \mathbf{n}$, p denotes pressure, $\boldsymbol{\tau}$ is the viscous stress tensor and

$$\Theta_x = u\tau_{xx} + v\tau_{xy} + w\tau_{xz} \tag{2.30}$$

$$\Theta_y = u\tau_{yx} + v\tau_{yy} + w\tau_{yz} \tag{2.31}$$

$$\Theta_z = u\tau_{zx} + v\tau_{zy} + w\tau_{zz} \tag{2.32}$$

The above system is completed with the equation of state for perfect gases:

$$p = (\gamma - 1)\rho \left[E - \frac{u^2 + v^2 + w^2}{2} \right] \tag{2.33}$$

In case the local Mach number gets close zero (typical for WT simulations) there is large disparity in the wave propagation speeds. The speed of sound (c) becomes very large

compared to the flow velocity (V) and completely deteriorates the stability and convergence properties of the system. In such cases, the equations are modified by applying **Low Mach Preconditioning** that acts on the time derivatives of the equations and basically modifies the speed of sound. By that, the convergence and stability characteristics of the system are improved. In MaPFlow Eriksson's Preconditioning Matrix [121] is implemented, due to its successful use in [122].

2.2.1.2 Space Integration and Implementation

In MaPFlow the flow variables are computed and stored at cell centers. Assuming that the cell volume remains unchanged:

$$\frac{\partial}{\partial t} \int_D \mathbf{U} dD = D \frac{d\mathbf{U}}{dt} \tag{2.34}$$

where

$$\mathbf{U} = \frac{1}{D} \int_D \mathbf{U}_{exact} dD \tag{2.35}$$

and

$$\int_D \mathbf{Q} dD = D\mathbf{Q} \tag{2.36}$$

where

$$\mathbf{Q} = \frac{1}{D} \int_D \mathbf{Q}_{exact} dD \tag{2.37}$$

The **surface integral** of equation (2.26) sums the fluxes over the faces of every cell. The fluxes are assumed to be piecewise constant over the cell faces and their values are computed at the face center:

$$\oint_{\partial D} (\mathbf{F}_c - \mathbf{F}_v) \, dS = \sum_{f=1}^{N_f} \left(\mathbf{F}_{c_f} - \mathbf{F}_{v_f} \right) \Delta S_f \tag{2.38}$$

The **discretized form** of equation (2.26) becomes:

$$\frac{d\mathbf{U}}{dt} = -\frac{1}{D} \sum_{f=1}^{N_f} \left(\mathbf{F}_{c_f} - \mathbf{F}_{v_f} \right) \Delta S_f + \mathbf{Q} \tag{2.39}$$

The **Convective Fluxes** $\left(\mathbf{F}_{c_f} \right)$ are evaluated by solving the local Riemann problem between the neighboring cells (I, J) of each face (f), using the Roe's approximate Riemann solver [112], which is a flux-difference scheme:

$$\mathbf{F}_{c_f} = \frac{1}{2} [\mathbf{F}_c(\mathbf{V}_R) + \mathbf{F}_c(\mathbf{V}_L) - |\mathbf{A}_{\mathbf{Roe}}|_f (\mathbf{V}_R - \mathbf{V}_L)] \tag{2.40}$$

where, the Left and Right states ($\mathbf{V}_L, \mathbf{V}_R$) of the primitive variables $\left(\mathbf{V} = (\rho, u, v, w, p)^T \right)$ of the face are computed using a Piecewise Linear Reconstruction (PLR) scheme:

$$\begin{aligned} \mathbf{V}_L &= \mathbf{V}_I + \Psi_I(\nabla \mathbf{V}_I \cdot \mathbf{r}_L) \\ \mathbf{V}_R &= \mathbf{V}_J - \Psi_J(\nabla \mathbf{V}_J \cdot \mathbf{r}_R) \end{aligned} \tag{2.41}$$

where $\mathbf{r}_L, \mathbf{r}_R$ denote the distance vectors pointing from the cell centers to the face center (Figure 2.12) and Ψ is the Venkatakrishnan limiter function [113] that reduces the gradients.
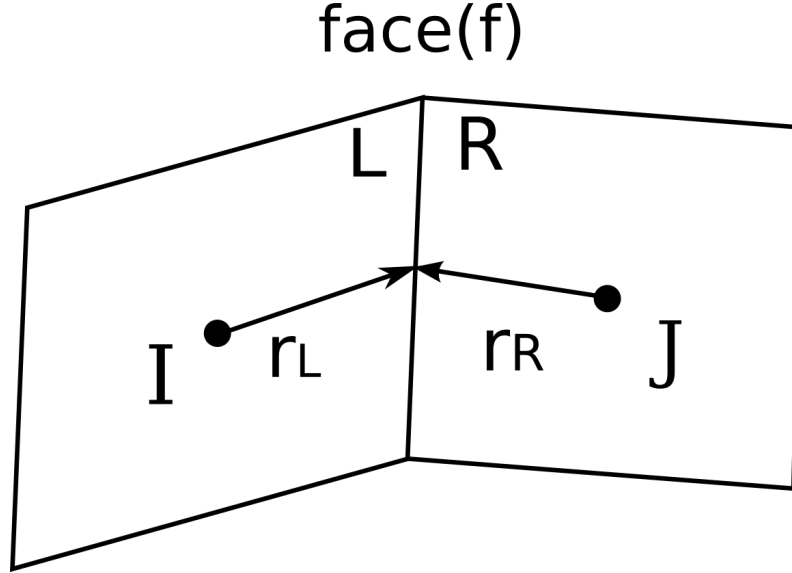
Figure 2.12. *Reconstruction of variables on a face f.*

In equation (2.40) $|\mathbf{A_{Roe}}|$ is constructed using the absolute values of the eigenvalues and the right eigenvector matrix R:

$$|\mathbf{A_{Roe}}| = \mathbf{R}^{-1}|\mathbf{\Lambda}|\mathbf{R} \tag{2.42}$$

In case the preconditioned system of equation is used, the eigenvalues and the eigenvectors of the preconditioned system must be used $(\mathbf{\Lambda}_\Gamma, \mathbf{R}_\Gamma)$. Hence, $|\mathbf{A_{Roe}}|$ is changed to (according to [123]):

$$
\begin{aligned}
|\mathbf{A_{\Gamma Roe}}| &= |\mathbf{\Gamma}^{-1}\mathbf{\Gamma A_{Roe}}| \\
&\simeq \mathbf{\Gamma}^{-1}|\mathbf{\Gamma A_{Roe}}| \\
&\simeq \mathbf{\Gamma}^{-1}\mathbf{R}_\Gamma^{-1}|\mathbf{\Lambda}_\Gamma|\mathbf{R}_\Gamma
\end{aligned}
\tag{2.43}
$$

In equation (2.41), the gradients are computed at the corresponding cell centers using the Green-Gauss formulation:

$$\nabla \mathbf{V} \approx \frac{1}{D} \int_{\partial D} \mathbf{V}\mathbf{n}dS \tag{2.44}$$

which in the Cell-Centered scheme takes the form:

$$\nabla \mathbf{V}_I \approx \frac{1}{D} \sum_{J=1}^{N_f} \frac{1}{2}(\mathbf{V}_I + \mathbf{V}_J)\mathbf{n}_{IJ}\Delta S_{IJ} \tag{2.45}$$

For the computation of the **Viscous Fluxes** $\left(\mathbf{F}_{v_f}\right)$ a central 2nd order scheme is used:

$$\mathbf{V}_{IJ} = \frac{1}{2}\left(\mathbf{V}_I + \mathbf{V}_J\right) \tag{2.46}$$

while for the gradients, the Green-Gauss formula is applied using the face averaged values $\mathbf{V}_{IJ}$ as defined in equation (2.46) but supplemented with a directional derivative [124]:

$$\nabla\mathbf{V}_{IJ} = \overline{\nabla\mathbf{V}_{IJ}} - \left[\overline{\nabla\mathbf{V}_{IJ}} \cdot \mathbf{t}_{IJ} - \left(\frac{\partial\mathbf{V}}{\partial l}\right)_{IJ}\right] \cdot \mathbf{t}_{IJ} \tag{2.47}$$

where

$$\overline{\nabla\mathbf{V}_{IJ}} = \frac{1}{2}\left(\nabla\mathbf{V}_I + \nabla\mathbf{V}_J\right) \tag{2.48}$$

is the mean gradient

$$\left(\frac{\partial\mathbf{V}}{\partial l}\right)_{IJ} \approx \frac{\mathbf{V}_J - \mathbf{V}_I}{l_{IJ}} \tag{2.49}$$

and l_{IJ} is the distance between cell centers I and J and $\mathbf{t}_{IJ}$ is the unit vector pointing from cell center I to cell center J.

2.2.1.3   Time Integration and Implementation

For the temporal discretization, the method of lines is used. This means that temporal and spatial discretization are done separately leading for every control volume to the following equation:

$$\frac{d\left(D_I\mathbf{U}_I\right)}{dt} + \mathbf{R}_I = \mathbf{0} \tag{2.50}$$

where $\mathbf{R}_I = \left[\sum\limits_{f=1}^{N_f}\left(\mathbf{F}_{c_f} - \mathbf{F}_{v_f}\right)\Delta S_f - D\mathbf{Q}\right]_I$. In comparison to equation (2.39), the form of equation (2.50) is more general in the sense that the control volume may vary in time.

Temporal discretization can be either explicit or implicit. Explicit methods use the $\mathbf{U}^n$ known solution and march in time using the corresponding residual $\mathbf{R}^n$ to obtain solution at $(t + \Delta t)$. On the other hand the implicit schemes use $R(\mathbf{U}^{n+1}) = \mathbf{R}^{n+1}$ to obtain the new solution and are favored because they allow larger time-steps. Since $\mathbf{R}^{n+1}$ is unknown, the following linear approximation is used:

$$\mathbf{R}^{n+1} \approx \mathbf{R}^n + \left(\frac{\partial\mathbf{R}}{\partial\mathbf{U}}\right)_n \Delta\mathbf{U}^n, \quad \Delta\mathbf{U}^n = \mathbf{U}^{n+1} - \mathbf{U}^n \tag{2.51}$$

In MaPFlow, a finite difference scheme is used for the time derivative (see [125]):

$$\frac{d\left(D_I\mathbf{U}_I\right)}{dt} = \frac{1}{\Delta t}\left[\phi_{n+1}\left(D_I\mathbf{U}_I\right)^{n+1} + \phi_n\left(D_I\mathbf{U}_I\right)^n + \phi_{n-1}\left(D_I\mathbf{U}_I\right)^{n-1} + \phi_{n-2}\left(D_I\mathbf{U}_I\right)^{n-2} + \dots\right] \tag{2.52}$$

Depending on the choice of ϕ_n the corresponding Backwards Difference Formulae (BDF) of the temporal scheme are defined. *BDF2OPT* refers to a class of optimized, 2nd

order, backward difference methods with an error half as large as the conventional 2nd order scheme [119].

Table 2.1. *Backwards Difference Schemes*

order	ϕ_{n+1}	ϕ_n	ϕ_{n-1}	ϕ_{n-2}
1st	1	-1	0	0
2nd	3/2	-2	1/2	0
3rd	11/6	-3	3/2	$-1/3$
BDF2OPT	$3/2 - \phi_{n-2}$	$-2 + 3\phi_{n-2}$	$1/2 - 3\phi_{n-2}$	$-0.58/3$

Even in **steady–state simulations**, a **pseudo-unsteady** technique is followed. For steady state simulations in MaPFlow, a 1st order scheme is chosen to march the solution in pseudo-time until convergence is reached. At 1st order, after linearizing $\vec{R}^{n+1}$ (see equation (2.51)) and by rearranging the terms, the final system of discrete equations is obtained in which the system matrix defines the *implicit operator* and the *explicit operator* of the scheme:

$$\underbrace{\left[\frac{D_I}{\Delta t_I} + \left(\frac{\partial \mathbf{R}}{\partial \mathbf{U}}\right)_I\right]}_{\text{Implicit Operator}} \Delta \mathbf{U}_I^n = \underbrace{-\mathbf{R_I^n}}_{\text{Explicit Operator}} \tag{2.53}$$

In order to facilitate convergence, the **Local Time Stepping** technique is used [86]. The time step for steady–state computation can be defined using the spectral radii of each cell. Consequently, a different time step may be defined for each cell:

$$\Delta t_I = CFL \frac{D_I}{\left(\hat{\Lambda}_c + C\hat{\Lambda}_v\right)_I} \tag{2.54}$$

where $\hat{\Lambda}_c, \hat{\Lambda}_v$ is the sum of convective and viscous eigenvalues over all cell faces. The constant which multiplies the viscous spectral radius is usually set as $C = 4$ [124].

The convective spectral radius is defined by:

$$(\hat{\Lambda}_c)_I = \sum_{J=1}^{N_f} (|\mathbf{u}_{IJ} \cdot \mathbf{n}_{IJ}| + c_{ij}) \Delta S_{IJ} \tag{2.55}$$

where $|\mathbf{u}_{IJ} \cdot \mathbf{n}_{IJ}|$ and c_{ij} are the normal velocity and speed of sound respectively over the various faces of area ΔS_{IJ} of a control volume.

The viscous spectral radius is defined by:

$$(\hat{\Lambda}_v)_I = \frac{1}{D_I} \sum_{J=1}^{N_f} [max(\frac{4}{3\rho_{IJ}}, \frac{\gamma_{IJ}}{\rho_{IJ}})(\frac{\mu_L}{Pr_L} + \frac{\mu_T}{Pr_T})_{IJ}(\Delta S_{IJ})^2] \tag{2.56}$$

where $\gamma_{IJ} = \left.\frac{C_p}{C_v}\right|_{IJ}$ is the adiabatic index and ρ_{IJ} is the density of the fluid, μ_L and μ_T denote the laminar and turbulent dynamic viscosity coefficients respectively, whereas Pr_L and Pr_T are the respective laminar and turbulent Prandtl numbers.

However, if **Time True Computations** are to be performed, one global time–step value

has to be employed for all control volumes, usually $\Delta t = min\,(\Delta t_I)$ or a user defined value. In Time True computations temporal discretization is crucial, because any remaining numerical error propagates in the flow as a disturbance. In order to minimize temporal errors higher order schemes should be used in conjunction with the **Dual Time–Stepping** technique [126].

By setting, $\mathbf{R}_I^* = \dfrac{d(D_I\mathbf{U}_I)}{dt} + \mathbf{R}_I$ equation (2.50) becomes $\mathbf{R}_I^* = 0$, resembling a steady–state equation. The Dual–Step approach adds an extra time-like derivative in the transport equation that refers to a different "time variable" τ, called "pseudo–time". The variables in the "pseudo–time" problem are denoted by $\vec{U}^*$ because they do not satisfy the original unsteady problem of equation (2.50) until convergence. Using this approach the unsteady problem of every true time–step is transformed into a steady one in which the following equation is solved in the "pseudo–time" τ:

$$\frac{\partial(D_I\mathbf{U}_I^*)}{\partial\tau} + \mathbf{R}_I^* = \mathbf{0} \tag{2.57}$$

or,

$$\frac{\partial(D_I\mathbf{U}_I^*)}{\partial\tau} + \frac{\partial(D_I\mathbf{U}_I^*)}{\partial t} + R(\mathbf{U}^*) = \mathbf{0} \tag{2.58}$$

When equation (2.57) converges in "pseudo–time" τ, $\mathbf{R}_I^* = 0$ and $\mathbf{U}_I^* = \mathbf{U}_I^{n+1}$ which satisfies the original unsteady problem in time–step $n + 1$.

The discretised form of equation (2.58) can be written as:

$$\frac{D_I^{n+1}\Delta\mathbf{U}_I^{*k}}{\Delta\tau_I} + \frac{1}{\Delta t}\left[\phi_{n+1}\left(D_I\mathbf{U}_I^{*k+1}\right)^{n+1} + \phi_n\,(D_I\mathbf{U}_I)^n + \phi_{n-1}\,(D_I\mathbf{U}_I)^{n-1}\right] + \mathbf{R}_I^{k+1} = \mathbf{0} \tag{2.59}$$

where $\Delta\mathbf{U}_I^{*k} = \mathbf{U}_I^{*k+1} - \mathbf{U}_I^{*k}$ and k denotes sub–iteration, thus, $\Delta\mathbf{U}_I^{*k} = \mathbf{0} \Rightarrow \mathbf{U}_I^{*k+1} = \mathbf{U}_I^{*k} = \mathbf{U}_I^{n+1}$.

By setting $\mathbf{R}_I^{*k+1} = \dfrac{1}{\Delta t}\left[\phi_{n+1}\left(D_I\mathbf{U}_I^{*k+1}\right)^{n+1} + \phi_n\,(D_I\mathbf{U}_I)^n + \phi_{n-1}\,(D_I\mathbf{U}_I)^{n-1}\right] + \mathbf{R}_I^{k+1}$ we may apply an Implicit Scheme in the Dual Time–Step procedure and linearize the unsteady residual $\mathbf{R}_I^{*k+1}$ as:

$$\mathbf{R}_I^{*k+1} \approx \mathbf{R}_I^{*k} + \left(\frac{\partial\mathbf{R}_I^*}{\partial\mathbf{U}_I^*}\right)_k \Delta\mathbf{U}_I^{*k} \tag{2.60}$$

where

$$\mathbf{R}_I^{*k} = \frac{1}{\Delta t}\left[\phi_{n+1}\left(D_I\mathbf{U}_I^{*k}\right)^{n+1} + \phi_n\,(D_I\mathbf{U}_I)^n + \phi_{n-1}\,(D_I\mathbf{U}_I)^{n-1}\right] + \mathbf{R}_I^k \tag{2.61}$$

and

$$\left(\frac{\partial\mathbf{R}_I^*}{\partial\mathbf{U}_I^*}\right)_k = \left(\frac{\partial\mathbf{R}_I}{\partial\mathbf{U}_I^*}\right)_k + \frac{1}{\Delta t}\left[\phi_{n+1}\,(D_I)^{n+1}\right] \tag{2.62}$$

By substituting the above defined expressions (equations (2.60),(2.61),(2.62)) in equation (2.59), the final discretised form of equation (2.58) is obtained:

$$\left[\frac{D_I^{n+1}}{\Delta\tau_I} + \phi_{n+1}\frac{D_I^{n+1}}{\Delta t} + \left(\frac{\partial\mathbf{R}_I}{\partial\mathbf{U}_I^*}\right)_k\right]\Delta\mathbf{U}_I^{*k} = -\mathbf{R}_I^k - \mathbf{Q}_{I,dual}^k \tag{2.63}$$

It is noted here that the "pseudo time–step" $\Delta\tau_I$ is defined as in the steady–state computations using local time–stepping equation (2.54).

The dual–step unsteady source–like terms $\mathbf{Q}^k_{I,dual}$ are given by:

$$\mathbf{Q}^k_{I,dual} = \frac{1}{\Delta t}\left[\phi_{n+1}\left(D_I\mathbf{U}^{*k}_I\right)^{n+1} + \phi_n\left(D_I\mathbf{U}_I\right)^n + \phi_{n-1}\left(D_I\mathbf{U}_I\right)^{n-1}\right] \Rightarrow$$

$$\mathbf{Q}^k_{I,dual} = \underbrace{\frac{1}{\Delta t}\left[\mathbf{U}^n_I\left(\phi_{n+1}D^{n+1}_I + \phi_nD^n_I + \phi_{n-1}D^{n-1}_I\right)\right]}_{\mathbf{U}^n_I\frac{dD_I}{dt}}$$

$$+ \frac{1}{\Delta t}\left[\phi_{n+1}\left(\mathbf{U}^{*k\,n+1}_I - \mathbf{U}^n_I\right)D^{n+1}_I + \phi_{n-1}\left(\mathbf{U}^{n-1}_I - \mathbf{U}^n_I\right)D^{n-1}_I\right] \qquad (2.64)$$

For undeformable grids $\frac{dD_I}{dt} = 0$, thus:

$$\mathbf{Q}^k_{I,dual} = \frac{1}{\Delta t}\left[\phi_{n+1}\left(\mathbf{U}^{*k\,n+1}_I - \mathbf{U}^n_I\right)D^{n+1}_I + \phi_{n-1}\left(\mathbf{U}^{n-1}_I - \mathbf{U}^n_I\right)D^{n-1}_I\right] \qquad (2.65)$$

2.2.1.4 Implementation of Deforming Grids

In Fluid Structure Interaction (FSI) configurations the grid must deform. For the Eulerian CFD solver part, two are the main aspects distinguishing the analysis followed so far that need to be taken care of. The first one is the change of the cell volume that needs to be considered $\left(\frac{dD_I}{dt} \neq 0\right)$ and the second one is the grid deformation method that needs to ensure that the grid lines do not overlap.

Grid deformation renders the cell volume $D(t)$ time dependent. Even though the time derivative of the cell volume can be estimated by a backwards difference scheme as shown before $\left(\frac{dD_I}{dt} = \phi_{n+1}D^{n+1}_I + \phi_nD^n_I + \phi_{n-1}D^{n-1}_I\right)$, in MaPFlow the so called Geometric Conservation Law (GCL), proposed by Thomas and Lombard [127], is preferred:

$$\frac{d}{dt}\int_{D(t)} dD = \oint_{\partial D(t)} \mathbf{V}_f \cdot \mathbf{n}_f\,dS_f \qquad (2.66)$$

The principle of GCL is that a uniform flow solution must remain unchanged regardless of the grid motion. Various numerical implementations of the GCL are found in the literature (e.g [128]). In MaPFlow that of [129] is adopted, which consists of adding a source term to the original equations. Starting from the integral form of the equations and assuming volume averaged approximation,

$$\frac{d}{dt}(\mathbf{U}D) + \mathbf{R} = \mathbf{0} \Rightarrow$$

$$\frac{d\mathbf{U}}{dt}D + \frac{dD}{dt}\mathbf{U} + \mathbf{R} = \mathbf{0}$$

So, by introducing (2.66),

$$\frac{d\mathbf{U}}{dt}D + \mathbf{R} = -\mathbf{U}\oint_{\partial D(t)} \mathbf{V}_f \cdot \mathbf{n}_f\,dS_f \qquad (2.67)$$

and applying (2.52), the following discrete formulation is obtained,

$$\frac{1}{\Delta t}\left[\phi_{n+1}\mathbf{U}^{n+1} + \phi_n\mathbf{U}^n + \phi_{n-1}\mathbf{U}^{n-1} + \phi_{n-2}\mathbf{U}^{n-2} + \dots\right]D^{n+1} = -\mathbf{R}^{n+1} - \left[\mathbf{U}\oint_{\partial D(t)}\mathbf{V}_f \cdot \mathbf{n}_f dS_f\right]^{n+1} \quad (2.68)$$

In this way, the same velocity distribution is used in order to compute the face integrals in equation (2.38) and the time derivative of the cell volume, thus, ensuring a compatibility between the explicit operator $\mathbf{R}$ and the dual–step unsteady source term $\mathbf{Q}_{dual}$. Otherwise, the estimation of $\frac{dD_I}{dt}$ through a backwards difference scheme introduces numerical errors that yield in incompatibility between $\mathbf{R}$ and $\mathbf{Q}_{dual}$ and, thus, a wrong solution of the flow variables $\mathbf{U}$. It is noted that for rigid body motions $\oint_{\partial D(t)}\mathbf{V}_f \cdot \mathbf{n}_f dS_f \approx 0$.

For grid deformation, the work by Zhao [90] is followed. The idea in Zhao's scheme is to propagate the displacements of the solid boundaries into the grid nodes without changing the far–field boundary while keeping the same grid topology. This is carried out at nodal level as follows:

$$\mathbf{d}r(node) = f(node)\mathbf{d}r(node_{wall}) \quad (2.69)$$

where $\mathbf{d}r$ is the displacement of an arbitrary grid node, $\mathbf{d}r(node_{wall})$ is the displacement of the corresponding/closest node that belongs to the solid boundary and f is the propagation function decaying exponentially in space:

$$f(x) = \frac{ly^2(x)}{lx^2(x) + ly^2(y)} \quad (2.70)$$

$$lx(x) = \frac{1 - \exp(-d(x)/d_{max})}{(e-1)/e}$$
$$ly(x) = \frac{1 - \exp(1 - d(x)/d_{max})}{1 - e} \quad (2.71)$$

where $d(x)$, is the distance of the node to the corresponding/nearest solid node and d_{max} is the maximum distance of all nodes from the solid boundary, ensuring that the far–field nodes remain in their undeformed positions. It is noted that $\mathbf{d}r(node)$ is superimposed to any rigid body motion undergone by the nodes.

2.2.1.5 Implementation of the Actuator Line model

In an actuator line modelling approach, the actual geometry of the rotor blades is not resolved. Instead, the blades are modelled as a set of blade elements along their axes as shown in Figure 2.13. The blade loads are computed on specific control points along the blade span through a blade element analysis in conjunction with $2D$ polars. The reaction of the computed aerodynamic forces of the control points are then applied to the flow as external forcing (source terms) on the cells swept by the blades during their rotation. In order to avoid numerical instabilities, the source terms are spread across the cells surrounding the control points through a $3D$ Gaussian convolution [7] (see Figure 2.14).
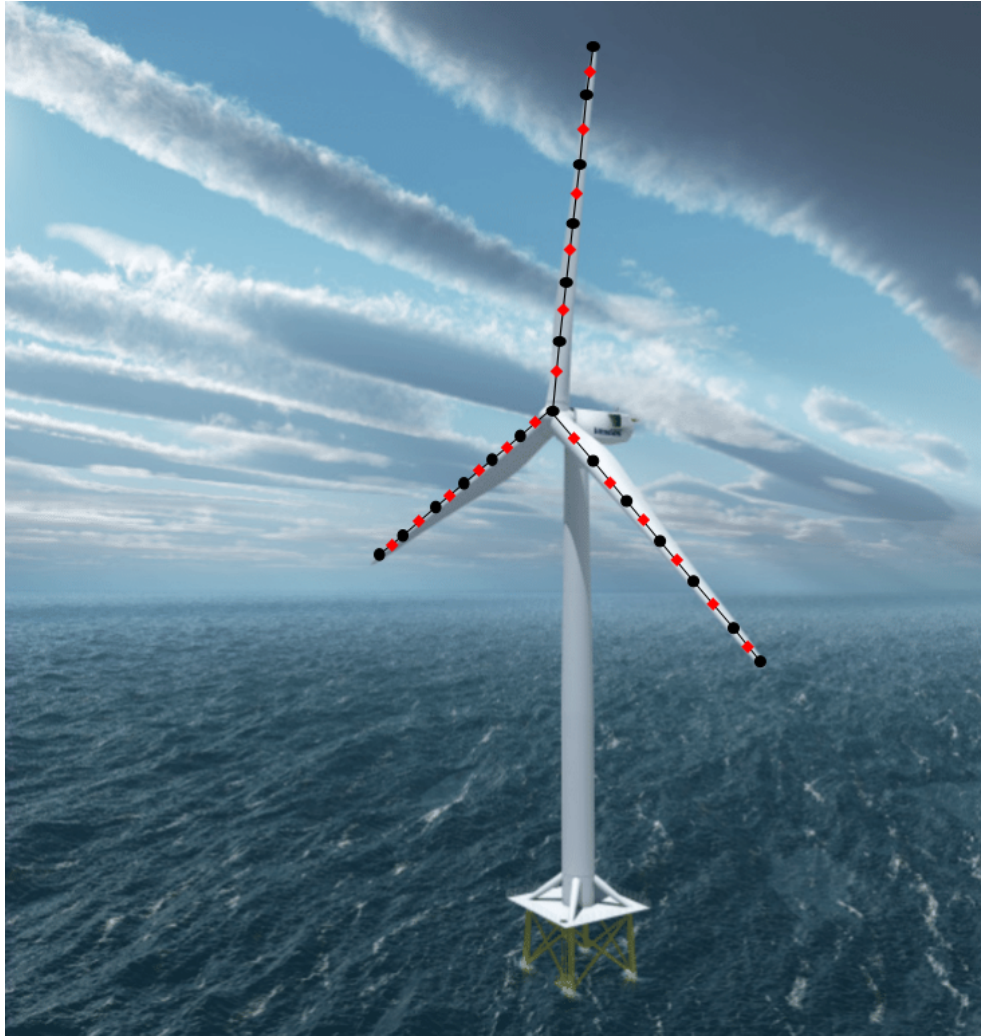
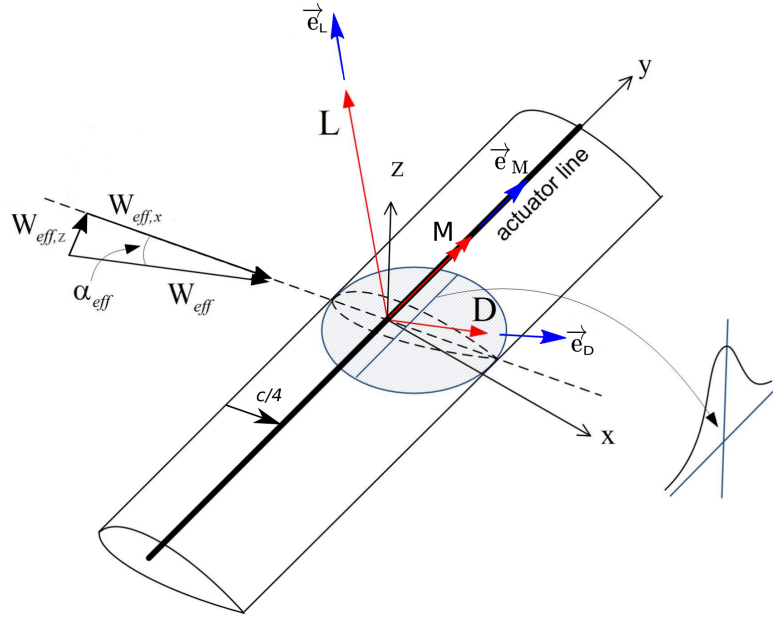**Figure 2.13.** *Actuator Line modelling of a WT rotor blades. Blade element nodes and control points are depicted as black circles and red diamonds respectively.*
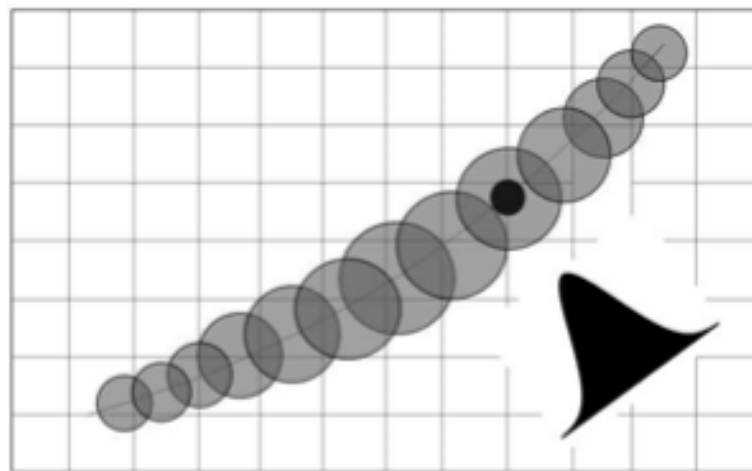
Figure 2.14. *Actuator Line modelling of a blade. Gaussian projection of the blade element forces. Image copied from [130].*

As stated before, Lift, Drag and Moment on every strip are computed through a blade element analysis, as shown in Figure 2.15 and detailed in equations (2.72).

Figure 2.15. *Actuator Line modelling of a blade. Blade element analysis and Gaussian projection of the resulting aerodynamic forces.*
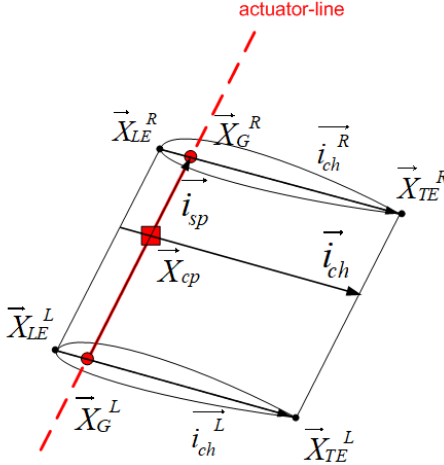
$$\alpha_{eff} = arctan\frac{W_{eff,z}}{W_{eff,x}}$$

$$L = \frac{1}{2}\rho W_{eff}^2 C_L(\alpha_{eff})c\Delta r$$

$$D = \frac{1}{2}\rho W_{eff}^2 C_D(\alpha_{eff})c\Delta r$$

$$M = \frac{1}{2}\rho W_{eff}^2 C_M(\alpha_{eff})c^2\Delta r \qquad (2.72)$$

$$\mathbf{f}_{cp} = L\mathbf{e}_L + D\mathbf{e}_D$$

$$\mathbf{m}_{cp} = M\mathbf{e}_M$$

where α_{eff} is the effective angle of attack, $C_L(\alpha_{eff})$, $C_D(\alpha_{eff})$ and $C_M(\alpha_{eff})$ are the lift, drag and moment coefficients for the specific angle of attack, ρ is the density of the fluid, W_{eff} is the norm of the local $2D$ inflow velocity, c is the blade element characteristic chord, Δr is the width of the blade element, and $\mathbf{e}_L$, $\mathbf{e}_D$ and $\mathbf{e}_M$ are the unit vectors in the direction of lift, drag and moment respectively.

In order to compute the local $2D$ inflow velocity $\mathbf{W}_{eff}$ (the radial component of the inflow velocity is neglected), the orientation of the blade element needs to be defined. This is performed through the computation of the Rotation Matrix of the blade element $\left(\mathbf{A}_{cp}\right)$ by following a multi–body approach, as shown in Figure 2.16 and explained in equations (2.73). In order to do so, apart from the control point of each blade element, a few more auxiliary points may be defined. Such are a pair of nodes at the edges of the blade element along the quarter–chord line $\left(\mathbf{X}_G^{L,R}\right)$ and the Leading and Trailing Edge points of the corresponding sections $\left(\mathbf{X}_{LE}^{L,R} \,\&\, \mathbf{X}_{TE}^{L,R}\right)$. Consequently a total number of 7 points on

each blade element are needed in order to perform the kinematic analysis. These points follow all the rigid body motions (e.g. azimuthal rotation and pitching motion) of the blades and the elastic deformations (e.g. transnational displacements due to bending and torsion) if elasticity is included in the analysis. In this way, the local twist, pitch and torsion angle of the blade element are inherently accounted for in the computation of the effective angle of attack when expressing the inflow velocity in the local coordinate system of the blade element.

Blade Element Orientation

Figure 2.16. *Actuator Line modelling of a blade. Orientation of the blade element is defined in a multi-body approach by computing its Rotation Matrix A_{cp}.*

$$
\begin{aligned}
\mathbf{W}_{eff} &= \mathbf{A}_{cp}^{T}\left(\mathbf{U}_{fl} - \mathbf{U}_{b}\right) \ where \ W_{eff,y} \equiv 0 \\
\mathbf{U}_{eff} &= W_{eff,x}\mathbf{i}_{ch} + W_{eff,z}\mathbf{i}_{nrm} \\
\mathbf{e}_{D} &= \mathbf{U}_{eff}/\left|\mathbf{U}_{eff}\right| \\
\mathbf{e}_{L} &= \mathbf{e}_{D} \times \mathbf{i}_{sp} \\
\mathbf{e}_{M} &= \mathbf{i}_{sp}
\end{aligned} \tag{2.73}
$$

where $\mathbf{W}_{eff}$ is the local $2D$ inflow velocity expressed in the local coordinate system of the blade element, $\mathbf{U}_{eff}$ is the local $2D$ inflow velocity expressed in the inertial frame, $\mathbf{U}_{fl}$ is the flow velocity interpolated to the control point from the neighbouring cells solution, $\mathbf{U}_{b}$ is the body motion of the control point (containing the rigid body velocity and the velocity of the elastic deformations), and $\mathbf{i}_{ch}$, $\mathbf{i}_{sp}$ and $\mathbf{i}_{nrm}$ are the unit vectors in the chord–wise, span–wise and normal direction of the blade element respectively.

The reaction of body forces and their work are then imported as source terms in the momentum and energy equations of the cells that are swept by the blades during their rotation. In order to avoid singularities, the body forces and their corresponding work are

numerically spread across a few cells using a $3D$ isotropic Gaussian distribution:

$$\mathbf{f}_\epsilon = \mathbf{f}_{cp}\eta_\epsilon$$
$$\mathbf{f}_c = -\sum_{i=1}^{N_{cp}} \mathbf{f}_{cp}\eta_\epsilon(cp_i, cell) \tag{2.74}$$

where:

- $\mathbf{f}_\epsilon$ is the projected force per unit volume [N/m^3];

- $\mathbf{f}_{cp}$ is the computed force on the actuator line emission (control) point [N];

- $\eta_\epsilon = \frac{1}{(\epsilon\sqrt{\pi})^3}e^{-\left(\frac{d}{\epsilon}\right)^2}$ is a $3D$ isotropic Gaussian distribution function;

- $d = |\mathbf{x}_{cp} - \mathbf{x}_c|$ is the distance between the actuator line emission point and the point where the force is applied [m];

- ϵ is the Gaussian kernel that defines the projection width [m].

The actuator line control points define the location of different blade elements that have specific Lift (L), Drag (D) and Moment (M) depending on their airfoil type, chord and span lengths and the incoming flow velocity that determines the effective angle of attack. They are placed at the mid–span of the blade element they represent, along it's quarter–chord line and are the center of the blade element forces distribution. In the Actuator Line (AL) methodology implemented in MaPFlow, the incoming flow velocity is directly sampled on the control points as well [131]. The reason is that the control points are also the centers of the blades' bound vorticity, where the blade local flow effects (upwash and downwash created by the bound vortex) vanish. Hence, a consistent estimation of the inflow velocity is performed. The velocity at the control points is estimated through a distance and volume weighted interpolation to the computed velocities of the neighbouring cells using Radial Basis Functions (RBF) [132]. In that sense the actuator line control points serve as both the kinematic analysis centers and the emission points of the aerodynamic forces.

Even though recommended by [133], tip correction models are not used in the current implementation, since the three-dimensional flow–field containing tip and root vortices can be fully resolved, provided that an adequately fine grid resolution is used in the vicinity of the actuator lines. In [134] and Section 3.1.1.2 it is shown that with a small enough characteristic cell length (Δx) of up to $R/90$ (R is the rotor radius), the isotropic Gaussian distribution of the aerodynamic forces is sufficient to accurately predict the radial distribution of the blade forces and to resolve the tip and root vortices. For this reason and for sake of simplicity, it is preferred over more sophisticated projection techniques proposed in [135, 136, 137, 130].

Both Cartesian and cylindrical grids can be used in the region of the actuator lines. However, cylindrical grids are inherently non–uniform and hence their use complicates significant aspects of the AL implementation, such as the inflow velocity interpolation on the control points. For this reason Cartesian grids are usually preferred. Both structured

and unstructured grids can be employed, as long as the characteristic cell length (Δx) is kept fine (and preferably constant) in the vicinity of the actuator lines.

As a rule of thumb, in most AL implementations the time step value is chosen so that the tip of the actuator line sweeps no more than one cell per time step $\left(\Delta t \leq \frac{\Delta x}{V_{tip}}\right)$. However, according to [134] and as is shown in Section 3.1.1.2 a more strict approach of the above rule of thumb $\left(\Delta t \leq 0.5 \frac{\Delta x}{V_{tip}}\right)$ is required for WT simulations.

With respect to the radial resolution Δr, accuracy is maintained when it is chosen to be fine enough so that the spherical regions around the body forces sufficiently overlap with each other (see Figure 2.14). In this way a continuous force distribution along the blade is secured. In [134] and Section 3.1.1.2 it is shown that at most double the grid spacing ($\Delta r \leq 2\Delta x$) is adequate when uniform spacing along the blade span is employed. Geometric refinement towards the two edges (root and tip) has also been tested, but it turned out to make no difference, since the actuator line spacing ends up to be really fine.

There are numerous advantages when following the AL approach:

1. CFD grid is not forced to follow the blades rotation;

2. Overset grids methodologies can be avoided when interaction between rotor wake and other configurations (e.g., WT tower, helicopter fuselage, other rotors) is to be assessed;

3. Aeroelastic simulations can be performed without many implementation difficulties, as the computational grid does not need to deform along with the blades.

The above render the AL model befitting for complex aeroelastic analyses, provided that the loads are accurately predicted. The main weakness of AL is its dependence on tabulated 2D airfoil data. The correct estimation of aerodynamic loads in stall conditions is critical in aeroelastic simulations. For this reason, a dynamic stall model needs to be used. In the AL methodology implemented in MaPFlow, the extended ONERA model [138] is used. The delay parameter of the original ONERA model, which accounts for dynamic stall delay in deep stall conditions is omitted. Moreover, the leading edge vortex and the vortex shedding effect considered by Truong [52] in more recent versions of the ONERA model are not included in the present implementation. However, these are not expected to significantly affect the aerodynamic and structural loads of large modern WTs as most of them are pitch regulated. Consequently, all cases of normal operating conditions deal with at most light stall conditions, with the maximum effective angle of attack lying in the vicinity of ($C_{L_{max}}$) where the leading edge vortex is not present. Analytical description and implementation details of the Dynamic Stall model utilized in the current AL implementation can be found in [139]. Nevertheless, 2D polars, even though corrected for unsteady aerodynamics and dynamic stall effects, still cannot account for unsteady phenomena due to vortex shedding (e.g., when massive flow separation takes place or secondary cross-flow effects at the scale of chord length appear). In such cases (e.g. stand–still configurations where the blades operate at nearly a 90° angle of attack) the actual geometry of the rotor blades needs to be accurately resolved.

2.2.1.6 Turbulence Generation in MaPFlow

2.2.1.6.1 Mann's generator of synthetic turbulence

Turbulent fields can be generated through spectral computational methods. In the present research, the one developed by Mann [104, 105, 8] has been used. The Mann model creates a synthetic $3D$ incompressible turbulent field based on the $3D$ von–Karman energy spectrum tensor representation of turbulence derived from Rapid Distortion Theory (RDT) of isotropic turbulence. A $3D$ Fast Fourier Transform (FFT) is then used to generate all three velocity components by summing a set of wave–number vectors, each with the appropriate amplitude and a random phase. The anisotropy of turbulence due to shear and the blocking effect of the ground are described through a parameter Γ that is connected to the "lifetime" of the eddies. By setting the value of the parameter Γ to 0, isotropic turbulent flows are modelled. Apart from Γ, the user needs to define the size of the largest energy–containing eddies through a length–scale parameter L and a parameter $a\epsilon^{2/3}$ containing the Kolmogorov length scale a and ϵ that defines the dissipation rate of the turbulent kinetic energy per unit mass. The produced turbulent field has shown to have the same 2nd order statistics with the atmospheric turbulence. The resulting spectral energy density distribution is adjusted by the values of Γ, $a\epsilon^{2/3}$ and L. For $\Gamma = 3.9$ the produced spectrum follows the distribution of the Kaimal spectrum for neutral stable conditions. Detailed instructions on how to choose the values of these parameters for various turbulence conditions based on the free–stream Turbulence Intensity (TI), the hub–height Z_{hub} and the wind speed at hub–height V_{hub} can be found in [140]. For neutral stable conditions and medium turbulence intensity the following expressions can be followed:

$$\sigma_1 = TI * V_{hub}$$

$$\sigma_{iso} = 0.55\sigma_1$$

$$\Lambda_1 = \begin{cases} 0.7Z_{hub}, & \text{if } Z_{hub} \leq 60m \\ 42m, & \text{if } Z_{hub} \geq 60m \end{cases} \tag{2.75}$$

$$L = 0.8\Lambda_1$$

$$a\epsilon^{2/3} = 1.453L^{-2/3}\sigma_{iso}^2$$

$$\Gamma = 3.9, \text{ for Kaimal spectrum}$$

The turbulent field is expressed as a set of time-series of the velocity fluctuations with respect to a mean velocity field. These time-series of velocity fluctuations are stored at the nodes of a plane perpendicular to the mean wind speed. By using Taylors' frozen turbulence hypothesis the sequence of instants is attributed to a sequence of distances between these planes in the direction of the mean wind speed. Consequently, the output of the generator is a box named "Mann box" (see Figure 2.17) that contains the velocity fluctuations. The axis of the mean wind speed is referred to as the time axis.
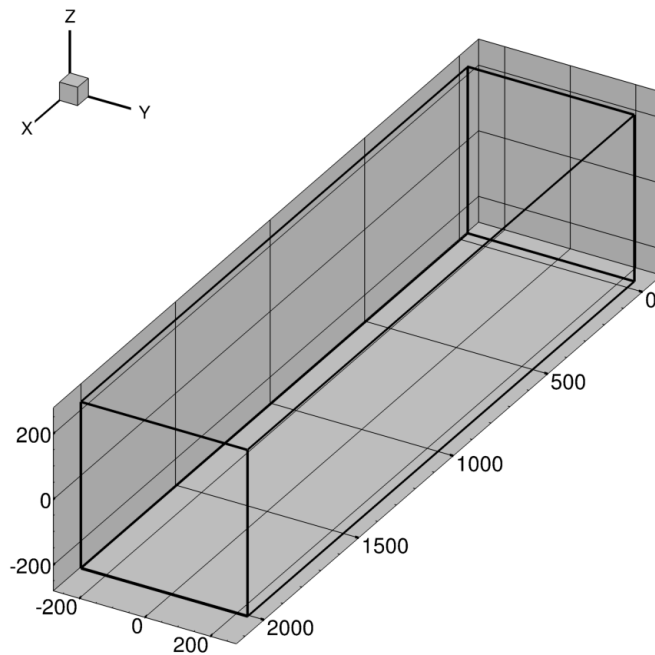
Figure 2.17. *Mann box with* 512*,* 128 *and* 128 *points in the x, y, and z axes.*

Detailed instructions concerning the discretization of the Mann box are given in [141]. The number of nodes in the three directions (axial/longitudinal, lateral and vertical) of the box must be a power of two for efficient FFT computations. In the longitudinal direction, the number of points is determined by the length of the time history required. The maximum wavelength (length of the Mann box) used is the length of the turbulence history to be generated (the mean wind speed multiplied by the duration of the required time series). The minimum wavelength is twice the longitudinal spacing of points, which is the mean wind speed divided by the maximum frequency of interest. In the lateral and vertical directions, fewer points may be used. The maximum wave–length in these directions must be significantly greater than the rotor diameter, since the solution is spatially periodic, with period equal to the maximum wavelength in each direction. Consequently, in cases where the required time series exceeds the duration of the Mann box, its time–history may be repeated until the end of the simulation.

2.2.1.6.2 Implementation of the Actuator Disk methodlogy

The most commonly adopted approach in order to apply a pre-defined turbulent field in the computational domain is to superimpose the velocity fluctuations to the mean velocity at the inlet boundary. However, in order to ensure that the inlet turbulent field is not altered significantly while getting convected downstream, a pretty fine grid is needed. The region of interest is usually placed far away from the inlet in order to avoid boundary effects. This means that a huge amount of computational cells needs to be used in the upstream area in order to preserve turbulence, thus, exploding the computational cost of the simulation. Alternatively, an immersed boundary approach can be used, so that the turbulent fluctuations are imposed on an internal region of the computational domain

located close to the region of interest. This saves computational resources and leads to a less diffused turbulent profile impacting the region of interest. This approach was used by Gilling [142] for the simulation of turbulent flows over airfoils and by Troldborg et al in [143, 107] for the simulation of atmospheric flows. The typical approach used in those studies in order to impose the turbulent fluctuations was to introduce time varying body forces (source terms in the momentum and energy equations) in a cross-section upstream to the region of interest that resembles the methodology of the Actuator Disk (AD). In this case however, the body forces are computed based on $1D$ momentum theory in conjunction with the Bernoulli equation:

$$\mathbf{f}_p = \frac{\rho \mathbf{U}'}{\Delta n}\left(U_n + \frac{1}{2}U_n'\right) \tag{2.76}$$

where $\mathbf{f}_p$ is the force per unit volume required to drive the fluid velocity from $\mathbf{U}$ to $\mathbf{U} + \mathbf{U}'$. $\mathbf{U}$ and $\mathbf{U}'$ are vectors containing the three components of the mean and the fluctuating velocity. U_n and U_n' are the magnitude of the mean and the fluctuating velocity in the direction of the mean wind speed. Δn is the grid spacing normal to the AD. In order to avoid numerical instabilities, these source terms are spread in the direction normal to the AD using a $1D$ Gaussian convolution:

$$\mathbf{f}_e = \mathbf{f}_p \eta_\epsilon$$
$$\eta_\epsilon = \frac{1}{\epsilon \sqrt{\pi}} e^{-\left(\frac{n-n_d}{\epsilon}\right)^2} \tag{2.77}$$

where ϵ is the Gaussian kernel that defines the projection width and $n - n_d$ is the normal distance from a grid point to the turbulence plane. Besides adding the source terms to the momentum equations, the work of the source terms can also be added to the energy equation as:

$$f_w = \mathbf{f}_e \cdot \mathbf{U}_c \tag{2.78}$$

where $\bar{U}_c$ is the velocity at the cell that the source terms are applied on.

2.2.1.6.3 Implementation of the Generation Zone methodology

In this work, an alternative approach for imposing a given velocity profile is tested. Instead of confining the turbulence actuator region to a single plane (the plane of the AD) and few computational cells around this plane, as a result of the Gaussian smearing, the idea is to spread the generation of the turbulent profile in a zone that is called a Generation Zone (GZ). The cells located inside this zone are assigned with source terms that drive the solution to the imposed velocity $\mathbf{U}_{tar} = \mathbf{U} + \mathbf{U}'$:

$$\mathbf{S}_c = C\rho_c\left(\mathbf{U}_{tar} - \mathbf{U}_c\right)$$
$$C = a * e^{-\left[\frac{x - x_s}{0.2\left(x_e - x_s\right)}\right]} \tag{2.79}$$

Regularization function C
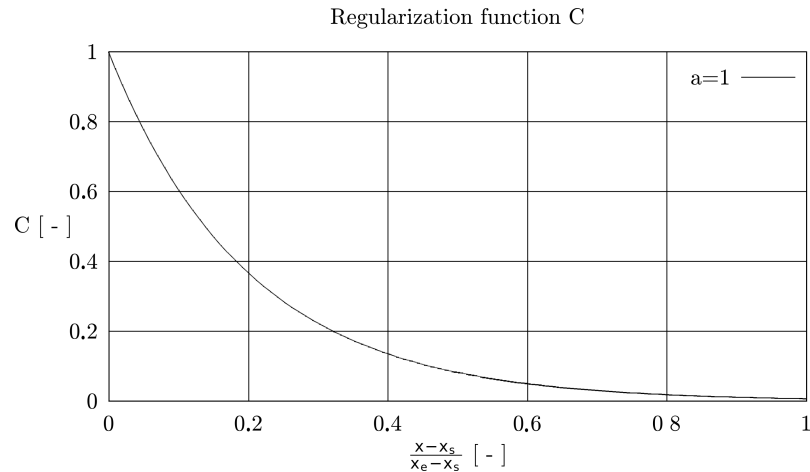
Figure 2.18. *Function C regulating the intensity of the Generation Zone. Maximum value of C is set at the start of the zone and then decays smoothly (as a first order filter) towards zero by the end of the zone.*

C is a function that regulates the intensity of the source terms and ρ_c is the air density in the computational cell that the source term is applied on. The maximum value of C is set through the parameter a. The start point of the GZ is denoted by x_s, while the end point by x_e and x is the position in the mean wind speed direction of the cells that lie within the zone. The parameter 0.2 ensures that the effect of the source terms of the GZ decays with the same rate as a first order filter and is damped by the end of the zone (see Figure 2.18). The desired numerical solution (e.g. a turbulent velocity profile) is obtained implicitly, which means that the solver needs to converge to that solution through the numerical procedure. The source terms, should be able to drive the solution to the desired one, while at the same time maintain the convergence properties of the method. Large values of a may lead to numerical instabilities, while small ones may not be able to effectively drive the desired one. A reasonable rule of thumb would be to use the maximum value of a for which the simulation runs properly. The maximum value of a may alter depending on the GZ length and other numerical parameters of the simulation.

The fact that the maximum value of C is set at the starting plane of the zone drives the solution of the nearby cells pretty close to the desired velocity profile. This is clearly depicted in Figure 2.19, where the time-series of the axial velocity and the corresponding spectrum that are produced with the GZ method are compared against the ones produced by the conventional methodology of the AD and the input signals produced by the Mann generator. It is obvious, that the GZ creates a velocity profile that is almost identical to the desired one. This is clearly not the case when it comes to the AD and the reason is that its source terms are computed based on potential approach ($1D$ momentum equations in conjunction with the Bernoulli equation) which is not fully compatible with a CFD solver. Moreover, the smooth decay of the source terms towards the end plane of the GZ ensures that the velocity profile created by the end of the zone is a true solution of the equations solved and compatible with the solver settings used (e.g. spatial and temporal discretization scheme and order, type of preconditioner, e.t.c.). Consequently, no numerical instabilities are expected.
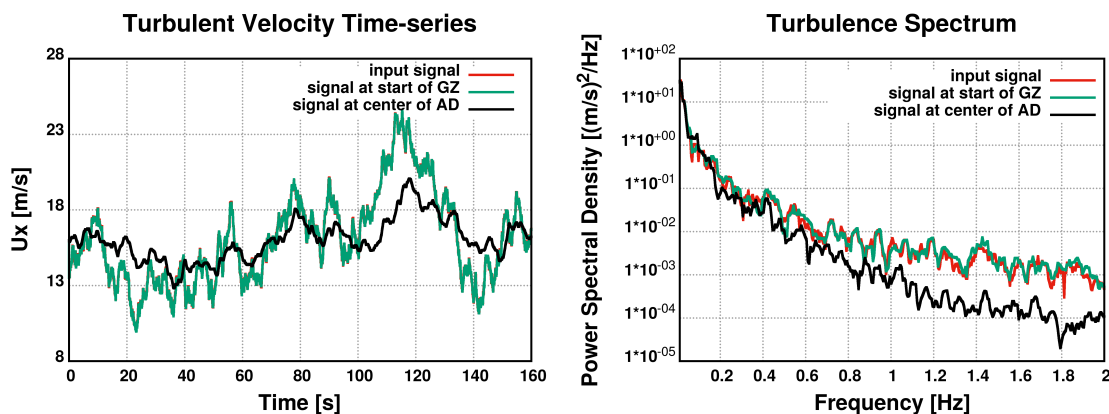
Figure 2.19. *Velocity time-series (left) and spectra (right) captured at start of GZ and center of AD, where the source terms are the strongest. Contrary to AD, the GZ creates a velocity profile that is almost identical to the desired one.*

The idea was first introduced in [144] (there referred to as "sponge zone") for absorbing free-surface waves in order to avoid reflection of waves from outlet boundaries. However, for the first time in [106] the same approach was used in order to generate a wave velocity profile and the idea of the Generation Zone was born. In that project, the GZ was placed near the far-field boundary of a domain. By only extending a few wavelengths (2 or more) and with 150 cells per wavelength, the GZ was able to precisely reproduce the desired velocity profile of the wave.

Nevertheless, the efficiency of the methodology is not that high when it comes to turbulent velocity profiles. In turbulent fields, the velocity profile is composed by multiple wave signals whose wavelengths vary in a wide range. The presence of very small wavelengths (the maximum frequency may go up to $10Hz$) renders the use of 150 cells per minimum wavelength not viable in terms of computational cost. Furthermore, the $3D$ nature of the current application of the methodology is an additional factor that leads to greater numerical diffusion compared to the $2D$ simulations it was applied regarding waves generation. Another crucial difference between waves and turbulence, is that turbulence is essentially dissipative, while waves are not. In fact, gravity is an important preservation factor when it comes to wave propagation. On the other hand, turbulence cannot maintain itself but depends on its environment to obtain energy. For these reasons, the turbulence spectrum at the end of the GZ is already slightly changed compared to the one created by Mann's generator, or the one produced at the start of the zone (see Figure 2.20). The most notable differences are observed in the higher frequency region ($> 1.4Hz$), where much less computational cells per wavelength exist compared to lower frequencies ($\leq 1.4Hz$). However, the fact that the numerical solution is obtained implicitly and is compatible with the solver settings, leads to a velocity profile that is less sensitive to numerical diffusion when convected downstream compared to the one created by the standard approach of the AD. In order to justify this statement, the spectra obtained by the two methodologies at the point of interest (hub center location of the WT) are directly compared in Figure 2.21. The newly proposed methodology is able to create a spectrum

which is less diffused compared to the conventional method.
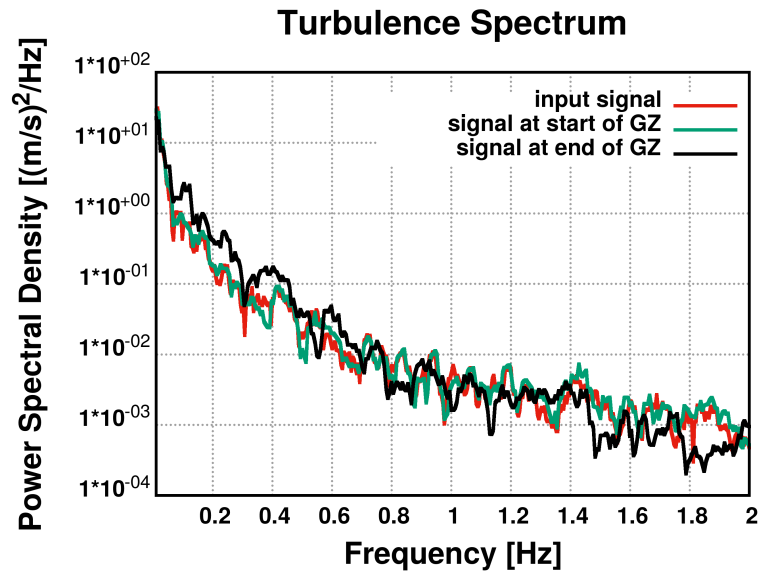
Figure 2.20. *The velocity spectra captured at the start and end plane of the GZ are compared against the desired one. The turbulence spectrum at the end of the GZ is already changed compared to the one created by Mann's generator, or the one produced at the start of the zone*
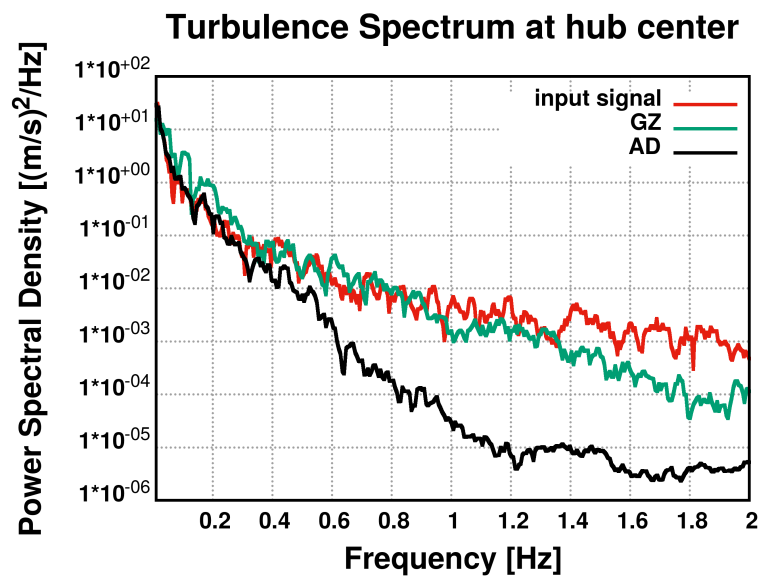
Figure 2.21. *The velocity spectra captured at the point of interest (e.g. rotor hub center) with the two methodologies are compared against the desired one. GZ is able to create a spectrum which is less diffused compared to AD.*

2.2.2 The Lagrangian CFD solver

In a Lagrangian formulation (material coordinates), the flow-field is represented by following the evolution of a number of particles along their trajectories. In that sense, particles act as flow marker points that are assigned with volume V_p and carry mass M_p, dilatation Θ_p, vorticity $\boldsymbol{\Omega}_p$ and pressure Π_p, regarded as the volume integrals of the continuous flow quantities density ρ, dilatation θ, vorticity $\boldsymbol{\omega}$ and pressure p respectively. In material coordinates, the flow equations take the form:

$$
\begin{aligned}
\frac{d\mathbf{Z}_p}{dt} &= \mathbf{U}_p \\
\frac{dV_p}{dt} &= V_p\,\theta_p \\
\frac{dM_p}{dt} &= 0 \\
\frac{d\boldsymbol{\Omega}_p}{dt} &= V_p\left[(\boldsymbol{\omega}\cdot\nabla)\mathbf{U} + \frac{1}{\rho^2}\nabla\rho\times\nabla p + \nu\nabla^2\boldsymbol{\omega}\right]_p \\
\frac{d\Theta_p}{dt} &= V_p\left[2\|\nabla\mathbf{U}\| - \frac{1}{\rho}\nabla^2 p + \frac{1}{\rho^2}\nabla\rho\cdot\nabla p + \nu\frac{4}{3}\nabla^2\theta\right]_p \\
\frac{d\Pi_p}{dt} &= V_p\left[(1-\gamma)p\theta + (\gamma-1)\left(\nabla\cdot(\boldsymbol{\tau}\cdot\mathbf{U}) - \mathbf{U}\cdot(\nabla\cdot\boldsymbol{\tau})\right)\right]_p
\end{aligned}
$$

(2.80)

where d/dt denotes the material time derivative, and $(\cdot)_p$ indicates evaluation at the position of particle p. $\nabla\cdot\boldsymbol{\tau} = \mu\left(\frac{4}{3}\nabla\theta - \nabla\times\boldsymbol{\omega}\right)$ denotes the divergence of the viscous stress tensor, and $\nu = \mu/\rho$ is the kinematic viscosity, which here is assumed constant.

The flow equations are supplemented with the Helmholtz's decomposition theorem (2.81), which states that every velocity field $\mathbf{u}$ can be expressed as the sum of a rot-free potential part $\mathbf{u}_\phi$ and a div-free vortical one $\mathbf{u}_\omega$, alongside a constant velocity component representing the undisturbed velocity field at infinity $\mathbf{U}_\infty$. The potential part is defined through a scalar potential ϕ $\left(\mathbf{u}_\phi = \nabla\phi\right)$ and is associated with the compressibility effects expressed by the dilatation of the flow θ ($\theta = \nabla\cdot\mathbf{u}$), whereas the vortical part is defined through a vector potential (stream-function) $\boldsymbol{\psi}$ ($\mathbf{u}_\omega = \nabla\times\boldsymbol{\psi}$) which is associated with the free vorticity of the flow $\boldsymbol{\omega}$ ($\boldsymbol{\omega} = \nabla\times\mathbf{u}$). Consequently, the scalar and vector potential satisfy the Poisson equation (2.82).

$$
\mathbf{u}\,(\mathbf{x}, t) = \mathbf{U}_\infty + \mathbf{u}_\phi\,(\mathbf{x}, t) + \mathbf{u}_\omega\,(\mathbf{x}, t)
$$

(2.81)

$$
\begin{aligned}
\nabla^2\phi &= \nabla\cdot\mathbf{u} = \theta \\
\nabla^2\boldsymbol{\psi} &= -\nabla\times\mathbf{u} = -\boldsymbol{\omega}
\end{aligned}
$$

(2.82)

By using Green's theorem, the velocity field $\mathbf{u}$ can be expressed in integral form:

$$
\mathbf{u}\,(\mathbf{x}) = \mathbf{U}_\infty + \int_D \left[\theta(\mathbf{y})\nabla G(\mathbf{r}) + \boldsymbol{\omega}(\mathbf{y})\times\nabla G(\mathbf{r})\right] dD(\mathbf{y}) + \int_S \left[\mathbf{n}\cdot\mathbf{u}(\mathbf{y})\nabla G(\mathbf{r}) + \mathbf{n}\times\mathbf{u}(\mathbf{y})\times\nabla G(\mathbf{r})\right] dS(\mathbf{y})
$$

(2.83)

where $G\,(\mathbf{r})$ is the Green's function for the Laplace operator, $\mathbf{r} = \mathbf{x} - \mathbf{y}$ and $S = \partial D$. Computational cost is dominated by the space convolution integral in equation (2.83).

For N particles, the associated cost is proportional to N^2, which can easily explode as N becomes large and the intended duration of the simulation is long. In order to reduce computational cost, the Particle Mesh (PM) technique is employed, and the Poisson equation (2.82) is solved for the scalar potential ϕ and the stream function ψ. In such a manner, computational cost is minimized from N^2 to $N \log N$. Computational performance is also enhanced by using Cartesian grids in order to discretize the Lagrangian domain, thus, enabling the use of fast Poisson solvers [145]. Particularly, in HoPFlow, the James–Lackner algorithm is used [146].

The PM framework is also employed in order to evaluate the Right Hand Side (RHS) of (2.80). The Lagrangian particles solution is interpolated to the PM nodes, and the desired differentiations are easily computed through finite difference schemes. Consequently, the RHS terms are first evaluated on the PM nodes, and then they are interpolated back to the particles positions. Afterwards, time marching is performed through a standard 4th order Runge–Kutta explicit scheme. In every sub–step of Runge–Kutta, intermediate convection steps are carried out, requiring intermediate evaluations of velocity, which are also conducted with the PM technique.

At the end of each time-step, remeshing is applied in order to recover full coverage of the computational domain and ensure a regular distribution of the numerical particles. Remeshing is a standard procedure in order to prevent excessive concentration or spreading of particles. In this way, the consistency and accuracy of the numerical solution is preserved.

For a given number of particles $\{\mathbf{Z}_p^n, M_p^n, V_p^n, \boldsymbol{\Omega}_p^n, \Theta_p^n, \Pi_p^n\}$, the sub-steps taken in the n_{th} Lagrangian time-step can be listed as follows:

Step 1: Project $\{M_p^n, \Theta_p^n, \boldsymbol{\Omega}_p^n, \Pi_p^n\}$ on the PM grid and obtain ρ_{ijk}^n, θ_{ijk}^n, $\boldsymbol{\omega}_{ijk}^n$, p_{ijk}^n

Step 2: Solve $\nabla^2 \phi = \theta$, $\nabla^2 \psi = -\boldsymbol{\omega}$ and obtain ϕ_{ijk}^n, ψ_{ijk}^n, $\mathbf{u}_{ijk}^n$

Step 3: Compute the RHS terms of equation (2.80), (e.g. $\nabla \rho_{ijk}^n$, ∇p_{ijk}^n, $\nabla \mathbf{u}_{ijk}^n$) on the PM grid;

Step 4: Interpolate all grid-based data q_{ijk}^n at the particle positions q_p^n

Step 5: Update all particle properties (integrate equation (2.80) in time)

Step 6: Re-mesh if needed

2.2.3 The Hybrid Lagrangian–Eulerian CFD solver HoPFLow

The rationale behind the application of the hybrid CFD solver HoPFlow is to combine an Eulerian approach close to solid–wall boundaries with a Lagrangian one for the rest of the domain. In this way, both the solid–wall and the exact far–field boundary conditions are satisfied in accuracy within the Eulerian and Lagrangian framework 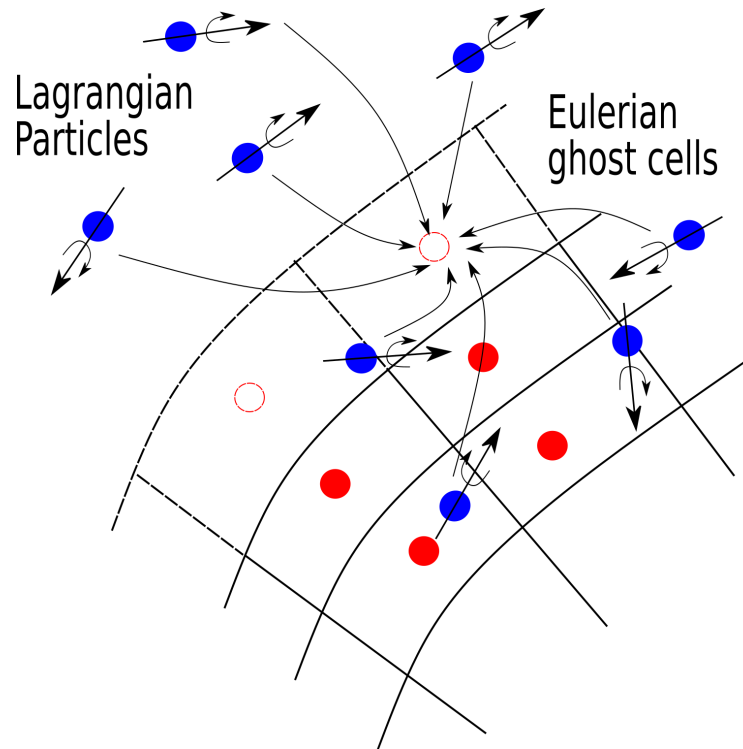respectively. The Lagrangian particles are distributed over the whole computational domain, overlapping with the Eulerian computational cells close to solid boundaries (see Figure 2.22). The Eulerian part of the hybrid solver solves the compressible Navier–Stokes equations under a cell–centered finite-volume approach in a confined region (D_E) around solid-wall boundaries (S_B). The Lagrangian part solves the compressible flow equations as well, in their material form, based on particle representation of the essential flow quantities, e.g. mass, pressure, dilatation and vorticity [67].
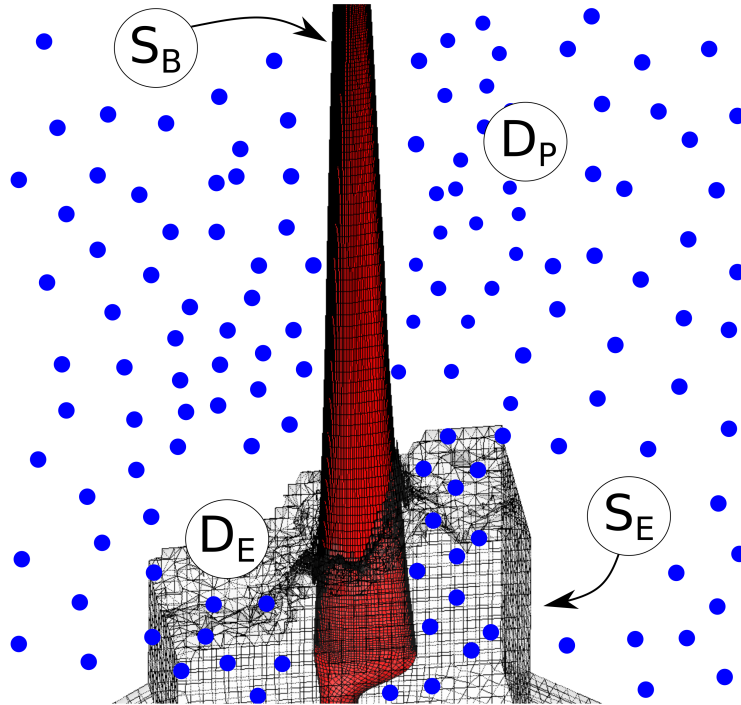
Figure 2.22. *Decomposition of Eulerian (D_E) and Lagrangian (D_P) computational domains. S_B denotes the solid-wall boundaries, and S_E the far-field of the Eulerian domain. The Lagrangian particles are distributed over the whole computational domain, overlapping with the Eulerian computational cells close to solid boundaries.*

The Eulerian and Lagrangian solutions are coupled in two ways. In the Lagrangian to Eulerian direction, the Lagrangian part provides the proper flow conditions on the outer boundaries of the Eulerian domain S_E. In order to do so, the Lagrangian solution is interpolated from the PM nodes (or, in a more generic approach, from the Lagrangian particle positions) to the ghost cells of the Eulerian grid (see Figure 2.23). The fluxes at the Eulerian boundary S_E may now be evaluated from the Riemann invariants and MaPFlow shall be capable of computing the flow–field close to the wall boundaries in the detail and accuracy that is provided by the Eulerian framework.
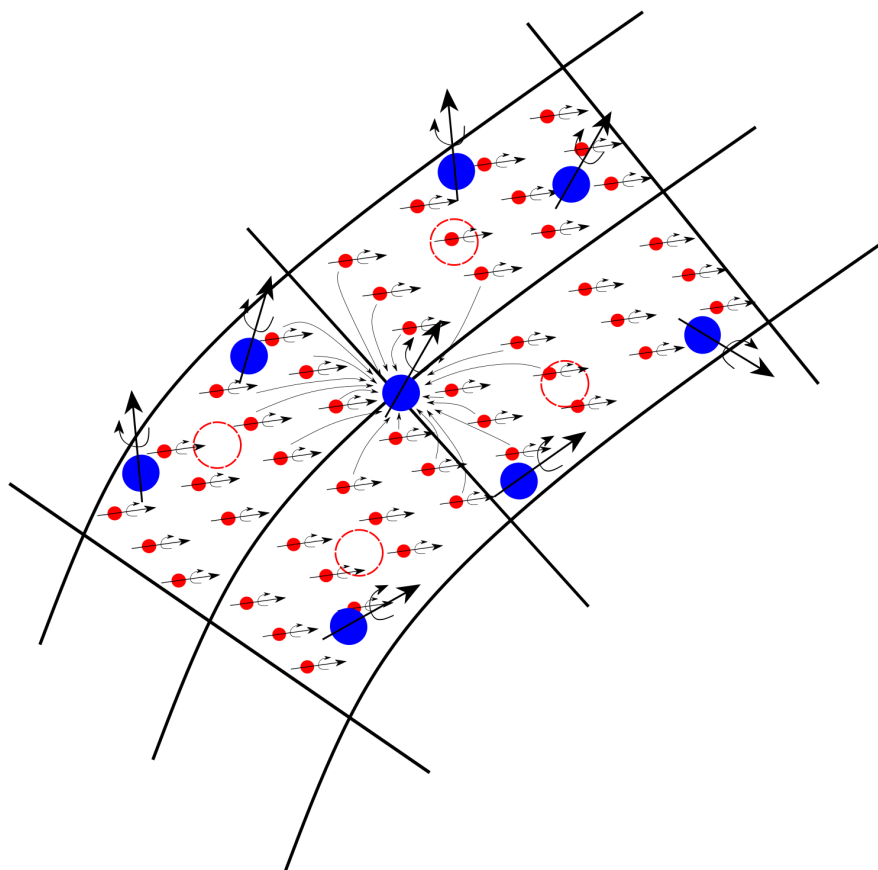
Figure 2.23. *The Lagrangian particles solution is interpolated to the ghost cells of the Eulerian sub-domain to define its far-field boundary conditions. Lagrangian particles are depicted as solid blue circles. Solid and dotted red circles denote the centers of the Eulerian cells and ghost cells, respectively.*

The closure of the coupling is achieved by correcting the flow information on the PM nodes (more generally on the Lagrangian particles) that lie within the Eulerian domain D_E and then by updating the whole Lagrangian field. In order to do so, the Eulerian solution is transformed into particles that carry mass, dilatation, vorticity, pressure and volume $(\rho, \theta, \boldsymbol{\omega}, p, V)_E$. The Eulerian particles need to be densely populated and regularly placed within the Eulerian computational cells, so that full coverage of the PM nodes is ensured (see Figure 2.24). The flow quantities of the Eulerian particles are interpolated from the cell–centered values based on a purely geometric approach using iso–parametric finite element approximations. The presence of solid boundaries is taken into account as surface (singular) particles that carry dilatation θ_s and vorticity $\boldsymbol{\omega}_s$, but no pressure, volume and mass. These particles only affect the solution of the Poisson equation (2.82) as contribution in $\mathbf{n} \cdot \mathbf{u}(\mathbf{y})$ and $\mathbf{n} \times \mathbf{u}(\mathbf{y})$ in the surface convolution related to boundary terms of equation (2.83) and must not be convected during time marching. The corrected Lagrangian particles information is then used in order to update the whole Lagrangian field and, thus, ensure that it is a smooth extension of the Eulerian one. In this way, the presence of solid–wall boundaries is effectively communicated from the Eulerian to the Lagrangian part.

The steps followed for the coupling between the Lagrangian and the Eulerian solver are depicted in the flow chart displayed in Figure 2.25. The corresponding implementation details have been thoroughly analyzed in [4, 147, 148, 45].

Figure 2.24. *The Eulerian solution is used in order to correct the Lagrangian particles that lie within the Eulerian sub-domain. The corrected Lagrangian particles information is then used in order to update the whole Lagrangian field and ensure that it is a smooth extension of the Eulerian one. Lagrangian particles are depicted as solid blue circles. Dotted red circles denote the centers of the Eulerian cells. Small solid red circles illustrate the Eulerian particles that correct the Lagrangian ones.*
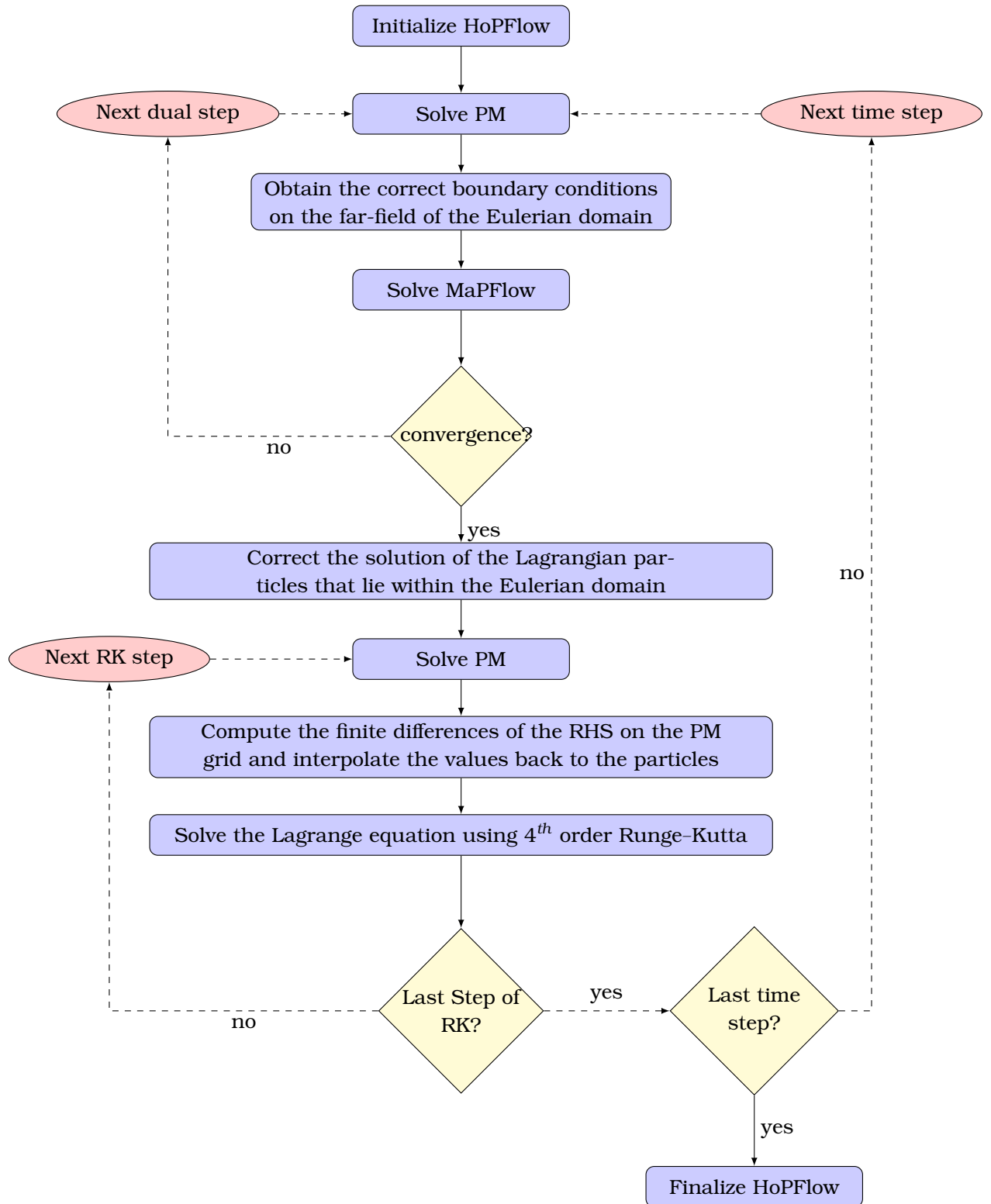
Figure 2.25. *Flowchart of the hybrid solver HoPFlow.*

2.3 Fluid Structure Interaction on beam–structured configurations

2.3.1 Aeroelastic coupling

Aeroelastic coupling consists of the interaction between the aerodynamic and elastodynamic modules within every time step of the numerical process. In order to do so, there are two different options of similar fidelity. The first one (full coupling) is to combine the two systems and solve them as one; alongside with their off–diagonal coupling terms (see Figure 2.26a). In this way the solution of the two systems are concurrently updated. Alternatively, the two systems can be solved separately (see Figure 2.26b). In this approach, the off–diagonal terms of the aeroelastic system are neglected and are "treated" as boundary terms of the two separate systems. The solution of the two systems are updated sequentially, by applying internal iterations until convergence is achieved for both. Within every internal iteration, compatibility information is exchanged between the systems (strong coupling) based on the solution of the previous iteration. In this way, it is easy to interchange between various aerodynamic or structural models of varying fidelity. Nevertheless, every pair of models needs an interface protocol of its own.

The aerodynamic code provides the elasto–dynamic module with loads, whereas the structural model provides kinematics to the aerodynamic one. More precisely, the distribution of the aerodynamic loads along the body, computed by the aerodynamic model, is fed to the structural dynamic module so that the work of the external loads in equation (2.11) can be estimated. In turn, the deformed coordinates and the deflection velocities at the nodes of the blade surface grid are computed by the structural analysis model and communicated to the aerodynamic module in order to define the correct solid–wall boundary conditions. This procedure is repeated within every time–step until convergence of both the aerodynamic and elastic solution is attained.

(a) *Fully coupled aeroelastic system.*   (b) *Strongly coupled aeroelastic system.*
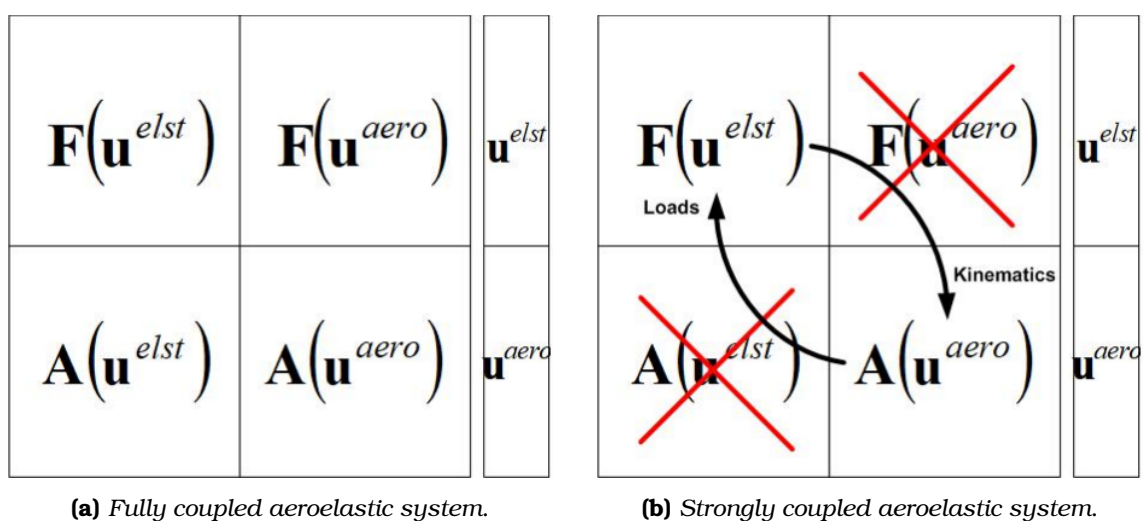
Figure 2.26. *Matrix form of aeroelastic equations.*

2.3.1.1 Kinematic (aerodynamic) boundary conditions

In an aeroelastic code the structural dynamics module needs to provide the aerodynamic solver with the correct kinematic boundary conditions (positions and velocities), so that both the rigid body motion and the elastic deformations of the body are properly accounted for at every point of its aerodynamic grid. In the current framework, the elasto–dynamic analysis of the various components of a configuration is based on a beam modelling approach. This means that the kinematics information which is concentrated on the beam axes, needs to be properly projected on the blade surface points of the aerodynamic grid (see Figure 2.27).

In particular, the primary kinematics information is concentrated on the nodes of the $1D$ Timoshenko beam finite elements ($\hat{\mathbf{u}}(t)$) and gets distributed along the beam axis through the shape function ($\mathbf{N}(y)$) of the finite elements. In this way, the elastic deformations of any arbitrary point along the beam can be defined ($\mathbf{u}(y, t) = \mathbf{N}(y)\hat{\mathbf{u}}(t)$) and then they are projected to all the blade surface points that belong to the corresponding cross–section ($\mathbf{u}_L(\mathbf{r}_L, t) = \mathbf{S}(x_L, z_L)\mathbf{u}(y_L, t)$).

This means that in a linear Euler–Bernoulli modelling of a beam, in order to calculate the elastic deformation of an aerodynamic point P, one could just simply project this point to the structural axis of the beam and acquire all the needed information as described above. However, in the current framework, non–linear beam (body) modelling is accomplished by connecting consecutive linear Timoshenko beams through non–linear constraint equations (see Section 2.1.3). Hence, the cross–sections of a beam, although still planar (warping is neglected), are not perpendicular to the structural axis ($\theta_x \neq w', \theta_z \neq -u'$). Therefore, for every aerodynamic point P one needs to know: i) the beam (sub–body) it belongs to and ii) the local co–ordinates of the point P with respect to the beam local co–ordinate system defined in the initial undeformed state ($\mathbf{r}_{L0}^k$), as shown in Figure 2.28. Consequently, a mapping between the aerodynamic and structural grids should precede the time–marching of the aeroelastic analysis.

The position and velocity of any blade surface point is computed by using the multi–body kinematics equations (2.1):

$$\mathbf{r}_G^P = \mathbf{R}^k + \mathbf{T}^k\left(\mathbf{r}_L^P + \mathbf{S}\left(x_L^P, z_L^P\right)\mathbf{u}^k\left(y_L^P, t\right)\right)$$

$$\dot{\mathbf{r}}_G^P = \dot{\mathbf{R}}^k + \dot{\mathbf{T}}^k\left(\mathbf{r}_L^P + \mathbf{S}\left(x_L^P, z_L^P\right)\mathbf{u}\left(y_L^P, t\right)\right) + \mathbf{T}^k\left(\mathbf{S}\left(x_L^P, z_L^P\right)\dot{\mathbf{u}}\left(y_L^P, t\right)\right)$$

where $\mathbf{r}_G^P(rig) = \mathbf{R}^k + \mathbf{T}^k\mathbf{r}_L^P$ is the rigid body motion part and $\mathbf{r}_G^P(el) = \mathbf{T}^k\left(\mathbf{S}\left(x_L^P, z_L^P\right)\mathbf{u}\left(y_L^P, t\right)\right)$ is the elastic deformation. This is sufficient for all the grid–free aerodynamic models (BEMT and FVW codes) and the actuator–based CFD methods (e.g. Actuator Line), where the aerodynamic bodies move freely inside the computational domain. A few more parameters need to be considered in the Eulerian formulations when the actual geometry of the body is resolved and the rest of the grid nodes need to comply with the motion of the aerodynamic bodies.

There are various implementation options permitting body motion and aeroelastic

analyses within an Eulerian CFD framework, like Immersed Boundary Methods (IBMs) [87], Overset grids [89] or Deforming grids [90], each coping with the aforementioned problem more or less differently and raising different issues, such as temporal discontinuity of regional cells, loss of conservativeness or deterioration of grid quality respectively. In the following paragraphs, emphasis is given to Overset and Deforming grids implementations details, as they are the ones used in the present research (the Lagrangian domain of the hybrid solver serves as the coupling domain between distinct and separately discretised sub–structures of the computational domain in the same way as Overset grids techniques).

In an Overset grids approach, every aerodynamic body has its own grid, confined in a narrow regions around its solid–wall boundaries and separate from the rest body–fitted grids. Their interaction is accounted for with the aid of a stationary background grid applying field communication, through which the different body–fitted grids move freely. Consequently, the elastic deflections of the body surface nodes can be expanded undamped to the rest of the body–fitted grid nodes, as if they were part of the body ($\mathbf{u}_L(\mathbf{r}_L, t) = \mathbf{S}(x_L, z_L)\mathbf{u}(y_L, t)$). In this way, the initial topology of the grid is not affected by the elastic deflections (and rigid body motion in general) of the body and, thus, the grid quality remains more or less intact (see Figure 2.29).

In cases where a single Eulerian domain contains all the deforming bodies, the grid needs to follow the motion of the various bodies whilst keeping the connectivity of the nodes unchanged. The Deforming grids approach may efficiently serve such cases whilst preserving the accuracy of the numerical approach and confining computational cost. There are multiple grid deformation techniques implemented in MaPFlow, such as the one proposed by Rendal and Allen [149], where Radial Basis Functions are used to interpolate the displacements of the inner grid nodes based on the displacements of the body surface nodes [150]. In the present work, the algorithm of Zhao [90] (see Section 2.2.1.4), in which the deformation of the grid nodes gets diminished through an exponential function as the distance from the body gets higher, is used. However, the motion of a grid node is explicitly determined by the motion of its closest body surface node, thus, significantly limiting computational cost.

In both of the aforementioned grid deformation techniques (rigid deformation, exponentially damped deformation) the velocity of the grid nodes is computed by applying a 1st order finite differences scheme between the position of the previous time–step and the current time–step iteration. A linear distribution of the velocity is assumed over the faces based on the values of their nodes and the GCL is applied in order to estimate the time derivative of the volume of the cells.
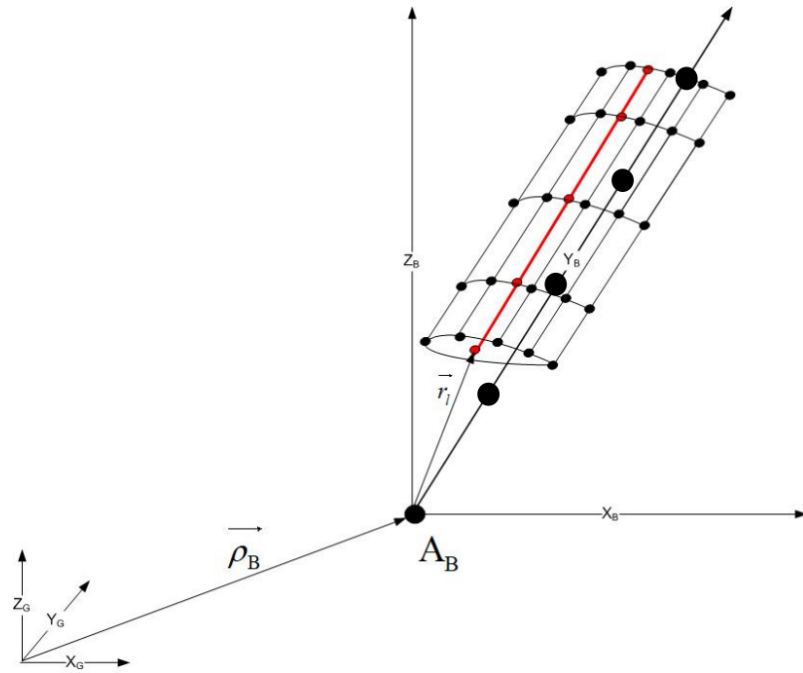
Figure 2.27. *In an aeroelastic framework, the aerodynamic and structural grid nodes are expressed in the same kinematics framework.*
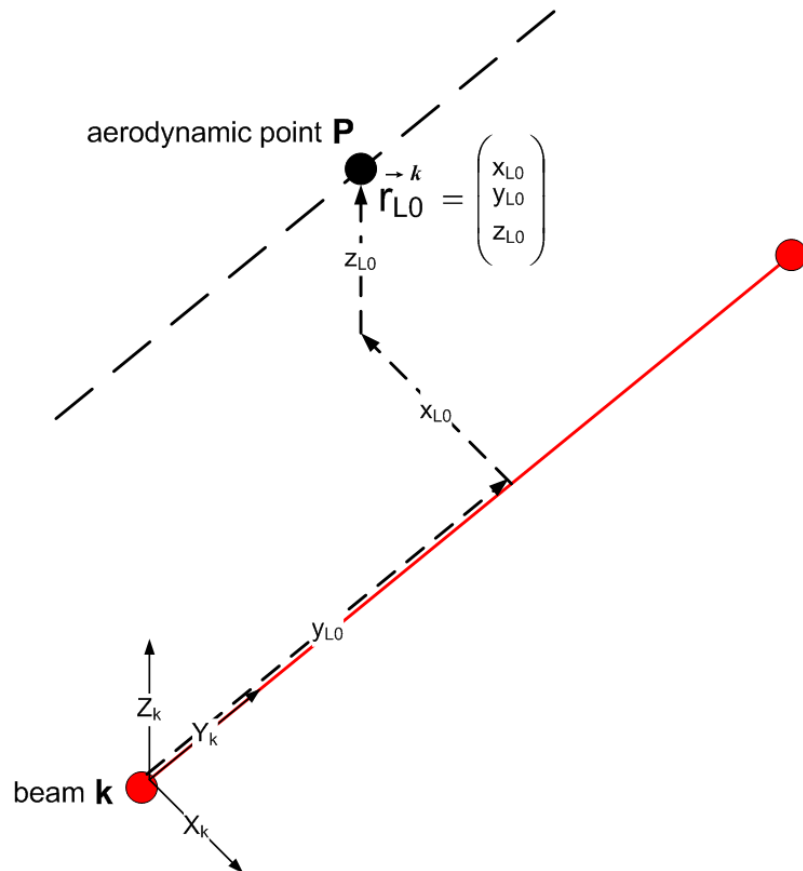
Figure 2.28. *Mapping between the structural and aerodynamic grid is applied in the initial undeformed state and is based on the local co-ordinates of the aerodynamic point P with respect to its local beam co-ordinate system.*

Deformed blade
Undeformed blade
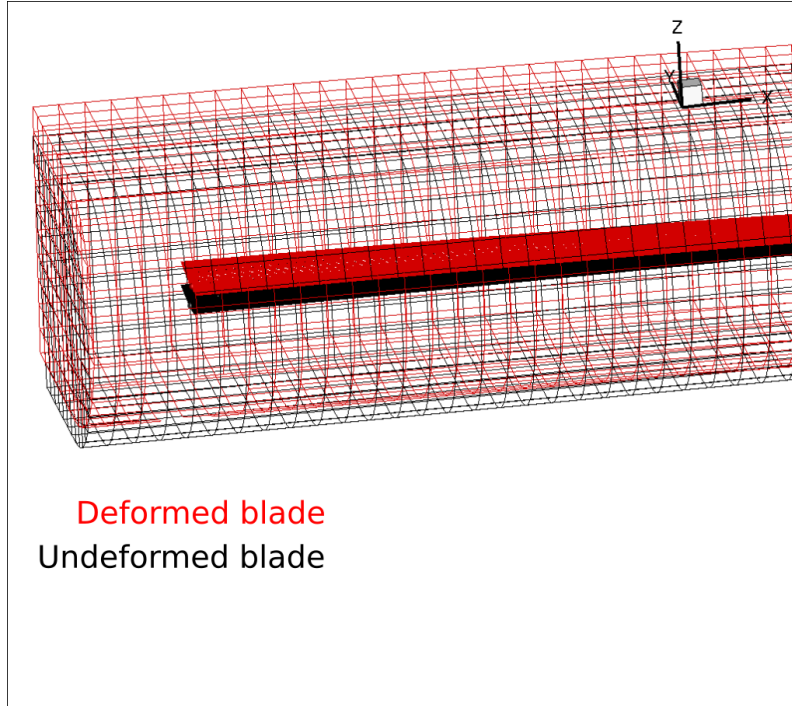
Figure 2.29. *Rigid deformation of the body–fitted grid nodes in an Overset grids formulation. Elastic deflections of the body surface nodes are expanded undamped to the rest of the grid nodes. Consequently, the initial topology and the quality of the grid remain intact.*

2.3.1.2 Dynamic (structural) boundary conditions

External loads (dominated by the aerodynamic forces and moments) act as dynamic condition to the structural module. The utter goal is to estimate their virtual work in equation (2.11). To that end, the aerodynamic code provides a $1D$ line distribution of forces and moments along the body axis to the elasto–dynamic module (beam modelling) by following a two–step procedure:

i) the aerodynamic forces are integrated from pressure and viscous stresses (surface friction) over the aerodynamic surface grid in strips according to equation (2.84) (see Figure 2.30):

$$
\begin{aligned}
\mathbf{f}_{aer}(s) &= \frac{\sum_p \mathbf{f}_p \Delta s_p \mathrm{W}_1\left(\frac{s_p - s}{\Delta s}\right)}{\Delta s} \\
\mathbf{m}_{aer}(s) &= \frac{\sum_p \mathbf{r}_p \times \mathbf{f}_p \Delta s_p \mathrm{W}_1\left(\frac{s_p - s}{\Delta s}\right)}{\Delta s}
\end{aligned}
\tag{2.84}
$$

where $\sum_p$ denotes summation over the panels that formulate the surface grid of the body, $\mathbf{f}_p$ is the total force exerted on the panel surface in N/m (pressure and viscous stresses are multiplied with the area of the panel and then normalized by the length of the panel along the span–wise direction of the body), $\mathbf{r}_p$ is the distance in m between the control point of the panel and the control point of the strip (the control points over successive strips form the aerodynamic reference line), s_p is the arc length in m of the control point of the panel, s is the arc length in m of the

control point of the strip, Δs_p is the length of the panel in m along the span–wise direction of the body, Δs is the length of the strip in m along the span–wise direction of the body and $W_1(h)$ is a $1D$ interpolation function. In the present work, the M_1 interpolation function is used (for others see [55]).

This results in a line distribution of normalized forces ($\mathbf{f}_{aer}(s)$) and moments ($\mathbf{m}_{aer}(s)$) along the *aerodynamic reference line* (usually set at quarter–chord).

ii) this distribution is transferred to the *structural reference line* (the line with respect to which the structural properties are defined), by taking into account their in between offset (Δx) as indicated in equation (2.85):

$$
\begin{aligned}
\mathbf{f}_{str}(s) &= \mathbf{f}_{aer}(s) \\
\mathbf{m}_{str}(s) &= \mathbf{m}_{aer}(s) + \Delta x \times \mathbf{f}_{aer}(s)
\end{aligned}
\tag{2.85}
$$

In general, the two lines can be offset with respect to each other (see Figure 2.31). Due to the above offset an extra twisting moment must be communicated when transferring loads from the aerodynamic line to the elastic line. The above offset must also be taken into account when transferring deflections and velocities from the elastic line to the aerodynamic line, as rotations around the structural axis induce translations at the aerodynamic points.

In the blade–element based aerodynamic methods (BEMT, LL, AL) the computation of normalized loads over strips along the aerodynamic reference line is part of the standard procedure. Likewise, in CFD, the grid is divided into strips along the body axis. If the surface elements are densely populated over the aerodynamic reference line (highly likely for standard CFD grid resolutions), reasonably smooth distributions of aerodynamic loads are generated. Otherwise, the forces of a surface element may be regularly distributed over multiple points inside the element in order to increase the density of the force points. Finally, it needs to be stressed that the aerodynamic reference line is considered as an actual part of the body and, for this reason, it follows its deformation.

In order to transfer the aerodynamic loads distribution from the aerodynamic reference line to the structural reference line, a mapping needs to be applied between the two lines. In general, the $1D$ discretization of the aerodynamic and structural reference lines is different. In the aerodynamic model, the reference line is divided into a number of aerodynamic strips over which aerodynamic loads are computed and considered uniformly distributed. With regard to the structural model, the elastic line of a single blade can be shared among several connected beams (sub–bodies), which in turn are discretized into a number of linear finite elements. The above definitions for the aerodynamic strips, the structural elements and the corresponding grids are shown in Figure 2.31a. The correspondence of the aerodynamic and structural grids is defined based on a material co–ordinate s_0 in the initial undeformed state (see Figure 2.31b). The material co–ordinate s_0 represents the arc length of every point with respect to the reference line it belongs and has a unitary numbering along the blade, no matter how many sub–bodies have been

used to describe it. If the blade is straight, s_0 coincides with the radial y co–ordinate of the blade local system. The need for introducing the material co–ordinate s_0 stems from the fact that when the blade is deformed the structural nodes are displaced in all directions and, depending on the deformation field, the length of the deformed blade changes (increases in case of pure tension, decreases in case of bending deflection).
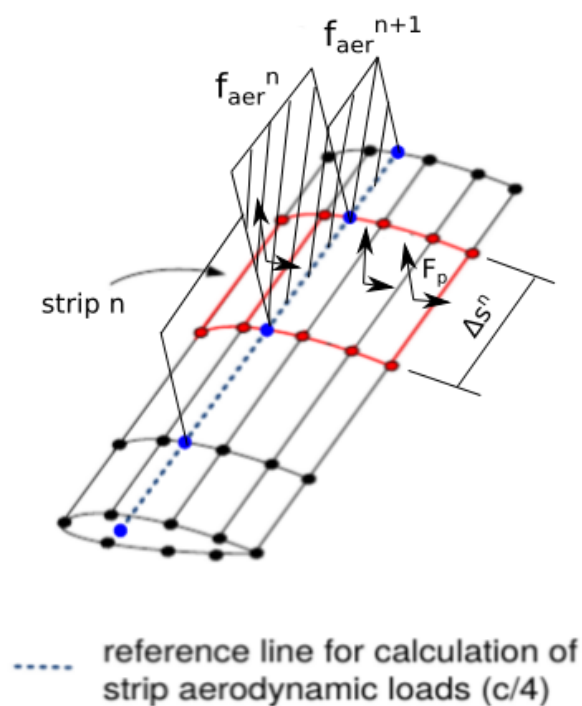
Figure 2.30. *Definition of the aerodynamic reference line in a CFD aerodynamic grid. Strips are defined along the body axis. The loads on the strips are computed by integrating pressure and viscous stresses over the surface grid panels that lie within the strip.*
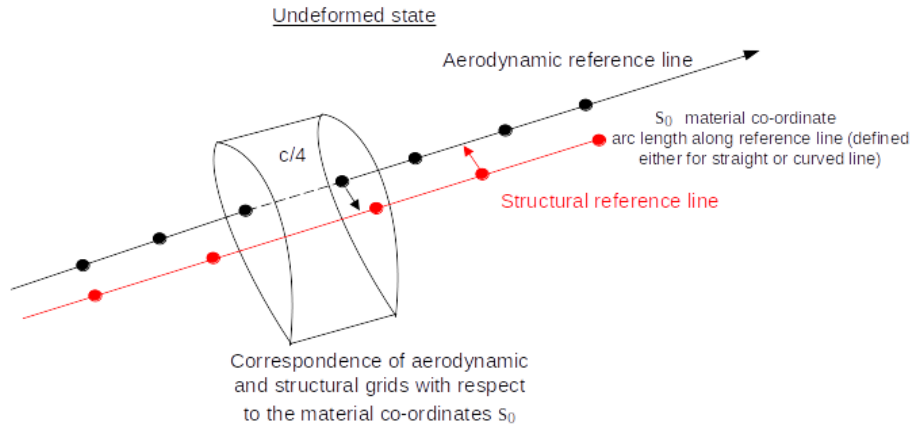
(a) *Undeformed state.*
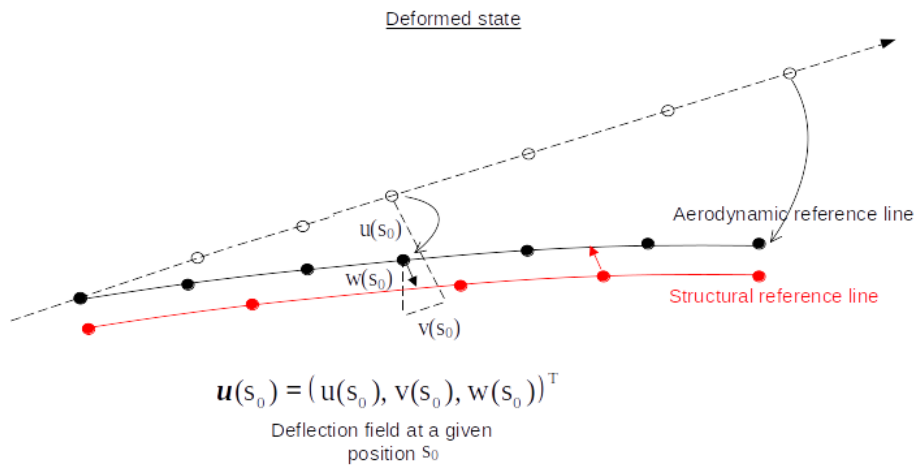
(b) *Deformed state.*

Figure 2.31. *Correspondence between the aerodynamic and structural grids is based on the material co-ordinate s_0 and is defined in the initial undeformed state.*

Chapter 3

AL modelled rotor blades using MaPFlow

In this chapter, the results produced through aeroelastic simulations of a WT rotor and a model helicopter Main Rotor (MR) under smooth free–stream flow conditions are presented. Then, aeroelastic analyses of a full WT configuration (tower, shaft, rotor) operating in turbulent wind conditions follow. The aerodynamic analysis of the rotor blades is based on the Actuator Line (AL) model implemented in MaPFlow. Results are compared against the ones produced by a standard Blade Element Momentum Theory (BEMT) model and a classical Lifting Line (LL) approach. These two models constitute standard state–of–the–art approaches for the aeroelastic analysis of WT and helicopter rotors, at least on industrial level. In any case, the elasto–dynamic analysis of the rotor blades is performed through GAST. In helicopter MR simulations, experimentally measured data are used as an extra reference.

3.1 Smooth free–stream flow cases

This section addresses the aeroelastic operation of both WT and helicopter rotors under smooth free–stream flows. First, the effect of multiple numerical parameters involved in the AL model will be assessed in purely aerodynamic simulations where the elastic deflections of the blades are neglected (rigid blades assumption). The extracted conclusions are then transferred and extended in the respective aeroelastic simulations, where GAST–AL results are compared against experimental measurements and computational predictions by lower fidelity aerodynamic models; namely BEMT and LL, which are the standard options in WT and helicopters design respectively.

3.1.1 Aeroelastic analysis of a WT rotor

In this section, aeroelastic simulations are performed for the DTU 10MW Reference Wind Turbine (DTU 10MW RWT) rotor operating at 8 and 11 m/s wind speed at various yaw misalignment angles from $-30°$ to $+30°$. The rotor blades are modelled as actuator lines in a purely Eulerian context, using MaPFlow. The structural dynamics analysis is performed through GAST and the rotor blades are modelled as beam assemblies, in order for non–linear geometric phenomena to be properly accounted for. The two systems are solved separately, but tightly coupled. First, aerodynamic simulations (blades deformations neglected) are performed at 11 m/s axial wind speed case in order to investigate the

effect of numerical parameters (e.g. spreading of aerodynamic forces, grid and time–step resolution, grid set–up) on the predicted aerodynamic loads. Then, aeroelastic simulations are performed at all the aforementioned wind speed cases and the produced results are compared against BEMT and LL predictions.

3.1.1.1 The DTU10MW Reference Wind Turbine

The DTU 10MW RWT is an IEC Class 1A conceptual WT that was designed during the Light Rotor project [151]. The Light Rotor project has been initiated as a cooperation between DTU Wind Energy and Vestas; its goal was to describe the design of a large scale light–weight WT with conventional methods and techniques in order to serve as a reference to future advanced rotor designs. Although the project mainly focused on the design of the rotor, the entire WT (tower, drive–train, rotor) was developed in order to understand the effect of the entire system (structural dynamics of the blades, the tower and the drive–train) on the rotor performance. The DTU 10MW RWT design was based on an up–scaling of the conceptual NREL 5MW RWT [152]. Later, it was employed as the reference turbine in a number of research projects, such as the INNWIND.EU European project [153] that among others addressed the design of large scale (10-20 MW) and cost effective WTs and the development of new modelling tools, capable of analyzing large scale innovative turbine systems.

DTU 10MW RWT is a traditional 3–bladed, upwind, horizontal axis WT (see Figure 3.1). It employs variable speed and pitch control systems. Its basic operational and geometrical characteristics are listed in Table 3.1, whereas more details can be found in [9].

Table 3.1. *Basic operational and geometrical characteristics of the DTU 10MW RWT.*

Wind Regime	IEC Class 1A
Rotor Orientation	Clock–wise rotation / Upwind
Control	Variable–Speed / Pitch–Regulated / Yaw–Control
Operational Wind Speed	$4 - 25\ m/s$
Rated Wind Speed	$11.4\ m/s$
Rated Power	$10MW$
Number of Blades	3
Rotor Diameter	$178.3m$
Hub Diameter	$5.6m$
Hub Height	$119m$
Range of Rotor Speed	$6 - 9.6\ rpm$
Maximum Tip Speed	$90\ m/s$
Hub Overhang	$7.1\ m/s$
Shaft Tilt	$5°$
Blade Pre–cone Angle	$2.5°$
Blade Pre–bend	$3.332\ m$
Blade, Nacelle and Tower Mass	$227962\ kg$, $446036\ kg$, $628442\ kg$
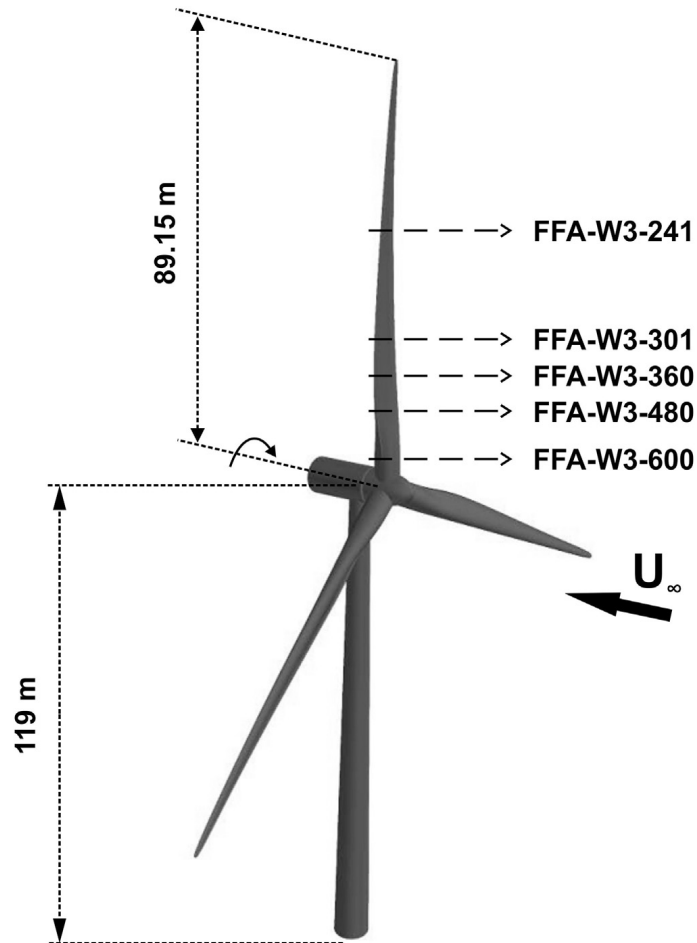
Figure 3.1. *Sketch of the DTU 10MW RWT. Image copied from [154].*

3.1.1.2 Numerical investigation

In this section, aerodynamic simulations are performed for the DTU 10MW RWT rotor operating at 11 m/s axial wind speed (partial load operation). Constant rotational speed and pitch angle of the blades are considered (open loop operation). The rotor blades are modelled as actuator lines in a purely Eulerian context, using MaPFlow. The goal is to investigate the effect of multiple numerical parameters (e.g. spreading of aerodynamic forces, grid and time–step resolution, grid set–up) on the produced aerodynamic loads. Any engineering correction model that needs case specific tuning (e.g. tip correction models) is neglected and the numerical parameters that affect the produced results in a more generic way are investigated in detail. A new way to define the projection width of the computed aerodynamic forces (firstly proposed in [134]) is applied, which is based on the standard 3D Gaussian convolution described in 2.2.1.5 and leads to a straightforward grid independent solution under moderate computational requirements.

The set–up of an AL model involves multiple numerical parameters that affect the produced results. In particular, the method used in the projection of the blade forces onto the CFD grid plays an important role in the intensity of the produced tip and root vortices [155], which, in turn, affects the computed blade loads. A great deal of research effort has been devoted to determining the best option of body force projec-

tion [135, 136, 137, 130]. A common requirement for the successful application of all these methods is the adoption of really fine grid resolution around the blades and in particular close to the blades tip. The alternative is to use a coarse grid and account for the tip vortex effect through proper tip loss correction [133, 156] or smearing correction [157, 158] models. In most of the above discussed studies, AL results are compared against results produced by LL models [47] or BEMT models that use Prandtl's tip correction [40]. Apart from the specific technique for blade forces projection, there are multiple additional numerical parameters that have to be carefully determined in order to acquire an accurate distribution of aerodynamic loads. Such are: the time–step value of the unsteady simulations, the number of strips used in order to discretise the actuator lines or/and the computational grid set–up.

The AL numerical parameters in WT simulations have been calibrated on an axial case at 11 m/s uniform wind speed. The blades are evenly distributed and considered to be rigid. Structural deflections alongside prebend, cone, and tilt angle of the blades are neglected, so that the configuration is as simple as possible for this parametric study. As a result, we end up with a purely axisymmetric case. In order to reduce computational cost, only one blade has been resolved in the rotating frame, with the use of periodic boundaries and in steady–state condition. The domain is a cylindrical section of 10 rotor diameters (10D) radius (see Figure 3.2a) and of 20D length (see Figure 3.2b). Structured and uniform meshing under maximum grid resolution is applied in a thin region surrounding the actuator line. The structured area extends adequately around the actuator line, so that maximum accuracy is acquired in resolving the Gaussian projection of loads (see Figure 3.3). The characteristic length of this region is denoted by Δx. This fine region is followed by an unstructured and slightly coarser area that resolves the near wake region, which is characterized by high velocity gradients and significantly affects the development of the aerodynamic forces over the rotor. This area extends up to 1D upstream, 3D downstream, and 1D radially from the actuator line, so that the wake expansion fits in. The characteristic length of this region is denoted by Δw.

(a) *Axial view.* (b) *Lateral view.*
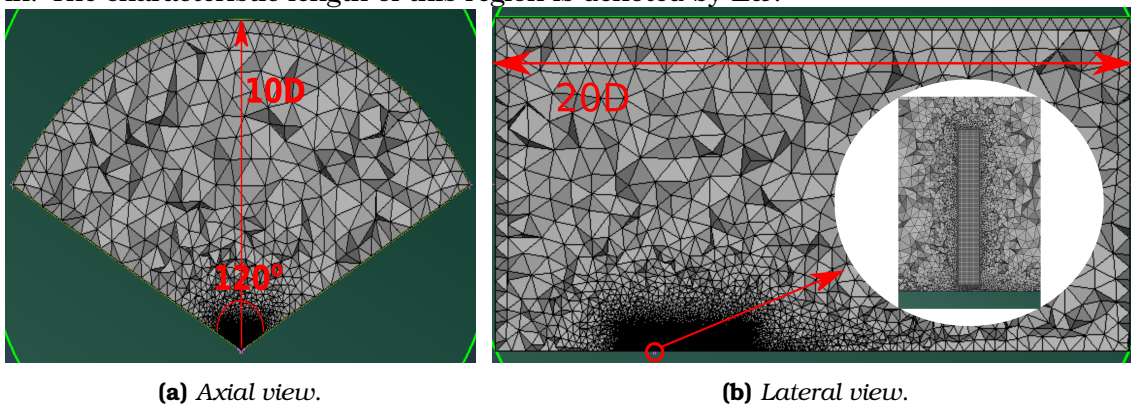
Figure 3.2. *Axial (a) and lateral (b) view of the computational domain in the axisymmetric case for the DTU 10MW RWT rotor at 11 m/s wind speed. Only 1 out of 3 blades is resolved. The blade is modelled as an actuator line that is located inside a cylindrical section of a 10D radius and a 20D length. Periodic boundary conditions have been applied to the circumferential sides. In light of the above and in order to reduce computational requirements, a steady–state simulation has been performed in the rotating frame.*
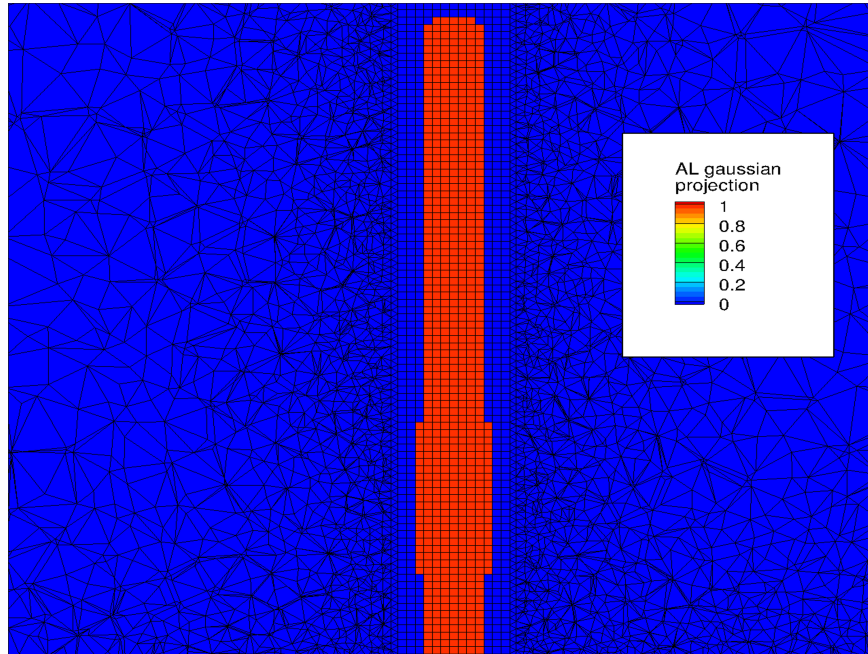
Figure 3.3. *Gaussian projection of the aerodynamic forces of the actuator line. The cells that lie within the distribution are painted in red. The support of the projected forces is fully included in a fine, structured and uniform region, so that maximum accuracy is acquired.*

Grid Dependency Analysis

First Δx is calibrated. The corresponding results are presented in Table 3.2 and Figure 3.4. Each column lists the extracted power in MW, with respect to different values of Δx and for various approaches in defining the Gaussian kernel value ϵ. The standard approach in defining ϵ proportionally to Δx [7] fails to provide a grid independent solution. Since the blade geometry is not resolved, flow does not perceive the presence of a solid body. The volume of the blade is regarded as the volume of the distributed aerodynamic forces of the actuator line, as shown in Figure 3.3. Consequently, when $\Delta x \rightarrow 0$ the "blade" volume degenerates and numerically disappears, along with the blade forces. As a remedy, the Gaussian distribution kernel ϵ may vary proportionally to the chord c of each blade section in order to take into account the effect of the blade geometry [135]. In this study, the proportionality factor 0.47 is chosen so that the Gaussian projection of the aerodynamic forces extends up to $1c$ around the emission points. (The projection width of the Gaussian distribution is $3\sigma = \frac{3}{\sqrt{2}}\epsilon$. If the projection width is decided to extend up to $1c$ around the emission points, then $c = \frac{3}{\sqrt{2}}\epsilon$ or $\epsilon \simeq 0.47c$.) This approach can resolve in detail the blade geometry and, thus, leads to a grid independent solution. However, the reduction of the chord close to the tip, results in very small values of ϵ thereby, even less than Δx, leading to numerical singularities that are avoided only when very fine grid resolution is employed in the AL vicinity. Then, computational cost is unbearably penalized, especially in unsteady simulations with many blades and rotors. In an attempt to restrain computational requirements, the two former approaches may be combined by setting a lower bound for ϵ, $\epsilon_{min} = 2\Delta x$, as proposed by [7]. According to Figure 3.4, this allows for grid independent and accurate solution under moderate grid resolution and,

thus, reasonable computational cost. Based on the results in Table 3.2, $\Delta x = R/90$ seems to be a good trade-off between accuracy and computational cost.

Table 3.2. *Variation of power [MW] with increasing the structured region characteristic length Δx [m]. Convergence with respect to Δx when different approaches for defining the Gaussian distribution kernel ϵ are adopted. Reference power corresponds to minimum values $\Delta x = R/180$. The hybrid approach $\epsilon = max(2\Delta x, 0.47c)$ provides an accurate and grid independent solution at $\Delta x = R/90$, by using less than $1/4$ of the cells needed when the geometric approach $\epsilon = 0.47c$ is employed (with $\Delta x = R/180$).*

Δx	$\epsilon = 2\Delta x$	$\epsilon = 0.47c$	$\epsilon = max(2\Delta x, 0.47c)$
$R/30$ $(151 \cdot 10^3$ cells$)$	+31.4%	+67.5%	+9.2%
$R/60$ $(283 \cdot 10^3$ cells$)$	+22.6%	−37.6%	+2.6%
$R/90$ $(495 \cdot 10^3$ cells$)$	+15.1%	−20.7%	−0.8%
$R/120$ $(884 \cdot 10^3$ cells$)$	+9.5%	−10.1%	−1.5%
$R/150$ $(1.500 \cdot 10^6$ cells$)$	+4.5%	−3.9%	−0.9%
$R/180$ $(2.290 \cdot 10^6$ cells$)$	7.921 MW	9.202 MW	9.362 MW
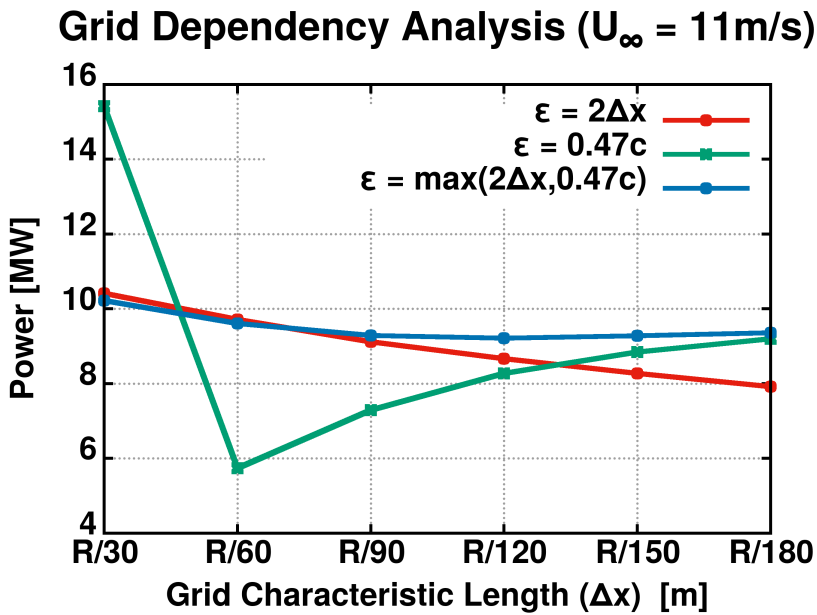
Figure 3.4. *Variation of power [MW] with increasing the structured region characteristic length Δx [m] for AL modelled WT rotor simulations. Comparison among different approaches of defining the Gaussian kernel ϵ. The standard approach $\epsilon = 2\Delta x$ fails to provide a grid independent solution. The geometric approach $\epsilon = 0.47c$ is successful under excessively fine grid resolutions. The hybrid approach $\epsilon = max(2\Delta x, 0.47c)$ provides an accurate and grid independent solution under moderate grid resolution. The values printed in this Figure are listed in Table 3.2.*

Wake region characteristic length Δw is examined in Table 3.3. The crucial aspect in choosing Δw is the detail in resolving near wake velocity and vorticity. Apparently, as Δw gets finer, the accuracy of the predicted flow field is enhanced, which comes at an extra computational cost. This improvement does not imply any additional benefits in load predictions which is the main focus of the present work. For this reason, $\Delta w = 10\Delta x$

is considered a good compromise between accuracy and computational cost. However, if wake dynamics is important (simulation of many aligned WT rotors, interacting with each other), Δw should be refined as much as possible in order to reduce numerical diffusion in the wake.

Table 3.3. *Variation of power [MW] with increasing wake region characteristic length Δw [m]. Reference power corresponds to minimum value $\Delta w = 5\Delta x$. $\Delta w = 10\Delta x$ provides a good trade-off between accuracy (within 1% of the reference value) and computational cost when rotor loads are to be captured. All the different Δw values have been tested by using the hybrid approach $\epsilon = max(2\Delta x, 0.47c)$ to define the Gaussian kernel ϵ. Refinement should be considered in wake dynamics studying in order to reduce numerical diffusion.*
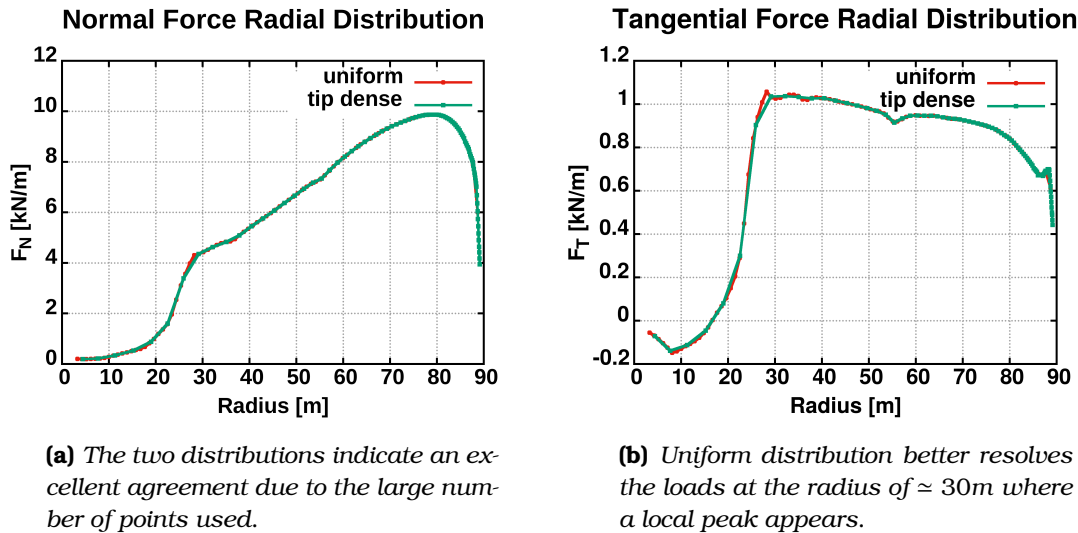
Δw	Power [MW]
$20\Delta x$ $(340 \cdot 10^3$ *cells*$)$	+2.2%
$10\Delta x$ $(495 \cdot 10^3$ *cells*$)$	+0.9%
$5\Delta x$ $(1.653 \cdot 10^6$ *cells*$)$	9.202 MW

Blade Grid Dependency Analysis

The outcome of the investigation for the effect of the number of strips (#*strips*) (AL control points are located at the center of each strip) and their distribution pattern in the power output is shown in Table 3.4 and Figure 3.5. As a first step, the AL control points are uniformly distributed along the blade span, thus, leading to a constant strip length (Δr). The parameter #*strips* is not independently studied, except through the correlation of Δr with Δx. In Table 3.4, it is clear that $\Delta r \leq 3\Delta x$ is a reasonable choice for defining Δr that can thereafter be used as a rule of thumb. Nevertheless, since #*strips* adds no significant computational cost, the ratio $\Delta r = 1.5\Delta x$ is proposed for the WT AL simulations, in order to ensure a smooth representation of the radial distribution of aerodynamic forces. Figure 3.5a and 3.5b present a comparison between a uniform distribution of control points ($\Delta r = 1.5\Delta x$) with a non–uniform one, with the same number of points. Non–uniformity implies a coarse discretization close to the root that gradually gets finer as we approach the tip. As seen in Figure 3.5, where the normal (3.5a) and tangential (3.5b) force along the blade span are plotted for the two different discretisations, the two distributions almost coincide due to the large number of points used. Uniform distribution better resolves the loads at the radius of $\simeq 30m$ where a local peak appears in particular in the tangential force. No advantage is observed at the tip region when employing denser distribution of points. It is easy to understand that due to the large number of control points along the blade span, a non–uniform distribution adds no extra benefit. Consequently, constant strip length Δr is proposed for the sake of simplicity.

Table 3.4. *Variation of power [MW] with increasing blade grid size Δr [m]. Reference power corresponds to minimum value $\Delta r = \Delta x$. $\Delta r = 3\Delta x$ provides an accurate and grid independent solution. However, since #strips adds no significant computational cost, more control points may be used ($\Delta r \leq 3\Delta x$) in order to ensure a smooth representation of the radial distribution of aerodynamic forces.*

Δr	Power [MW]
$4\Delta x$	-1.8%
$3\Delta x$	$+0.1\%$
$2\Delta x$	$+0.06\%$
Δx	9.286 MW

(a) *The two distributions indicate an excellent agreement due to the large number of points used.*

(b) *Uniform distribution better resolves the loads at the radius of $\simeq 30m$ where a local peak appears.*

Figure 3.5. *Normal (a) and tangential (b) force radial distribution in a purely aerodynamic axial case of the DTU 10MW RWT rotor at 11 m/s wind speed. Comparison between uniform distribution of control points against a non-uniform one with the same number of points (60) but concentrated in dense distribution towards the tip. Very good agreement is shown in the distributions of both components. The uniform distribution better resolves the loads close to the root. No advantage is observed at the tip region when employing denser distribution of control points. Hence, a non-uniform distribution adds no extra benefit, provided that a sufficiently large amount of control points is already employed.*

Time-step Dependency Analysis

Next, the time-step Δt is investigated. In most AL implementations, the maximum allowed value of Δt is selected so that the blade tip crosses a maximum of one cell within two consecutive time–steps $\left(\Delta t = \Delta x/V_{tip}\right)$. However, based on the results in Table 3.5, a more strict approach of the above rule of thumb $\left(\Delta t = 0.5\Delta x/V_{tip}\right)$ is required for WT simulations. Table 3.5 results have been extracted by a typical unsteady, 3-bladed rotor simulation on a full–scale grid.

Table 3.5. *Variation of power [MW] with increasing time-step Δt [sec]. Reference power corresponds to minimum value $\Delta t = 0.25\Delta x/V_{tip}$. $\Delta t = 0.5\Delta x/V_{tip}$ provides a good trade-off between accuracy (within 1% of the reference value) and computational cost when rotor loads are to be captured. All the different time-step values have been tested by using the hybrid approach $\epsilon = max(2\Delta x, 0.47c)$ to define the Gaussian kernel ϵ.*

Δt	Power [MW]
$\Delta x/V_{tip}$	-2.0%
$0.5\Delta x/V_{tip}$	-0.2%
$0.25\Delta x/V_{tip}$	9.631 MW

Grid set-up

Another aspect to be examined is the grid type employed. Fully unstructured, structured, and hybrid grids can be used. Structured grids are orthogonal but with high aspect ratio cells. On the other hand, unstructured grids result in a good aspect ratio, but orthogonality is lost. Computational cost is sensitive to the type of grid employed. For this reason, grid structure needs to be properly examined, both in terms of computational cost and accuracy of the produced results (in this case, aerodynamic forces predictions). In Table 3.6 the total number of grid cells and the power output of four different grid setups are listed, which are visualized in Figure 3.6. In Figure 3.6a, a fully structured grid (*"setup1"*) is shown with $8.9 \cdot 10^6$ cells. The area nearby the rotor is kept uniform and fine with a characteristic length of $\Delta x = R/90$, followed by a gradual coarsening up to $\Delta w = 10\Delta x$ at the limits of the near wake region and a more steep one up to the outer boundaries of the grid. Figure 3.6b illustrates two grid strategies similar to the one used in the periodic, steady–state simulations. Particularly, in *"setup2"* a fine and structured area is considered around the blade with length $\Delta x = R/90$, while the rest of the domain is unstructured. Again the near wake region has a characteristic length of $\Delta w = 10\Delta x$ and the total amount of grid cells is $2.9 \cdot 10^6$. The only difference in *"setup3"* is that the AL vicinity is unstructured, thus, exploding the number of cells to $6.2 \cdot 10^6$. Finally, a hexahedral grid (*"setup4"*) is shown in Figure 3.6c with a total number of $1.9 \cdot 10^6$ cells. The characteristic length of $\Delta x = R/90$ close to the rotor and $\Delta w = 10\Delta x$ in the near wake region have been maintained in this setup. Based on Table 3.6, all 4 grid setups produce similar results. *"setup3"* shows the greatest discrepancy ($\simeq 2\%$) due to the reduced accuracy in the AL region provoked by the unstructured grid. Consequently, *"setup4"* is qualified due to its minimum number of grid cells.

Table 3.6. *Variaton of power [MW] with different grid setup. Reference power corresponds to grid "setup4". All the different grid setups produce similar results. "setup3" shows the greatest discrepancy due to the unstructured grid in the actuator lines region. "setup4" is preferable to the rest, as it provides an accurate solution (concerning rotor loads estimation) under a minimum number of computational cells. All the different grid setups have been tested by using the hybrid approach $\epsilon = max(2\Delta x, 0.47c)$ to define the Gaussian kernel ϵ.*

Grid type	Power [MW]
*setup*1 $(8.9 \cdot 10^6$ *cells*)	-0.12%
*setup*2 $(2.9 \cdot 10^6$ *cells*)	-0.17%
*setup*3 $(6.2 \cdot 10^6$ *cells*)	$+1.93\%$
*setup*4 $(1.9 \cdot 10^6$ *cells*)	9.607 MW
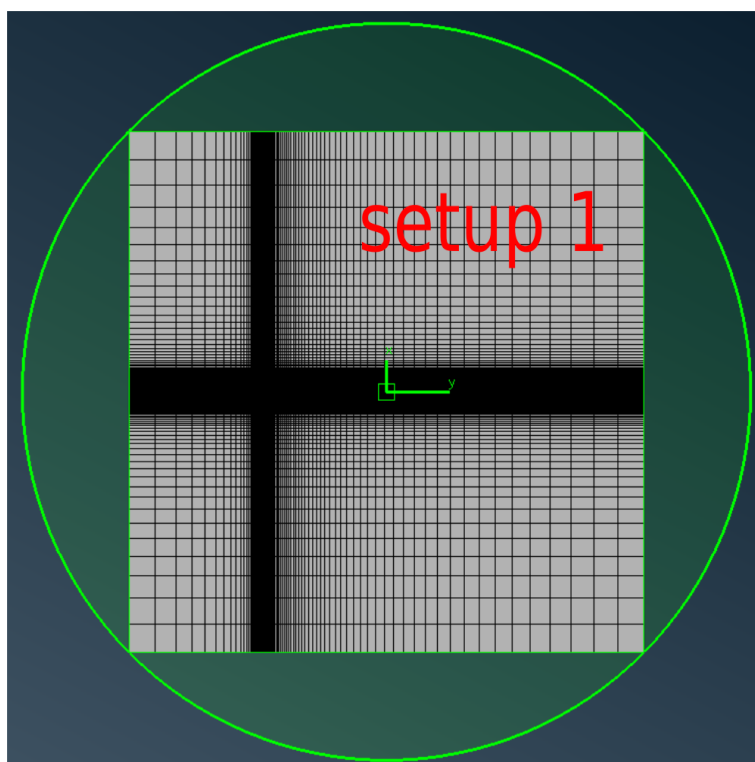
(a) *Structured grid setup.*

Figure 3.6. *Cont.*
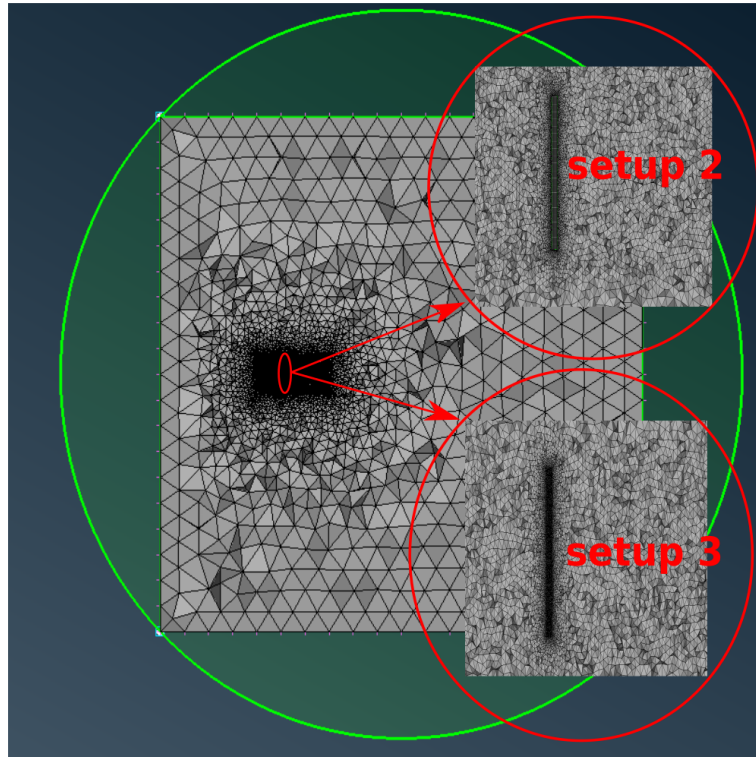
(b) *Unstructured grids setup.*
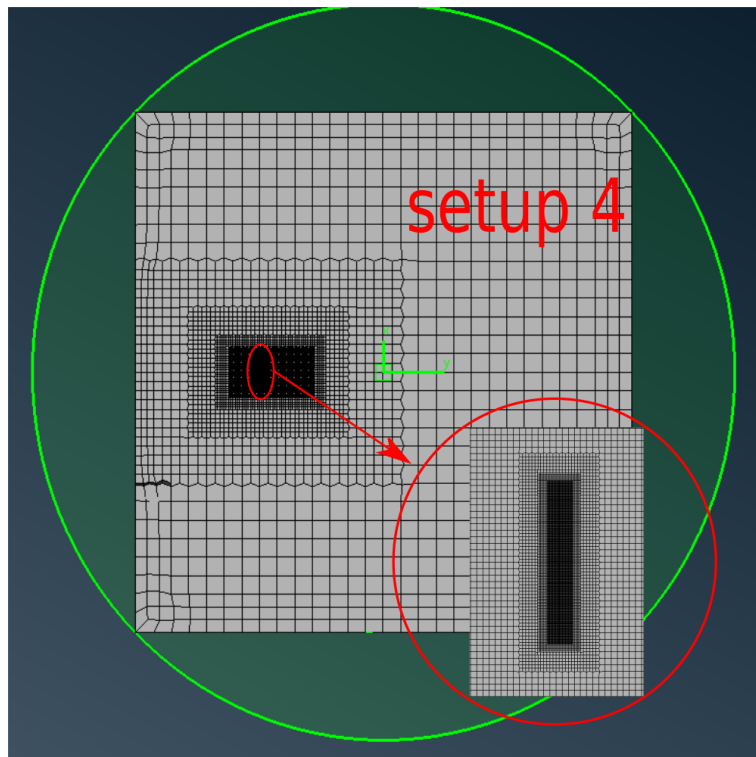
(c) *Hexahedral grid setup.*

Figure 3.6. *Simple grid setups, structured (a), unstructured (b) and hexahedral with haning nodes (c), used for AL modelled WT rotor simulations. No solid–walls are present. The region close to the actuator lines is uniform and fine (with characteristic length of $\Delta x = R/90$). Grid coarsening is employed towards the near wake region (characteristic length up to $\Delta w = 10\Delta x$) and a steeper one follows up to the far-field boundaries.*

3.1.1.3 Comparison against BEMT and LL predictions

In this section, aeroelastic simulations results using the AL model as the aerodynamic analysis tool are compared against reference results obtained using lower fidelity aerodynamic tools. The rotor of the conceptual DTU 10MW RWT is modelled. This WT has been developed by DTU and was employed as a reference turbine in a number of research projects (e.g., INNWIND.EU see [9]). Herein, the 5° tilt angle of the rotor, the 2.5° pre–cone angle of the blades, and the 3.332 m prebend at the blade tip have been properly considered (see Table 3.1). Constant free–stream flow conditions are simulated for the wind speeds of 8 and 11 m/s. Yaw misalignment conditions are considered as well, where free–stream flow angle ranges from −30° to +30°. Constant rotational speed and blade pitch angle is assumed for all cases, as described in Table 3.7. The azimuth angle is assumed to be zero when the blade points upwards (opposite to the ground). The airfoil data used for the blade element analysis on the control points of all the different aerodynamic models have been generated by DTU, using the in–house CFD solver EllipSys2D [159] in fully turbulent $2D$ simulations. Blade loads and elastic displacements results are depicted as azimuthal variations and radial distributions along the blade span. Comparisons are made between a standard BEMT model and the classical LL approach under the framework of Free Vortex Wake (FVW) modelling [42].

WT aeroelastic anaysis within the Wind Energy sector are usually based on BEMT models, as they are fast and reliable in simple flow cases. Therefore, they have been widely employed in design and analysis. For this reason, BEMT results are regarded as reference data in these WT simulations. However, when analyzing complex aerodynamic conditions (yaw misalignment or high shear of the atmospheric boundary layer), the LL model constitutes a more accurate alternative due to the detailed vortex particle representation of the wake. On the contrary, the original BEMT formulation is based on the assumption of a uniform, axi–symmetric and steady–state inflow. The dynamic response of the wake due to time varying conditions is accounted for through an engineering dynamic inflow model [49]. The inflow model is actually a first order filter equation, which imposes a time delay on rotor induction and therefore on rotor loads when the thrust changes in time. It assumes the wake structure to be a cylindrical vortex sheet with a radius equal to that of the rotor and is tuned based on free–vortex–wake aerodynamic model results. In yaw misalignment cases, the induced velocity is corrected through the introduction of an extra term that models the asymmetric distribution of the induced velocities over the rotor disk due to wake skewness [49]. Consequently, LL results will be used as an extra reference in the complex free–stream flow conditions (yaw misalignment cases), where AL and BEMT results are expected to deviate.

Table 3.7. *Operational data for the DTU 10MW RWT under constant wind speed.*

| Wind Speed (m/s)	Yaw misalignment (°)	Rotational Speed (rpm)	Pitch Anlge (°)
8	$-30, -15, 0, 15, 30$	6.423	0
11	$-30, -15, 0, 15, 30$	8.837	0

Structural verification

Table 3.8 lists the predicted natural frequencies of GAST and other state–of–the–art aeroelastic tools (based on beam models) that were used in the Work Package 2 of the INNWIND.EU project for the DTU 10MW RWT blades. The predicted frequencies are compared to 3D FEM predictions obtained with NISA FEM code [160]. In Figure 3.7, the first modes of the isolated rotor blade are depicted, where an overall good agreement among the models is observed in all components, apart from the 1st torsional mode, where GAST predicts a slightly lower torsion angle along the blade span. Moreover, a strong flapwise component is predicted by the 3D FEM code which is not identified by GAST. More details can be found in [161].

Table 3.8. *DTU 10MW RWT blade natural frequencies. Comparison among different structural models (GAST - multi–body & 1st order Timoshenko beam, NEREA - Generalized Timoshenko beam, Cp-Lambda - Geometrically Exact beam, HAWC2 - 1st order Timoshenko beam, NISA - 3D FEM) used in WP2 of the INNWIND.EU project. Beam models slightly underestimate the lower frequencies (former 5) compared to the 3D FEM model, however they agree well with each other. In higher frequencies (latter 3), minor discrepancies among the beam models appear (maximum $\simeq$ 2.3%) and a small underestimation of the natural frequencies compared to 3D FEM (maximum $\simeq$ 12%).*

Mode	GAST	NEREA	Cp-Lambda	HAWC2	NISA
1st *flap*	0.62	0.62	0.62	0.61	0.64
1st *edge*	0.94	0.94	0.94	0.93	0.96
2nd *flap*	1.76	1.74	1.76	1.74	1.85
2nd *edge*	2.80	2.79	2.80	2.77	2.86
3rd *flap*	3.59	3.52	3.60	3.57	3.76
1st *torsion*	5.40	5.36	—	6.60	6.01
3rd *edge*	5.73	5.61	5.74	5.70	5.82
4th *flap*	6.09	6.03	6.11	6.11	—
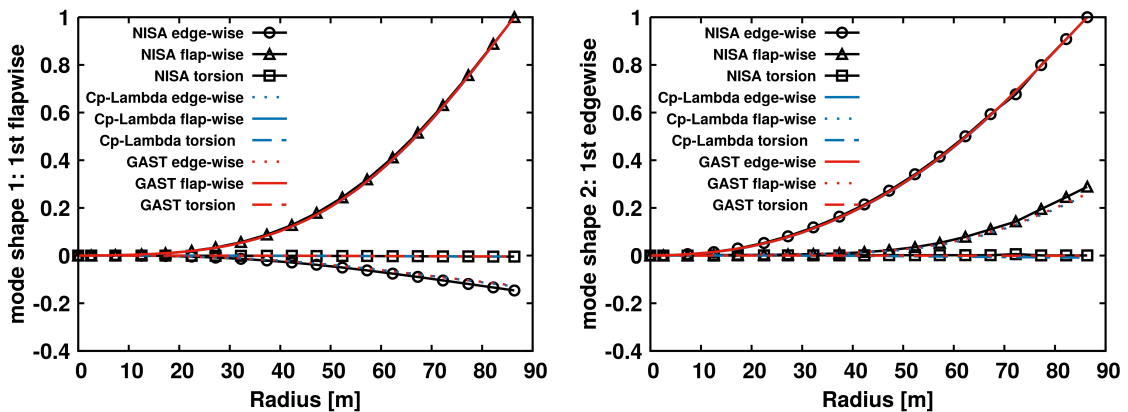
Figure 3.7. *Cont.*
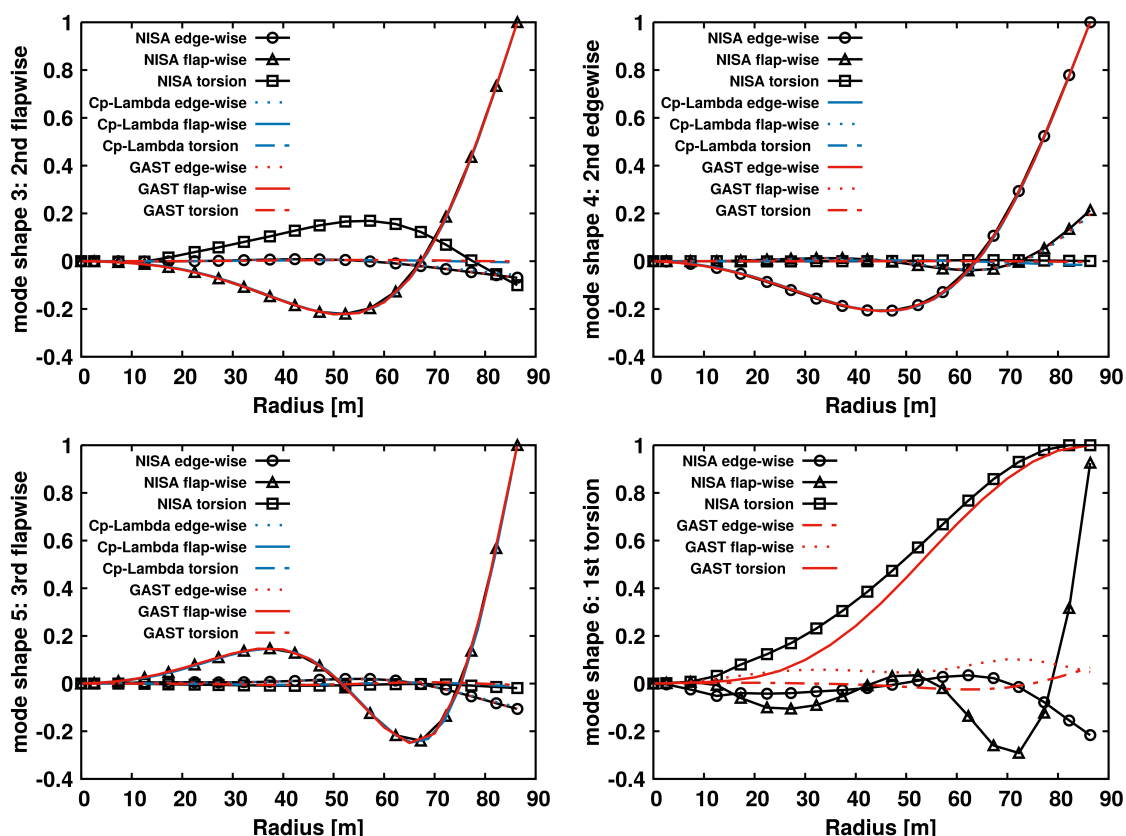
Figure 3.7. *DTW 10MW RWT! blade mode-shapes. Comparison among different structural models (GAST - 1st order Timoshenko beam, Cp-Lambda - Geometrically Exact beam, NISA - 3D FEM) used in WP2 of the INNWIND.EU project. An overall good agreement is observed in most of the presented modes. GAST predicts a slightly lower torsion angle along the blade span in the 1st torsion mode. Moreover, a strong flapwise component is predicted by the 3D FEM code which is not identified by GAST.*

3.1.1.3.1 Axial flow cases

In Figure 3.8, the edgewise bending moment (M_{edge}) at the blade root and the corresponding deflection at the blade tip (U_{edge}) are shown for axial wind speed at 8 and 11 m/s. Nearly perfect agreement is achieved among the different aerodynamic models. Edgewise loads and deflections are mainly driven by gravitational loads. Consequently, deviations among different aerodynamic analysis methodologies are expected to be small. This conclusion is valid in yaw misalignment cases as well. For this reason, the corresponding figures are omitted in the yaw misalignment section.

Root Edgewise Moment

Tip Edgewise Deflection
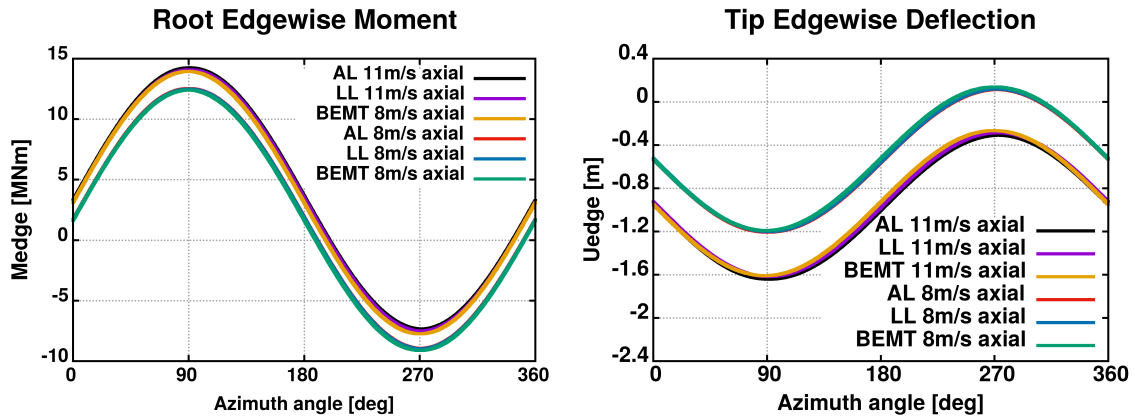
(a) *Edgewise bending moment at the blade root.*   **(b)** *Edgewise deflection at the blade tip.*

Figure 3.8. *Edgewise bending moment at the blade root (a) and the respective tip deflection (b) at 8 and 11 m/s axial wind speed. Comparison among different aerodynamic methods coupled with the same structural module. Almost total agreement is observed among the different aerodynamic models due to the fact that edgewise loads and deflections are driven by gravitational loads.*

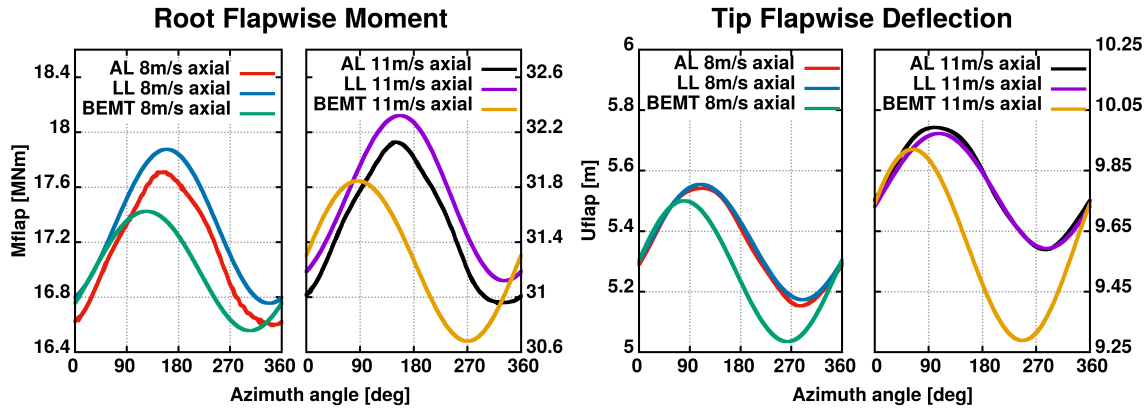Figure 3.9 depicts the flapwise bending moment (M_{flap}) at the blade root and the corresponding deflection at the blade tip (U_{flap}) for axial wind speed at 8 and 11 m/s. The once per rotor revolution (1P) variation appears as a result of the 5° tilt angle of the rotor that shifts the maximum loading towards the azimuth position of 180°. Good agreement is observed in the mean values (maximum difference 1.8% at 8 m/s and 1.3% at 11 m/s). Furthermore, all the models predict a small amplitude of the 1P variation ($\leq$ 3.25% of the mean load at 8 m/s and $\simeq$ 1.9% of the mean load at 11 m/s). Nevertheless, BEMT appears to have a phase difference of approximately 35° at 8 m/s and 70° at 11 m/s, while the AL and LL results match perfectly with each other. Results for the predicted by the different models mean load, amplitude, and phase are tabulated in Table 3.9. The phase difference in the BEMT results are due to the omission of the wake skewness effect induced by the tilt angle of the rotor in BEMT model. On the other hand, the detailed description of the flow–field within the CFD and the FVW frameworks, renders the AL and LL models (respectively) capable accurately estimating the positioning and evolution of the emitted wake vortices with respect to the rotor plane and hence account for the varying wake induction over it. Finally, the quality of agreement is similar among the different models in the flapwise deflection.

(a) *Flapwise bending moment at the blade root.*

(b) *Flapwise deflection at the blade tip.*

Figure 3.9. *Flapwise bending moment at the blade root (a) and the respective tip deflection (b) at 8 and 11 m/s axial wind speed. Comparison among different aerodynamic methods coupled with the same structural module. BEMT slightly underestimates the flapwise moment mean values (maximum difference 1.8% at 8 m/s and 1.3% at 11 m/s) compared to the higher fidelity models. It also shows a phase difference of approximately 35° at 8 m/s and 70° at 11 m/s, which is attributed to disregarding the wake skewness effect induced by the tilt angle of the rotor. Very good agreement is observed between the higher fidelity models predictions. Similar remarks can be made for the tip deflection.*

Table 3.9. *Flapwise bending moment at the blade root at 8 and 11 m/s axial wind speed. Comparison among different aerodynamic models. Good agreement is observed in the mean values and amplitudes predictions by all three models (maximum difference 1.8% at 8 m/s and 1.3% at 11 m/s). BEMT shows a phase difference that increases with the wind speed and is attributed to disregarding the wake skewness effect induced by the tilt angle of the rotor.*

	8 m/s			11 m/s		
	Mean Value	**Amplitude**	**Phase**	**Mean Value**	**Amplitude**	**Phase**
BEMT	17.004 MNm	0.434 MNm	124 °	31.270 MNm	1.863 MNm	86 °
LL	17.307 MNm	0.560 MNm	160 °	31.700 MNm	1.895 MNm	156 °
AL	17.151 MNm	0.559 MNm	156 °	31.531 MNm	1.865 MNm	149 °

As Figure 3.10 shows, the different aerodynamic models are in good agreement regarding the twisting moment (M_{tw}) at the blade root. Very small differences are noted in the mean value of the tip torsion angle (about 0.02° at 8 m/s and 0.04° at 11 m/s). The phase differences seen in M_{flap} and U_{flap} have vanished herein.
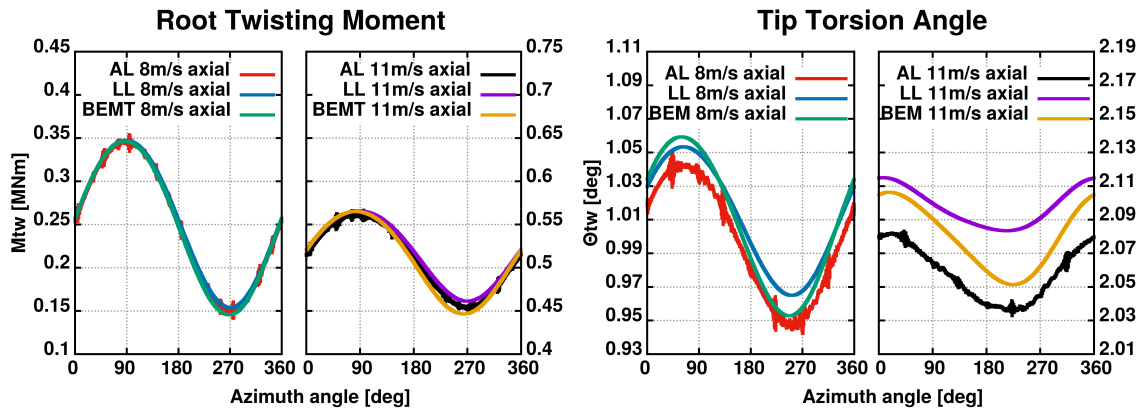
(a) *Twisting moment at the blade root.* **(b)** *Torsion angle at the blade tip.*

Figure 3.10. *Twisting moment at the blade root (a) and torsion angle at the blade tip (b) at* 8 *and* 11 *m/s axial wind speed. Comparison among different aerodynamic methods coupled with the same structural module. Very good agreement is observed among the different models predictions both in the loads and the deflections.*

Comparison of the aerodynamic models

It needs to be stressed, that in LL and AL models, the blade "perceives" the wake-induced velocity in a different way compared to BEMT. This is attributed to the detailed description of the 3D flow field by the FVW and the CFD methodologies respectively. Figure 3.11a verifies the correct effect of the tip correction model used in BEMT [40], as the aerodynamic forces are effectively reduced close to the tip. As depicted in Figure 3.11b however, axial induction factor computed by BEMT has a constant level difference and an increase towards the tip. This is the result of applying Prandtl's tip correction formula directly on the thrust coefficient C_T in order to reduce the aerodynamic loads close to the tip. In the root region, no corresponding correction model has been used to capture the effect of root vortices. For this reason, the axial induction factor there drops to zero.

Back to the tip region, the same pattern holds for LL, but for a different reason. In this case, it is a result of the excessively strong vortices released from the tip. The exaggeration in tip vortices intensity, stems from the fact that the non–zero circulation of the last strip of the blade is followed by zero circulation after that. In vortex methodologies, this sharp drop of circulation is directly translated to very high vorticity of the near wake filaments close to the tip. This is a fundamental difference between LL and AL, as the latter affects the flow through momentum exchange between the fluid and the blade. Another difference between the two models comes from the method of computing the wake–induced velocity. In LL, the computation is performed directly on the control points of the strips through the application of Biot–Savart law. On the other hand, in this AL implementation the control point velocity is computed based on a distance and volume weighted interpolation to the surrounding cells velocities using Radial Basis Functions [132]. For these reasons, the induced velocity predicted by the AL model tends to zero towards the tip along with blade normal force. This is confirmed in [162], where the wake–induced velocity by a FVW flow–field solver is first computed on the nodes of a stationary back–ground grid and then is interpolated to the control points of the blade, in a similar approach to the one followed

in the AL model. In this case, the radial distribution of the wake–induction tends to zero towards the tip.

A comparison of the predicted circulation distribution along the span is shown in Figure 3.11c. AL effectively predicts a circulation distribution that decreases sharply close to the tip. However, this is not reflected on the axial induction factor the same way with LL (Figure 3.11b). It is therefore shown that in AL, the axial induction factor is not directly related to circulation radial variation as in the case of LL, or to an engineering correction model as in the case of BEMT. The increased values of circulation in the root vicinity of LL can be justified by the potential nature of LL that changes circulation proportionally to the angle of attack. The higher circulation predicted by the LL model is related to the high values of the angle of attack at the root of the blade (see Figure 3.11d) and the fact that the LL model presumes a 2π slope for the lift variation of the cylindrical sections close to the root (although this is not valid for those thick non–aerodynamic sections). Then, an a posteriori correction on loads is performed to account for the reduced (or even zero) lift of these sections and the higher drag. In BEMT and AL analyses, the computation of the induction and the loads are in tight connection with the local airfoil polars. To sum up, the main differences among the models in predicting the above mentioned flow parameters are limited to the blade tip and root regions.
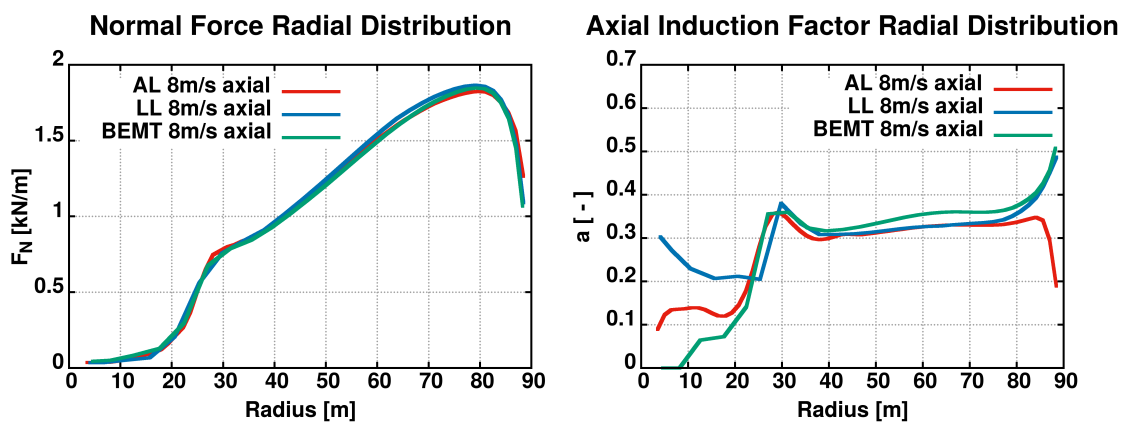
(a) *Normal force radial distribution. Good agreement in the aerodynamic forces reduction close to the tip, indicating the effectiveness of the tip loss correction model used in BEMT.*

(b) *Axial induction factor radial distribution. BEMT prediction shows a constant level difference compared to the higher fidelity models that originates in the crude estimation of the wake induction, whereas the higher fidelity models agree well with each other. The abrupt increase towards the tip is the result of the direct application of the tip correction on the thrust coefficient C_T. The same pattern is predicted by the LL model, as a result of the excessively strong vortices emitted from the tip. AL predicted induction tends to zero in a more physical representation computed through an interpolation from the neighbouring cells.*

Figure 3.11. *Cont.*

Circulation Radial Distribution

Angle of Attack Radial Distribution
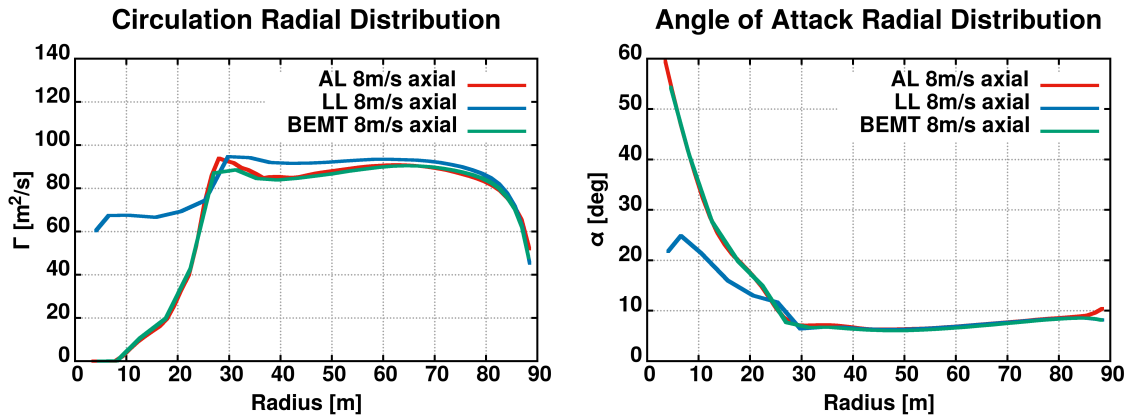
(c) *Circulation radial distribution. Good agreement is shown in the circulation drop close to the tip by all aerodynamic models. A small level difference is observed by LL and an unnatural increase towards the root that stems from the computation of circulation proportionally to the effective angle of attack.*

(d) *Radial distribution of the effective angle of attack. Very good agreement is achieved among the different models prediction, apart from the root region where the LL model underestimates the angle of attack compared to the other two models. This is related to the root vortices emitted in the LL model and the strong downwash they induce.*

Figure 3.11. *Normal force (a), axial induction factor (b), circulation (c) and angle of attack (d) radial distributions at 8 m/s axial wind speed. Averaging over the final revolution of the simulation. Comparison among different aerodynamic methods coupled with the same structural module.*

3.1.1.3.2 Yawed flow cases

Figure 3.12 depicts the flapwise bending moment of the blade root at 8 and 11 m/s wind speed, for yaw misalignment angles of ±15° and ±30°, respectively. A mean value difference is observed among BEMT and the two higher fidelity models that increases with yaw angle ($\simeq$ 3.5% at ±15° and $\simeq$ 8.5% at ±30°). Mean wind speed has a smaller impact. Nevertheless, the amplitude of the variation changes similarly for all three methods. Moreover, a phase difference in the range 35°–45° among BEMT and the other two models exists in all cases. The corresponding deflections at the blade tip are depicted in Figure 3.13, presenting qualitatively similar results with the moments.

Root Flapwise Moment

AL yaw +15⁰ —— **LL yaw +15⁰** —— **BEMT yaw +15⁰** ——
AL yaw -15⁰ —— **LL yaw -15⁰** —— **BEMT yaw -15⁰** ——

(a) $\pm 15°$ *yaw at* 8 *and* 11 *m/s wind speed.*

Root Flapwise Moment

AL yaw +30⁰ —— **LL yaw +30⁰** —— **BEMT yaw +30⁰** ——
AL yaw -30⁰ —— **LL yaw -30⁰** —— **BEMT yaw -30⁰** ——
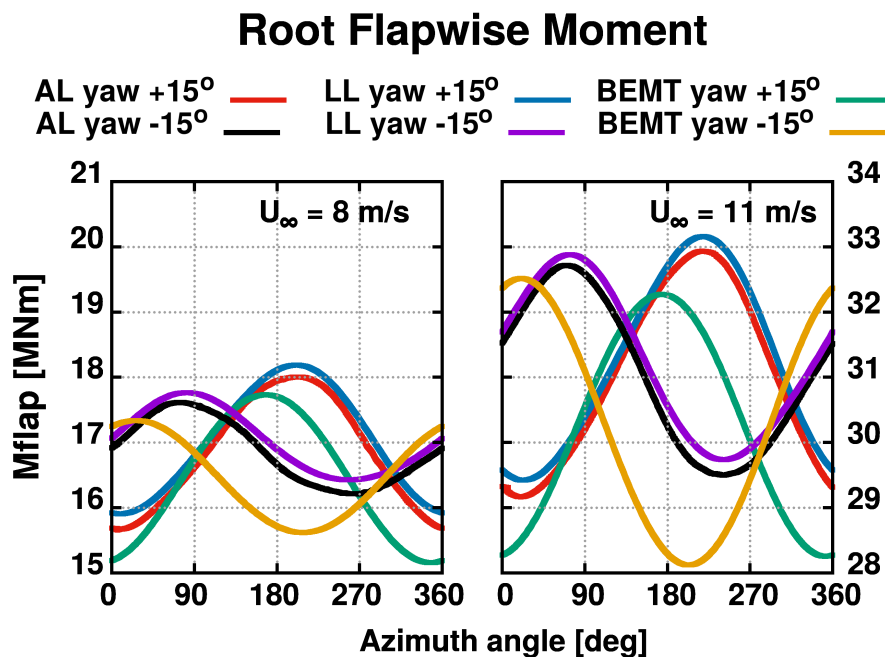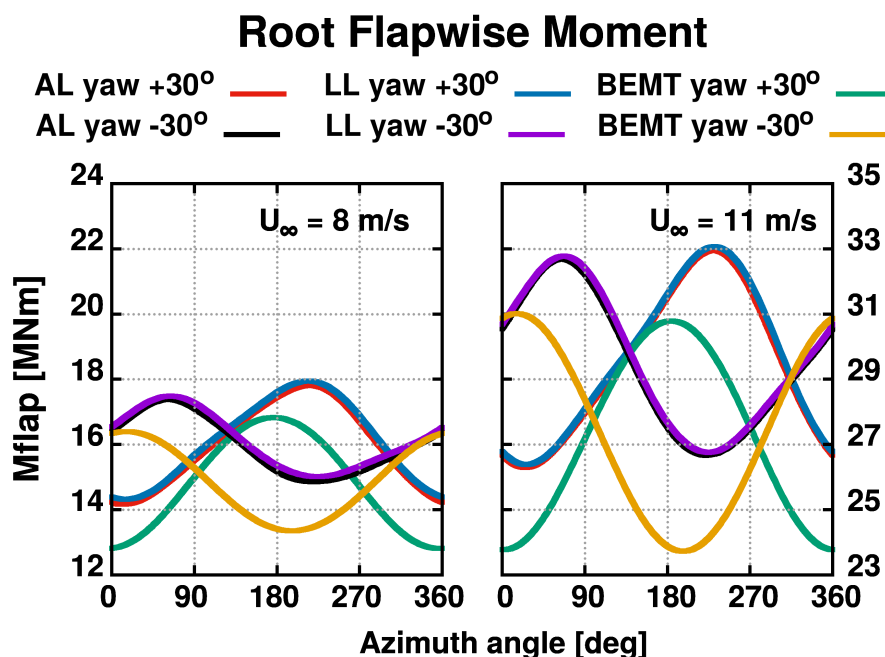
(b) $\pm 30°$ *yaw at* 8 *and* 11 *m/s wind speed.*

Figure 3.12. *Flapwise bending moment of blade root at* $\pm 15°$ *(a) and* $\pm 30°$ *(b) yawed wind speed at* 8 *and* 11 *m/s. Comparison among different aerodynamic methods coupled with the same structural module. BEMT shows a mean value underestimation that increases with yaw angle and a constant phase difference. Good agreement is shown between the higher fidelity models.*

Tip Flapwise Deflection

AL yaw +15° —— LL yaw +15° —— BEMT yaw +15° ——
AL yaw -15° —— LL yaw -15° —— BEMT yaw -15° ——

(a) ±15° yaw at 8 and 11 m/s wind speed.

Tip Flapwise Deflection

AL yaw +30° —— LL yaw +30° —— BEMT yaw +30° ——
AL yaw -30° —— LL yaw -30° —— BEMT yaw -30° ——

(b) ±30° yaw at 8 and 11 m/s wind speed.

Figure 3.13. *Flapwise deflection of blade tip at ±15° (a) and ±30° (b) yawed wind speed at 8 and 11 m/s. Comparison among different aerodynamic methods coupled with the same structural module. Similar remarks with the respective loads (see Figure 3.12) can be made here as well, indicating that flapwise deflection is mainly driven by the corresponding loads.*

Figure 3.14 shows the twisting moment of the blade root at 8 and 11 m/s wind speed, for yaw misalignment angles of ±15° and ±30°. The corresponding torsion angles at the blade tip are depicted in Figure 3.15. Very good agreement is observed both for the mean values and for the amplitudes of the variations. The phase differences of BEMT

107

encountered in the flapwise signals are not present, or at least are much less pronounced herein. The torsion angle is not only driven by the aerodynamic twisting moment but also by the flapwise bending loads as a result of very high flapwise deflection that gives rise to a twisting of the section due to non–linear geometric coupling effects [38]. This is also justified by the phase difference in the torsion angle signals, comparing positive and negative yaw angles, which agrees with the corresponding phase difference of the flapwise signals.
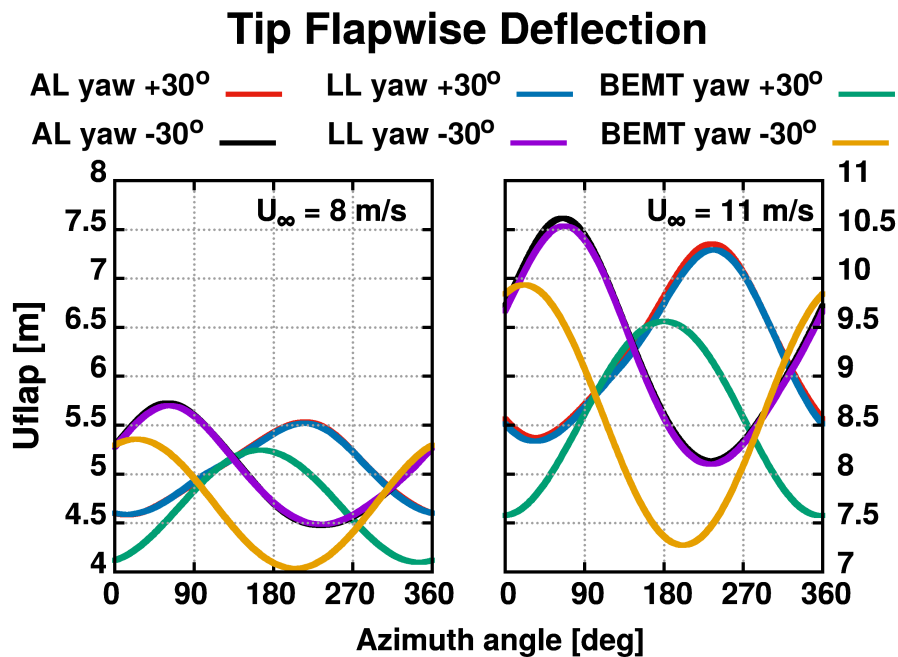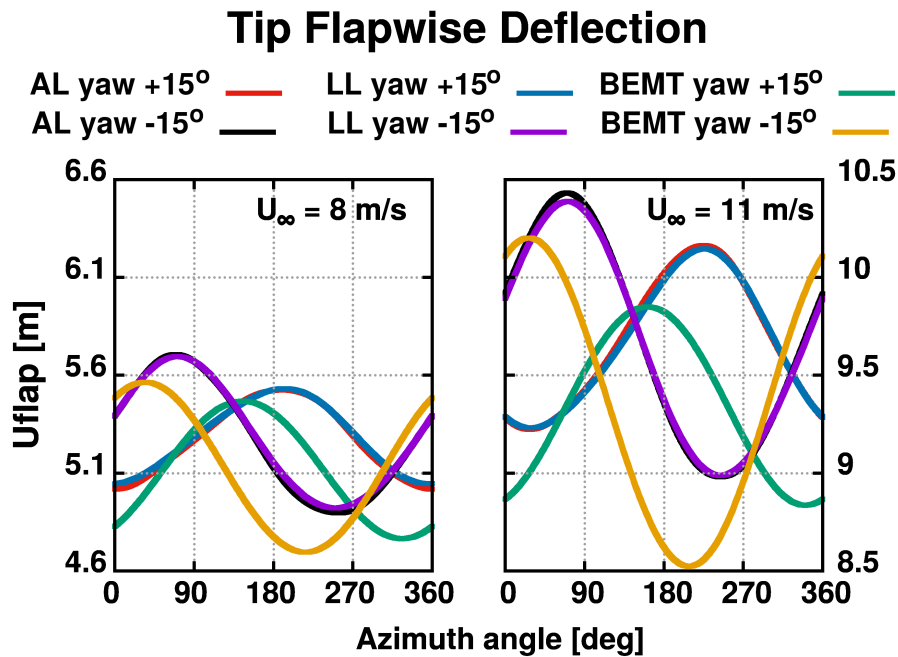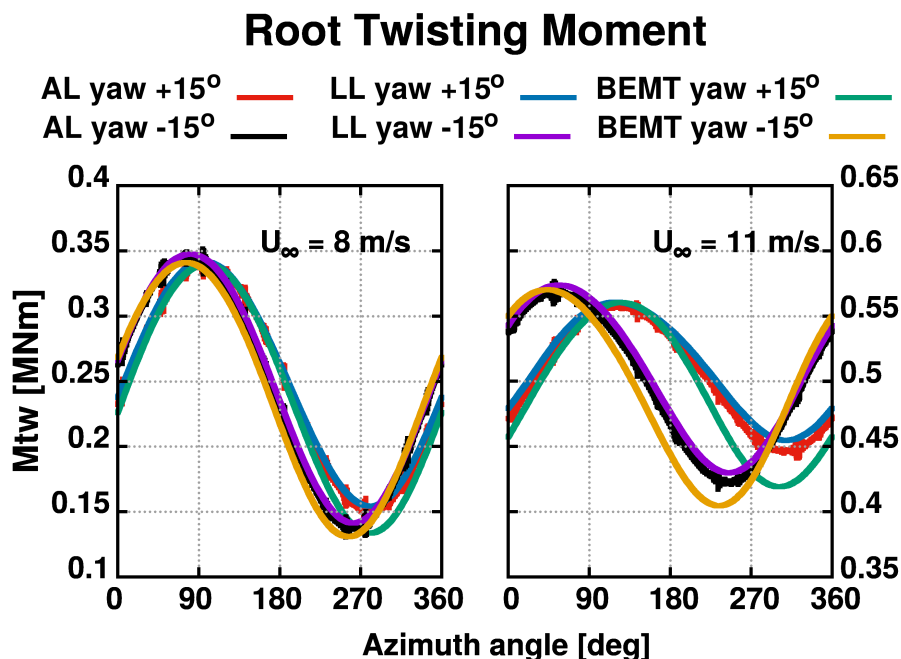

(a) ±15° *yaw at* 8 *and* 11 *m/s wind speed.*
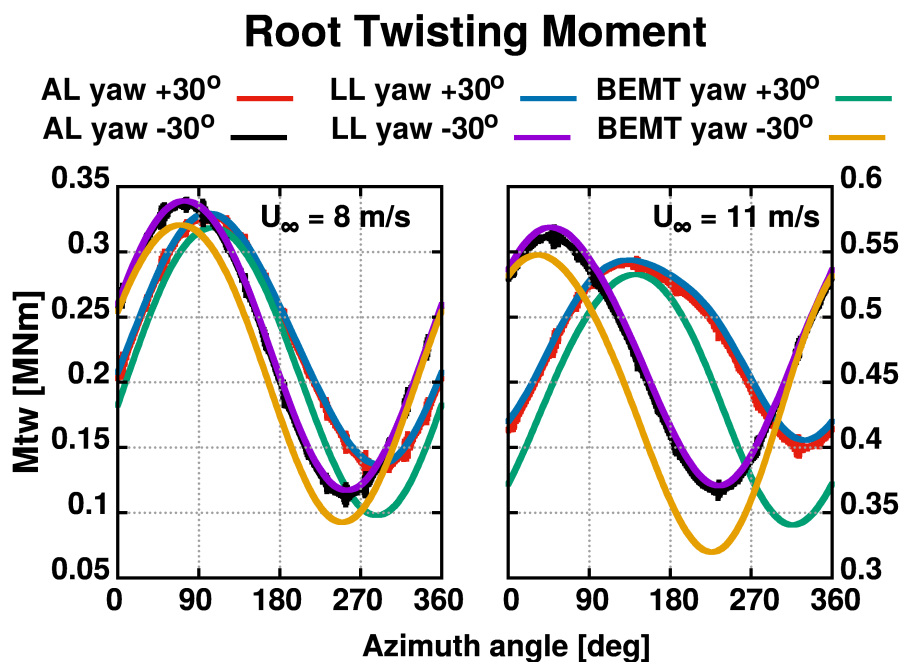
(b) ±30° *yaw at* 8 *and* 11 *m/s wind speed.*

Figure 3.14. *Twisting moment of blade root at* ±15° *(a) and* ±30° *(b) yawed wind speed at* 8 *and* 11 *m/s. Comparison among different aerodynamic methods coupled with the same structural module. Good agreement is shown among the different models predictions.*

Tip Torsion Angle

AL yaw +15° —— **LL yaw +15°** —— **BEMT yaw +15°** ——
AL yaw -15° —— **LL yaw -15°** —— **BEMT yaw -15°** ——

(a) *±15° yaw at 8 and 11 m/s wind speed.*

Tip Torsion Angle

AL yaw +30° —— **LL yaw +30°** —— **BEMT yaw +30°** ——
AL yaw -30° —— **LL yaw -30°** —— **BEMT yaw -30°** ——

(b) *±30° yaw at 8 and 11 m/s wind speed.*
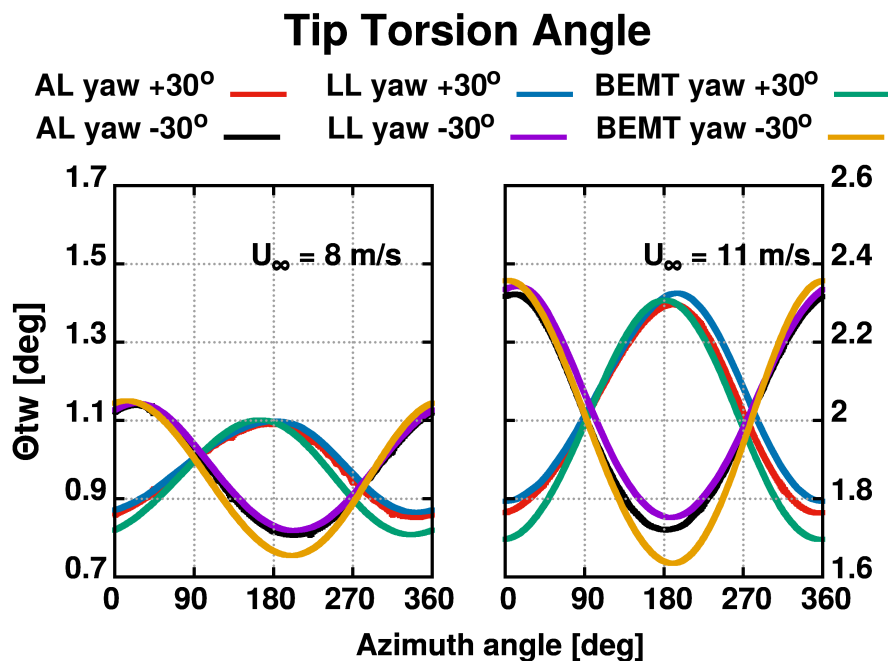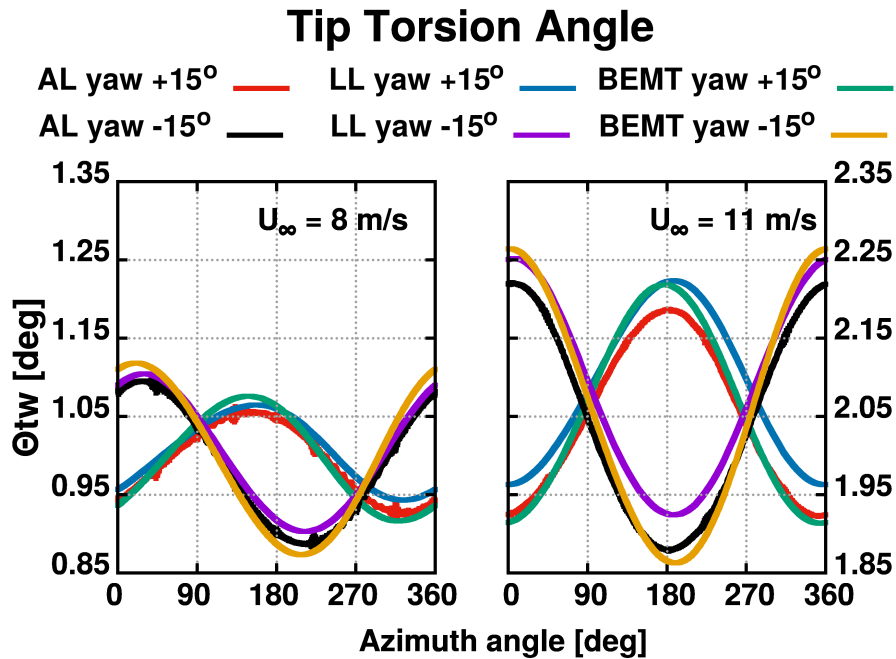
Figure 3.15. *Torsion angle of blade tip at ±15° (b) and ±30° (b) yawed wind speed at 8 and 11 m/s. Comparison among different aerodynamic methods coupled with the same structural module. Good agreement is shown among the different models predictions. The increased phase difference between positive and negative yaw angles compared to the respective loads (see Figure 3.14) indicates that the torsion angle is not only driven by the aerodynamic twisting moment, but also by the flapwise bending moments (see Figure 3.12) as a result of the very high flapwise deflection (see Figure 3.13) that brings about geometric couplings.*

In summary, the main differences among the three models mainly concern the flapwise moments (Figure 3.12) and deflections (Figure 3.13). A deviation in between 4% and 10% is observed in the mean value, alongside with a phase difference of about 35° to 45°. This can be attributed to the differences encountered in the axial induction factor (axial component of wake induced velocity divided by the reference velocity, which in WT applications is the wind speed) seen in Figure 3.16. Clearly, AL and LL predict lower mean values compared to BEMT, which is in line with the level difference shown in the axial cases (see Figure 3.11b) and explains the level difference of moments and deflections (lower induction results in higher inflow velocity and therefore in higher loads). This difference grows as the yaw angle increases. Furthermore, AL and LL predict higher variation amplitude of the induction than BEMT at all wind speeds and yaw angles with a phase difference of about 20° to 45°, close to the one seen in the flapwise moments and deflections. At positive yaw angles, both at a wind speed of 8 and 11 m/s, all aerodynamic models predict the maximum loading around the azimuth angle of 180°. The reason for that is the increased relative velocity seen by the blade at this azimuth position, due to its clockwise rotation. There, the in–plane component of the wind is superimposed to the rotational speed of the blade. Apart from that, the effect of the wake skewness is important. It is the origin of the differences among the different aerodynamic models. The variation in the axial induction factor is much less pronounced in BEMT results (7% to 15% of the mean value), which, in turn, leads to decreased phase shifting of the loads due to the wake skewness effect as compared to AL and LL models, where the amplitudes are higher (12.5% to 29% of the mean value). Minimum–induced velocity is predicted by all models close to the azimuth angle of 270°, thus, shifting maximum loads towards a greater azimuth position. The lower minimum–induced velocity predicted by AL and LL explains the 35° to 45° phase difference in the flapwise moments and deflections. Similar results are observed at negative yaw angles, but with a phase shift of 180° compared to positive values. The reason of the above differences is that, in the AL and LL models, the wake induction is inherently included in the flow field and wake computations while in the BEMT it is determined by an engineering yaw correction model.

Axial Induction Factor at 75%R

AL yaw +15° ⎯⎯ LL yaw +15° ⎯⎯ BEMT yaw +15° ⎯⎯
AL yaw -15° ⎯⎯ LL yaw -15° ⎯⎯ BEMT yaw -15° ⎯⎯

(a) ±15° *yaw at 8 and 11 m/s wind speed.*

Axial Induction Factor at 75%R

AL yaw +30° ⎯⎯ LL yaw +30° ⎯⎯ BEMT yaw +30° ⎯⎯
AL yaw -30° ⎯⎯ LL yaw -30° ⎯⎯ BEMT yaw -30° ⎯⎯

(b) ±30° *yaw at 8 and 11 m/s wind speed.*
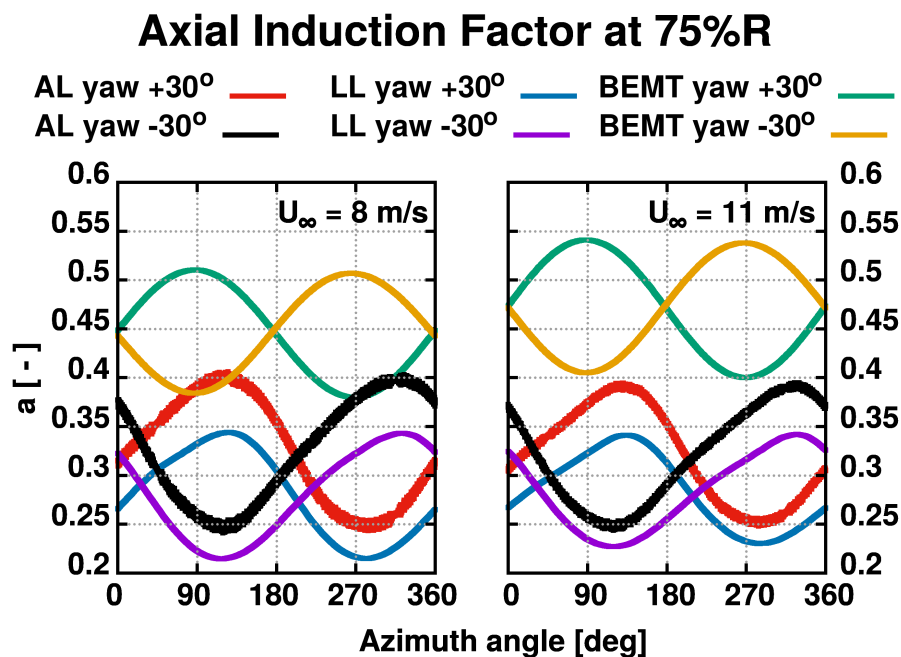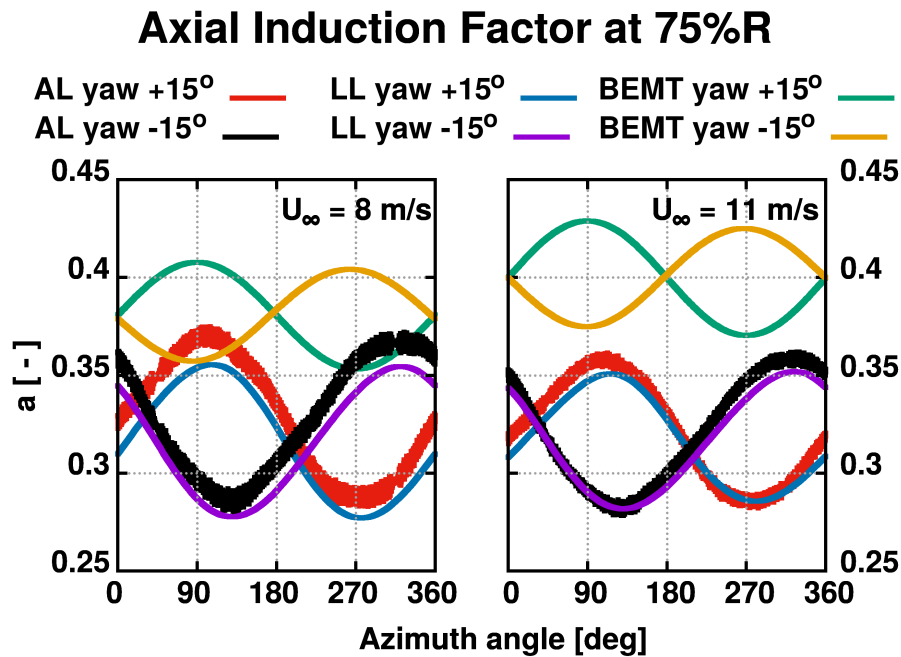
Figure 3.16. *Axial induction factor at 75%R of the blade at ±15° (a) and ±30° (b) yawed wind speed at 8 and 11 m/s. Comparison among different aerodynamic methods coupled with the same structural module.* BEMT *predicts greater mean values that grow with yaw angle. This is in line with the lever difference shown in the axial cases (see Figure 3.11b). Moreover,* BEMT *predicts lower amplitudes (7% to 15% of the mean value) and a phase difference (about 20° to 45°) that are related to its crude estimation of the wake skewness effect through an engineering yaw correction model (wake skewness induced by the tilt angle of the rotor is neglected). Good agreement is shown between the higher fidelity models predictions, where again a minor level difference is observed that is attributed to the different techniques in computing the wake induced velocity (see Section 3.1.1.3.1). Nevertheless, there is very good agreement in the amplitude and phase.*

3.1.2 Aeroelastic analysis of a helicopter MR

In this section, aeroelastic simulations are performed for the MR of the model BO105 used in the HeliNoVi wind tunnel experimental campaign [10]. Computations are performed in forward flight conditions at low (12.3 m/s), medium (50.5 & 50.9 m/s) and high (69.6 & 69.9 m/s) flight speed. The rotor blades are modelled as actuator lines in a purely Eulerian context, using MaPFlow. The structural dynamics analysis is performed through GAST and the rotor blades are modelled as beam assemblies, in order for non–linear geometric phenomena to be properly accounted for. The two systems are solved separately, but tightly coupled. First, aerodynamic simulations (blades deformations neglected) are performed at the low speed case (12.3 m/s) in order to investigate the effect of multiple numerical parameters (e.g. grid and time–step resolution) on the predicted aerodynamic loads. Then, aeroelastic simulations are performed at all the aforementioned flight speed cases and the produced results are compared against experimental measurements and LL predictions.

3.1.2.1 The HeliNoVi experimental campaign

The Helicopter Noise and Vibration (HeliNoVi) reduction project was performed in April 2002, in an open–jet facility of the German-Dutch wind tunnel (DNW) as a joint effort of Eurocopter Deutschland GmbH (ECD), German Aerospace Center (DLR), French Aerospace Lab (ONERA), VIBRATEC France, Netherlands Aerospace Center (NLR), SENER Spain, National Technical University of Athens (NTUA) and DNW to generate a comprehensive database for noise and vibration measurements. The objective was to investigate the potential of tail rotor noise and helicopter vibration reduction by modifying important design parameters such as the position of the tail rotor, the sense of rotation and its rotations speed, as well as the main rotor to fuselage distance. The model rotor was a 1 : 2.45 Mach and dynamically scaled BO105 hingeless rotor (see Figure 3.17) operating in forward flight cases of full helicopter configurations (Main Rotor, Fuselage and Tail Rotor). Hub loads and blade loads at various span–wise positions have been measured with load sensors (strain gauges and accelerometers). Additionally, Stero Pattern Recognition (SPR) was used for the first time in order to determine the blade deflections, whereas Particle Image Velocimetry (PIV) measurements have been performed in order to obtain the detailed flow–field in the vicinity of the MR and the evaluation of wake structures.

The basic geometric characteristics of the model MR used in the experimental campaign can be found in Table 3.10.

Figure 3.17. *BO105 helicopter wind tunnel model used in the HeliNoVi experimental campaign. Image copied from [10].*

Table 3.10. *Summary of the basic geometric characteristics of the model MR used in the HeliNoVi experimental campaign.*

Characteristic	Symbol	Value
Mast angle (tilt forward)	a_{sft}	3°
Rotor radius	R	2 m
Blade chord	c	0.121 m
Number of blades	N_b	4
Rotor solidity	σ	0.077
Non–dim. root cut–out	r_a	0.22
Non–dim. zero twist radius	r_{tw}	0.75
Blade linear twist	Θ_{tw}	$-8°/R$
Airfoil	modified ~ trailing edge tab	NACA23012
Tab length	t_L	5 mm
Tab thickness	t_{th}	0.9 mm

3.1.2.2 Numerical investigation

Following the preceding analysis for the effect of the AL numerical parameters on WT rotor loads, a helicopter MR is examined. The AL numerical parameters Δx, Δr and Δt are tested on case 851 of the HeliNoVi experimental campaign [10], which is a forward flight case at 12.3 m/s flight speed. The elastic deformation of the blades is neglected in this study as well. Many of conclusions drawn through the respective WT analysis (see Section 3.1.1.2) have been used here without further investigation, namely:

- As depicted in Figure 3.18, a hexahedral grid set–up has been utilized;

- The ratio $\Delta w = 10\Delta x$ is used again for the near wake region;

- The Gaussian kernel is defined by the relationship $\epsilon = max(2\Delta x, 0.47c)$.

Grid Dependency Analysis

In Table 3.11, the rotor thrust predictions are listed with respect to different values of Δx. Thrust is preferred as a metric over power in this case, due to its higher sensitivity to changes in the numerical parameters in helicopter cases. Ratio $\Delta x = c/8$ is considered to be the optimal compromise between accuracy and computational cost.

Table 3.11. *Variation of thrust [kN] with increasing the actuator lines region characteristic length Δx [m]. Reference thrust corresponds to minimum value $\Delta x = c/10$. The hybrid approach $\epsilon = max(2\Delta x, 0.47c)$ provides an accurate and grid independent solution at $\Delta x = c/8$.*

Δx	Thrust
$c/4$ $(830 \cdot 10^3$ *cells*$)$	−3.4%
$c/6$ $(1.65 \cdot 10^6$ *cells*$)$	−1.7%
$c/8$ $(4.22 \cdot 10^6$ *cells*$)$	−0.6%
$c/10$ $(9.33 \cdot 10^6$ *cells*$)$	4.706 kN
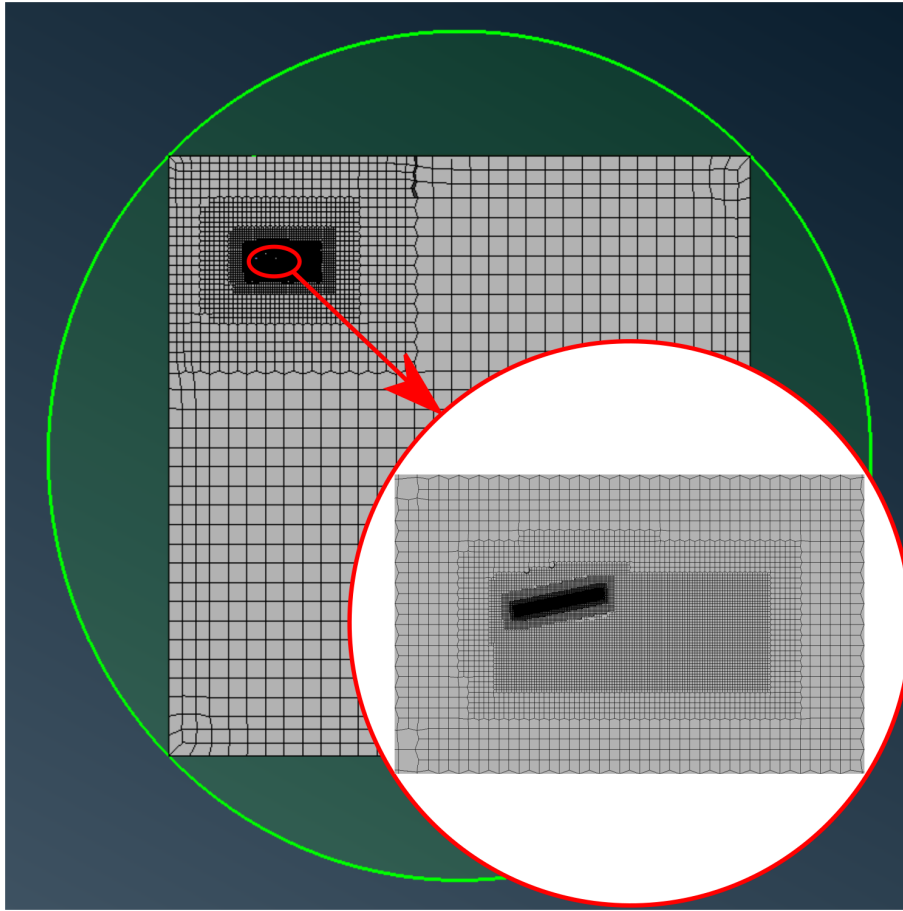
Figure 3.18. *MR hexa grid setup. Simple hexahedral grid setup with haning nodes, used for AL modelled Helicopter MR simulations. The whole computational domain is discretized in cells (no solid–walls are present). The region close to the actuator lines is uniform and fine (with characteristic length of $\Delta x = c/8$). Grid coarsening is employed towards the near wake region (characteristic length up to $\Delta w = 10\Delta x$) and a steeper one follows up to the far-field boundaries.*

Blade Grid Dependency Analysis

In Table 3.12, the effect of *#strips* is investigated. Due to constant airfoil along the blade span, reasonable accuracy in thrust prediction is obtained even with a lower number of control points. For MR simulations, a uniform distribution of control points with $\Delta r = 2\Delta x$ is used. Since *#strips* does not penalize computational cost, the main criterion for choosing this parameter is the smooth radial distribution of the aerodynamic forces.

Table 3.12. *Variation of thrust [kN] with increasing blade grid size Δr [m]. Reference thrust corresponds to minimum value $\Delta r = 2\Delta x$. $\Delta r = 4\Delta x$ provides an accurate and grid independent solution. However, since #strips adds no significant computational cost, more control points may be used ($\Delta r \leq 4\Delta x$) in order to ensure a smooth representation of the radial distribution of aerodynamic forces.*

Δr	Thrust
$4\Delta x$	-0.16%
$3\Delta x$	-0.07%
$2\Delta x$	4.679 kN

Time-step Dependency Analysis

The time–step Δt is investigated in Table 3.13. In this case, the rule of thumb $\left(\Delta t = \Delta x / V_{tip}\right)$ seems to be satisfactory. Overall blade grid and time resolution requirements are found to be relaxed in the helicopter case as higher values for Δr and Δt provided (#*strips*) and time independent loads.

Table 3.13. *Variation of thrust [kN] with increasing time-step Δt [s]. Reference thrust corresponds to minimum value $\Delta t = 0.25\Delta x / V_{tip}$. $\Delta t = \Delta x / V_{tip}$ provides a good trade-off between accuracy (within 1% of the reference value) and computational cost when rotor loads are to be captured.*

Δt	*Thrust*
$2\Delta x / V_{tip}$	−4.0%
$\Delta x / V_{tip}$	−0.9%
$0.5\Delta x / V_{tip}$	−0.01%
$0.25\Delta x / V_{tip}$	4.683 kN

3.1.2.3 Comparison against measurements and LL predictions

In this section, aeroelastic simulations are performed in forward flight conditions at low (12.3 *m/s*), medium (50.5 & 50.9 *m/s*) and high (69.6 & 69.9 *m/s*) flight speed. Operational details can be found in Table 3.14. AL results are compared against measurements and LL predictions. Comparisons of predictions and measurements are made for blade loads and elastic displacements and the results are presented as azimuthal variations. 0° azimuth corresponds to the blade pointing towards the tail boom. Furthermore, a discrete Fourier analysis has been performed to blade loads. The results have been expressed in terms of amplitude and phase for the harmonic frequencies of the highest energy content. The corresponding mean values are presented in tabulated form. In the wind tunnel tests, all blades where instrumented with load sensors, therefore blade loads for all blades were obtained. In the comparisons, predictions are compared to data from all available sensors. The missing data in some of the comparisons are due to broken or malfunctioning sensors.

Table 3.14. *Operational data for the simulated cases of the HeliNoVi experimental campaign.*

| Case:	851	844	847	983	907	918
Flight Speed (m/s)	12.3	50.5	69.6	12.3	50.9	69.9
Air density (kg/m^3)	1.19956	1.20347	1.19578	1.19304	1.19081	1.19713
Temperature (°C)	21.5	20.6	22.6	23.9	23.6	23.0
Pitch Attitude (°)	+3.0	−2.6	−8.2	+3.1	−2.7	−8.2
(positive nose up)						
Roll Attitude (°)	−0.2	−2.8	−5.1	−0.3	−2.7	−5.2
(positive advancing side down)						
Rotational Speed (rpm)	1047	1050	1050	1051	1051	1051
Collective Pitch (°)	7.6	7.2	11.6	7.8	7.3	11.7
Lateral Pitch (°)	2.8	1.0	0.7	2.7	1.1	0.7
Longitudinal Pitch (°)	−0.2	−2.7	−5.5	−0.2	−2.7	−5.4
Thrust (N)	3774.7	3857.5	3999.5	3787.3	3883.1	4008.4
Pitch Moment (Nm)	132.4	220.6	231.0	152.7	223.3	226.6
(positive nose up)						
Roll Moment (Nm)	33.1	37.5	86.9	22.6	48.9	84.7
(positive advancing side down)						

Structural verification

In Figure 3.19, the predicted by GAST Campbell diagram (rotational speed range 0–1050 rpm) of the BO105 model blade is compared against the one produced by a commercial code and provided by ECD to the HeliNoVi consortium. Very good agreement is observed at all the presented mode frequencies, with minor discrepancies at the 1st torsional frequencies.
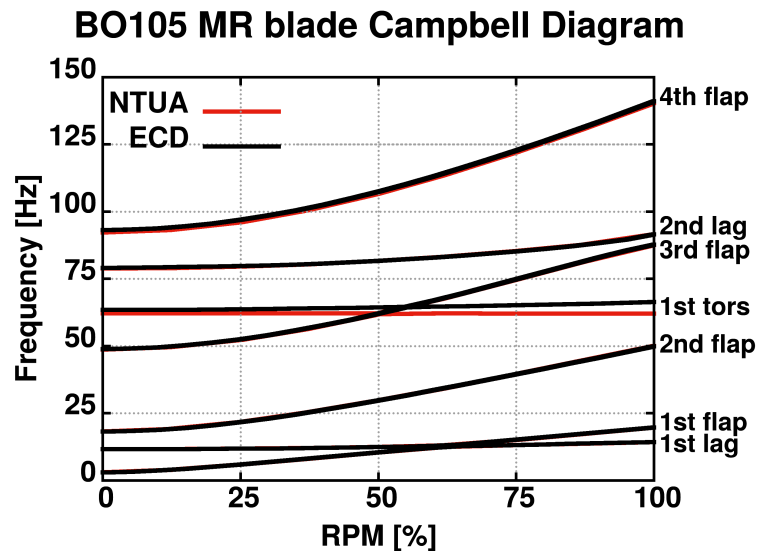
Figure 3.19. *Campbell diagram of an isolated BO105 model MR blade used in the HeliNoVi experimental campaign. Comparison among the natural frequencies produced by GAST and a commercial code (provided by ECD). Very good agreement is observed at all the presented mode frequencies, with minor discrepancies at the 1st torsional frequencies.*

For a fair comparison against experimental measurements, the control angles (collective and cyclic pitch) have been trimmed based on a feedback control algorithm which aims at matching the predicted hub loads (thrust force, pitching and rolling moment) to the measured ones. The latter are considered as the target values of the control loop. Figure 3.20 compares the predicted by the two aerodynamic models MR pitch control angles against those used in the wind tunnel test campaign. Very good agreement is observed for all flight speeds in the collective and longitudinal pitch, whereas for lateral pitch there is an increasing deviation with the flight speed with a maximum difference of $2°$ at 70 m/s.
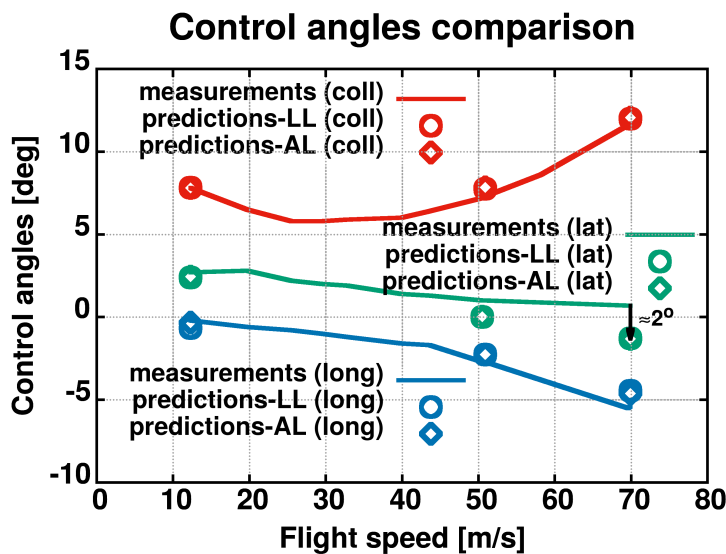

Figure 3.20. *Control angles comparison. Trimmed simulation values vs experimental measurements. Good agreement is observed at all the simulated flight speeds for the collective and longitudinal pitch. A small deviation is observed for lateral pitch that increases with flight speed up to $2°$ at 70 m/s. Almost total agreement is achieved between the two computational models.*

3.1.2.3.1 Forward Flight case at 12 m/s

Notable differences, both in the mean value, as well as in the amplitude of the once per rotor revolution (1/rev) variation are observed in the lead–lag bending moment (Figure 3.21a). Load variations due to high frequency harmonics are well captured by the AL simulations. The LL model predicts a smoother variation of loads at higher frequencies, while the predicted signal is slightly shifted with respect to AL predictions and measurements. In the lead–lag deflections (Figure 3.21b), predictions lead with respect to measurements. It is noted that positive deflection is in the lag direction. This is common in all three flight speeds and is mainly attributed to the technique used to measure blade deflections in the experimental campaign. SPR that was used for the first time in the HARTII and HeliNoVi projects, has been repeatedly reported to show a consistent 2–4 cm ($\simeq 1-2\%$) translational offset in the lag direction with respect to numerous and of varying fidelity computational method results [163, 164, 165]. In [10], the flexibility of the drive train system and the hub, which are regarded as infinitely stiff in our simulations, are

considered as an extra source of discrepancies between measurements and predictions. The "soft" drive train system used in the experimental campaign allows for a torsion angle at the end of the shaft that is dictated by the mean value of the lead–lag bending moment at the root of the blades. In turn, a positive (towards the lag direction) level shift of the blade tip deflections is to be expected. Nevertheless, the 1/rev amplitude of the variation is well predicted by the computational models, but the high frequency oscillations seen in measurements seem to be almost completely damped in both simulations.
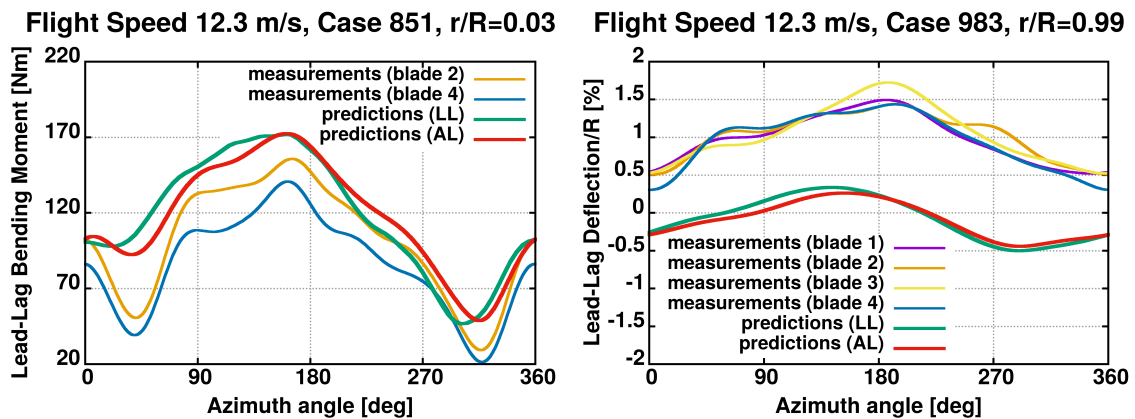

(a) *Lead-lag moment at $r/R = 0.03$. Mean value is overestimated by $\simeq 17\%$ in the computational predictions. 1/rev amplitude is fairly predicted (overestimated by 6% (LL) and 2% (AL) of the mean value) with a small phase lead (19° (LL) and 6° (AL)). Higher frequency components are fairly predicted by the models.*

(b) *Lead-lag deflection at $r/R = 0.99$. Measured signal shows an $\simeq 1\%$ offset in the lag direction with respect to computational predictions that is attributed to the SPR method used to determine deflections and the infinitely stiff drive train assumed in the simulations. Excellent agreement between measurements and LL results concerning 1/rev amplitude and a 7% underestimation by the AL. Moreover, a small phase lead of 30° (LL) and 20° (AL) is shown in the current harmonic. Higher frequency oscillations are almost completely damped in simulations.*

Figure 3.21. *Forward flight at 12.3 m/s, cases 851 (a) and 983 (b) of the HeliNoVi experimental campaign. Lead-lag moment at $r/R = 0.03$ (a) and deflection at $r/R = 0.99$ (b). Comparison between computational predictions and experimental measurements. Positive in the lag direction.*

Good agreement is observed in the mean value of the flapwise bending moment (Figure 3.22a). The 1/rev amplitude is fairly predicted. High frequency variations seen in the measurements (mainly 2/rev and 3/rev) are effectively reproduced by the simulations, with a small under–prediction of the respective amplitudes in LL results. Furthermore, a minor phase difference is seen in AL predictions which appears to be more pronounced in the LL predictions. The 1/rev flapwise deflection amplitude (Figure 3.22b) is clearly under–predicted by the two computations, which however agree well with each other. The high frequency variations seen in measurements are again effectively predicted.

Flight Speed 12.3 m/s, Case 851, r/R=0.1465

Flight Speed 12.3 m/s, Case 983, r/R=0.99
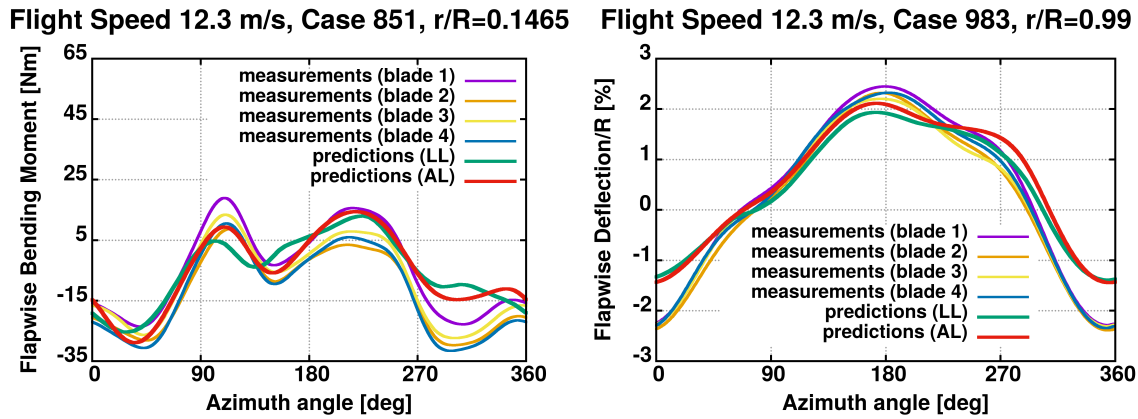
(a) *Flapwise moment at r/R = 0.1465. Mean value predictions are within the experimental range. 1/rev amplitude is slightly underestimated (6% by LL and 3% by AL) with a phase lag of ≃ 20°. Higher harmonics are effectively predicted by the computational models.*

(b) *Flapwise deflection at r/R = 0.99. Computational models predict higher mean value, whereas 1/rev amplitude is clearly underestimated with a phase lag of ≃ 10°. Higher harmonics are effectively predicted by the computational models.*

Figure 3.22. *Forward flight at 12.3 m/s, cases 851 (a) and 983 (b) of the HeliNoVi experimental campaign. Flapwise moment at r/R = 0.1465 (a) and deflection at r/R = 0.99 (b). Comparison between computational predictions and experimental measurements.*

Regarding twisting moment (Figure 3.23a), a small difference is seen in the predicted mean value. A clear 3/rev variation is seen in measurements, which is slightly under–predicted by the simulations. The mean value of the torsion angle is well predicted by the models (Figure 3.23b), however with almost zero 1/rev amplitude. Although the measured signal exhibits a dominant 3/rev variation, a small 1/rev component is also noted. The 3/rev variation is well captured by the simulations, while a small phase shift is observed. The high frequency ripple in the LL simulation is related to higher harmonics or some higher frequency mode due to the BVI phenomena. This does not appear in the AL results due to the increased numerical diffusion of the AL analysis associated with the coarser far wake grid.

Flight Speed 12.3 m/s, Case 851, r/R=0.332

Flight Speed 12.3 m/s, Case 983, r/R=0.99
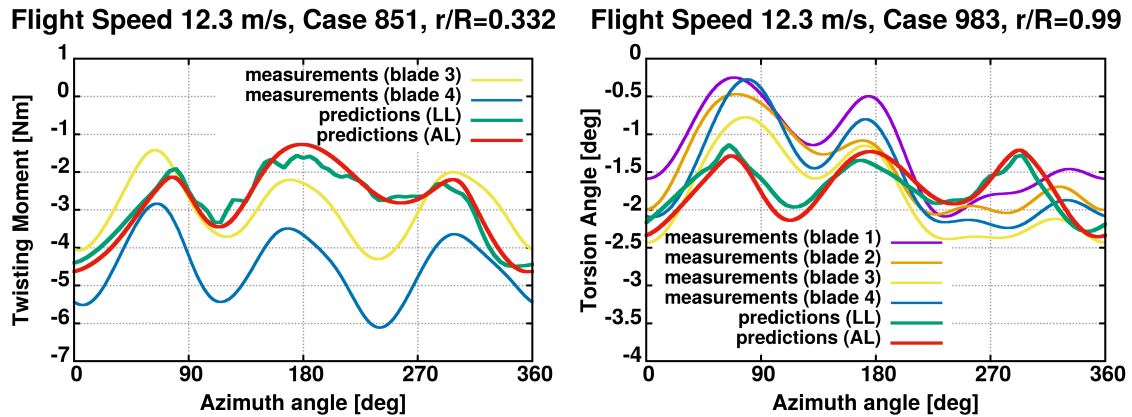
(a) *Twisting moment at r/R = 0.332. Mean value is slightly overestimated by ≃ 5%. Computational models predict clearly greater 1/rev (≃ 13%). However, the 3/rev seen in measurements are effectively predicted by the computational models, although slightly underpredicted. Higher frequency oscillations seen in the LL signal are effectively damped by AL. This is attributed to the increased numerical diffusion of the Eulerian framework.*

(b) *Torsion angle at r/R = 0.99. Mean value is fairly predicted but the 1/rev amplitude is almost completely damped. 3/rev harmonic seen in measurements are effectively predicted by the computational models, although slightly underestimated and with a phase lag of 25° for LL and 15° for AL predictions.*

Figure 3.23. *Forward flight at 12.3 m/s, cases 851 (a) and 983 (b) of the HeliNoVi experimental campaign. Twisting moment at r/R = 0.332 (a) and torsion angle at r/R = 0.99 (b). Comparison between computational predictions and experimental measurements.*

3.1.2.3.2 Forward Flight case at 50 m/s

Much better agreement is achieved in the lead–lag moment (Figure 3.24a) compared to the previous case. The mean value is slightly overestimated (≃ 17%), whereas the 1/rev amplitude is fairly predicted. However, the 4/rev harmonic excited in the experiment seems to have a much smaller amplitude in the simulations. The excitation of the 4/rev in the measurements could be related to a miss–placement of the 2*nd* lead-lag mode in close proximity to the 4/rev frequency (70*Hz*) in the experimental set–up. The higher damping of the mode in the simulations is attributed to higher aerodynamic damping by the models and a miss–tuning of the structural damping of the corresponding mode. Regarding the lead–lag deflection (Figure 3.24b), similar remarks can be made as in the low speed case.

In flapwise bending moment (Figure 3.25a), predictions are in line with measurements. There is very good agreement in the mean value and a minor underestimation of the 1/rev amplitude. Again, higher harmonics are less pronounced in the simulations. Predictions of the flapwise deflection (Figure 3.25b) have a small offset with respect to experimental data, whereas the 1/rev amplitude is computed correctly. Both 2/rev and 3/rev harmonics are excited in the measurements, while in the predictions 3/rev component almost vanishes. The main difference is observed in the 3*rd* and 4*th* quadrants of the azimuth circle.

The comparison regarding the torsion moment (Figure 3.26a) shows good agreement in the mean value and a small under–estimation of the amplitude of 1/rev. 2/rev load varia-

tions measured in the experiments are fairly predicted by the simulations. In torsion angle (Figure 3.26b) there is a good agreement in the mean value and a small over–prediction of the amplitude of 1/rev variation. 2/rev oscillations are reproduced by the simulations, however 3/rev frequencies that are excited in the measurements seem to have zero amplitude in the predictions. Moreover, a phase difference towards lower azimuth angles is seen in the simulations results.

The reason why higher than 2/rev frequencies have small amplitude in the simulations is most probably the use of a global Rayleigh type structural damping [166] which cannot reproduce correctly the exact modal damping of each vibration direction.
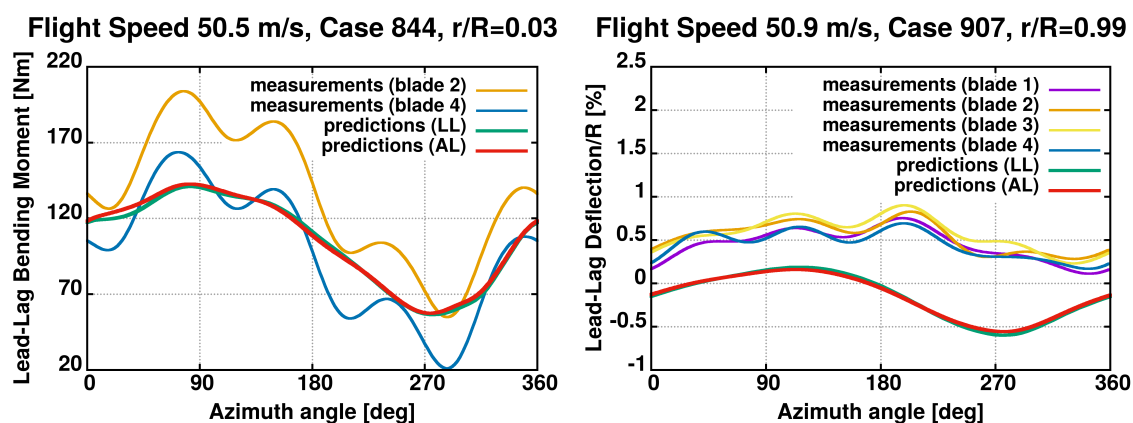
(a) *Lead-lag moment at r/R = 0.03. Mean value is slightly overestimated (≃ 17%) by the computational models but the 1/rev amplitude is fairly predicted (approximately +7% of the mean value for LL and +2.5% for AL). A phase lead of ≃ 20° for LL and ≃ 7° for AL is reported. 4/rev harmonic excited in measurements is almost completely damped by the computational models. This could be attributed to a miss–placement of the 2nd lead–lag mode close to the 4/rev natural frequency (70Hz) in the experimental set–up. Excessive damping of this harmonic by the computational models is attributed to the use of a global Rayleigh structural damping that is not properly tuned for higher natural frequencies.*

(b) *Lead-lag deflection at r/R = 0.99. Measured signal shows an ≃ 1% offset in the lag direction with respect to computational predictions that is attributed to the SPR method used to determine deflections and the infinitely stiff drive train assumed in the simulations. 1/rev amplitude is fairly predicted with a phase lag of ≃ 30° (LL) and ≃ 20° (AL). 4/rev harmonic excited in measurements is almost completely damped by the computational models.*

Figure 3.24. *Forward flight at 50 m/s, cases 844 (a) and 907 (b) of the HeliNoVi experimental campaign. Lead-lag moment at r/R = 0.03 (a) and deflection at r/R = 0.99 (b). Comparison between computational predictions and experimental measurements. Positive in the lag direction.*

Flight Speed 50.5 m/s, Case 844, r/R=0.1465

Flight Speed 50.9 m/s, Case 907, r/R=0.99
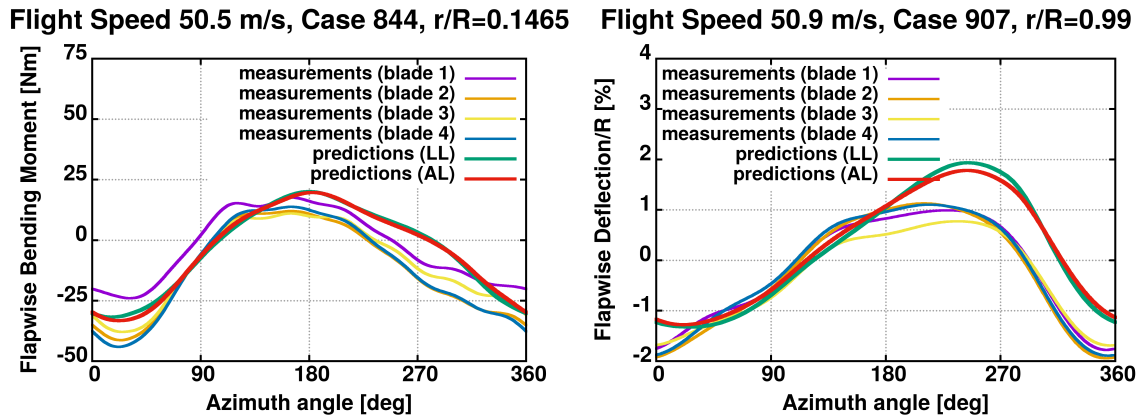
(a) *Flapwise moment at r/R = 0.1465. Mean value is fairly predicted by the computations. 1/rev amplitude is slightly underestimated with a phase lag of ≃ 20°. Higher harmonics seen in measurements are less pronounced in the simulations, as a result of a global Rayleigh type structural damping that excessively damps higher frequencies.*

(b) *Flapwise deflection at r/R = 0.99. Mean value is overestimated in computational predictions. 1/rev amplitude is fairly predicted but an approximately 10° lag is reported. Higher harmonics seen in measurements are less pronounced in predictions.*

Figure 3.25. *Forward flight at 50 m/s, cases 844 (a) and 907 (b) of the HeliNoVi experimental campaign. Flapwise moment at r/R = 0.1465 (a) and deflection at r/R = 0.99 (b). Comparison between computational predictions and experimental measurements.*

Flight Speed 50.5 m/s, Case 844, r/R=0.332

Flight Speed 50.9 m/s, Case 907, r/R=0.99
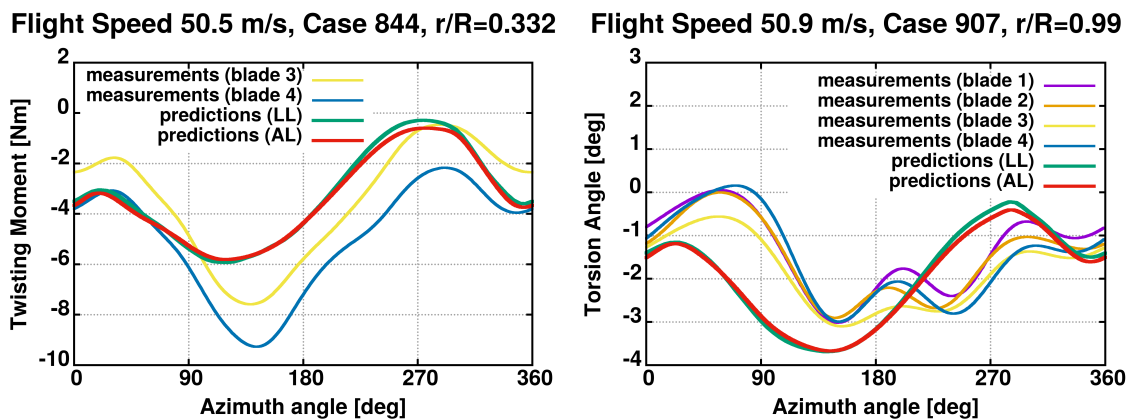
(a) *Twisting moment at r/R = 0.332. Mean value is fairly predicted by the computations. 1/rev amplitude is underestimated (−15% (LL) and −20% (AL)) with a 35° phase lead. 2/rev harmonic is effectively predicted.*

(b) *Torsion angle at r/R = 0.99. Mean value is fairly predicted, but the 1/rev amplitude is slightly overestimated. 2/rev harmonic is effectively predicted, but the 3/rev oscillations seen in measurements are clearly damped in computations.*

Figure 3.26. *Forward flight at 50 m/s, cases 844 (a) and 907 (b) of the HeliNoVi experimental campaign. Twisting moment at r/R = 0.332 (a) and torsion angle at r/R = 0.99 (b). Comparison between computational predictions and experimental measurements.*

3.1.2.3.3 Forward Flight case at 70 m/s

In the lead–lag moment comparison shown in Figure 3.27a, both the mean value and the amplitude of the 1/rev variation match very well. As in the previous case, the 4/rev harmonic excited in the experiment is much less pronounced in the simulations. Concerning the lead–lag deflection (Figure 3.27b), similar remarks can be made as in both previous speeds cases.

The mean value in the flapwise moment signals (Figure 3.28a) is clearly overestimated. There is good agreement regarding the 1/rev amplitude, but with a phase lag of approximately 40°. However, 2/rev variations are more pronounced in the simulations. On the contrary, the 3/rev harmonic that is excited in measurements is slightly damped in predictions. The comparison between flapwise deflection (Figure 3.28b) is in line with the one of the previous case (Figure 3.25b). The difference in the mean value is more pronounced herein. On the contrary, the amplitude of 1/rev is fairly predicted and 2/rev variations are captured by predictions, but their amplitude is smaller compared to measurements.

Concerning torsional moment (Figure 3.29a) and angle (Figure 3.29b), similar remarks can be made as in the previous speed case.
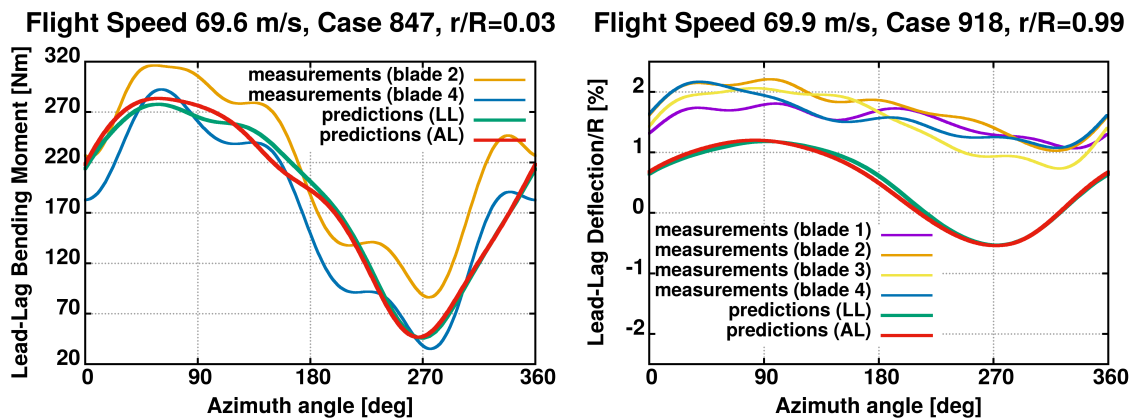
(a) *Lead-lag moment at $r/R = 0.03$. Mean value and 1/rev amplitude match very well. Higher harmonics (especially 4/rev) excited in measurements are less pronounced in simulations results. This could be attributed to a miss-placement of the 2nd lead-lag mode close to the 4/rev natural frequency (70Hz) in the experimental set-up. Excessive damping of this harmonic by the computational models is attributed to the use of a global Rayleigh structural damping that is not properly tuned for higher natural frequencies.*

(b) *Lead-lag deflection at $r/R = 0.99$. Measured signal shows an $\simeq 1\%$ offset in the lag direction with respect to computational predictions that is attributed to the SPR method used to determine deflections and the infinitely stiff drive train assumed in the simulations. 1/rev amplitude is fairly predicted with a phase lag of $\simeq 9°$ (LL) and $\simeq 5°$ (AL). 4/rev harmonic excited in measurements is almost completely damped by the computational models.*

Figure 3.27. *Forward flight at 70 m/s, cases 847 (a) and 918 (b) of the HeliNoVi experimental campaign. Lead-lag moment at $r/R = 0.03$ (a) and deflection at $r/R = 0.99$ (b). Comparison between computational predictions and experimental measurements.*

Flight Speed 69.6 m/s, Case 847, r/R=0.1465

Flight Speed 69.9 m/s, Case 918, r/R=0.99

(a) *Flapwise moment at r/R = 0.1465. Mean value is clearly overestimated by the computational models (≃ 60%). 1/rev amplitude is fairly predicted but with a phase lag of ≃ 40°. 2/rev harmonic is more pronounced in the simulations. On the other hand, 3/rev seen in measurements are slightly damped in the computational predictions.*

(b) *Flapwise deflection at r/R = 0.99. Mean value is clearly overestimated by the computational models and 1/rev amplitude is fairly predicted but with a phase lag of ≃ 60°, in line with the differences reported in flapwise bending moment. Higher harmonics are effectively predicted by the computations, but the respective amplitudes are slightly underestimated.*

Figure 3.28. *Forward flight at 70 m/s, cases 847 (a) and 918 (b) of the HeliNoVi experimental campaign. Flapwise moment at r/R = 0.03 (a) and deflection at r/R = 0.99 (b). Comparison between computational predictions and experimental measurements.*

Flight Speed 69.6 m/s, Case 847, r/R=0.332

Flight Speed 69.9 m/s, Case 918, r/R=0.99

(a) *Twisting moment at r/R = 0.332. Mean value is slightly overestimated by the computations (13% (LL) and 10% (AL)). 1/rev amplitude is slightly underestimated by AL predictions with a 20° phase lead for both computational models. 2/rev harmonic is effectively predicted.*

(b) *Torsion angle at r/R = 0.99. Mean value is fairly predicted but 1/rev amplitude is slightly overestimated (≃ 1°). 2/rev harmonic is effectively predicted, but the 3/rev oscillations seen in measurements are clearly damped in computations.*

Figure 3.29. *Forward flight at 70 m/s, cases 847 (a) and 918 (b) of the HeliNoVi experimental campaign. Twisting moment at r/R = 0.332 (a) and torsion angle at r/R = 0.99 (b). Comparison between computational predictions and experimental measurements.*

3.1.2.3.4 Harmonic Analysis

As stated in previous paragraphs, computational simulations over–predict the mean value of the lead–lag moment at the low speed case. In Table 3.15, it is shown that this difference is about 17% both for the LL and AL results. However, in the medium and high flight speed, the predicted mean values are within the scatter zone of the measurements of the different blades. The corresponding deflections in Table 3.16 show an $\simeq$ 1% difference. This is consistent in all three flight speeds and is totally in line with the comments made in the previous paragraph.

The mean value of the flapwise bending moment is fairly predicted by the two aerodynamic models at 12.3 and 50.5 m/s, whereas an over–estimation of about 1.5 Nm is observed at 69.6 m/s. This difference may seem large ($\simeq$ 60%), however it is smaller than the maximum difference of $\simeq$ 2.5 Nm among different blades measurements. As far as the flapwise deflection is concerned, the computational results consistently predict slightly higher mean values at all flight speeds with a maximum difference of $\simeq$ 0.4% at 69.9 m/s.

Finally, the simulations predict slightly smaller absolute mean values of the twisting moment at all the assessed cases. This difference increases with the flight speed up to 13% at 69.6 m/s. On the other hand, very good agreement is achieved in the tip torsion angle, where a maximum difference of $\simeq$ 0.15° is noted at 50.9 m/s.

Both in cases where the predicted values are close to the measured ones and in cases where discrepancies are noted, AL and LL seem to be in good agreement with each other.

Fourier analysis is performed on loads. Based on the analysis of the previous sections, where the azimuthal variation signals have been presented, similar conclusions with respect to the harmonic content are expected to be drawn for deflections.

Table 3.15. *Forward flight cases of the HeliNoVi experimental campaign at low, medium and high flight speed. Mean values of blade structural loads. Comparison between computational predictions and experimental measurements. An overall good agreement is observed in lead-lag bending moment (slightly overestimated by $\simeq$ 17% at 12 m/s) and flapwise bending moment (overestimated by $\simeq$ 60% at 70 m/s). Twisting moment is slightly overestimated at all flight speeds. Computational predictions agree very well with each other.*

|		Blade 1	Blade 2	Blade 3	Blade 4	LL	AL
	$\overline{M_{lag}}$ [Nm]	—	100.86	—	85.26	117.93	117.31
12.3 m/s	$\overline{M_{flap}}$ [Nm]	−4.38	−11.91	−8.51	−12.13	−4.95	−5.22
	$\overline{M_{tors}}$ [Nm]	—	—	−2.94	−4.49	−2.80	−2.80
	$\overline{M_{lag}}$ [Nm]	—	135.17	—	97.65	104.68	105.62
50.5 m/s	$\overline{M_{flap}}$ [Nm]	−2.83	−12.12	−9.84	−11.99	−4.10	−4.19
	$\overline{M_{tors}}$ [Nm]	—	—	−3.49	−5.02	−3.28	−3.39
	$\overline{M_{lag}}$ [Nm]	—	217.76	—	173.15	186.84	186.71
69.6 m/s	$\overline{M_{flap}}$ [Nm]	−2.53	−5.01	−5.19	−4.94	−0.91	−0.97
	$\overline{M_{tors}}$ [Nm]	—	—	−4.36	−5.64	−3.79	−3.91

Table 3.16. *Forward flight cases of the HeliNoVi experimental campaign at low, medium and high flight speed. Mean values of blade deflections. Comparison between computational predictions and experimental measurements. Lead–lag deflections show a consistent ≃ 1% difference that is attributed to the SPR method used to determine deflections and the infinitely stiff drive train assumed in the simulations. Flapwise deflections are slightly overestimated in computations at all flight speeds, but torsion angle is fairly predicted. Computational predictions agree very well with each other.*

|		Blade 1	Blade 2	Blade 3	Blade 4	LL	AL
12.3 m/s	$\overline{U_{lag}/R}$ [%]	0.99	1.04	1.05	0.97	−0.07	−0.09
	$\overline{U_{flap}/R}$ [%]	0.45	0.25	0.30	0.36	0.49	0.61
	$\overline{\Theta_{tors}}$ [deg]	−1.21	−1.45	−1.79	−1.53	−1.70	−1.72
50.9 m/s	$\overline{U_{lag}/R}$ [%]	0.45	0.54	0.58	0.45	−0.15	−0.15
	$\overline{U_{flap}/R}$ [%]	−0.17	−0.22	−0.31	−0.16	0.22	0.24
	$\overline{\Theta_{tors}}$ [deg]	−1.36	−1.52	−1.84	−1.53	−1.94	−1.98
69.9 m/s	$\overline{U_{lag}/R}$ [%]	1.51	1.72	1.50	1.57	0.46	0.45
	$\overline{U_{flap}/R}$ [%]	0.34	0.27	0.05	0.29	0.71	0.72
	$\overline{\Theta_{tors}}$ [deg]	−1.72	−1.87	−2.43	−2.05	−2.41	−2.46

In Figure 3.30a, the amplitude of the 1/rev, 2/rev and 4/rev variations are shown for the lead–lag bending moment. These are the highest excited harmonics. Both 1/rev and 2/rev amplitudes are fairly predicted by the computational tools, except from a difference in the 1/rev amplitude at 50 m/s (≃ 15% of the mean value) and the 2/rev amplitude at 70 m/s (≃ 6.5% of the mean value for the LL and ≃ 5% for the AL). The 4/rev harmonic exhibits much higher amplitudes compared to predictions. This is attributed to a possible miss–match of the 2*nd* lead–lag mode of the wind tunnel model with respect to the design value. The corresponding frequency approaches 4/rev in the test, which explains its high excitation. The 2*nd* lead–lag frequency is predicted at 91.58 Hz by the computational structural beam model, well apart from the 4/rev (70 Hz) and close to the design value. This explains the low excitation of the 4/rev harmonic in predictions. Better agreement is shown in phase computations (Figure 3.30b) where a maximum phase shift is observed in the 4/rev at the high speed case (70° for LL and 110° for AL).

The flapwise bending moment amplitudes (Figure 3.31a) are generally predicted consistently. However, in 3/rev harmonic frequency, a maximum phase shift of 120° is seen at the medium flight speed in the LL results and 110° at the high flight speed in the AL results (see Figure 3.31b).

Finally, the amplitudes of the different harmonic frequencies of the twisting moment are shown in Figure 3.32a. A maximum difference of about 13% of the mean value is observed at the 1/rev amplitude of the low speed case for the LL results. The corresponding difference increases to 15.5% for the AL case. Furthermore, the 3/rev amplitude, that seems to be in the measurements of the low speed case, is slightly under–predicted by the simulations (10% of the mean value in LL and 6.5% in the AL results). The greatest phase difference (Figure 3.32b) is observed in the 1/rev phase of the low speed case, where a phase shift of 100° is noted in the LL results case and 110° in the AL case.
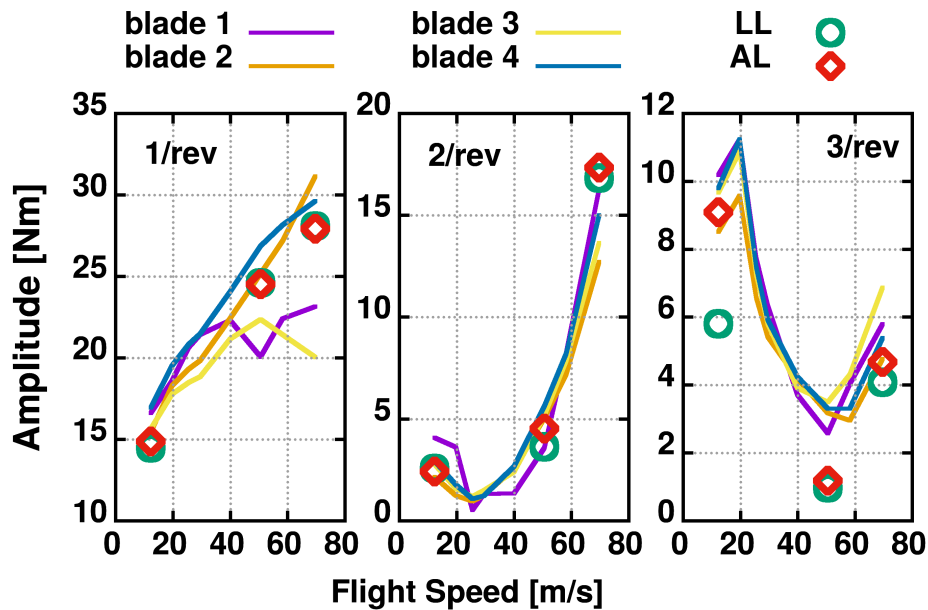
Lead-Lag Moment Harmonic Analysis, r/R=0.03
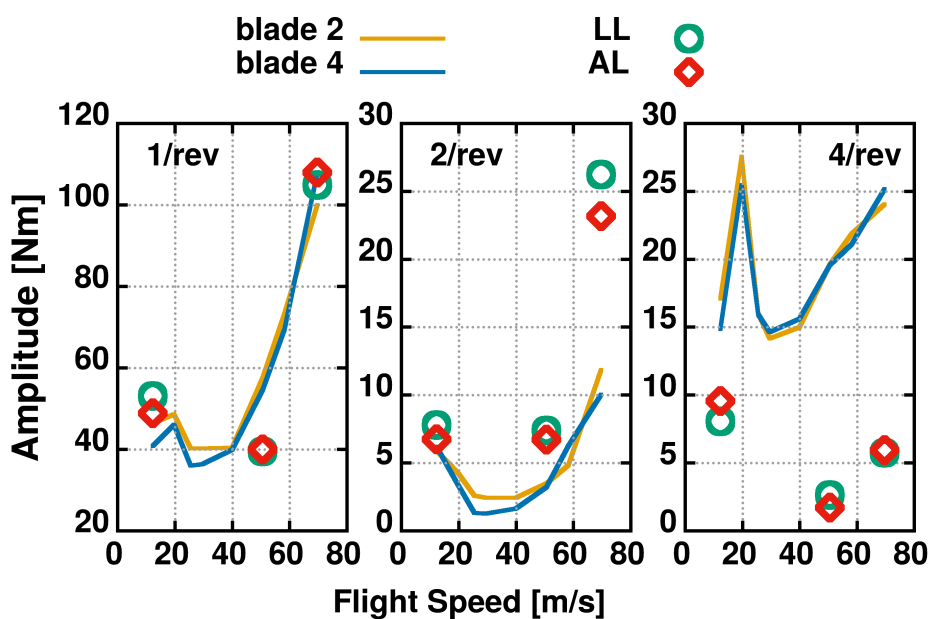
(a) *Amplitude of lead-lag bending moment harmonics. An overall good agreement is observed in 1/rev (slightly underestimated by $\simeq$ 15% of the mean value at 50 m/s) and 2/rev (slightly overestimated by $\simeq$ 6.5% of the mean value at 70 m/s) amplitudes. 4/rev harmonics excited in measurements are much less pronounced by computational tools predictions. This could be attributed to a miss-placement of the 2nd lead-lag mode close to the 4/rev natural frequency (70Hz) in the experimental set-up. Excessive damping of this harmonic by the computational models is attributed to the use of a global Rayleigh structural damping that is not properly tuned for higher natural frequencies. Computational predictions agree very well with each other.*

Lead-Lag Moment Harmonic Analysis, r/R=0.03
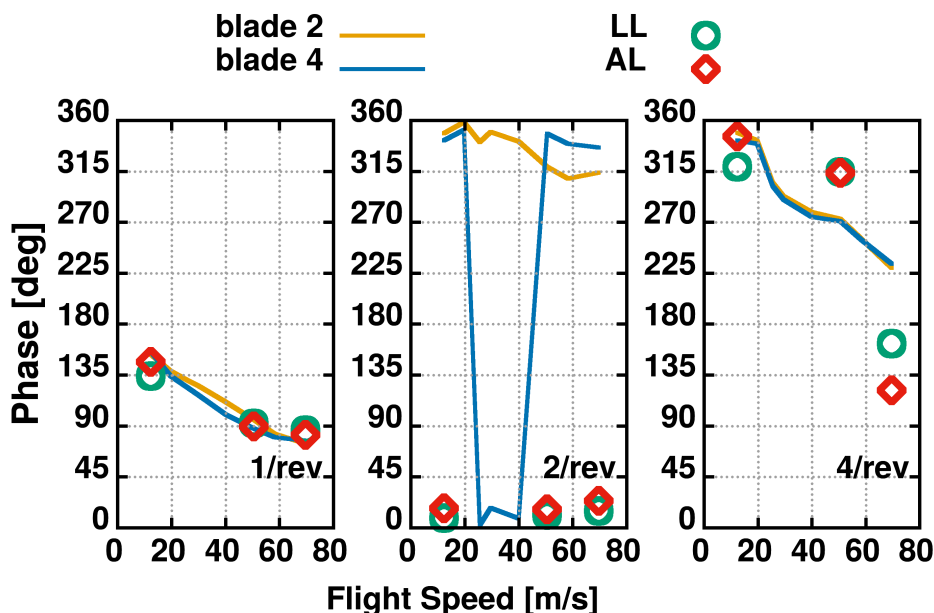
(b) *Phase of lead-lag bending moment harmonics. An overall good agreement is observed, especially in lower harmonics (highest energy content). The maximum phase shift is in 4/rev at the high speed case (70° for LL and 110° for AL). Computational predictions agree well with each other.*
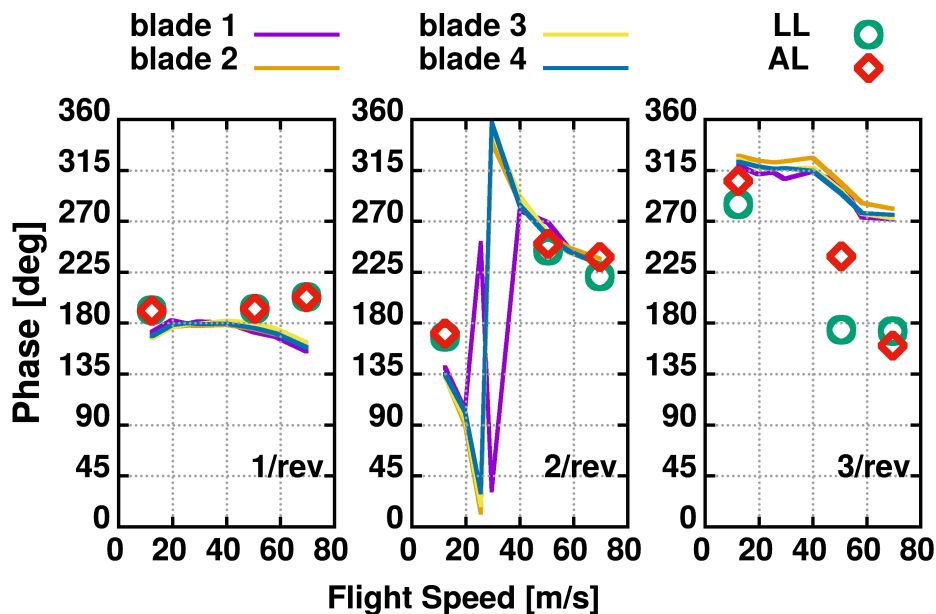
Figure 3.30. *Harmonic analysis of lead-lag bending moment. Amplitude (a) and phase (b) of frequencies with the highest energy content.*

Flapwise Moment Harmonic Analysis, r/R=0.1465

(a) *Amplitude of flapwise bending moment harmonics. An overall good agreement is observed, especially in lower harmonics (highest energy content). Computational predictions agree very well with each other, except from 3/rev amplitude of 12 m/s flight speed where AL predictions are closer to experimental measurements.*

Flapwise Moment Harmonic Analysis, r/R=0.1465

(b) *Phase of flapwise bending moment harmonics. An overall good agreement is observed, especially in lower harmonics (highest energy content). Maximum phase shift is observed in 3/rev at the medium speed case (120° for the LL results) and at high flight speed (110° for the AL). Computational predictions agree very well with each other.*

Figure 3.31. *Harmonic analysis of Flapwise bending moment. Amplitude (a) and phase (b) of frequencies with the highest energy content.*

Twisting Moment Harmonic Analysis, r/R=0.332
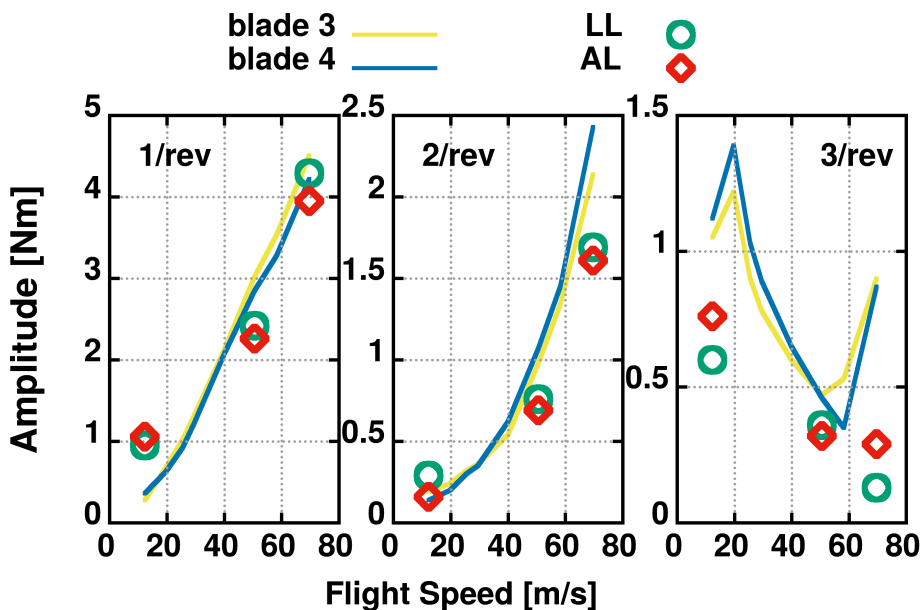
(a) *Amplitude of twisting moment harmonics. An overall good agreement is observed. Maximum difference is observed in 1/rev at the low speed case (+13% for the LL results and +15.5% for the AL). Computational predictions agree very well with each other.*

Twisting Moment Harmonic Analysis, r/R=0.332

(b) *Phase of twisting moment harmonics. An overall good agreement is observed. Maximum phase shift is observed in 1/rev at the low speed case (100° for the LL results) and at high flight speed (110° for the AL). Computational predictions agree very well with each other.*
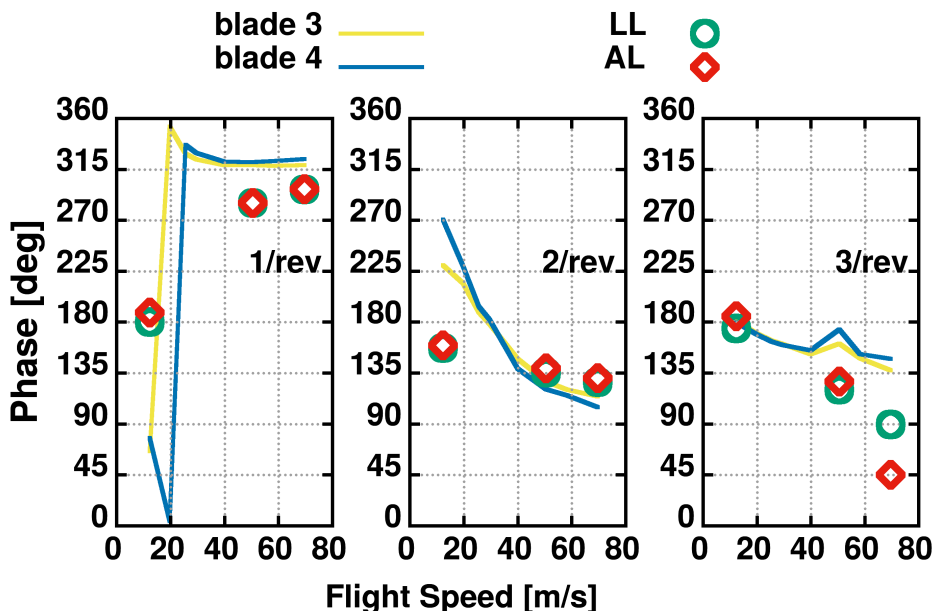
Figure 3.32. *Harmonic analysis of twisting moment. Amplitude (a) and phase (b) of frequencies with the highest energy content.*

3.2 Turbulent free–stream flow cases

In this section, the aeroelastic response of a WT operating under turbulent inflow conditions is simulated within a CFD framework. The utter goal is:

i. to investigate the mutual interaction between a WT rotor and a stochastic atmospheric inflow

ii. to assess how much the loading of the various WT components may change due to the effect of the WT on the local inflow conditions.

First, the numerical reproduction of turbulent atmospheric fields in a CFD context is performed. This is accomplished by using the model of Mann [8] to generate a synthetic $3D$ turbulence field (indicative instructions given in Section 2.2.1.6.1) and the method of the Generation Zone (presented in Section 2.2.1.6.3) in order to impose the turbulent velocity fluctuations of the Mann box onto the mean wind field provided by the CFD code. A set of simulations reproducing only the turbulent wind field without the presence of a WT are initially performed, in order to investigate the effect of multiple numerical parameters (e.g. grid resolution, length of the zone) on the spectral characteristics of the reproduced turbulent field. Then, aeroelastic simulations are performed for the isolated rotor of the DTU 10MW RWT operating at $V_\infty = 16 m/s$ mean wind speed at axial and $+30°$ yawed flow cases. Moreover, a full WT configuration (tower, shaft and rotor) operating inside the Atmospheric Boundary Layer (ABL) is simulated in the present analysis. The flow–field inside the boundary layer is initialized based on a logarithmic distribution of the wind velocity in the axial direction that is also continually imposed as the inlet boundary condition. The boundary layer length is set to $\delta = 1200 m$ and the surface roughness to $z_0 = 0.1 m$. Axial wind speed at hub height ($Z_{hub} = 119 m$) is set to $V_{hub} = 16 m/s$. Neutral stability conditions at 14% Turbulence Intensity (TI) are assumed for all the different cases tested, that correspond to Normal Turbulence Model (NTM) of the IEC standard. The rotor blades are modelled as ALs, using MaPFlow. The structural dynamics analysis of the various WT components is performed through GAST and the rotor blades are modelled as beam assemblies, in order for non–linear geometric phenomena to be properly considered. The two systems are solved separately, but tightly coupled. The coupled GAST–AL results are compared against computational predictions of the GAST–BEMT model, which as already discussed is the standard modelling approach in WT design.

3.2.1 Numerical investigation

In this section, turbulent wind field simulations in the absence of a WT are performed at 16 m/s axial mean wind speed with 14% TI. The synthetic turbulent field is produced with the the model of Mann [8]. The maximum frequency resolved by the produced Mann box is $f_{max} \simeq 5.85 Hz$ that corresponds to a $\Delta x_{Mann} = 1.367 m$ spacing in the longitudinal direction (the maximum frequency of interest is the mean wind speed divided by the minimum wavelength, which is twice the longitudinal spacing of the grid points in the Mann box). The maximum frequency resolved is set to that value, because higher

frequencies in the response of the WT (greater than 1 Hz) show much less energy content compared to lower ones (see Figure 3.33) and hence do not significantly contribute to the WT loading. The length of the produced Mann box is $L_{Mann} \simeq 11200m$ that corresponds to a total number of 8192 grid points in the longitudinal direction and a time duration of $T_{Mann} \simeq 700s$ (the desired length of Mann box equals the mean wind speed multiplied by duration of the required time series). The proposed by [102] time duration of turbulent inflow simulations is 10 minutes. In the lateral and vertical direction 32 points have been used with $\Delta y_{Mann} = \Delta z_{Mann} = 8m$ that result in planes of $248m \times 248m = 61504m^2$ and are much greater than the rotor disk area ($\simeq 25000m^2$) that is used in the aeroelastic simulations to follow.
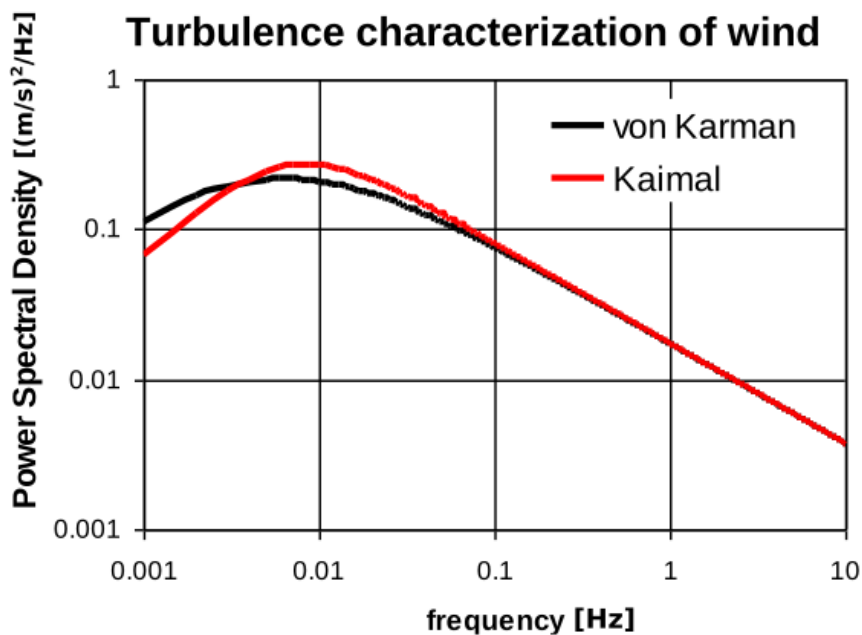
Figure 3.33. *Kaimal and von Karman energy spectrum for wind modelling. Frequencies higher than 1 Hz show much lower energy content compared to lower frequencies.*

The method of Generation Zone (GZ) is then used in order to superimpose the turbulent velocity fluctuations onto the mean wind field. This is accomplished through source terms that are applied in the momentum and energy equations of the cells located inside the zone. In this way, the nearby velocity field is forced to the desired (turbulent) one. The zone must be placed sufficiently far from the rotor disk, so that the local velocity field is not that heavily influenced by the rotor and vice versa. Otherwise, the effect of the rotor in the formation of the overall flow–field (expansion and deceleration of the flow) will be consumed by the strong source terms of the GZ. However, as the zone is placed further upstream from the rotor plane, the grid resolution needs to get finer so that the turbulent field will not be altered significantly while getting convected downstream. In Figure 3.34, it is shown that a good compromise between accuracy and computational cost is to place the GZ approximately $1R$ upstream of the rotor plane. In the following simulations, the end of the zone is fixed at $1R$ upstream of the rotor hub, whereas the starting plane

is defined by the length of the zone. The GZ length is later investigated in detail along with other numerical parameters such as the grid resolution. The goal of the following paragraphs is to assess the sensitivity of the spectral characteristics of the turbulent field we end up with at the rotor plane (region of interest). The great difference between the minimum and maximum wave–lengths of simulated turbulence ($\lambda_{min} \simeq 2.734m$ and $\lambda_{max} = 11200m$) dictate the application of LES turbulence modelling, so that multiple turbulent scales are accounted for. Consequently, large eddies (larger than the grid size) are directly resolved, whereas smaller ones (Sub-Grid Scale (SGS)) are modelled with the algebraic SGS model of Smagorisnky [167].
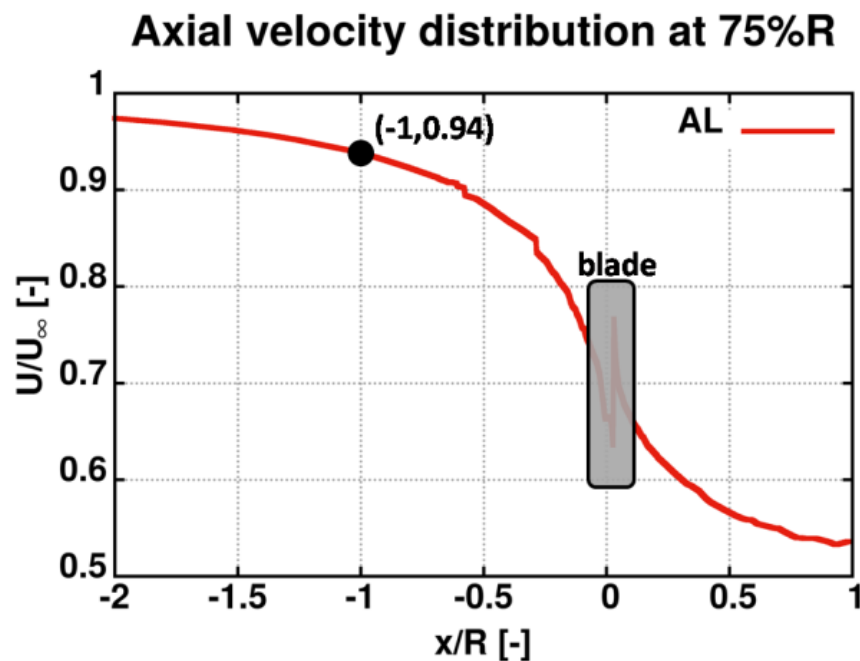
Figure 3.34. *Axial velocity distribution at 75%R radial position extracted from an aero-dynamic simulation of the DTU 10MW RWT isolated rotor (modelled as actuator lines) operating at $11m/s$ axial wind speed. X and Y axes are normalized with rotor radius and free-stream velocity. Axial velocity is at 94% of U_∞ at 1 rotor radius upstream, indicating small interaction between the rotor and the free-stream flow in this region.*

Grid set-up

The computational domain used in these simulations is a box of 20 rotor diameters ($20D$) length in the longitudinal direction ($5D$ upstream and $15D$ downstream) and $20D$ in the lateral and vertical directions ($10D$ around the center of the box where the rotor hub center will be placed in the aeroelastic simulations to follow). Structured and uniform meshing under maximum grid resolution is applied in a region extending $1R$ upstream, $2D$ downstream in order to better resolve the development of the wake deficit and its impact on the aerodynamic forces and $1.5R$ around the center of the box so that the flow expansion fits in when the WT is present. GZ is placed at the beginning of this structured area that for this reason extends slightly further upstream, depending on the length of the GZ, as illustrated in Figure 3.35. However, the end plane of the GZ is always placed $1R$ upstream of the box center. The characteristic length of this region is denoted by Δx.
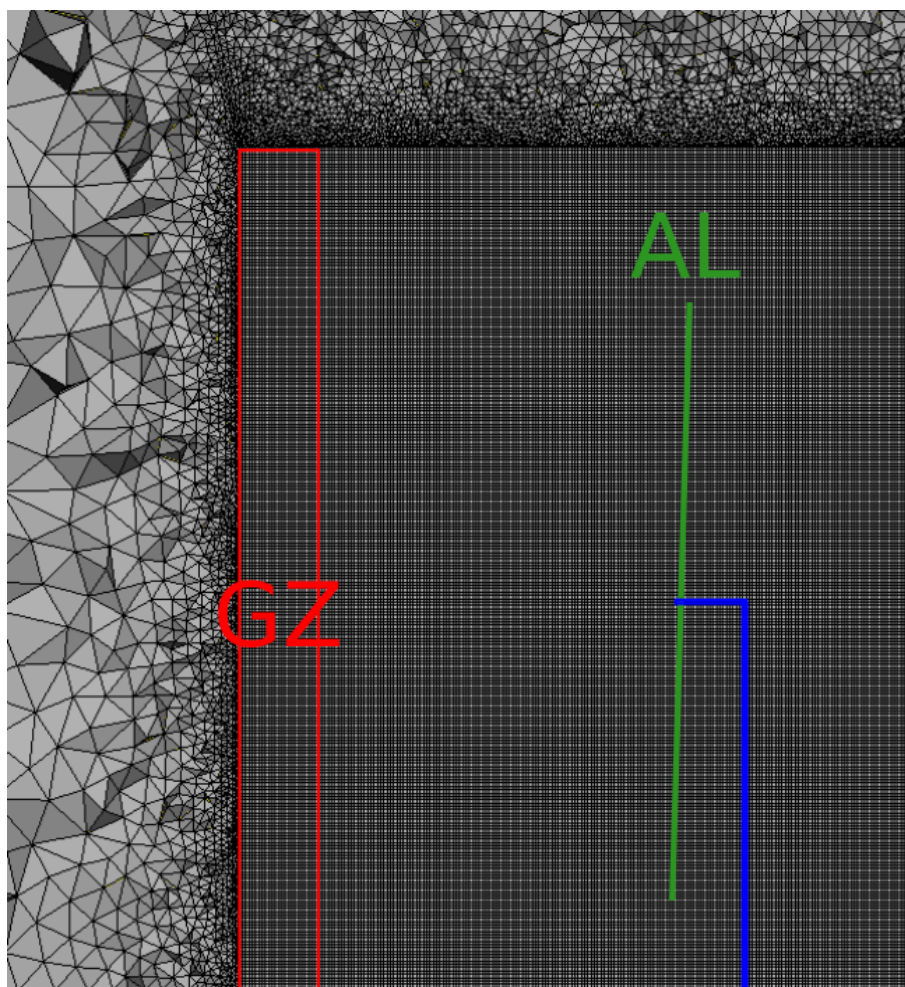
Figure 3.35. *Side view of the computational domain used in the turbulent flow simulations of the DTU 10MW RWT rotor at* 16 *m/s mean wind speed. The rotor blades are modelled as actuator lines and are located inside a box of* 20D *length and* 10D *radius around the rotor hub center. The end plane of the GZ is placed* 1R *upstream of the rotor. The whole GZ is inside an equidistant region of maximum grid resolution in order to better resolve the turbulent wake structures.*

Grid Dependency Analysis

The first parameter checked is the characteristic length (denoted by Δx) of the structured and equidistant region that contains the GZ and the turbulent eddies (in the aeroelastic simulations that follow, the WT and the near wake vortices are also inside this region). A maximum of $\Delta x = 1m$ has been used in all 3 directions (longitudinal, lateral and vertical) throughout the equidistant region, based on findings of Section 3.1.1.2 ($\Delta x = R/90 \simeq 1m$ in a uniform and structured region around the rotor has been found to provide a grid independent solution yielding both affordable and accurate estimation of the aerodynamic loads when they are simulated as actuator lines). In order to restrain computational cost, finer values of Δx are tested only in the longitudinal direction, employing them from the beginning of the fine region and up to 10m upstream of the center of the domain (hub center will be placed there in the aeroelastic simulations). This approach is adopted, so that the Gaussian projection of the aerodynamic forces of the actuator lines is fully

included in the uniform region, according to the instructions in Section 3.1.1.2. Three different values of Δx have been tested ($\Delta x = 1m, 0.5m, 0.25m$) and the corresponding grid size (number of cells) is listed in Table 3.17. The spectra of the axial velocity that we end up with at the rotor plane are compared against the input spectrum in Figure 3.36. Both fixed point (sampled at the WT hub center) and rotating point (sampled at 75%R) samplings are depicted. For the fixed point sampling spectra, the finest grid resolutions seem to better preserve the high frequency content of the wind fluctuations ($\geq 1Hz$) (see Figure 3.36a). However, all three different grid resolutions end up in lower energy content compared to the target. The reason for these differences is grid diffusion acting from the GZ up to the WT plane. Use of even finer grids in order to reduce numerical diffusion leads to prohibitive computational cost. It needs to be highlighted, that the ultimate objective of this study is to produce a turbulent field that will be later used for the investigation of the interaction between the stochastic atmospheric inflow and the aeroelastic response of a WT. Hence, this numerical set–up is meant to be used in multiple and long lasting simulations (the proposed by [102] time duration of turbulent inflow simulations is 10 minutes). Moderate grid resolutions must be employed so that the resulting computational cost remains affordable. After all, frequencies greater than $1Hz$ have much lower energy content and, thus, minor contribution to the excitation of the WT. For this reason, the value $\Delta x = 1m$ is considered to be acceptable. Moreover, the spectrum of the axial velocity captured by a rotating point at 75%R is shown in Figure 3.36b. The rotational velocity of the sampling point is the same as the rotational velocity of the WT considered in the following aeroelastic simulations. In this case, the energy content of all the depicted frequencies is well captured even for the coarse grid of $\Delta x = 1m$. The reason is that due to the rotation of the sampling point, the energy content of turbulence is concentrated on the frequency of rotation and its harmonics. The rotating sampling spectrum shows the energy content of turbulent excitation at it is perceived by the rotating blades of the WT. For this reason, it is considered to be much more significant as a metric compared to fixed point sampling. Overall, $\Delta x = 1m$ ends up providing an accurate estimation of the turbulent excitation under moderate grid resolution both for the fixed and rotating point sampling. For this reason it is adopted for the discretization of the fine equidistant region in the aeroelastic simulations to follow.

Table 3.17. *Grid size (in million cells) vs grid characteristic length Δx [m] employed upstream of the rotor hub in the longitudinal direction of the fine and structured region that contains the GZ and the produced turbulent structures. $\Delta x = \Delta y = \Delta z = 1m$ is used in the remaining region in the longitudinal direction and everywhere in lateral and vertical directions.*

Δx	#cells
$1m$	48.4 M
$0.5m$	56.9 M
$0.25m$	73.8 M
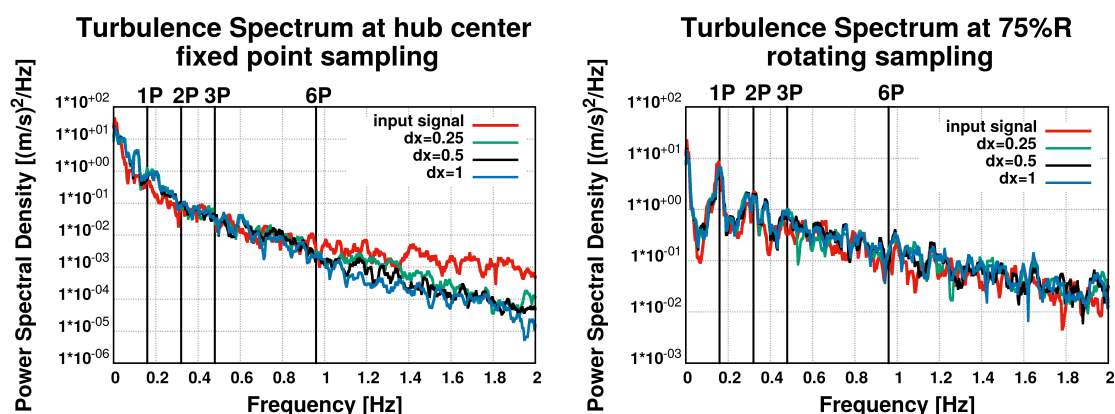
(a) *Turbulence spectrum of axial velocity captured at rotor hub center. Fixed point sampling.*

(b) *Turbulence spectrum of axial velocity captured at 75%R. Rotating point sampling.*

Figure 3.36. *Axial velocity spectra, captured at the plane of interest (rotor plane) with different grid resolutions are compared against the desired one (input). Fixed point sampling at hub center (a) and rotating point sampling at 75%R (b). Numerical diffusion is the main source of discrepancies. Lower energy content is captured in frequencies ≥ 1Hz at fixed point sampling. Finer grid resolutions are slightly closer to the input spectrum. All different grid resolutions predict comparable energy content at all the depicted frequencies of rotating point sampling.*

GZ Length Dependency Analysis

A number of simulations have been performed in order to check how much does the GZ length (measured in number of cells in longitudinal direction) affect the resulting spectra of the axial velocity at the rotor plane. In Figure 3.37, it is shown that 2 cells are not enough to produce reasonable spectra at the rotor plane. The GZ length needs to be at least 5 cells long to sufficiently preserve the wind fluctuations. Frequencies higher than $1Hz$ are again not adequately resolved in the fixed point sampling (see Figure 3.37a) and no significant improvement is reported when more than 5 cells are employed. However, very good agreement is shown in the energy content of all the depicted frequencies in the rotating sampling (see Figure 3.37b). This means that a GZ length of at least 5 cells is acceptable. Since there is no big difference in total amount of grid cells when greater lengths of GZ are employed, 20 cells are used in the following aeroelastic simulations.
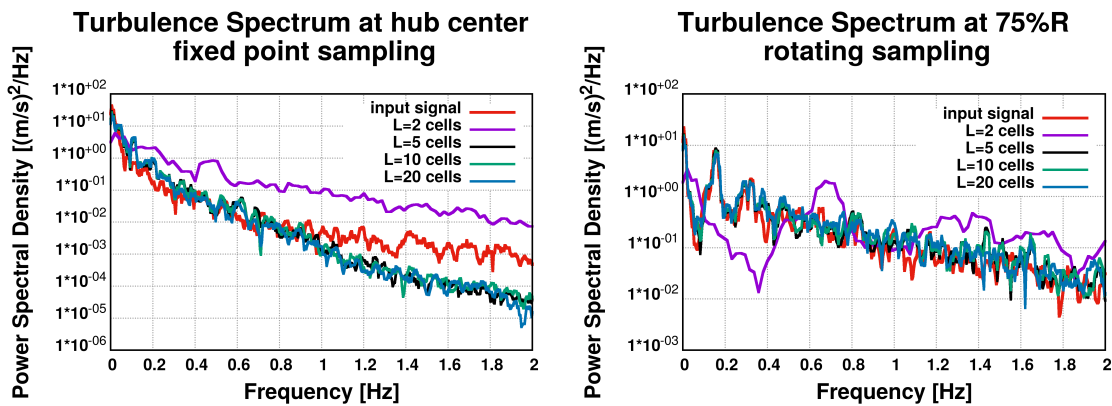
(a) *Turbulence spectrum of axial velocity captured at rotor hub center. Fixed point sampling.*

**(b)** *Turbulence spectrum of axial velocity captured at 75%R. Rotating point sampling.*

Figure 3.37. *Axial velocity spectra, captured at the plane of interest (rotor plane) with different lengths of GZ (measured in number of cells in longitudinal direction) are compared against the desired one (input). Fixed point sampling at hub center (a) and rotating point sampling at 75%R (b). Non-realistic spectra are produced when only 2 cells are used in GZ length. Reasonable spectra are captured when at least 5 cells are employed. Lower energy content is captured in frequencies ≥ 1Hz at fixed point sampling. Use of more than 5 cells does not significantly improve the produced fixed point spectrum. All GZ implementations with at least 5 cells predict comparable energy content, similar to the desired one, at all the depicted frequencies at rotating point sampling.*

3.2.2 Comparison against BEMT predictions

In this section, turbulent inflow aeroelastic simulations results using the AL model as the aerodynamic analysis tool are compared against reference results obtained by a standard BEMT model. 3 different cases are addressed at 16 m/s mean wind speed; i) an isolated WT rotor at axial mean wind, ii) an isolated WT rotor at +30° yaw misalignment, and iii) a full WT (tower, shaft, rotor) operating inside the ABL. In the latter case, 16 m/s refers to the mean wind speed at hub height. Only the rotor blades are included in the aerodynamic analysis, whereas shaft and tower are modelled as elastic beams without external aerodynamic forcing. The modelled WT is the conceptual DTU 10MW RWT, which has been analyzed in Section 3.1.1.1. Constant rotational speed at 9.6 rpm and 12° blade pitch angle is assumed for all cases (WT controller continually regulating rotational speed and pitch angle is not enabled in the simulations). The azimuth angle is assumed to be zero when the blade points upwards (opposite to the ground). Flapwise bending moments (based on Section 3.1.1 results, flapwise bending moment dictates the overall loading of the rotor blades) at the root of the blades and the tower (when present) are depicted as time history and azimuthal variations. The above loads are also provided in the frequency domain, by performing an Fast Fourier Transform (FFT) analysis in the corresponding time–history signals. Finally, rain–flow counting [168] is applied in order to determine the number of fatigue cycles that exist in the time–history and extract the Damage Equivalent Loads (DEL).
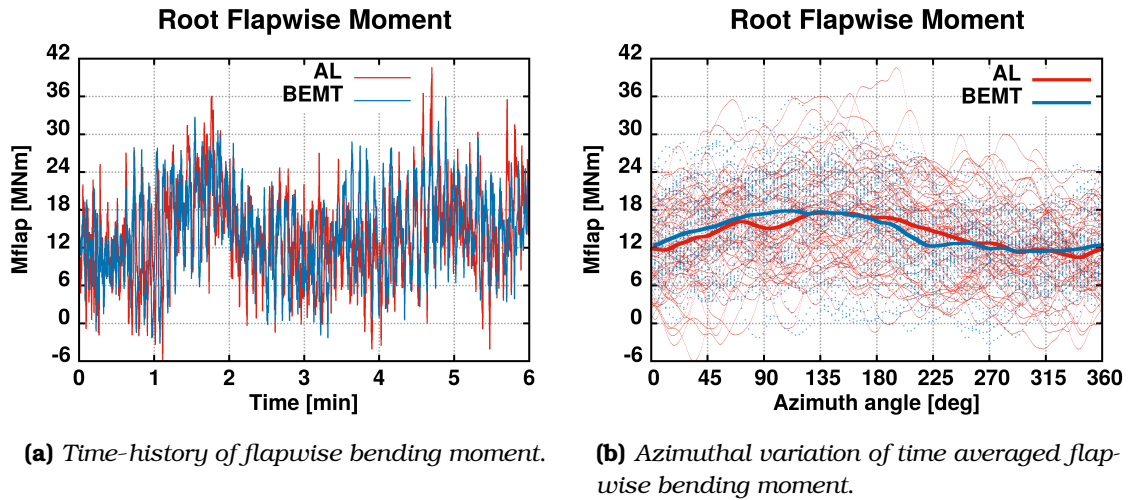
3.2.2.1 Axial flow case

Turbulent eddies generated by the GZ and the wake produced by the aeroelastic AL model on the axial mean flow case are visualized in Figure 3.38 by plotting Q–Criterion iso–surfaces [169]. In Figure 3.39a, the corresponding time–history of the flapwise bending moment measured at the root of the 1st blade is shown, where an overall good correlation is observed between AL and BEMT predictions for a 6 minutes simulation. In order to assess the differences between the two models predictions, the respective azimuthal variation is shown in Figure 3.39b. Dots indicate the instantaneous predicted values, whereas the solid lines indicate the azimuthally averaged values. An overall good agreement is shown in the mean value, amplitude and phase predictions of the averaged signal between AL and BEMT. This is expected based on the good agreement shown in axial flow cases under constant wind in Section 3.1.1.3.1. However, AL results for the flapwise bending moment exhibit higher energy values at higher frequencies (beyond 5P). This is in line with the higher energy observed in the spectrum of the rotational sampled wind at the rotor plane shown in Figure 3.36b). This is also captured in Figure 3.40a, where the spectral density of the flapwise moment is shown. It needs to be stressed that in BEMT simulations, as opposed to CFD ones, the turbulent field is directly imposed on the rotor plane and hence no discrepancies are expected with respect to the turbulent field produced by the Mann's model. Indeed, AL shows slightly greater energy content in higher frequencies ($\geq 0.8Hz$) as compared to BEMT. This explains the increased range of the AL predicted loads in the large number of cycles (≥ 80) (see Figure 3.40b) and the corresponding difference in the computed DEL.
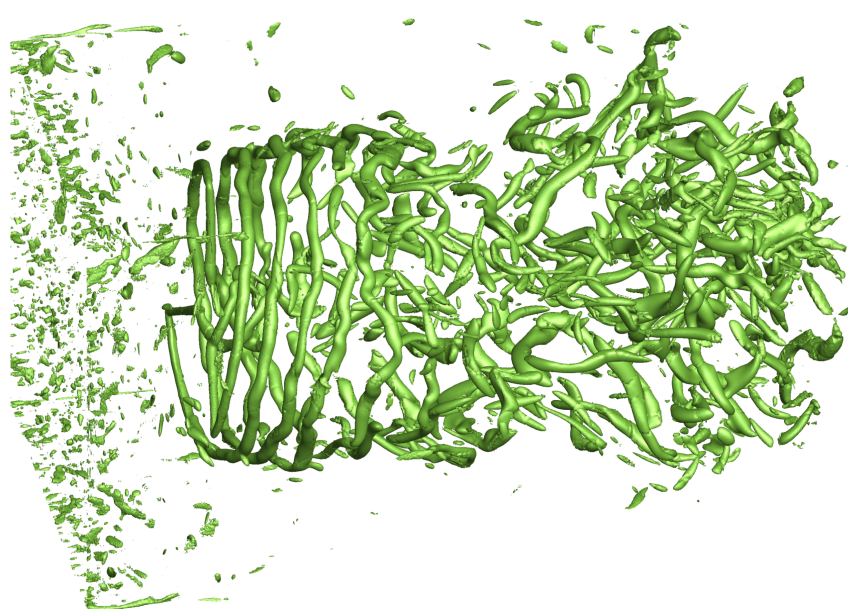
Figure 3.38. *Turbulent eddies and wake visualization of the DTU 10MW RWT rotor operating at 16 axial mean wind speed under NTM conditions. Rotor blades are modelled as actuator lines, whereas the turbulent eddies are produced with the method of GZ. Vorticity structures are visualized by plotting Q–Criterion iso–surfaces.*

(a) *Time-history of flapwise bending moment.*

(b) *Azimuthal variation of time averaged flap-wise bending moment.*

Figure 3.39. *Flapwise bending moment measured at the root of the 1st blade expressed as time-history (a) and azimuthal variation (b) for axial mean wind speed at 16 m/s. Good agreement is observed in mean value, amplitude and phase of the averaged signal predictions between the two models. Higher frequency excitation is shown in the AL results that originates in the effect of numerical diffusion on the produced turbulent spectrum at the rotor plane.*

(a) *FFT of flapwise bending moment.*

(b) *RFC of flapwise bending moment.*
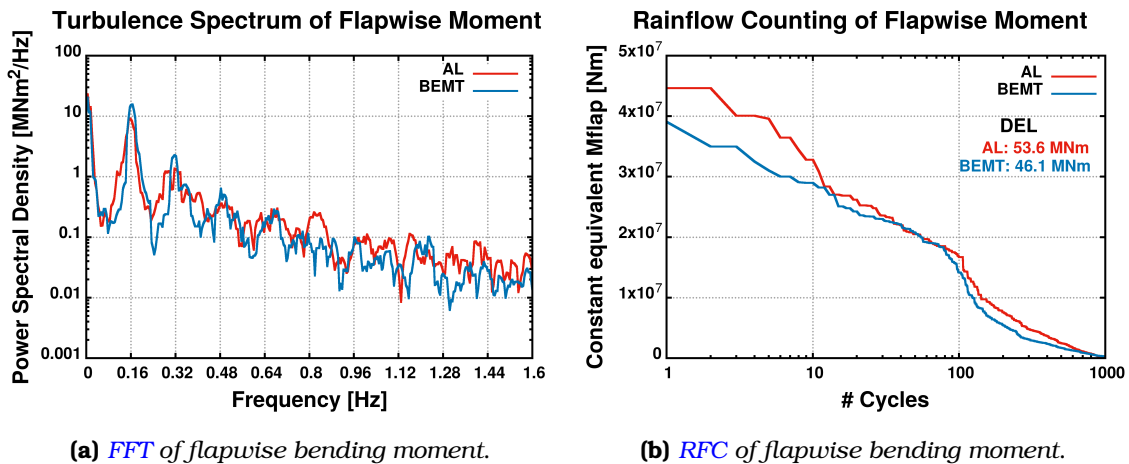
Figure 3.40. *FFT (a) and RFC (b) of flapwise bending moment measured at the root of the 1st blade for axial mean wind speed at 16 m/s. Higher energy content excitation is shown in higher frequencies ($\geq$ 0.8Hz) of AL results that originates in the effect of numerical diffusion on the produced turbulent spectrum at the rotor plane. This leads to increased range of loads in the large number of cycles ($\geq$ 80) and, in turn, to greater DEL.*

3.2.2.2 Yawed flow case

In Figure 3.41a, the time–history of the flapwise bending moment predicted at the root of the 1st blade is shown for the case of a mean wind with +30° yaw misalignment. As in the case of the axial mean wind, an overall good correlation is observed between AL and BEMT predictions for a 6 minutes simulation. The differences between the two models predictions are more clearly depicted in the corresponding azimuthal variation shown in Figure 3.41b. Dots indicate the instantaneous predicted values, whereas the solid lines indicate the azimuthally averaged values. As in the yawed flow cases under constant wind (see Section 3.1.1.3.2), an overestimation of $\simeq 9\%$ is observed by BEMT in the mean value and $\simeq 29\%$ in the amplitude. Moreover, an $\simeq 35°$ phase difference is noted. These differences are attributed to the omission of the wake skewness in BEMT simulations. Consequently, no increased wake induction is considered, due to the relative angle between the wake and the rotor plane. On the other hand, this is inherently accounted for in the AL simulations, thanks to the CFD framework through which the wake vortices are described. For this reason, the minimum load predicted in BEMT simulations is at $\simeq 225°$ azimuthal position, whereas in the AL predictions it is at $\simeq 260°$, closer to 270° where the wake induced velocities are minimized. The difference in 1P amplitude is also captured in Figure 3.42a as a notable difference in the peak at the rotational frequency (0.16Hz). This explains the increased load ranges of BEMT in the low number of cycles (≤ 100) that are computed by the Rain-Flow Counting (RFC) method (see Figure 3.42b) and the corresponding difference in the computed DEL.

(a) *Time-history of flapwise bending moment.*   **(b)** *Azimuthal variation of time averaged flap-wise bending moment.*
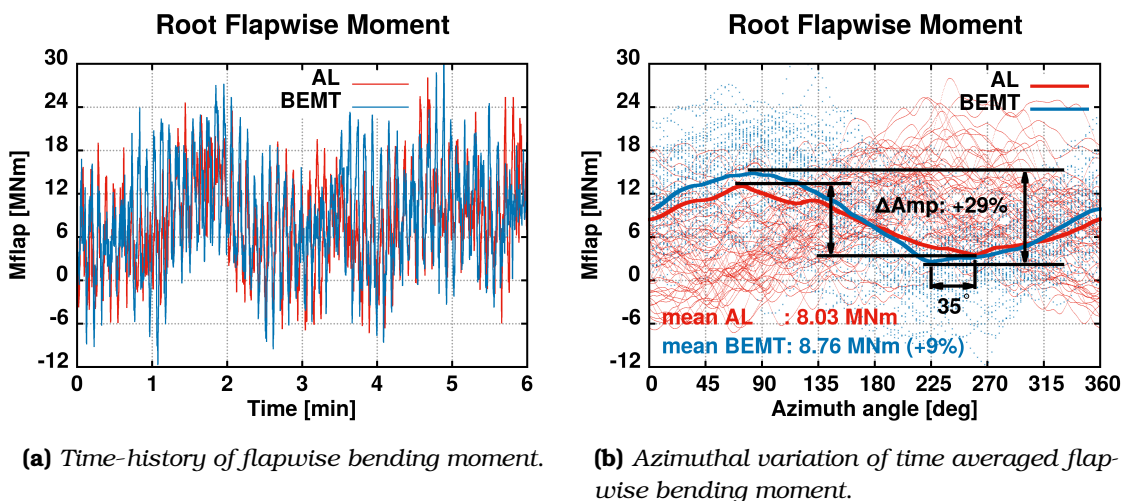
Figure 3.41. *Flapwise bending moment measured at the root of the 1st blade expressed as time-history (a) and azimuthal variation (b) for +30° yawed mean wind speed at 16 m/s. BEMT overestimates the mean value and the 1P amplitude by approximately 9% and 29% respectively. Moreover an $\simeq 35°$ phase shift is observed. Those differences are attributed to the detailed description of the wake vortices in the AL simulations due to the CFD framework. Hence, more accurate estimation of the wake induced velocities is accomplished.*

(a) *FFT of flapwise bending moment.*
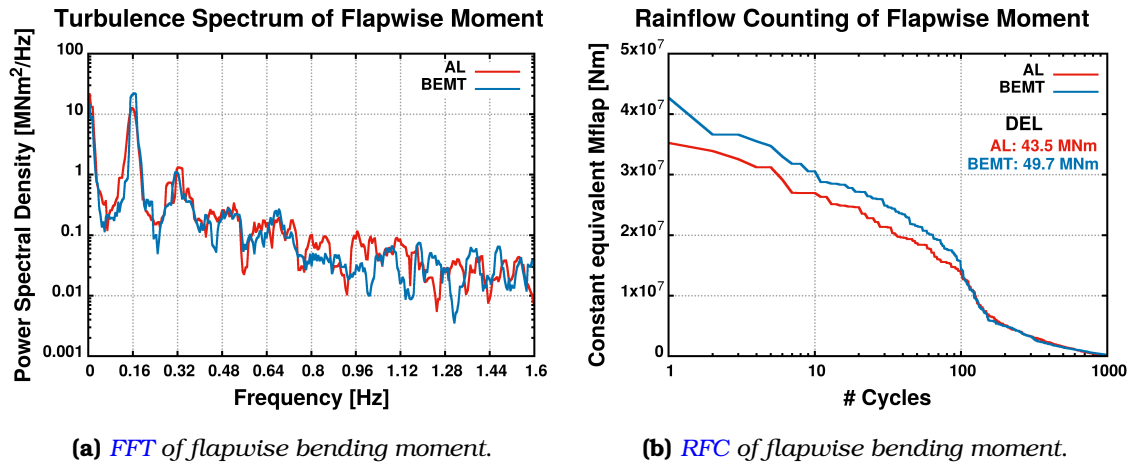

(b) *RFC of flapwise bending moment.*

Figure 3.42. *FFT (a) and RFC (b) of flapwise bending moment measured at the root of the 1st blade for +30° yawed mean wind speed at 16 m/s. A greater peak is predicted in BEMT simulations at the rotational frequency (0.16Hz), that is directly related to the overestimation of the 1P amplitude seen in Figure 3.41b. This leads to increased load ranges at low number of cycles ($\leq$ 100) and, in turn, to greater DEL.*

3.2.2.3 Atmoshperic boundary layer flow case

In Figure 3.43a, the time–history of the flapwise bending moment predicted at the root of the 1st blade is shown for the case of the full WT operating inside the ABL. As in the previous cases, an overall good correlation is observed between AL and BEMT predictions, which however show a significant level difference herein. The differences between the two models predictions are more clearly depicted in the corresponding azimuthal variation shown in Figure 3.41b. Dots indicate the instantaneous predicted values, whereas the solid lines indicate the azimuthally averaged values. An overall good agreement is observed in the phase of the averaged response. However, mean value is underestimated by $\simeq$ 26% in BEMT simulations, whereas the amplitude is overestimated by $\simeq$ 35%. The difference in 1P amplitude is also depicted in Figure 3.44a as a notable difference in the peak value of the spectrum at the rotational frequency (0.16Hz). This explains the increased range of loads predicted by BEMT in the intermediate number of cycles (20 − 100) that are computed by the RFC method (see Figure 3.44b). On the other hand, greater energy content response is shown in higher frequencies ($\geq$ 0.8Hz) of AL results that, as discussed in Section 3.2.2.1, originates in the effect of the numerical procedure on the produced turbulent spectrum at the rotor plane. This counteracts the difference in intermediate number of cycles and, for this reason, the computed by the two different models DEL are similar.

(a) *Time-history of flapwise bending moment.*

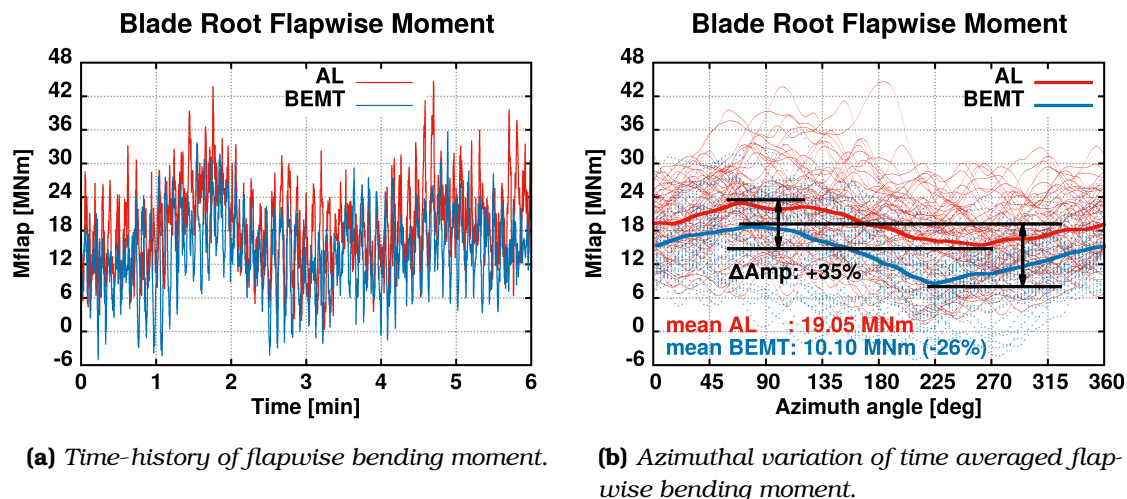**(b)** *Azimuthal variation of time averaged flapwise bending moment.*

Figure 3.43. *Flapwise bending moment measured at the root of the 1st blade expressed as time-history (a) and azimuthal variation (b) for a full WT operating inside the ABL. The axial velocity is 16 m/s at hub height. BEMT underestimates the mean value by approximately 26% and overestimates the 1P amplitude by approximately 35%. Those differences are attributed to the detailed description of the wake vortices in the CFD framework and the effect of the rotor and the ground on the turbulent wind inflow, that is properly accounted for in AL simulations.*

(a) *FFT of flapwise bending moment.*

(b) *RFC of flapwise bending moment.*
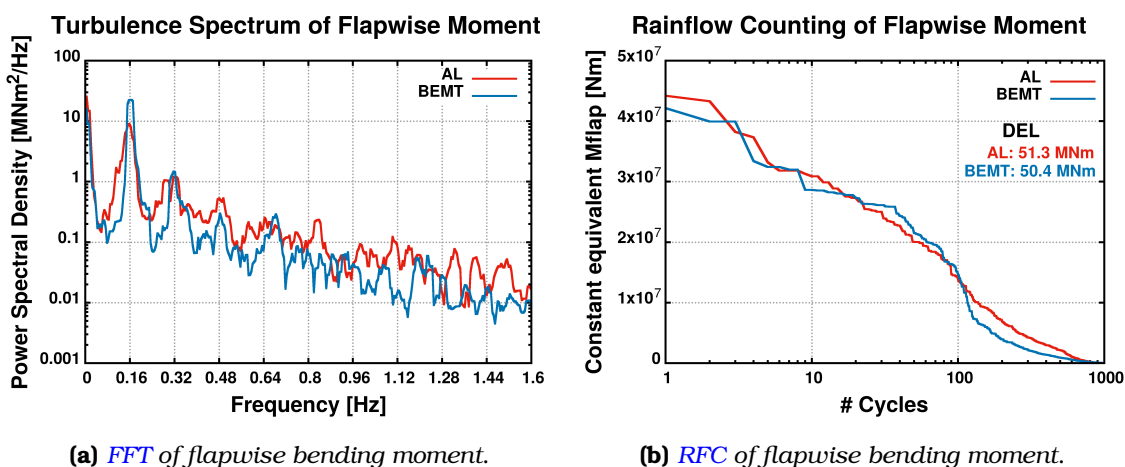
Figure 3.44. *FFT (a) and RFC (b) of flapwise bending moment measured at the root of the 1st blade for a full WT operating inside the ABL. The axial velocity is 16 m/s at hub height. A greater peak is predicted in BEMT simulations at the rotational frequency (0.16Hz), that is directly related to the overestimation of the 1P amplitude seen in Figure 3.43b. This leads to greater range of loads at the intermediate number of cycles (20 − 100). Greater energy content response is shown in higher frequencies ($\geq$ 0.8Hz) of AL results that originates in the effect of the numerical procedure on the produced turbulent spectrum at the rotor plane. This leads to greater range of loads at the large number of cycles ($>$ 100). Hence, the computed DEL by the two models end up being similar.*

As in the yaw case, the differences in the flapwise bending moment at the root of the blades are attributed to the detailed description of the local flow conditions close to the rotor in the AL simulation. In the CFD framework, varying inflow conditions on the rotor

disk are properly resolved. On the contrary, in the reference BEMT module a simplified representation of the inflow conditions is considered. The dynamic response of the wake due to time varying conditions is accounted for through an engineering dynamic inflow model [49]. The inflow model is actually a first order filter equation, which imposes a time delay on rotor induction and therefore on rotor loads when the thrust changes in time. It is shown in Section 3.1.1.3.2, that as the flow conditions get more complex, the modelling of the local inflow in BEMT simulations becomes less accurate.

In order to better understand the origin of the differences in the flapwise bending moment predictions (Figure 3.43b), the measured height distribution of the axial velocity inside the ABL of the AL simulation is shown in Figure 3.45a. Axial velocity is averaged in time and measured at the rotor plane. The analytical profile corresponds to the averaged logarithmic profile of the ABL for axial velocity of V_{hub} = 16 m/s at the hub height (Z_{hub} = 119 m) and for surface roughness of z_0 = $0.1m$, that is developed without the presence of the WT. Greater axial velocity above the hub height, leads to near wake being convected downstream faster compared to lower regions. As opposed to BEMT, this is properly accounted for in the AL model and leads to lower induction on the upper part of the rotor. This explains the level difference in the flapwise bending moment predictions on the upper part of the rotor (approximately from 315° to 45° azimuth angle), shown in Figure 3.41b. Moreover, a significant acceleration of the local inflow is measured on the lower part of the rotor (below hub height). This is clearly depicted in the measured height distribution of the mean axial velocity when the WT is present (averaged profile), as shown in Figure 3.45a. Due to the blocking effect of the rotor on the flow and the downwash induced by the emitted wake, the measured distribution was anticipated to show reduced values compared to the analytical profile (mean profile when the rotor is not present) throughout the height of the WT. Even though this is true for heights greater than $70m$, significant acceleration is noted up to this height. This is attributed to the contraction of the flow between the lower part of the rotor and the ground, as illustrated in Figure 3.45b. This reasoning is confirmed by the axial velocity field shown in Figure 3.46. The increased axial component of inflow velocity on the lower part of the rotor results in greater angle of attack from 135° to 225° azimuth angle (see Figure 3.47) and explains the plateau formed in the AL predictions. On the other hand, due to the simplified modelling of the inflow, BEMT is not able to predict the acceleration on the lower part of the rotor and leads to reduction of the angle of attack in the corresponding azimuthal positions. This explains the level difference in the flapwise bending moment predicted by the two models (see Figure 3.41b) on the lower part of the rotor (approximately from 135° to 225° azimuth angle), but also the difference in the overall amplitude predictions. To sum up; i. lower induction on the upper part of the rotor and ii. acceleration of the local inflow on the lower part of the rotor in the AL simulations result in a level and amplitude difference of the AL and BEMT predicted angle of attack (see Figure 3.47). These differences are directly reflected in the flapwise bending moment shown in Figure 3.43b.

Shear wind speed profile
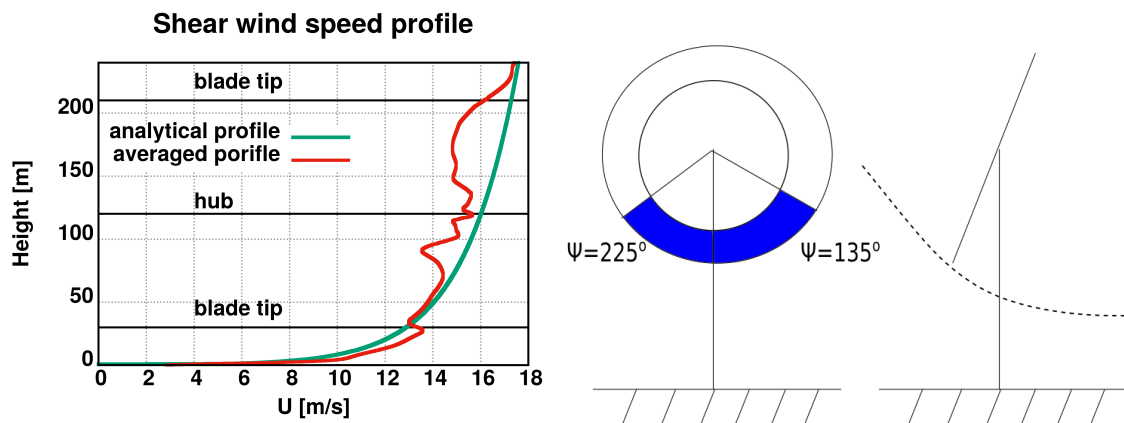
(a) *Height distribution of mean (averaged in time) axial velocity (red) in AL simulation, measured at rotor plane. Comparison against analytical (undisturbed) profile (green) that corresponds to a mean (averaged in time) profile when the WT is not present.*

(b) *Schematic representation of rotor and ground. Visualization of their effect on accelerating the local inflow on the lower part of the rotor.*

Figure 3.45. *Height distribution of the mean axial velocity measured at the rotor plane (a) and schematic representation of the WT and the ground forming an aerodynamic nozzle (b). Due to the WT rotor blocking the flow, the measured axial velocity (red line) is expected show lower values compared to the analytical profile (green line) that corresponds to an undisturbed distribution when the WT is not present. This is true for heights greater than $\simeq 70m$ and up to the higher tip of the rotor plane. The acceleration observed at the lower part of the rotor $\simeq 0 - 70m$ is attributed to the nozzle formed between the ground and the lower part of the rotor.*
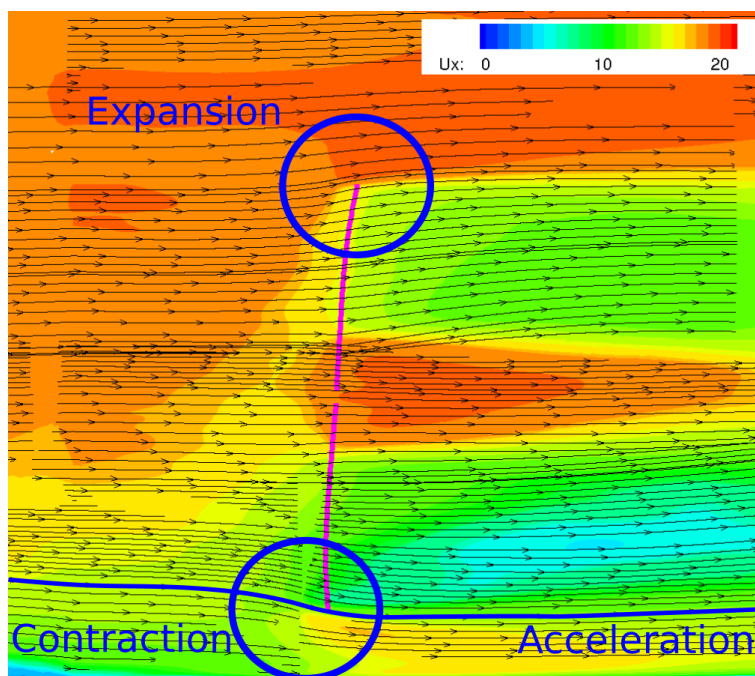
Figure 3.46. *Mean axial velocity field close to the rotor for a full WT operating inside the ABL. The axial velocity is 16 m/s at hub height. The effect of the rotor and the ground on the flow is accounted for in detail thanks to the CFD framework. Expansions of the flow is shown at the upper part of the rotor. Contraction of the flow is observed between the lower part of the rotor and the ground that accelerates the local flow.*

Angle of attack at 75%R
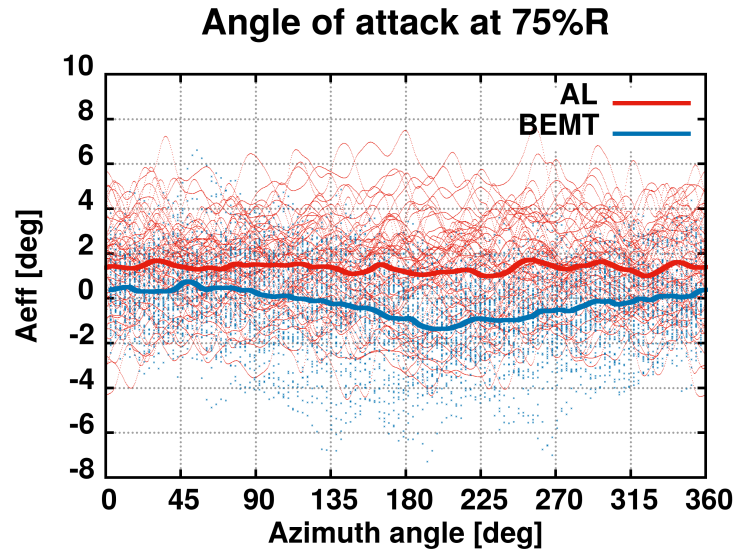
Figure 3.47. *Azimuthal variation of the averaged effective angle of attack measured at 75% radial station of the 1st blade. Full WT case operating inside the ABL. The axial velocity is 16 m/s at hub height. BEMT underestimates the mean value by $\simeq 2°$ and overestimates the 1P amplitude. Minimum values are predicted between 135° and 225° azimuthal angle in BEMT results. AL predictions show a flat variation throughout the azimuthal circle. This is attributed to the acceleration of the local inflow at the lower part of the rotor that leads to mitigation of the expected reduction between 135° and 225°.*

The greater mean value of the rotor blades loads predicted by the AL model (see Figure 3.43) lead to increased loading of the tower, both in terms of mean value and amplitude. This is clearly depicted in Figure 3.48 where the for–aft bending moment at the bottom of the tower is shown as time–series (Figure 3.48a) and azimuthal variation in the time averaged signal (Figure 3.48b). BEMT predicts lower mean value ($\simeq -22\%$) and 3P amplitude ($\simeq -46\%$) compared to AL results. However, an overall good agreement is observed in the phase due to the corresponding phase agreement in the flapwise bending moment at the root of the rotor blades. The difference in 3P amplitude of the for–aft bending moment at the root of the tower is also depicted in Figure 3.49a as a difference in the peak value of the spectrum at 0.48Hz which is 3 times the rotational frequency of the rotor blades. This explains the large differences in the equivalent loads predicted by the two models that are computed by the RFC method (Figure 3.49b). It is noted that the nacelle is omitted in the computational set–up. This leads to a significant mass reduction at the top of the tower, that increases the natural frequency of the for–aft mode from $\simeq 0.31Hz$ to $\simeq 0.77Hz$.

(a) *Time-history of for-aft bending moment.*

(b) *Azimuthal variation of time averaged for-aft bending moment.*
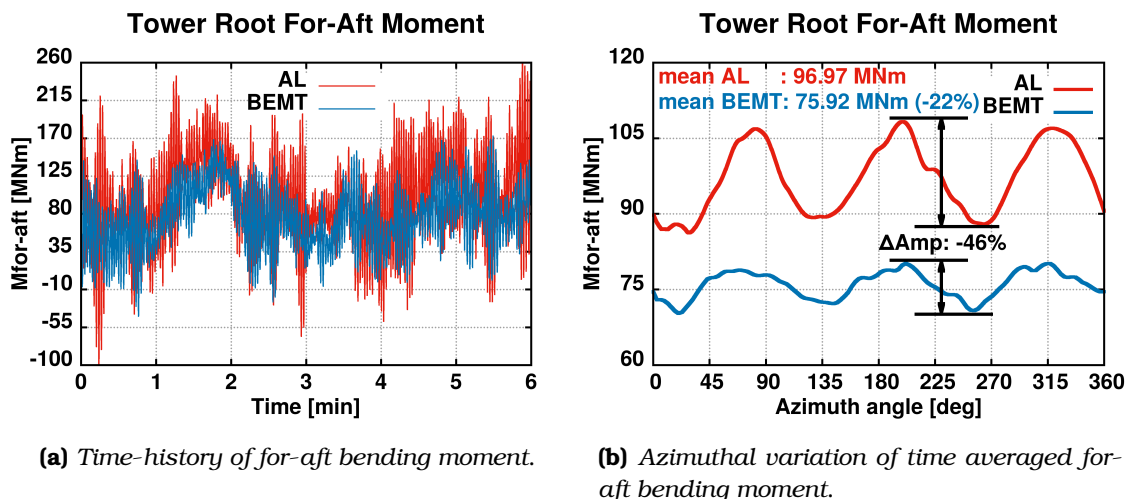
Figure 3.48. *For-aft bending moment measured at the root of the tower expressed as time-history (a) and azimuthal variation of the time averaged signal (b) for a full WT operating inside the ABL. The axial velocity is 16 m/s at hub height. BEMT underestimates the mean value by approximately 22% and the 3P amplitude by approximately 46%. Those differences are attributed to the mean value difference in the flapwise bending moment measured at the root of the blades, shown in Figure 3.43b.*

(a) *FFT of for-aft bending moment.*

(b) *RFC of for-aft bending moment.*
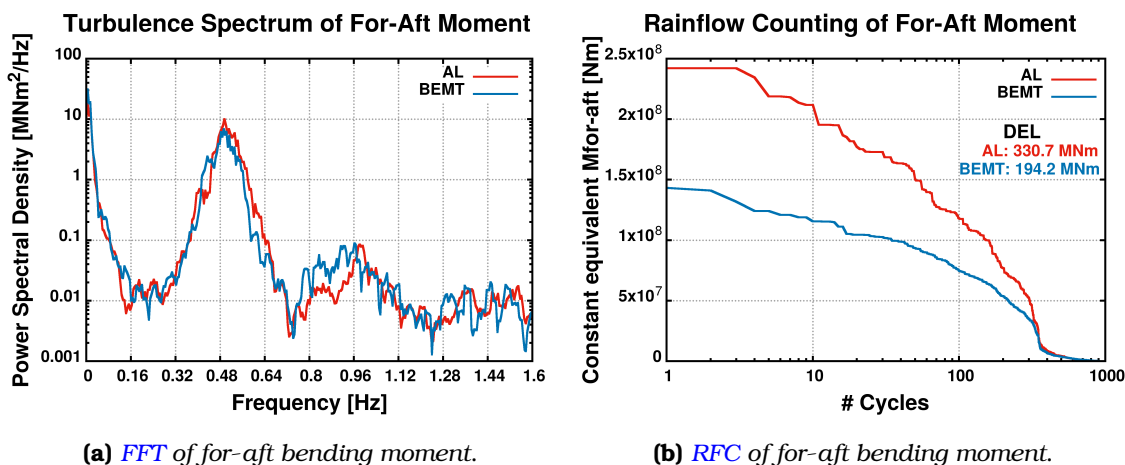
Figure 3.49. *FFT (a) and RFC (b) of for-aft bending moment measured at the root of the tower for a full WT operating inside the ABL. The axial velocity is 16 m/s at hub height. A greater peak is predicted in AL simulations at 0.48Hz, which is 3 times the rotational frequency of the blades. This originates in the increased mean value of the blade loads predicted by AL (Figure 3.43b). In turn, greater equivalent loads are computed by AL for all number of cycles.*

3.3 Conclusions

In this chapter, the accuracy of an AL model is assessed in aeroelastic simulations of WT and helicopter rotors. In WT cases, both constant wind speed and turbulent flow simulations are conducted. Comparisons are presented against a standard BEMT model and a classical LL approach, which are considered as state of the art in WT and helicopters design respectively. All the different aerodynamic modules are coupled with the same structural solver, GAST. In helicopter cases, AL results are compared against experimental data and LL predictions.

First, a detailed investigation of the numerical parameters of the AL model is performed. For WT simulations, it is found that a number of 90 cells in the rotor radius provides a grid independent solution, whilst a three times coarser discretization is suggested for the actuator lines. For the helicopter simulations, a number of 8 cells in the blade chord is sufficient. Time step is defined based on the grid resolution and tip velocity. A grid resolution 10 times the one used in the vicinity of the actuator lines is found to be sufficient for the near wake region, in order for an accurate estimation of the wake induction on the rotor to be accomplished. Various grids set–up are tested, showing minor effect on the computed blade loads, but having great differences in the resulting computational cost. A hexahedral grid set–up with hanging nodes is preferred, as it is found yielding accurate results under minimum number of grid cells. Finally, a new rule of thumb is proposed for computing the Gaussian kernel that leads to a grid independent and accurate solution under moderate grid resolution. Hence, the Gaussian kernel is chosen to vary with the chord length, but a lower bound of twice the grid spacing is also set in order to avoid too small kernel values at the blade tip.

In the WT cases under constant wind speed, comparisons among the AL module, a standard BEMT model, and a LL approach are presented. At simple axial cases, good agreement is achieved by all three models in terms of loads and deflections predictions. Deviations between BEMT and the other two models occur at yawed flow cases, due to simplified modelling of the inflow conditions in BEMT that does not properly take into account the positioning and evolution of the emitted wake vortices with respect to the rotor plane. These differences become more pronounced as the flow conditions get more complex (e.g. as yaw angle increases). However, excellent agreement between AL and LL is observed in all the examined cases, due to the detailed representation of the flow–field thanks to the CFD and Free Vortex Wake frameworks respectively. In contrast to LL, AL predicted wake–induced velocities tend to zero near the blade tip. The same difference between these two models is observed in the circulation close to the blade root.

For the Helicopter MR simulations, AL predictions are validated against LL simulation results and wind tunnel measurements of the HeliNoVi experiment. In general, predictions are close to the experimental measurements and when differences occur the two models results seem to agree well with each other. Nevertheless, at low speed cases, in which wake–induced effects are stronger, the AL model achieves a better phase agreement with experimental data but also increased aerodynamic damping due to increased numerical diffusion.

In turbulent flow cases, a novel approach is assessed in order to impose the velocity fluctuations of a predefined turbulent field onto an averaged flow–field, within an Eulerian CFD context. The approach is based on source terms imposed upstream to a region of interest that drive the solution of the nearby flow–field to the desired one. This newly proposed methodology provides better representation of the intended spectral characteristics on the region of interest compared to other conventional approaches. This originates in spreading the source terms in a large zone and regulating their intensity through proper space functions within that zone. Hence, a very accurate representation of the intended flow–field is achieved in the region where the source terms have their maximum values. Moreover, reduced numerical diffusion is accomplished when the turbulent field gets convected downwards. A zone length of at least 5 grid cells is required so that the spectral characteristics of the produced turbulent field are close to the desired ones. Moreover, a uniform grid resolution of 90 cells in the rotor radius for all the near wake region is found to be sufficient for an accurate estimation of the mutual interaction between the rotor and the ambient turbulence.

In WT simulations under turbulent inflow, comparisons between the AL module and a standard BEMT model are made in terms of loading on the various WT components, in particular rotor blades and tower. As in the constant wind speed cases, good agreement is achieved at simple axial cases, whereas differences occur at more complex flow cases. The detailed description of the flow–field within the CFD framework, provides the AL model with the ability to accurately account for the varying wake induction on the rotor plane and the effect of the rotor and the ground on the local turbulent inflow. These are not properly regarded in simple BEMT approaches yielding in significant differences concerning the predictions in loading and wear, of the various WT components.

Overall, AL results show significant differences compared to BEMT predictions that get more intense as the flow conditions get more complex. Most of them originate in the detailed description of the flow–field close to the rotor provided by the CFD framework. On the other hand, AL results share the same level of accuracy with the ones produced by the LL method, when it comes to blade loads and deflections in isolated rotor cases. Although much more affordable than resolving the whole blades geometry, AL simulations remain at least 2 orders of magnitude more computationally demanding than LL. The main advantage of the AL method, is that the effect of the rotor and ground on the local turbulent inflow are accounted for in detail within the CFD context under moderate computational requirements. This is not easily resolved in a potential FVW framework, where the consideration of viscous effects close to the ground and the modelling of turbulence can be tricky.

Chapter 4

# Fully resolved rotor blades using HoPFlow

In this chapter, the results produced by an aerodynamic simulation of a model Wind Turbine (WT) rotor and an aeroelastic simulation of a model helicopter Main Rotor (MR) under smooth free–stream flow cases are presented and compared against measurements and other CFD based predictions. The actual geometry of the rotor blades is now fully resolved in a hybrid Lagrangian–Eulerian context, using HoPFlow. The value of the present method lies in multi–body and aeroelastic applications in which there are multiple, mutually interacting regions of interest within the computational space [170]. The Lagrangian sub–domain serves as the background coupling domain between the moving Eulerian sub–domains in the same way that overset grids function in standard Eulerian CFD simulations. Lagrangian methods are advantageous compared to overset approaches, as they minimize numerical diffusion and therefore preserve wake structures and flow disturbances. HoPFlow and coupled GAST–HoPFlow results are compared against experimental measurements and computational predictions by other CFD solvers.

4.1 Aerodynamic analysis of a WT rotor

In this section, aerodynamic simulations are performed for the New MEXICO WT model rotor. The goal is firstly to investigate the effect of multiple numerical parameters (e.g. blade surface grid, time–step value, PM discretisation length) on the predicted aerodynamic loads when the hybrid Eulerian–Lagrangian CFD solver HoPFlow is employed in the aerodynamic analysis. A thorough comparison of blade loads is then performed against experimental measurements and computational results from the Eulerian counterpart (MaPFlow) of the hybrid solver and other CFD solvers predictions. Blade loads are depicted as span–wise distribution of aerodynamic loads and pressure distribution at specific span–wise positions. The axial velocity distribution (parallel to the direction of the wind), predicted at constant span–wise positions, representing the wake deficit formation, will be compared as well. The test case is the run no. 266, which is a 14.7 m/s axial flow case at 425 rpm of the New MEXICO experimental campaign [11, 12] that corresponds to a tip speed ratio of $\lambda = 6.81$ and a pitch angle of 2.3° nose down.

4.1.1 The New MEXICO experimental campaign

The New Mexico experiment was partially funded by the INNWIND.EU project [153] and was a follow–up to the MEXICO experiment [171]. The New MEXICO WT model rotor is a 4.5 m diameter 3–bladed rotor (see Figure 4.1). It consists of three different airfoil shapes at the root (DU91-W2-250), mid-span (RISØ A1-21) and tip (NACA 64418) region of the blade according to Table 4.1. The twist and chord distribution of the blade are shown in Table 4.2. Turbulent transition is triggered with trip tapes of 5 mm width and 0.2 mm thickness placed at 10% of the chord on both the pressure and suction sides of the blade. Results from numerical investigations concerning test cases from the MEXICO and the New MEXICO experimental campaigns can be found in [172, 173, 174, 175, 176, 177, 178].
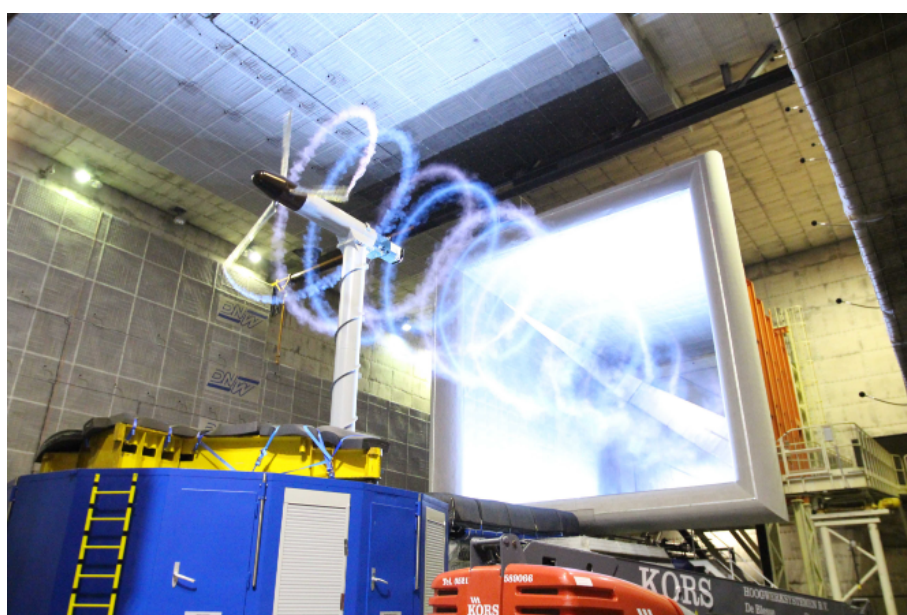
Figure 4.1. *Set-up of the New MEXICO experimental campaign. Tip vortices visualization with smoke. Image copied from [11].*

Table 4.1. *New MEXICO WT model rotor blade airfoils.*

Radius [m]	r/R	Airfoil
0.45–1.025	20–45%	DU91-W2-250
1.225–1.475	55–65%	RISØ A1-21
1.675–2.25	75–100%	NACA 64418

Table 4.2. *New MEXICO WT model rotor blade radial distribution of twist and chord.*

Radius [m]	Twist [°]	Chord [mm]
0.21	0	195
0.23	0	195
0.235	0	90
0.300	0	90
0.375	8.2	165
0.450	16.4	240
0.675	12.1	207
0.900	8.3	178
1.025	7.1	166
1.125	6.1	158
1.225	5.5	150
1.350	4.8	142
1.475	4.0	134
1.575	3.7	129
1.675	3.2	123
1.800	2.6	116
2.025	1.5	102
2.165	0.7	92
2.193	0.469	82
2.232	0.231	56
2.250	0.0	11

4.1.2 Numerical investigation

In this section, a detailed calibration of the most significant numerical parameters involved in the computational set–up of the hybrid model is performed; namely, the blades' surface grid, the time–step value and the PM discretization length.

Blade Surface Grid Dependency Analysis

First, the blades surface grid is investigated in the Eulerian solver framework. The domain is a cylinder of a 20 rotor diameters (20D) length (5D upstream and 15D downstream) and a 10D radius (see Figure 4.2). In order to take into account the near–wake effect on the aerodynamic loads, the region close to the rotor blades is kept fine. This (blue rectangle in Figure 4.2) is a cylindrical region that extends up to 1D upstream, 3D downstream, and 1D radially from the rotor hub center, so that the wake expansion fits in. These simulations consider that the whole grid is rotating about the rotor hub center.
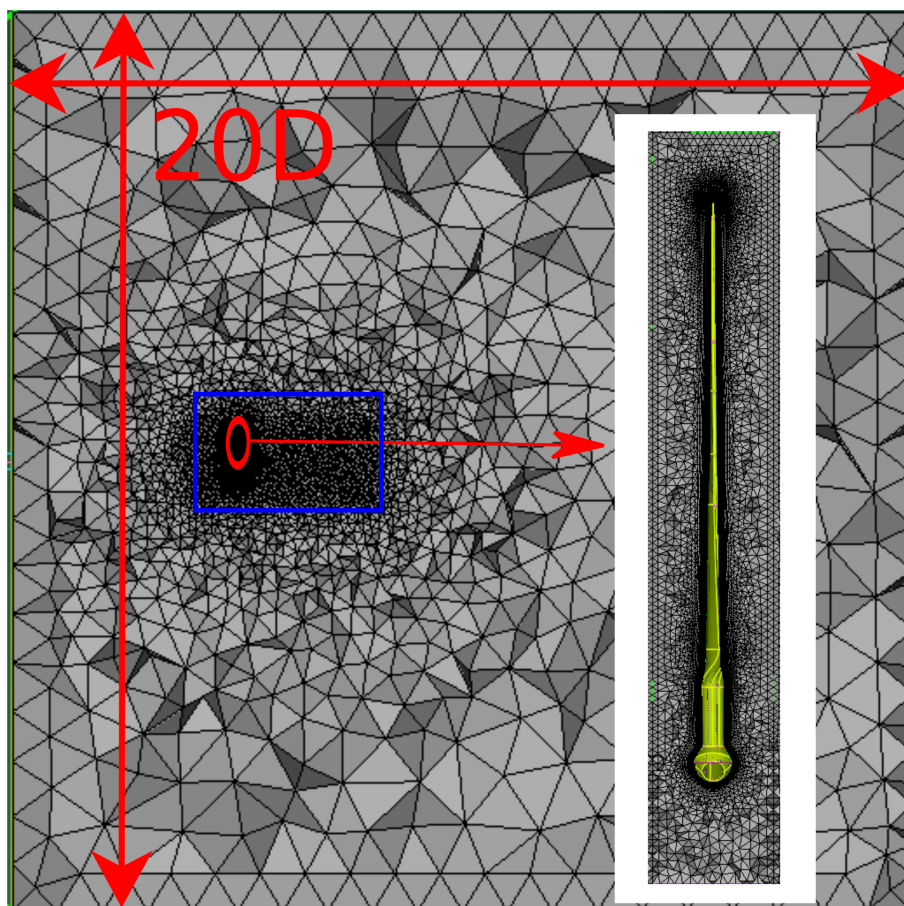
Figure 4.2. *Lateral view of the computational domain (cylinder) used by the Eulerian solver (MaPFlow) for the axial test case no. 266 of the New MEXICO experimental campaign. A fine region is considered around the rotor (blue box), so that the effect of near wake fits is. This region is chosen to reach up to 1D upstream, 3D downstream and 0.75D radially from the rotor center, in order to also account for wake expansion. The outer region of the grid extends up to 5D upstream, 15D downstream and 10D radially.*

Results from three different blade grids are reported, employing 5280, 20350 and 56260 surface cells for the blade discretization. In the coarse grid, 66 cells describe the airfoil shape and 80 cells cover the span–wise direction. Similarly, in the medium and fine surface grids, 110×185 and 194×290 surface elements are employed respectively. The corresponding total amount of grid cells are $1.4 \cdot 10^6$, $4.8 \cdot 10^6$ and $11 \cdot 10^6$ cells, respectively. The integrated rotor loads produced by the three grids are presented in Table 4.3. The coarse blade discretization underestimates the thrust value by $\simeq 3.8\%$ and the torque by $\simeq 13.9\%$ with respect to the finest grid, whereas the corresponding differences for the medium blade discretization are 2.3% and 3.9%, respectively. Based on the above, the medium surface blade discretization (110×185 blade surface cells and $4.8 \cdot 10^6$ total amount of cells) provides a reasonable compromise between accuracy and computational cost. For this reason, the specific set-up is used in the following simulations. It also needs to be stressed, that due to the early presence of trip–tapes in the experimental set–up, at 10% of the chord on both the pressure and suction sides of the blade, fully turbulent simulations are conducted.

Table 4.3. *New MEXICO WT model rotor thrust and torque estimation by the Eulerian solver (MaPFlow) with respect to different blade surface grids. The test case is the run no. 266 of the experimental campaign. Reference values correspond to finest grid results. The medium blade discretization* 110×185 *is preferred to the rest, as it provides a good compromise between accuracy (concerning integrated rotor loads estimation) and computational cost.*

chord $\times$ span (overall)	Thrust	Torque
$66 \times 80 \left(1.4 \cdot 10^6 \ cells\right)$	-3.8%	-13.9%
$110 \times 185 \left(4.8 \cdot 10^6 \ cells\right)$	-2.3%	-3.9%
$194 \times 290 \left(11 \cdot 10^6 \ cells\right)$	1875.2 [N]	317.55 [Nm]

Time-step Dependency Analysis

In order to investigate how the selected time–step affects the aerodynamic loads, a number of different time–step values (dt) have been tested. As one may see in Table 4.4, the time–step values have been defined with reference to the rotor rotation period (T) (certain number of time steps per revolution). All the listed time–step values provide acceptable results as the greatest differences shown are an $\simeq 2\%$ under–estimation of the thrust value at $dt = T/360$ and an $\simeq 1.8\%$ over–estimation of the torque at $dt = T/720$. However, the final choice of the time–step value for the hybrid solver simulations is also dependent on the grid discretization because of the CFL condition, as will be pointed out in the next paragraphs.

Table 4.4. *New MEXICO WT model rotor thrust and torque estimation by the Eulerian solver (MaPFlow) with respect to different time-step values. The test case is the run no. 266 of the experimental campaign. Reference values correspond to finest time-step value results. All the different time-step values produce similar results. $dt = T/360$ and $dt = T/720$ (T is the rotor revolution period) show the greatest discrepancies concerning thrust and torque estimation respectively.*

	Thrust	Torque
$dt = T/360$	-2.0%	$+0.3\%$
$dt = T/720$	-0.1%	$+1.8\%$
$dt = T/1440$	-0.9%	$+1.1\%$
$dt = T/2880$	-0.2%	$+1.4\%$
$dt = T/5760$	1846.6 [N]	301.79 [Nm]

HoPFlow Grid set-up

In the hybrid solver simulations, the Eulerian sub–domain is restricted to a narrow region around the rotor blades. In particular, it consists of cylinders that surround the rotor blades and extend at least up to one local chord away from the largest section of the blade, as is recommended in [148] and illustrated in Figure 4.3. The greatest chord length of the specific blade is approximately 240 mm at 20% of its radius. The Eulerian grid consists of hexahedral cells (structured-type) close to the blade surface in order to better represent the boundary layer properties, whilst it is unstructured at the rest of the domain. Another numerical parameter that needs to be considered is that the largest dimension of the Eulerian cells should not exceed the PM discretization length. Otherwise,

the number of Eulerian particles (particles generated within the Eulerian grid) may not be sufficient to ensure dense population within the PM grid. Typically, this restriction concerns the surface discretization of the Eulerian sub–domain far–field (S_E); however, care needs to be taken of the span–wise discretization of the blade as well. This justifies the great number of cells used in the span–wise direction of the blade surface grids that were tested before. The Eulerian sub–domain that is used in the hybrid solver simulations consists of 4.1 millon computational cells.

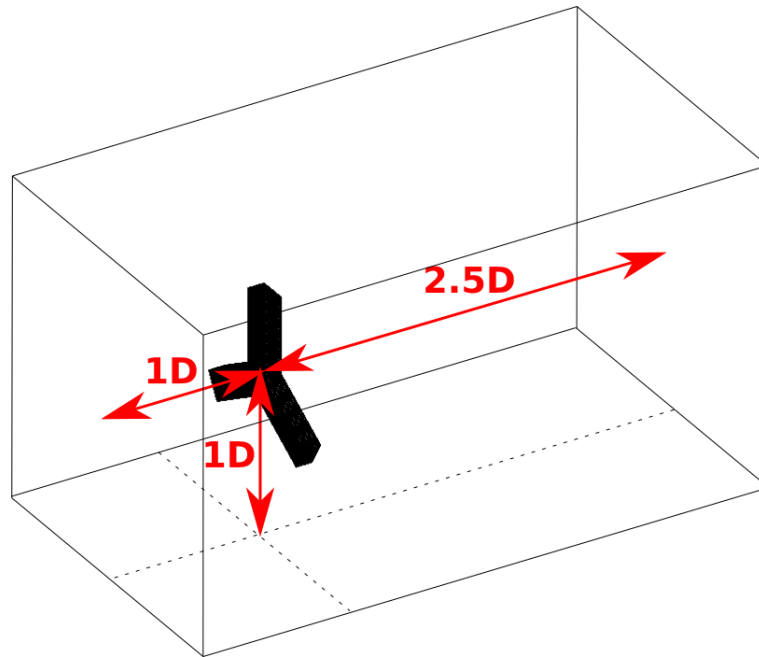The Lagrangian sub–domain is defined as a box that covers the entire computational domain, extending from $1D$ upstream up to $2.5D$ downstream and $1D$ radially about the rotor hub center. In Figure 4.4, the placement and the extent of the two sub–domains is depicted. As stated in Section 2.2.2, the Lagrangian sub–domain is discretised with the use of the PM technique and by employing uniform Cartesian grids. The different values of the PM discretisation length ($DXpm$) were chosen to vary proportionally to the local chord length at 75% of the blade radius, which is approximately 120 mm and, from now on, will be denoted by c.
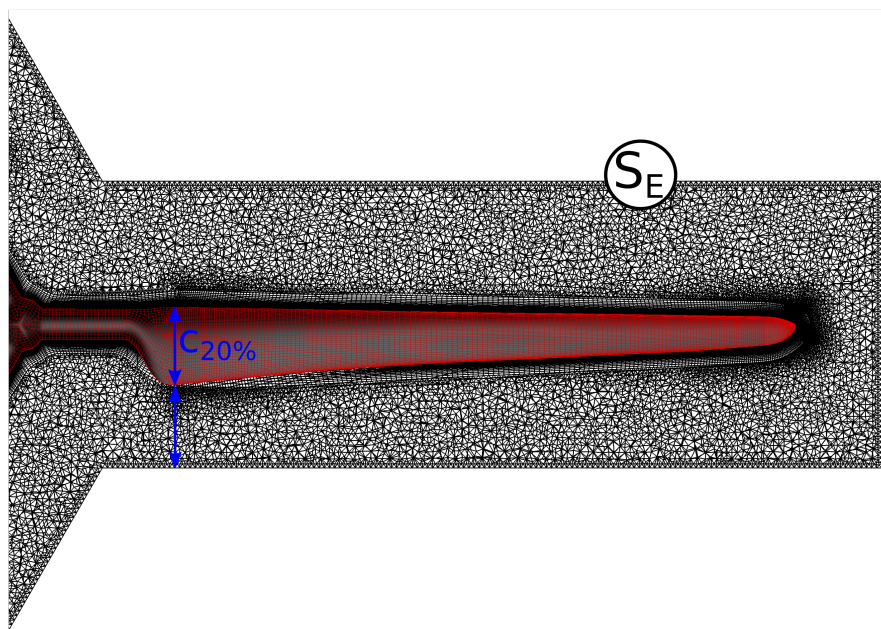
Figure 4.3. *The Eulerian sub-domain defined in the hybrid solver (HoPFlow) simulations consists of cylindrical sections around the rotor blades and totals $4. \cdot 10^6 1$ computational cells. The cylindrical sections extend at least 1 local chord away from the largest section of the blade (at $\simeq 20\%R$). The region close to blade surface is of structured type (hexahedral cells) in order to accurately resolve the boundary layer. The characteristic length of the largest Eulerian cells (typically located at the far-field S_E of the Eulerian sub-domain) does not exceed the PM discretization length.*

Figure 4.4. *Visualization of the Lagrangian and the Eulerian sub-domains in the hybrid solver simulations. Details for the Eulerian sub-domain can be found in Figure 4.3. The Lagrangian sub-domain is a box that extends* 1D *upstream,* 2.5D *downstream and* 1D *radially from the rotor hub center.*

It also needs to be stressed, that not the actual hub geometry, as illustrated in Figure 4.5, has been modelled. The root of the blade is modeled as a cylindrical section while the geometry of the spinner is not included in the simulations.
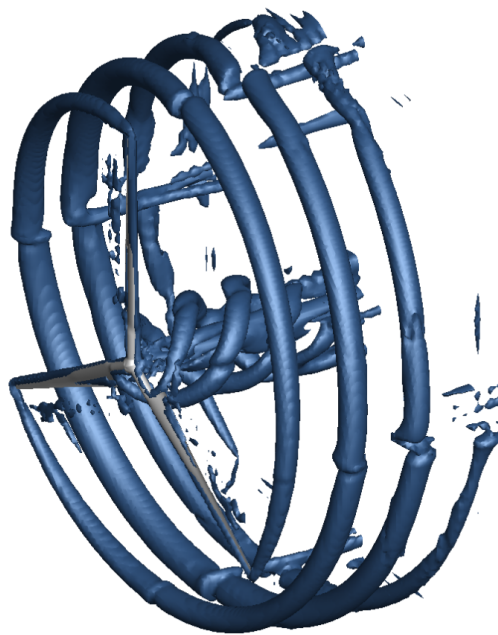
Figure 4.5. *Hybrid solver wake visualization with* Q *criterion. Tower and nacelle are omitted in the computational set-up. This allows for root vortices to be emitted in the simulations.*

PM Grid Dependency

In Table 4.5, the integrated rotor loads predicted for the different values of *DXpm* are listed. Five different values of *DXpm* have been tested, *DXpm* = 1*c*, *DXpm* = 0.5*c*, *DXpm* = 0.35*c*, *DXpm* = 0.25*c* and *DXpm* = 0.20*c*, which correspond to 2, 3 , ≃ 4, 5 and 6 PM nodes per chord, respectively. It needs to be stressed that the time–step values employed in these simulations correspond to more than 360 steps per rotor revolution, complying with the results of the previous time–step dependency analysis. Nevertheless, for the hybrid solver simulations, there is one extra restriction. Since the time–marching scheme is explicit, the time–step values need to respect the CFL condition. Consequently, *dt* = *T*/540, *dt* = *T*/900, *dt* = *T*/1440, *dt* = *T*/1800 and *dt* = *T*/2160 have been utilized for the *DXpm* = 1*c*, *DXpm* = 0.5*c*, *DXpm* = 0.35*c*, *DXpm* = 0.25*c* and *DXpm* = 0.20*c* simulations, respectively.

In Figure 4.6, it is shown that the differences in the predicted rotor loads decrease as *DXpm* gets smaller, with values less than *DXpm* = 0.35*c* (at least 4 points per chord length) providing a good compromise between accuracy and computational cost. Apart from the integrated rotor loads, the detailed description of the radial distribution of the aerodynamic loads is also of great importance. Table 4.6 shows the normalized forces and moments at 60% of the span, predicted by the different values of *DXpm*. The loads of the specific radial position experience the highest sensitivity with respect to the numerical parameters (this will be also shown in the next paragraphs). For this reason, the rest of the available span–wise positions are omitted in this table. It needs to be stressed, that the tangential normalized loads (F_T/dr) and the resulting rotor Torque, are very sensitive to changes of the numerical parameters. This is attributed to their overall small values and to the fact that they are driven by the drag forces of the blade. As a result, in order to obtain a grid independent solution for the blade radial distribution of aerodynamic loads, at least 5 PM nodes per chord length (*DXpm* ≤ 0.25*c*) need to be used. However, it also needs to be highlighted (see Table 4.5) that as *DXpm* gets smaller, the total number of PM nodes increases dramatically, thus, substantially penalizing computational cost. Based on all the above remarks, *DXpm* = 0.25*c* seems to provide the best compromise between accuracy and computational cost.

Table 4.5. *PM grid dependency analysis for New MEXICO WT model rotor simulations with the hybrid CFD solver (HoPFlow). Rotor thrust and torque estimation for different PM discretisation lengths DX_{pm}. Tabulated data of Figure 4.6. Reference values correspond to minimum value DXpm = 0.20c (c is the local chord length at 75%R) results. Time–step values have been set so that the CFL condition gets respected (T is the rotor revolution period). PM discretization with DXpm ≤ 0.35c (≥ 4 PM points per c) provides a grid independent solution concerning integrated rotor loads.*

DXpm	dt	PM Nodes	PM Nodes per c	Thrust	Torque
1*c*	*T*/540	$1.1 \cdot 10^6$	2	+17.7%	+53.8%
0.50*c*	*T*/900	$7.3 \cdot 10^6$	3	+4.1%	−1.3%
0.35*c*	*T*/1440	$23.3 \cdot 10^6$	4	+0.5%	+0.7%
0.25*c*	*T*/1800	$52.2 \cdot 10^6$	5	+0.03%	+0.25%
0.20*c*	*T*/2160	$123.2 \cdot 10^6$	6	1796.3 [N]	293.6 [Nm]
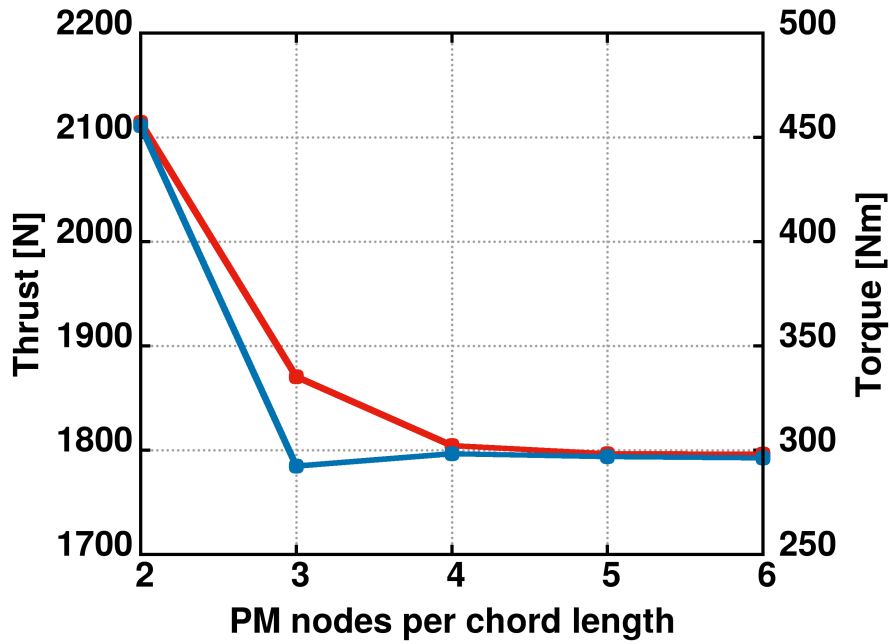
Figure 4.6. *Rotor thrust and torque estimation with respect to the number of PM nodes per characteristic chord length (chord length at 75%R). ≥ 4 PM points per chord length provide a grid independent solution concerning integrated rotor loads. Values printed in this Figure are listed in Table 4.5.*

Table 4.6. *Normalized aerodynamic loads estimation at 60%R with respect to different PM discretisation lengths. Reference values correspond to minimum value DXpm = 0.20c. Loads at other radial positions are neglected, because the loads of the specific position are the most sensitive to the numerical parameters. DXpm ≤ 0.25c is required in order to accurately acquire the radial distribution of the aerodynamic loads.*

DXpm	F_N/dr (60%R)	F_T/dr (60%R)	M_{tw}/dr (60%R)
$1c$	+16.06%	+50.42%	+18.44%
$0.50c$	+4.15%	−4.57%	+8.29%
$0.35c$	+0.98%	+5.81%	+1.03%
$0.25c$	+0.42%	+1.24%	−1.27%
$0.20c$	356.8 [N/m]	35.44 [N/m]	4.876 [Nm/m]

4.1.3 Comparison against measurements and other CFD predictions

In this paragraph, the simulation results by the Eulerian solver, MaPFlow, and the hybrid solver, HoPFlow ($DXpm$ = 0.25c), are compared against available experimental data and computational predictions by other CFD solvers of similar accuracy, such as the incompressible solver EllipSys3D [179, 180] and the compressible solver Wind Multi–Block of CENER [181].

In Figure 4.7, the gauge pressure ($p_\infty - p$) distributions predicted by different CFD solvers at various radial positions are compared against experimental measurements. Very good agreement is observed between computational predictions and experimental measurements at the radial stations close to the root (25%R and 35%R). A minor level shift towards lower pressure is predicted by MaPFlow and HoPFlow on the suction side that is attributed to the fact that the spinner geometry is not included in the NTUA computations (see Figure 4.5). This allows for root vortices to be produced while the local acceleration induced by the nacelle is neglected. Both predict reduced local angle of attack (geometric angle of attack $\simeq$ 14° at 25%R and $\simeq$ 13° at 35%R) away from the stall region, thus, reducing the pressure level at the suction side. Very good agreement is also observed close to the tip (82%R and 92%R). The predicted and measured distributions of both the pressure and suction sides are very close to each other. A minor difference in the suction side pressure predictions by EllipSys3D at 92%R is attributed to the incompressible flow equations solved along with the high local Mach number ($M_{92\%R}$ = 0.27). Significant discrepancies with respect to measured data are observed at the mid–span of the blade (60%R). The pressure side predictions match very well with each other and with the experimental values. On the other hand, the suction side pressure close to the leading edge is underestimated by all computational models, which however agree very well with each other. This difference is connected to the abrupt change of the airfoil profile in the mid–span region (see Table 4.1) and to the fact that the RISØ A1-21 airfoil used thereby has a much different zero lift angle compared to the preceding DU91-W2-250 (root) and the following NACA 64418 (tip). In [11], this is reported to be the main reason for the systematic over–prediction of the measured suction side pressure compared to computational predictions. The causes were not clarified during the New MEXICO project and, for this reason, the quasi–2D polars of the stationary blade are compared to the 3D sectional characteristics of the rotating blade in Figure 4.8. A significant lift offset of $\Delta C_L \simeq$ 0.33 is reported at the geometric angle of attack in which the airfoil operates in the examined test case, that justifies the reported difference between predictions and measurements at 60%R. Whether this offset originates from the three-dimensional set–up, a misalignment in the geometric angle of attack or the Reynolds number difference was not clarified during the project and still remains a subject of further investigation.
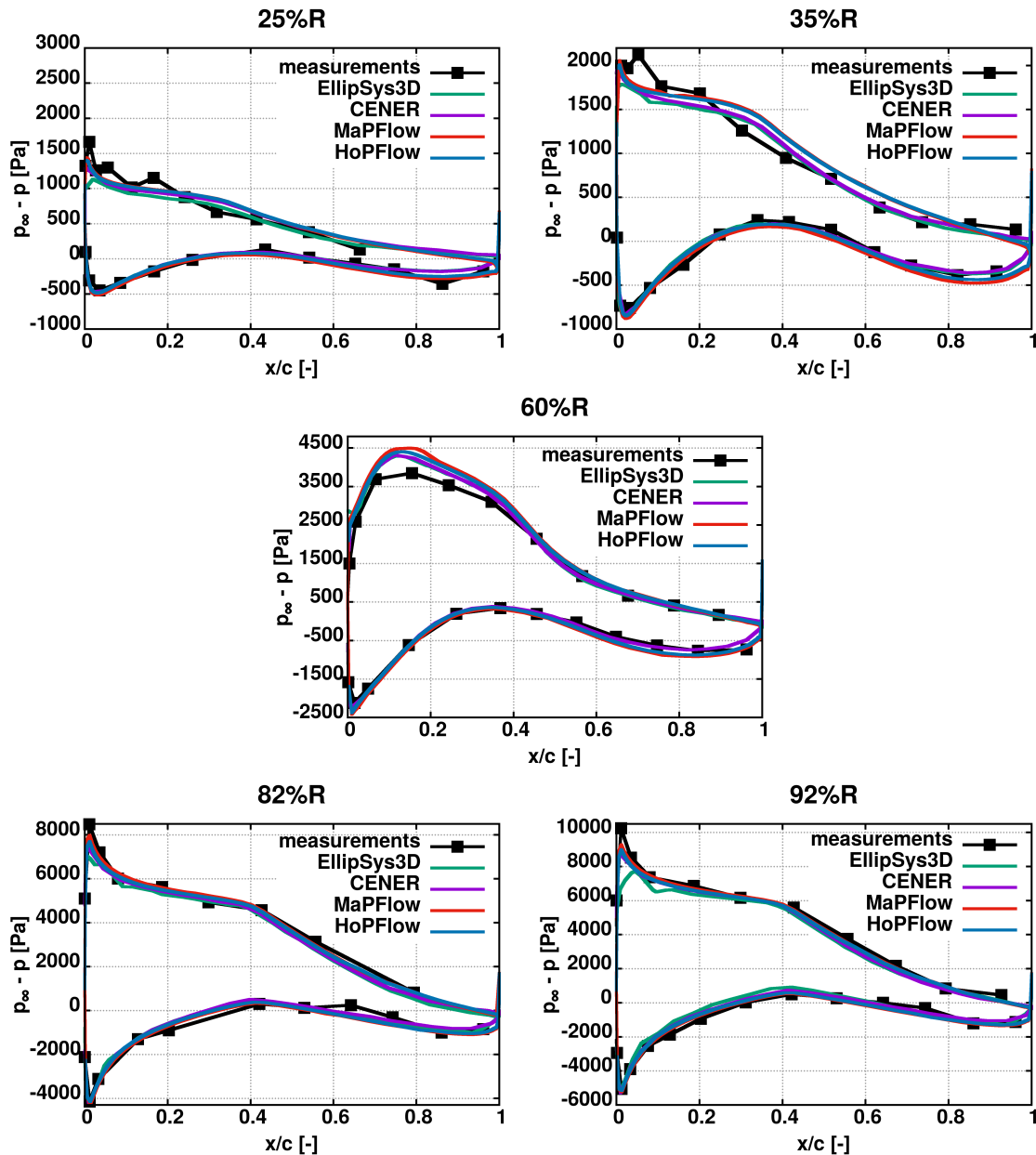
Figure 4.7. *Pressure distribution at different radial positions. Comparison among computational predictions by different CFD solvers (EllipSys3D – incompressible solver, CENER – compressible solver, MaPFlow – compressible solver, HoPFlow – compressible hybrid Lagrangian–Eulerian solver) and experimental measurements. Very good agreement is observed between computational predictions and measurements at the root (25%R, 35%R) and the tip region (82%R, 92%R). The different suction side pressure prediction close to the leading edge by the incompressible solver EllipSys3D at 92%R is attributed to the increased local Mach number ($M_{92\%R} = 0.27$). The most notable discrepancies are observed at 60%R, where the suction side pressure close to the leading edge is slightly underestimated by all computational predictions, which however agree very well with each other.*

(a) *Sectional lift at 60%R.*

(b) *Sectional drag at 60%R.*
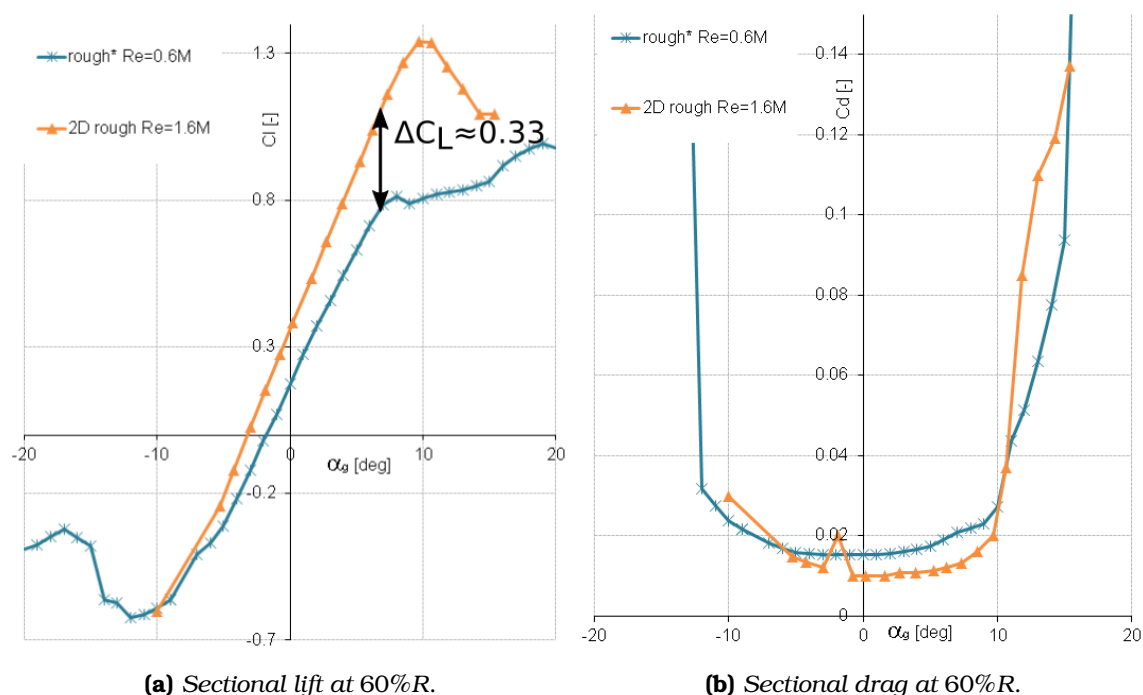
Figure 4.8. *Comparison between quasi-2D (stationary blade) and 3D (rotating blade) sectional characteristics of the RISØ A1-21 airfoil, measured during the New MEXICO experimental campaign. A significant offset between the quasi-2D and the 3D lift curves is reported. The slope of the 3D lift curve is smaller. These differences cannot be fully justified by the different Reynolds numbers and the 3D effects. Images copied from [11].*

In Table 4.7 and Figure 4.9, the normal and tangential forces distribution along the blade span are depicted where an overall good comparison is shown. It needs to be stressed that, as in the CFD predictions, the experimental values for the aerodynamic forces result from integrating the measured pressure distributions shown in Figure 4.7. However, due to the low number of installed pressure taps in the experimental set–up and the approximation of a linear variation of pressure between two consecutive taps, a level of uncertainty is to be expected concerning the measured forces. The maximum discrepancies with respect to the experimental values are observed about the mid–span of the blade (60%). An $\simeq 22\%$ and $\simeq 18\%$ higher normal force is predicted by the Eulerian and the hybrid solver respectively compared to the measured value. The corresponding differences in the tangential force are $\simeq 28\%$ and $\simeq 21\%$. Both are attributed to the over–prediction of the measured suction side pressure (see Figure 4.7). Even though the percentage differences concerning normal forces at the root of the blade (25% and 35%) are slightly bigger, they are not considered that important. The high percentage difference originates in the small values of the forces, whereas the absolute error in the loads estimation is quite smaller. This statement is confirmed by the very good agreement shown in the corresponding pressure distributions in Figure 4.7. Very good agreement is also achieved at the tip region (82% and 92%), where the hybrid solver results are slightly closer to the measured values compared to those of its Eulerian counterpart. This is the region where the effect of the tip vortices is significant in the computations of the aerody-

namic forces. Hence, the differences in the predicted loads are attributed to the increased numerical diffusion of the Eulerian methodology resulting from the gradual coarsening of the computational grid towards the far–field. Consequently, the wake is dissipated when convected downstream, and its upstream induced effect (downwash) is not properly resolved, yielding in over–estimation of aerodynamic loads. On the other hand, the Lagrangian formulation of the Navier–Stokes equations reduces numerical diffusion in the off–body region. Consequently, the emitted tip vortices are effectively preserved and the near–wake deficit is formed in greater detail, yielding in a more physical representation of the downwind flow–field with increased axial induction and, thus, reduced loads compared to the Eulerian solver predictions.

The latter statement is also verified in Figure 4.10, where wake velocity predictions by HoPFlow and MaPFlow are compared to measurements. In particular, the axial velocity distribution (parallel to the direction of the wind), predicted at constant span–wise positions is presented. For the radial position of 1.4 m ($\simeq$ 60%), both the Eulerian and the Lagrangian solver provide acceptable predictions. The Eulerian solver predicts slightly higher values of the axial velocity downstream (reduced near–wake deficit) and is closer to the measurements of the New MEXICO experiment, whereas the hybrid solver agrees with the measurements of the old MEXICO. The two solvers are in good agreement with each other and with the experimental measurements in the upstream region. In the second radial position at 1.8 m (80%), the Eulerian solver predicts higher values for the axial velocity downwards, whereas the hybrid solver results agree with both experimental measurements, not only in the predicted level but also in the slope of the downstream axial velocity variation. This shows that, opposed to the predictions of its Eulerian counterpart, the wake deficit formed in the hybrid solver simulations is close to the one formed during the wind tunnel experiment. The differences are again attributed to the reduced numerical diffusion of the Lagrangian–Vorticity formulation of the hybrid solver in the near–wake region that preserves the wake structures with greater success. Of course, numerical diffusion is an inevitable feature of all numerical methodologies and cannot be completely eliminated. In particle methods, remeshing is the main source of numerical diffusion and it gets increased alongside with the PM grid spacing.

Finally, in Table 4.8, the measured and computationally predicted rotor loads are listed. The hybrid solver seems to predict a thrust value that is closer to the measured value (overestimated by $\simeq$ 9%), as compared with the Eulerian solver (overestimated by $\simeq$ 13%). Better agreement with measurements is achieved in torque prediction by both computational tools (HoPFlow under–predicts the torque value by $\simeq$ 7% and MaPFlow by $\simeq$ 4%).

To sum up, simulations results by various CFD solvers are very close to measurements in the root and tip regions. Small discrepancies are reported in the mid–span of the blade, which are attributed to the over–prediction of the measured suction side pressure. However, computational predictions agree very well with each other. The tip region loading dictates the overall loading and performance of the rotor. This explains why the differences in the integrated rotor loads are not substantial. The slightly smaller values of aerodynamic forces (closer to the experimental ones) predicted by the hybrid solver are

attributed to the reduced numerical diffusion and, thus, the increased wake induction due to the Lagrangian formulation used in the off–body region.

Table 4.7. *Radial distribution of normal and tangential forces. Comparison between computational predictions and experimental measurements. Tabulated data of Figure 4.9. Reference values correspond to experimental measurements. The hybrid solver predicts reduced aerodynamic forces compared to the Eulerian ones at all the different radial positions that overall are closer to the measured values. This is attributed to the increased numerical dissipation of the Eulerian formulation in the wake region that ends up in reduced wake induced velocities.*

Radius	F_N [N/m]			F_T [N/m]		
	Measurements	MaPFlow	HoPFlow	Measurements	MaPFlow	HoPFlow
25%	119.0	+29%	+25%	31.98	−11%	−14%
35%	198.1	+8%	+7%	27.23	+21%	+14%
60%	303.4	+22%	+18%	29.76	+28%	+21%
82%	421.9	+6%	+3%	44.22	+7%	+2%
92%	452.9	+1%	−1%	43.37	+7%	+4%

(a) *Normal forces radial distribution.*

(b) *Tangential forces radial distribution.*
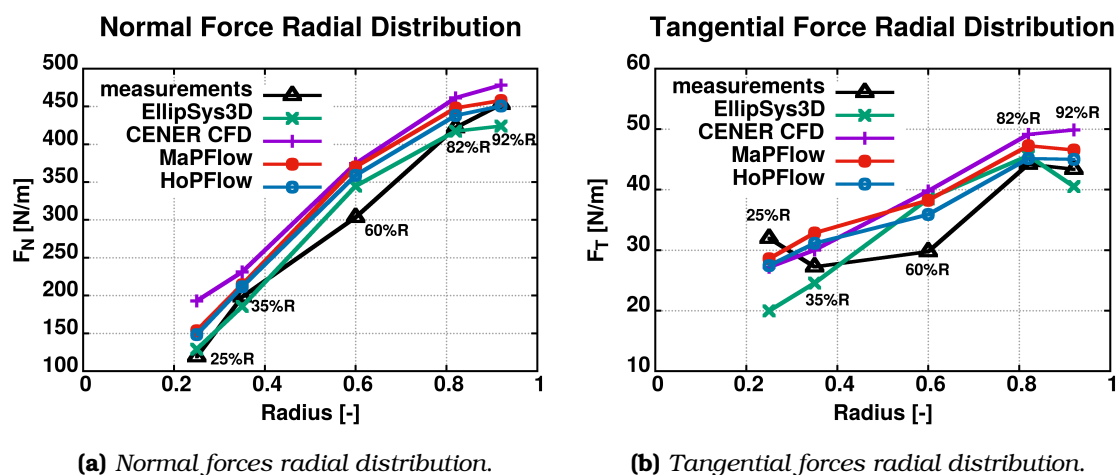
Figure 4.9. *Radial distribution of normal (a) and tangential (b) forces. Comparison among computational predictions by different CFD solvers (EllipSys3D – incompressible solver, CENER – compressible solver, MaPFlow – compressible solver, HoPFlow – compressible hybrid Lagrangian–Eulerian solver) and experimental measurements. The NTUA results printed in this Figure are listed in Table 4.7. Good agreement is observed at most radial positions. At 60%R where the differences from measured values are greatest, the computational models predictions agree well with each other. Overall, HoPFlow predicted loads are lower compared to MaPFlow and CENER (the two compressible Eulerian solvers) and slightly closer to the experimental values. Underestimation of loads by EllipSys3D at most radial positions (even compared to measured values) is attributed to solving the incompressible flow equations.*
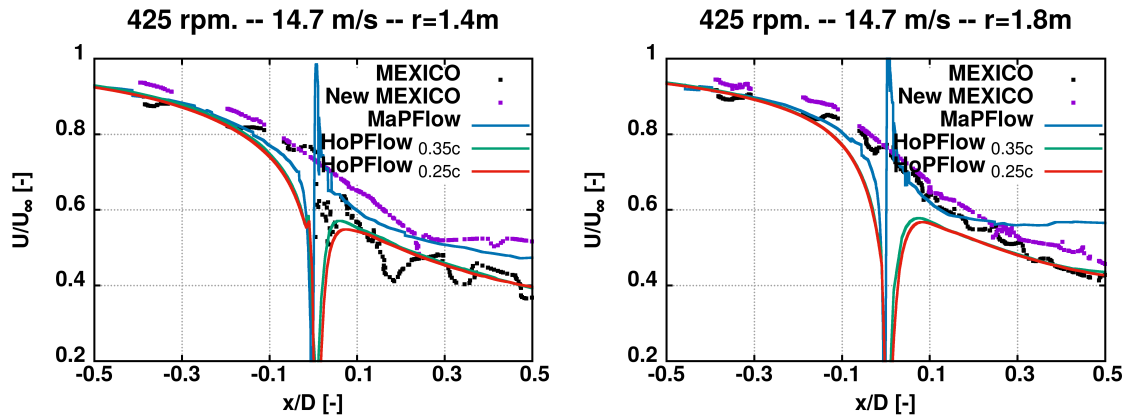
Figure 4.10. *Axial velocity distribution at constant radial positions r = 1.4 m (left) and r = 1.8 m (right). X and Y axes have been normalized with rotor diameter D = 4.5m and free-stream velocity U∞ = 14.7m/s respectively. Comparison between computational predictions and experimental measurements. Good agreement is observed in the upstream region at both radial positions. The Eulerian solver predicts higher values for the axial velocity in the downstream (wake) region. This is attributed to the increased numerical diffusion of the Eulerian formulation. Moreover, the slope of the axial velocity reduction downstream of the rotor (wake deficit) is fairly captured by the hybrid solver, opposed to the Eulerian one. This is again associated with the reduced numerical diffusion of the Lagrangian–Voricity formulation of the hybrid solver in the wake region that preserves the wake structures more efficiently than the Eulerian finite volume approach.*

Table 4.8. *Thrust (N) and Torque (Nm) estimation of New MEXICO WT model rotor for the axial case of run no. 266. Comparison between computational predictions (produced by the hybrid CFD solver HoPFlow and its Eulerian counterpart MaPFlow) and experimental measurements. Reference values correspond to measured values. Thrust is overestimated by both computational models, with the hybrid solver predictions being closer to the experimental measurements. Torque is better predicted but slightly underestimated by both computations. The overall reduced integrated loads predicted by the hybrid solver compared to its Eulerian counterpart are attributed to the increased wake downwash, due to the reduced numerical diffusion of the Lagrangian formulation in the wake region.*

	Thrust	Torque
MaPFlow	+13%	−4%
HoPFlow	+9%	−7%
measurements	1620.1 [N]	319.33 [Nm]

4.1.4   Computational Requirements

In Table 4.9, a comparison concerning the computational cost of the Eulerian and two hybrid solver simulations is made. In the former, a coarse PM grid (*DXpm* = 0.50*c*) has been used, whereas in the latter, the fine PM grid (*DXpm* = 0.25*c*) has been used, in which the PM grid dependency analysis resulted. It is noted that the PM grids for which computational costs are presented result in similar forces predictions, within a 5% margin (see Table 4.6). Due to the usage of uniform PM grids, even the coarse discretization length ends up in approximately 2 times more computational elements than the ones used in the Eulerian solver simulation, which rises to 12 times if the fine discretization length is employed. Nevertheless, the Eulerian solver simulation needs more rotor revolutions in order to achieve convergence of aerodynamic loads. This is because the Lagrangian method exactly satisfies the boundary conditions at infinity, and therefore, the required number of revolutions for the convergence of the loads depends only on the distance that the wake has traveled away from the rotor disk plane. On the other hand, in the Eulerian simulation, the convergence rate depends on the extent of the domain, which dictates the reflection of the numerical errors and the coarsening of the grid in the far–field, which regulates their decay rate. The differences in the utilized time–step values (expressed as steps per rotor revolution) come from the fact the CFL condition needs to be respected in the hybrid simulations, as no preconditioning has been applied to the Lagrangian formulation of the flow equations (2.80). This explains the greater number of steps per revolution required by the fine grid simulation. Even though the amount of PM nodes used in the fine grid simulation is an order of magnitude greater than the ones used in the coarse grid simulation, the computational time–lengths of the time–steps are comparable. This is due to the fact that in the coarse grid simulation, more sub–iterations are needed to accomplish a converged time–step solution. Furthermore, fewer processors have been used in the specific simulation. Overall, the computational cost of the coarse PM grid hybrid simulation is 1.4 times higher than that of the Eulerian solver simulation, whereas the fine PM grid hybrid simulation costs 5.7 times more than the Eulerian one.

In Figure 4.11a, the normal force distribution computed by the three different simulations is depicted. The distributions predicted by the Eulerian and the coarse grid hybrid simulation are close to each other, whereas the distribution predicted by the fine grid hybrid simulation is slightly closer to the experimental values. In Figure 4.11b, the pressure distribution at 60% of the blade is depicted. The coarse grid hybrid simulation results exhibit a small shift towards lower pressure with respect to measured data–sets and other predictions, which results from the insufficient density of the PM grid used. However, these deviations in pressure do not significantly affect the overall aerodynamic force prediction.

Table 4.9. *Computational cost comparison among Eulerian and two hybrid solver simulations, with coarse and fine PM. Due to uniform PM discretization implemented in HoPFlow, the coarse and fine PM simulations end up in 2 and 12 times more computational elements than the Eulerian simulation respectively. Nevertheless, the predicted aerodynamic loads are within 6% according to Tables 4.6 and 4.7 and Figure 4.11, with the coarse PM being slightly closer to fine PM results and experimental values. Time-step values employed in the hybrid simulations are smaller than the Eulerian one due to the CFL condition that needs to be respected in order to successfully solve the non-preconditioned Lagrangian equations of the flow. However, satisfying the exact boundary conditions in the Lagrangian sub-domain far-field leads to greater convergence rate and less number of rotor revolutions needed in the hybrid solver simulations. Consequently, the total computational costs of the three simulations are comparable, with the Eulerian simulation having approximately double computational cost per element compared to the hybrid simulations.*

Solver	Computational Elements	Revolutions	$\dfrac{Steps}{Revolution}$	$\dfrac{Sec}{Step}$	$\dfrac{Sub-Iterations}{Step}$	Processors	Corehours
MaPFlow	$4.8M$ [a]	10	1440	3.5	9	480	6720
HoPFlow$_{coarse}$	$7.3M$ [b] $+ 4.1M$ [a]	6	900	76.75	17	80	9210
HoPFlow$_{fine}$	$52.2M$ [b] $+ 4.1M$ [a]	6	1800	81	9	120	38,800

[a] Number of computational cells.

[b] Number PM nodes.

(a) *Radial distribution of normal forces.*

(b) *Pressure distribution at 60% of the blade.*
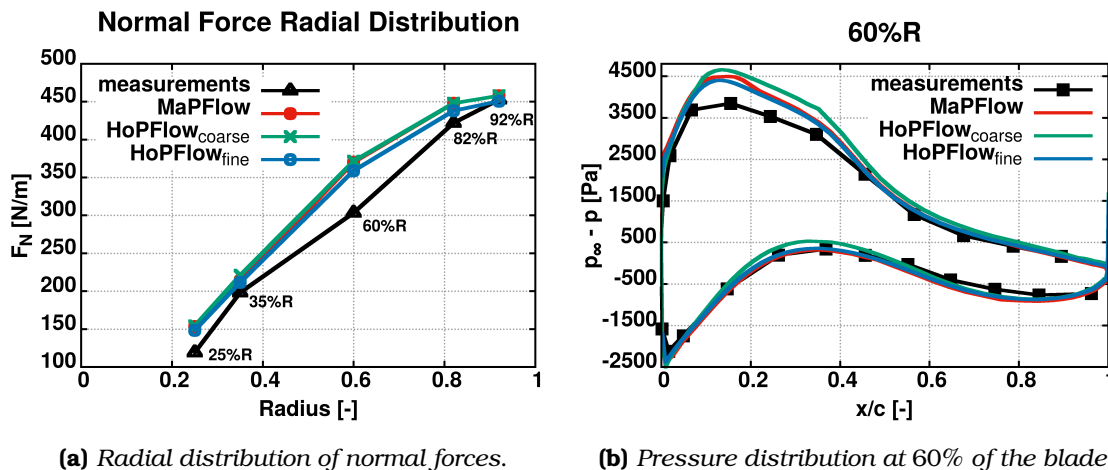
Figure 4.11. *Comparison of aerodynamic forces between computational predictions and experimental measurements. According to Table 4.9, the simulations experience comparable computational costs. In turn, the predicted aerodynamic loads (a) and pressure distribution (b) are close to each other, with the fine PM results being slightly closer to experimental values.*

4.2 Aeroelastic analysis of a helicopter rotor

In this section, aeroelastic simulations of the MR of a BO105 helicopter model are presented. HoPFlow is used for the aerodynamic analysis, in which the rotor blades are fully resolved. The fuselage and rotor hub geometries are omitted in the simulations. The structural dynamics analysis is performed through GAST and the rotor blades are modelled as beam assemblies, in order for non–linear geometric phenomena to be properly accounted for. The aerodynamic and structural problems are solved separately, but tightly coupled. The test case is the Base–Line case of the HARTII experimental campaign [13], which is a descent flight at 33 m/s. First, the most important numerical parameters (grid set–up and resolution, time–step value, # dual–steps) are examined. The produced aeroelastic results (wake geometry, aerodynamic loads at 87% radial station, structural loads close to the blade root and the corresponding deflections at the blade tip) are then compared against experimental measurements and computational predictions extracted from other CFD based aeroelastic simulations performed. The corresponding structural dynamics analyses are based on beam models as well. Results from these computational predictions are copied from [163, 164].

4.2.1 The HARTII experimental campaign

The second higher Harmonic control and Aeroacoustic Rotor Test (HARTII) was performed in October 2001, in an open–jet facility of the German-Dutch wind tunnel (DNW) as a joint effort of the U.S. Army Aero-Flight Dynamics Directorate (AFDD), NASA Langley (NL), German Aerospace Center (DLR), French Aerospace Lab (ONERA) and DNW to generate a comprehensive database of wake geometry, aerodynamic and structural loads, blade deflections and acoustic radiation measurements. The objective was to provide a comprehensive experimental database for code validation and technical interchange of expertise in rotorcraft analysis and modelling. The model rotor was a 1 : 2.45 Mach and dynamically scaled BO105 hingeless rotor operating in descent flight conditions in which strong Blade Vortex Interaction (BVI) is expected.

A detailed description of the HARTII data and how they were measured is available in the test documentation [13] and has been reported in numerous papers and reports [182, 183, 184, 185, 186]. A subset of the data has been released to the international community in 2005 with the opening of the HARTII International Workshop. Since then numerous workshops have been held at both the European Rotorcraft Forum (ERF) and the Annual Forum of the American Helicopter Society (AHS) with increasing participation from rotorcraft research establishments and the industry worldwide. The database of the HARTII project are now accessible via `www.dlr.de/ft/HART-II`.

The operational conditions used in the workshop were two Higher Harmonic Control (HHC) cases (a Minimum–Noise and a Minimum–Vibration case) and a Base–Line case without HHC. The most important variables that determine the conditions for the Base–Line case of the HARTII experimental campaign are listed in Table 4.10.

Table 4.10. *Summary of the simulation conditions for the HARTII Base-Line case.*

| Characteristic	Symbol	Value
Rotor geometry		
Rotor radius	R	2 m
Blade chord	c	0.121 m
Number of blades	N_b	4
Rotor solidity	σ	0.077
Non–dim. root cut–out	r_a	0.22
Non–dim. zero twist radius	r_{tw}	0.75
Blade linear twist	Θ_{tw}	$-8°/R$
Airfoil	modified $\sim$ trailing edge tab	NACA23012
Tab length	t_L	5 mm
Tab thickness	t_{th}	0.9 mm
Wind tunnel data		
Air pressure	p_∞	100.97 kPa
Air temperature	T_∞	17.3 $°C$
Air density	ρ_∞	1.2055 k/m^3
Speed of sound	c_∞	341.7 m/s
Wind speed	V_∞	32.9 m/s
Mach number	M_∞	0.0963 m/s
Operational data		
Rotational speed	Ω	109.12 rad/s
Hover blade tip Mach number	M_h	0.639 rad/s
Rotor shaft angle of attack	a_s	5.3°
Wind tunnel interference angle	Δa_s	$-0.8°$
Advance ratio	μ	0.151
Rotor thrust	T	3300 N
Roll moment (positive advancing side down)	M_x	20 Nm
Pitch moment (positive nose up)	M_y	-20 Nm
Rotor power	P	18.3 kW
Collective control angle	Θ_{coll}	3.8°
Lateral cyclic control angle	Θ_c	1.92°
Longitudinal cyclic control angle	Θ_s	$-1.34°$
Mean steady elastic tip torsion	Θ_{el}	$-1.09°$

4.2.2   Numerical investigation

The objective of this section is to assess the effect of the grid and the time–step on the aerodynamic loads predictions. To this end, the measured normal aerodynamic force ($C_N M^2$) and twisting moment ($C_M M^2$) at $87\%R$ radial station are the reference. Because of that, aeroelastic simulations are used. For a fair comparison with the experimental measurements, the control angles (collective and cyclic pitch) of the simulations are trimmed based on a feedback control algorithm in order to match the predicted hub loads (thrust force, pitching and rolling moment) to the measured ones.

Eulerian grid set–up

In the standard approach followed in HoPFlow simulations, every aerodynamic body has its own near–body Eulerian grid, typically of unstructured type, following its motion (rigid body motion and elastic deflections). The off–body region is filled with particles and the field communication is applied by solving the Navier–Stokes equations in a Lagrangian approach. In order to compute the convectional terms of the particles in accuracy, the off–body region is discretized in a uniform Cartesian stationary grid called Particle Mesh (PM). This concept is illustrated in Figure 4.12a and resembles the standard Overset grids approach followed in Eulerian CFD. From now on, this grid structure will be referred to as the "blades" set–up.

In order to estimate the grid resolution effect on the computed aerodynamic loads, different values of PM discretisation lengths (DX_{PM}) need to be tested, starting from $DX_{PM} = c/4$. However, the use of uniform PM in the current HoPFlow implementation does not allow for finer grid resolutions to be tested, as the resulting number of PM nodes explodes and, thus, computational cost becomes prohibitive. To circumvent this problem, the different rotor blades are incorporated within a single Eulerian disk–shaped grid that is confined in a narrow region close to the rotor and extra grid refinement is applied on the Eulerian disk. The Eulerian disk follows the rotor motion (rigid body motions that are common for all the blades), such as helicopter attitudes and azimuthal rotation. The motion that is different for every blade (pitching motion and elastic deflections) is projected from the blade surface nodes to the internal nodes of the disk by following the Zhao deforming grid method (see Section 2.2.1.4). This concept is illustrated in Figure 4.12b and, from now on, will be referred to as the "disk" set–up.

In both cases of the Eulerian grid sub–domains ("blades", "disk"), only the pure aerodynamic part of the blades is modelled. The blade holder (elliptical form), the hub cylinder and the fuselage are omitted in the simulations. The PM grid is defined as a box that encapsulates the entire computational domain, extending $1.5R$ upstream, $3R$ downstream, $1.5R$ transversely, $0.5R$ towards the top and $1R$ towards the bottom from the rotor hub center. It is discretised by employing uniform Cartesian grids under a constant discretization length of $DXpm = c/4$. Larger domains have been tested, but no significant differences are found.
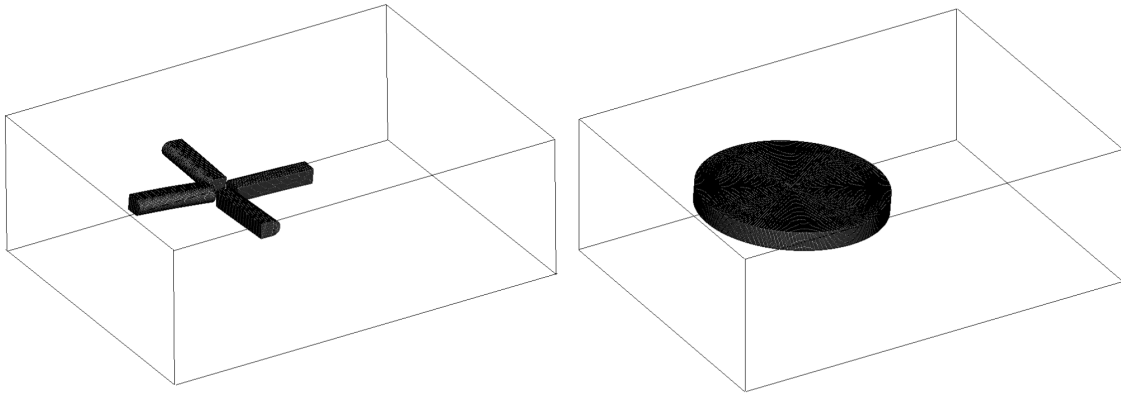
(a) *"blades" set-up. Every blade has its own Eulerian grid, confined in a narrow region around it and separate from the other blade-fitted grids. Their interaction (field communication) is accounted for through the PM (Lagrangian background grid). The rigid body motion (e.g. azimuthal rotation, pitching motion) and elastic deflections of a blade are transferred from the surface nodes to the rest of its blade-fitted Eulerian grid nodes.*

(b) *"disk" set-up. A single Eulerian domain contains all the blades. Their interaction (field communication) is accounted for directly by the Eulerian solver. The Eulerian disk follows the rigid body motions that are common for all the blades (e.g. helicopter attitudes, azimuthal rotation). Individual rigid motion and elastic deformations are extrapolated from the blade surface to the space and the grid is accordingly deformed.*

Figure 4.12. *Different grids set-up employed in helicopter main rotor aerorelastic simulations using HoPFlow. Black solid lines indicate the boundaries of the PM used in the Lagrangian sub-domain. PM is a box that extends $1.5R$ upstream, $3R$ downstream, $0.5R$ to the top, $1R$ to the bottom and $1.5R$ to the lateral sides of the rotor center. In "blades" set-up (a) the space between the different blades is discretized solely in a PM with $DX_{PM} = c/4$, whereas in "disk" set-up (b) the rotor blades are inside a finer single Eulerian sub-domain (disk formed) with $DX_{Eul} = c/8, c/12, c/16$.*

In this way the region close to the rotor may by refined within the Eulerian framework, by following a similar approach to the one used in Section 3.1.2.3 for the Actuator Line (AL) cases. This is depicted in Figure 4.13. It needs to be stressed, that in the following analyses, uniform grid spacing has been adopted throughout the whole Eulerian disk and its characteristic length is denoted by DX_{Eul}. Moreover and contrary to the "blades" set–up, the interaction between the rotor blades (field communication) is accounted for directly by the Eulerian solver. No intermediary intervention of the Lagrangian sub–domain is needed, which is solely assigned with the task of providing far–field boundary conditions at the boundaries of the disk. Consequently, no information is lost through the interpolation schemes used to transfer the flow–field information from one sub–domain to the other. Consequently, numerical diffusion is reduced, not only due to grid refinement, but also due to minimizing the transfer of the flow information from one sub–domain to the other. This is clearly shown in Figure 4.14, where the vorticity structures created in the early steps of an aeroelastic simulation are compared between the 'blades" and 'disk" set–ups. The vorticity contours shown are extracted from the same PM background grid. Yet, the corrections in the Eulerian near–body region drastically reduce numerical

diffusion when the 'disk" set–up is employed. On the other hand, the Eulerian corrections are less efficient in the 'blades" set–up.
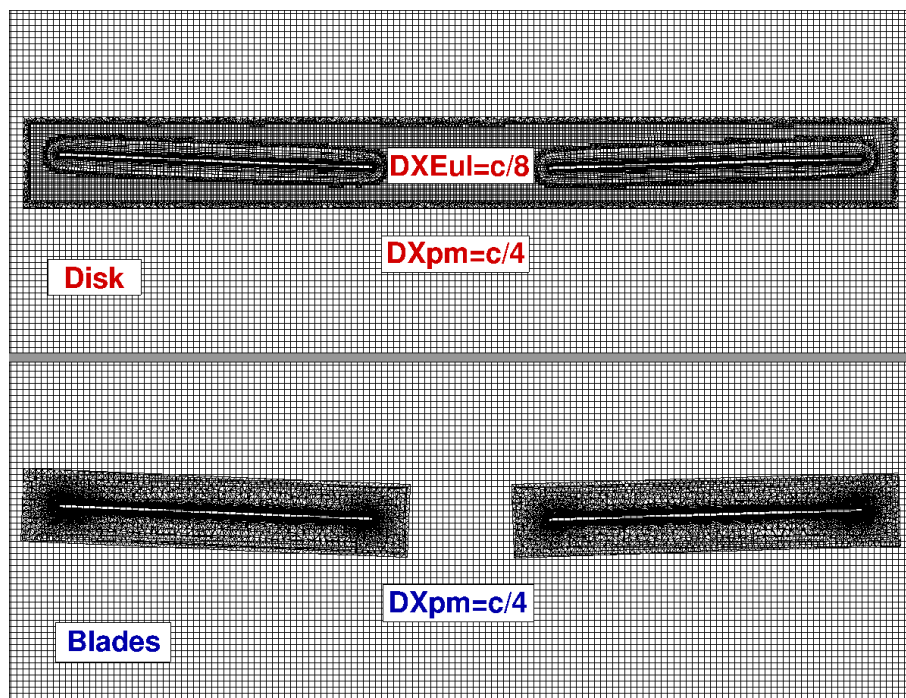
Figure 4.13. *Close to solid boundaries grid set–up. Comparison between the fineness of discretization in the rotor region. In "blades" set–up (down) the space between the different blades is discretized solely in a PM with $DX_{PM} = c/4$, whereas in "disk" set–up (up) a much finer discretization is accomplished through an Eulerian sub-domain (disk formed) with $DX_{Eul} = c/8, c/12, c/16 < DX_{PM}$.*
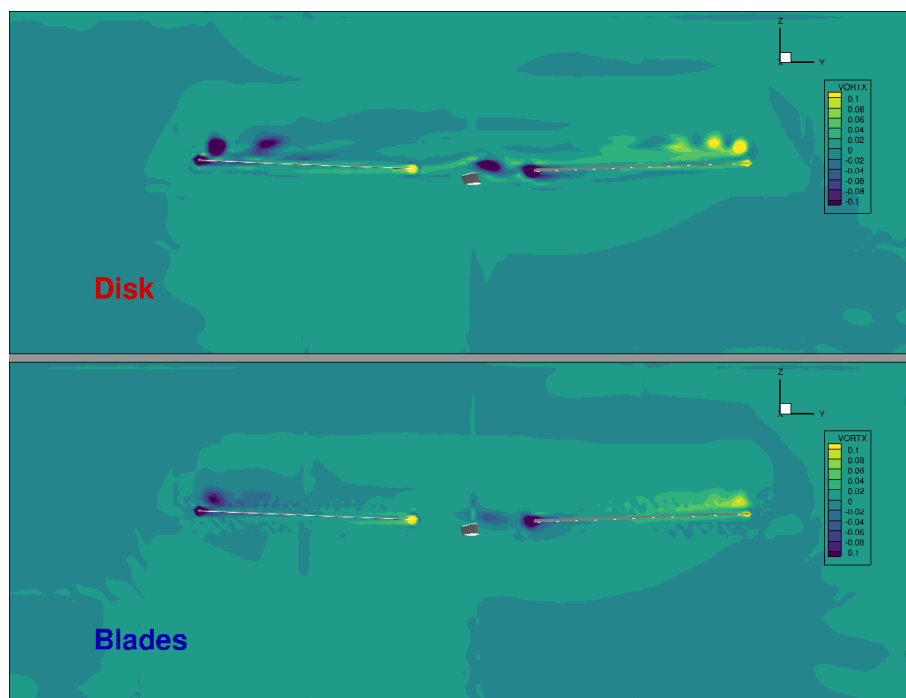
Figure 4.14. *Vorticity contours in the close to solid boundaries region. By employing a fine Eulerian sub-domain ("disk" set-up) the diffusion of the near wake vortices is reduced compared to the coarse PM used in "blades" set-up.*

Grid dependency

In Table 4.11, the mean values of the normalized aerodynamic loads predictions are listed with respect to different grid refinement attempts. The blade surface grid used in these simulation consists of 14308 elements, 138 cells to describe the airfoil shape and 100 cells in the span–wise direction. 720 time–steps have been used in rotor revolution, each divided in 8 dual–steps. The corresponding control angles and the torsion angle at the blade tip are listed in Table 4.12. The azimuthal variation of the normalized aerodynamic loads is depicted in Figure 4.15. The medium Eulerian disk set–up provides a grid independent solution and a good compromise between accuracy and computational cost at $DX_{PM} = c/4$ and $DX_{Eul} = c/12$. The difference from the fine disk set–up is -0.6% for $\overline{C_N M^2}$ and -1.2% for $\overline{C_M M^2}$. A significant level difference is reported with respect to the measured values that gets minimized as the grid gets finer for $C_N M^2$ (up to $\simeq -8\%$ for the fine disk set–up). Small improvement from grid refinement is reported for $C_M M^2$ which is predicted almost twice (in absolute) the measured one ($\simeq -70\%$). This brings about an almost double value for the tip torsion angle ($\simeq 1.5°$ difference), which, in turn, explains the $\simeq 1°$ difference in the collective pitch angle. Good agreement is observed in the cyclic pitch amplitudes ($< 0.5°$ difference). For this reason, an overall good agreement is reported in trend of the azimuthal variation of the aerodynamic loads in Figure 4.15.

The great difference in the aerodynamic twisting moment is frequent for most CFD based predictions, as shown in Section 4.2.3. This is attributed to the tab that has been used in the airfoil profile of the rotor blades in order to confine the increase of C_M with the angle of attack. Due to the small length of the tab ($\simeq 4\%c$), a great number of points is expected to be required in the trailing edge region to effectively predict its aerodynamic effect, thus, implying increased computational cost. Hence, if the tab is poorly resolved a level difference in the torsion angle is to be expected. Increasing the collective pitch during the trim procedure, seems to be a reasonable engineering compromise. The reduced mean value of the aerodynamic normal force at 87% is also frequent for most CFD based predictions. In the NTUA predictions, it is related to the poor prediction of the BVI in the advancing side of the rotation ($0° - 90°$).

In Figure 4.15a, we see an overall better agreement with the experimental measurements when the disk set–up is employed in HoPFlow simulations. BVI induced variations of the aerodynamic loads show up in the 1st and 4th quadrants, although less pronounced compared to measurements, especially in the $0° - 60°$ region. Moreover, the local peaks at $70°$ and $250°$ are predicted closer to the measured values. These are attributed to the reduced numerical diffusion brought about by the disk set–up, as explained in paragraph 4.2.2. Grid refinement in the Eulerian sub–domain efficiently leads to a grid independent solution. Small differences remain with respect to experimental measurements, that are not attributed to the grid resolution. This indicates the effect of another physical mechanism, apart from numerical diffusion, that weakens BVI, especially in the 1st quadrant. This is examined in detail in Section 4.2.3.

Table 4.11. *Variation of the number of grid cells and normalized aerodynamic loads with increasing the refinement of the Eulerian sub-domain. Reference values correspond to experimental measurements. A small difference in the mean value of the normal aerodynamic force is reported ($\simeq 10\%$). A significant difference is shown in the mean value of the twisting moment ($\simeq 70\%$). Grid refinement in the Eulerian sub-domain (disk set-up) does not significantly improve the predicted mean values.*

	Discretisation	**# Eulerian cells**	$\overline{C_N M^2}$	$\overline{C_M M^2}$
HoPFlow blades	$DX_{PM} = c/4$	$4.8M$	-14.1%	-80.8%
HoPFlow disk coarse	$DX_{PM} = c/4 \,\&\, DX_{Eul} = c/8$	$6.16M$	-10.3%	-71.9%
HoPFlow disk medium	$DX_{PM} = c/4 \,\&\, DX_{Eul} = c/12$	$12.45M$	-9.0%	-70.4%
HoPFlow disk fine	$DX_{PM} = c/4 \,\&\, DX_{Eul} = c/16$	$26.65M$	-8.3%	-68.8%
Experiment	-	$-$	0.0902	-0.0026

Table 4.12. *Control angles comparison among trimmed simulation values for different Eulerian sub-domains. The computationally predicted $\overline{C_M M^2}$ is almost twice (in absolute) the measured one (see Table 4.11). This almost doubles the predicted tip torsion angle ($\simeq 1.5°$ difference), that, in turn, leads to an $\simeq 1°$ increase in the collective pitch angle. Good agreement ($< 0.5°$ difference) is observed in the cosinus pitch amplitude. This difference is slightly greater in the sinus pitch amplitude, however it gets smaller as the Eulerian sub-domain gets finer.*

	collective	**cos**	**sin**	**tip torsion**
HoPFlow blades	$4.83°$	$1.45°$	$-0.55°$	$-2.74°$
HoPFlow disk coarse	$4.81°$	$1.63°$	$-0.78°$	$-2.60°$
HoPFlow disk medium	$4.81°$	$1.58°$	$-0.91°$	$-2.58°$
HoPFlow disk fine	$4.68°$	$1.50°$	$-0.97°$	$-2.57°$
Experiment	$3.8°$	$1.92°$	$-1.34°$	$-1.09°$ *
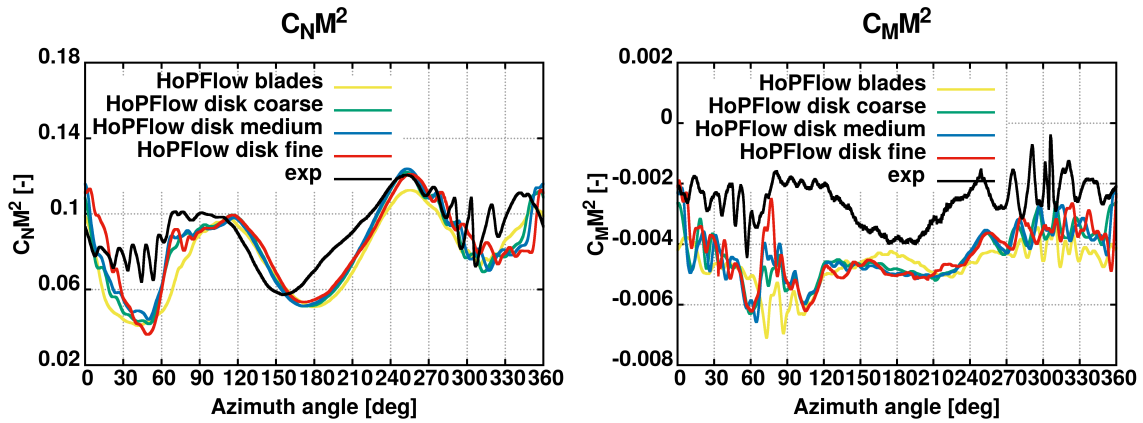
* Averaged over all four blades.

(a) *Non-dimensional normal aerodynamic force at 87% radial station. A small level difference in the 1st and 4th quadrants is reported between the predictions and experimental measurements. This explains the mean value differences reported in Table 4.11. Better agreement is shown in the 2nd and 3rd quadrants where the level is fairly well predicted (maximum at 250° slightly underestimated in blades set-up) but with an $\simeq 20°$ phase lag of the minimum (minimum at 180° (blades) , 170° (disk) and 155° (measurements)). Disk set-up results predict mild BVI (compared to measurements) in the 1st and 4th quadrants, whereas in blades set-up the BVI induced variations of the aerodynamic force are almost completely damped.*

(b) *Non-dimensional aerodynamic twisting moment at 87% radial station. A level difference is reported between the computational predictions and experimental measurements ($\simeq -80\%$ (blades) and $\simeq -70\%$ (disk)). The variations trend is fairly predicted by the disk set-up, apart from the $120° - 210°$ curvature which is almost completely flattened. The BVI in the 1st and 4th quadrants are fairly predicted by the models, with a minor phase lag in the 4th quadrant.*

Figure 4.15. *Non-dimensional normal aerodynamic force (a) and twisting moment (b) at 87% radial station. Comparison among HoPFlow predictions under different Eulerian sub-domains and experimental measurements. Computational predictions are improved when the disk set-up is employed. No great improvements are reported as the Eulerian sub-domain (disk set-up) gets finer.*

Blade Surface Grid dependency

In Table 4.13, the mean values of the normalized aerodynamic loads predictions are listed with respect to different blade surface grid refinement attempts. The corresponding control angles and the torsion angle at the blade tip are listed in Table 4.14. The azimuthal variation of the normalized aerodynamic loads is depicted in Figure 4.16. Three different blade grids have been tested, employing 7324, 14308 and 28224 surface cells for every blade discretization. In the coarse grid, 96 cells were used to describe the airfoil shape and 70 cells were used in the span–wise direction, whilst in the medium and fine grids, the corresponding number of cells were 138×100 and 201×130, respectively. The corresponding total amount of grid cells are 12.42, 12.45 and $14.84 \cdot 10^6$ cells, respectively. In these simulations, 720 time–steps have been used in rotor revolution, each divided in 8 dual–steps. Again, no great improvements are observed as the blade surface grid gets finer, especially in $C_N M^2$ predictions, indicating the effect of a physical mechanism (not numerical convergence) on the reported differences. The twisting moment level shifts

towards the measured one, but no great improvement is reported. An excessive grid refinement could possibly bridge the gap ($\simeq 70\%$), but the computational cost would rise prohibitively. As stated in the previous paragraph, the increase of the collective pitch angle through the trimming procedure seems like an affordable engineering remedy. Finally, no crucial differences are observed among the different blade grids concerning the the azimuthal variation of the aerodynamic loads. As a result of the above, the medium blade surface grid is considered to provide the best compromise between accuracy and computational cost.

Table 4.13. *Variation of number of surface panels and normalized aerodynamic loads with increasing the refinement of blade surface grid. Reference values correspond to experimental measurements. All the different surface grids have been tested by employing the medium disk set-up (Eulerian sub-domain grid). A small difference in the mean value of the normal aerodynamic force is reported ($\simeq 10\%$). A significant difference is shown in the mean value of the twisting moment ($\simeq 70\%$) that gets smaller as the blade surface grid gets finer. Nevertheless, the differences among the various blade surface grids are not considered to be crucial.*

	# Eulerian cells	# surface panels	$\overline{C_N M^2}$	$\overline{C_M M^2}$
HoPFlow blade grid coarse	$12.42M$	7324	-10.8%	-79.3%
HoPFlow blade grid medium	$12.45M$	14308	-9.0%	-70.4%
HoPFlow blade grid fine	$14.84M$	28224	-9.3%	-62.5%
Experiment	-	–	0.0902	-0.0026

Table 4.14. *Control angles comparison among trimmed simulation values for different blade surface grids and experimental values. The computationally predicted $\overline{C_M M^2}$ is almost twice (in absolute) the measured one (see Table 4.13). This almost doubles the predicted tip torsion angle ($\simeq 1.5°$ difference), that, in turn, leads to an $\simeq 1°$ increase in the collective pitch angle. Good agreement ($< 0.5°$ difference) is observed in the cosinus and sinus pitch amplitudes.*

	collective	cos	sin	tip torsion
HoPFlow blade grid coarse	$4.87°$	$1.51°$	$-0.91°$	$-2.68°$
HoPFlow blade grid medium	$4.81°$	$1.58°$	$-0.91°$	$-2.58°$
HoPFlow blade grid fine	$4.74°$	$1.62°$	$-0.94°$	$-2.53°$
Experiment	$3.8°$	$1.92°$	$-1.34°$	$-1.09°$ *
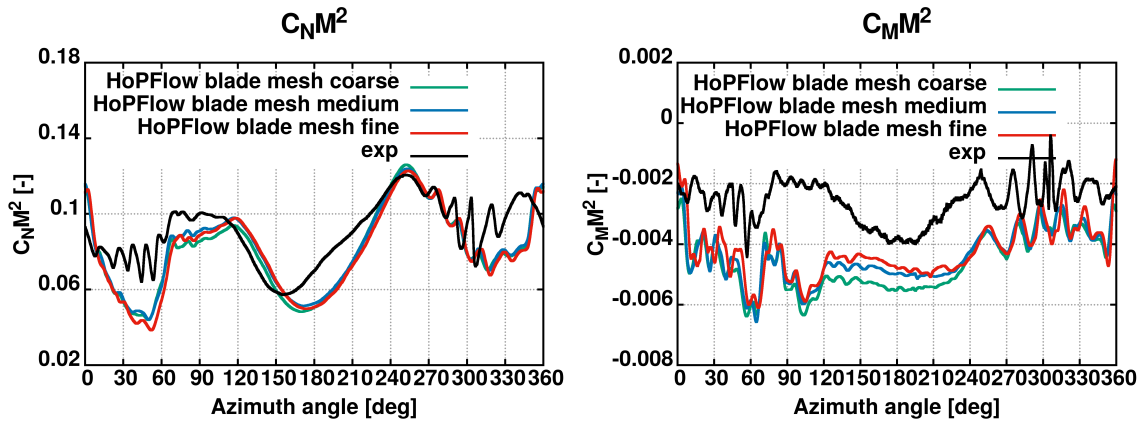
* Averaged over all four blades.

$$C_N M^2$$

$$C_M M^2$$

(a) *Non-dimensional normal aerodynamic force at 87% radial station. A small level difference in the 1st and 4th quadrants is reported between the computational predictions and experimental measurements. This explains the mean value differences reported in Table 4.13. Better agreement is shown in the 2nd and 3rd quadrants where the level is fairly well predicted. Local maximum at range $60° - 120°$ and minimum at $150°$ are slightly underestimated by computational models, with an $\simeq 20°$ phase lag. Maximum at $250°$ is fairly well predicted (slightly overestimated) by computational models. Medium and fine surface grids are closer to measurements than the coarse one. BVI in 1st quadrant is almost completely smoothed out in computations. The respective BVI in the 4th quadrant is effectively predicted, but less pronounced along with a minor lag.*

(b) *Non-dimensional aerodynamic twisting moment at 87% radial station. A level difference is reported between the computational predictions and experimental measurements that gets smaller as the blade grid mesh gets finer. Overall, medium and fine grid predictions are relatively closer to each other compared to the coarse one. The variations trend is fairly predicted, apart from the $120° - 210°$ curvature which is almost completely flattened. The BVI in the 1st and 4th quadrants are fairly predicted by all the different grids (fine grid produces sharper spikes), with a minor phase lag in the 4th quadrant.*

Figure 4.16. *Non-dimensional normal aerodynamic force (a) and twisting moment (b) at 87% radial station. Comparison among HoPFlow predictions under different blade surface grids and experimental measurements. No great differences are observed for the various blade surface grids tested herein. Overall, medium and fine grid predictions are relatively closer to each other compared to the coarse one.*

Dual-steps Dependency

In order to properly investigate how the selected time–step affects the aerodynamic loads, the PM must be refined accordingly to the time–step value. Very big time–step values (according to the PM characteristic length) cannot be used due to the CFL stability condition that needs to be respected in the hybrid simulations. This is because we do not apply preconditioning in the Lagrangian formulation of the flow equations (2.80). On the other hand, very small time–step values cannot be used either. This is attributed to the remeshing technique that is applied at the end of every time-step in order to recover full coverage of the computational domain and ensure a regular distribution of the numerical particles. Remeshing is a standard procedure to prevent excessive concentration or spreading of particles and, in this way, preserve the consistency and accuracy of the numerical solution. However, when very small time–step values are employed, it also prevents the flow information from convecting downwards, thus, blocking the conver-

gence of the numerical procedure. In the present study, no finer PM discretization than $DX_{PM} = c/4$ are employed, as the computational cost becomes prohibitive. Consequently, a constant time–step value of $\Delta t = T/720$ (T is the rotor rotation period) is employed in all the presented simulations.

Therefore, instead of the time–step value, the number of dual–steps performed within every time–step is tested. In Table 4.15, the mean values of the normalized aerodynamic loads predictions are listed with respect to different number of dual–steps employed. The corresponding control angles and the torsion angle at the blade tip are listed in Table 4.16. The azimuthal variation of the normalized aerodynamic loads is depicted in Figure 4.17. The blade surface grid used in these simulation consists of 14308 elements and the total amount of grid cells that the Eulerian disk is discretized in is $12.45 \cdot 10^6$. No great differences are observed as the number of dual–steps increases, concerning the mean value of the predicted aerodynamic loads (slightly improved) and the trimmed control angles. However, when it comes to azimuthal variation of the aerodynamic loads, better agreement with measurements regarding the phase of the BVI spikes in the 4th quadrant is achieved. As a result of the above, the use of 12 dual–steps is considered to provide the best compromise between accuracy and computational cost.

Table 4.15. *Variation of normalized aerodynamic loads with increasing the number of dual steps (# Dual-steps) used within every time-step. Reference values correspond to experimental measurements. All the different # Dual-steps have been tested by employing the medium disk set-up and the medium blade surface grid (Eulerian sub-domain grid). A small difference in the mean value of the normal aerodynamic force is reported ($\approx$ 10%). A significant difference is shown in the mean value of the twisting moment ($\approx$ 70%) that gets smaller as the # Dual-steps is increased. Nevertheless, the differences among the various # Dual-steps are not considered to be crucial.*

	$\overline{C_N M^2}$	$\overline{C_M M^2}$
HoPFlow 8 Dual–steps	−9.0%	−70.4%
HoPFlow 12 Dual–steps	−8.3%	−65.2%
HoPFlow 16 Dual–steps	−7.9%	−63.4%
Experiment	0.0902	−0.0026

Table 4.16. *Control angles comparison among trimmed simulation values for different number of dual steps. The computationally predicted $\overline{C_M M^2}$ is almost twice (in absolute) the measured one (see Table 4.15). This almost doubles the predicted tip torsion angle ($\approx$ 1.5° difference), that, in turn, leads to an $\approx$ 1° increase in the collective pitch angle. Good agreement ($\leq$ 0.6° difference) is observed in the cosinus and sinus pitch amplitudes.*

	collective	cos	sin	tip torsion
HoPFlow 8 Dual–steps	4.81°	1.58°	−0.91°	−2.58°
HoPFlow 12 Dual–steps	4.81°	1.65°	−0.82°	−2.52°
HoPFlow 16 Dual–steps	4.80°	1.68°	−0.78°	−2.48°
Experiment	3.8°	1.92°	−1.34°	−1.09° *
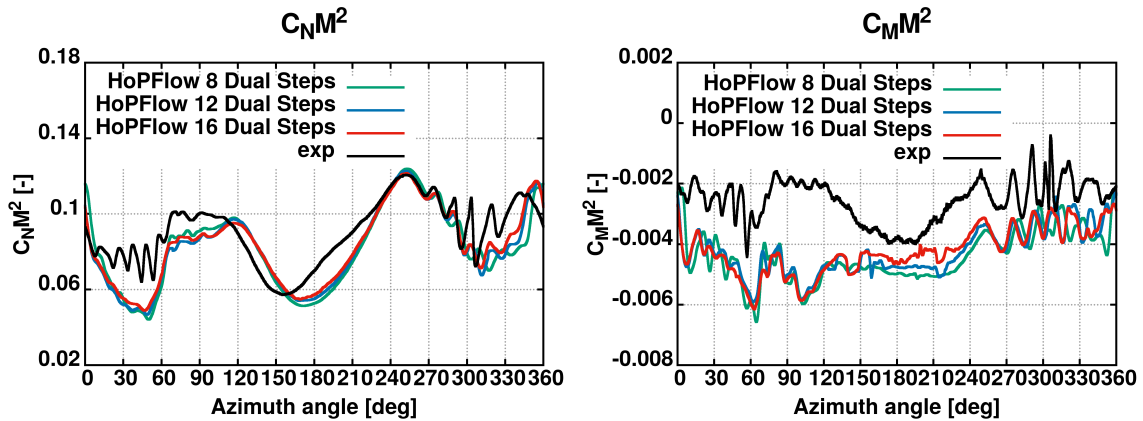
* Averaged over all four blades.

(a) *Non-dimensional normal aerodynamic force at 87% radial station. A small level difference in the 1st and 4th quadrant is reported between the computational predictions and experimental measurements. This explains the mean value differences reported in Table 4.15. Better agreement is shown in the 2nd and 3rd quadrants where the level is fairly predicted. Local maximum at range $60° - 120°$ and minimum at $150°$ are slightly underestimated by computational models, with an $\simeq 20°$ phase lag. Maximum at $250°$ is fairly predicted (slightly overestimated) by computational models. BVI in 1st quadrant is almost completely smoothed out in computations. The respective BVI in the 4th quadrant is effectively predicted, but less pronounced along with a minor lag when 8 Dual-steps are used. 12 and 16 Dual-steps simulations agree well with measurements and with each other regarding the phase of the BVI spikes.*

(b) *Non-dimensional aerodynamic twisting moment at 87% radial station. A level difference is reported between the computational predictions and experimental measurements that gets smaller as number of Dual-steps increases. The variations trend is fairly predicted, apart from the $120° - 210°$ curvature which is almost completely flattened. The BVI in the 1st and 4th quadrants are fairly predicted by all the simulations results, with a minor phase lag in the 4th quadrant when 8 Dual-steps are used. 12 and 16 Dual-steps simulations agree well with measurements and with each other regarding the phase of the BVI spikes.*

Figure 4.17. *Non-dimensional normal aerodynamic force (a) and twisting moment (b) at 87% radial station. Comparison between experimental measurements and HoPFlow predictions when different number of Dual-steps are used per time-step. No great differences are observed for the number of Dual-steps tested herein. 12 and 16 Dual-steps simulations accomplish better agreement with measurements regarding the phase of the BVI spikes in the 4th quadrant.*

4.2.3 Comparison against measurements and other CFD based aeroelastic predictions

In this section, computational results produced by the coupled HoPFlow–GAST aeroelastic solver are compared against measurements and computational predictions extracted from other CFD based aeroelastic simulations. First, a comparison concerning the natural frequencies and mode–shapes predicted by the different structural solvers is performed. Comparison of aeroelastic predictions and measurements is made for blade loads (aerodynamic loads and structural/reaction loads) and elastic deflections and the results are presented as azimuthal variations. The corresponding mean values are presented in tabulated form. Furthermore, a comparison concerning the produced wake

geometry is performed by estimating the position of specific tip vortices traces on a lateral plane of the advancing and retreating sides. The results of computations performed by other research centers are extracted from [163, 164], where more details can be found. It needs to be stressed that the NTUA did not participate in the HARTII project and the respective results have been appended to original images copied from [163, 164].

In Table 4.17 the structural dynamics and aerodynamic codes used by the different research centers and the consortium of the HARTII project are listed. All the structural dynamics codes are based on beam–structures modelling, whereas CFD codes are used for the aerodynamic analyses. Short presentation of the most important features of the individual codes is given in the following paragraphs, whereas more details can be found in [163, 164]. It needs to be pointed out that DLR results are extracted by a less expensive comprehensive code that has been found to be the best performing among various comprehensive codes in [165]. Its structural dynamics analysis is based on a modal approach, whereas aerodynamics is estimated through semi-empirical math models for loads calculations implemented within a prescribed wake context. Nevertheless, DLR results are shown to be overall comparable with the high fidelity CFD/beam–FEM methods.

Table 4.17. *Structural dynamics (beam FEM) and aerodynamics (CFD) codes used by different groups of researchers participated in HARTII experimental campaign.*

Researcher's group	Label	Structural Dynamics code	CFD code
U.S. Army aero/flight–dynamics dir.	AFDD1	CAMRADII	OVERFLOW
U.S. Army aero/flight–dynamics dir.	AFDD2	RCAS	Helios
NASA–Langley	NL1	CAMRADII	OVERFLOW
NASA–Langley	NL2	CAMRADII	FUN3D
Georgia Institute of Technology	GIT1	DYMORE4	FUN3D
Georgia Institute of Technology	GIT2	DYMORE2	GENCAS
Konkuk University	KU	CAMRADII	KFLOW
University of Maryland	UM	UMARC	TURNS
German Aerospace Center	DLR	S4	N/A
National Technical University of Athens	NTUA	GAST	HoPFlow

Structural verification

In Table 4.18 the structural dynamics codes used by the different research centers that participated in the HARTII project are listed. All the structural dynamics codes (except from S4 used by DLR) model the rotor blades as beams discretized using FEM. Non–linear phenomena are properly taken into account either implicitly (CAMRADII, DYMORE, RCAS, UMARC), or through non–linear connections in a multi–body context (GAST).

The Campbell diagram (Figure 4.18a) and the natural frequencies computed at nominal rotation speed (Figure 4.18b) show a good agreement in the lower frequencies of the

10 lowest frequency modes depicted. Small differences occur on the higher frequencies at all rotational velocities. These differences are not expected to play a significant role in the aeroelastic results, as the last 3 modes (2nd torsion, 3rd lag and 5th flap) do not contribute significantly to the overall blade deflections. Nevertheless, the NTUA model shows an overall good agreement with other computational predictions at nominal rotational speed, lying systematically within the scatter range. In Figure 4.19, the corresponding mode–shapes are depicted. Again, very good agreement is observed for the first modes whilst minor deviations occur on the higher ones. The fact that the torsional modes begin from a non–zero root deflection is attributed to the pitch spring that is considered in the root of the blade in order to represent the stiffness of the pitch link mechanism that connects the blade with the hub. The pitch spring stiffness value is calibrated so that a non–dimensional 1st torsion frequency of 3.77 is captured. The pitch spring stiffness in the NTUA simulations is set to 800 Nm/rad, whereas the values used by the group participants vary from 400 to 2336 Nm/rad.

Table 4.18. *Structural dynamics codes (short description of discretisation method) used by different groups of researchers.*

Structural Dynamics code	Researcher's group	Developer	Discretization method
CAMRADII	*AFDD*1 *NL*1 *NL*2 *KU*	commercial	*non − linear beam FEM*
DYMORE	*GIT*1 *GIT*2	Georgia Institute of Technology	*multi − body non − linear beam FEM*
RCAS	AFDD2	U.S. Army	*multi − body non − linear beam FEM*
UMARC	UMD	University of Maryland	2nd *order Euler − Bernouli beam FEM*
S4	DLR	German Aerospace Center	*modal approach*
GAST	NTUA	National Technical University of Athens	*multi − body 1st order Timoshenko beam FEM*

(a) *Campbell diagram.*

(b) *Natural frequencies at 100%RPM.*
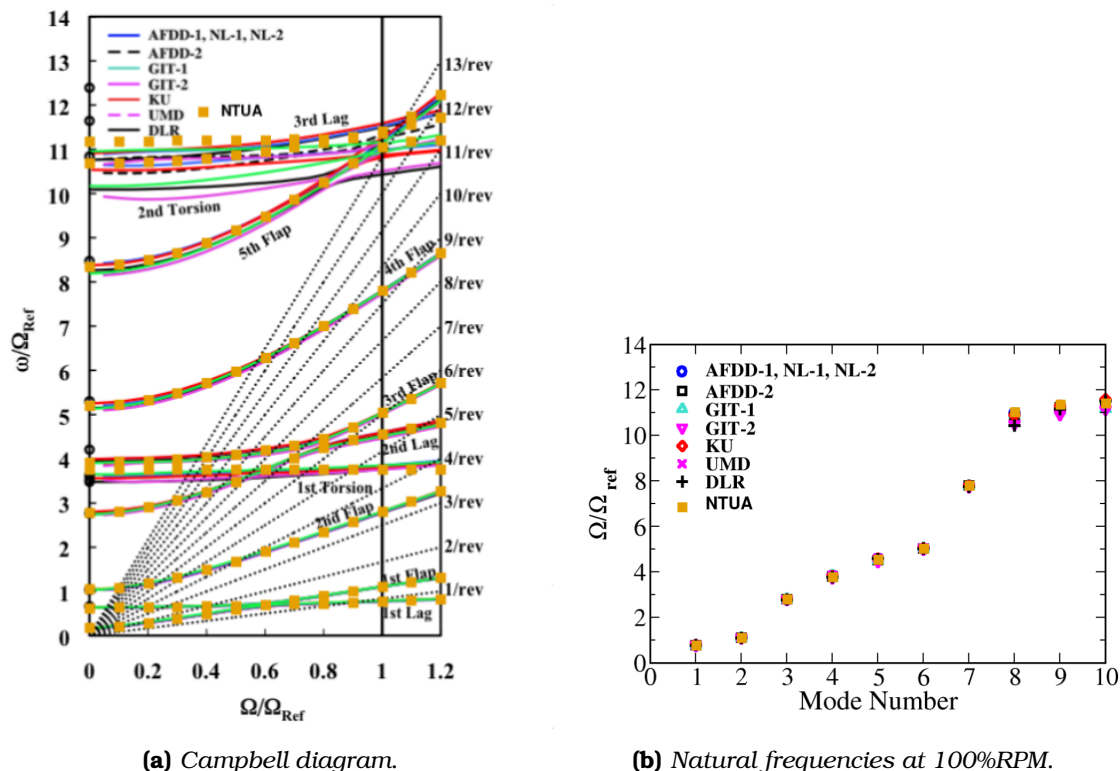
Figure 4.18. *BO105 model rotor natural frequencies predicted by different structural dynamics methodologies (beam based models) among various institutions and research centers. Very good agreement is observed among the predictions computed by all the different structural models, especially for the lower natural frequencies, whilst minor deviations occur on the higher ones.*
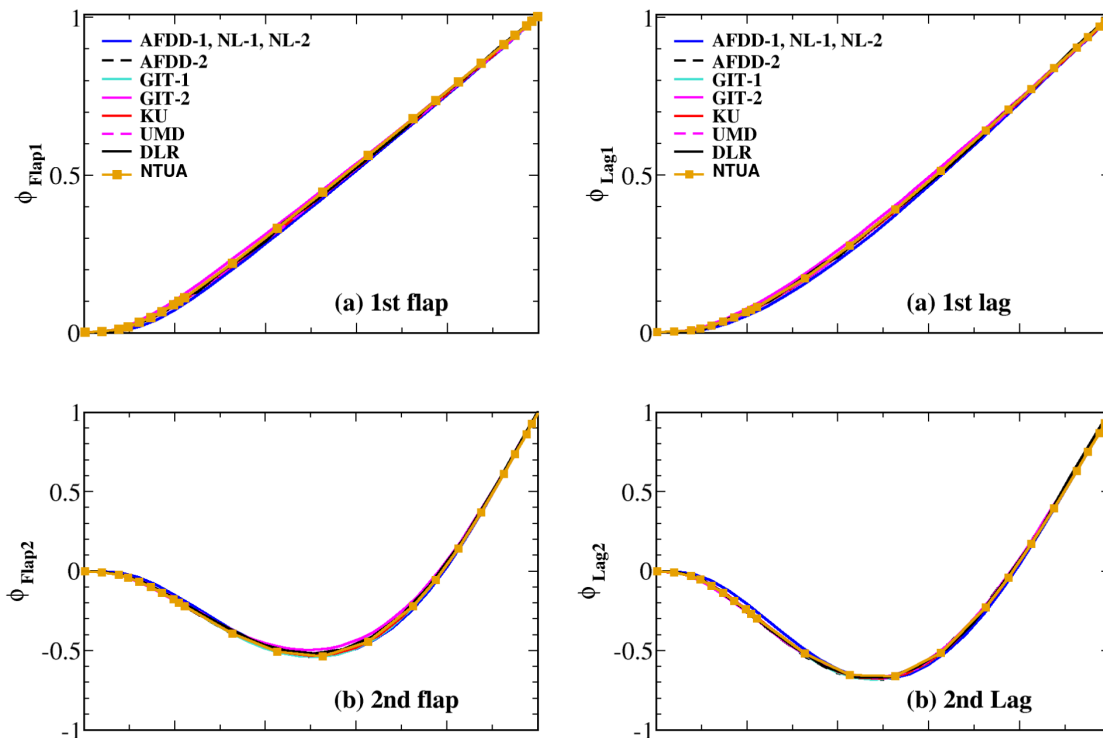
Figure 4.19. *Cont.*
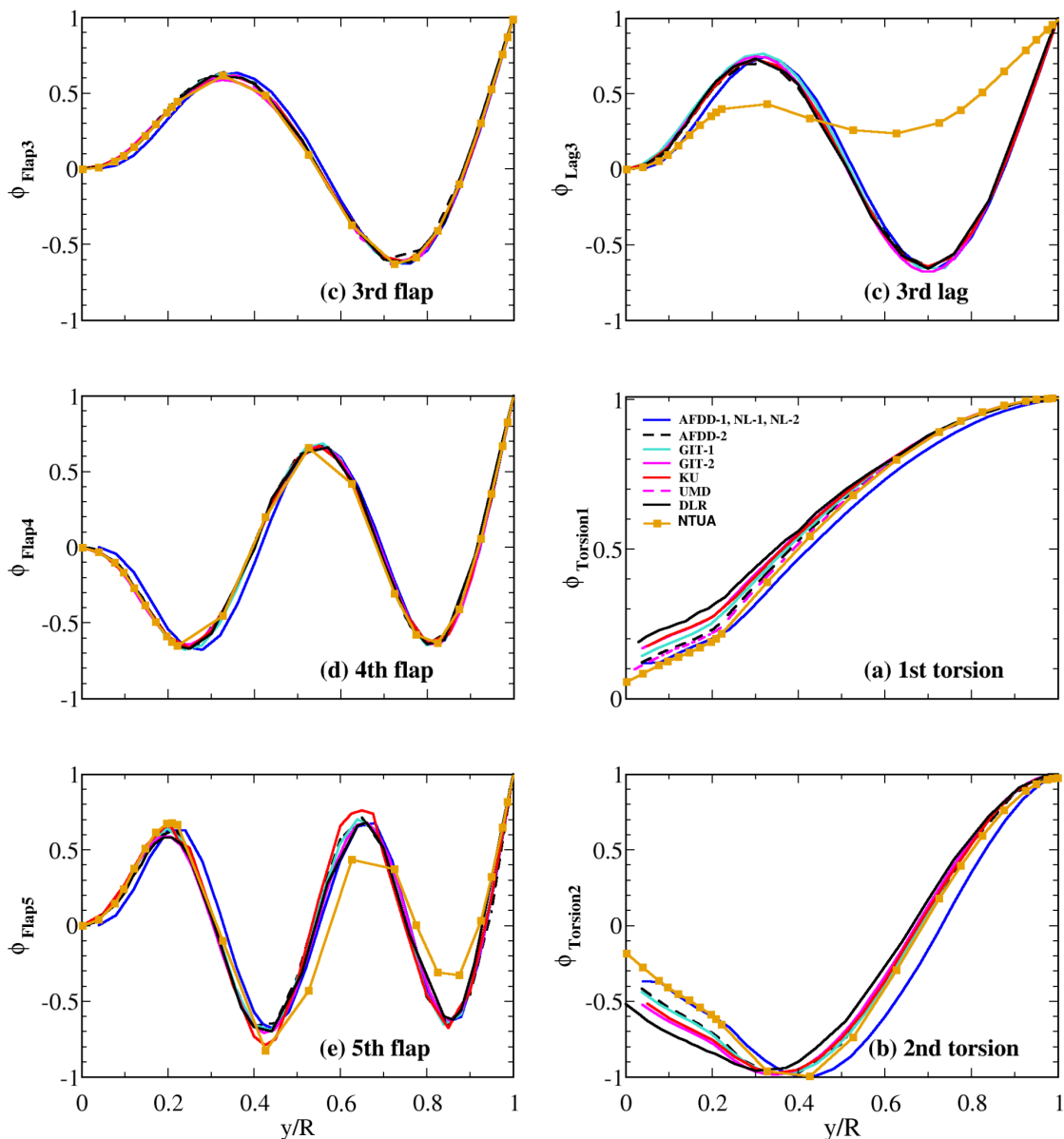
Figure 4.19. *BO105 model rotor mode-shapes predicted by different structural dynamics methodologies (beam based models) among various institutions and research centers. Very good agreement is observed among the predictions computed by all the different structural models. The NTUA predictions deviate from the rest computational models results for the 5th flap and 3rd lag mode. The respective natural frequencies at nominal rotational speed (see Figure 4.18b) are shown to be at least an order of magnitude greater than the lower ones. For this reason, these discrepancies are not considered significant for the total blade deflection prediction in aeroelastic simulations.*

Aeroelastic analysis

In Table 4.19 the CFD based aerodynamic analysis codes used by the different research centers that participated in the HARTII project or later workshops are listed. Both unstructured and structured (high order) codes have been used. Moreover, Overset grids and hybrid Eulerian/Lagrangian approaches have been employed. It is noted that the hybrid CFD codes used by GIT2 (GENCAS) and UMD (TURNS) follow a potential Lagrangian

approach (Free Vortex Wake) in the off–body region, contrary to HoPFlow in which the field communication is applied by solving the Lagrangian formulation of the compressible Navier-Stokes equations.

Table 4.19. *Aerodynamics codes (short description of discretisation method) used by different groups of researchers.*

CFD code	Researcher's group	Developer	Discretization method
OVERFLOW	*AFDD*1 *NL*1	NASA	structured NS
FUN3D	*NL*2 *GIT*1	NASA	unstructured NS
Helios	AFDD2	U.S. Army	*Overset NS unstructured near − body structured off − body*
KFLOW	KU	Konkuk University	*Overset NS unstructured near − body structured off − body*
GENCAS	GIT2	Georgia Institute of Technology	hybrid NS/FW
TURNS	UMD	University of Maryland	hybrid NS/FW
HoPFlow	NTUA	National Technical University of Athens	hybrid NS/PM

In Table 4.20 the mean values of blade loads (aerodynamic and structural loads) and elastic deflections predicted by different codes are compared against the measured values. Significant differences in the mean value of the aerodynamic twisting moment ($C_M M^2$) are reported for most CFD based computational predictions. As explained before (paragraph 4.2.2), this is attributed to the difficulty (excessive cost) in properly resolving the tab that has been used in the airfoil profile of the rotor blades in order to confine the increase in C_M with the angle of attack. This, in turn, leads to a big level difference in the mean value of the structural twisting moment (M_{tw}) and consequently in the torsion angle at the blade tip (Θ_{tors}). The differences in the torsion angle (up to $\simeq 1.5°$) are bridged (at least concerning the geometric angle of attack) by adjusting the collective pitch during the trim procedure. Moreover, differences between predictions and measurements are reported in the mean values of the aerodynamic normal force ($C_N M^2$) at 87% radial station. The big differences between measurements and computational predictions regarding the mean values of structural bending moments (M_{flap} and M_{lag}) cannot be justified by the differences in the aerodynamic forces. In [163, 164, 165] they are attributed to the calibration of strain gauges on non–rotating blades in the experimental set–up. It is, thus, suspected that a bias due to centrifugal forces may be undergone in measured values. For this reason, the differences in structural bending moments are not reflected in the tip flapwise deflection (U_{flap}), where an overall good agreement is reported. In the tip lead–lag deflections (U_{lag}), measurements lag with respect to all CFD predictions

(positive deflection is in the lag direction). This is common with the forward flight speed cases of the HeliNoVi experimental campaign showed in Section 3.1.2.3. In [163, 164, 165] it is mainly attributed to the technique used to measure blade deflections in these experimental campaigns. Stero Pattern Recognition (SPR) that was used for the first time in the HARTII and HeliNoVi projects, has been repeatedly reported to show a consistent 2–4 cm ($\simeq$ 1 − 2%) translational offset in the lag direction with respect to numerous and of varying fidelity computational method results. In [10], the flexibility of the drive train system and the hub, which are regarded as infinitely stiff in the simulations, are considered as extra sources for discrepancies between measurements and predictions. The "soft" drive train system used in the experimental campaign allows for a torsion angle at the end of the shaft that is dictated by the mean value of the lead–lag bending moment at the root of the blades. In turn, a positive (towards the lag direction) level shift of the blade tip deflections is to be expected.

Table 4.20. *Mean values of non-dimensional aerodynamic loads (normal force $C_N M^2$ and twisting moment $C_M M^2$ at 87% of the blade), structural moments (flapwise moment M_{flap} and lead-lag moment M_{lag} at 17% of the blade and twisting moment M_{tw} at 33% of the blade) and elastic deflections (flapwise displacement U_{flap}, lead-lag displacement U_{lag} and torsion angle Θ_{tors} at blade tip). Comparison between experimental measurements and computational predictions extracted from CFD based aeroelastic simulations (structural dynamics analyses are based on beam models) performed by various institutions and research centers.*

|	$\overline{C_N M^2}$ [−]	$\overline{C_M M^2}$ [−]	$\overline{M_{flap}}$ [Nm]	$\overline{M_{lag}}$ [Nm]	$\overline{M_{tw}}$ [Nm]	$\overline{U_{flap}}$ [$z_{el}/R * 100$]	$\overline{U_{lag}}$ [$x_{el}/R * 100$]	$\overline{\Theta_{tors}}$ [°]
AFDD1	0.0775	−0.0039	3.87	51.67	−0.01	−0.914	−0.679	−1.894
AFDD2	0.0766	−0.0032	2.56	47.04	−7.85	−0.955	0.783	−1.438
GIT1	0.0723	−0.0035	−3.14	0.00	−4.49	−0.939	0.000	−1.995
GIT2	0.0787	−0.0046	−1.61	56.78	−5.69	−0.997	0.675	−2.384
KU	0.0800	−0.0027	−0.84	−9.94	−3.49	−0.879	−0.354	−1.232
NL1	0.0782	−0.0040	3.19	57.21	48.36	−0.915	−0.460	−1.922
NL2a	0.0820	−0.0029	3.41	58.12	−3.62	−0.777	−0.318	−1.151
NL2b	0.0814	−0.0030	3.52	58.12	−3.71	−0.778	−0.307	−1.167
UMD	0.0892	−0.0025	−13.62	−2.94	−2.94	−0.657	−0.244	−1.204
DLR	0.0863	−0.0027	−12.48	15.02	−1.31	−1.036	1.345	−0.724
NTUA	0.0821	−0.0043	−8.71	65.98	−5.54	−0.792	−0.317	−2.519
Experiment	0.0902	−0.0026	−9.27	−10.25	−2.90	−0.871	1.399*	−1.09*

* Averaged over all four blades.

In Figure 4.20, the azimuthal variation of the non–dimensional normal aerodynamic force (a) and twisting moment (b) at 87% radial station is shown. Due to the big level differences reported in Table 4.20, mean values have been removed, so that the overall trend is assessed. In Figure 4.20a, it is shown that the NTUA (along with GIT1 and NL2) underestimates the $C_N M^2$ in the 1st quadrant and fails to predict the strong BVI induced fluctuations. The trend in the $60° − 120°$ is not effectively predicted and the local peak is predicted with an $\simeq 20°$ phase lag. Nevertheless this is in line with most computational predictions. The overestimation of the minimum (in the $150° − 180°$ range) and the maximum (at $\simeq 250°$) in the NTUA predictions originates in the removal of the mean

value. Otherwise, very good agreement is reported in Figure 4.17a. The BVI is effectively predicted in the 4th quadrant, whereas the local maximum close to 345° is slightly shifted ($\simeq 10°$) towards higher azimuth angle compared to measurements and other computational predictions. An overall good agreement is observed in $C_M M^2$ shown in Figure 4.20b between the NTUA results and measurements. The overall trend is effectively predicted except from the $120° - 210°$ dip which is flattened in the NTUA predictions, yet within the range of other computational predictions. Nevertheless, the BVI in the 1st and 4th quadrants are in phase with measurements and fairly predicted concerning their strength.
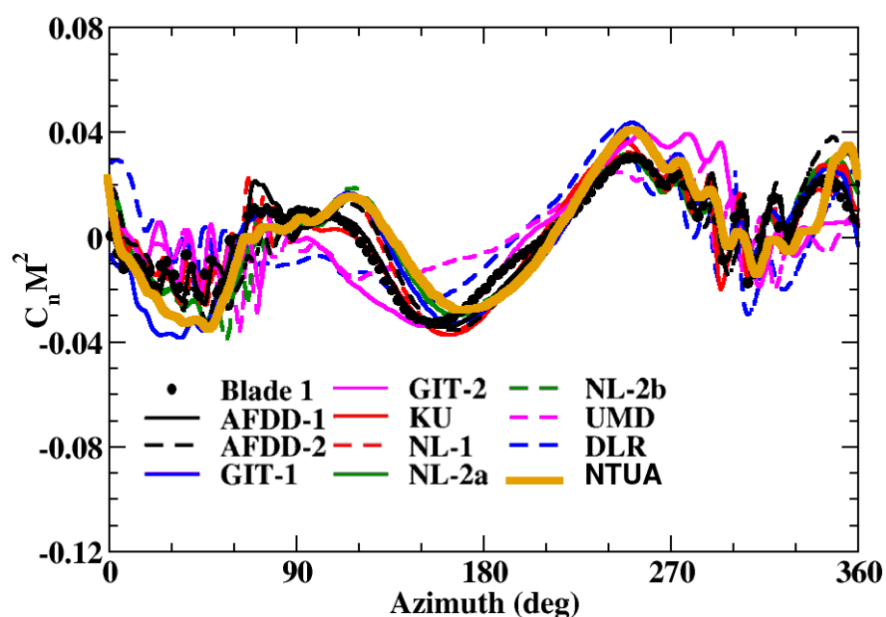
(a) *Non–dimensional normal aerodynamic force at 87% radial station. Means removed. The NTUA predictions underestimate the normal force over the 1st quadrant compared to measurements. However, it is still within the range of other computational predictions. The BVI induced fluctuations are almost completely damped. Better agreement is shown in the 2nd and 3rd quadrants where the level is fairly predicted, but with an $\simeq 20°$ phase lag from measurements, which however is in line with most computational predictions. BVI in the 4th quadrant is effectively represented but slightly less pronounced compared to measurements. Local maximum close to 345° is overestimated and slightly shifted ($\simeq 10°$ lag) to measurements and other computational predictions.*

Figure 4.20. *Cont.*
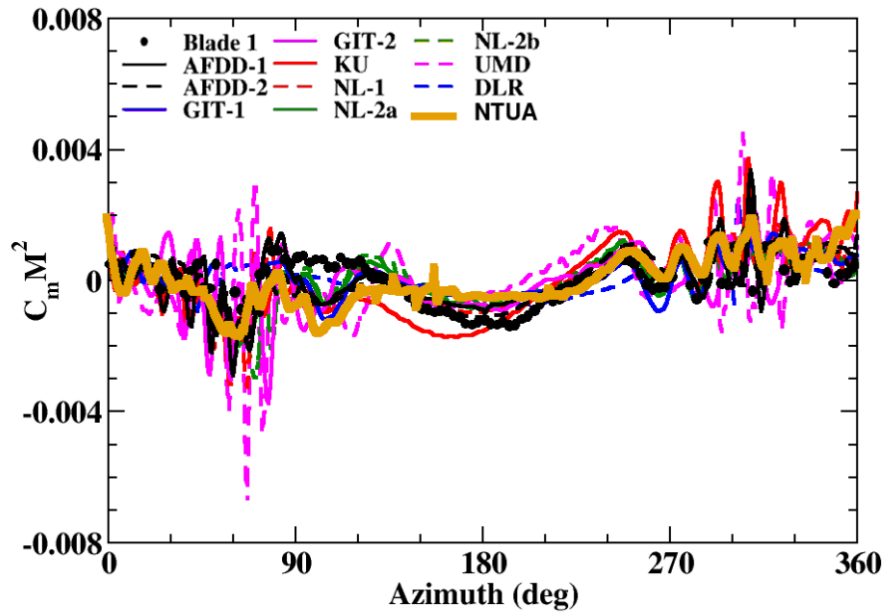
(b) *Non-dimensional aerodynamic twisting moment at 87% radial station. Means removed. The variation trend is fairly predicted, apart from the $120° - 210°$ curvature which is almost completely flattened in the NTUA and most computational results. The NTUA results slightly under-predict the twisting moment in the range $70° - 135°$ and over-predict it in $345° - 5°$. However, it is still within the range of other computational predictions. The BVI in the 1st and 4th quadrants are fairly predicted.*

Figure 4.20. *Non-dimensional normal aerodynamic force (a) and twisting moment (b) at 87% radial station. Comparison between experimental measurements and computational predictions extracted from other CFD based aeroelastic simulations. An overall good agreement is observed against measurements. In most cases where discrepancies occur, the NTUA results are in line with most of the other computational predictions.*

In order to better assess the differences seen in the azimuthal variation of the aerodynamic loads, the wake geometry generated by the simulations needs to be examined. The position of the vortex structures, especially of the tip vortices, is crucial for the accurate estimation of the aerodynamic loading in strong BVI regions. In descent cases, these are usually found in the 1st and 4th quadrants, where the blades are approximately parallel to the vortices. In Figures 4.21 and 4.22, the wake structures generated in the NTUA simulations are depicted at two snap–shots when the 1st blade is at 20° (sub–figures a) and 70° (sub–figures c) azimuthal position. The location of specific tip vortices at the same azimuthal positions was experimentally identified in various lateral planes ($y/R = ±0.4, +0.55, ±0.7, ±0.85, ±0.97$) of the advancing (+) and retreating (−) side by analyzing PIV maps in order to estimate the vortex centers. However, only the vortex center locations at $y/R = ±0.7$ are presented herein, as a higher quality camera was used for image capturing in these planes. The vortices position in the simulations have been identified as the center of the largest vortices in the corresponding planes through visual inspection. Therefore, an additional error due to personal judgment is to be expected. The specific tip vortices tracked are defined in [13] and may be seen in red circles in Figures 4.21a, 4.21c, 4.22a and 4.22c. The vortex center positions are given with respect to the local hub coordinate system.

In Figure 4.21b, the measured and computationally predicted position of the tip vortices at $y/R = +0.7$ (advancing side) is shown. The fact that the tip vortices predicted by the NTUA, GIT1 and NL2 in the 1st quadrant (captured at $\Psi = 20°$ azimuthal position) are located $\simeq 5\%R$ lower compared to the measured ones explains why these code fail to predict BVI and they overall underestimate $C_N M^2$ in the corresponding region. Moreover the 4th vortex center of the specific azimuthal position is untraceable in the NTUA predictions. This is attributed to the strong root vortices that are emitted from the blades cut–out (in Figure 4.12a it is shown that the inner part of the blades and the hub are not included in the NTUA simulations), that according to Figure 4.21a seem to drastically interfere with the tip vortices and either partially (3rd tip vortex), or completely (4th tip vortex) break their structure. This assumption is amplified by the fact that the blade holders that connect the blades with the hub and the top of the hub cylinder have been also neglected in GIT1 and NL2 simulations (see Figure 4.23), thus, allowing for root vortices to be emitted from the inner parts of the blades. Better agreement is shown in the tip vortices that are located in the 2nd quadrant (captured at $\Psi = 70°$ azimuthal position). However, again the 2nd and 3rd tip vortices are placed below the measured ones. This explains the different trend compared to measurements of the aerodynamic loads in the $60° − 90°$ region.

In Figure 4.22b, the measured and computationally predicted position of the tip vortices at $y/R = −0.7$ (retreating side) is shown. Very good agreement is observed in the location estimation of the tip vortices at both the 3rd (captured at $\Psi = 20°$ azimuthal position) and 4th (captured at $\Psi = 70°$ azimuthal position) quadrants. The fact that the 2nd tip vortex of the 4th quadrant is untraceable in the NTUA and GIT1 predictions is again associated with the strong root vortices and explains the phase lag of the last $C_N M^2$ peak (slightly before $360°$) in the NTUA predictions. Nevertheless, the overall good agreement in the retreating side is not unexcepted, due to the more consistent results of the aerodynamic loads predictions in the corresponding region.

Finally, it also needs to be stressed that omitting the fuselage in the NTUA simulations is an important aspect concerning BVI events, especially in the advancing side. Tip vortices experience a displacement due to the presence of fuselage that affects their positioning with respect to the hub, thus, influencing the strength of BVI. Another possibly significant factor is the correction of the angle of attack that is usually applied in order to account for the wind tunnel interference in the rotor thrust estimation. Such engineering corrections have been found to be very effective when it comes to integrated hub loads predictions. However, their effect in more sensitive aspects, such as the tip vortices positioning with respect to the rotor hub, has not been yet thoroughly investigated.
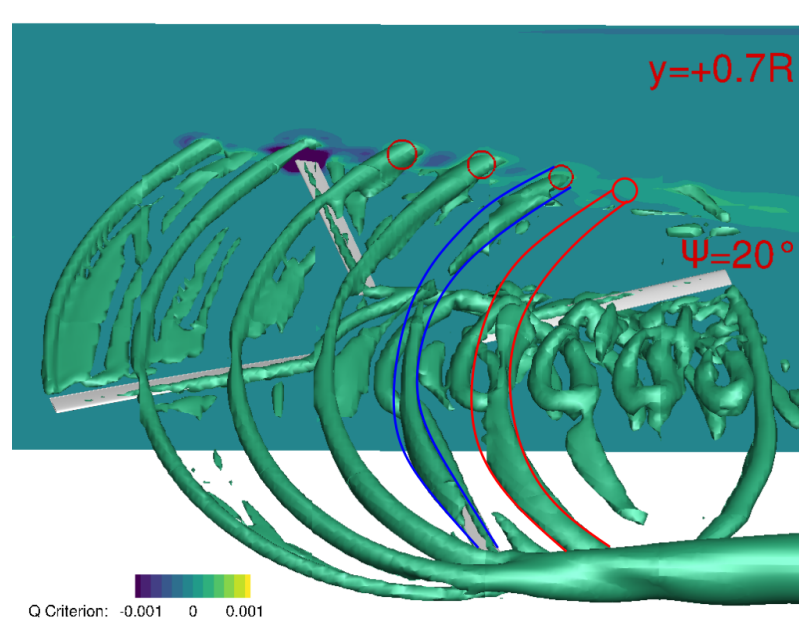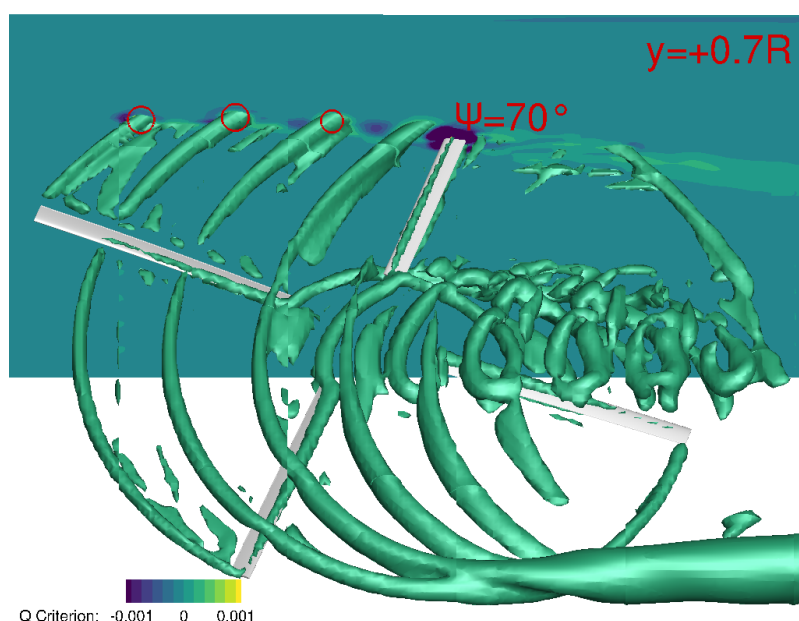
(a) *Visualisation of the wake structures created in the NTUA simulations under Q-criterion and the respective contour at 70% lateral position of the advancing side (y = 0.7R), when the 1st blade is at 20° azimuth angle. Strong root vortices are emitted from the aerodynamic root cut-out of the blades. Root vortices seem to drastically interfere with the tip vortices and break their structure. This is illustrated in the 3rd and 4th tip vortex cases, where their trajectories are partially (3rd tip vortex depicted in blue line) or fully (4th tip vortex estimated in red line) broken by the root vortices. Consequently, they are expected to be miss-located compared to measurements.*
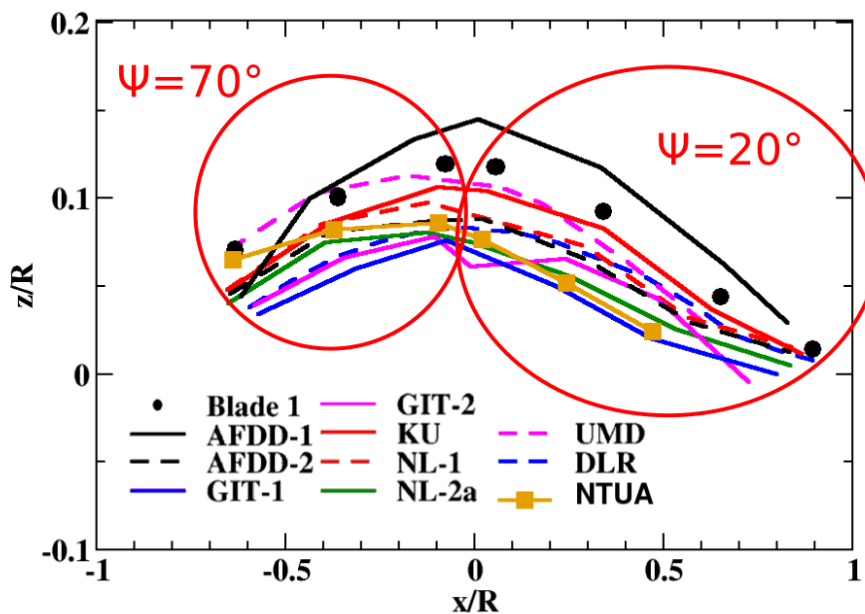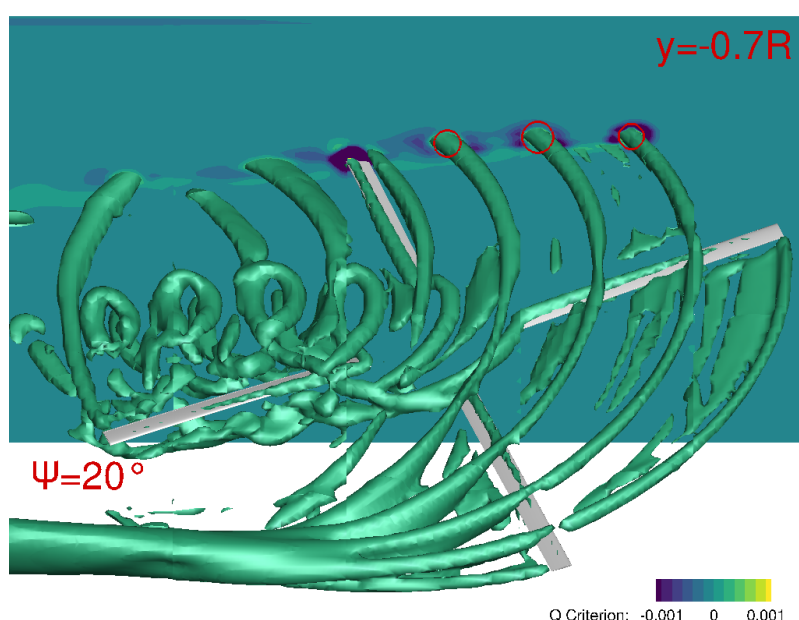

(b) *Position of the tip vortices, expressed in the hub local coordinate system, at 70% lateral position of the advancing side (y = 0.7R), when the 1st blade is at 20° and 70° azimuth angles. Most of the tip vortices traces that lie within the 1st quadrant (x/R ≥ 0), where BVI is encountered, are miss-located in the NTUA simulations, placed ≃ 5%R lower than the measured ones, yet within the range of other computational predictions. Better agreement is observed in the 2nd quadrant (x/R ≤ 0).*

Figure 4.21. *Cont.*

(c) *Visualisation of the wake structures created in the NTUA simulations under Q–criterion and the respective contour at 70% lateral position of the advancing side (y = 0.7R), when the 1st blade is at 70° azimuth angle. Root vortices do not heavily interfere with the tip vortices. Consequently, they are expected to be located correctly.*

Figure 4.21. *Position of the tip vortices in the advancing side (y=0.7R), when the 1st blade is at 20° and 70° azimuth angles. Visualisation of the wake structures created in the NTUA simulations (a,c) and comparison between experimental measurements and computational predictions extracted from various CFD based aeroelastic simulations (b).*

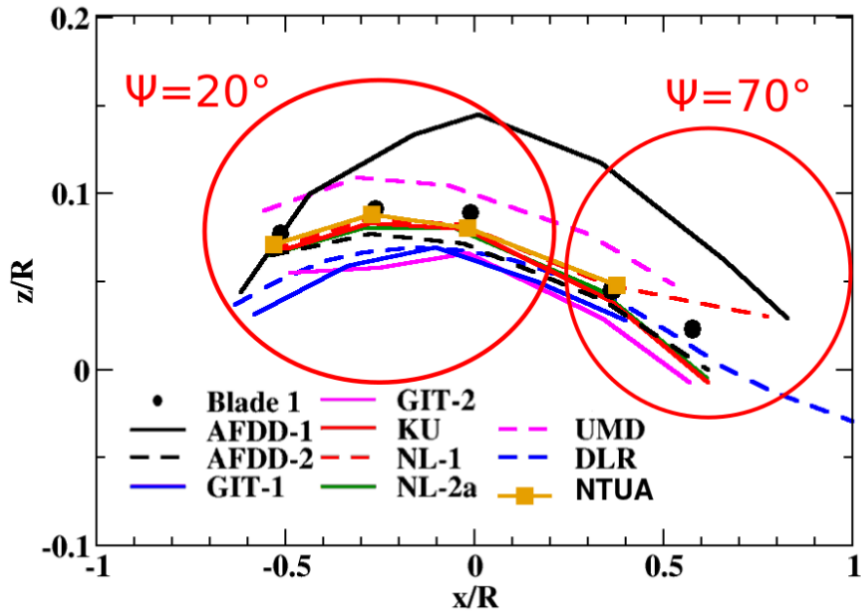**(a)** *Visualisation of the wake structures created in the NTUA simulations under Q–criterion and the respective contour at 70% lateral position of the retreating side (y = −0.7R), when the 1st blade is at 20° azimuth angle. Root vortices do not heavily interfere with the tip vortices. Consequently, they are expected to be located correctly.*

Figure 4.22. *Cont.*

(b) *Position of the tip vortices, expressed in the hub local coordinate system, at 70% lateral position of the retreating side (y = −0.7R), when the 1ˢᵗ blade is at 20° and 70° azimuth angles. Most of the tip vortices positions are fairly predicted by the NTUA. The 5ᵗʰ tip vortex tracked does not intersect with the plane of interest.*
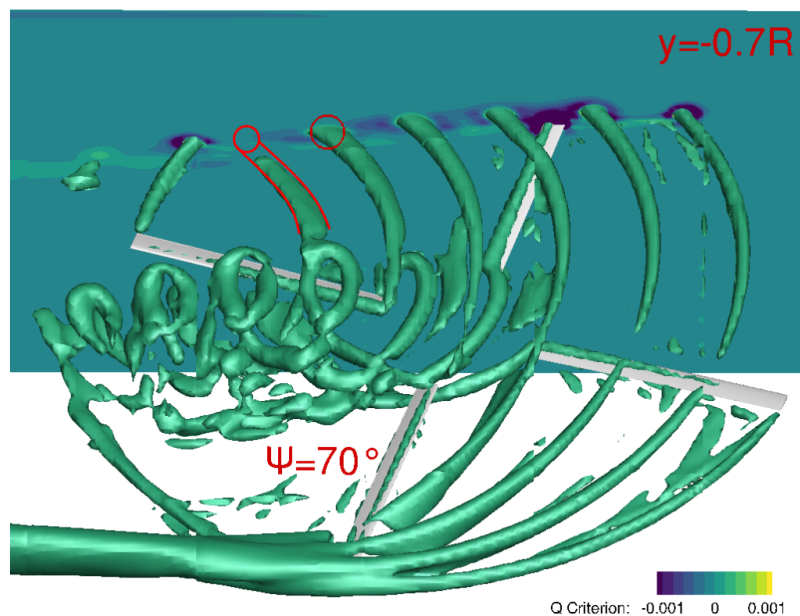
(c) *Visualisation of the wake structures created in the NTUA simulations under Q–criterion and the respective contour at 70% lateral position of the retreating side (y = −0.7R), when the 1ˢᵗ blade is at 70° azimuth angle. The 2ⁿᵈ tip vortex is partially diffused and does not intersect with the plane of interest.*

Figure 4.22. *Position of the tip vortices at 70% lateral position of the retreating side (y = −0.7R), when the 1ˢᵗ blade is at 20° and 70° azimuth angles. Visualisation of the wake structures created in the NTUA simulations (a,c) and comparison between experimental measurements and computational predictions extracted from various CFD based aeroelastic simulations (b).*
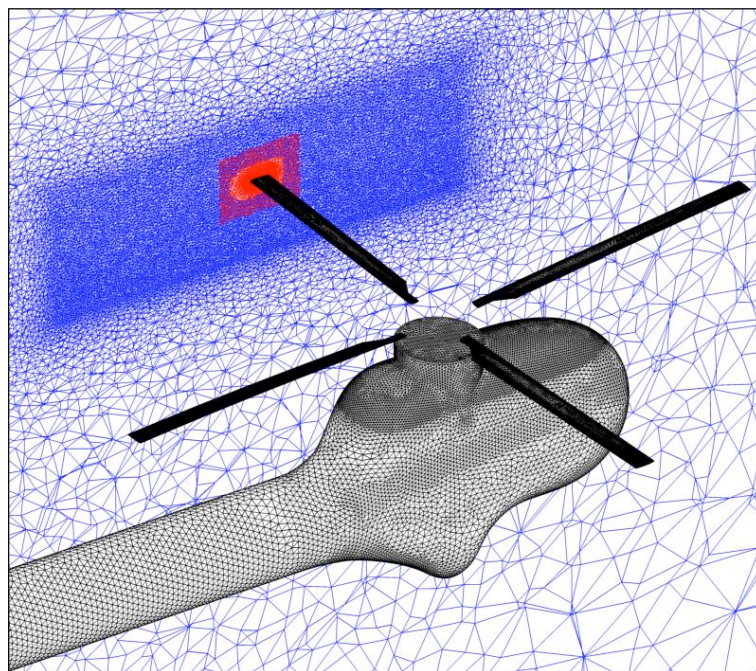
189

Figure 4.23. *Grid set–up employed in FUN3D aeroelastic simulations performed by GIT1 and NL2. Image copied from [163, 164]. The inboard portions of the blades (transition from the aerodynamic root cut–out to the blade holder) are properly modelled. The blade holders (elliptical or cylindrical sections) that connect the blades with the hub and the top of the hub cylinder have been neglected. Consequently, root vortices are expected to be emitted from the inner parts of the blades.*

In the following Figures presenting the structural moments, only the strain gauges measurements of the 1st blade are depicted. Hence, an estimation of the blade to blade differences can only be made through the respective differences in deflections measurements.

In Figure 4.24, the lead–lag bending moment at 17% of the blade (a) and the corresponding deflection at the blade tip (b) are shown. Due to the big level differences reported in Table 4.20, mean values have been removed and emphasis is placed on load variations. Good agreement is observed among the NTUA results, measurements and other computational predictions. The phase of the dominant once per rotor revolution (1/rev) harmonic variation in the lead–lag signal is well predicted in the lead–lag moment (see Figure 4.24a). The corresponding amplitude is slightly overestimated, which however is typical for most simulations. The flattened plateau in the peak region is effectively predicted, although slightly narrowed compared to measurements. Higher harmonics are almost completely damped in the NTUA and most of the other simulations, thus, indicating increased numerical diffusion and damping. As far as the NTUA simulations is concerned, this can be justified by the use a global Rayleigh type structural damping [166] which cannot reproduce correctly the exact modal damping of higher frequency modes. A miss–placement of a higher lead–lag mode close to a harmonic of the rotational frequency in the experimental set–up could be also possible. Concerning the lead–lag deflection (see Figure 4.24b) good agreement is observed both in the phase and the amplitude of the 1/rev harmonic. Higher harmonics seen in the lead–lag bending moment are less pronounced herein.

In Figure 4.25, the flapwise bending moment at 17% of the blade (a) and the corresponding deflection at the blade tip (b) are shown. Due to the big level differences reported in Table 4.20, the mean value of the flapwise moment has been removed in Figure 4.25a and emphasis is placed on load variations. Great differences in amplitude and phase are shown among many computational predictions and experimental measurements. This is attributed to the low (in absolute) hub moments (see Table 4.10) that, in turn, minimize the amplitude of the flapwise moment, rendering it very sensitive even to minor discrepancies. This explains the phase differences seen among measurements and many computational predictions. In particular, the $\simeq 55°$ phase lag of the NTUA results for the high azimuth angle peak (measured at $\simeq 340°$) originates in the corresponding phase lag of $C_N M^2$ (see Figure 4.20a). Nevertheless, the overall amplitude and the 2/rev trend seen in measurements is effectively reproduced in the NTUA results. In the flapwise deflection depicted in Figure 4.25b, good agreement is shown in the predicted mean value, whereas the 1/rev amplitude is slightly underestimated in the NTUA predictions. The 2/rev behaviour seen in measurements is predicted but slightly underestimated in the NTUA results. The phase differences seen herein are in line with the phase differences reported in the flapwise moment, but slightly shifted towards higher azimuth angles (phase lag) due to inertial effect.

In Figure 4.26, the twisting moment at 33% of the blade (a) and the corresponding torsion angle at the blade tip (b) are shown. Due to the big level differences reported in Table 4.20, the mean value of the twisting moment has been removed in Figure 4.26a and emphasis is placed on load variations. The overall amplitude and phase are fairly predicted by the NTUA. The excessive reduction shortly before 90° originates in the corresponding underestimation of $C_M M^2$ in the vicinity of 60° (see Figure 4.20b). Respectively, the plateau behaviour in the $120° - 180°$ region originates in the flattening of the dip in $C_M M^2$ in the same region. In the torsion angle depicted in Figure 4.26b an $\simeq 1.5°$ difference is reported compared to measurements. The torsion level predicted by the NTUA is still comparable to the one predicted by other simulations (GIT1,GIT2,NL1,AFDD1) and originates in the level difference of $C_M M^2$ reported in Table 4.20. The overall amplitude and phase are fairly predicted by the NTUA, in line with the twisting moment reports. The excessive torsion angle shortly before 90° is again in line with the differences shown in the corresponding moment.
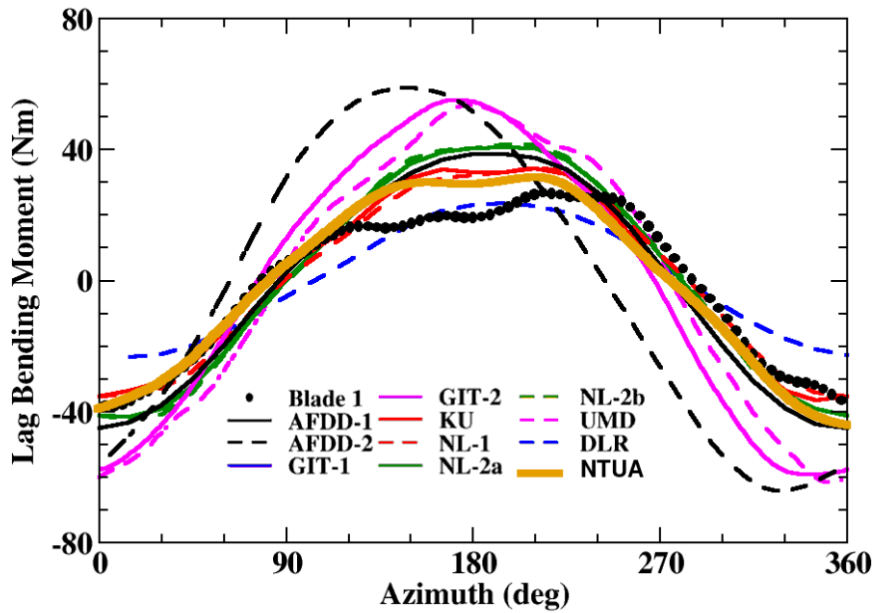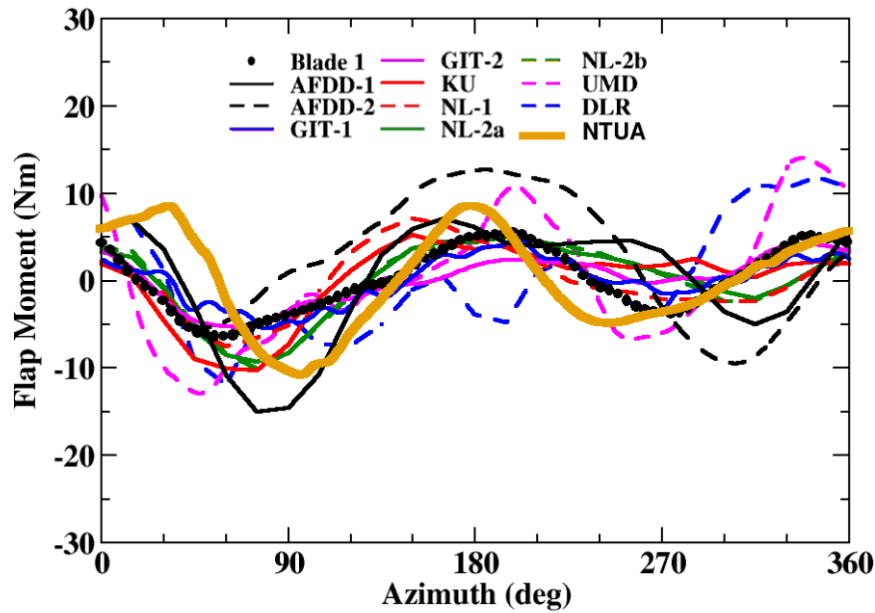
(a) *Lead-lag bending moment at 17% radial station. Positive in the lag direction. Mean removed. 1/rev amplitude is slightly overestimated in the NTUA results as a result of higher peak prediction (in the range 90° − 270°) compared to measurements, which however is in line with most computational predictions. The flattened plateau behaviour is effectively predicted in the NTUA results, but in a more narrow region compared to measurements. Again, this is in line with most computational predictions. Higher harmonics seen in measurements are less pronounced in all computational results.*
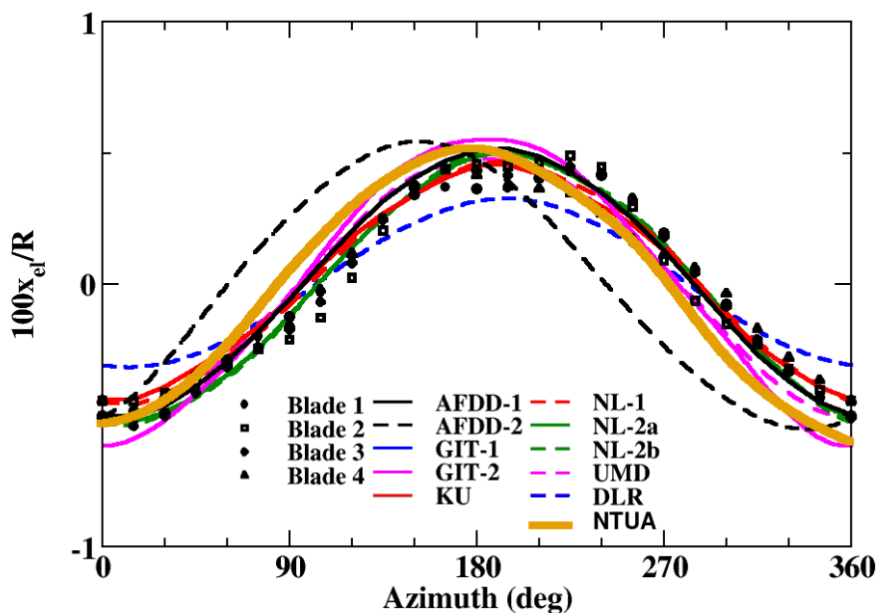
(b) *Lead-lag deflection at blade tip. Positive in the lag direction. Mean removed. Good agreement is observed both in the amplitude and phase of the 1/rev harmonic among experimental measurements, the NTUA predictions and most of the other computational results. Higher harmonic variations shown in the lead-lag bending moment measurements are less pronounced herein.*

Figure 4.24. *Lead-lag bending moment at 17% radial station (a) and tip deflection (b). Positive in lag direction. Comparison between experimental measurements and computational predictions extracted from various CFD based aeroelastic simulations. An overall good agreement is observed against measurements. In most cases where discrepancies occur, the NTUA results are in line with most of the other computational predictions.*

(a) *Flapwise bending moment at 17% radial station. Mean removed. 2/rev behaviour of the measured signal is effectively predicted, but slightly overestimated by the NTUA. Amplitude and phase differences form measurements are also reported in many computational predictions. This is attributed to the rotor trim targeting for zero hub moments that leads to minimization of flapping moment amplitude.*
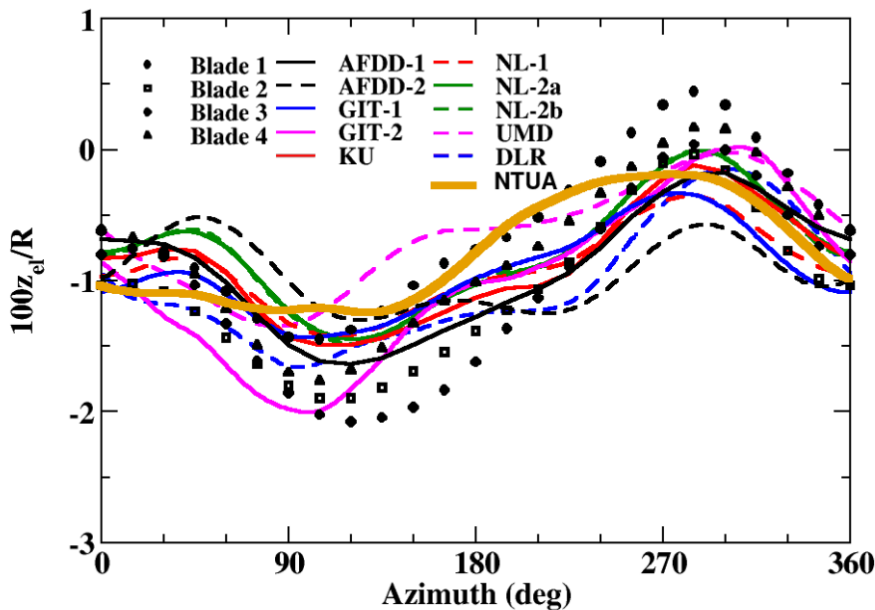
(b) *Flapwise deflection at blade tip. Good agreement is shown in the mean value between measurements and all the different computational models predictions. A dominant 1/rev behaviour is observed along with a 2/rev of much lower amplitude. 1/rev and 2/rev amplitudes are slightly underestimated by the NTUA. Phase differences form measurements are also reported in the NTUA and many other computational predictions.*

Figure 4.25. *Flapwise bending moment at 17% radial station (a) and tip deflection (b). Deflection is relative to pre-cone. Comparison between experimental measurements and computational predictions extracted from various CFD based aeroelastic simulations. Dominant 1/rev and 2/rev harmonics are effectively predicted in the NTUA results. However, amplitude and phase differences form measurements are reported, which is common for most computational predictions.*
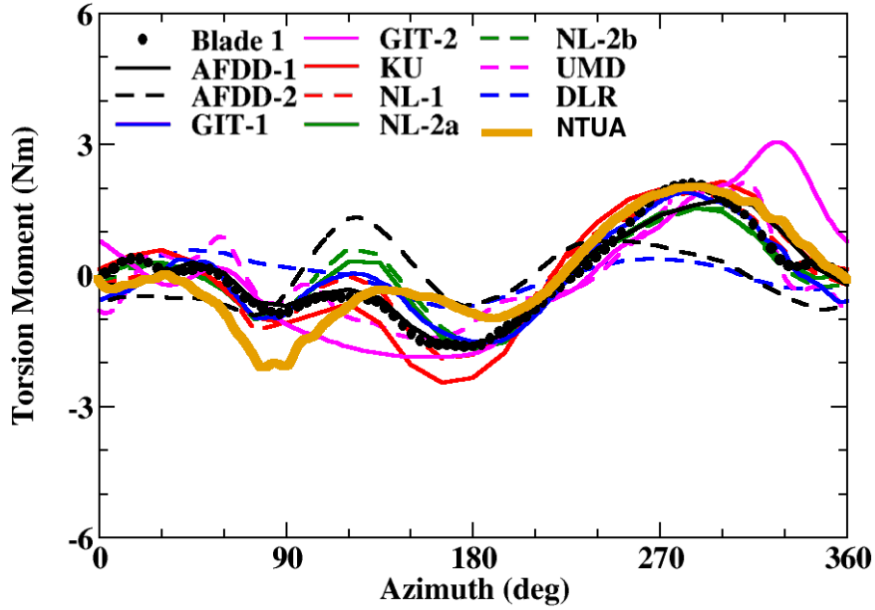
(a) *Twisting moment at 33% radial station. Mean removed. A fair prediction is observed by the NTUA and most of the other computational predictions. The amplitude is overall predicted well. The excessive reduction close to $90°$ and the flattened curvature in the $120° − 180°$ region predicted by the NTUA that are directly related to different behaviour of the predicted $C_M M^2$ from the measured on (see Figure 4.20b) in the same regions.*
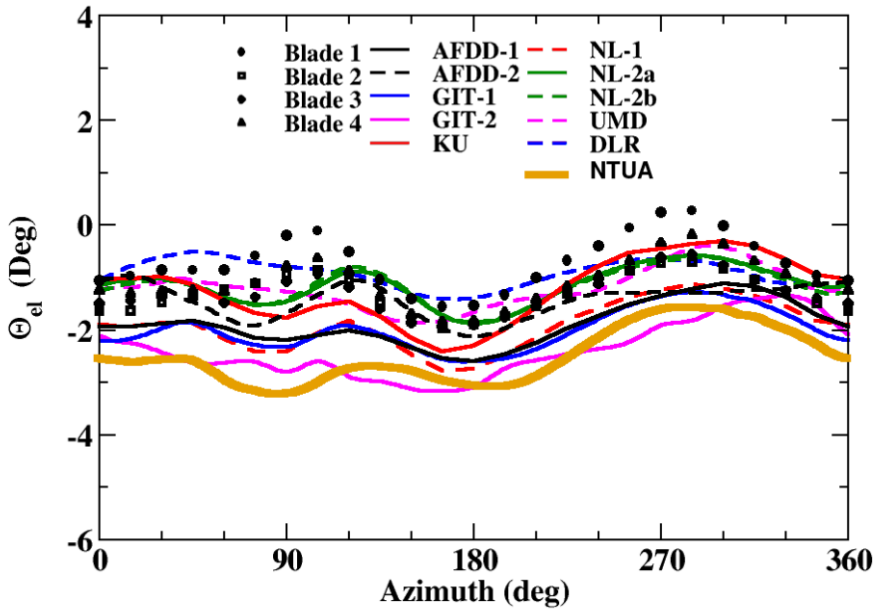
(b) *Torsion angle at blade tip. An $\simeq 1.5°$ level difference is reported between the NTUA predictions and measured data, which originates in the respective mean offset of $C_M M^2$ (see Table 4.20). Small improvement from grid refinement is shown in Section 4.2.2. The NTUA predicted mean value is still comparable to other computational results (GIT,NL1,AFDD1). The amplitude and phase are overall predicted well.*

Figure 4.26. *Twisting moment at 33% radial station (a) and tip torsion angle (b). Tip torsion is relative to pre-twist and control angles. Comparison between experimental measurements and computational predictions extracted from various CFD based aeroelastic simulations. An overall good agreement is observed against measurements and other computational predictions.*

4.3 Conclusions

In this chapter, the accuracy of the hybrid CFD solver HoPFlow is assessed in the aerodynamic analysis of an axial flow case around the model WT rotor used in the New MEXICO experimental campaign [11, 12]. Moreover, the coupled GAST–HoPFlow solver is validated in the aeroelastic analysis of the model BO105 helicopter rotor operating in the conditions of the Base–Line descent case of the HARTII experiment [13]. In this way, this newly composed CFD based aeroelastic analysis tool is evaluated over a wide part of the sub–sonic region. On the lower Mach values (in the root region of the WT rotor) re–circulations may appear, while the onset of weak shock–waves is to be expected near the helicopter's blades tip (higher Mach values).

First, a detailed investigation is performed on the effect of the numerical parameters of HoPFlow on the produced results of the WT aerodynamic analysis. It is found that under a PM discretisation with 5 nodes per chord length (in this analysis the characteristic chord length is assumed to be the one at 75% of the blade), HoPFlow predicts the loading of rotor blades with great accuracy. HoPFlow results are compared against experimental measurements and predictions produced by MaPFlow, the Eulerian counterpart of HoPFlow, and other CFD solvers. Results are presented as integrated rotor loads, radial distribution of aerodynamic forces and moments, pressure distributions at various span–wise positions along the rotor blades and axial flow distributions along a line being at a constant radial positions. Deviations from the measured loads are observed in the middle region of the blade. However, very good agreement is shown with all the other CFD solvers predictions. These discrepancies are attributed to the abrupt change of the airfoil profile used in the mid–span region and its much different zero lift angle compared to the preceding (root) and the following (tip) airfoils. Hence, the accuracy of the hybrid solver HoPFlow in the predicted pressure distributions along the whole blade span is found to be comparable with the one of standard Eulerian CFD codes. This indicates that the near–body flow–field (boundary layer solution) is described in detail and, thus, confirms that the coupling method that determines the boundary conditions for the confined Eulerian grid is adequate and consistent. Furthermore, it is shown that the Lagrangian formulation followed in the off–body region reduces numerical diffusion significantly compared to standard Eulerian solvers. For this reason, the wake vortices are resolved more effectively and the near–wake deficit is formed in greater accuracy (in better agreement with the wind tunnel measurements). Nevertheless, the cost of the hybrid approach is overwelming for a single rotor simulation. A remedy for moderating the computational cost is the application of multi–level/telescopic PM grids [42], finer in the vicinity of the body and coarser in the far–domain.

A detailed numerical investigation of HoPFlow parameters is also performed for the aeroelastic analysis of the helicopter rotor. In this case, it is found that a fine grid resolution under a constant characteristic length of $c/12$ (c is the chord length of the helicopter rotor blades that remains constant over the whole blade span) is needed in the region close to the rotor. However, due to the use of uniform PM grids in the current HoPFlow implementation, such a fine discretization over the whole computational domain

renders the cost of this kind of numerical set–ups prohibitive. For this reason, the far–domain is discretized under a PM with a characteristic length of $c/4$ and the required grid refinement in the region close to the rotor is applied on the Eulerian sub–domain. Hence, the need for the development of multi–level/telescopic PM grids [42] is stressed herein as well. GAST–HoPFlow results, are compared against wind tunnel data and predictions by other CFD based aeroelastic solvers. The comparison concerns azimuthal variation of aerodynamic loads measured at 87% radial station, azimuthal variation of structural loads close to the root of the blades, azimuthal variation of the corresponding deflections at the tip of the blades and position of tip vortices traces on a lateral plane of the advancing and retreating sides of the rotor. Significant differences are reported in the mean values of the azimuthal variations compared to measurements, which however are frequent for most CFD based predictions. Most of them are related to experimental mechanisms that are not easily reproduced in the numerical set–up (e.g. aerodynamic effect of the blade tab, stiffness of the drive–train system, of the shaft and of the pitch–link mechanism), poor calibration or malfunctioning/broken sensors for loads measurements, or the use of immature techniques (SPR) for estimating blade deflections. Nevertheless the overall trend is fairly well predicted by the GAST–HoPFlow aeroelastic solver. In cases that discrepancies appear, very good agreement is shown with all the other CFD solvers predictions. Consequently, the coupling between the aerodynamic solver HoPFlow and the structural dynamics solver GAST is confirmed and the accuracy of the aeroelastic solver is found to be comparable to that of other CFD based aeroelastic codes.

Chapter 5

Conclusions

In this chapter, a synopsis of the work done in this thesis is performed. The main objectives and the most significant conclusions drawn from this research are then summarized. Finally, indicative topics for future research and development are proposed.

5.1 Synopsis

The main objective of this thesis was the development of a high fidelity aeroelastic analysis tool for rotor configurations, capable of analyzing complex flow phenomena over a wide part of the sub–sonic region and under the same computational framework. The structural dynamics problem is solved by GAST, an in–house elasto–dynamic analysis module, the development of which has started in previous theses [1, 2] and continued in the present. In GAST, the structural analysis of a Wind Turbine is applied by approximating its various components as Timoshenko beams, discretized under a 1D FEM approach. In order to broaden the scope of GAST in the present thesis, the kinematic and dynamic analysis part was reformed to follow a multi–body dynamics methodology. In this way, the various components of a configuration are allowed to independently move in space and are connected into a full configuration through proper kinematic and dynamic constraints that are realized by satisfying non–linear connection equations [36]. Consequently, GAST may now be used for the structural dynamics analysis of any arbitrary configuration consisting of slender components. Another important advantage of the multi–body approach compared to other similar implementations is that the dynamic equations, including those of constraints, are linearized allowing, thus, to perform eigenvalue stability analyses. The system of dynamic equations is provided in a linearized state space form.

The aerodynamic analysis is based on MaPFlow [4], an in–house CFD code that solves the compressible URANS equations. In order to accurately analyze low Mach flow regions (e.g. WT applications), preconditioning is applied to the system of the flow equations [123]. During this thesis the method of the Actuator Line (AL) [92] was implemented in MaPFlow, where the blades of a rotor are simulated as a set of control points along their axes. In this way, the "blades" (group of control points) are allowed to move freely inside the computational grid and their aerodynamic loads are applied to the flow field as source terms on the computational cells they slice during their rotation. The AL model was then

coupled with GAST, in order to be applicable to aeroelastic analyses of rotors. In this approach, multi–body and aeroelastic simulations are facilitated, while computational cost is restrained. Opposed to standard design tools, such modelling options were found adequate for describing in detail the varying inflow conditions of complex flow cases. Furthermore, in order to reproduce the true (atmospheric) conditions in which a WT operates, the method of Generation Zone (GZ) was implemented in MaPFlow in order to impose a pre–defined turbulent field (produced with Mann's model [8]) onto a mean flow–field within a CFD context.

In order to describe the actual geometry of the rotor blades (or other moving bodies) and to resolve load–driving conditions that are related to it (e.g. flow separation, shock waves), the hybrid CFD solver HoPFlow [4] is used. In HoPFlow, multi–body and aeroelastic applications are facilitated by a domain decomposition approach that is followed in order to combine the standard Eulerian CFD formulation, implemented in MaPFlow, close to the solid boundaries with a Lagrangian CFD approach for the rest of the domain. Hence the actual geometry of any arbitrary body may be described through a body–fitted grid that is confined in a narrow region around its solid–wall boundaries. HoPFlow has been coupled with GAST during the present study. In the coupled HoPFlow–GAST context, the positions and velocities of the blade surface nodes are defined through the multi–body kinematics framework, based on the kinematics of the corresponding structural body (beam). The individual rigid motion and elastic deformations of a body are then extrapolated from its surface to the surrounding grid nodes either un–damped, or by applying a deforming grid approach.

5.2   Remarks

This study aimed at the development of a general application high accuracy aeroelastic analysis tool. For the aerodynamic problem, this is effectively accomplished by employing CFD analysis. For the structural dynamics part, a multi–body dynamics framework was incorporated to the elasto–dynamics solver along with non–linear kinematic and dynamic equations in order to connect the different bodies into a full configuration. The flexible components are numerically treated in the context of $1D$ beam FEM analysis. Consequently, this newly formed aeroelastic analysis tool employs high level of fidelity in the modelling of both the aerodynamics and the structural dynamics and is capable of simulating a wide variety of complex load path configurations. However, the applications tested herein are limited to rotor configurations.

AL modelled rotor blades using MaPFlow

By employing an AL representation of the rotor blades and by incorporating turbulent wind conditions (through the method of GZ) within the CFD context, this newly developed aeroelastic code may serve as an holistic and cost–effective design tool especially for WTs, and for rotor applications in general. AL has been widely used in studying the generation and convection of WT rotor wakes [6, 7], due to the detailed description of the flow–field that the CFD framework provides. However, in [134] it is found capable of predicting also the radial distribution and azimuthal variation of loads, of both WT and helicopter rotor

blades, in accuracy and under moderate computational requirements. The fact that the computation of the blade loads is based on the use of predefined airfoil polars makes the AL model similar to BEMT and LL options, which are considered as state of the art in WT and helicopter rotors design respectively. Polar based approaches perform exceptionally in the mid–span and tip region of the blades that dictate the overall performance of the rotor. On the other hand, they poorly describe the root region in which separation and secondary flows phenomena are present, which however in modern large WT designs are treated engineeringly through Vortex Generators and Gurney Flaps [187, 188, 189]. It is therefore shown that the new GAST–AL module befits the current trend in designing pitch regulated WT rotors that do not operate in deep stall conditions. The validation of this new highly accurate, but cost–effective aeroelastic module consists of:

i) aeroelastic simulations of the isolated rotor of the DTU 10MW RWT [9] under smooth and turbulent free stream flow in axial wind and yaw misalignment cases;

ii) full configuration of the DTU 10MW RWT (rotor blades, shaft and tower included) operating within the Atmospheric Boundary Layer (ABL) in neutral atmospheric conditions (turbulent wind).

Results were compared against computational results produced using the same structural solver coupled with lower fidelity aerodynamic models; namely a Blade Element Momentum Theory (BEMT) based model and a standard Lifting Line (LL) approach.

Good agreement is achieved between all three models predictions at simple axial flow cases, in terms of loads and deflections predictions. Deviations occur between BEMT and the higher fidelity models (LL and AL) in yawed flow cases that become more pronounced as the flow conditions get more complex (e.g. increase of yaw angle). However, excellent agreement between AL and LL is observed in all the examined flow cases. These differences, originate in the detailed description of the flow–field within the CFD (AL) and the FVW (LL) frameworks. Hence, the AL and LL models manage to account for the varying wake induction on the rotor plane, due to complex flow conditions. This is not properly regarded in simple BEMT approaches due to the simplified modelling of the rotor inflow. Similar remarks are made in WT simulations under turbulent wind, where significant differences are reported between AL and BEMT predictions in terms of rotor blades loading. Due to the CFD framework, the AL model is able to consider the effect of the rotor and the ground on local turbulent inflow conditions. The differences shown in the rotor blades loads are directly reflected in the loading and wear of the rest of WT component, such as the tower. Concerning the representation of a turbulent flow–field within a CFD context, it needs to be stressed that the approach of GZ was used for the first time in order to impose the velocity fluctuations of a predefined turbulent field onto an averaged flow–field. GZ was able to create turbulent fields that are closer to the turbulent field produced by the Mann's model, compared to conventional methodologies found in literature.

The newly created coupled GAST–AL aeroelastic model has been also validated in aeroelastic simulations of the Main Rotor (MR) of the model BO105 helicopter used in the HeliNoVi experimental campaign [10]. The examined test cases consider forward

flight conditions at low, medium and high flight speed. In these cases, AL produced results were compared against LL predictions and wind tunnel measured data. In general, computational results were close to measured data and when differences occurred the two models predictions were in good agreement with each other.

Overall, AL results show significant differences compared to BEMT predictions that get more intense as the flow conditions get more complex. Most of them originate in the detailed description of the flow–field close to the rotor that the CFD framework provides. On the other hand, AL results share the same level of accuracy with the ones produced by the LL method, when it comes to blade loads and deflections in isolated rotor cases. Although much more affordable than resolving the whole blades geometry, AL simulations remain at least 2 orders of magnitude more computationally demanding than LL. The main advantage of the AL method, is that the effect of the rotor and ground on the local turbulent inflow are accounted for in detail within the CFD context under moderate computational requirements. This is not easily resolved in a potential Free Vortex Wake (FVW) framework, where the consideration of viscous effects close to the ground and the modelling of turbulence can be tricky.

Fully resolved blades using HoPFlow

For an accurate aeroelastic analysis of slender bodies undergoing large deflections and operating within complex flow fields the actual geometry of the rotor blades needs to be resolved. This was accomplished by coupling GAST with HoPFlow, a compressible hybrid Eulerian–Lagrangian CFD solver that employs a domain decomposition approach in order to combine a Lagrangian representation of the back–ground flow–field through numerical particles with an Eulerian approach close to the solid wall boundaries (bodies). The validation of this newly formed high fidelity aeroelastic solver consists of both WT and helicopter rotors simulations. To that end, its accuracy is assessed in complex local flow phenomena and over a wide part of the sub–sonic region. On the lower Mach values (in the root region of the WT rotor), detached flow conditions are produced, while weak shock–waves appear near the helicopter's blades tip (higher Mach values). The simulated cases concern:

i) aerodynamic analysis of the model WT rotor used in the New MEXICO experimental campaign [11, 12] for an axial flow case at 14.7 m/s;

ii) aeroelastic analysis of the MR of the model BO105 helicopter used in the HARTII experimental campaign [13] for the Base–Line descent case at 33 m/s flight speed.

The accuracy and the features of the coupled GAST–HoPFlow aeroelastic solver were evaluated by comparing its results against experimental measurements and predictions produced by other CFD based aeroelastic codes.

In both cases, the hybrid CFD code was able to predict the aerodynamic loads of the blades in great accuracy (comparable to that of standard CFD solvers). Consequently, the resulting structural loads and the corresponding deflections were estimated fairly well. The same remark can be made for the flow–field developed in the region close to the rotors. In fact, it is shown in the WT aerodynamic analysis case that the reduced

numerical diffusion of the Lagrangian formulation followed in the off–body region leads to better preservation of wake structures and, thus, to a more accurate estimation of the developed wake deficit compared to its Eulerian counterpart MaPFlow. The above remarks confirm that the coupling method between the Eulerian and the Lagrangian sub–domains that determines the boundary conditions for the confined Eulerian grid is adequate and consistent. The same conclusion is drawn for the coupling between the structural module and the aerodynamic solver. Hence, the aeroelastic behaviour of the full rotor configuration is well predicted (close to measured data) by the new aeroelastic solver. In cases where deviations are observed with respected to experimental measurements, the simulations results agree well with the computational predictions of other CFD based aeroelastic solvers. These deviations are mainly attributed to small geometrical differences between the models used in wind tunnel tests and computational simulations.

Nevertheless, it needs to be stressed that the cost of the hybrid approach is excessive for a single rotor simulation. A remedy for moderating the computational cost is the application of multi–level/telescopic Particle Mesh (PM) grids [42], finer in the vicinity of the body and coarser in the far–domain. The benefit for paying this increased computational cost (using fine PM grids in the entire computational domain) lies in unsteady applications where interaction phenomena (e.g. rotor–rotor interactions) are prominent or in cases where the accurate characterization of the far–wake dynamics is required. It is also attractive for aeroelastic analyses in which a standard Eulerian methodology relies on the use of overset grids and the corresponding coupling between different sub–domains, which penalizes computational cost.

5.3   Recommendations for future work

The recommendations proposed next concern improvements and development of the individual solvers and suggestions for future research of technological interest.

Development

From a methodological point of view, there are various development options capable of increasing the accuracy, reducing computational requirements and enhancing the stability of the presented solvers, namely:

1. development of a higher order and more accurate beam model (e.g. Geometrically Exact Timoshenko [33]) as an alternative to the use of multiple sub–bodies in order to describe non–linear structural phenomena.This approach will only slightly affect computational cost and not the level of accuracy, as shown in [190]. This is because by applying the geometrically exact representation at every point along the blade and not in a discrete manner from one sub–body to another relaxes the requirements on number of elements (sub–bodies) needed in the analysis;

2. application of multi–level/telescopic PM grids [42], finer in the vicinity of the body and coarser in the far–domain;

3. generation of synthetic turbulence using particles and simulation of the exact geometry of the various components of a full WT configuration operating in turbulent

inflow conditions through the coupled GAST–HoPFlow solver;

4. preconditioning of the Lagrangian formulation of the flow equations in order to increase the stability of the hybrid CFD solver HoPFlow in low Mach number regions and, thus, permit the employment of larger time–step values and accelerate the simulations.

Technological research

The newly created CFD based aeroelastic solver may be efficiently used, in its current form, in order to investigate:

1. the interaction between multiple rotors, such as wind farm simulations, where rotor wake diffusion has an impact on the performance of the downwind turbines, or the interaction between the main rotor wake and other components of a helicopter (e.g. horizontal stabilizers, tail rotor) where stability or acoustic issues occur in specific flight cases;

2. the effect of large scale vortex structures on the loading and wear of various components of a full configuration (e.g. rotor blades, WT tower). Such cases are the massive separation of the flow around a helicopter fuselage and the induced vibration loads on the rotor blades, or a WT rotor in parked/idling conditions, where the rotor blades operate at extremely high angles of attack ($\simeq 90°$) deeply within the stall region of their airfoils.

Bibliography

[1] Vasilis A Riziotis and Spyros G Voutsinas. *GAST: A general aerodynamic and structural prediction tool for wind turbines*. *EWEC-CONFERENCE-*, pages 448–452. BOOKSHOP FOR SCIENTIFIC PUBLICATIONS, 1997.

[2] Dimitris I. Manolas. *Hydro-aero-elastic analysis of offshore wind turbines*. Ph.D. Thesis, National Technical University of Athens, School of Mechanical Engineering, 2016.

[3] Tohid Bagherpour, XM Li, DI Manolas and VA Riziotis. *Modeling of material bend-twist coupling on wind turbine blades*. *Composite Structures*, 193:237–246, 2018.

[4] Georgios Papadakis. *Development of a hybrid compressible vortex particle method and application to external problems including helicopter flows*. Ph.D. Thesis, National Technical University of Athens, School of Mechanical Engineering, 2014.

[5] Sandip Ghosal. *An analysis of numerical errors in large-eddy simulations of turbulence*. *Journal of Computational Physics*, 125(1):187–206, 1996.

[6] Stefan Ivanell, Jens N. Sørensen, Robert Mikkelsen and Dan Henningson. *Analysis of numerically generated wake structures*. *Wind Energy*, 12(1):63–80, 2009.

[7] Niels Troldborg, Jens N. Sorensen and Robert Mikkelsen. *Numerical simulations of wake characteristics of a wind turbine in uniform inflow*. *Wind Energy*, 13(1):86–99, 2010.

[8] Jakob Mann. *Atmospheric turbulence*. *DTU Wind Energy, Technical university of Denmark, Denmark, DK-4000 Roskilde*, 2012.

[9] Christian Bak, Frederik Zahle, Robert Bitsche, Taeseong Kim, Anders Yde, Lars Christian Henriksen, Morten Hartvig Hansen, José Pedro Albergaria Amaral Blasques, Mac Gaunaa and Anand Natarajan. *The DTU 10-MW Reference Wind Turbine*. 2013.

[10] H. J. Langer, O. Dieterich, S. Oerlemans, O. Schneider, B. V.D. Wall and J. Yin. *The EU HeliNOVI project - wind tunnel investigations for noise and vibration reduction*. *31st European Rotorcraft Forum*, 2005, 2005.

[11] JG Schepers and K Boorsma. *New MEXICO experiment, Preliminary overview with initial validation*. 2014.

[12] K. Boorsma and J. G. Schepers. *Rotor experiments in controlled conditions continued: New Mexico.* *Journal of Physics: Conference Series*, 753(2), 2016.

[13] Berend Gvan der Wall. *A comprehensive rotary-wing data base for code validation: the HART II international workshop.* *Aeronautical Journal*, 115(1164):91, 2011.

[14] Dewey H Hodges and G Alvin Pierce. *Introduction to structural dynamics and aeroelasticity*, volume 15. cambridge university press, 2011.

[15] Carlos ES Cesnik and Dewey H Hodges. *VABS: a new concept for composite rotor blade cross-sectional modeling.* *Journal of the American helicopter society*, 42(1):27–38, 1997.

[16] José Pedro Blasques. *User's Manual for BECAS.* *Technical University of Denmark*, 2012.

[17] Junuthula Narasimha Reddy. *Mechanics of laminated composite plates and shells: theory and analysis.* CRC press, 2003.

[18] JB Kosmatka and PP Friedmann. *Vibration analysis of composite turbopropellers using a nonlinear beam-type finite-element approach.* *AIAA journal*, 27(11):1606–1614, 1989.

[19] Carlos Cesnik, Vladislav Sutyrin and Dewey Hodges. *A refined composite beam theory based on the variational-asymptotical method.* *34th Structures, Structural Dynamics and Materials Conference*, page 1616, 1993.

[20] Giorgia Guma, Philipp Bucher, Patrick Letzgus, Thorsten Lutz and Roland Wüchner. *High-fidelity aeroelastic analyses of wind turbines in complex terrain: fluid–structure interaction and aerodynamic modeling.* *Wind Energy Science*, 7(4):1421–1439, 2022.

[21] Peretz P Friedmann. *Rotary-Wing Aeroelasticity: Current Status and Future Trends.* *AIAA Journal*, 42(10):1953–1972, 2004.

[22] M. O.L. Hansen, J. N. Sørensen, S. Voutsinas, N. Sørensen and H. Aa Madsen. *State of the art in wind turbine aerodynamics and aeroelasticity.* *Progress in Aerospace Sciences*, 42(4):285–330, 2006.

[23] Lin Wang, Xiongwei Liu and Athanasios Kolios. *State of the art in the aeroelasticity of wind turbine blades: Aeroelastic modelling.* *Renewable and Sustainable Energy Reviews*, 64:195–210, 2016.

[24] Stig Øye. *FLEX4. Simulation of wind turbine dynamics.* 1996.

[25] EA Bossanyi and D Quarton. *GH bladed.* *Garrad Hassan*, 2003.

[26] Jason M Jonkman, Marshall L Buhl Jr and others. *Fast user's guide. National Renewable Energy Laboratory, Golden.* *Technical Report No. NREL/EL-500-38230*, 2005.

[27] Oliver A Bauchau and James I Craig. *Euler-Bernoulli beam theory*. *Structural analysis*, pages 173–221, 2009.

[28] Eugenio Oñate. *Structural analysis with the finite element method. Linear statics: volume 2: beams, plates and shells*. Springer Science & Business Media, 2013.

[29] V. A. Riziotis, S. G. Voutsinas, E. S. Politis, P. K. Chaviaropoulos, A. M. Hansen, H. A. Madsen and F. Rasmussen. *Identification of structural non-linearities due to large deflections on a 5MW wind turbine blade*. *European Wind Energy Conference and Exhibition 2008*, 1:102–112, 2008.

[30] Dewey H Hodges and Earl H Dowell. *Nonlinear equations of motion for the elastic bending and torsion of twisted nonuniform rotor blades*. Technical report, 1974.

[31] Juan C Simo. *A finite strain beam formulation. The three-dimensional dynamic problem. Part I*. *Computer methods in applied mechanics and engineering*, 49(1):55–70, 1985.

[32] Dewey H Hodges. *A mixed variational formulation based on exact intrinsic equations for dynamics of moving beams*. *International journal of solids and structures*, 26(11):1253–1273, 1990.

[33] Dewey H Hodges. *Geometrically exact, intrinsic theory for dynamics of curved and twisted anisotropic beams*. *AIAA journal*, 41(6):1131–1137, 2003.

[34] Christoph Meier, Alexander Popp and Wolfgang A Wall. *An objective 3D large deformation finite element formulation for geometrically exact curved Kirchhoff rods*. *Computer Methods in Applied Mechanics and Engineering*, 278:445–478, 2014.

[35] Christoph Meier, Alexander Popp and Wolfgang A Wall. *A locking-free finite element formulation and reduced models for geometrically exact Kirchhoff rods*. *Computer Methods in Applied Mechanics and Engineering*, 290:314–341, 2015.

[36] O. A. Bauchau, C. L. Bottasso and Y. G. Nikishkov. *Modeling rotorcraft dynamics with finite element multibody procedures*. *Mathematical and Computer Modelling*, 33(10-11):1113–1137, 2001.

[37] V. A. Riziotis, S. G. Voutsinas, D. I. Manolas, E. S. Politis and P. K. Chaviaropoulos. *Aeroelastic analysis of pre-curved rotor blades*. *European Wind Energy Conference and Exhibition 2010, EWEC 2010*, 2:1173–1202, 2010.

[38] D. I. Manolas, V. A. Riziotis and S. G. Voutsinas. *Assessing the Importance of Geometric Nonlinear Effects in the Prediction of Wind Turbine Blade Loads*. *Journal of Computational and Nonlinear Dynamics*, 10(4):1–15, 2015.

[39] O. A. Bauchau. *Flexible multibody dynamics*, volume 176. 2011.

[40] H. Glauert. *Airplane Propellers*. *Aerodynamic Theory*, pages 169–360, 1935.

[41] Helge Aagaard Madsen, Vasilis Riziotis, Frederik Zahle, Torben Juul Larsen, Evangelos Politis, Martin O L Hansen, Herman Snel and Francesco Grasso. *BEM modeling of inflow with shear in comparison with advanced model results*. The Science of Making Torque from Wind, (June):1–12, 2010.

[42] Spyros G. Voutsinas. *Vortex methods in aeronautics: How to make things work*. International Journal of Computational Fluid Dynamics, 20(1):3–18, 2006.

[43] SG Voutsinas, MA Belessis and KG Rados. *Investigation of the yawed operation of wind turbines by means of a vortex particle method*. AGARD CONFERENCE PROCEEDINGS AGARD CP, pages 11–11. AGARD, 1995.

[44] Forrester T Johnson, Edward N Tinoco and N Jong Yu. *Thirty years of development and application of CFD at Boeing Commercial Airplanes, Seattle*. Computers & Fluids, 34(10):1115–1151, 2005.

[45] Theologos E. Andronikos. *Hovering helicopter interaction with the ground and bluff bodies : A CFD based investigation*. Ph.D. Thesis, National Technical University of Athens, School of Mechanical Engineering, 2022.

[46] Martin Hansen. *Aerodynamics of Wind Turbines*. Routledge, 2015.

[47] Ludwig Prandtl. *Applications of modern hydrodynamics to aeronautics*. US Government Printing Office, 1921.

[48] JG Schepers and H Snel. *Dynamic inflow. Yawed conditions and partial span pitch control*. 1995.

[49] Spyros G. Voutsinas, Vasilis A. Riziotis and P. Chaviaropoulos. *Non-linear aerodynamics and fatigue loading on wind turbines operating at extreme sites*. 35th Aerospace Sciences Meeting and Exhibit, (January):1–15, 1997.

[50] Theodore Theodorsen. *GENERAL THEORY OF AERODYNAMIC INSTABILITY AND THE MECHANISM OF*. Annual Report of the National Advisory Committee for Aeronautics, 268:413, 1935.

[51] J Gordon Leishman and TS Beddoes. *A Semi-Empirical model for dynamic stall*. Journal of the American Helicopter society, 34(3):3–17, 1989.

[52] Khiem Van Truong. *Modeling aerodynamics, including dynamic stall, for comprehensive analysis of helicopter rotors*. Aerospace, 4(2), 2017.

[53] Dale M Pitt and David A Peters. *Theoretical prediction of dynamic-inflow derivatives*. 1980.

[54] Helge Aagaard Madsen and Flemming Rasmussen. *A near wake model for trailing vorticity compared with the blade element momentum theory*. Wind Energy: An International Journal for Progress and Applications in Wind Power Conversion Technology, 7(4):325–341, 2004.

[55] Georges Henri Cottet, Petros D Koumoutsakos and others. *Vortex methods: theory and practice*, volume 8. Cambridge university press Cambridge, 2000.

[56] P. Koumoutsakos and A. Leonard. *High-Resolution simulations of the flow around an impulsively started cylinder using vortex methods*. *Journal of Fluid Mechanics*, 296:1–38, 1995.

[57] L. A. Barba, A. Leonard and C. B. Allen. *Advances in viscous vortex methods - Meshless spatial adaption based on radial basis function interpolation*. *International Journal for Numerical Methods in Fluids*, 47(5):387–421, 2005.

[58] R Hockney and J Eastwood. *Computer simulations using particles mcgraw-hill*. *New York*, 61, 1981.

[59] Benoit Couet, Oscar Buneman and Anthony Leonard. *Simulation of three-dimensional incompressible flows with a vortex-in-cell method*. *Journal of Computational Physics*, 39(2):305–328, 1981.

[60] Serge G Huberson and Spyros G Voutsinas. *Particles and grid*. *Computers & fluids*, 31(4-7):607–625, 2002.

[61] Leslie Greengard and Vladimir Rokhlin. *A fast algorithm for particle simulations*. *Journal of computational physics*, 73(2):325–348, 1987.

[62] Leslie Greengard and Vladimir Rokhlin. *A new version of the fast multipole method for the Laplace equation in three dimensions*. *Acta numerica*, 6:229–269, 1997.

[63] Rick Beatson and Leslie Greengard. *A short course on fast multipole methods*. *Wavelets, multilevel methods and elliptic PDEs*, 1:1–37, 1997.

[64] Joseph J Monaghan and Robert A Gingold. *Shock simulation by the particle method SPH*. *Journal of computational physics*, 52(2):374–389, 1983.

[65] J. J. Monaghan. *Smoothed particle hydrodynamics*. *Reports on Progress in Physics*, 68(8):1703–1759, 2005.

[66] Milad Rakhsha, Christopher E. Kees and Dan Negrut. *Lagrangian vs. Eulerian: An analysis of two solution methods for free-surface flows and fluid solid interaction problems*. *Fluids*, 6(12), 2021.

[67] Jeff D. Eldredge, Tim Colonius and Anthony Leonard. *A vortex particle method for two-dimensional compressible flow*. *Journal of Computational Physics*, 179(2):371–399, 2002.

[68] Philippe Parmentier, Grégoire Winckelmans and Philippe Chatelain. *A Vortex Particle-Mesh method for subsonic compressible flows*. *Journal of Computational Physics*, 354:692–716, 2018.

[69] Spyros G Voutsinas and Dimitris G Triantos. *Aeroacoustics of full helicopter configurations using vortex particle flow approximation*. *2Q00MW (M*, page 175, 1999.

[70] Philippe Chatelain, Alessandro Curioni, Michael Bergdorf, Diego Rossinelli, Wanda Andreoni and Petros Koumoutsakos. *Billion vortex particle direct numerical simulations of aircraft wakes*. Computer Methods in Applied Mechanics and Engineering, 197(13-16):1296–1304, 2008.

[71] Theologos E. Andronikos, George Papadakis and Vasilis Riziotis. *Aerodynamic analysis of helicopter in interaction with wind Turbine's wake*. 44th European Rotorcraft Forum 2018, ERF 2018, 1:342–354, 2018.

[72] Ludwig Prandtl. *Applications of modern hydrodynamics to aeronautics*. US Government Printing Office, 1925.

[73] W. F. Phillips and D. O. Snyder. *Modern adaptation of Prandtl's classic lifting-line theory*. Journal of Aircraft, 37(4):662–670, 2000.

[74] Spyros G Voutsinas and Dimitris G Triantos. *High resolution aerodynamic analysis of full helicopter configurations*. 1999.

[75] Luigi Morino. *A general theory of unsteady compressible potential aerodynamics*. Technical report, NASA, 1974.

[76] John L Hess. *Calculation of potential flow about arbitrary three-dimensional lifting bodies*. Technical report, Douglas Aircraft Co Long Beach CA, 1972.

[77] Charles Hirsch. *Numerical computation of internal and external flows*. Computational methods for inviscid and viscous flows, 2, 1990.

[78] Randall J LeVeque. *Finite volume methods for hyperbolic problems*, volume 31. Cambridge university press, 2002.

[79] Bernardo Cockburn and Chi Wang Shu. *Runge-Kutta discontinuous Galerkin methods for convection-dominated problems*. Journal of scientific computing, 16:173–261, 2001.

[80] Thomas A Zang, Craig L Streett and M Yousuff Hussaini. *Spectral methods for CFD*. Technical report, 1989.

[81] David C Wilcox and others. *Turbulence modeling for CFD*, volume 2. DCW industries La Canada, CA, 1998.

[82] Myoungkyu Lee, Nicholas Malaya and Robert D Moser. *Petascale direct numerical simulation of turbulent channel flow on up to 786k cores*. Proceedings of the International Conference on High Performance Computing, Networking, Storage and Analysis, pages 1–11, 2013.

[83] Wolfgang Rodi, Joel H Ferziger, Michael Breuer, Mathieu Pourquié and others. *Status of large eddy simulation: results of a workshop*. Transactions-American Society of Mechanical Engineers Journal of Fluids Engineering, 119:248–262, 1997.

[84] Jochen Fröhlich and Dominic Von Terzi. *Hybrid LES/RANS methods for the simulation of turbulent flows*. *Progress in Aerospace Sciences*, 44(5):349–377, 2008.

[85] M Giles, M Drela and W THOMPKINS, JR. *Newton solution of direct and inverse transonic Euler equations*. *7th Computational Physics Conference*, page 1530, 1985.

[86] Dimitri J Mavriplis and Antony Jameson. *Multigrid solution of the Navier-Stokes equations on triangular meshes*. *AIAA journal*, 28(8):1415–1425, 1990.

[87] Rajat Mittal and Gianluca Iaccarino. *Immersed boundary methods*. *Annu. Rev. Fluid Mech.*, 37:239–261, 2005.

[88] R. Steijl and G. Barakos. *Sliding mesh algorithm for CFD analysis of helicopter rotor-fuselage aerodynamics*. *International Journal for Numerical Methods in Fluids*, 58(5):527–549, 2008.

[89] Z.J. Wang. *A Fully Conservative Interface Algorithm for Overlapped Grids*. *Journal of Computational Physics*, 122(1):96–106, 1995.

[90] Y. Zhao, J. Tai and F. Ahmed. *Simulation of micro flows with moving boundaries using high-order upwind FV method on unstructured grids*. *Computational Mechanics*, 28(1):66–75, 2001.

[91] Jens N Sørensen and Asger Myken. *Unsteady actuator disc model for horizontal axis wind turbines*. *Journal of Wind Engineering and Industrial Aerodynamics*, 39(1-3):139–149, 1992.

[92] Jens Nørkær Sørensen and Wen Zhong Shen. *Numerical modeling of wind turbine wakes*. *Journal of Fluids Engineering, Transactions of the ASME*, 124(2):393–399, 2002.

[93] Mark Drela. *XFOIL: An analysis and design system for low Reynolds number airfoils*. *Low Reynolds number aerodynamics*, pages 1–12. Springer, 1989.

[94] P. K. Chaviaropoulos, I. G. Nikolaou, K. A. Aggelis, N. N. Soerensen, J. Johansen, M. O. L. Hansen, M. Gaunaa, T. Hambraus, H. Von Geyr, Ch Hirsch, K. Shun, S. G. Voutsinas, G. Tzabiras, Y. Perivolaris and S. Z. Dyrmose. *Viscous and aeroelastic effects on wind turbine blades. the VISCEL project. Part I:3D Navier-Stokes rotor simulations*. *Wind Energy*, 6(4):365–385, 2003. Cited By :32.

[95] Sven Schmitz and Jean Jacques Chattot. *A coupled Navier-Stokes/Vortex-Panel solver for the numerical analysis of wind turbines*. *Computers and Fluids*, 35(7):742–745, 2006. Special Issue Dedicated to Professor Stanley G. Rubin on the Occasion of his 65th Birthday.

[96] J L Guermond, S Huberson and W Z Shen. *Simulation of 2D external viscous flows by means of a domain decomposition method*. *Journal of Computational Physics*, 108(2):343–352, 1993.

[97] Paul Ploumhans, GS Winckelmans, John K Salmon, Anthony Leonard and MS Warren. *Vortex methods for direct numerical simulation of three-dimensional bluff body flows: application to the sphere at Re= 300, 500, and 1000*. *Journal of Computational Physics*, 178(2):427–463, 2002.

[98] Georges Henri Cottet. *Particle-grid Domain Decomposition Methods for the Navier-Stokes Equations in Exterior Domain*. Ecole polytechnique, Centre de mathématiques appliquées, 1990.

[99] Phuriwat Anusonti-Inthra and Matt Floros. *Coupled CFD and particle vortex transport method: Wing performance and wake validations*. *38th Fluid Dynamics Conference and Exhibit*, page 4177, 2008.

[100] Christopher Stone, Earl Duque, Christopher Hennes and Adrin Gharakhani. *Rotor wake modeling with a coupled Eulerian and vortex particle method*. *48th AIAA Aerospace Sciences Meeting Including the New Horizons Forum and Aerospace Exposition*, page 312, 2010.

[101] Gregory Scott Oxley. *A 2-D hybrid euler-compressible vortex particle method for transonic rotorcraft flows*. Ph.D. Thesis, Carleton University, 2009.

[102] International Electrotechnical Commission and others. *Wind energy generation systems-Part 1: Design requirements*. *International Electrotechnical Commission: Geneva, Switzerland*, 2019.

[103] VA Riziotis, PK Chaviaropoulos and SG Voutsinas. *Development of a State-of-the Art Aeroelastic Simulator for Horizontal Axis Wind Turbines: Part 2: Aerodynamic Aspects and Application*. *Wind Engineering*, pages 423–440, 1996.

[104] Jakob Mann. *The spatial structure of neutral atmospheric surface-layer turbulence*. *Journal of fluid mechanics*, 273:141–168, 1994.

[105] Jakob Mann. *Wind field simulation*. *Probabilistic engineering mechanics*, 13(4):269–282, 1998.

[106] Dimitris Ntouras and George Papadakis. *A coupled artificial compressibility method for free surface flows*. *Journal of Marine Science and Engineering*, 8(8), 2020.

[107] Niels Troldborg, Jens N. Sørensen, Robert Mikkelsen and Niels N. Sørensen. *A simple atmospheric boundary layer model applied to large eddy simulations of wind turbine wakes*. *Wind Energy*, 17(4):657–669, 2014.

[108] A. Bazoune, Y. A. Khulief and N. G. Stephen. *Shape functions of three-dimensional Timoshenko beam element*. *Journal of Sound and Vibration*, 259(2):473–480, 2003.

[109] Alexander Stäblein and Morten Hartvig Hansen. *Timoshenko beam element with anisotropic cross-sectional properties*. *ECCOMAS Congress 2016: VII European Congress on Computational Methods in Applied Sciences and Engineering*. European Community on Computational Methods in Applied Sciences, 2016.

[110] Joseph Katz and Allen Plotkin. *Low-speed aerodynamics*, volume 13. Cambridge university press, 2001.

[111] George Karypis and Vipin Kumar. *METIS: A software package for partitioning unstructured graphs*. *Partitioning Meshes, and Computing Fill-Reducing Orderings of Sparse Matrices, Version*, 4(0), 1998.

[112] P. L. Roe. *Characteristic-Based Schemes for the Euler Equations*. *Annual Review of Fluid Mechanics*, 1:337–365, 1986.

[113] Venkat Venkatakrishnan. *On the accuracy of limiters and convergence to steady state solutions*. *31st Aerospace Sciences Meeting*, page 880, 1993.

[114] Philippe Spalart and Steven Allmaras. *A one-equation turbulence model for aerodynamic flows*. *30th aerospace sciences meeting and exhibit*, page 439, 1992.

[115] Florian R Menter. *Two-equation eddy-viscosity turbulence models for engineering applications*. *AIAA journal*, 32(8):1598–1605, 1994.

[116] Robin Blair Langtry, FR Menter, SR Likki, YB Suzen, PG Huang and S Völker. *A correlation-based transition model using local variables—part II: test cases and industrial applications*. 2006.

[117] Mikhail L Shur, Philippe R Spalart, Mikhail Kh Strelets and Andrey K Travin. *A hybrid RANS-LES approach with delayed-DES and wall-modelled LES capabilities*. *International journal of heat and fluid flow*, 29(6):1638–1649, 2008.

[118] Robert Biedron and James Thomas. *Recent enhancements to the FUN3D flow solver for moving-mesh applications*. page 1360, 2009.

[119] Veer N. Vatsa, Mark H. Carpenter and David P. Lockard. *Re-evaluation of an optimized second order backward difference (BDF2OPT) scheme for unsteady flow applications*. *48th AIAA Aerospace Sciences Meeting Including the New Horizons Forum and Aerospace Exposition*, 2010.

[120] Yousef Saad. *Iterative methods for sparse linear systems*. SIAM, 2003.

[121] L E Eriksson. *A preconditioned Navier-Stokes solver for low Mach number flows*. *Computational fluid dynamics' 96 (Paris, 9-13 September 1996)*, pages 199–205, 1996.

[122] VG Asouti, DI Papadimitriou, DG Koubogiannis and KC Giannakoglou. *Low Mach number preconditioning for 2D and 3D upwind flow solution schemes, on unstructured grids*. *5th GRACM International Congress, Cyprus*, 2005.

[123] Varvara G Asouti. *Aerodynamic analysis and design methods at high and low speed flows, on multiprocessor platforms*. Ph.D. Thesis, PhD thesis, National Technical University of Athens, 2009.

[124] Jiri Blazek. *Computational fluid dynamics: principles and applications*. Butterworth-Heinemann, 2015.

[125] Robert Biedron, Veer Vatsa and Harold Atkins. *Simulation of unsteady flows using an unstructured Navier-Stokes solver on moving and stationary grids*. page 5093, 2005.

[126] Antony Jameson. *Time dependent calculations using multigrid, with applications to unsteady flows past airfoils and wings*. page 1596, 1991.

[127] P. D. Thomas and C. K. Lombard. *Geometric conservation law and its application to flow computations on moving grids*. *AIAA Journal*, 17(10):1030–1037, 1979.

[128] Dimitri J Mavriplis and Zhi Yang. *Construction of the discrete geometric conservation law for high-order time-accurate simulations on dynamic meshes*. *Journal of Computational Physics*, 213(2):557–573, 2006.

[129] Hyung Taek Ahn and Yannis Kallinderis. *Strongly coupled flow/structure interactions with a geometrically conservative ALE scheme on general hybrid meshes*. *Journal of Computational Physics*, 219(2):671–696, 2006.

[130] Pankaj K. Jha and Sven Schmitz. *Actuator curve embedding - An advanced actuator line model*. *Journal of Fluid Mechanics*, 834:1–11, 2018.

[131] Luis A Martínez-Tossas, Matthew J Churchfield and Stefano Leonardi. *Large eddy simulations of the flow past wind turbines: actuator line and disk modeling*. *Wind Energy*, 18(6):1047–1060, 2015.

[132] Shengxin Zhu. *Compactly supported radial basis functions: How and why?* (12):24–29, 2012.

[133] Wen Zhong Shen, Jens Nørkær Sørensen and Robert Mikkelsen. *Tip loss correction for actuator/Navier-Stokes computations*. *Journal of Solar Energy Engineering, Transactions of the ASME*, 127(2):209–213, 2005.

[134] Nikos Spyropoulos, George Papadakis, John M Prospathopoulos and Vasilis A. Riziotis. *Investigating the Level of Fidelity of an Actuator Line Model in Predicting Loads and Deflections of Rotating Blades under Uniform Free-Stream Flow*. *Applied Sciences*, 11(24):12097, 2021.

[135] Michael Shives and Curran Crawford. *Mesh and load distribution requirements for actuator line CFD simulations*. *Wind Energy*, (August 2012):n/a–n/a, 2012.

[136] Pankaj K. Jha, Matthew J. Churchfield, Patrick J. Moriarty and Sven Schmitz. *Guidelines for volume force distributions within actuator line modeling of wind turbines on large-eddy simulation-type grids*. *Journal of Solar Energy Engineering, Transactions of the ASME*, 136(3):1–11, 2014.

[137] Matthew J. Churchfield, Scott Schreck, Luis A. Martínez-Tossas, Charles Meneveau and Philippe R. Spalart. *An advanced actuator line method for wind energy applications and beyond. 35th Wind Energy Symposium, 2017*, (January):1–20, 2017.

[138] D Petot. *Dynamic stall modelling using differential equations.* 1989.

[139] Kai Wang, Vasilis A. Riziotis and Spyros G. Voutsinas. *Aeroelastic stability of idling wind turbines. Wind Energy Science*, 2(2):415–437, 2017.

[140] B S En. *IEC 61400-1:2005. Wind Turbines–Part 1: Design Requirements.* 3:60, 2005.

[141] Tony Burton, Nick Jenkins, David Sharpe and Ervin Bossanyi. *Wind energy handbook.* John Wiley & Sons, 2011.

[142] L. Gilling and N. N. Sørensen. *Imposing resolved turbulence in CFD simulations. Wind Energy*, 14(5):661–676, 2011.

[143] Niels Troldborg, Jens N. Sørensen and Robert Mikkelsen. *Actuator line simulation of wake of wind turbine operating in turbulent inflow. Journal of Physics: Conference Series*, 75(1), 2007.

[144] Stefan Mayer, Antoine Garapon and Lars S Sørensen. *A fractional step method for unsteady free-surface flow with applications to non-linear wave dynamics. International Journal for Numerical Methods in Fluids*, 28(2):293–315, 1998.

[145] Ronald F. Boisvert. *a Fourth Order Accurate Fast Direct Method for the Helmholtz Equation.* Αριθμός version 3. ACADEMIC PRESS, INC., 1984.

[146] Gregory T. Balls and Phillip Colella. *A finite difference domain decomposition method using local corrections for the solution of poisson's equation. Journal of Computational Physics*, 180(1):25–53, 2002.

[147] Giorgos Papadakis and Spyros G. Voutsinas. *In view of accelerating CFD simulations through coupling with vortex particle approximations. Journal of Physics: Conference Series*, 524(1), 2014.

[148] George Papadakis and Spyros G. Voutsinas. *A strongly coupled Eulerian Lagrangian method verified in 2D external compressible flows. Computers and Fluids*, 195:104325, 2019.

[149] Thomas CS Rendall and Christian B Allen. *Efficient mesh motion using radial basis functions with data reduction algorithms. Journal of Computational Physics*, 228(17):6231–6249, 2009.

[150] Konstantinos Theodorakis, Dimitris Ntouras and George Papadakis. *Investigation of a submerged fully passive energy-extracting flapping foil operating in sheared inflow. Journal of Fluids and Structures*, 113:103674, 2022.

[151] Christian Bak, Robert Bitsche, Anders Yde, Taeseong Kim, Morten H. Hansen, Frederik Zahle, Mac Gaunaa, José Blasques, Mads Døssing, Jens Jakob Wedel Heinen and Tim Behrens. *Light rotor: The 10-MW Reference Wind Turbine*. *European Wind Energy Conference and Exhibition 2012, EWEC 2012*, 1:532–541, 2012.

[152] Jason Jonkman, Sandy Butterfield, Walter Musial and George Scott. *Definition of a 5-MW reference wind turbine for offshore system development*. Technical report, National Renewable Energy Lab.(NREL), Golden, CO (United States), 2009.

[153] Peter Hjuler Jensen and Anand Natarajan. *INNWIND. EU. Overview of project and recent results*. *EERA DeepWind 2014-11th Deep Sea Offshore Wind R&D Conference*, 2014.

[154] Abdolrahim Rezaeiha, Ricardo Pereira and Marios Kotsonis. *Fluctuations of angle of attack and lift coefficient and the resultant fatigue loads for a large horizontal axis wind turbine*. *Renewable Energy*, 114:904–916, 2017.

[155] L a Martinez Tossas and S Leonardi. *Wind Turbine Modeling for Computational Fluid Dynamics December 2010 − December 2012 Wind Turbine Modeling for Computational Fluid Dynamics*. (July):57, 2013.

[156] Jens N. Sørensen, Kaya O. Dag and Néstor Ramos-García. *A refined tip correction based on decambering*. *Wind Energy*, 19(5):787–802, 2016.

[157] Alexander R. Meyer Forsting, Georg Raimund Pirrung and Néstor Ramos-García. *A vortex-based tip/smearing correction for the actuator line*. *Wind Energy Science*, 4(2):369–383, 2019.

[158] Kaya Onur Dağ and Jens Nørkær Sørensen. *A new tip correction for actuator line computations*. *Wind Energy*, 23(2):148–160, 2020.

[159] F Bertagnolio, NN Sørensen and J Johansen. *Status for the Two-Dimensional Navier-Stokes Solver EllipSys2D*, volume 1282. 2001.

[160] T Fancev, D Grgic and I Saban. *NISA FEM Support in Seismic Qualification of Small Class 1E Electric Motors*. 1996.

[161] D. I. Manolas, G. R. Pirrung, A. Croce, M. Roura, V. A. Riziotis, H. A. Madsen, C. Pizarro, S. G. Voutsinas and F. Rasmussen. *Cross comparison of aeroelastic state-of-the-art design tools on a 10 MW scale wind turbine*. *European Wind Energy Association Annual Conference and Exhibition 2015, EWEA 2015 - Scientific Proceedings*, 2015.

[162] H. Aa. Madsen, V. Riziotis, F. Zahle, M.O.L. Hansen, H. Snel, F. Grasso, T.J. Larsen, E. Politis and F. Rasmussen. *Blade element momentum modeling of inflow with shear in comparison with advanced model results*. *Wind Energy*, 15(1):63–81, 2012.

[163] Marilyn J Smith, Joon W Lim, Berend Gvan der Wall, James D Baeder, Robert T Biedron, D Douglas Boyd Jr, Buvana Jayaraman, Sung N Jung and Byung Young Min. *An assessment of CFD/CSD prediction state-of-the-art using the HART II international workshop data*. *68th Annual Forum of the American Helicopter Society, Ft. Worth, TX*, 2012.

[164] Marilyn J Smith, Joon W Lim, Berend Gvan der Wall, James D Baeder, Robert T Biedron, D Douglas Boyd, Buvana Jayaraman, Sung N Jung and Byung Young Min. *The HART II international workshop: an assessment of the state of the art in CFD/CSD prediction*. *CEAS Aeronautical Journal*, 4:345–372, 2013.

[165] Berend Gvan der Wall, Joon W Lim, Marilyn J Smith, Sung N Jung, Joëlle Bailly, James D Baeder and D Douglas Boyd. *The HART II international workshop: an assessment of the state-of-the-art in comprehensive code prediction*. *CEAS Aeronautical Journal*, 4:223–252, 2013.

[166] Ray W Clough and Joseph Penzien. *Dynamics of Structures McGraw-Hill*. *Inc Editor*, 1993.

[167] Joseph Smagorinsky. *General circulation experiments with the primitive equations: I. The basic experiment*. *Monthly weather review*, 91(3):99–164, 1963.

[168] Masanori Matsuishi and Tatsuo Endo. *Fatigue of metals subjected to varying stress*. *Japan Society of Mechanical Engineers, Fukuoka, Japan*, 68(2):37–40, 1968.

[169] Julian CR Hunt, Alan A Wray and Parviz Moin. *Eddies, streams, and convergence zones in turbulent flows*. *Studying turbulence using numerical simulation databases, 2. Proceedings of the 1988 summer program*, 1988.

[170] George Papadakis, Vasilis A. Riziotis and Spyros G. Voutsinas. *A hybrid Lagrangian-Eulerian flow solver applied to elastically mounted cylinders in tandem arrangement*. *Journal of Fluids and Structures*, 113:103686, 2022.

[171] JG Schepers, K Boorsma, T Cho, S Gomez-Iradi, P Schaffarczyk, WZ Shen, T Lutz, B Stoevesandt, S Schreck, D Micallef and others. *Analysis of Mexico wind tunnel measurements. Final report of IEA Task 29, Mexnext (Phase 1)*. 2012.

[172] A. Bechmann, N. N. Sørensen and F. Zahle. *CFD simulations of the MEXICO rotor*. *Wind Energy*, 14(5):677–689, 2011.

[173] M. Carrión, R. Steijl, M. Woodgate, G. Barakos, X. Munduate and S. Gomez-Iradi. *Computational fluid dynamics analysis of the wake behind the MEXICO rotor in axial flow conditions*. *Wind Energy*, 18(6):1023–1045, 2015.

[174] Borja Plaza, Rafael Bardera and Sergio Visiedo. *Comparison of BEM and CFD results for MEXICO rotor aerodynamics*. *Journal of Wind Engineering and Industrial Aerodynamics*, 145:115–122, 2015.

[175] Niels N. Sørensen, F. Zahle, K. Boorsma and G. Schepers. *CFD computations of the second round of MEXICO rotor measurements*. *Journal of Physics: Conference Series*, 753(2), 2016.

[176] Yaoru Qian, Zhenyu Zhang and Tongguang Wang. *Comparative study of the aerodynamic performance of the new MEXICO rotor under yaw conditions*. *Energies*, 11(4), 2018.

[177] Rafael V. Rodrigues and Corinne Lengsfeld. *Development of a computational system to improve wind farm layout, Part I: Model validation and near wake analysis*. *Energies*, 12(5), 2019.

[178] P. García Regodeseves and C. Santolaria Morros. *Unsteady numerical investigation of the full geometry of a horizontal axis wind turbine: Flow through the rotor and wake*. *Energy*, 202:117674, 2020.

[179] Jess A Michelsen. *Block structured Multigrid solution of 2D and 3D elliptic PDE's*. Department of Fluid Mechanics, Technical University of Denmark, 1994.

[180] Niels N Sørensen. *General purpose flow solver applied to flow over hills*. 1995.

[181] S. Iradi Gomez. *CFD for Horizontal Axis Wind Turbines*. Ph.D. Thesis, University of Liverpool, 2009.

[182] Berend Gvan der Wall. *2nd HHC aeroacoustic rotor test (HART II)-Part I: Test Documentation*. 2003.

[183] Joon W Lim, Chee Tung, Yung H Yu, Casey L Burley, Thomas Brooks, Doug Boyd, Berend Van Der Wall, Oliver Schneider, Hugues Richard and Markus Raffel. *HART-II: Prediction of blade-vortex interaction loading*. Technical report, NATIONAL AERONAUTICS AND SPACE ADMINISTRATION MOFFETT FIELD CA ROTORCRAFT . . . , 2003.

[184] Berend Gvan der Wall, Casey L Burley, Yung Yu, Hugues Richard, Kurt Pengel and Philippe Beaumier. *The HART II test–measurement of helicopter rotor wakes*. *Aerospace Science and Technology*, 8(4):273–284, 2004.

[185] Berend Gvan der Wall and Casey L Burley. *2nd HHC aeroacoustic rotor test (HART II)-Part II: representative results*. 2005.

[186] Oliver Schneider. *Analysis of SPR measurements from HART II*. *Aerospace Science and Technology*, 9(5):409–420, 2005.

[187] YG Perivolaris and SG Voutsinas. *A cfd performance analysis of vortex generators used for boundary layer control on wind turbine blades*. *Proceedings of the European Wind Energy Conference, Copenhagen, Denmark*, volume 10, pages 4626–6247, 2001.

[188] Hanns Mueller-Vahl, Georgios Pechlivanoglou, CN Nayeri and CO Paschereit. *Vortex generators for wind turbine blades: A combined wind tunnel and wind turbine parametric study*. Turbo Expo: Power for Land, Sea, and Air, volume 44724, pages 899–914. American Society of Mechanical Engineers, 2012.

[189] L Chng, J Alber, D Ntouras, G Papadakis, N Kaufmann, P Ouro and M Manolesos. *On the combined use of Vortex Generators and Gurney Flaps for turbine airfoils*. *Journal of Physics: Conference Series*, 2265(3):032040, 2022.

[190] Anthoula N Panteli, Dimitris I Manolas, Vasilis A Riziotis and Konstantinos V Spiliopoulos. *Comparative study of two geometrically non-linear beam approaches for the coupled wind turbine system*. *Journal of Wind Engineering and Industrial Aerodynamics*, 231:105231, 2022.

[191] Konstantinos Diakakis. *Computational analysis of transitional and massively separated flows with application to Wind Turbines*. Ph.D. Thesis, National Technical University of Athens, School of Mechanical Engineering, 2019.

[192] F. Moukalled, L. Mangani and M. Darwish. *The Finite Volume Method in Computational Fluid Dynamics*, volume 113 at *Fluid Mechanics and Its Applications*. Springer International Publishing, Cham, 2016.

Εκτεταμενη Ελληνικη Περιληψη

Στο κεφάλαιο αυτό παρατίθεται μια εκτεταμένη περίληψη της διατριβής γραμμένη στα Ελληνικά.

Α Εισαγωγη

Οι Ανεμογεννήτριες (ΑΓ) και τα ελικόπτερα είναι χαρακτηριστικά τεχνολογικά επιτεύγματα τα οποία αξιοποιούν τις ατμοσφαιρικές ροές για την παραγωγή ωφέλιμου έργου. Η εκμετάλλευση του ανέμου για την παραγωγή ηλεκτρικής ενέργειας είναι εδώ και χρόνια εφικτή χάρη στις ΑΓ. Συνεπώς, για τη μείωση του κόστους παραγωγής της ηλεκτρικής ενέργειας από τον άνεμο είναι επιθυμητή τόσο η μείωση του κόστους κατασκευής των ΑΓ, όσο και η αύξηση της απόδοσής τους. Αντίστοιχα, στον τομέα των ελικοπτέρων παρατηρείται ραγδαία ανάπτυξη τα τελευταία χρόνια με στόχο τη βελτίωση της ασφάλειας και της απόδοσης των εναέριων μεταφορών, αλλά και άλλων υπηρεσιών που αυτά παρέχουν, όπως η πυρόσβεση, οι γεωργικές εργασίες κ.α. Με αυτό το σκεπτικό, η έρευνα στις μέρες μας κατευθύνεται στην ανάπτυξη αξιόπιστων υπολογιστικών εργαλείων, ικανών να προβλέπουν όλα τα επιμέρους σύνθετα φυσικά φαινόμενα που λαμβάνουν χώρα κατά τη διάρκεια της αλληλεπίδρασης ενός δρομέα με τον αέρα, ούτως ώστε αυτά να αναλυθούν με ακρίβεια και να γίνουν πλήρως κατανοητά. Τέτοια εργαλεία είναι ιδιαίτερα χρήσιμα στη φάση του σχεδιασμού και μπορούν να βοηθήσουν σημαντικά στη βελτίωση της ασφάλειας και της απόδοσης τόσο των ΑΓ, όσο και των ελικοπτέρων.

Στην προσπάθεια μείωσης του κόστους παραγωγής της αιολικής ενέργειας, οι ΑΓ αυξάνουν σε μέγεθος. Με τη σειρά τους, τα πτερύγια του δρομέα γίνονται όλο και μεγαλύτερα, συνεπώς και πιο εύκαμπτα. Σαν αποτέλεσμα, υφίστανται μεγάλες παραμορφώσεις που επηρεάζουν σημαντικά τόσο την ελαστο-δυναμική τους συμπεριφορά, όσο και το κοντινό πεδίο ροής, δημιουργώντας έτσι ένα σύνθετο αεροελαστικό φαινόμενο. Αντίστοιχα, οι δρομείς των ελικοπτέρων χαρακτηρίζονται από πολύπλοκους μηχανισμούς λειτουργίας με πολύ εύκαμπτα πτερύγια, συνιστώντας έτσι ένα ιδιαίτερα σύνθετο δυναμικό σύστημα με έντονα μη-γραμμικές αποκρίσεις. Εύλογα, επομένως, προκύπτει η ανάγκη δημιουργίας υπολογιστικών εργαλείων υψηλής ακρίβειας για τη λεπτομερή ανάλυση σύνθετων αεροελαστικών φαινομένων, ούτως ώστε να βοηθηθεί ο σχεδιασμός τέτοιων πολύπλοκων και εύκαμπτων κατασκευών.

Στόχος αυτής της διατριβής είναι η ανάπτυξη και η πιστοποίηση ενός υπολογιστικού εργαλείου υψηλής ακρίβειας για την αεροελαστική ανάλυση δρομέων. Για την εξασφάλιση τόσο της γενικότητας σε σχέση με την εφαρμογή, όσο και της υψηλής ακρίβειας, το κομμάτι της δυναμικής ανάλυσης βασίζεται στη μέθοδο της Δυναμικής Πολλαπλών Σωμάτων (Multi–Body Dynamics), ενώ για την αεροδυναμική ανάλυση χρησιμοποιούνται μέθοδοι Υπολογιστικής

Ρευστομηχανικής (Computational Fluid Dynamics – CFD) που βασίζονται στην επίλυση των εξισώσεων Navier–Stokes. Τα δύο αυτά συστήματα (ελαστο-δυναμικό και αεροδυναμικό) επιλύονται ξεχωριστά, ενώ η σύνδεσή τους πραγματοποιείται μέσω ενός ειδικά διαμορφωμένου πρωτοκόλλου επικοινωνίας που βασίζεται στη λογική των εσωτερικών επαναλήψεων. Με αυτόν τον τρόπο είναι δυνατή η εύκολη εναλλαγή μεταξύ μοντέλων διαφορετικού κόστους και ακρίβειας.

Ο ελαστο-δυναμικός κώδικας που αναπτύχθηκε στην παρούσα διατριβή είναι μία νέα έκδοση του GAST [1] και του hGAST [2] που αναπτύχθηκαν στο εργαστήριο αεροδυναμικής στο πλαίσιο προηγούμενων διδακτορικών διατριβών. Όπως και στις προηγούμενες εκδόσεις του GAST, οι διάφορες συνιστώσες μίας κατασκευής (ΑΓ, ελικόπτερο κ.α.) μοντελοποιούνται σαν δοκοί. Η ελαστική τους ανάλυση βασίζεται στη θεωρία δοκών Timoshenko και η διακριτοποίησή των διαφορικών τους εξισώσεων στο χώρο πραγματοποιείται μέσω της Αρχής των Δυνατών Έργων (Principle of Virtual Work) και της Μεθόδου των Πεπερασμένων Στοιχείων (Finite Element Method – FEM). Στη νέα μορφή του κώδικα, ωστόσο, η κινηματική και η δυναμική ανάλυση που ακολουθείται για τη σύνδεση των επιμέρους συνιστωσών σε μία ενιαία κατασκευή είναι γενικής εφαρμογής και δεν περιορίζεται σε ΑΓ. Για το σκοπό αυτό, ακολουθείται η μέθοδος της Δυναμικής Πολλαπλών Σωμάτων και η σύνδεση μεταξύ δύο ανεξάρτητα κινούμενων σωμάτων (δοκών) πραγματοποιείται μέσω της επαλήθευσης κατάλληλων μη–γραμμικών κινηματικών και δυναμικών εξισώσεων σύνδεσης [36]. Ως εκ τούτου, ο GAST μπορεί πλέον να προσομοιώνει τη λειτουργία οποιασδήποτε διάταξης αποτελείται από δοκούς.

Σε προηγούμενες εκδόσεις του, ο GAST είχε συνδεθεί με το RAFT [103], έναν χαμηλού κόστους και ακρίβειας αεροδυναμικό κώδικα ανάλυσης δρομέων που βασίζεται στη μέθοδο Δίσκου Ορμής και Στοιχείων Πτερύγωσης (Blade Element Momentum Theory – BEMT), και τον GenUVP [42], έναν αεροδυναμικό κώδικα μέσης ακρίβειας που μοντελοποιεί αεροδυναμικά σώματα οποιασδήποτε γεωμετρίας (κινούμενα ή μη) μέσω των Μεθόδων των Συνοριακών Στοιχείων (Boundary Element Methods – BEM) και τον ομόρρου τους μέσω Στοιχείων Ελεύθερης Στροβιλότητας (Free Vortex Wake – FVW). Λόγω της αδυναμίας αυτών των μεθοδολογιών να περιγράψουν με ακρίβεια τα έντονα συμπιεστά και συνεκτικά φαινόμενα, η νέα έκδοση του GAST συνδέθηκε, στο πλαίσιο αυτής της διατριβής, με το MaPFlow και το HoPFlow [4], δύο αεροδυναμικούς κώδικες υψηλής ακρίβειας που επιλύουν τις συμπιεστές εξισώσεις Navier–Stokes. Ο υπολογιστικός κώδικας MaPFlow επιλύει τις συμπιεστές μη-μόνιμες εξισώσεις Navier–Stokes για ένα χρονικά μέσο πεδίο κατά Reynolds (URANS). Η χωρική διακριτοποίηση των εξισώσεων γίνεται μέσω ενός κεντροκυψελικού σχήματος πεπερασμένων όγκων (cell–centered finite volume scheme), ενώ για την επιτυχή περιγραφή της ροής σε περιοχές όπου ο αριθμός Mach είναι χαμηλός (σύνηθες κατά τη λειτουργία ΑΓ), εφαρμόζεται προσταθεροποίηση (preconditioning) των εξισώσεων της ροής. Η ολοκλήρωση τους στο χώρο και στο χρόνο πραγματοποιείται με τη χρήση σχημάτων 2ης τάξης. Σε εφαρμογές πολλαπλών σωμάτων, όπου συνυπάρχουν περισσότερα του ενός σώματα και κινούνται στο χώρο ανεξάρτητα το ένα από το άλλο (π.χ. αλληλεπίδραση δρομέα ΑΓ και εδάφους), η μοντελοποίηση των αεροδυναμικών σωμάτων γίνεται με τη μέθοδο της Γραμμής Δράσης (Actuator Line - AL). Στην περίπτωση αυτή, το πτερύγιο ενός δρομέα αντικαθίσταται από μία αλληλουχία σημείων ελέγχου (control points) που τοποθετούνται κατά τον

άξονα του πτερυγίου σχηματίζοντας μία γραμμή και πραγματοποιούν χωρίς περιορισμούς όλες τις κινήσεις του πτερυγίου εντός του υπολογιστικού πλέγματος. Για κάθε ένα από αυτά τα σημεία ελέγχου υπολογίζεται μέσω της πεδιακής λύσης μία φαινόμενη ταχύτητα ροής και με τη βοήθεια πινακοποιημένων αδιάστατων συντελεστών (2D polars) πραγματοποιείται μία εκτίμηση των αντίστοιχων αεροδυναμικών δυνάμεων του πτερυγίου στη θέση αυτή. Με τη μέθοδο της Γραμμής Δράσης, περιορίζεται σημαντικά το υπολογιστικό κόστος, με αποτέλεσμα να καθίσταται δυνατή η χρήση του νέου αυτού αεροελαστικού εργαλείου (GAST–AL) και για σειρές τρεξιμάτων κατά τη φάση του σχεδιασμού. Στην περίπτωση αυτή, και ιδίως κατά το σχεδιασμό ΑΓ, απαιτείται η ανάλυση της λειτουργίας τους σε τυρβώδεις συνθήκες ανέμου. Για το σκοπό αυτό, κατά τη διάρκεια αυτής της διατριβής αναπτύχθηκε και ενσωματώθηκε στο MaPFlow μία νέα μεθοδολογία για την υπέρθεση ενός τυρβώδους προφίλ διαταραχών ταχυτήτων σε ένα μέσο πεδίο ανέμου. Η μοντελοποίηση της πραγματικής γεωμετρίας ενός αεροδυναμικού σώματος σε εφαρμογές πολλαπλών σωμάτων είναι δυνατή με τη χρήση του υβριδικού CFD κώδικα HoPFlow. Στην περίπτωση αυτή, η χωρική διατύπωση (Eulerian formulation) των εξισώσεων της ροής επιλύεται από το MaPFlow σε ένα σωματόδετο πλέγμα που περιορίζεται κοντά στο εκάστοτε αεροδυναμικό σώμα, ενώ μακριά από τα σώματα οι εξισώσεις της ροής διατυπώνονται στην υλική τους έκφραση (Lagrangian formulation) και η εξέλιξη της ροής περιγράφεται παρακολουθώντας την κίνηση και την αλλαγή των ροϊκών μεγεθών που χαρακτηρίζουν ορισμένα υλικά σωματίδια (Lagrangian Particles) που δρουν σαν ροϊκοί σημειακοί δείκτες.

Συνοψίζοντας, στην παρούσα διατριβή αναπτύχθηκε ένα νέο υπολογιστικό εργαλείο υψηλής ακρίβειας, για την αεροελαστική ανάλυση δρομέων. Λόγω της γενικότητας στην εφαρμογή των επιμέρους μεθοδολογιών που χρησιμοποιήθηκαν για την δημιουργία του, το νέο αυτό εργαλείο είναι σε θέση να προσομοιώνει διαφορετικού τύπου δρομείς (π.χ. δρομείς οριζόντιων και κατακόρυφων ΑΓ, κύριο και ουραίο στροφείο ελικοπτέρου, drones, αεροπορικές έλικες κ.α.), που λειτουργούν κάτω από ένα μεγάλο εύρος αριθμών Mach στην υπο–ηχιτική περιοχή, όπως και άλλων αεροδυναμικών κατασκευών που μπορούν να μοντελοποιηθούν σαν διατάξεις δοκών (π.χ. πλήρεις διατάξεις ανεμογεννητριών και ελικοπτέρων, διατάξεις από φωτοβολταϊκά πάνελ κ.α.). Για το λόγο αυτό, στην παρούσια διατριβή εξετάζονται δρομείς τόσο ΑΓ, όσο και ελικοπτέρων. Για την πιστοποίηση της υψηλής του ακρίβειας, τα αποτελέσματά του νέου αυτού αεροελαστικού κώδικα συγκρίνονται με πειραματικές μετρήσεις και υπολογιστικές προβλέψεις που παράχθηκαν από άλλα εργαλεία παρόμοιας ακρίβειας. Τέλος, σύγκριση πραγματοποιείται και με υπολογιστικές προβλέψεις ήδη πιστοποιημένων προγραμμάτων αεροελαστικής ανάλυσης δρομέων, αλλά χαμηλότερης ακρίβειας, που αναπτύχθηκαν παλαιότερα στο εργαστήριο Αεροδυναμικής του ΕΜΠ. Τα εργαλεία αυτά χρησιμοποιούν πιο οικονομικά και λιγότερο ακριβή αεροδυναμικά μοντέλα που βασίζονται στη μέθοδο BEMT και στη μέθοδο της Γραμμής Άνωσης (Lifting Line – LL), μέθοδοι οι οποίες χρησιμοποιούνται κατά κόρον στη φάση του σχεδιασμού δρομέων ΑΓ και ελικοπτέρων αντίστοιχα.

Το οικονομικό αεροελαστικό εργαλείο GAST–AL χρησιμοποιήθηκε για την ανάλυση της λειτουργίας του δρομέα της πρότυπης ΑΓ 10MW που σχεδιάστηκε στο DTU [151], υπό σταθερές και τυρβώδεις συνθήκες ανέμου. Δοκιμάστηκαν συνθήκες αξονικής ροής και ροής υπό διάφορες γωνίες απόκλισης για διαφορετικές ταχύτητες ανέμου, ενώ εξετάστηκε και η

περίπτωση της λειτουργίας της πλήρους διάταξης της ΑΓ (πύργος, άξονας, δρομέας) υπό τυρβώδεις συνθήκες ανέμου και εντός του οριακού στρώματος του εδάφους. Τα αποτελέσματα του νέου αυτού εργαλείου συγκρίνονται με αυτά που παράγονται όταν ο ίδιος ελαστοδυναμικός κώδικας (GAST) συνδέεται με τη μέθοδο BEMT και τη μέθοδο LL. Στις απλές περιπτώσεις της αξονικής ροής παρατηρείται πολύ καλή συμφωνία μεταξύ των διαφορετικών υπολογιστικών εργαλείων, ενώ διαφορές προκύπτουν στην περίπτωση των πιο σύνθετων συνθηκών λειτουργίας (ροή με απόκλιση ανέμου, ροή εντός του οριακού στρώματος του εδάφους) μεταξύ του χαμηλότερης ακρίβειας μοντέλου BEMT και των άλλων δύο μεγαλύτερης ακρίβειας μοντέλων (LL και AL), οι προβλέψεις των οποίων συμφωνούν πάρα πολύ καλά μεταξύ τους. Ειδικά στην περίπτωση της λειτουργίας της ΑΓ σε τυρβώδη άνεμο και εντός του οριακού στρώματος του εδάφους αναδεικνύεται η ικανότητα του νέου αυτού εργαλείου να περιγράφει με ακρίβεια σύνθετα ροϊκά φαινόμενα και να προβλέπει επιτυχώς την αλληλεπίδραση μεταξύ του δρομέα και του εδάφους με την ατμοσφαιρική τύρβη. Ακόμη, εξετάστηκε η περίπτωση του μοντέλου του δρομέα ελικοπτέρου που χρησιμοποιήθηκε στο πείραμα HeliNOVI [10] για συνθήκες ευθείας πτήσης σε μικρές, μεσαίες και μεγάλες ταχύτητες. Εδώ, τα αποτελέσματα του νέου εργαλείου (GAST–AL) συγκρίνονται με πειραματικές μετρήσεις και με τις προβλέψεις που προκύπτουν όταν χρησιμοποιείται το αεροδυναμικό μοντέλο που βασίζεται στη θεωρία LL. Σε αυτήν την περίπτωση παρατηρείται μία γενικά καλή συμφωνία μεταξύ των προβλέψεων και των πειραματικών μετρήσεων, ενώ όταν προκύπτουν διαφορές, τα δύο υπολογιστικά εργαλεία συμφωνούν πολύ καλά μεταξύ τους.

Το πιο ακριβές, αλλά και με μεγαλύτερες υπολογιστικές απαιτήσεις, αεροελαστικό εργαλείο GAST–HoPFlow είναι σε θέση να μοντελοποιεί την πραγματική γεωμετρία πολλών και ανεξάρτητα κινούμενων σωμάτων. Για την πιστοποίηση της ακρίβειας των αποτελεσμάτων του, χρησιμοποιήθηκε αρχικά για την αεροδυναμική ανάλυση του μοντέλου δρομέα ΑΓ που μελετήθηκε στο πείραμα New MEXICO [11]. Η πολύ καλή σύγκριση των υπολογισμών των αεροδυναμικών φορτίων των πτερυγίων, τόσο με τις πειραματικές μετρήσεις, όσο και με υπολογιστικές προβλέψεις από άλλους CFD κώδικες επαληθεύουν τη διαδικασία σύνδεσης μεταξύ του χωρικού (Eulerian) επιλύτη MaPFlow, που χρησιμοποιείται στην περιοχή κοντά στα σώματα, και του σωματιδιακού (Lagrangian) επιλύτη που χρησιμοποιείται στο μακρινό πεδίο. Ακόμη, η μειωμένη αριθμητική διάχυση που χαρακτηρίζει την υλική διατύπωση των εξισώσεων της ροής στο μακρινό πεδίο, οδηγεί σε μία πιο ακριβή πρόβλεψη του ελλείματος ταχύτητας που διαμορφώνεται κατάντι και σε καλύτερη συμφωνία με τις πειραματικές μετρήσεις σε σχέση με την περίπτωση που χρησιμοποιείται ο Eulerian επιλύτης MaPFlow. Στη συνέχεια, ο αεροελαστικός επιλύτης GAST–HoPFlow χρησιμοποιήθηκε για την αεροελαστική ανάλυση του μοντέλου του δρομέα ελικοπτέρου που χρησιμοποιήθηκε στο πείραμα HARTII [13] σε συνθήκες πτήσης καθόδου. Και σε αυτήν την περίπτωση η σύγκριση των αποτελεσμάτων του νέου αυτού εργαλείου, τόσο με πειραματικές μετρήσεις, όσο και με προβλέψεις από άλλους υπολογιστικούς κώδικες αντίστοιχης ακρίβειας είναι πολύ καλή και πιστοποιεί την ακρίβεια των επιμέρους επιλυτών και την ορθότητα της διαδικασίας που ακολουθήθηκε για τη σύνδεσή τους.

Βʹ Μεθοδολογία

Στην ενότητα αυτή παρατίθεται το θεωρητικό υπόβαθρο στο οποίο βασίζονται οι υπολογιστικοί κώδικες που χρησιμοποιούνται στην παρούσα διατριβή. Πρώτα αναλύεται ο ελαστο-δυναμικός κώδικας GAST και στη συνέχεια ακολουθούν ο Eulerian CFD επιλύτης MaPFlow, (έμφαση δίνεται στις μεθόδους που αναπτύχθηκαν κατά τη διάρκεια αυτής της διατριβής, δηλαδή στη μέθοδο της Γραμμής Δράσης (AL) και στη μέθοδο της Ζώνης Παραγωγής (Generation Zone – GZ), για την επιβολή των τυρβωδών διαταραχών ταχύτητας σε ένα μέσο πεδίο) και ο υβριδικός CFD επιλύτης HoPFlow.

Βʹ.1 Ο *ελαστοδυναμικος επιλυτης* GAST

Η ελαστο–δυναμική απόκριση ενός συστήματος αναλύεται με τη χρήση του επιλύτη GAST [1, 29, 37, 38]. Ο GAST προσεγγίζει μία συνολική κατασκευή σαν ένα σύνολο από επιμέρους τμήματα (δοκούς), για τη δυναμική ανάλυση των οποίων ακολουθείται η μέθοδος της Δυναμικής Πολλαπλών Σωμάτων (βλέπε Εικόνα 5.1). Σύμφωνα με αυτήν, ένα τοπικό σύστημα συντεταγμένων [$O(x, y, z)$] είναι προσδεδεμένο στην αρχή της κάθε δοκού (P1), με βάση το οποίο καθορίζονται οι ελαστικές παραμορφώσεις της. Η θέση και ο προσανατολισμός ενός σώματος k καθορίζονται με βάση το Διάνυσμα Θέσης $\mathbf{R}^k$ και το Μητρώο Στροφής $\mathbf{T}^k$ του συστήματος συντεταγμένων του. Έτσι, η δυναμική συμπεριφορά ενός οποιουδήποτε σημείου που ανήκει στο σώμα k μπορεί να καθοριστεί με βάση τις εξισώσεις της Δυναμικής Πολλαπλών Σωμάτων:

$$
\begin{aligned}
\mathbf{r}_G^k &= \mathbf{R}^k + \mathbf{T}^k \left(\mathbf{r}_L^k + \mathbf{S}\mathbf{u}^k(t) \right) \\
\dot{\mathbf{r}}_G^k &= \dot{\mathbf{R}}^k + \dot{\mathbf{T}}^k \left(\mathbf{r}_L^k + \mathbf{S}\mathbf{u}^k(t) \right) + \mathbf{T}^k \left(\mathbf{S}\dot{\mathbf{u}}^k(t) \right) \\
\ddot{\mathbf{r}}_G^k &= \ddot{\mathbf{R}}^k + \ddot{\mathbf{T}}^k \left(\mathbf{r}_L^k + \mathbf{S}\mathbf{u}^k(t) \right) + 2\dot{\mathbf{T}}^k \left(\mathbf{S}\dot{\mathbf{u}}^k(t) \right) + \mathbf{T}^k \left(\mathbf{S}\ddot{\mathbf{u}}^k(t) \right)
\end{aligned}
\tag{5.1}
$$

όπου $\mathbf{r}_L^k = \left(x_L^k, y_L^k, z_L^k \right)^T$ είναι οι τοπικές συντεταγμένες του σημείου στην αρχική απαραμόρφωτη κατάσταση, $\mathbf{u}^k = \left(u^k, v^k, w^k, \theta_x^k, \theta_y^k, \theta_z^k \right)^T$ είναι το διάνυσμα των τοπικών παραμορφώσεων (μετατοπίσεις και γωνίες), ενώ $\dot{\mathbf{u}}^k = \left(\dot{u}^k, \dot{v}^k, \dot{w}^k, \dot{\theta}_x^k, \dot{\theta}_y^k, \dot{\theta}_z^k \right)^T$ και $\ddot{\mathbf{u}}^k = \left(\ddot{u}^k, \ddot{v}^k, \ddot{w}^k, \ddot{\theta}_x^k, \ddot{\theta}_y^k, \ddot{\theta}_z^k \right)^T$ είναι οι αντίστοιχες ταχύτητες και επιταχύνσεις (όλα ορίζονται στο τοπικό σύστημα συντεταγμένων του σώματος k). Το μητρώο $\mathbf{S}$ δίνεται από τον τύπο:

$$
\mathbf{S} = \begin{bmatrix} 1 & 0 & 0 & 0 & z_L^k & 0 \\ 0 & 1 & 0 & -z_L^k & 0 & x_L^k \\ 0 & 0 & 1 & 0 & -x_L^k & 0 \end{bmatrix}
\tag{5.2}
$$
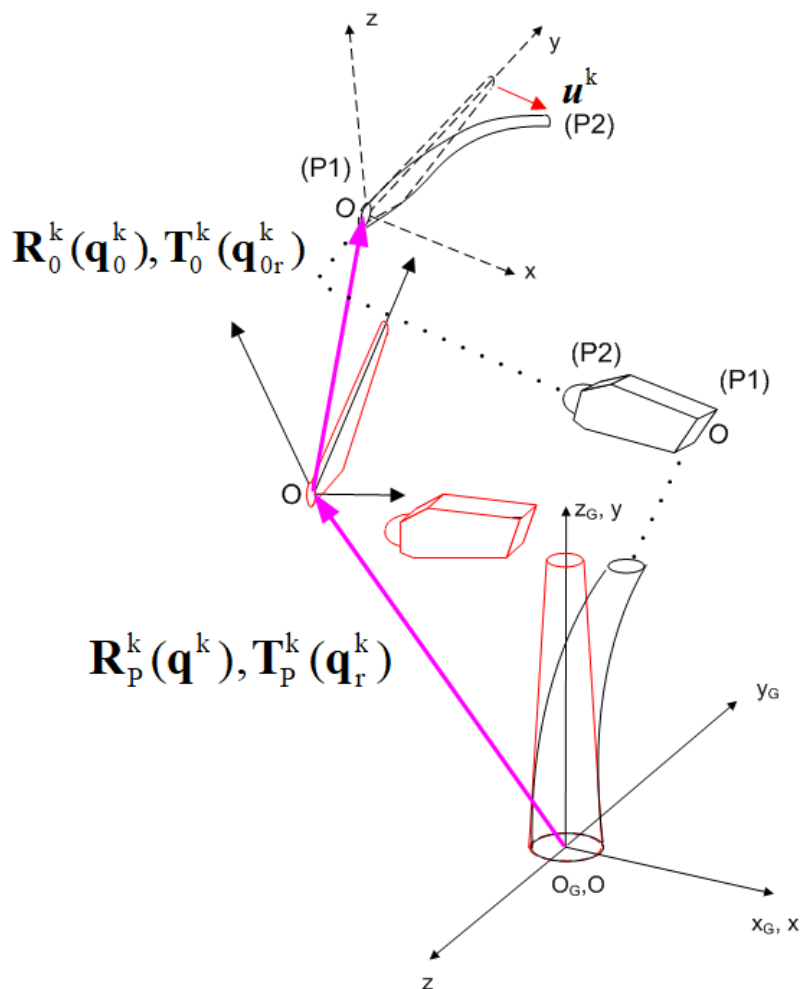
Figure 5.1. *Μοντελοποίηση της διάταξης ανεμογεννήτριας με βάση τη Μέθοδο των Πολλαπλών Σωμάτων. Η αρχική απαραμόρφωτη κατάσταση απεικονίζεται με κόκκινη γραμμή, ενώ η παραμορφωμένη κατάσταση με μαύρη. Οι κινηματικοί βαθμοί ελευθερίας* $\mathbf{q}^k$ *ενός σώματος k καθορίζονται από τις κινήσεις που κάνει το σώμα από μόνο του, ενώ οι τοπικοί κινηματικοί βαθμοί ελευθερίας* $\mathbf{q}_0^k$ *καθορίζονται από τα σώματα με τα οποία συνδέεται το σώμα k.*

Το διάνυσμα θέσης $\mathbf{R}^k$ και το Μητρώο Στροφής $\mathbf{T}^k$ ενός σώματος k καθορίζονται ως προς το αδρανειακό σύστημα σύστημα συντεταγμένων $[O_G (x_G, y_G, z_G)]$ με βάση τους κινηματικούς βαθμούς ελευθερίας $\mathbf{q}^k = \left[\mathbf{q}_t^k, \mathbf{q}_r^k \right]^T$, οι οποίοι χωρίζονται σε γραμμικές μετακινήσεις $\left(\mathbf{q}_t^k \right)$ και γωνίες στροφής $\left(\mathbf{q}_r^k \right)$ που μπορεί να μεταβάλλονται στο χρόνο ή να παραμένουν σταθερές. Εκτός από όλες τις μετακινήσεις και τις γωνίες στροφής που υφίσταται το σώμα k λόγω των δικών του κινήσεων, το διάνυσμα θέσης $\mathbf{R}^k$ και το Μητρώο Στροφής $\mathbf{T}^k$ του σώματος καθορίζονται επιπλέον από ένα σετ τοπικών κινηματικών βαθμών ελευθερίας $\mathbf{q}_0^k = \left[\mathbf{q}_{0t}^k, \mathbf{q}_{0r}^k \right]^T$, οι οποίοι χωρίζονται σε σε γραμμικές μετακινήσεις $\left(\mathbf{q}_{0t}^k \right)$ και γωνίες στροφής $\left(\mathbf{q}_{0r}^k \right)$ που υφίσταται το σώμα k λόγω της σύνδεσής του με άλλα σώματα (π.χ. τα πτερύγια μιας ανεμογεννήτριας υφίστανται επιπλέον μετακινήσεις και γωνίες στροφής λόγω της παραμόρφωσης του πύργου). Οι τιμές του $\mathbf{q}_0^k$ υπολογίζονται ικανοποιώντας κατάλληλες μη-γραμμικές εξισώσεις σύνδεσης μεταξύ των επιμέρους δοκών της συνολικής κατασκευής. Από αυτήν την άποψη, μπορεί να ειπωθεί ότι οι ελαστικές παραμορφώσεις των σωμάτων που είναι συνδεδεμένα με τη δοκό k,

αθροίζονται/συσσωρεύονται στο $\mathbf{q}_0^k$ και οι μεγάλες αυτές κινήσεις πραγματοποιούνται από το σώμα k υπό τη μορφή μεγάλων κινήσεων απαραμόρφωτου σώματος (rigid–body motion). Έτσι, οι σχέσεις για τον υπολογισμό του Διανύσματος Θέσης $\mathbf{R}^k$ και του Μητρώου Στροφής $\mathbf{T}^k$ ενός σώματος k παίρνουν τη μορφή:

$$
\begin{aligned}
\mathbf{R}^k &= \mathbf{R}_p^k\left(\mathbf{q}^k, t\right) + \mathbf{T}_p^k\left(\mathbf{q}_r^k, t\right)\mathbf{R}_0^k\left(\mathbf{q}_0^k, t\right) \\
\mathbf{T}^k &= \mathbf{T}_p^k\left(\mathbf{q}_r^k, t\right)\mathbf{T}_0^k\left(\mathbf{q}_{0r}^k, t\right)
\end{aligned}
\tag{5.3}
$$

όπου τα μητρώα στροφής $\mathbf{T}_p^k$ και $\mathbf{T}_0^k$ υπολογίζονται σαν μία αλληλουχία από διαδοχικές στοιχειώδεις στροφές γύρω από έναν άξονα (στροφές Euler):

$$
\mathbf{T} = \mathbf{T}_1\left(q_r^1\right)\mathbf{T}_2\left(q_r^2\right)\cdots\mathbf{T}_{m-1}\left(q_r^{m-1}\right)\mathbf{T}_m\left(q_r^m\right)
$$

ενώ τα διανύσματα θέσης $\mathbf{R}_p^k$ και $\mathbf{R}_0^k$ υπολογίζονται σαν μία αλληλουχία από στοιχειώδεις στροφές, κάθε μιας από τις οποίες προηγείται μία στοιχειώδης μετακίνηση κατά μήκος ενός άξονα:

$$
\mathbf{R} = \mathbf{R}_1\left(q_t^1\right) + \mathbf{T}_1\left(q_r^1\right)\left(\mathbf{R}_2\left(q_t^2\right) + \mathbf{T}_2\left(q_r^2\right)\cdots\mathbf{R}_{m-1}\left(q_t^{m-1}\right) + \mathbf{T}_{m-1}\left(q_r^{m-1}\right)\mathbf{R}_m\left(q_t^m\right)\right)
$$

όπου $m = 6$ για τα $\mathbf{R}_0^k$ και $\mathbf{T}_0^k$, ενώ μπορεί να πάρει οποιαδήποτε τιμή για τον καθορισμό των $\mathbf{R}_p^k$ και $\mathbf{T}_p^k$.

Όλα τα εύκαμπτα τμήματα μιας κατασκευής μοντελοποιούνται σαν δοκοί, για την ελαστική ανάλυση των οποίων χρησιμοποιείται η γραμμική θεωρία δοκών Timoshenko μαζί με την καταστατική εξίσωση για τη σχέση τάσεων–τροπών στις διατομές των δοκών που ισχύει στην ελαστική περιοχή (νόμος του Hook):

$$
\textbf{Timoshenko:}\quad \int_A \rho\mathbf{S}^T\mathbf{T}^{k^T}\ddot{\mathbf{r}}_G^k\,dA = \begin{bmatrix} F_x' \\ F_y' \\ F_z' \\ M_x' + F_z - F_y w' \\ M_y' \\ M_x' - F_x + F_y u' \end{bmatrix}^k + \begin{bmatrix} \text{εξωτερικα φορτια} \\ \text{και αντιδασεις} \\ \text{συνδεδεμενων} \\ \text{σωματων} \end{bmatrix} \Bigg\} \Rightarrow
$$

$$
\textbf{Καταστατική:}\quad \mathbf{F}^k = \mathbf{K}^k \epsilon^k
$$

$$
\int_A \rho\mathbf{S}^T\mathbf{T}^{k^T}\ddot{\mathbf{r}}_G^k\,dA = \left(\mathbf{K}_1^k\mathbf{u}'^k\right)' + \left(\mathbf{K}_2^k\mathbf{u}^k\right)' + \left(\mathbf{K}_3^k\mathbf{u}'^k\right) + \left(\mathbf{K}_4^k\mathbf{u}^k\right) + \text{εξωτερικα φορτια}
\tag{5.4}
$$

όπου το $()' = \frac{\partial}{\partial y}$ συμβολίζει τη χωρική παράγωγο στην αξονική κατεύθυνση y της δοκού, ενώ τα $\mathbf{K}_1^k$, $\mathbf{K}_2^k$, $\mathbf{K}_3^k$ και $\mathbf{K}_4^k$ ορίζονται αναλυτικά στην Ενότητα 2.1.2.1. Οι όροι $F_y w'$ και $F_y u'$ στις εξισώσεις των ροπών γύρω από τους x και z άξονες αντίστοιχα είναι οι μόνοι μη–γραμμικοί όροι που έχουν διατηρηθεί στο σετ των δυναμικών εξισώσεων της δοκού. Ο λόγος είναι ότι αυτοί οι όροι αυξάνουν τη φαινόμενη δυσκαμψία της δοκού ανάλογα με το τετράγωνο της γωνιακής ταχύτητας.

Συνδυάζοντας την εξίσωση (5.4) με την Αρχή των Δυνατών Έργων προκύπτει η ασθενής μορφή των εξισώσεων της δοκού:

$$
\int_L \delta\mathbf{u}^{kT} \left[\int_A \rho \mathbf{S}^T \mathbf{T}^{kT} \left[\ddot{\mathbf{R}}^k + \ddot{\mathbf{T}}^k \left(\mathbf{r}_L^k + \mathbf{S}\mathbf{u}^k(t) \right) + 2\dot{\mathbf{T}}^k \left(\mathbf{S}\dot{\mathbf{u}}^k(t) \right) + \mathbf{T}^k \left(\mathbf{S}\ddot{\mathbf{u}}^k(t) \right) \right] dA \right] dy =
$$
$$
-\int_L \delta\mathbf{u'}^{kT} \left(\mathbf{K}_1^k \mathbf{u'}^k \right) dy - \int_L \delta\mathbf{u'}^{kT} \left(\mathbf{K}_2^k \mathbf{u}^k \right) dy + \int_L \delta\mathbf{u}^{kT} \left(\mathbf{K}_3^k \mathbf{u'}^k \right) dy + \int_L \delta\mathbf{u}^{kT} \left(\mathbf{K}_4^k \mathbf{u}^k \right) dy
$$

+ εργο των εξωτερικων δυναμεων + συνοριακοι οροι

$$(5.5)$$

Η διακριτοποιμένη μορφή των εξισώσεων της δοκού που παρουσιάζεται στην εξίσωση (5.6) επιτυγχάνεται εφαρμόζοντας στην εξίσωση (5.5) τη Μέθοδο των Πεπερασμένων Στοιχείων και προσεγγίζοντας τις ελαστικές παραμορφώσεις ενός στοιχείου ως $\mathbf{u}(y, t) = \mathbf{N}(y)\,\hat{\mathbf{u}}(t)$, όπου $\mathbf{N}(y)$ είναι το μητρώο των Συναρτήσεων Μορφής του στοιχείου και $\hat{\mathbf{u}}(t)$ οι χρονικά εξαρτώμενοι ελαστικοί βαθμοί ελευθερίας του στοιχείου, που ορίζονται αναλυτικά στην Ενότητα 2.1.2.1.

$$
\int_{L_e} \mathbf{N}^T(y) \int_A \rho \mathbf{S}^T \mathbf{S} dA \mathbf{N}(y)\, dy\, \ddot{\hat{\mathbf{u}}}(t)
$$
$$
+ \int_{L_e} \mathbf{N}^T(y) \int_A \rho \mathbf{S}^T \mathbf{T}^{kT} 2\dot{\mathbf{T}}^k \mathbf{S} dA \mathbf{N}(y)\, dy\, \dot{\hat{\mathbf{u}}}(t)
$$
$$
+ \int_{L_e} \mathbf{N}^T(y) \int_A \rho \mathbf{S}^T \mathbf{T}^{kT} \ddot{\mathbf{T}}^k \mathbf{S} dA \mathbf{N}(y)\, dy\, \hat{\mathbf{u}}(t)
$$
$$
+ \int_{L_e} \mathbf{N'}^T(y) \mathbf{K}_1^k \mathbf{N'}(y) dy\, \hat{\mathbf{u}}(t) + \int_{L_e} \mathbf{N'}^T(y) \mathbf{K}_2^k \mathbf{N}(y) dy\, \hat{\mathbf{u}}(t) \qquad (5.6)
$$
$$
- \int_{L_e} \mathbf{N}^T(y) \mathbf{K}_3^k \mathbf{N'}(y) dy\, \hat{\mathbf{u}}(t) - \int_{L_e} \mathbf{N}^T(y) \mathbf{K}_4^k \mathbf{N}(y) dy\, \hat{\mathbf{u}}(t) =
$$
$$
- \int_{L_e} \mathbf{N}^T(y) \int_A \rho \mathbf{S}^T \mathbf{T}^{kT} \ddot{\mathbf{R}}^k dA dy - \int_{L_e} \mathbf{N}^T(y) \int_A \rho \mathbf{S}^T \mathbf{T}^{kT} \ddot{\mathbf{T}}^k \mathbf{r}_L^k dA dy
$$

+εργο των εξωτερικων δυναμεων + συνοριακοι οροι

Οι παραπάνω μη–γραμμικές εξισώσεις γραμμικοποιούνται ως προς τους κινηματικούς και τους ελαστικούς βαθμούς ελευθερίας, ακολουθώντας τη Μέθοδο των Διαταραχών:

$$
\mathbf{q} = \mathbf{q}^0 + \Delta\mathbf{q},\ \dot{\mathbf{q}} = \dot{\mathbf{q}}^0 + \Delta\dot{\mathbf{q}},\ \ddot{\mathbf{q}} = \ddot{\mathbf{q}}^0 + \Delta\ddot{\mathbf{q}}
$$
$$
\mathbf{u} = \mathbf{u}^0 + \Delta\mathbf{u},\ \dot{\mathbf{u}} = \dot{\mathbf{u}}^0 + \Delta\dot{\mathbf{u}},\ \ddot{\mathbf{u}} = \ddot{\mathbf{u}}^0 + \Delta\ddot{\mathbf{u}}
$$

$$(5.7)$$

Η γραμμικοποιημένη μορφή των εξισώσεων ενός πεπερασμένου στοιχείου παίρνει τη μορφή:

$$
\mathbf{M}_e^a \Delta\ddot{\mathbf{u}} + \mathbf{C}_e^a \Delta\dot{\mathbf{u}} + \mathbf{K}_e^a \Delta\mathbf{u} + \mathbf{M}_e^q \Delta\ddot{\mathbf{q}} + \mathbf{C}_e^q \Delta\dot{\mathbf{q}} + \mathbf{K}_e^q \Delta\mathbf{q} = \mathbf{Q}_e \qquad (5.8)
$$

όπου τα γενικευμένα μητρώα μάζας, απόσβεσης, δυσκαμψίας και δυνάμεων του στοιχείου ορίζονται αναλυτικά στην Ενότητα 2.1.2.1.

Συγκεντρώνοντας τα μητρώα κατά μήκος των διαδοχικών πεπερασμένων στοιχείων μίας δοκού, το σύστημα των εξισώσεων της δοκού παίρνει τη μορφή της Εικόνας 5.2.
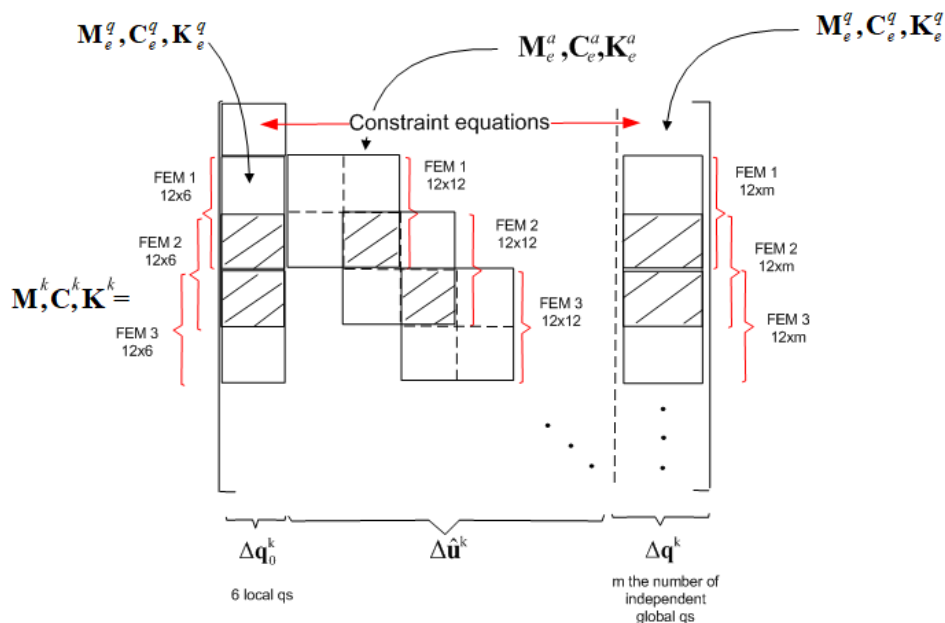
Figure 5.2. *Η μορφή του συστήματος των εξισώσεων μίας μεμονωμένης δοκού χτίζεται συγκεντρώνοντας όλα τα μητρώα κατά μήκος των διαδοχικών πεπερασμένων στοιχείων της δοκού.*

Η σύνδεση των ξεχωριστών δοκών σε μία συνολική διάταξη επιτυγχάνεται με την ικανοποίηση κατάλληλων μη–γραμμικών κινηματικών και δυναμικών εξισώσεων σύνδεσης. Στη γενική περίπτωση της σύνδεσης μεταξύ δύο δοκών r και m, η μία καθορίζει την κινηματική (θέση και προσανατολισμός) του κοινού σημείου σύνδεσης, ενώ η δεύτερη καθορίζει την φόρτισή του (βλέπε Εικόνα 5.3).
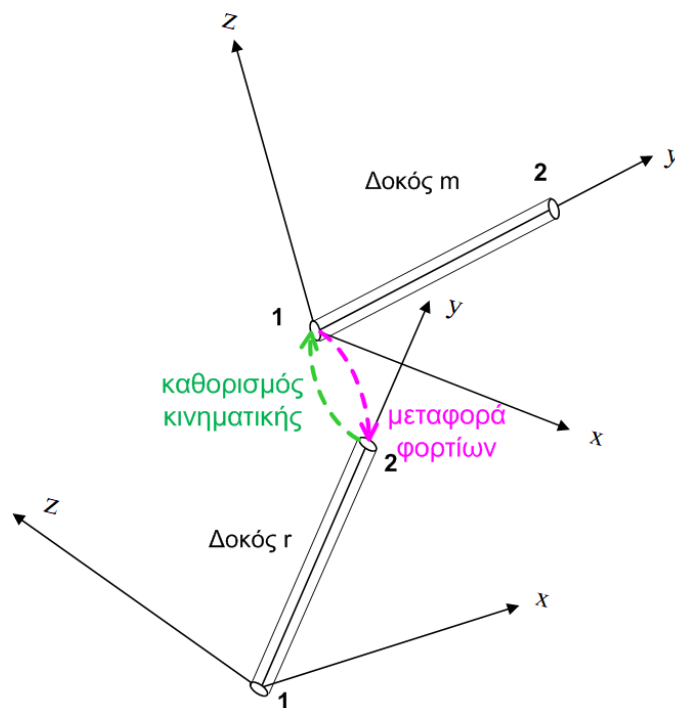
Figure 5.3. *Συνθήκες σύνδεσης μεταξύ δύο δοκών. Η πρώτη (r) καθορίζει την κινηματική του κοινού σημείου σύνδεσης, ενώ η δεύτερη (m) καθορίζει τη φόρτισή του.*

227

Οι κινηματικές συνθήκες σύνδεσης, συνήθως παίρνουν τη μορφή Dirichlet οριακών συν-θηκών με βάση τις οποίες καθορίζονται οι τιμές των τοπικών κινηματικών βαθμών ελευθερίας $\mathbf{q}_0^k = \left[\mathbf{q}_{0t}^k, \mathbf{q}_{0r}^k\right]^T$ της κάθε δοκού. Οι μη–γραμμικές κινηματικές εξισώσεις για τη σταθερή σύν-δεση μεταξύ δύο δοκών r και m έχουν τη μορφή:

$$\mathbf{r}_G^m (P1 \; or \; P2) - \mathbf{r}_G^r (P1 \; or \; P2) - \mathbf{d}_0^{r,m} = \mathbf{0}$$
$$\boldsymbol{\theta}^{r,m} - \boldsymbol{\theta}_0^{r,m} = \mathbf{0}$$

(5.9)

όπου $\mathbf{d}_0^{r,m}$ και $\boldsymbol{\theta}_0^{r,m}$ η απόσταση και η γωνία αντίστοιχα, μεταξύ των σημείων σύνδεσης (P1 ή P2 της δοκού r και P1 ή P2 της δοκού m). Τα διανύσματα $\mathbf{r}_G^m$ και $\mathbf{r}_G^r$ υπολογίζονται με βάση το αδρανειακό σύστημα συντεταγμένων από την εξίσωση (5.1) και οι σχετικές γωνίες $\boldsymbol{\theta}^{r,m}$ υπολογίζονται γύρω από τους άξονες του τοπικού συστήματος συντεταγμένων της δοκού r σύμφωνα με τις εξισώσεις [36]:

$$\cos \theta_i^{r,m} \left(\mathbf{e}_j^m \cdot \mathbf{e}_k^r\right) - \sin \theta_i^{r,m} \left(\mathbf{e}_k^m \cdot \mathbf{e}_k^r\right) = 0$$

(5.10)

$$\cos \theta_i^{r,m} = \left(\mathbf{e}_k^m \cdot \mathbf{e}_k^r\right)$$
$$\sin \theta_i^{r,m} = \left(\mathbf{e}_j^m \cdot \mathbf{e}_k^r\right)$$

(5.11)

όπου $\mathbf{e}_i^r$ και $\mathbf{e}_i^m$ είναι τα μοναδιαία διανύσματα βάσης που καθορίζουν τον προσανατολισμό των διατομών των δοκών r και m αντίστοιχα.

Οι δυναμικές συνθήκες σύνδεσης συμπληρώνουν τις κινηματικές και καθορίζουν τη φόρ-τιση του κοινού σημείου σύνδεσης. Υλοποιούνται μεταφέροντας τα φορτία αντίδρασης από τον κόμβο της δοκού που δέχεται την κινηματική (έστω το σημείο P1 της δοκού m) στον κόμβο της δοκού που καθορίζει την κινηματική του κοινού σημείου σύνδεσης (έστω το σημείο P2 της δοκού r). Τα φορτία αντίδρασης στους δύο κόμβους ενός πεπερασμένου στοιχείου *e* υπολογίζονται με βάση την εξίσωση (5.12):

$$\begin{bmatrix} \mathbf{Q}^R(1) \\ \mathbf{Q}^R(2) \end{bmatrix} = \mathbf{M}_e^a \Delta\ddot{\mathbf{u}} + \mathbf{C}_e^a \Delta\dot{\mathbf{u}} + \mathbf{K}_e^a \Delta\mathbf{u} + \mathbf{M}_e^q \Delta\ddot{\mathbf{q}} + \mathbf{C}_e^q \Delta\dot{\mathbf{q}} + \mathbf{K}_e^q \Delta\mathbf{q} - \mathbf{Q}_e$$

(5.12)

Οι πρώτες 6 γραμμές $\mathbf{Q}^R(1)^T$ είναι τα φορτία αντίδρασης (δυνάμεις και ροπές) στον 1ο κόμβο του στοιχείου, ενώ οι τελευταίες 6 γραμμές $\mathbf{Q}^R(2)^T$ είναι τα φορτία αντίδρασης στο 2ο κόμβο. Τα φορτία αυτά είναι εκφρασμένα στο τοπικό σύστημα συντεταγμένων της δοκού που περιέχει το συγκεκριμένο στοιχείο (έστω η δοκός m). Επομένως, οι αντιδράσεις αυτών στο σημείο της δοκού που δέχεται τα φορτία (έστω το σημείο P2 της δοκού r) προκύπτουν από τη σχέση:

$$\mathbf{Q}^R(2)^r = -\mathbf{T}^{r\,T} \mathbf{T}^m \mathbf{Q}^R(1)^m$$

(5.13)

Με αυτόν τον τρόπο, ορίζονται πλήρως οι οριακές συνθήκες μίας δοκού (κινηματική ή φορτία στα δύο άκρα) και το σύστημα που προκύπτει για την περίπτωση δύο συνδεδεμένων δοκών r και m παίρνει τη μορφή:
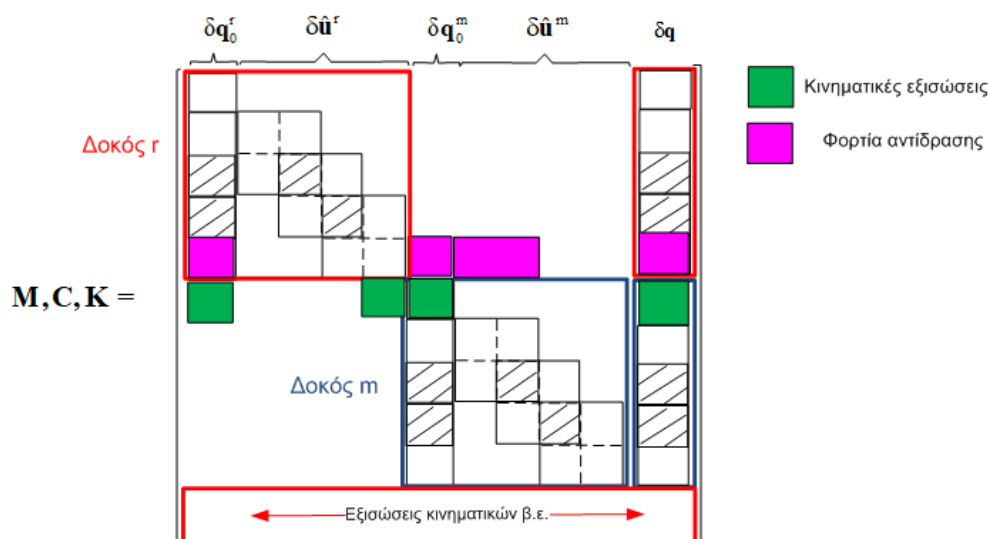
Figure 5.4. *Η μορφή του συστήματος για την περίπτωση της άκαμπτης σύνδεσης μεταξύ δύο δοκών r και m. Η δοκός r καθορίζει την κινηματική του κοινού σημείου σύνδεσης, ενώ η δοκός m τη φόρτισή του.*

Τα πολύ εύκαμπτα σώματα που υφίστανται μεγάλες παραμορφώσεις, μοντελοποιούνται σαν μία αλληλουχία από διαδοχικές γραμμικές δοκούς Timoshenko που συνδέονται μεταξύ τους. Έτσι, οι μεγάλες παραμορφώσεις ενός πολύ εύκαμπτου σώματος χτίζονται σταδιακά, αθροίζοντας τις μικρές παραμορφώσεις (γραμμικές και γωνιακές) των προηγούμενων δοκών Timoshenko σε μεγάλες μετακινήσεις και γωνίες στροφής που εκφράζονται μέσω του διανύσματος θέσης και του μητρώου στροφής των δοκών που ακολουθούν και υπολογίζονται με βάση τις παραπάνω μη–γραμμικές εξισώσεις σύνδεσης. Με αυτόν τον τρόπο, ο ελαστο–δυναμικός κώδικας GAST, είναι σε θέση να προβλέπει με ακρίβεια τα μη–γραμμικά γεωμετρικά και αεροελαστικά φαινόμενα που προκύπτουν λόγω μεγάλων παραμορφώσεων, χρησιμοποιώντας τη γραμμική θεωρία Timoshenko στο επίπεδο τον δοκών, αλλά λαμβάνοντας υπ' όψιν τα μη–γραμμικά φαινόμενα στα σημεία σύνδεσης.

B.2 Ο Eulerian *επιλύτης* MaPFlow

Ο MaPFlow είναι ένας κλασσικός Eulerian CFD επιλύτης που αναπτύχθηκε στο Εργαστήριο Αεροδυναμικής του ΕΜΠ στο πλαίσιο προηγούμενων διδακτορικών διατριβών [4, 191]. Επιλύει τις συμπιεστές μη–μόνιμες εξισώσεις Navier–Stokes για ένα χρονικά μέσο πεδίο κατά Reynolads (URANS). Η χωρική διακριτοποίηση των εξισώσεων γίνεται μέσω ενός κεντροκυψελικού σχήματος πεπερασμένων όγκων. Ο MaPFlow μπορεί να χειριστεί τόσο δομημένα, όσο και μη–δομημένα πλέγματα. Η παραλληλοποίησή του γίνεται σύμφωνα με το πρωτόκολλο επικοινωνίας MPI, ενώ η διαμέριση του πλέγματος στους ξεχωριστούς επεξεργαστές (grid partitioning) υλοποιείται με τη βοήθεια της βιβλιοθήκης METIS [111]. Οι όροι συναγωγής υπολογίζονται επιλύοντας ένα πρόβλημα ασυνέχειας Riemann μεταξύ δύο γειτονικών κελιών, χρησιμοποιώντας τον προσεγγιστικό επιλύτη του Roe [112]. Για τον υπολογισμό των μεταβλητών της ροής στα σύνορα μιας υπολογιστικής κυψέλης ακολουθείται η διαδικασία της 'ανακατασκευής' (reconstruction) των μεταβλητών, θεωρώντας γραμμική μεταβολή της λύσης στον πεπερασμένο όγκο (Piecewise Linear Reconstruction). Για την

αποτροπή των ακραίων τιμών των μεταβλητών στη διεπιφάνεια μεταξύ δύο κελιών, χρησιμοποιείται ο 'περιοριστής' (limiter) του Venkatakrishnan [113], ενώ οι παράγωγοι των μεταβλητών υπολογίζονται στα κέντρα των υπολογιστικών κυψελών είτε με τη μέθοδο του Green–Gauss [124], είτε με τη μέθοδο των Ελαχίστων Τετραγώνων [192]. Οι όροι συναγωγής διακριτοποιούνται χρησιμοποιώντας ένα κεντρικό σχήμα 2ης τάξης. Για την επιτυχή περιγραφή της ροής σε περιοχές όπου ο αριθμός Mach είναι χαμηλός, πραγματοποιείται 'προσταθεροποίηση' (preconditioning) των εξισώσεων της ροής χρησιμποιώντας το Μητρώο Προσταθεροποίησης του Eriksson [121]. Ο MaPFlow διαθέτει πολλές επιλογές για τη μοντελοποίηση της τύρβης, όπως το μοντέλο μίας εξίσωσης των Spalart–Allmaras [114] ή το μοντέλο δύο εξισώσεων $k - \omega$ SST του Menter [115], ενώ ακόμα υπάρχει και η δυνατότητα περιγραφής των μεγάλων δομών στροβιλότητας (δινών) μέσω των μεθόδων LES (για τη μοντελοποίηση των δινών μικρής κλίμακας χρησιμοποιείται το αλγεβρικό μοντέλο του Smagorinsky [167]), DES και DDES [117]. Η ολοκλήρωση των εξισώσεων στο χρόνο πραγματοποιείται μέσω ενός 'άρρητου' (implicit) σχήματος πεπερασμένων διαφορών 2ης τάξης [125, 118] που συνδυάζεται με την τεχνική των 'εσωτερικών ψευδο–χρονικών βημάτων' (dual time–stepping) [119] για τη βελτίωση της σύγκλισης. Τέλος, η επίλυση του γραμμικοποιημένου συστήματος πραγματοποιείται χρησιμοποιώντας την επαναληπτική μέθοδο Gauss–Seidel, μαζί με τη μέθοδο 'αναδιάταξης' (reordering) Reverse Cuthill–Mckee για την ισχυροποίηση της διαγώνιας μορφής του συστήματος [120].

B.2.1 Η μεθοδος της Γραμμης Δρασης – AL

Για την εύκολη διαχείριση εφαρμογών Πολλαπλών Σωμάτων (Multi–Body applications) (π.χ. ανάλυση πολλαπλών δρομέων), αλλά και τον ταυτόχρονο περιορισμό του υπολογιστικού κόστους για την ανάλυσή τους, ενσωματώθηκε στο MaPFlow κατά τη διάρκεια αυτής της διατριβής η μέθοδος της Γραμμής Δράσης (Actuator Line – AL). Στη μέθοδο αυτή, το πεδίο ροής επιλύεται χωρίς να λαμβάνεται αυστηρά υπ' όψιν η φυσική παρουσία ενός σώματος εντός του υπολογιστικού χωρίου. Αντίθετα, το σώμα αυτό μοντελοποιείται σαν μία αλληλουχία από σημεία ελέγχου (control points) κατά τον κύριο άξονά του, που σχηματίζουν μία γραμμή (βλέπε Εικόνα 5.5). Η γραμμή αυτή έχει τη δυνατότητα να κινείται και να παραμορφώνεται ελεύθερα μέσα στο πλέγμα του υπολογιστικού χωρίου, κάτι το οποίο είναι ιδιαίτερα βολικό σε αεροελαστικές προσομοιώσεις πολλαπλών σωμάτων.
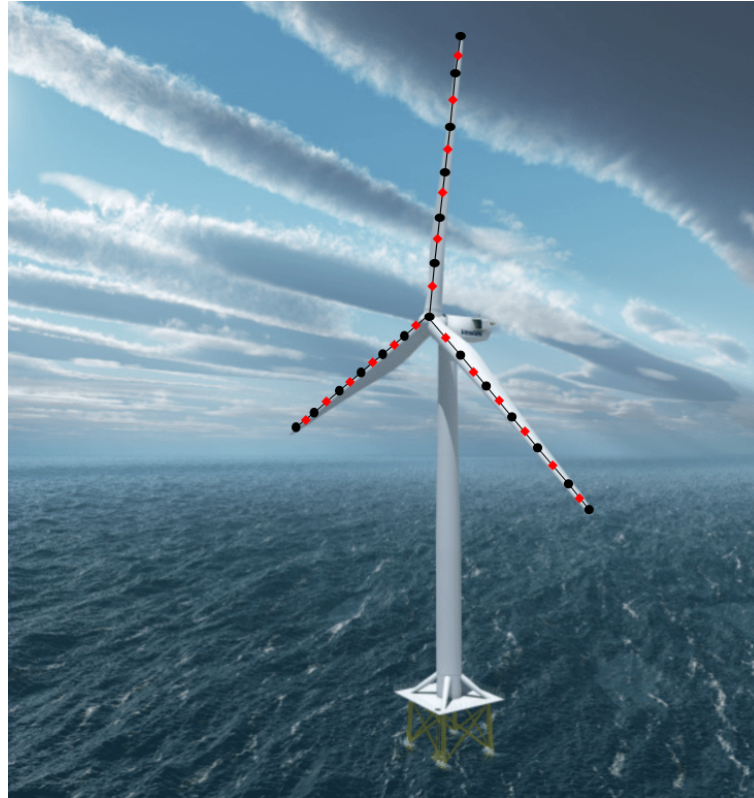
Figure 5.5. *Μοντελοποίηση των πτερυγίων ενός δρομέα ΑΓ με τη μέθοδο Γραμμής Δράσης. Τα σημεία ελέγχου στο κέντρο των στοιχείων πτερύγωσης απεικονίζονται με κόκκινες τελείες, ενώ τα άκρα των στοιχείων πτερύγωσης με μαύρες τελείες.*

Τα σημεία ελέγχου της γραμμής συνήθως τοποθετούνται στα κέντρα των στοιχείων πτερύγωσης στα οποία διακριτοποιείται το υπό μελέτη σώμα (π.χ. πτερύγιο). Σε κάθε ένα από αυτά τη σημεία ελέγχου υπολογίζεται μία τοπική ταχύτητα $\mathbf{W}_{eff}$ (local inflow velocity) μέσω παρεμβολών από τη λύση των υπολογιστικών κελιών που τα περιβάλλουν. Στην παρούσα υλοποίηση της μεθόδου χρησιμοποιούνται συναρτήσεις ΡΒΦ [132] για την πραγματοποίηση των παρεμβολών με βάση τον όγκο και την απόσταση των γειτονικών υπολογιστικών κελιών. Με βάση αυτήν την ταχύτητα, υπολογίζεται και η γωνία πρόσπτωσης a_{eff} του στοιχείου πτερύγωσης. Με αυτήν τη γωνία πρόσπτωσης και τη βοήθεια πινακοποιημένων καμπυλών C_L, C_D, C_M υπολογίζονται τα αεροδυναμικά φορτία του πτερυγίου στη θέση των σημείων ελέγχου ($\mathbf{f}_{cp}, \mathbf{m}_{cp}$), όπως περιγράφεται στην εξίσωση (5.14) και φαίνεται στην Εικόνα 5.6.

$$a_{eff} = arctan\frac{W_{eff,z}}{W_{eff,x}}$$

$$L = \frac{1}{2}\rho W_{eff}^2 C_L(a_{eff})c\Delta r$$

$$D = \frac{1}{2}\rho W_{eff}^2 C_D(a_{eff})c\Delta r$$

$$M = \frac{1}{2}\rho W_{eff}^2 C_M(a_{eff})c^2\Delta r$$

$$\mathbf{f}_{cp} = L\mathbf{e}_L + D\mathbf{e}_D$$

$$\mathbf{m}_{cp} = M\mathbf{e}_M$$

(5.14)
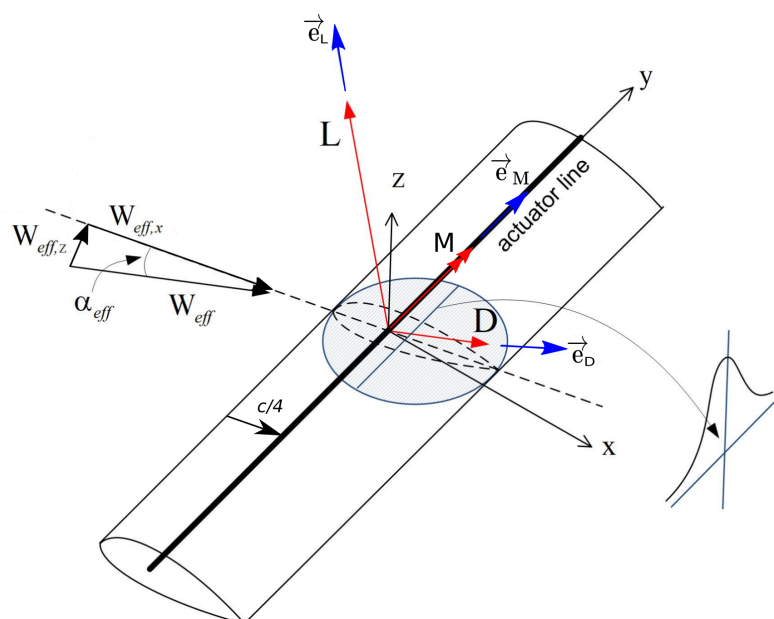
Figure 5.6. *Μοντελοποίηση ενός πτερυγίου με τη μέθοδο Γραμμής Δράσης. Ανάλυση στοιχείων πτερύγωσης για τον υπολογισμό των αεροδυναμικών φορτίων στα σημειά ελέγχου του πτερυγίου και προβολή των αεροδυναμικών δυνάμεων στο χώρο μέσω μιας 3Δ κατανομής Gauss.*

Στη συνέχεια, και για λόγους αριθμητικής ευστάθειας, οι αντιδράσεις αυτών των φορτίων κατανέμονται στο χώρο μέσω μιας 3Δ κατανομής Gauss και μοντελοποιούνται σαν όροι πηγής στα υπολογιστικά κελιά που βρίσκονται εντός αυτής της κατανομής (βλέπε εξίσωση (5.15) και Εικόνα 5.7). Τέλος, οι εξισώσεις της ροής επιλύονται λαμβάνοντας υπ' όψιν τους συγκεκριμένους όρους πηγής, το πεδίο της ροής ανανεώνεται λαμβάνοντας υπ' όψιν την 'παρουσία' του αεροδυναμικού σώματος που μοντελοποιείται σαν Γραμμή Δράσης και η διαδικασία αυτή επαναλαμβάνεται έως ότου συγκλίνει.

$$\mathbf{f}_\epsilon = \mathbf{f}_{cp}\eta_\epsilon$$
$$\mathbf{f}_c = -\sum_{i=1}^{N_{cp}} \mathbf{f}_{cp}\eta_\epsilon(cp_i, cell) \tag{5.15}$$

όπου :

- $\mathbf{f}_\epsilon$ είναι η δύναμη ανά μονάδα όγκου $[N/m^3]$ που προβάλεται στο υπολογιστικό πλέγμα;

- $\mathbf{f}_{cp}$ είναι η δύναμη $[N]$ που υπολογίζεται σε ένα τυχαίο σημείο ελέγχου του σώματος;

- $\eta_\epsilon = \frac{1}{(\epsilon\sqrt{\pi})^3}e^{-\left(\frac{d}{\epsilon}\right)^2}$ είναι η συνάρτηση της 3Δ κατανομή Gauss $[1/m^3]$;

- $d = |\mathbf{x}_{cp} - \mathbf{x}_c|$ είναι η απόσταση $[m]$ μεταξύ του σημείου ελέγχου $\mathbf{x}_{cp}$ και του σημείου $\mathbf{x}_c$ στο οποίο εφαρμόζεται η κατανεμημένη δύναμη;

- ϵ είναι η τυπική απόκλιση της κατανομής Gauss $[m]$ που καθορίζει και το πλάτος της κατανομής.
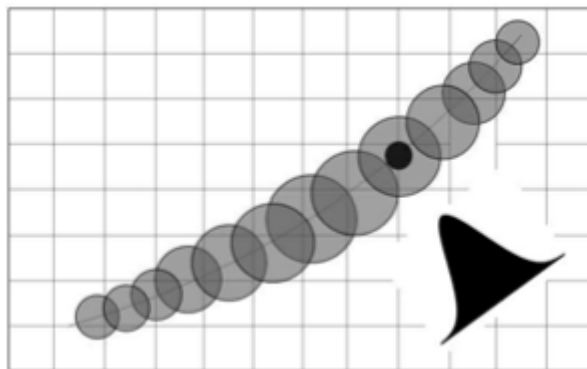
Figure 5.7. *Μοντελοποίηση ενός πτερυγίου με τη μέθοδο Γραμμής Δράσης. Προβολή των αεροδυναμικών δυνάμεων στο χώρο μέσω μιας 3Δ κατανομής Gauss. Η εικόνα δημοσιεύτηκε πρώτη φορά στο [130].*

### Β.2.2 Η μέθοδος της Ζώνης Παραγωγής – GZ

Για να υπάρχει η δυνατότητα χρήσης του αεροελαστικού κώδικα GAST-AL στη φάση του σχεδιασμού δρομέων ΑΓ, πρέπει να υπάρχει η δυνατότητα προσομοίωσης ατμοσφαιρικών (τυρβωδών) συνθηκών ροής. Για αυτό το σκοπό, κατά τη διάρκεια αυτής της διατριβής, αναπτύχθηκε και ενσωματώθηκε στο MaPFlow η μέθοδος της Ζώνης Παραγωγής (GZ) για την επιβολή των τυρβωδών διαταραχών ταχύτητας σε ένα μέσο πεδίο CFD.

Το πρώτο πράγμα που πρέπει να γίνει για την αναπαράσταση ενός τυρβώδους πεδίου ανέμου σε ένα περιβάλον CFD είναι η δημιουργία ενός συνθετικού τυρβώδους πεδίου. Αυτό επιτυγχάνεται με ένα εξωτερικό εργαλείο το οποίο δημιουργεί μία αλληλουχία από διαταραχές ταχύτητας $\mathbf{U}'$ γύρω από ένα μέσο πεδίο ταχύτητας $\mathbf{U}$ και τις αποθηκεύει σε διαδοχικά επίπεδα κάθετα στην κατεύθυνση της ροής. Το εργαλείο που χρησιμοποιήθηκε στο πλαίσιο αυτής της διατριβής βασίζεται στο μοντέλο του Mann [104, 105, 8].

Σε δεύτερη φάση, αυτές οι διαταραχές ταχυτήτων πρέπει να προστεθούν στο μέσο πεδίο που περιγράφεται σε ένα περιβάλλον CFD. Αυτό επιτυγχάνεται με την επιβολή όρων πηγής $\mathbf{S}_c$ σε ορισμένα κελιά του υπολογιστικού χωρίου, ούτως ώστε η λύση της ταχύτητας αυτών των κελιών να οδηγηθεί στην επιθυμητή $\mathbf{U}_{tar} = \mathbf{U} + \mathbf{U}'$. Αυτοί οι όροι πηγής απλώνονται σε μία ζώνη (Ζώνη Παραγωγής) κοντά στο επίπεδο της ΑΓ. Οι τιμές τους εξαρτώνται τόσο από τη χρονική στιγμή, όσο και από τη θέση και την τρέχουσα ταχύτητα των υπολογιστικών κελιών στα οποία επιβάλλονται, όπως φαίνεται στην εξίσωση (5.16). Η ένταση των όρων πηγής ρυθμίζεται μέσω μίας συνάρτησης C, η οποία παίρνει τη μέγιστη τιμή της στην αρχή της Ζώνης Παραγωγής (x_s) και τείνει στο 0 προς το τέλος της (x_e) (βλέπε Εικόνα 5.8). Το γεγονός ότι οι όροι πηγής έχουν εξαφανιστεί μέχρι το τέλος της ζώνης σημαίνει ότι εκεί καταλήγουμε με ένα προφίλ ταχυτήτων το οποίο είναι σε συμφωνία με τις υπολογιστικές παραμέτρους που χρησιμοποιούμε (π.χ. τύπος των εξισώσεων που επιλύονται, τάξη αριθμητικού σχήματος κ.α.), με αποτέλεσμα να μην υπάρχει σημαντικός κίνδυνος αριθμητικών αστάθειων κατά τη διάρκεια της προσομοίωσης.

$$\mathbf{S}_c = C\rho_c\left(\mathbf{U}_{tar} - \mathbf{U}_c\right)$$
$$C = a * e^{-\left[\dfrac{x - x_s}{0.2\left(x_e - x_s\right)}\right]} \tag{5.16}$$
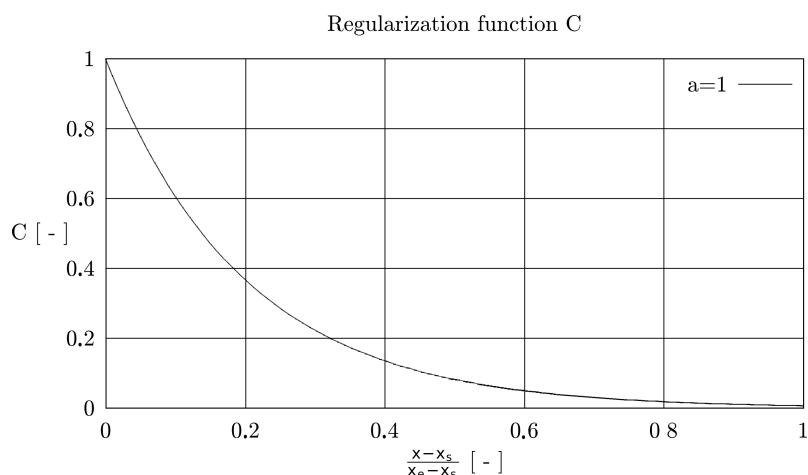
Figure 5.8. *Η συνάρτηση C ρυθμίζει την ένταση των όρων πηγής της Ζώνης Παραγωγής. Παίρνει τη μέγιστη τιμή της στην αρχή της ζώνης (x_s) και τείνει ομαλά στο 0 προς το τέλος της (x_e).*

Η παράμετρος a που καθορίζει τη μέγιστη τιμή της συνάρτησης C ρυθμίζεται από τον χρήστη. Αυτό σημαίνει ότι οι όροι πηγής εντός της Ζώνης Παραγωγής μπορούν να γίνουν όσο ισχυροί χρειάζεται ούτως ώστε, τουλάχιστον στην αρχή της ζώνης, να επιτευχθεί ακριβώς το επιθυμητό προφίλ ταχυτήτων. Ο ισχυρισμός αυτός επιβεβαιώνεται από την Εικόνα 5.9, όπου συγκρίνονται τα φάσματα της αξονικής ταχύτητας που παράγει η μέθοδος της Ζώνης Παραγωγής (GZ) και η συμβατική μέθοδος του Δίσκου Δράσης (Actuator Disk – AD) σε σχέση με το φάσμα που παράγει το μοντέλο του Mann. Αυτό έχει σαν αποτέλεσμα, και το φάσμα με το οποίο καταλήγουμε στο επίπεδο του δρομέα της ΑΓ, όταν χρησιμοποιούμε τη μέθοδο του GZ, να είναι πολύ πιο κοντά στο επιθυμητό σε σχέση με αυτό που καταλήγουμε όταν χρησιμοποιούμε τη συμβατική μέθοδο του AD (βλέπε Εικόνα 5.10).
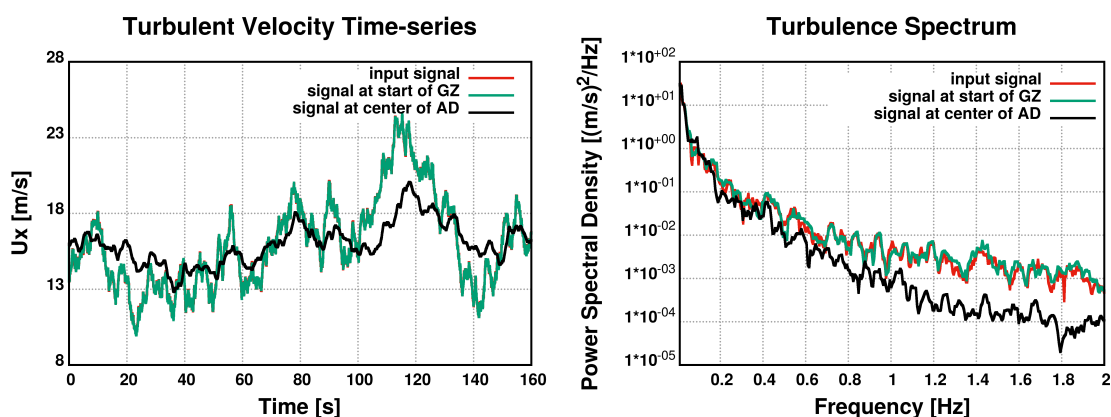
Figure 5.9. *Αξονική ταχύτητα στο πεδίο του χρόνου (αριστερά) και στο πεδίο των συχνοτήτων (δεξιά). Σε αντίθεση με το προφίλ που παράγεται στο κέντρου του AD, το προφίλ που παράγεται στην αρχή του GZ είναι σχεδόν ίδιο με το επιθυμητό προφίλ που παράγεται από το μοντέλο του Mann.*
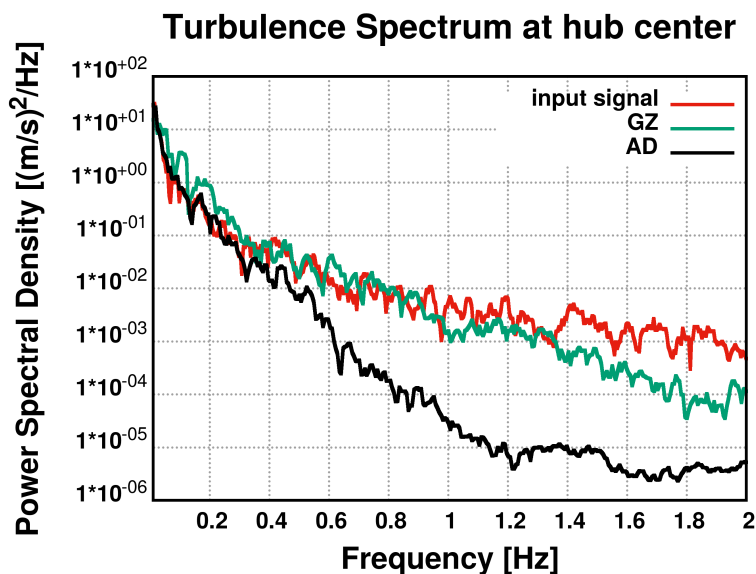
Figure 5.10. *Το φάσμα αξονικής ταχύτητας στο κέντρο του επιπέδου του δρομέα της ΑΓ, όπως υπολογίζεται από τη μέθοδο του GZ και του AD. Η μέθοδος του GZ καταλήγει σε ένα φάσμα που είναι πολύ πιο κοντά στο επιθυμητό σε σχέση με τη μέθοδο του AD.*

Βʹ.3   Ο *υβριδικος* Lagrangian–Eulerian *επιλυτης* HoPFlow

Ο υβριδικός Lagrangian–Eulerian CFD επιλύτης HoPFlow βασίζεται στο διαχωρισμό του υπολογιστικού χωρίου σε δύο επιμέρους υπο–πεδία (βλέπε Εικόνα 5.11). Στο ένα, το οποίο περιορίζεται κοντά στα στερεά σύνορα, ακολουθείται η Eulerian περιγραφή των εξισώσεων της ροής, ούτως ώστε να επαληθεύονται με ακρίβεια οι συνθήκες τοίχου. Μακριά από τα σώματα επιλύονται οι εξισώσεις της ροής στην υλική τους διατύπωση, η οποία επαληθεύει ακριβώς τις συνθήκες της αδιατάραχτης ροής στο άπειρο, ενώ ακόμη παρουσιάζει μειωμένη (θεωρητικά μηδενική) αριθμητική διάχυση. Με αυτόν τον τρόπο συνδυάζονται τα πλεονεκτήματα των δύο διατυπώσεων, με αποτέλεσμα να αυξάνεται η ακρίβεια των υπολογισμών και να περιορίζεται το υπολογιστικό κόστος. Χάρη στο διαχωρισμό των επιμέρους πεδίων, διευκολύνεται ακόμη η μοντελοποίηση πολλών σωμάτων που κινούνται και παραμορφώνονται ανεξάρτητα το ένα από το άλλο.

Η σύνδεση μεταξύ των δύο πεδίων είναι ισχυρή και επιτυγχάνεται μέσω μίας αμφίδρομης επικοινωνίας. Αρχικά η πεδιακή λύση παρεμβάλεται από τα υλικά σωματίδια στα εξωτερικά όρια του Eulerian πεδίου, καθορίζοντας έτσι τις οριακές του συνθήκες (βλέπε Εικόνα 5.12). Στη συνέχεια, οι εξισώσεις της ροής επιλύονται στην Eulerian μορφή τους. Με βάση την Eulerian λύση διορθώνονται, μέσω παρεμβολών, και τα ροϊκά μεγέθη των υλικών σωματιδίων που βρίσκονται εντός του Eulerian πεδίου (βλέπε Εικόνα 5.13). Τέλος, ολόκληρο το Lagrangian πεδίο ανανεώνεται, ούτως ώστε να καταλήξει να είναι μία ομαλή συνέχεια του Eulerian πεδίου.
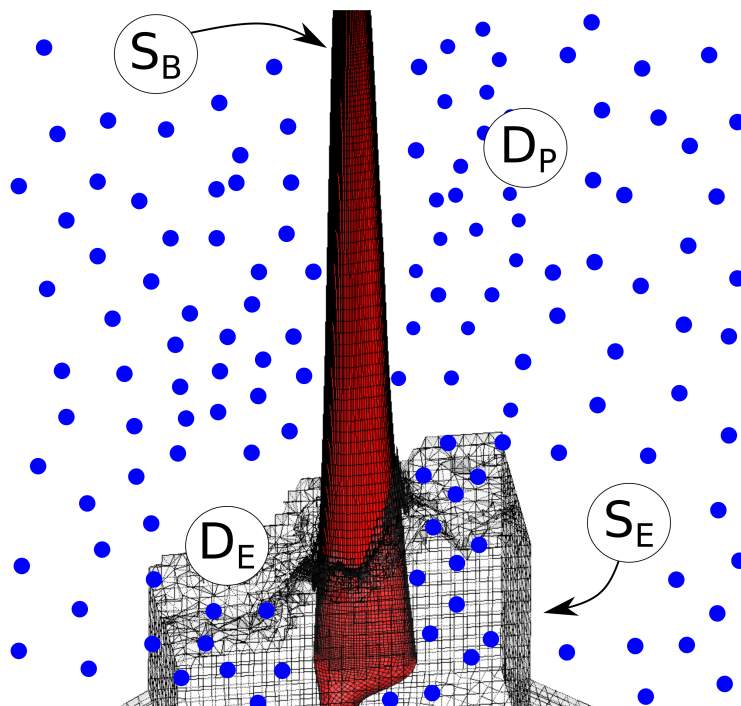
Figure 5.11. *Διαχωρισμός του Eulerian (D_E) και του Lagrangian (D_P) πεδίου. Με S_B συμβολίζονται τα στερεά σύνορα (τοίχος) και με S_E τα εξωτερικά σύνορα του Eulerian πεδίου. Τα Lagrangian σωματίδια βρίσκονται παντού μέσα στο υπολογιστικό χωρίο και επικαλύπτουν τα υπολογιστικά κελιά του Eulerian πεδίου.*
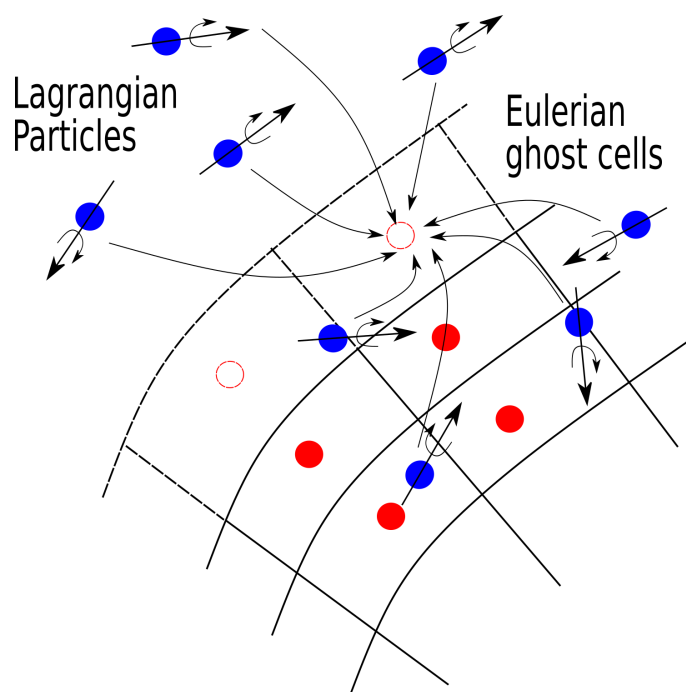
Figure 5.12. *Τα ροϊκά μεγέθη των υλικών σωματιδίων παρεμβάλλονται στα ghost cells του Eulerian πεδίου. Με αυτόν τον τρόπο καθορίζονται οι οριακές του συνθήκες. Τα υλικά σωματίδια απεικονίζονται ως συμπαγείς μπλε κύκλοι. Οι συμπαγείς και διακεκομμένοι κόκκινοι κύκλοι συμβολίζουν τα κέντρα των υπολογιστικών κελιών και των ghost cells του Eulerian πεδίου αντίστοιχα.*
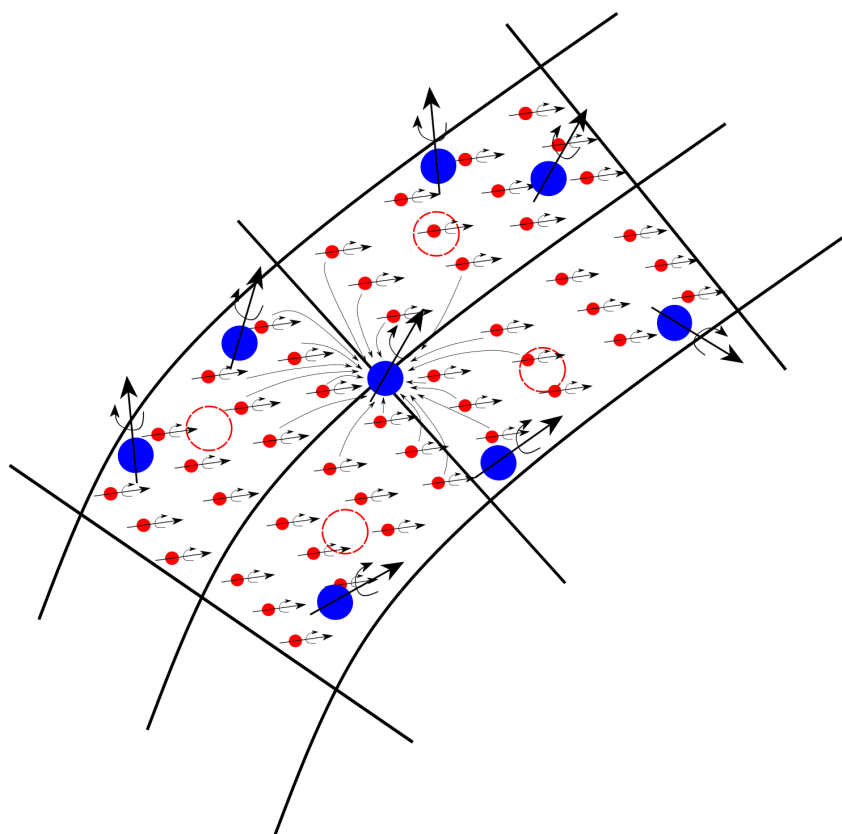
Figure 5.13. *Η Eulerian λύση χρησιμοποιείται για να διορθωθούν τα ροϊκά μεγέθη των υλικών σωματιδίων που βρίσκονται εντός του Eulerian πεδίου. Στη συνέχεια, η πληροφορία από τα διορθωμένα υλικά σωματίδια χρησιμοποιείται για την ανανέωση ολόκληρου του Lagrangian πεδίου, ούτως ώστε να εξασφαλιστεί η ομαλή συνέχεια μεταξύ των δύο. Τα υλικά σωματίδια απεικονίζονται ως συμπαγείς μπλε κύκλοι. Οι διακεκομμένοι κόκκινοι κύκλοι συμβολίζουν τα κέντρα των υπολογιστικών κελιών του Eulerian πεδίου. Οι μικροί συμπαγείς κόκκινοι κύκλοι συμβολίζουν τα Eulerian σωματίδια που διορθώνουν τα μπλε Lagrangian σωματίδια.*

Στη Lagrangian διατύπωση των εξισώσεων της ροής, τα ροϊκά μεγέθη συγκεντρώνονται σε υλικά σωματίδια και η εξέλιξη του πεδίου παρακολουθείται ακολουθώντας τις τροχιές αυτών των σωματιδίων και καταγράφοντας την αλλαγή στα ροϊκά τους μεγέθη. Στη διατύπωση που ακολουθείται στο HoPFlow, τα υλικά σωματίδια μεταφέρουν μάζα M_p, διόγκωση Θ_p, στροβιλότητα $\mathbf{\Omega}_p$, πίεση Π_p και όγκο V_p [67], ενώ για την επίλυση της Lagrangian μορφής των εξισώσεων της ροής, η οποία είναι υπερβολικού τύπου, χρειαζόμαστε ακόμα την ταχύτητα $\mathbf{U}_p$ και τις παραγώγους των παραπάνω ροϊκών μεγεθών $\partial \mathbf{Q}_p$, $\partial \mathbf{U}_p$:

$$\mathbf{Q}_p(t) = \begin{bmatrix} M \\ \Theta \\ \mathbf{\Omega} \\ \Pi \\ V \end{bmatrix}_p^T$$

$$\frac{d\mathbf{Q}_p}{dt}(t) = \mathbf{F}\left(\mathbf{Q}_p, \mathbf{U}_p, \partial \mathbf{Q}_p, \partial \mathbf{U}_p, t\right)$$

(5.17)

Για τον υπολογισμό του πεδίου της ταχύτητας χρησιμοποιείται το θεώρημα διαχωρισμού ταχυτήτων του Helmholtz, με βάση το οποίο η ταχύτητα ενός πεδίου $\mathbf{u}\left(\mathbf{x}, t\right)$ μπορεί να περιγραφεί σαν άθροισμα της επ' άπειρο ταχύτητας $\mathbf{U}_\infty$ και μιας ταχύτητας διαταραχής που περιγράφεται από ένα βαθμωτό δυναμικό φ $\left(\mathbf{u}_\phi = \nabla\phi\right)$ και ένα διανυσματικό δυναμικό (ροϊκή συνάρτηση) $\boldsymbol{\psi}$ ($\mathbf{u}_\omega = \nabla \times \boldsymbol{\psi}$):

$$\mathbf{u}\left(\mathbf{x}, t\right) = \mathbf{U}_\infty + \mathbf{u}_\phi\left(\mathbf{x}, t\right) + \mathbf{u}_\omega\left(\mathbf{x}, t\right) \tag{5.18}$$

Οι τιμές των φ και $\boldsymbol{\psi}$ υπολογίζονται επιλύοντας τις εξισώσεις Poisson της ροής, οι οποίες εισάγουν άμεσα τον ελλειπτικό χαρακτήρα της ροής στη διατύπωση που ακολουθείται από το HoPFlow:

$$\begin{aligned} \nabla^2\phi &= \nabla \cdot \mathbf{u} = \theta \\ \nabla^2\boldsymbol{\psi} &= -\nabla \times \mathbf{u} = -\boldsymbol{\omega} \end{aligned} \tag{5.19}$$

Οι εξισώσεις Poisson στο HoPFlow λύνονται με τη χρήση της μεθόδου του Particle Mesh (PM) [58, 59, 60]. Αυτό σημαίνει ότι τα ροϊκά μεγέθη προβάλλονται από τις θέσεις των υλικών σωματιδίων στους κόμβους του δομημένου πλέγματος PM (βλέπε Εικόνα 5.14), όπου επιλύονται οι εξισώσεις Poisson και υπολογίζονται τα φ και $\boldsymbol{\psi}$. Στο πλέγμα αυτό πραγματοποιούνται και όλες οι παραγωγίσεις που απαιτούνται για να υπολογιστεί η ταχύτητα και όποια άλλη παράγωγος υπάρχει στο δεξί μέλος των εξισώσεων (5.17). Στη συνέχεια, όλα τα μεγέθη που έχουν υπολογιστεί στους κόμβους του PM παρεμβάλλονται στις θέσεις των υλικών σωματιδίων. Με γνωστό πλέον το δεξί μέλος των εξισώσεων (5.17), τα υλικά σωματίδια μετακινούνται στο χώρο και τα ροϊκά τους μεγέθη ανανεώνονται μέσω ενός σχήματος ολοκλήρωσης Runge–Kutta 4ης τάξης.
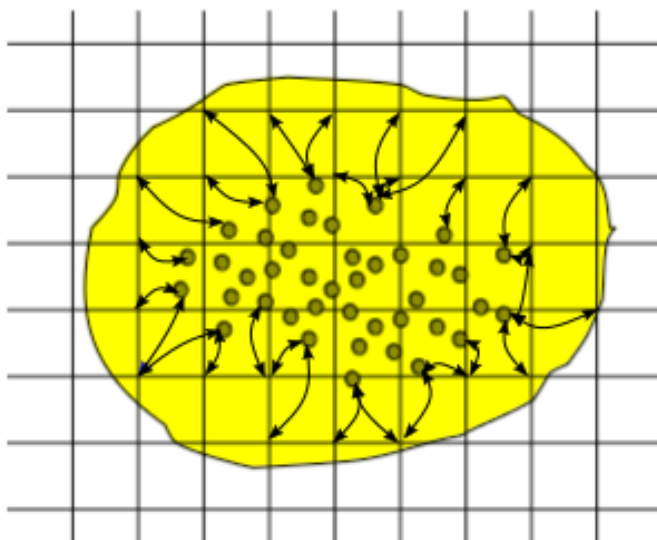
Figure 5.14. *Στη μέθοδο του PM, ένα δομημένο πλέγμα καλύπτει το Lagrangian χωρίο. Οι τιμές των θ και ω παρεμβάλλονται στους κόμβους του με βάση τις αντίστοιχες τιμές των υλικών σωματιδίων. Οι εξισώσεις Poisson λύνονται στο δομημένο πλέγμα και στη συνέχεια οι τιμές των φ και ψ που υπολογίστηκαν παρεμβάλλονται πίσω στα υλικά σωματίδια. Το δομημένο αυτό πλέγμα μπορεί ακόμα να χρησιμοποιηθεί και για τον υπολογισμό όλων των απαιτούμενων παραγώγων που συναντώνται στο δεξί μέλος των εξισώσεων της ροής.*

C *Αποτελεσματα*

Στην ενότητα αυτή παρατίθενται τα αποτελέσματα που προκύπτουν από τη χρήση των νέων εργαλείων, που αναπτύχθηκαν στο πλαίσιο αυτής της διατριβής, για την αεροελαστική ανάλυση δρομέων ΑΓ και ελικοπτέρων. Το νέο GAST–AL εργαλείο εφαρμόζεται για την αεροελαστική ανάλυση του δρομέα της πρότυπης ΑΓ 10MW που σχεδιάστηκε στο DTU [151], υπό σταθερές και τυρβώδεις συνθήκες ανέμου, ενώ ο αεροελαστικός κώδικας GAST–HoPFlow χρησιμοποιείται για την αεροδυναμική ανάλυση του μοντέλου δρομέα ΑΓ που μελετήθηκε στο πείραμα New MEXICO [11] και για την αεροελαστική ανάλυση του μοντέλου του δρομέα ελικοπτέρου που χρησιμοποιήθηκε στο πείραμα HARTII [13]. Στόχος είναι η επιβεβαίωση της ορθής λειτουργίας των νέων αεροελαστικών εργαλείων και η ανάδειξη των πλεονεκτημάτων τους σε σχέση με τις συμβατικές μεθοδολογίες που χρησιμοποιούνται κατά τη φάση του σχεδιασμού των δρομέων ΑΓ και ελικοπτέρων.

C.1 *Τα αποτελεσματα του αεροελαστικου εργαλεου* **GAST–AL**

Σ' αυτήν την υποενότητα, το νέο αεροελαστικό εργαλείο GAST–AL χρησιμοποιείται για την αεροελαστική ανάλυση της πρότυπης ΑΓ 10MW που σχεδιάστηκε στο DTU [151], όταν αυτή λειτουργεί σε συνθήκες σταθερού και τυρβώδους ανέμου. Τα αποτελέσματα της ανάλυσης συγκρίνονται με αυτά που παράγονται από άλλα, ήδη πιστοποιημένα αεροελαστικά εργαλεία, που χρησιμοποιούν τις αεροδυναμικές μεθόδους LL και BEMT. Στόχος είναι η επιβεβαίωση της ορθής λειτουργίας του νέου αεροελαστικού εργαλείου GAST–AL, αλλά και η ανάδειξη των πλεονεκτημάτων του σε σχέση με τις δύο πιο συμβατικές αεροδυναμικές μεθόδους.

C.1.1 *Λειτουργια ΑΓ σε σταθερο ανεμο*

Πρώτα εξετάζεται η περίπτωση της αεροελαστικής λειτουργίας της ΑΓ σε σταθερό άνεμο για δύο διαφορετικές ταχύτητες ανέμου και για διάφορες γωνίες απόκλισης, όπως φαίνεται στον Πίνακα 5.1. Ειδικά για την περίπτωση της αξονικής ροής (μηδενική απόκλιση ανέμου), πραγματοποιείται στην Εικόνα 5.15 σύγκριση της ακτινικής κατανομής του κάθετου αεροδυναμικού φορτίου και του συντελεστή αξονικής επαγωγής που υπολογίζονται όταν χρησιμοποιούνται τρία διαφορετικά αεροδυναμικά μοντέλα που βασίζονται στις μεθόδους BEMT, LL και AL. Χρειάζεται να τονιστεί ότι τα μοντέλα LL και AL εκτιμούν με πολύ διαφορετικό τρόπο το κατώρευμα του ομόρρου απ' ότι η μέθοδος BEMT, χάρη στη λεπτομερή αναπαράσταση του 3Δ πεδίου της ροής που προσφέρουν οι FVW και CFD μεθοδολογίες αντίστοιχα. Η Εικόνα 5.15α επιβεβαιώνει την ορθή λειτουργία του μοντέλου ακροπτερυγίου που χρησιμοποιεί το BEMT [40], καθώς αυτά τείνουν στο μηδέν κοντά στο άκρο. Ωστόσο, η Εικόνα 5.15β δείχνει ότι ο συντελεστής αξονικής επαγωγής που υπολογίζεται από το BEMT είναι σταθερά πιο υψηλός από τις προβλέψεις των άλλων δύο αεροδυναμικών μοντέλων. Μάλιστα οι υπερβολικά μεγάλες τιμές που υπολογίζονται κοντά στο ακροπτερύγιο οφείλονται στην τεχνητή αύξηση αυτών από το μοντέλο ακροπτερυγίου του Prandtl, προκειμένου να μειωθούν τα αεροδυναμικά φορτία. Το αντίστοιχο μοντέλο στη ρίζα δεν έχει χρησιμοποιηθεί στις συγκεκριμένες προσομοιώσεις και γι' αυτό οι τιμές του συντελεστή αξονικής επαγωγής εκεί τείνουν στο μηδέν. Αντίστοιχη συμπεριφορά παρουσιάζουν και οι προβλέψεις του LL

στην περιοχή του ακροπτερυγίου. Στην περίπτωση αυτή, ωστόσο, οι υπερβολικά μεγάλες τιμές του συντελεστή αξονικής επαγωγής οφείλονται στους πολύ ισχυρούς στροβίλους που απελευθερώνονται από το άκρο του πτερυγίου και αντίστοιχα στο πολύ ισχυρό κατόρευμα που αυτοί επάγουν. Η μεγάλη ένταση των στροβίλων ακροπτερυγίου δικαιολογείται από την απότομη πτώση της κυκλοφορίας όσο πλησιάζουμε στο άκρο του πτερυγίου. Αυτή είναι και η βασική διαφορά μεταξύ των μοντέλων LL και AL, καθώς η ένταση των στροβίλων που σχηματίζει το AL δεν καθορίζονται από τη μεταβολή της κυκλοφορίας στα πτερύγια, αλλά από τη συναλλαγής ορμής μεταξύ πτερυγίων και ροής. Αυτός είναι ένας βασικός λόγος για τον οποίον ο συντελεστής αξονικής επαγωγής που υπολογίζει το AL μειώνεται όσο πλησιάζουμε στο ακροπτερύγιο. Ένας ακόμη πολύ σημαντικός λόγος για αυτήν τη συμπεριφορά είναι ο τρόπος με τον οποίον υπολογίζεται η επαγώμενη ταχύτητα από τον ομόρρου στα πτερύγια. Στο LL, αυτή υπολογίζεται απευθείας από τα στοιχεία στροβιλότητας του ομόρρου πάνω στα σημεία ελέγχου του πτερυγίου, ενώ στο AL υπολογίζεται μέσω παρεμβολών από την πεδιακή λύση των γειτονικών κελιών.

Στην Εικόνα 5.16 φαίνεται η αζιμουθιακή μεταβολή της ροπής πτερύγισης στη ρίζα των πτερυγίων και η αντίστοιχη παραμόρφωση στο ακροπτερύγιο. Η 1P διακύμανση οφείλεται στην κλίση 5° του άξονα του δρομέα (βλέπε Πίνακα 3.1). Καλή είναι η συμφωνία που παρατηρείται στη μέση τιμή της ροπής (μέγιστη διαφορά 1.8% στα 8 m/s και 1.3% στα 11 m/s) και στο πλάτος. Ωστόσο, η ροπή που προβλέπει το BEMT παρουσιάζει μία διαφορά φάσης περίπου 35° στα 8 m/s και 70° στα 11 m/s σε σχέδη με τα δύο άλλα μοντέλα, τα οποία συμφωνούν σχεδόν απόλυτα μεταξύ τους. Η διαφορά αυτή οφείλεται στο γεγονός ότι το συγκεκριμένο μοντέλο BEMT δεν έχει τον τρόπο να αντιλαμβάνεται την κλίση του ομόρρου ως προς τον δρομέα και τη διαφορά που αυτή επιφέρει στην ένταση του κατωρεύματος που επάγεται στις διαφορετικές γωνίες αζιμουθίου. Αντίθετα, η λεπτομερής περιγραφή του 3Δ πεδίου που παρέχουν οι FVW και CFD μεθοδολογίες, καθιστούν την πρόβλεψη τέτοιων φαινομένων ιδιαίτερα ακριβή από τα LL και AL μοντέλα αντίστοιχα. Αντίστοιχα είναι και τα συμπεράσματα που προκύπτουν από την ανάλυση της παραμόρφωσης του ακροπτερυγίου στην κατεύθυνση της πτερύγισης.

Αντίστοιχα, στην Εικόνα 5.17 παρουσιάζεται η ροπή πτερύγισης στη ρίζα των πτερυγίων για τις ίδιες ταχύτητες ανέμου, αλλά με απόκλιση +15° και +30°. Στην περίπτωση αυτή, παρατηρείται μία σημαντική διαφορά στη μέση τιμή που υπολογίζει το BEMT σε σχέση με τα δύο άλλα μοντέλα, η οποία μεγαλώνει όσο αυξάνει και η απόκλιση του ανέμου ($\simeq$ 3.5% στις +15° και $\simeq$ 8.5% στις +30°). Ακόμη, παρατηρείται μία σταθερή διαφορά φάσης μεταξύ 35°–45°. Οι αποκλίσεις αυτές οφείλονται στις διαφερικές τιμές που υπολογίζουν τα μοντέλα για τον συντελεστή αξονικής επαγωγής (βλέπε Εικόνα 5.18). Όπως και στην περίπτωση της αξονικής ροής (βλέπε Εικόνα 5.15δ), το BEMT προβλέπει μεγαλύτερες τιμές για το συντελεστή αξονικής επαγωγής από τα άλλα δύο μοντέλα, κάτι που δικαιολογεί τη μικρότερη μέση τιμή της ροπής πτερύγισης (μεγαλύτερη επαγώμενη ταχύτητα οδηγεί σε μικρότερη φαινόμενη ταχύτητα και μικρότερη γωνία πρόσπτωσης). Το διαφορετικό πλάτος και η διαφορά φάσης που παρατηρείται στο συντελεστή αξονικής επαγωγής (περίπου 20° με 45°) οδηγεί στη διαφορά φάσης που παρατηρείται και στα φορτία. Το BEMT υπολογίζει τη μέγιστη ροπή πτερύγισης κοντά στις 180°, γιατί εκεί η συνιστώσα του ανέμου που είναι παράλληλη στο

Table 5.1. *Συνθήκες λειτουργίας της DTU 10MW πρότυπης ΑΓ υπό σταθερό άνεμο.*

| Ταχύτητα Ανέμου (m/s)	Απόκλιση Ανέμου (°)	Γωνιακή Ταχύτητα (rpm)	Γωνία Βήματος (°)
8	0, 15, 30	6.423	0
11	0, 15, 30	8.837	0
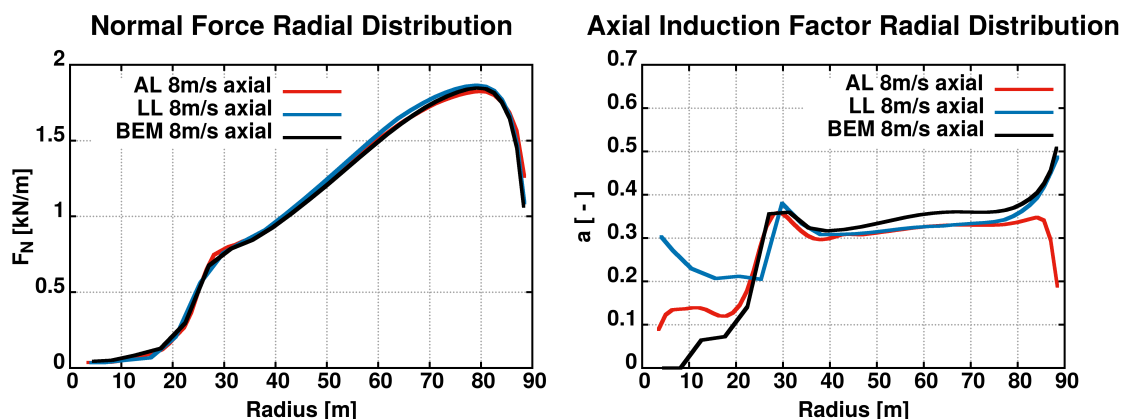
(a) *Ατκινική κατανομή της κάθετης αεροδυναμικής δύναμης. Η καλή συμφωνία των αποτελεσμάτων κοντά στο ακροπτερύγιο υποδηλώνει την αποτελεσματική δράση του μοντέλου διόρθωσης των φορτίων ακροπτερυγίου που χρησιμοποιείται από τη μέθοδο BEMT.*

(b) *Ακτινική κατανομή του συντελεστή αξονικής επαγωγή. Οι προβλέψεις του BEMT παρουσιάζουν μία σταθερή υπερεκτίμηση σε σχέση με τις άλλες δύο πιο ακριβείς μεθόδους, οι οποίες συμφωνούν πολύ καλά μεταξύ τους. Η διαφορά αυτή οφείλεται στην πρόχειρη εκτίμηση των επαγώμενων ταχυτήτων του ομόρρου από το BEMT. Η απότομη αύξηση κοντά στο ακροπτερύγιο οφείλεται στο μοντέλο ακροπτερυγίου, το οποίο επιτυγχάνεται μέσω της τεχνητής αύξησης του συντελεστή αξονικής επαγωγής στην περιοχή αυτή. Παρόμοια συμπεριφορά παρουσιάζει και το LL, αλλά αυτό λόγω των υπερβολικά ισχυρών στροβίλων που αποβάλλονται από το άκρο του πτερυγίου. Αντίθετα, το AL προβλέπει μία φυσιολογική πτώση του συντελεστή αξονικής επαγωγής κοντά στο άκρο του πτερυγίου. Η διαφορά αυτή οφείλεται κυρίως στο διαφορετικό τρόπο υπολογισμού της επαγώμενης ταχύτητας από τον ομόρρου, αφού στο LL αυτή υπολογίζεται απευθείας από τα στοιχεία στροβιλότητας του ομόρρου πάνω στα σημεία ελέγχου του πτερυγίου, ενώ στο AL υπολογίζεται μέσω παρεμβολών από την πεδιακή λύση των γειτονικών κελιών.*

Figure 5.15. *Ακτινική κατανομή της κάθετης αεροδυναμικής δύναμης (a) και του συντελεστή αξονικής επαγωγής (b) σε αξονική ροή με ταχύτητα ανέμου στα 8 m/s. Μέση τιμή στην τελευταία περιστροφή. Σύγκριση μεταξύ διαφορετικών αεροδυναμικών μοντέλων (Γραμμή Δράσης (AL), Γραμμή Άνωσης (LL), Δίσκος Ορμής και Στοιχεία Πτερύγωσης (BEMT)), συνδεδεμένων με τον ίδιο ελαστο-δυναμικό επιλύτη (GAST).*

πεδίο του δρομέα προστίθεται στην ταχύτητα περιστροφής και αυξάνει τη συνολική φαινόμενη ταχύτητα. Εκτός από αυτό, η απόκλιση του ανέμου οδηγεί στην ταχύτερη απομάκρυνση του ομόρρου από το δρομέα κοντά στις 270°, με αποτέλεσμα οι επαγώμενες ταχύτητες να

είναι χαμηλότερες στη γύρω περιοχή και να μετατοπίζεται η μέγιστη φόρτιση προς αυτή τη γωνία αζιμουθίου. Σε αντίθεση με το BEMT, το φαινόμενο αυτό προβλέπεται με επιτυχία από το LL και το AL, γιατί μπορούν να περιγράψουν με ακρίβεια τη θέση και την εξέλιξη των δομών στροβιλότητας του ομόρρου χάρη στη λεπτομερή αναπαράσταση του 3Δ πεδίου της ροής από τις FVW και CFD μεθοδολογίες αντίστοιχα. Αυτός είναι και ο βασικός λόγος για τις διαφορές στη μέση τιμή, το πλάτος και τη φάση του συντελεστή αξονικής επαγωγής, ο οποίος με τη σειρά του επηρεάζει άμεσα και τα αεροδυναμικά φορτία που υπολογίζει το κάθε μοντέλο.
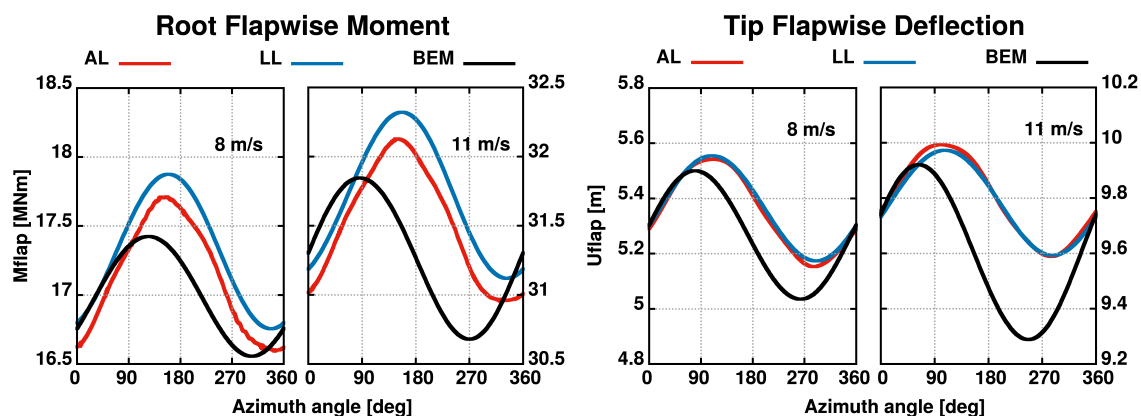
**(a)** *Ροπή πτερύγισης στη ρίζα του πτερυγίου.*

(b) *Παραμόρφωση ακροπτερυγίου στην κατεύθυνση της πτερύγισης.*

Figure 5.16. *Αζιμουθιακή μεταβολή της ροπής πτερύγισης στη ρίζα των πτερυγίων (a) και η αντίστοιχη παραμόρφωση ακροπτερυγίου (b) σε αξονική ροή με ταχύτητα ανέμου στα 8 και 11 m/s. Σύγκριση μεταξύ διαφορετικών αεροδυναμικών μοντέλων (Γραμμή Δράσης (AL), Γραμμή Άνωσης (LL), Δίσκος Ορμής και Στοιχεία Πτερύγωσης (BEMT)), συνδεδεμένων με τον ίδιο ελαστο-δυναμικό επιλύτη (GAST). Το BEMT ελαφρώς υποεκτιμά τη μέση τιμή των ροπών πτερύγισης (μέγιστη διαφορά 1.8% στα 8 m/s και 1.3% στα 11 m/s) σε σχέση με τις άλλες δύο πιο ακριβείς μεθόδους, οι οποίες συμφωνούν πολύ καλά μεταξύ τους. Επίσης, παρουσιάζει μία σημαντική διαφορά φάσης περίπου 35° στα 8 m/s και 70° στα 11 m/s, η οποία οφείλεται στην αδυναμία πρόβλεψης της διαφορετικής επίδρασης του ομόρρου στα αεροδυναμικά φορτία λόγω της κλίσης του σε σχέση με το επίπεδο του δρομέα. Παρόμοια είναι και τα συμπεράσματα που εξάγονται από τη σύγκριση της παραμόρφωσης του ακροπτερυγίου.*
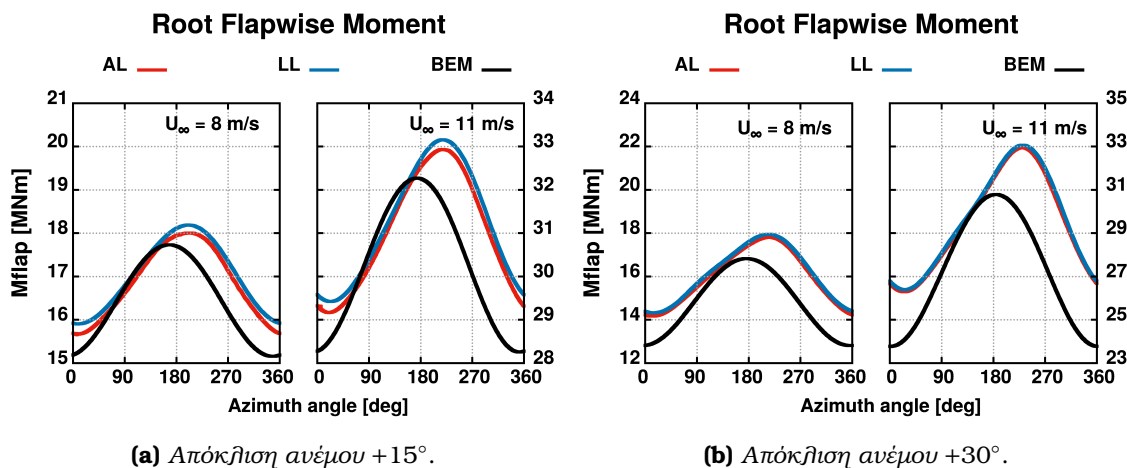
Root Flapwise Moment

(a) *Απόκλιση ανέμου +15°.* **(b)** *Απόκλιση ανέμου +30°.*

Figure 5.17. *Αζιμουθιακή μεταβολή της ροπής πτερύγισης στη ρίζα των πτερυγίων για ροή με απόκλιση ανέμου +15° (a) και +30° (b) και ταχύτητα ανέμου στα 8 και 11 m/s. Σύγκριση μεταξύ διαφορετικών αεροδυναμικών μοντέλων (Γραμμή Δράσης (AL), Γραμμή Άνωσης (LL), Δίσκος Ορμής και Στοιχεία Πτερύγωσης (BEMT)), συνδεδεμένων με τον ίδιο ελαστο-δυναμικό επιλύτη (GAST). Το BEMT ελαφρώς υποεκτιμά τη μέση τιμή των ροπών σε σχέση με τις άλλες δύο πιο ακριβείς μεθόδους, οι οποίες συμφωνούν πολύ καλά μεταξύ τους. Η διαφορά αυτή αυξάνει μαζί με τη γωνία απόκλισης του ανέμου (−3.5% στις +15° και −8.5% στις +30°). Επίσης, προβλέπει μία σημαντική αλλά σταθερή διαφορά φάσης περίπου 35° − 45° σε σχέση με τις άλλες δύο μεθόδους, οι οποίες και εδώ συμφωνούν πολύ καλά μεταξύ τους.*
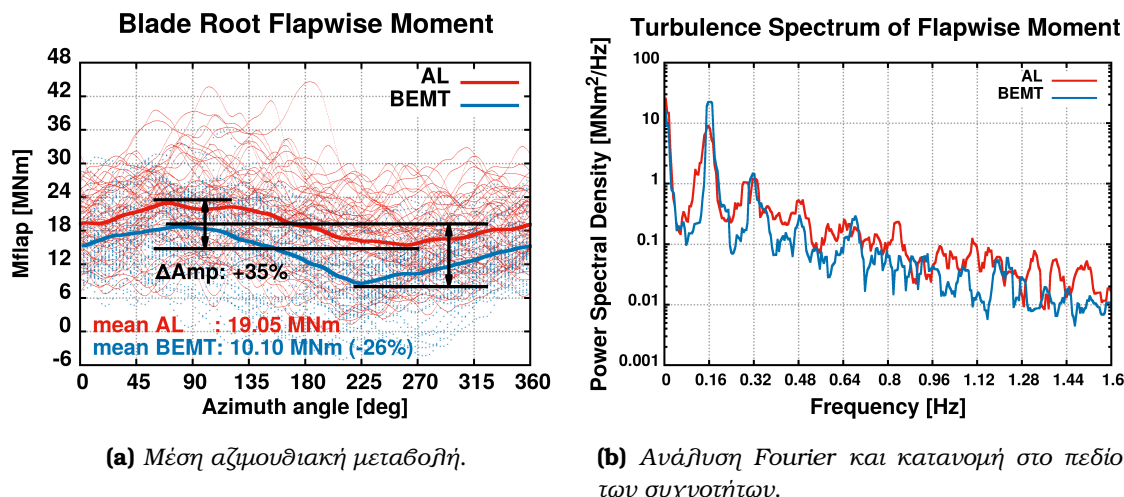

Axial Induction Factor at 75%R

(a) *Απόκλιση ανέμου +15°.* **(b)** *Απόκλιση ανέμου +30°.*
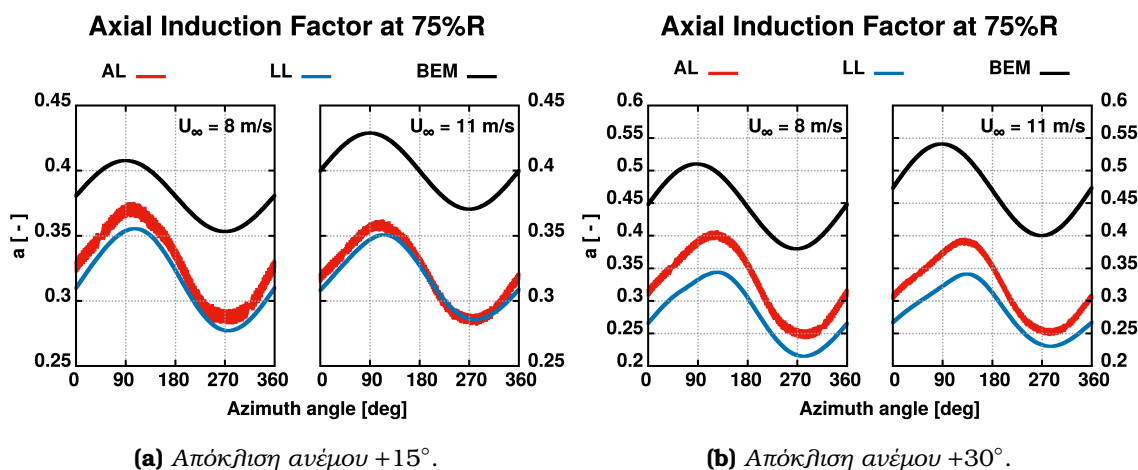
Figure 5.18. *Αζιμουθιακή μεταβολή του συντελεστή αξονικής επαγωγής στο 75% των πτερυγίων για ροή με απόκλιση ανέμου +15° (a) και +30° (b) και ταχύτητα ανέμου στα 8 και 11 m/s. Σύγκριση μεταξύ διαφορετικών αεροδυναμικών μοντέλων (Γραμμή Δράσης (AL), Γραμμή Άνωσης (LL), Δίσκος Ορμής και Στοιχεία Πτερύγωσης (BEMT)), συνδεδεμένων με τον ίδιο ελαστο-δυναμικό επιλύτη (GAST). Το BEMT προβλέπει μεγαλύτερη μέση τιμή από τα άλλα δύο μοντέλα που αυξάνει με την απόκλιση και την ταχύτητα του ανέμου (διαφορά από 7% έως 15% της μέσης τιμής). Ακόμη προβλέπει μία διαφορά φάσης που κυμαίνεται μεταξύ 20° και 45°. Και τα δύο συνδέονται με την αδυναμία της μεθόδου να προβλέψει με ακρίβεια τη διαφορετική επίδραση του ομόρρου λόγω της κλίσης του σε σχέση με το επίπεδο του δρομέα. Αντίθετα, πολύ καλή είναι η συμφωνία μεταξύ των δύο άλλων μοντέλων, με μια μικρή διαφορά στη μέση τιμή η οποία φαίνεται και στην Εικόνα 5.156 και συνδέεται με τη διαφορετική τεχνική υπολογισμού των επαγόμενων ταχυτήτων από τον ομόρρου.*

C.1.2   Λειτουργια ΑΓ σε τυρβωδη ανεμο

Στη συνέχεια, εξετάζεται η περίπτωση της αεροελαστικής λειτουργίας της πλήρους ΑΓ (πύργος, άξονας, δρομέας) σε μέσης έντασης τυρβώδη άνεμο ($TI = 14\%$) και εντός του οριακού στρώματος του εδάφους, για μέση ταχύτητα ανέμου στα 16 m/s στο ύψος του άξονα ($Z_{hub} = 119m$). Στην περίπτωση αυτή τα αποτελέσματα του αεροελαστικού μοντέλου GAST-AL συγκρίνονται με τα αντίστοιχα αποτελέσματα που παράγονται όταν ο ίδιος ελαστοδυναμικός επιλύτης GAST είναι συνδεδεμένος με ένα BEMT αεροδυναμικό μοντέλο.

Στην Εικόνα 5.19α φαίνεται η μέση αζιμουθιακή μεταβολή (συνεχείς γραμμές) της ροπής πτερύγισης που προβλέπουν τα δύο μοντέλα στη ρίζα των πτερυγίων του δρομέα. Οι τελείες δείχνουν τις στιγμιαίες προβλέψεις. Όπως και στις περιπτώσεις λειτουργίας σε σταθερό άνεμο, το BEMT υποεκτιμά τη μέση τιμή του φορτίου (εδώ κατά $\simeq 26\%$). Παρατηρείται και μία υπερεκτίμηση του πλάτους κατά $\simeq 35\%$ σε σχέση με το AL, η οποία φαίνεται και από τη διαφορά στο φάσμα της ροπής στη συχνότητα περιστροφής ($0.16Hz$) (βλέπε Εικόνα 5.19β). Και σε αυτήν την περίπτωση, οι διαφορές οφείλονται στην ακριβή περιγραφή της θέσης και της εξέλιξης των δομών στροβιλότητας του ομόρρου όταν χρησιμοποιείται το AL. Για να γίνει καλύτερα κατανοητό το φαινόμενο που κυριαρχεί σε αυτήν την περίπτωση, παρουσιάζεται στην Εικόνα 5.20α η υψομετρική κατανομή της μέσης αξονικής ταχύτητας στο επίπεδο του δρομέα της ΑΓ, όπως υπολογίζεται από το μοντέλο AL (κόκκινη γραμμή) και όπως προκύπτει από το αναλυτικό προφίλ (πράσινη γραμμή) που ισχύει όταν δεν υπάρχει η ΑΓ. Η μεγάλη αξονική ταχύτητα πάνω από το ύψος του άξονα, έχει σαν αποτέλεσμα τη γρήγορη απομάκρυνση των στροβίλων από το άνω τμήμα του δρομέα που οδηγεί σε μικρό κατώρευμα σε αυτήν την περιοχή. Σε αντίθεση με το BEMT, αυτή η συμπεριφορά προβλέπεται με ακρίβεια από το AL και οδηγεί σε μεγαλύτερα αεροδυναμικά φορτία στην αζιμουθιακή περιοχή $315°$ με $45°$. Λόγω της επιβράδυνσης που επιφέρει ο δρομέας στο κοντινό ανάντι πεδίο, θα περιμέναμε η κατανομή της αξονικής ταχύτητας που υπολογίζεται από το AL (κόκκινη καμπύλη) να χαρακτηρίζεται από χαμηλότερες τιμές σε σχέση με το αναλυτικό προφίλ (να βρίσκεται αριστερά της πράσινης καμπύλης). Αν και αυτό ισχύει για τα ύψη πάνω από τα $70m$, παρατηρείται μια σημαντική επιτάχυνση της αξονικής ταχύτητας μέχρι αυτό το ύψος. Αυτή η επιτάχυνση οφείλεται στην γεωμετρία ακροφυσίου που σχηματίζεται μεταξύ του εδάφους και του κάτω μέρους του δρομέα (βλέπε Εικόνα 5.20β), φαινόμενο το οποίο φαίνεται να προβλέπεται με επιτυχία από το AL (βλέπε Εικόνα 5.21). Η αύξηση της αξονικής ταχύτητας στο κάτω μέρος του δρομέα εμποδίζει την περεταίρω μείωση της γωνίας πρόσπτωσης στις γωνίες αζιμουθίου μεταξύ $135°$ και $225°$, όπως φαίνεται και από το πλατό που σχηματίζεται από το AL στην Εικόνα 5.22. Το φαινόμενο αυτό δεν μπορεί να προβλεφθεί από το BEMT, πράγμα που οδηγεί στην απότομη αύξηση της διαφοράς στη γωνία πρόσπτωσης, συνεπώς και στη ροπή πτερύγισης σε αυτή την αζιμουθιακή περιοχή (βλέπε Εικόνα 5.19α). Τα δύο αυτά φαινόμενα (i. μικρότερο κατώρευμα στο άνω τμήμα του δρομέα και ii. επιτάχυνση της ροής στο κάτω τμήμα του δρομέα) δεν μπορούν να περιγραφούν από το BEMT, αλλά προβλέπονται με επιτυχία από το AL, και εξηγούν τη διαφορά τόσο στη μέση τιμή, όσο και στο πλάτος της ροπής πτερύγισης που προβλέπουν τα δύο μοντέλα.

(a) *Μέση αζιμουθιακή μεταβολή.*

(b) *Ανάλυση Fourier και κατανομή στο πεδίο των συχνοτήτων.*

Figure 5.19. *Ροπή πτερύγισης στης ρίζα των πτερυγίων για ροή εντός του οριακού στρώματος του εδάφους με ταχύτητα ανέμου στα 16 m/s στο ύψος του άξονα. Μέση αζιμουθιακή μεταβολή (a) και κατανομή στο πεδίο των συχνοτήτων (b). Σύγκριση μεταξύ διαφορετικών αεροδυναμικών μοντέλων (Γραμμή Δράσης (AL), Δίσκος Ορμής και Στοιχεία Πτερύγωσης (BEMT)), συνδεδεμένων με τον ίδιο ελαστο-δυναμικό επιλύτη (GAST). Το BEMT υποεκτιμά τη μέση τιμή κατα 26% και υπερεκτιμά το 1P πλάτος κατά 35%. Αυτό αντικατοπτρίζεται και στη διαφορά στο φάσμα της ροπής στη συχνότητα περιστροφής (0.16Hz). Οι διαφορές αυτές οφείλονται στη λεπτομερή περιγραφή του πεδίου ροής στο CFD περιβάλον. Σαν αποτέλεσμα, η επίδραση του δρομέα και του εδάφους στο ανάντι πεδίο προβλέπονται με επιτυχία από το AL, κάτι το οποίο δεν λαμβάνεται καθόλου υπ΄ όψιν από το BEMT.*
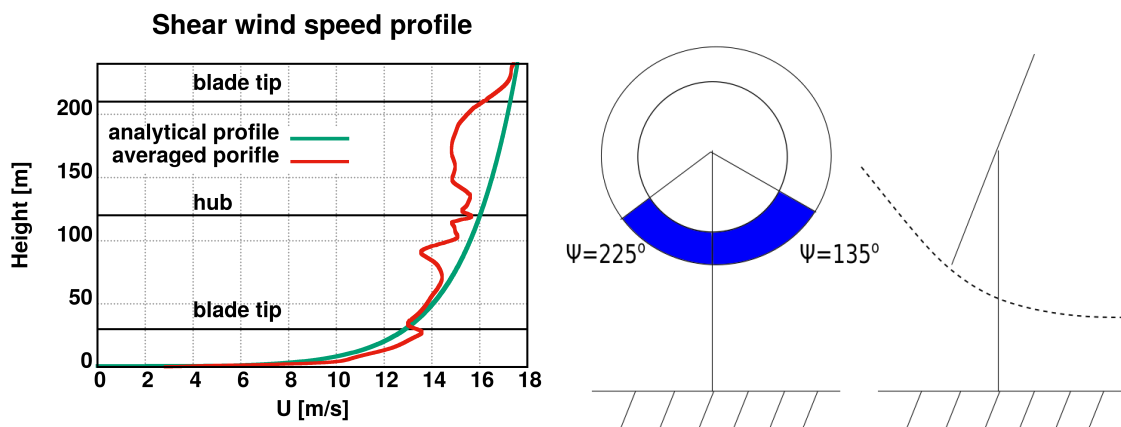

(a) *Υψομετρική κατανομή της μέσης αξονικής ταχύτητας που προβλέπει το AL (κόκκινη γραμή). Σύγκριση με το αναλυτικό προφίλ (πράσινη γραμμή), που αντιστοιχεί στο μέσο αδιατάραχτο προφίλ απουσία ΑΓ.*

(b) *Σχηματική αναπαράσταση ΑΓ και εδάφους. Η γεωμετρία ακροφυσίου που σχηματίζεται μεταξύ δρομέα και εδάφους έχει σαν αποτέλεσμα την επιτάχυνση της ροής στο κάτω τμήμα του δρομέα.*

Figure 5.20. *Υψομετρική κατανομή της μέσης αξονικής ταχύτητας (a) και σχηματική αναπαράσταση ΑΓ και εδάφους (b). Λόγω της επιβράδυνσης που επιφέρει η ΑΓ στη ροή, η αξονική ταχύτητα που προβλέπει η μέθοδος το AL (κόκκινη γραμμή) θα έπρεπε να έχει πιο χαμηλές τιμές από το μέσο αναλυτικό προφίλ (πράσινη γραμμή) που αντιστοιχεί στην κατανομή της μέσης αξονικής ταχύτητας απουσία ΑΓ. Αυτό ισχύει πάνω από τα 70m και μέχρι το άνω άκρο του δρομέα. Η επιτάχυνση που παρατηρείται στο κάτω μέρος του δρομέα (0 − 70m) οφείλεται στην γεωμετρία ακροφυσίου που σχηματίζεται μεταξύ του εδάφους και του κάτω μέρους του δρομέα.*
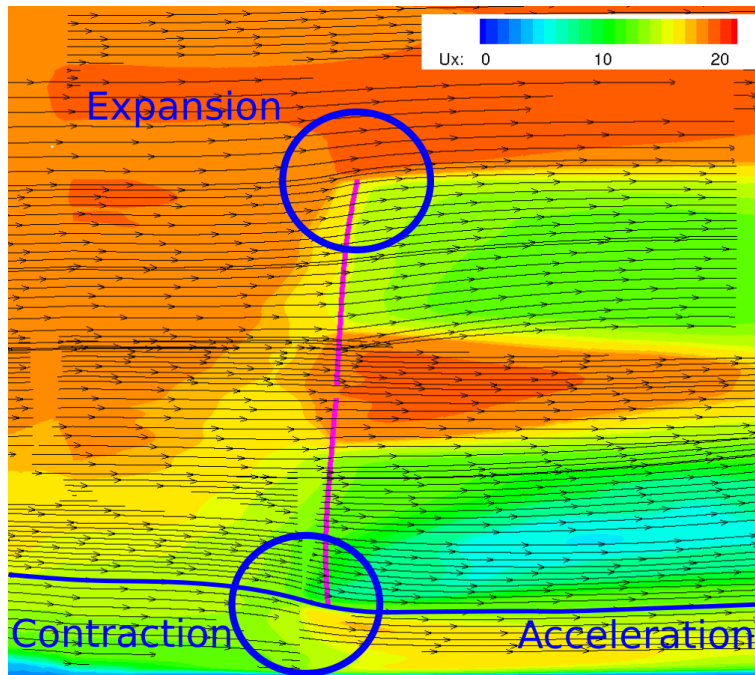
Figure 5.21. *Μέσο πεδίο αξονικής ταχύτητας κοντά στο επίπεδο του δρομέα. Η ταχύτητα στο ύψος της πλήμνης είναι* 16 m/s. *Η επίδραση του δρομέα και του εδάφους στη ροή περιγράφεται με ακρίβεια από τη λύση του CFD πεδίου. Στο πάνω μέρος του δρομέα παρουσιάζεται διαστολή της ροής, ενώ η συστολή της ανάμεσα στο έδαφος και στο κάτω μέρος του δρομέα οδηγεί σε επιτάχυνση της αξονικής ταχύτητας.*
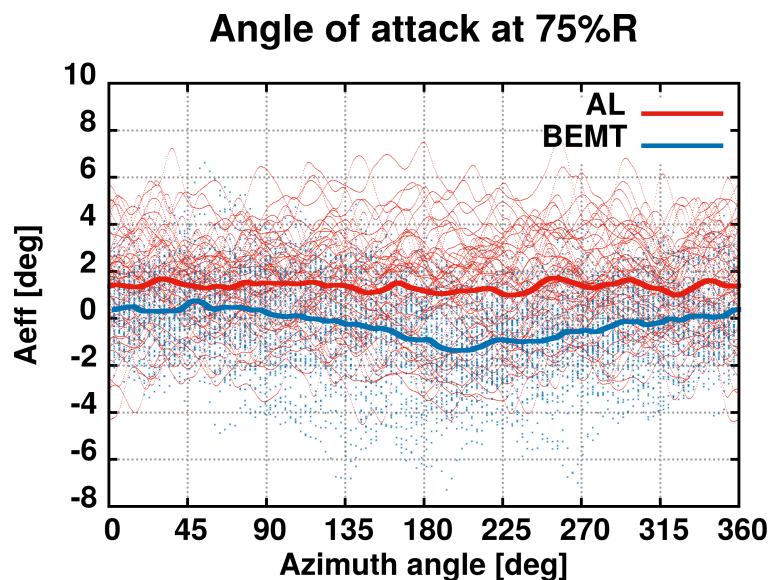
Figure 5.22. *Μέση αζιμουθιακή μεταβολή της γωνίας πρόσπτωσης στο* 75% *των πτερυγίων. Το BEMT υποεκτιμά τη μέση τιμή κατά* $\simeq 2°$ *και υπερεκτιμά το πλάτος της* 1P *μεταβολής. Ακόμη, προβλέπει την ελάχιστη τιμή της γωνίας πρόσπτωσης μεταξύ* 135° *και* 225°, *σε αντίθεση με τη μέθοδο το AL που υπολογίζει ένα σταθερό πλατό σε αυτήν την περιοχή. Αυτό οφείλεται στην γεωμετρία ακροφυσίου που σχηματίζεται μεταξύ του εδάφους και του κάτω μέρους του δρομέα και οδηγεί στην τοπική επιτάχυνση της αξονικής ταχύτητας, σταματώντας την περαιτέρω μείωση της γωνίας πρόσπτωσης στις γωνίες αζιμουθίου μεταξύ* 135° *και* 225°.

C.2 *Τα αποτελεσματα του αεροελαστικου εργαλεου* GAST–HoPFlow

Σ' αυτήν την υποενότητα, ο αεροελαστικός κώδικας GAST–HoPFlow χρησιμοποιείται για την αεροδυναμική ανάλυση του μοντέλου δρομέα ΑΓ που μελετήθηκε στο πείραμα New MEXICO [11] και για την αεροελαστική ανάλυση του μοντέλου του δρομέα ελικοπτέρου που χρησιμοποιήθηκε στο πείραμα HARTII [13]. Και στις δύο αυτές περιπτώσεις μοντελοποιείται η πραγματική γεωμετρία των πτερυγίων. Τα αποτελέσματα που παράγονται συγκρίνονται με πειραματικές μετρήσεις και υπολογιστικές προβλέψεις από άλλα αεροδυναμικά και αεροελαστικά εργαλεία που χρησιμοποιούν CFD κώδικες για την αεροδυναμική ανάλυση. Στόχος είναι η επιβεβαίωση της ορθής λειτουργίας του νέου αεροελαστικού κώδικα GAST–HoPFlow, αλλά και η ανάδειξη των πλεονεκτημάτων του υβριδικού CFD αεροδυναμικού κώδικα HoPFlow σε σχέση με τον συμβατικό Eulerian CFD επιλύτη MaPFlow.

C.2.1 *Αεροδυναμικη αναλυση δρομεα ΑΓ*

Πρώτα εξετάζεται η περίπτωση της αεροδυναμικής λειτουργίας του μοντέλου δρομέα ΑΓ που χρησιμοποιήθηκε στο πείραμα New MEXICO [11], τα γεωμετρικά χαρακτηριστικά του οποίου φαίνονται στους Πίνακες 4.1 και 4.2. Εδώ εξετάζεται η περίπτωση της αξονικής ροής σε ταχύτητα 14.7 m/s. Η γωνιακή ταχύτητα του δρομέα είναι 425 rpm, που αντιστοιχεί σε λόγο ταχύτητας ακροπτερυγίου λ = 6.81. Η γωνία βήματος των πτερυγίων είναι 2.3°.

Στην Εικόνα 5.23 φαίνεται η κατανομή της πίεσης σε διάφορες ακτινικές θέσεις κατά το εκπέτασμα των πτερυγίων. Οι πειραματικές μετρήσεις συγκρίνονται με τις προβλέψεις από διάφορους CFD αεροδυναμικούς κώδικες (EllipSys3D – ασυμπίεστος επιλύτης, CENER CFD – συμπιεστός επιλύτης, MaPFlow – συμπιεστός επιλύτης, HoPFlow – συμπιεστός υβριδικός Lagrangian–Eulerian επιλύτης). Πολύ καλή είναι η συμφωνία που παρατηρείται μεταξύ προβλέψεων και μετρήσεων τόσο κοντά στη ρίζα (25%R και 35%R), όσο και κοντά στο άκρο (82%R και 92%R) των πτερυγίων. Μια μικρή διαφορά στην πίεση που υπολογίζει ο ασυμπίεστος επιλύτης EllipSys3D στην πλευρά υποπίεσης στο 92%R οφείλεται στον σχετικά υψηλό τοπικό αριθμό Mach ($M_{92\%R}$ = 0.27). Η πιο σημαντική διαφορά εντοπίζεται κοντά στο κέντρο των πτερυγίων (60%R), όπου η πίεση που μετρήθηκε στην πλευρά υποπίεσης είναι πιο μεγάλη σε σχέση με αυτήν που προβλέπουν τα υπολογιστικά μοντέλα, τα οποία συμφωνούν πολύ καλά μεταξύ τους. Η διαφορά αυτή μεταξύ μετρήσεων και υπολογιστικών προβλέψεων συνδέεται με την απότομη αλλαγή αεροτομής στη συγκεκριμένη περιοχή (βλέπε Πίνακα 4.1) και στο γεγονός ότι η RISØ A1-21 που χρησιμοποιήθηκε στο μέσο των πτερυγίων έχει πολύ μεγάλη διαφορά στη γωνία μηδενικής άνωσης σε σχέση με τις άλλες δύο αεροτομές που χρησιμοποιήθηκαν στη ρίζα και στο άκρο. Η επίδραση που έχει αυτή η διαφορά μεταξύ των γειτονικών αεροτομών στα αεροδυναμικά φορτία φαίνεται να προβλέπεται με επιτυχία από όλα τα υπολογιστικά μοντέλα, αλλά να μην αποτυπώνεται στις μετρήσεις. Ο ισχυρισμός αυτός επιβεβαιώνεται και από τη σύγκριση της πειραματικής καμπύλης $C_L - a$ της συγκεκριμένης αεροτομής που μετρήθηκε στο 3Δ πτερύγιο και σε μία 2Δ αεροτομή (βλέπε Εικόνα 5.24). Μάλιστα, σημειώνεται μία σημαντική απόκλιση $\Delta C_L \simeq 0.33$ στη γεωμετρική γωνία λειτουργίας της αεροτομής. Οι λόγοι γι' αυτή τη διαφορά διερευνήθηκαν, αλλά χωρίς επιτυχία κατά τη διάρκεια διεξαγωγής του πειράματος New MEXICO.
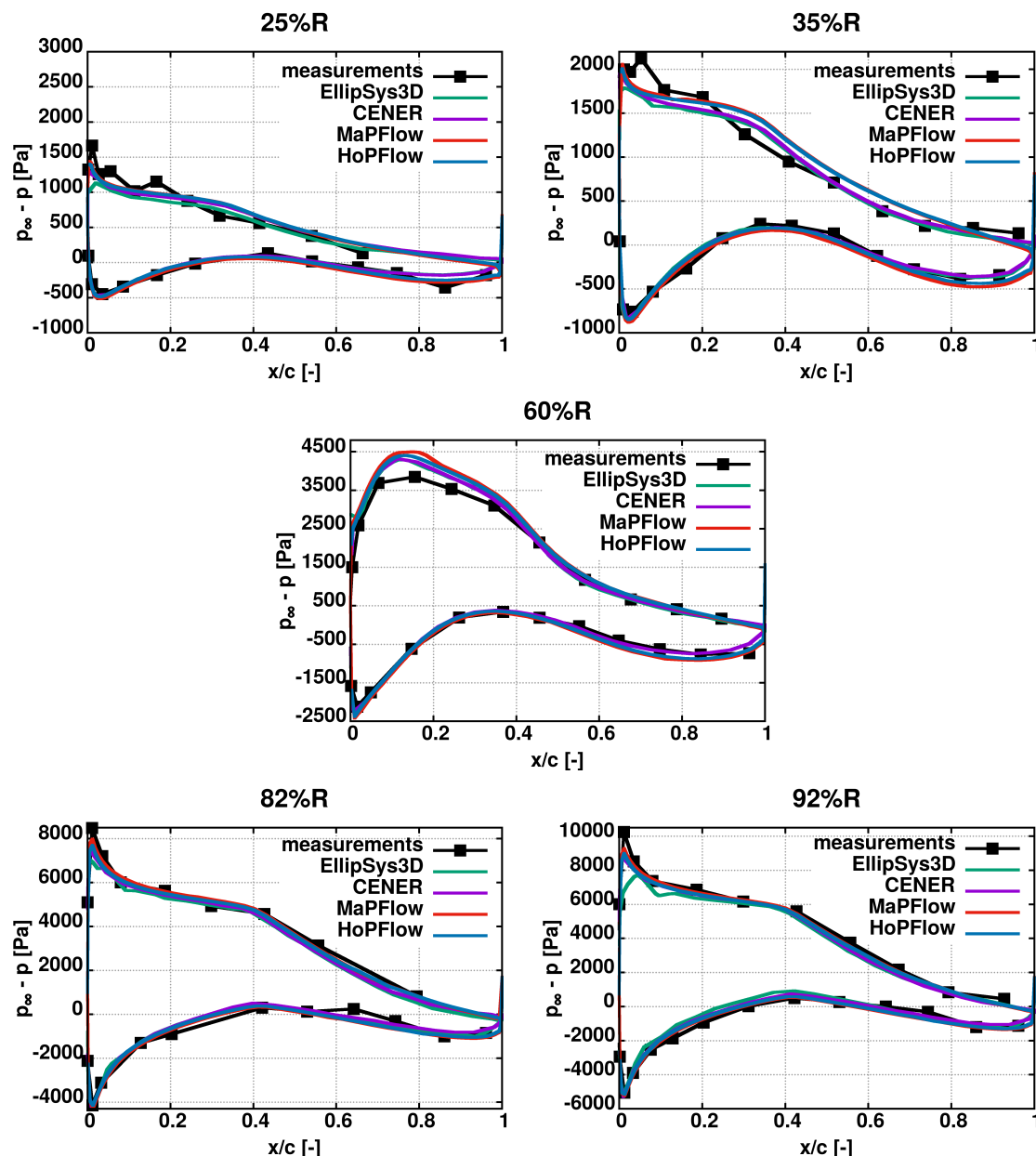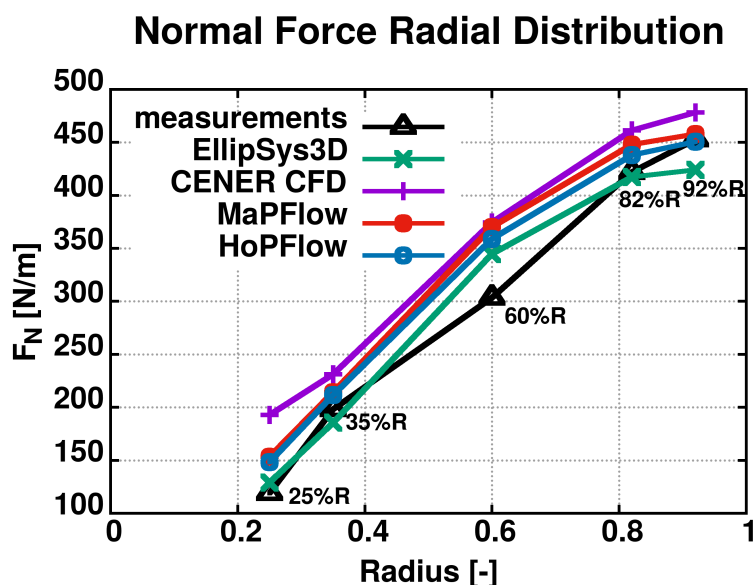
Figure 5.23. *Κατανομή πιέσεων σε διάφορες ακτινικές θέσεις. Σύγκριση μεταξύ υπολογιστικών προβλέψεων από διάφορους CFD κώδικες (EllipSys3D - ασυμπίεστος επιλύτης, CENER CFD - συμπιεστός επιλύτης, MaPFlow - συμπιεστός επιλύτης, HoPFlow - συμπιεστός υβριδικός Lagrangian-Eulerian επιλύτης) και πειραματικές μετρήσεις. Πολύ καλή συμφωνία παρατηρείται μεταξύ των υπολογιστικών προβλέψεων και των μετρήσεων κοντά στη ρίζα (25%R, 35%R) και στο άκρο του πτερυγίου (82%R, 92%R). Η διαφορετική πίεση στην πλευρά υποπίεσης που προβλέπει ο ασυμπίεστος επιλύτης EllipSys3D στο 92%R οφείλεται στον σχετικά υψηλό τοπικό αριθμό Mach ($M_{92\%R}$ = 0.27). Η πιο σημαντική διαφορά παρατηρείται στο 60%R, όπου η πίεση που μετρήθηκε στην πλευρά υποπίεσης είναι πιο υψηλή σε σχέση με τις προβλέψεις όλων των υπολογιστικών μοντέλων, τα οποία ωστόσο συμφωνούν πολύ καλά μεταξύ τους.*
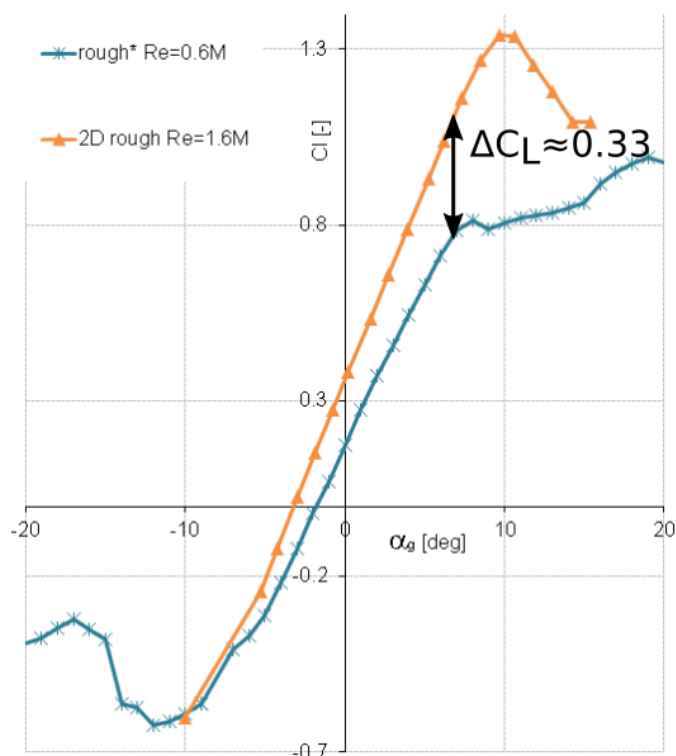
Figure 5.24. *Πειραματική καμπύλη $C_L - a$ για την αεροτομή RISØ A1-21 που χρησιμοποιήθηκε στο 60%R των πτερυγίων του δρομέα ΑΓ που μελετήθηκε στο πείραμα New MEX-ICO. Σύγκριση μεταξύ 2Δ και 3Δ μετρήσεων. Παρατηρείται μία σημαντική απόκλιση η οποία δεν μπορεί να αιτιολογηθεί πλήρως από τα 3Δ τοπικά φαινόμενα της ροής και από τη διαφορά στον αριθμό Reynolds. Η εικόνα δημοσιεύτηκε πρώτη φορά στο [11].*

Στην Εικόνα 5.25 φαίνεται η ακτινική κατανομή του κάθετου αεροδυναμικού φορτίου, όπου παρατηρείται μία καλή σύγκριση μεταξύ μετρήσεων και υπολογιστικών προβλέψεων. Αξίζει να σημειωθεί, ότι οι πειραματικές τιμές των αεροδυναμικών φορτίων προκύπτουν από ολοκλήρωση των πιέσεων που μετρήθηκαν στις αντίστοιχες θέσεις (βλέπε Εικόνα 5.23). Λόγω του μικρού αριθμού αισθητήρων πίεσης γύρω από τις αεροτομές και της θεώρησης γραμμικής κατανομής της πίεσης μεταξύ διαδοχικών αισθητήρων, οι πειραματικές εκτιμήσεις των φορτίων δεν είναι ιδιαίτερα ακριβείς, πράγμα το οποίο δικαιολογεί σε κάποιο βαθμό τις μικρές διαφορές που προκύπτουν στα φορτία ορισμένων ακτινικών θέσεων. Η πιο σημαντική διαφορά εντοπίζεται στο μέσο του πτερυγίου (60%R), όπου ο Eulerian επιλύτης MaPFlow και ο υβριδικός Lagrangian–Eulerian επιλύτης HoPFlow προβλέπουν $\simeq 22\%$ και $\simeq 18\%$ αντίστοιχα μεγαλύτερο φορτίο από την πειραματική εκτίμηση. Η διαφορά αυτή οφείλεται στη αντίστοιχη διαφορά πίεσης στην πλευρά υποπίεσης που αναλύθηκε παραπάνω. Από την άλλη μεριά, πολύ καλή είναι η συμφωνία των φορτίων κοντά στη ρίζα (25% και 35%) και στο άκρο (82% και 92%) των πτερυγίων. Μάλιστα, οι προβλέψεις του υβριδικού επιλύτη HoPFlow στο ακροπτερύγιο είναι ελαφρώς πιο κοντά στις πειραματικές μετρήσεις από αυτές του Eulerian επιλύτη MaPFlow. Ο λόγος έγκειται στο γεγονός ότι το HoPFlow επιλύει την υλική μορφή των εξισώσεων της ροής μακριά από τα σώματα (στην περιοχή του ομόρρου). Η μειωμένη αριθμητική διάχυση που χαρακτηρίζει την υλική περιγραφή των εξισώσεων, έχει σαν αποτέλεσμα την καλύτερη διατήρηση των δομών στροβιλότητας του ομόρρου και

συνεπώς τον πιο ακριβή υπολογισμό της επαγώμενης ταχύτητας των ακροστροβίλων. Τα φορτία στην περιοχή του ακροπτερυγίου είναι και αυτά που επηρεάζονται πιο έντονα από το κατώρευμα του ομόρρου και στα οποία φαίνονται πιο καθαρά τέτοιες διαφορές. Αντίθετα, η Eulerian περιγραφή της ροής που ακολουθεί το MaPFlow χαρακτηρίζεται από αυξημένη αριθμητική διάχυση στην περιοχή του ομόρρου, που οφείλεται στην αραίωση του υπολογιστικού πλέγματος μακριά από τα πτερύγια. Συνεπώς, οι δομές στροβιλότητας του ομόρρου διαλύονται γρήγορα όσο προχωρούν κατάντι, με αποτέλεσμα την υποεκτίμηση της επαγώμενης ταχύτητάς τους και την υπερεκτίμηση των αεροδυναμικών φορτίων του δρομέα. Αυτό έχει σαν αποτέλεσμα και την εσφαλμένη εκτίμηση του ελλείματος ταχύτητας που διαμορφώνεται κατάντι. Ο ισχυρισμός αυτός επιβεβαιώνεται από την Εικόνα 5.26, όπου παρουσιάζεται η κατανομή της αξονικής ταχύτητας για μία σταθερή ακτινική θέση στα 1.8 m (80%R). Αν και οι πειραματικές μετρήσεις και οι προβλέψεις του MaPFlow και του HoPFlow συμφωνούν πολύ καλά μεταξύ τους στην ανάντι περιοχή, το MaPFlow υπολογίζει μεγαλύτερες τιμές και διαφορετική κλίση ταχύτητας κατάντι. Αντίθετα, ο υβριδικός επιλύτης συμφωνεί πολύ καλά με τις μετρήσεις, επιβεβαιώνοντας έτσι την καλύτερη διαμόρφωση και διατήρηση της δομής του ομόρρου που επιτυγχάνεται χάρη στην υλική περιγραφή των εξισώσεων της ροής.

Figure 5.25. *Ακτινική κατανομή κάθετης αεροδυναμικής δύναμης. Σύγκριση μεταξύ υπολογιστικών προβλέψεων από διάφορους* CFD *κώδικες (EllipSys3D - ασυμπίεστος επιλύτης, CENER CFD - συμπιεστός επιλύτης, MaPFlow - συμπιεστός επιλύτης, HoPFlow - συμπιεστός υβριδικός Lagrangian-Eulerian επιλύτης) και πειραματικές μετρήσεις. Καλή συμφωνία παρατηρείται στις περισσότερες ακτινικές θέσεις. Στο* 60%R, *όπου υπάρχουν σημαντικές διαφορές μεταξύ των πειραματικών μετρήσεων και των υπολογιστικών προβλέψεων, τα αποτελέσματα των διάφορων υπολογιστικών μοντέλων συμφωνούν πολύ καλά μεταξύ τους. Γενικά, τα φορτία που υπολογίζει ο υβριδικός κώδικας HoPFlow είναι πιο μικρά σε σχέση με τους δύο συμπιεστούς κώδικες MaPFlow και CENER CFD και πιο κοντά στις πειραματικές μετρήσεις. Ο υπολογισμός χαμηλών φορτίων από τον επιλύτη EllipSys3D (σε κάποιες ακτινικές θέσεις τα φορτία που υπολογίζονται είναι πιο χαμηλά ακόμα και σε σχέση με τις πειραματικές μετρήσεις), αποδίδεται στην επίλυση των ασυμπίεστων εξισώσεων Navier-Stokes.*
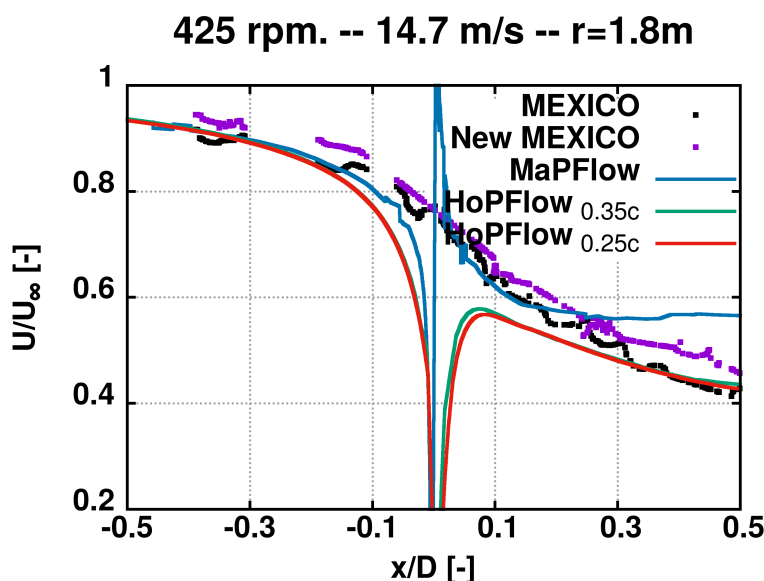
Figure 5.26. *Κατανομή αξονικής ταχύτητας στην κατεύθυνση του άξονα περιστροφής και σε σταθερή ακτινική θέση στο r = 1.8 m. Οι άξονες X και Y έχουν αδιαστατοποιηθεί με τη διάμετρο του δρομέα D = 4.5m και την ταχύτητα της αδιατάραχτης ροής U∞ = 14.7m/s αντίστοιχα. Σύγκριση μεταξύ υπολογιστικών προβλέψεων και πειραματικών μετρήσεων. Καλή συμφωνία παρατηρείται στην περιοχή ανάντι. Ο Eulerian επιλύτης MaPFlow προβλέπει πιο υψηλές τιμές στην κατάντι περιοχή (περιοχή ομόρρου) που αποδίδεται στην αυξημένη αριθμητική διάχυση της συγκεκριμένης μεθοδολογίας. Αντίθετα, τόσο οι τιμές, όσο και η κλίση της κατανομής που προβλέπει ο υβριδικός επιλύτης HoPFlow είναι σε καλή συμφωνία με τις πειραματικές μετρήσεις. Αυτό αποδίδεται στη μειωμένη αριθμητική διάχυση που παρουσιάζει η επίλυση των εξισώσεων της ροής στην υλική τους μορφή και έχει σαν αποτέλεσμα την καλύτερη διατήρηση των δομών στροβιλότητας του ομόρρου και συνεπώς την πιο ακριβή πρόβλεψη του ελλείματος ταχύτητας που διαμορφώνεται κατάντι.*

C.2.2 **Αεροελαστικη αναλυση δρομεα ελικοπτερου**

Στη συνέχεια, εξετάζεται η αεροελαστική λειτουργία του μοντέλου του δρομέα ελικοπτέρου που χρησιμοποιήθηκε στο πείραμα HARTII [13]. Εξετάζεται η Base–Line περίπτωση που αποτελεί πτήση καθόδου στα 33 m/s. Οι συνθήκες λειτουργίας αναφέρονται αναλυτικά στον Πίνακα 4.10. Τα αποτελέσματα του αεροελαστικού κώδικα GAST–HoPFlow συγκρίνονται με πειραματικές μετρήσεις και προβλέψεις από άλλα αεροελαστικά εργαλεία που χρησιμοποιούν μοντέλα δοκού για την ελαστική ανάλυση και CFD επιλύτες για την αεροδυναμική ανάλυση.

Στην Εικόνα 5.27 παρουσιάζεται η αζιμουθιακή μεταβολή του κάθετου ανηγμένου αεροδυναμικού φορτίου στο 87%R, όπου πραγματοποιείται σύγκριση μεταξύ μετρήσεων και υπολογιστικών προβλέψεων από διάφορα ερευνητικά κέντρα και πανεπιστήμια. Λόγω των σημαντικών διαφορών που παρατηρούνται σε αυτές (βλέπε Πίνακα 4.20), οι μέσες τιμές έχουν αφαιρεθεί και εξετάζεται μόνο η αζιμουθιακή μεταβολή γύρω από αυτές. Σε γενικές γραμμές, τα αποτελέσματα του GAST–HoPFlow (NTUA), συγκρίνονται καλά με τις μετρήσεις και τις υπόλοιπες προβλέψεις. Παρατηρείται μία μικρή υποεκτίμηση των φορτίων στο 1ο τεταρτημόριο και αδυναμία πρόβλεψης της έντασης με την οποία αλληλεπιδρούν οι δομές στροβιλότητας του ομόρρου με τα πτερύγια. Αντίστοιχη συμπεριφορά ωστόσο παρουσιάζουν

και οι προβλέψεις από άλλους κώδικες, η οποία δικαιολογείται από την εσφαλμένη θέση στην οποία βρίσκονται οι ακροστρόβιλοι που απελευθερώνονται από τα προπορευόμενα πτερύγια. Στην Εικόνα 5.28a φαίνεται πως οι θέσεις των ακροστροβίλων που προβλέπονται από το ΕΜΠ στο πρώτο τεταρτημόριο ($x/R \geq 0$), είναι περίπου $5\%R$ πιο χαμηλά από τις θέσεις που μετρήθηκαν στο πείραμα, ενώ καλύτερη είναι η συμφωνία στο 2ο τεταρτημόριο ($x/R \leq 0$). Αυτός είναι και ο λόγος για τον οποίον το μέγεθος του κάθετου αεροδυναμικού φορτίου υπολογίζεται σωστά μεταξύ 90° και 180°. Εκεί σημειώνεται μία διαφορά φάσης $\simeq 20°$ σε σχέση με τις μετρήσεις, η οποία ωστόσο είναι κοινή για τις περισσότερες υπολογιστικές προβλέψεις, που συμφωνούν πολύ καλά μεταξύ τους. Πολύ καλή είναι η πρόβλεψη των φορτίων στο 3ο και στο 4ο τεταρτημόριο, όπου μάλιστα περιγράφεται με ακρίβεια από το GAST–HoPFlow και η έντονη αλληλεπίδραση του ομόρρου με τα πτερύγια. Αυτό επιβεβαιώνεται και από την καλή θέση στην οποία υπολογίζονται οι ακροστρόβιλοι στην πλευρά υποχώρησης του δρομέα, όπως φαίνεται στην Εικόνα 5.28β.
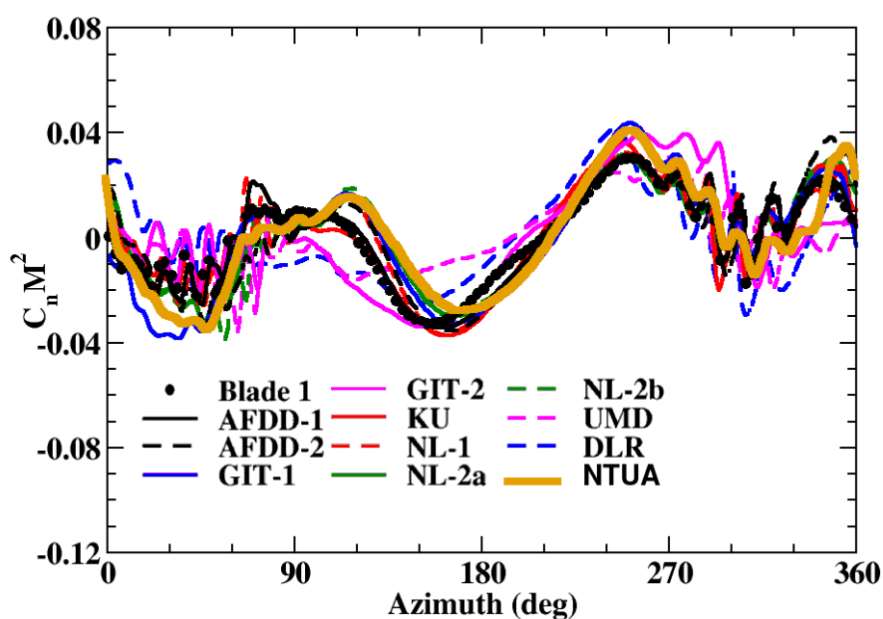
Figure 5.27. *Αδιάστατος συντελεστής κάθετου αξονικού αεροδυναμικού φορτίου στο $87\%R$. Σύγκριση μεταξύ πειραματικών μετρήσεων και προβλέψεων από beam–CFD αεροελαστικά μοντέλα. Οι μέσες τιμές έχουν αφαιρεθεί. Οι προβλέψεις του ΕΜΠ υποεκτιμούν τη δύναμη στο 1ο τεταρτημόριο σε σύγκριση με τις μετρήσεις· βρίσκονται, ωστόσο, εντός του εύρους των προβλέψεων των υπόλοιπων υπολογισμών. Ακόμη, δεν προβλέπεται έντονη διακύμανση του φορτίου λόγω αλληλεπίδρασης των πτερυγίων με τον ομόρρου, όπως φαίνεται στις μετρήσεις. Καλύτερη είναι η συμφωνία με τις μετρήσεις στο 2ο και 3ο τεταρτημόριο, όπου οι τιμές του φορτίου που προβλέπονται είναι στο σωστό εύρος, αλλά με μία υστέρηση περίπου $20°$. Αυτή η διαφορά φάσης με τις μετρήσεις υπάρχει στις προβλέψεις σχεδόν όλων των υπολογιστικών μοντέλων, τα οποία συμφωνούν πολύ καλά μεταξύ τους. Οι διακυμάνσεις του φορτίου στο 4ο τεταρτημόριο, λόγω αλληλεπίδρασης των πτερυγίων με τον ομόρρου, προβλέπονται επιτυχώς από το μοντέλο του ΕΜΠ, αλλά είναι ελαφρώς ασθενέστερες σε σχέση με τις μετρήσεις. Το τοπικό μέγιστο κοντά στις $345°$ υπερεκτιμάται και παρουσιάζει μία ελαφρά υστέρηση κοντά στις $10°$ σε σχέση με τις μετρήσεις και τις υπόλοιπες υπολογιστικές προβλέψεις.*
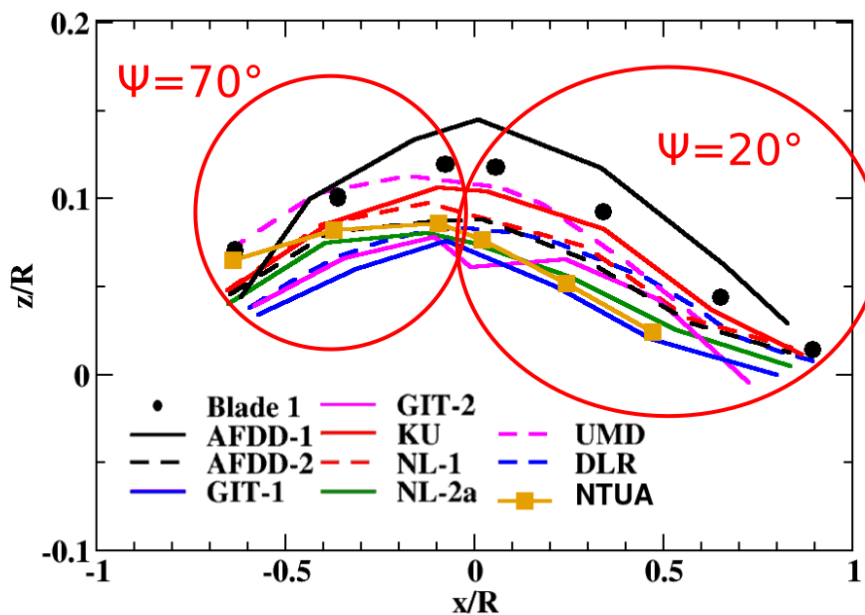
(a) *Πλευρά προχώρησης. Οι περισσότεροι από τους στροβίλους που εντοπίζονται στο 1ο τεταρτημόριο (x/R ≥ 0), όπου αναμένεται έντονη αλληλεπίδραση των πτερυγίων με τον ομόρρου, προβλέπονται σε λάθος θέσεις από το μοντέλο του ΕΜΠ, περίπου 5%R πιο χαμηλά από τις θέσεις που μετρήθηκαν στο πείραμα. Καλύτερη ωστόσο είναι η συμφωνία στο 2ο τεταρτημόριο (x/R ≤ 0).*
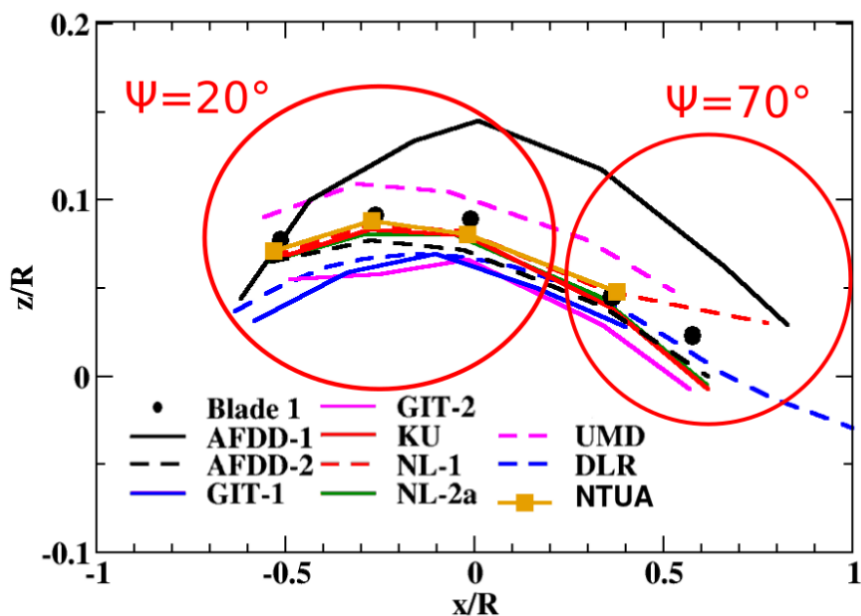

(b) *Πλευρά υποχώρησης. Οι θέσεις των περισσότερων ακροστροβίλων προβλέπονται με ακρίβεια από το μοντέλο του ΕΜΠ. Ο 5ος στρόβιλος, ωστόσο, δεν φαίνεται να βρίσκεται εντός των ορίων που παρουσιά-ζονται στην εικόνα.*

Figure 5.28. *Θέσεις των ακροστροβίλων στην πλευρά προχώρησης (y = 0.7R) (a) και υπο-χώρησης (y = −0.7R) (b), όταν το 1ο πτερύγιο βρίσκεται σε αζιμουθιακή γωνία 20° και 70°. Οι συντεταγμένες των στροβίλων εκφράζονται στο τοπικό σύστημα του δρομέα. Σύγκριση μεταξύ πειραματικών μετρήσεων και προβλέψεων από beam-CFD αεροελαστικά μοντέλα.*

Στην Εικόνα 5.29 φαίνεται η αζιμουθιακή μεταβολή της ροπής στην κατεύθυνση της πτερύγισης και της περιστροφής, όπως μετρήθηκε και υπολογίστηκε στο 17%R. Και σε αυτήν την περίπτωση, οι μέσες τιμές έχουν αφαιρεθεί και εξετάζεται η διακύμανση των φορτίων γύρω από αυτές. Στη ροπή πτερύγισης (Εικόνα 5.29α) παρατηρούνται σημαντικές διαφορές ως προς το πλάτος και τη φάση μεταξύ των μετρήσεων και των επιμέρους υπολογισμών. Ο λόγος είναι οι πολύ μικρές τιμές των ροπών στο μη στρεφόμενο σύστημα του δρομέα (βλέπε Πίνακα 4.10) που οδηγεί στην ελαχιστοποίηση του πλάτους της ροπής πτερύγισης. Αυτό έχει σαν αποτέλεσμα η ροπή που υπολογίζεται να καθίσταται ιδιαίτερα ευαίσθητη στις μικρο–διαφορές μεταξύ των μοντέλων (πειραματικών και υπολογιστικών). Παρ' όλα αυτά, η 2/rev διακύμανση που φαίνεται στις μετρήσεις, προβλέπεται με επιτυχία από το GAST–HoPFlow, αλλά ελαφρώς πιο έντονη σε σχέση με αυτές. Από την άλλη μεριά, πολύ καλή είναι η συμφωνία που παρατηρείται στη ροπή στην κατεύθυνση της περιστροφής (Εικόνα 5.29β). Η φάσης της κυρίαρχης 1/rev διακύμανσης προβλέπεται σωστά από το μοντέλο του ΕΜΠ, ενώ παρατηρείται μία ελαφρά υπερεκτίμηση του αντίστοιχου πλάτους, η οποία οφείλεται στην πρόβλεψη μεγαλύτερης τιμής για τη μέγιστη φόρτιση μεταξύ $90° − 270°$. Η συμπεριφορά αυτή είναι κοινή για τα περισσότερα υπολογιστικά μοντέλα. Αξίζει ακόμη να σημειωθεί ότι το πλατό που παρατηρείται σε αυτήν την περιοχή προβλέπεται με επιτυχία από το GAST–HoPFlow, αλλά ελαφρώς πιο στενό σε σχέση με τις πειραματικές μετρήσεις, κάτι το οποίο επίσης συνατάται στις περισσότερες υπολογιστικές προβλέψεις.
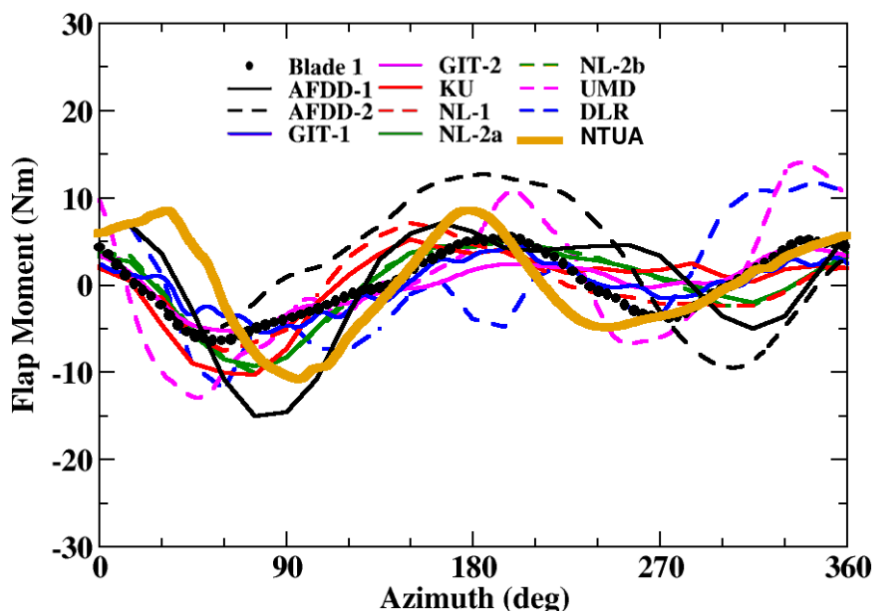
(a) *Ροπή κάμψης στην κατεύθυνση της πτερύγισης. Η 2/rev διακύμανση που φαίνεται στις μετρήσεις, προβλέπεται με επιτυχία από το μοντέλο του ΕΜΠ, αλλά ελαφρώς πιο έντονη. Διαφορές παρατηρούνται στο πλάτος και τη φάση μεταξύ όλων των υπολογιστικών προβλέψεων και των πειραματικών μετρήσεων, οι οποίες οφείλονται στις πολύ μικρές τιμές των ροπών στο μη στρεφόμενο σύστημα του δρομέα (βλέπε Πίνακα 4.10). Σαν αποτέλεσμα, ελαχιστοποιείται το πλάτος της ροπής πτερύγισης και καθίσταται ιδιαίτερα ευαίσθητη στις μικρο–διαφορές μεταξύ των μοντέλων.*
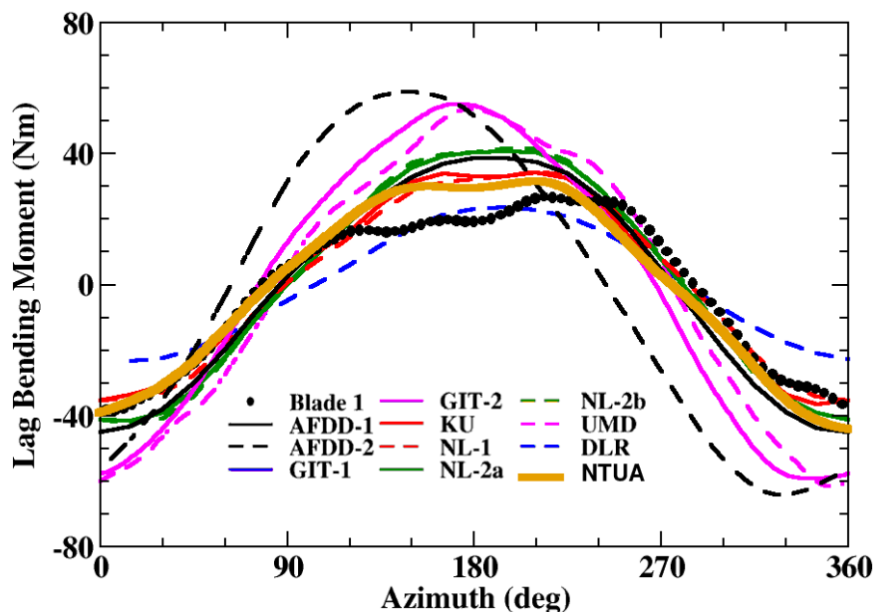
(b) *Ροπή κάμψης στην κατεύθυνση της περιστροφής. Θετική θεωρείται η κατεύθυνση αντίθετα της περιστροφής. Το πλάτος της 1/rev διακύμανσης προβλέπεται από το μοντέλο του ΕΜΠ ελαφρώς πιο μεγάλο σε σχέση με τις μετρήσεις. Αυτό οφείλεται στην πρόβλεψη μεγαλύτερης τιμής για τη μέγιστη φόρτιση μεταξύ 90° − 270°, το οποίο ωστόσο συναντάται στις περισσότερες υπολογιστικές προβλέψεις.*

Figure 5.29. *Ροπή κάμψης στην κατεύθυνση της πτερύγισης (a) και της περιστροφής (b) στο 17%R. Σύγκριση μεταξύ πειραματικών μετρήσεων και προβλέψεων από beam-CFD αεροελαστικά μοντέλα. Οι μέσες τιμές έχουν αφαιρεθεί. Σε γενικές γραμμές παρατηρείται μία καλή συμφωνία των προβλέψεων του ΕΜΠ σε σύγκριση με τις πειραματικές μετρήσεις, ενώ όπου παρατηρούνται διαφορές, τα αποτελέσματα του μοντέλου του ΕΜΠ είναι σε συμφωνία με τα υπόλοιπα υπολογιστικά μοντέλα.*

D   *Συμπεράσματα*

Κύριο στόχο αυτής της διατριβής αποτέλεσε η ανάπτυξη ενός αεροελαστικού εργαλείου υψηλής ακρίβειας για την ανάλυση δρομέων, ικανού να διαχειρίζεται εφαρμογές εντός ενός μεγάλου εύρους αριθμών Mach της υπο–ηχιτκής περιοχής σε ένα ενιαίο υπολογιστικό πλαίσιο.

Το κομμάτι της ελαστο–δυναμικής ανάλυσης το διαχειρίζεται ο GAST, ένας σερβο–αερο–ελαστο–δυναμικός επιλύτης για ΑΓ, ο οποίος αναπτύχθηκε στο Εργαστήριο Αεροδυναμικής του ΕΜΠ στο πλαίσιο προηγούμενων διδακτορικών διατριβών [1, 2] και συνεχίζει να αναπτύσσεται μέχρι και σήμερα. Στον GAST, η ελαστική ανάλυση μιας ΑΓ βασίζεται στη μοντελοποίηση των επιμέρους τμημάτων της σαν δοκούς Timoshenko, οι οποίες διακριτοποιούνται στο χώρο με τη μέθοδο των 1Δ Πεπερασμένων Στοιχείων (FEM). Για τη διεύρυνση του πεδίου εφαρμογής του GAST πέρα από τα όρια των ΑΓ, το κομμάτι της κινηματικής και της δυναμικής ανάλυσης αναμορφώθηκε, κατά τη διάρκεια αυτής της διατριβής, ώστε να ακολουθεί το πλαίσιο της θεωρίας Δυναμικής Πολλαπλών Σωμάτων (Multi–Body Dynamics). Με αυτόν τον τρόπο, τα επιμέρους τμήματα μιας οποιασδήποτε κατασκευής μπορούν να κινούνται στο χώρο ανεξάρτητα το ένα από το άλλο, ενώ η σύνδεσή τους σε μία ενιαία διάταξη υλοποιείται με την ικανοποίηση κατάλληλων μη–γραμμικών κινηματικών και

δυναμικών εξισώσεων σύνδεσης [36]. Συνεπώς, ο GAST είναι πλέον σε θέση να αναλύει την ελαστο–δυναμική συμπεριφορά οποιαδήποτε διάταξης αποτελείται από επιμήκη τμήματα που μπορούν με ακρίβεια να μοντελοποιηθούν σαν δοκοί.

Για το αεροδυναμικό πρόβλημα, η υψηλή ακρίβεια και η δυνατότητα γενικής εφαρμογής επιτυγχάνεται με την υιοθέτηση μεθόδων CFD. Γι' αυτό το λόγο, η αεροδυναμική ανάλυση του νέου αυτού εργαλείου βασίστηκε στο MaPFlow και το HoPFlow [4], έναν κλασσικό Eulerian CFD επιλύτη και έναν υβριδικό Lagrangian–Eulerian επιλύτη που αναπτύχθηκαν επίσης στο Εργαστήριο Αεροδυναμικής του ΕΜΠ κατά τη διάρκεια μιας προηγούμενων διατριβών [4, 191, 45]. Καθώς και οι δύο αεροδυναμικοί κώδικες επιλύουν τις συμπιεστές εξισώσεις Navier–Stokes, μπορούν να χρησιμοποιηθούν για την ανάλυση ενός μεγάλου εύρους αριθμών ·ατινΜαςη της υπο–ηχητικής περιοχής. Σαν πρώτο βήμα, και για τη δημιουργία μίας οικονομικής επιλογής που μπορεί να χρησιμοποιηθεί ακόμα και κατά τη φάση του σχεδιασμού δρομέων ΑΓ και ελικοπτέρων, ενσωματώθηκε στο MaPFlow και συνδέθηκε με τον GAST ένα μοντέλο Γραμμής Δράσης (AL), όπου τα πτερύγια ενός δρομέα μοντελοποιούνται σαν γραμμές από σημεία ελέγχου κατά τον άξονα των πτερυγίων. Οι γραμμές αυτές έχουν τη δυνατότητα να κινούνται και να παραμορφώνονται ελεύθερα μέσα στο υπολογιστικό πλέγμα. Με αυτόν τον τρόπο γίνονται πιο εύκολες οι εφαρμογές πολλαπλών σωμάτων σε ένα Eulerian CFD περιβάλλον, ενώ παράλληλα περιορίζεται σημαντικά το υπολογιστικό κόστος. Ακόμη, για να μπορεί αυτό το εργαλείο να χρησιμοποιηθεί σε όλες τις φάσεις του σχεδιασμού δρομέων ΑΓ, πρέπει να είναι δυνατή και η αναπαραγωγή των πραγματικών (ατμοσφαιρικών) συνθηκών λειτουργίας μιας ΑΓ. Γι' αυτό το λόγο, αναπτύχθηκε και ενσωματώθηκε στο MaPFlow και η μέθοδος της Ζώνης Παραγωγής (GZ), για την υπέρθεση ενός προφίλ διαταραχών της ταχύτητας λόγω τύρβης σε ένα μέσο CFD πεδίο. Μάλιστα, η μέθοδος GZ έδειξε να παράγει τυρβώδη πεδία που υφίστανται χαμηλότερη αριθμητική διάχυση και διατηρούν πιο αποτελεσματικά τα φασματικά χαρακτηριστικά τους σε σχέση με τις συμβατικές μεθοδολογίες που απαντώνται στη βιβλιογραφία. Το νέο GAST–AL αεροελαστικό μοντέλο εξετάστηκε τόσο σε εφαρμογές ΑΓ όσο και ελικοπτέρων. Σε αντίθεση με τα συνήθη εργαλεία που χρησιμοποιούνται κατά τη φάση του σχεδιασμού δρομέων, παρατηρήθηκε η ικανότητά του να υπολογίζει με ακρίβεια, κάτω από σύνθετες συνθήκες ροής και χωρίς ιδιαίτερα υψηλό υπολογιστικό κόστος τόσο τα φορτία των πτερυγίων, όσο και το πεδίο ροής που διαμορφώνεται κοντά. Μάλιστα, ιδιαίτερα σημαντική κρίνεται η ικανότητα του μοντέλου να προβλέπει με επιτυχία όχι μόνο την επίδραση της τύρβης στο δρομέα και την εξέλιξη του ομόρρου, αλλά και την επίδραση του δρομέα και του εδάφους στο ανάντι τυρβώδες πεδίο.

Για τις περιπτώσεις που απαιτείται η μοντελοποίηση της πραγματικής γεωμετρίας ενός σώματος (π.χ. για την πρόβλεψη της φόρτισης κάτω από συνθήκες που επηρεάζονται άμεσα από τη γεωμετρία του σώματος, όπως τα κύματα κρούσης ή οι έντονα αποκολλημένες ροές), αυτό είναι δυνατό με τη χρήση του υβριδικού Lagrangian–Eulerian CFD επιλύτη HoPFlow. Στην περίπτωση αυτή, η Eulerian διατύπωση των εξισώσεων της ροής επιλύεται από το MaPFlow σε ένα σωματόδετο πλέγμα που περιορίζεται κοντά στο εκάστοτε αεροδυναμικό σώμα, ενώ μακριά από τα σώματα, οι εξισώσεις της ροής διατυπώνονται στη Lagrangian έκφρασή τους και η εξέλιξη της ροής περιγράφεται παρακολουθώντας την κίνηση και την αλλαγή των ροϊκών μεγεθών που χαρακτηρίζουν ορισμένα υλικά σωματίδια που δρουν σαν

ροϊκοί σημειακοί δείκτες. Ο κώδικας HoPFlow συνδέθηκε με τον GAST στο πλαίσιο αυτής της διατριβής και το νέο αυτό αεροελαστικό εργαλείο εξετάστηκε τόσο σε εφαρμογές ΑΓ όσο και ελικοπτέρων. Και στις δύο περιπτώσεις φάνηκε ότι η ακρίβεια του GAST–HoPFlow στην πρόλεξη των φορτίων του δρομέα και στη διαμόρφωση του ομόρρου είναι τουλάχιστον παρόμοια με αυτή των κλασσικών CFD υπολογισμών, πράγμα που πιστοποιεί τόσο τη διαδικασία σύζευξης μεταξύ του Eulerian και του Lagrangian πεδίου, όσο και τη σύνδεση μεταξύ του ελαστο–δυναμικού επιλύτη GAST και του αεροδυναμικού επιλύτη HoPFlow.